DISSERTATION

SYNTHESIS AND CHARACTERIZATION OF BIOLOGICALLY RELEVANT REDOX-ACTIVE MOLECULES

Submitted by

Kateryna Kostenkova

Department of Chemistry

In partial fulfillment of the requirements

For the Degree of Doctor of Philosophy

Colorado State University

Fort Collins, Colorado

Summer 2023

Doctoral Committee:

Advisor: Debbie Crans

Joseph Zadrozny
Robert Paton
Deanna Worley

ABSTRACT

SYNTHESIS AND CHARACTERIZATION OF BIOLOGICALLY RELEVANT REDOX-ACTIVE MOLECULES

Redox chemistry is fundamental to several essential life processes, such as energy metabolism, respiration, and free radical formation. Many redox-active inorganic and organic molecules are promising agents to combat difficult-to-treat diseases, including cancer and tuberculosis. This dissertation covers the syntheses, studies of the fundamental chemical and biological properties of two vastly different classes of redox-active molecules, inorganic and organic molecules. Most of this work has investigated the fundamental development of hydrophilic, hydrophobic and amphiphilic redox-active vanadium complexes for the treatment of different types of cancer. The last chapter of this dissertation describes the studies of the fundamental properties of demethylmenaquinones which are biosynthetic precursors to menaquinones, lipid electron carriers essential for anaerobic bacterial respiration of several types of bacteria, including *Escherichia coli, Actinomadura madurae* and pathogenic *Mycobacterium tuberculosis*. Targeting bacterial electron transport chain disrupts respiration of pathogenic *Mycobacterium tuberculosis*, thus, studying the properties of demethylmenaquinone analogs is of great interest.

Chapter one, an introductory chapter, presents a comprehensive review of the developments in vanadium anticancer therapeutics over the last five years. The structural diversity of the vanadium-containing anticancer compounds, potential applications to various cancer cell lines, and different modes of delivery of highly cytotoxic vanadium species are described in detail. Vanadium gained interest for its anticancer applications after

bis(maltolato)oxovanadium(IV), an antidiabetic complexes studied in Phase II clinical trials, went off patent in September 2011. Previous studies with vanadium antidiabetic complexes, however, provided valuable information to understand the action of novel vanadium anticancer complexes, as cancer and diabetes target the same metabolic pathways.

Chapters two and three describe the syntheses, spectroscopic characterization, and cytotoxic studies of novel vanadium(V) catecholate complexes with pyridine-containing Schiff base ligands. According to previous reports, vanadium(V) Schiff base catecholate complexes are promising agents for glioblastoma treatment, and herein we investigated whether the presence of the pyridine ring on the Schiff base scaffold improves cytotoxicity and hydrolytic stability of the vanadium catecholato complexes. The studies showed that the presence of the pyridine ring improves hydrolytic stability of the V(V) catecholate complexes, yet it decreases their uptake into glioblastoma cells which result in the decrease of cytotoxicity of the complexes. Even though the stability increased and the compounds have enough time to get into cells, the efficacy of these complexes decreased. Chapter three further explores the redox properties and the redox reaction mechanism of vanadium(V) Schiff base catecholate complexes with pyridine-scaffolds and *tert*-butyl substituted catecholate ligands.

Chapter four describes the speciation studies and testing of vanadium(V) dipicolinate that enhance the effects of oncolytic viruses, non-pathogenic viruses that can infect and kill cancer cells. Additionally, the chapter describes ^{1}H and ^{51}V NMR studies carried out in model membrane interfaces. The data show that V(V) dipicolinates hydrolyze under physiological conditions and generate vanadate which ultimately enhances the spread of the oncolytic viruses. V(V) dipicolinates are located on the interface of the aqueous pool and hydrophobic region of model membranes which also contributes to their hydrolysis.

Chapter five describes Pt^{IV} and Mo^{VI} monosubstituted decavanadates, monoplatino(IV)nonavanadate(V) ($[H_2Pt^{IV}V^{V}_{9}O_{28}]^{5-}$, V_9Pt), and monomolybdo(VI)-

nonavanadate(V) ($[Mo^{VI}V^{V}_{9}O_{28}]^{5-}$, V_9Mo), and their ability to initiate signal transduction on the luteinizing hormone receptor (LHR) in CHO cells and their speciation chemistry under the biological experiments. The Pt^{IV} and Mo^{VI} monosubstituted decavanadates are large vanadium-oxo clusters that are structurally similar to decavanadate but have different charges. The results showed that both V_9Mo and V_9Pt affect LHR expression and do not inhibit cell growth which is different than the decavanadate ($[V_{10}O_{28}]^{6-}$, abbreviated V_{10}). Although all the clusters hydrolyze under the assay conditions lifetimes are different, and this was characterized using spectroscopic methods. Using the washing experiments, we were able to show that the V_9Pt and V_9Mo monosubstituted decavanadates do not associate with the cells and, hence, do not negatively affect cell growth, however, they are more effective in initiating signaling.

Chapter six describes initial efforts to study the fundamental properties of two truncated demethylmenaquinones, biosynthetic precursors for menaquinones. The studies are important to understand the fundamental differences between the chemical properties of menaquinones and demethylmenaquines which include 3D conformation and redox potential. Indeed, the development of inhibitors of *MenG, a* methyltransferase enzyme that coverts demethylmenaquines to form menaquinones*,* is a known target for drug development for antitubercular applications. Therefore, we investigated whether non-native demethylmenaquines would convert to menaquinones by the relevant enzymes present in the membrane preparations.

In summary, the first five chapters demonstrate 1) the diversity of applications of vanadium compounds for treatment of different types of cancer and 2) the efforts to develop vanadium-based anticancer therapeutics to treat different types of cancer. The final chapter describes efforts in fundamental studies preparing and characterizing the chemical properties the truncated demethylmenaquinones. In addition, we demonstrated that the membrane preparations of mycobacteria concerted the synthesized truncated demethylmenaquinone-2 and demethylmenaquinone-3 are processed to form menquinone-2 and menaquinone-3.

ACKNOWLEDGEMENTS

First, I would like to acknowledge my mentors from undergraduate and graduate careers for their support and encouragement of my professional goals and dreams. I would like to especially thank my PhD mentor, Prof. Debbie Crans, for her mentorship, encouragement to dream big and accomplish big, support and understanding during my PhD career. I would also like to thank Profs. Kerry Breno (Whitworth University), Michael Sardinia (Whitworth University), Melissa Reynolds (CSU) and Nancy Levinger (CSU) for their mentorship and support over the years. I would also like to thank Profs. Peter Lay (University of Sydney), Dean Crick (CSU) and Deborah Roess (CSU) for mentorship on collaborative research projects.

Second, I would like to thank current and former Crans group members for taking the time to mentor me and work with me on collaborative projects. I would like to give a special thanks to Heide Murakami, Skyler Markham, Andrew Bates, Jordan Koehn, Ben Peters, Cameron Van Cleave, Kaitlin Doucette, Allison Haase. I am thankful to have worked with all of you and have learned how to be a good scientist. I would also like to thank my undergraduate mentees for taking the time to work with me and help move the projects forward.

Finally, I would like to thank my friends and family for being there for me during my PhD journey. I would not have been where I am at today without your love and support! I would like to give special thanks to my parents, Alla Kostenkova and Oleg Kostenkov, my brother, Andrey Kostenkov, and my partner, Avery Turman, for being there with me through everything. I would also like to give a special thanks to my friends including Allie Adachi, Sarah Sanders, Amelia Haas, Kaija Olson, Rose Wipke, Brooke Bauman, Yuka Shimizu, Jeremiah White, Mortaza Derakshani, Tyler Milstein, the Koerper family, the Sokolov family, Tim and Iryna Grayson. Thank you for reminding me about enjoying life outside of graduate school! I am forever grateful to be a part of your lives and to have had fun memories with you!

PREFACE

Before starting graduate school, I was interested in ways to improve global healthcare and patient health. As a freshman at Whitworth University, I pursued a Biochemistry degree on a Pre-Medicine track in hopes to become a family physician. To gain experience in healthcare, I volunteered at a local hospital emergency room and quickly realized that a career in medicine was not for me. When I worked in a medicinal chemistry lab as a sophomore, I discovered my passion for research. I realized I could help patients by developing novel therapeutics to combat difficult-to-treat conditions and replacing current therapies that cause significant damage to patient health. As an undergraduate, I also worked as a Supplemental Instruction Facilitator for General and Organic chemistry for two years. My research and teaching experiences as an undergraduate student motivated me to continue my education at Colorado State University. I was fascinated with both inorganic and organic research which, ultimately, led me to pursuing a PhD in Bioinorganic and Bioorganic Chemistry.

As a bioinorganic and bioorganic chemist, I chose to pursue research projects in two different areas, vanadium chemistry and the chemistry of lipid-like electron carriers. Most of my dissertation research focused on the development of novel vanadium-based anticancer therapeutics. Among first-row transition metals with reported biological properties, vanadium is fascinating due to the variety of transition states, which results in an enormous structural diversity of vanadium complexes. Vanadium has recently gained attention for its anticancer applications, and I have worked on several projects focused on the development of vanadium anticancer complexes during my PhD. I sought the opportunities both at CSU and elsewhere to learn about NMR and EPR spectroscopies, and cyclic voltammetry in order to use these techniques to understand the fundamental chemical properties of the vanadium complexes I developed. I was fortunate to work on many vanadium projects with the collaborators from all over the world, including Australia, Canada, Brazil and Uruguay, and to learn about different areas of vanadium

chemistry from them. My bioorganic research focused on studying the fundamental properties of several lipid electron carriers, such as ubiquinones and demethylmenaquinones. I elucidated the 3D conformation of ubiquinone-2, a small, truncated analog of eukaryotic lipid electron carrier ubiquinone-10, using ^{1}H-^{1}H NOESY and ^{1}H-^{1}H ROESY NMR data. My research contributions helped identify the fundamental chemical properties of demethylmenaquinones, as well as their activity in bacteria.

During my PhD, I also discovered a passion for mentoring. I worked with ten undergraduate students from diverse backgrounds and with a variety of aspirations. Many of my students won highly competitive poster presentation awards and research fellowships at CSU. I also mentored junior PhD students in the Crans lab, helping them to define their research interests and teaching them a variety of techniques. I would like to continue mentoring junior chemistry researchers moving forward.

I look forward to applying my skills and expertise as a Postdoctoral Research Associate at the University of Minnesota College of Pharmacy where I will work on the development of novel antitubercular agents. I am grateful that my PhD experience has set me up for a promising research career in biological and medicinal chemistry.

DEDICATION

To my parents and my brother.

Thank you for your unconditional love and support through everything!

TABLE OF CONTENTS

Chapter 1 Recent Advances of Medicinal Properties of Vanadium Compounds: Cancer and Other Diseases

1.1 Introduction: Vanadium Compounds in Medicine

Vanadium is a non-essential first-row transition metal that has been underexplored for medicinal applications (Crans and Kostenkova, 2020, Van Cleave and Crans, 2019, Pessoa et al., 2015, Sharfalddin et al., 2022, Treviño et al., 2019, Gourdon et al., 2022). Five of the first-row transition - manganese, iron, cobalt, copper, and zinc - are essential to human health (Crans and Kostenkova, 2020). Three of the non-essential first-row transition metals, chromium, vanadium, and nickel, have beneficial biological effects for the treatment of disease. Chromium, vanadium, and nickel complexes have been investigated in clinical trials, and vanadium is the only non-essential element to exhibit both anticancer and antidiabetic properties (Crans and Kostenkova, 2020, Thompson et al., 2009). Vanadium and zinc are the two transition metals with the highest natural abundance in the Earth crust (0.008% and 0.019%) and many biological effects, yet zinc is an essential element but vanadium is not (Rehder, 2012, Crans and Kostenkova, 2020). Therefore, the biological and medicinal properties of vanadium compounds have been extensively reviewed (Crans and Kostenkova, 2020, Van Cleave and Crans, 2019, Pessoa et al., 2015, Scalese et al., 2022b). Vanadium compounds have entered 18 clinical trials as of May 2023 compared to for example 2,260 clinical trials with zinc which has also been extensively reviewed (Drewry and Gunning, 2011, Pellei et al., 2021, Hou et al., 2021). Previous studies with vanadium have investigated antidiabetic properties of vanadium compounds (Crans et al., 2003, Thompson et al., 2009, Thompson and Orvig, 2006, Willsky et al., 2011, Sakurai, 2002). More recently, anticancer properties of vanadium compounds have gained momentum in the bioinorganic chemistry and medicinal communities, mostly over the last five to ten years (Aureliano et al., 2023,

Crans et al., 2018, Crans and Kostenkova, 2020, Scalese et al., 2022b, Aureliano et al., 2021, Treviño et al., 2019, Scior et al., 2016).

A Web of Science search in May 2023 has shown a significant increase of publications of vanadium compounds in medicine over the last two decades (**Figure 1.1**). We have compared

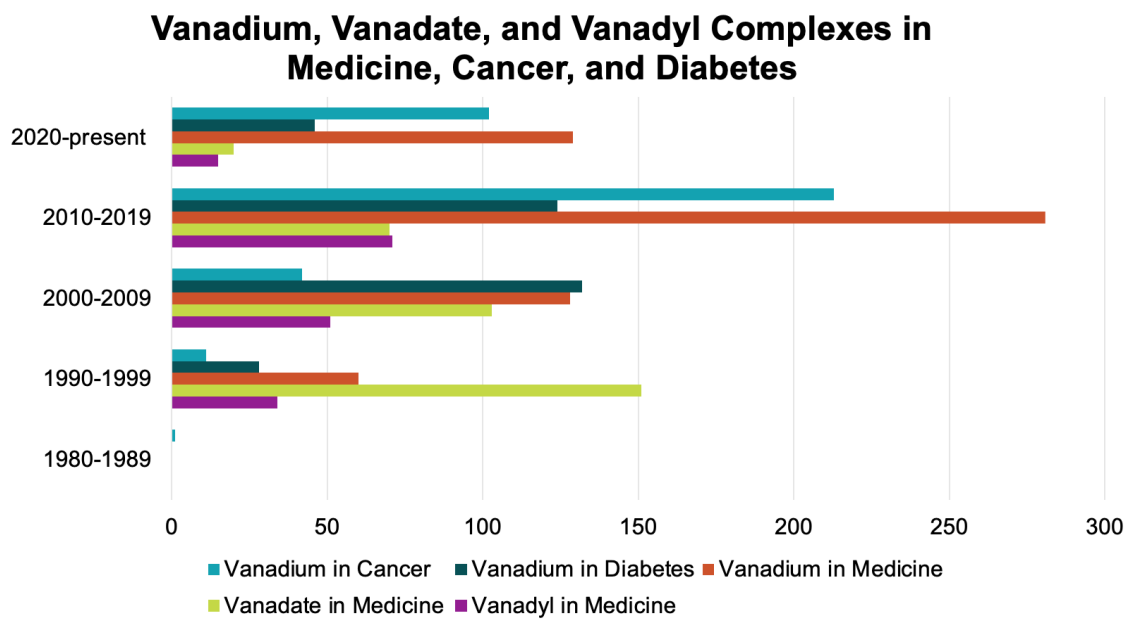

Figure 1.1. Number of reported studies using vanadyl, vanadate, and vanadium complexes in medicine, cancer, and diabetes. Studies were found by searching the phrases "vanadyl complexes in medicine," "vanadate complexes in medicine," and "vanadium complexes in medicine" on Web of Science.

the number publications mentioning vanadium in cancer and vanadium in diabetes. The findings show that both areas are a smaller sub-area within vanadium in medicine, although vanadium has gained attention for its anticancer applications over the last two decades. Reports of applications of vanadium complexes as antidiabetic agents in Web of Science would be expected to decrease when BMOV failed clinical trials and went off patent September 30, 2011 (Thompson et al., 2009, Thompson and Orvig, 2006, Crans, 2015). As showing **in Figure 1.1**, publications on antidiabetic agents have decreased after 2011. The interest in vanadium has then increased for cancer studies, its involvement in oxidative stress and emerging diseases, such as neurological

diseases, and SARS (Scior et al., 2021, Aureliano et al., 2023). Between 2018 and 2023, 269 peer-reviewed publications using vanadium as anticancer agents have been published. We anticipate that the number of publications involving vanadium in medicine and various diseases will continue to increase in the next five years.

As a transition metal ion, vanadium can be a countercation that neutralizes negatively charged residues on biomolecules (Kostenkova et al., 2022). Although these systems generally involve vanadium in lower oxidation states, a few systems involve vanadium in oxidation site V, such as cis-dioxovanadium cation. The most frequently observed cases are interactions with proteins, organelles, and involvement in oxidative stress. Interaction of vanadium with transferrin (Costa Pessoa and Tomaz, 2010) and other blood proteins have been extensively studied. Other enzymes have been reported to bind vanadium in place of its divalent countercation, and some structural details are emerging (Crans et al., 2004, Chasteen, 1983). The effects of vanadium on oxidative stress, lipid peroxidation and effects on reactive oxygen species (ROS) also involve cationic vanadium species (Aureliano et al., 2023). These modes of action involve Fenton and Haber-Weiss chemistries and various radical species (Valko et al., 2005, Valko et al., 2006). Since vanadium forms many different species under physiological conditions depending on the oxidation state, pH and metabolites present, the mode of action depends on the species present.

Vanadium in oxidation state five is in the form of vanadate ($H_2VO_4^-$, HVO_4^{2-}) which is a structural and electronic analog of phosphate (Crans et al., 2004, Chasteen, 1983). This form of vanadium can act as a substrate or an inhibitor by interaction with numerous phosphorylase enzymes, including various phosphatases and ribonucleases. The observed inhibition results from the ability of vanadate to bind to the active sites of those enzymes (Pessoa et al., 2015, Crans et al., 2017, Pessoa et al., 2021, Crans, 2015). The inhibition of protein tyrosine phosphatases is responsible for the effects of vanadium on signaling pathways (Crans, 2015). Physiological effects of vanadium are also caused by the inhibition of the Na^+ and K^+ ATPases; physiological roles include stimulating bone cell proliferation, bone collagen synthesis, neoplastic

transformations, and other antidiabetic actions (Pessoa et al., 2015). PTPs have a conservative Cys-His diad in their active site, just like the main protease M^{PRO}) in SARS-CoV (Scior et al., 2021, Semiz, 2022). The reported *in silico* modeling of 20 vanadium complexes in the active site of M^{PR} extend the use of vanadium complexes to treatment of SARS-CoV2-19 (Scior et al., 2021).

Several signaling pathways are affected by vanadium compounds, including protein tyrosine kinases receptor (Winter et al., 2012, Al-Quatati et al., 2013) and G-protein coupled receptors (Althumairy et al., 2020a, Althumairy et al., 2020b, Samart et al., 2020), of which the effects on the luteinizing hormone receptor (LHR) having been studied most extensively (Samart et al., 2020, Kostenkova et al., 2023). Recently, it was demonstrated that the signaling is sensitive to interaction with the lipid interface (Kostenkova et al., 2023, Samart et al., 2020). Vanadium compounds can activate and deactivate different signaling pathways, and this is important to their antitumoral action (Ferretti and León, 2022). Several signaling pathways activated by vanadium compounds have been identified and include the Mitogen-Activated Protein Kinase (MAPK) / Extracellular Signal-Regulated Kinase (ERK) signaling pathway, Phosphatidylinositol 3-Kinase (PI3K) / Protein Kinase B (AKT) signaling pathways, Caspase Signaling Pathway, Janus Kinase Protein (JAK) / Signal Transducer and Activator of Transcription Protein (STAT) signaling pathway, and Nuclear Factor Erythroid 2-Related Factor 2 (Nrf2) / Heme Oxygenase-1 (HO-1) signaling pathway. Signaling pathways that are inactivated include the Focal Adhesion Kinase (FAK) signaling pathway, autophagy signaling pathway, transforming growth factor-beta (TGFbeta) - Ephithelial to Mesenchymal Transition (EMT) signaling pathway, and Notch-1-signaling pathway. These pathways potentially lead to cell cycle arrest, ROS production and apoptosis, and the presence of vanadium induces tumor suppressor effects.

One challenge of using vanadium compounds for medicinal applications is the complex vanadium speciation chemistry under physiological conditions (Levina et al., 2017, Crans et al., 2013). Vanadium(V) complexes tend to hydrolyze into the vanadate ($H_2VO_4^-$) and a free ligand at physiological pH. Vanadate forms several colorless oxidovanadates with nuclearity of one (V_1,

monomer), two (V_2, dimer), four (V_4, tetramer) or five (V_5, pentamer) vanadium atoms, which rapidly interconvert in aqueous solution but can be observed by ^{51}V NMR spectroscopy (Crans et al., 2013). The oxidovanadates can furthermore have multiple protonation states depending on the pH. Vanadate can also form a polyoxidoanion composed of ten vanadium atoms to make up decavanadate ($V_{10}O_{28}^{6-}$ or abbreviated V_{10}) which is stable from pH 3-6.5 (Samart et al., 2018). The vanadium speciation chemistry under cellular conditions forms other coordination complexes and oxidovanadates, and it is difficult to know what the active species is [30]. Several oxidovanadates have been reported to cause antidiabetic (Aureliano and Crans, 2009), antituberculosis (Samart et al., 2018), and anticancer effects (Aureliano et al., 2022, Aureliano et al., 2021).

The toxicity of vanadium anticancer complexes presents another challenge and potential concern. Vanadium concentration in human blood plasma is reported in the range of 0.2-15 nM, and this concentration changes upon administration of vanadium compounds (Pessoa et al., 2015). However, according to human studies, the concentration of vanadium does not change linearly as the concentration of the treatment increases (Willsky et al., 2013). For example, several studies have shown that long-term administration of vanadium can cause accumulation in the bone. Still however, other metal-based cancer treatments, such as the protein/peptide vaccines for immunotherapy, use much more toxic metal adjuvants than vanadium, such as aluminum oxides salts (Kamta et al., 2017, Shaw et al., 2014).

The last decade of vanadium anticancer research has resulted in 269 peer-reviewed publications ,and consequentially, many promising vanadium compounds for cancer treatment have been identified. These compounds include vanadium salts, oxovanadium coordination complexes, and polyoxidovanadates. In this review, we highlight recent advances in vanadium anticancer research over the last five years and identify key studies with other prevalent diseases.

1.2 Anticancer Application of Vanadium Compounds

Vanadium salts were first reported to have anticancer properties in 1965 (Rehder, 2012, Kieler et al., 1965), followed by a report in 1986 that vanadocene, an organovanadium compound that has a vanadium ion sandwiched between two cyclopentadienyl rings, has antitumoral effects (Rehder, 2012, Köpf-Maier and Köpf, 1986). Vanadocene is the first non-oxo organovanadium species to have reported anticancer effects (Pessoa et al., 2015). Vanadocene has shown to induce apoptosis in HepG2 (human liver) cells, yet its mechanism of action remains unknown. Recent studies indicate that vanadocene does not cause primary DNA damage, meaning that its mechanism of action is different from the leading metal-based cancer treatment, cisplatin (Mahanty et al., 2021).

These initial reports have inspired further research of vanadium-based anticancer agents. In general, vanadium anticancer compounds induce apoptosis by disruption of cellular metabolism through generation of ROS, DNA damage, and alteration of organelles and signaling pathways (Pessoa et al., 2015, Vlasiou and Pafiti, 2021, Kioseoglou et al., 2015, Aureliano et al., 2023). The following sections will explore different classes of anticancer vanadium compounds, including vanadium salts, coordination complexes and polyoxidovanadates, and modes of administration of these agents.

1.2.1 Vanadium Coordination Complexes

1.2.1.1 V(IV/V) oxo Complexes

Vanadium oxo complexes contain one oxo group and constitute most of the novel vanadium anticancer agents reported over the last five years (**Figure 1.2**). Metvan

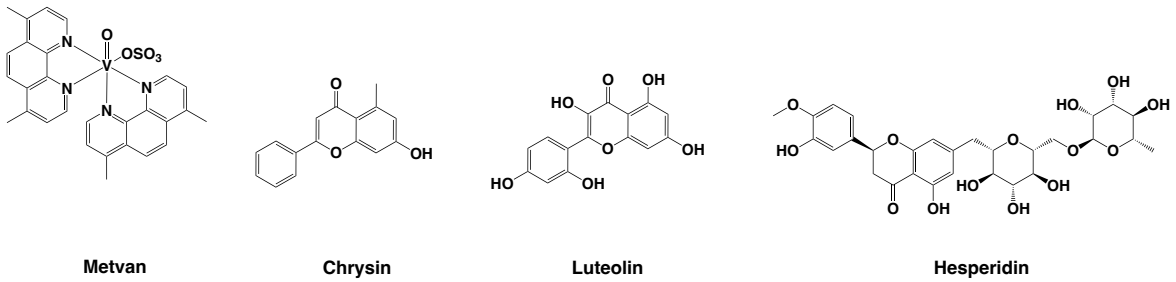

Figure 1.2. Oxovanadium complexes and flavonoid ligands reported to for anticarcinogenic vanadium complexes (Cacicedo et al., 2019, León et al., 2016, Roy et al., 2015b, Etcheverry et al., 2008).

($[V^{IV}O(OSO_3)(phen)_2]$ where phen = 1,10-phenanthroline) is a well-known vanadium(IV) oxo complex that has been initially reported for anticancer applications in early 2000s (Pessoa et al., 2015). Studies with metvan have recently suggested that it is a promising multitargeted anticancer complex with apoptosis-inducing activity in leukemia, glioblastoma, myeloma, and solid tumor cells (D'Cruz and Uckun, 2002). However, metvan undergoes hydrolysis in both PBS and MEM media which is confirmed by UV-Vis and EPR speciation data at pH 7.4, suggesting that the complex hydrolyzes upon entering cells. Therefore, recent studies have revisited its cytotoxicity (Nunes et al., 2021) . The toxicity of both complex and ligand were investigated, and the study established that the toxicity of the complex is mainly caused by the phen ligand, not vanadium itself, thus bringing into question the potential application of metvan as a cancer therapeutic in future studies (Nunes et al., 2021).

Vanadium oxo complexes with antioxidant flavonoid ligands have been explored because of the potential that resulting complexes would be very active (Etcheverry et al., 2008, Ferrer et al., 2006, Selvaraj and Krishnan, 2021, Islas et al., 2015, León et al., 2016, Martínez Medina et al., 2017). Several flavonoid ligands form complexes that affect gene expression, metabolic pathways, and cause DNA damage (Selvaraj and Krishnan, 2021). Flavonoids also inhibit several

ROS-producing enzymes, including monooxygenase, cyclooxygenase, lipoxygenase, NADH, and phospholipase (Selvaraj and Krishnan, 2021). Vanadium complexes reported with flavonoid ligands include quercetin, hesperidin, morin, silibinin, and chrysin (Selvaraj and Krishnan, 2021, Ferrer et al., 2006, Etcheverry et al., 2008, Naso et al., 2013, León et al., 2016). These complexes are cytotoxic against several cancer cell lines. This cytotoxicity is attributed to the pro-oxidant nature of flavonoid ligands and the ability of the complexes to generate ROS (Selvaraj and Krishnan, 2021). The nature of the vanadium-flavonoid complexes has been characterized by several techniques, including FTIR, UV-Vis, and elemental analysis (**Table 1.1**); however, crystal structures of these complexes remain elusive. Interestingly, some of the vanadium-flavonoid complexes are less cytotoxic than the corresponding ligands such as chrysin, suggesting that some structural differences exist that affect the anticancer potential of these materials. A better understanding of these differences would be desirable before further exploration of these systems for cancer treatment.

Table 1.1. Vanadium(IV/V) flavonoid complexes, their reported characterization, and observed biological activities of the complexes.

Complex	**Ligand**	**Reported Characterization**	**Reported Anticancer Properties**	**Reference**
$[VO(apigenin)(H_2O)_2]Cl$	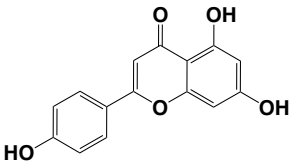 apigenin	Elemental analysis, TGA, diffuse reflection	Lung (A549) and cervix HeLa cancer cells	(Martínez Medina et al., 2017)
$[VO(dios)(OH)_3]Na_5 \cdot 6H_2O$	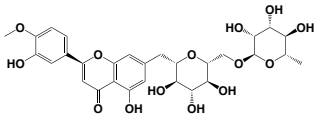 diosmin	Elemental analysis, UV-Vis, TGA	Lung (A549) and breast (T47D, SKBR3 and MDAMB231) cancer cell lines	(Naso et al., 2016)
$[VO(luteolin)_2]$	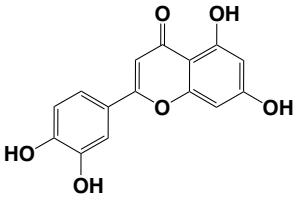 luteolin	UV-Vis, FTIR, ESI-MS	N/A, ROS formation was tracked using 1-diphenyl-2-picrylhydrazyl (DPPH)	(Roy et al., 2015b)
$[VO(Quer)_2EtOH]_n$	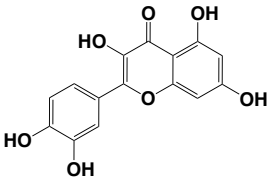 quercetin	UV-Vis, elemental analysis	Osteoblastic cell cultures: normal (MC3T3E1) and tumoral (UMR106),	(Ferrer et al., 2006)
$[VO(Hesp)(OH)_3]Na_4 \cdot 3H_2O$ (VOHesp)	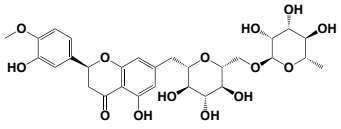 hesperidin	FTIR, elemental analysis	Rat osteosarcoma (UMR106) and human colon adenocarcinoma (Caco-2)	(Etcheverry et al., 2008)

Table 1.1. Vanadium(IV/V) flavonoid complexes, their reported characterization, and observed biological activities of the complexes.

$[VO(mor)_2H_2O]\cdot 5H_2O$ (VOmor)	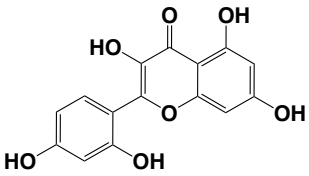 morin	UV-Vis, FTIR, elemental analysis, diffuse reflection	osteoblast (UMR106 and MC3T3E1), breast tumor (T47D and SKBR3) and breast epithelial cell lines	(Naso et al., 2013)
[VO(rutin)2]	Rutin	^{1}H NMR, ESI-MS, FTIR, UV-Vis	Oral subacute toxicity study in balb/c mice. Mortality observed at a dose of 120 mg/kg	(Roy et al., 2015a)
$[VO(chrysin)_2EtOH]_2$	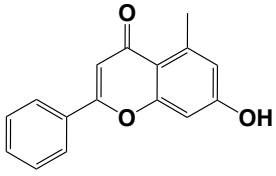 chrysin	FTIR, elemental analysis	Human osteosarcoma cell line (MG-63)	(León et al., 2016, Leon et al., 2013)

Several oxovanadium(IV) complexes have been reported as promising agents for photodynamic therapy due to their near-IR d-d light absorption (Gourdon et al., 2022). The complexes with N,N-donor dipyridophenazine (dppz) ligand have been reported in 2007, showing a weak d–d band around 840 and 700 nm and another one around 470 nm (Sasmal et al., 2007). The curcumin oxovanadium complexes have also been of interest for ROS production and DNA binding (Balaji et al., 2014, Banik et al., 2014). The oxovanadium curcumin complexes absorb light around 450 nm due to p-p* transitions and 720 nm due to their MC bands, resulting in good type I PDT effect with IC_{50} values of 10 μM under visible light irradiation in HeLa cells (Balaji et al., 2014, Banik et al., 2014). Oxovanadium(IV) complexes with BODIPY ligands are most

promising PDT agents upon irradiation at 535 nm due to the emission properties of BODIPY that

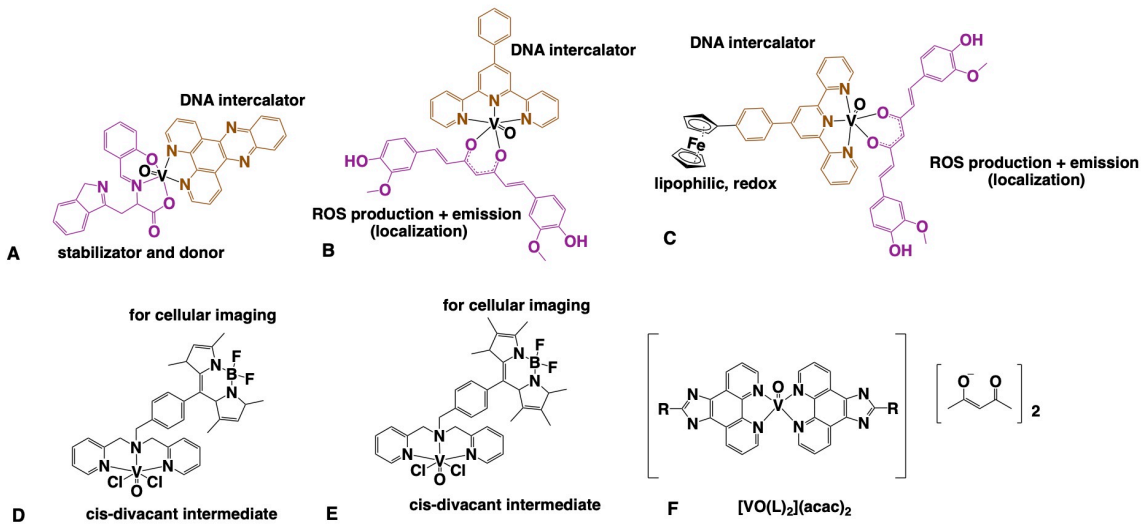

Figure 1.3. Representative oxovanadium(IV) complexes for PDT.

allow for cellular imaging (Kumar et al., 2020, Kumar et al., 2016). A recent study has also reported several oxovanadium(V) Schiff base complexes that accumulate complex in breast cancer cell lines and show cytotoxicity (Noriega et al., 2020). A novel imidazo[4,5-f][1,10] phenanthroline oxidovanadium(IV) complex had an IC_{50} of 8.2 μM in human keratinocytes (HaCaT) under visible light irradiation (Sanasam et al., 2020). The representative oxovanadium(IV) complexes for PDT are shown in **Figure 1.3.** Overall, the development of V(IV) complexes for PDT is an emerging area where a careful design of the ligands may result in vanadium complexes with favorable properties for both PDT and cancer treatment. For example, a novel two-dimensional (2D) vanadium-based nanosheets (Vanadene, V NSs) with polyvalent surfaces (V^{IV}/V^{V}) and high biodegradability were prepared by a liquid-phase exfoliation strategy (Nie et al., 2022). The polyvalent surface endowed its multiple capabilities to modulate TME through GSH consumption and O2 production via V^{V} and to catalyze a Fenton-like reaction to produce ·OH under a mild condition via V^{IV}. The V NSs-based nanocatalyst can be slowly

degraded into non-toxic species, enabling it to be innocuously eliminated from the body after completing tumor eradication by single drug injection and single NIR irradiation.

1.2.1.2 Vanadium Schiff base complexes: V^{IV}, V^{V} and mono and dioxo complexes

Schiff base ligands provide scaffolds that support diverse coordination modes and participate in many biological activities, making them desirable in catalysis as fluorescence sensors and in drug development (Pessoa et al., 2015). Vanadium Schiff base complexes, however, are susceptible to hydrolysis under physiological conditions. Thus, novel delivery methods of those complexes may be required to for further development of these compounds for therapeutic purposes (Levina et al., 2022). The class of vanadium Schiff base complexes continues to grow due to their convenient synthesis and characterization, in addition to the fact that the framework stabilizes complexes including metal ions in high oxidation states. Schiff base ligands have been used for decades to model coordination mode and reactivity of vanadium in biological systems in studies exploring the chemistry of haloperoxidase enzymes (Hernández et al., 2022).

In the last five years, oxovanadium(IV/V) Schiff base complexes for application as anticancer agents have been reported. While some of the reported complexes have IC_{50} > 50 μM or have comparable cytotoxicity to cisplatin (refer to (Kongot et al., 2019, Mokhtari and Mohammadnezhad, 2022, Hassan et al., 2022, Rodríguez et al., 2019)), several novel vanadium Schiff base complexes have high cytotoxicity, making them promising anticancer agents (**Figure 1.4**) (Bai et al., 2021). For example, a newly synthesized oxovanadium salan complex $(HNEt_3)[V^{V}O_2L]$ where L = H_2L = 4-((E)-(2-hydroxy-5-nitrophenylimino)methyl)benzene-1,3-diol] has demonstrated moderate cytotoxicity against colon cancer cell lines(HT-29, IC_{50} = 9.09 ± 0.03 μM) (Sahu et al., 2021) and low cytotoxicity against mouse embryonic fibroblast (NIH-3T3, IC_{50} = 79.77 ± 4.00 μM) cancer cell lines (Sahu et al., 2021). Vanadium(IV) naphthoylhydrazone complex

(**Figure 1.4A**) has been found to be a promising multitargeted anticancer complex with high

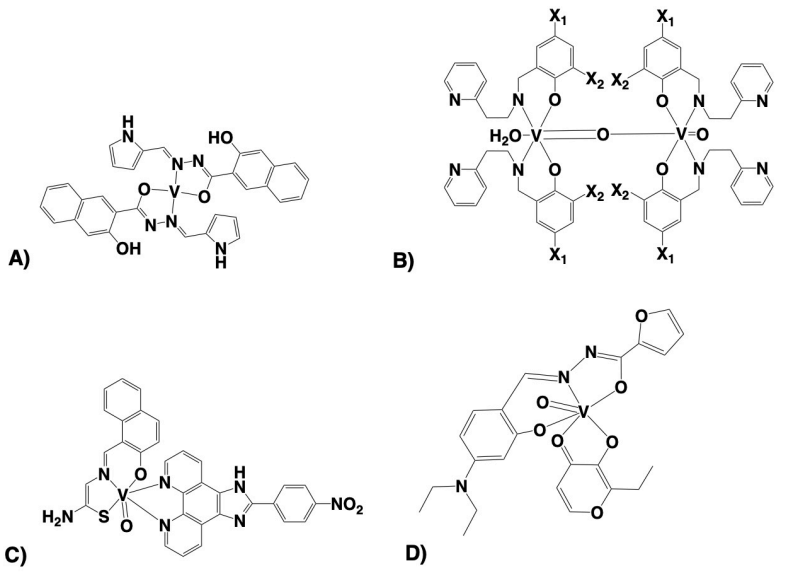

Figure 1.4. Oxidovanadium(IV/V) Schiff base complexes with reported anticancer properties.

cytotoxicity in lung (H1299, IC_{50} = 7.0 μM), breast (MCF7, IC_{50} = 0.73 μM), and colon (HCT116, IC_{50} = 1.12 μM) cancer cell lines (Ribeiro et al., 2019). A new series of vanadium dinuclear complexes of tridentate halogen-substituted Schiff bases with the $O \rightarrow V^{IV} = O \rightarrow V^{IV} = O$ core (**Figure 1.4B**) has been evaluated in ovarian (A2780), breast (MCF7), and prostate (PC3) cancer cells at 48 h (Rudbari et al., 2021). The results with these multitargeted anticancer compounds have shown that these complexes are highly cytotoxic with the IC_{50} values in the range of 3.9–17.2 μM (Rudbari et al., 2021).

VO(hntdtsc)(NPIP) shown in **Figure 1.4C** significantly inhibited the tumor growth and induced the apoptosis of cancer cells in mice xenograft models, according to the results of *in vivo* image detection, H&E pathological examination, and immunohistochemical detection of p16/Ki-67 protein expression (Bai et al., 2021). This complex was tested in several cell lines and was found to have an IC_{50} = 1.09 μM in Hela cells, 4.51 μM in BIU-87 cells and 7.61 μM in SPC-A-1 cells. An oxidovanadium [V^{V}OL(ema)] complex was synthesized using tridentate ONO donor ligands, **Figure 1.4D.** The *in vitro* cytotoxicity activity was tested against lung (A549) and colon

(HT-29) cancer cell lines, and a non-cancerous mouse fibroblast (NIH-3T3) cell line. The anticancer activity was manifested in an IC_{50} value of 4.4 ± 0.1 μM against the HT-29 cell line (Sahu et al., 2023). The complex induces cell cycle arrest at the G2/M phase and a dose-dependent cell apoptosis is triggered as measured by the cell apoptosis analysis via flow cytometry and confocal microscopy assays. The complex targets the mitochondria by disrupting the mitochondrial membrane potential and causes overproduction of intracellular reactive oxygen species, eventually leading to induced cell apoptosis (Sahu et al., 2023). Overall, recent reports have introduced several interesting oxovanadium(IV/V) complexes, although rigorous cytotoxicity assays are necessary to assure that the scaffolds used are not contributing to the observed cytotoxicity in cancer cell lines.

Vanadium(V) catecholate complexes are a subclass of vanadium Schiff base complexes with reported anticancer properties (**Figure 1.5**) (Crans et al., 2019b, Levina et al., 2020, Murakami et al., 2022).The studies by the Crans and Lay groups have shown that bulky hydrophobic substituents on the catecholate ligand increase hydrolytic stability and cytotoxicity in T98g (glioblastoma multiforme) cells, as these complexes readily hydrolyze under physiological conditions (Levina et al., 2020, Murakami et al., 2022). The modest hydrolytic stability makes vanadium(V) catecholate complexes suitable agents to treat glioblastoma via intratumoral injections; they are sufficiently stable to be administered, but are very reactive with tumors before any diffusion takes place (Levina et al., 2020, Levina et al., 2022). The spectroscopic properties

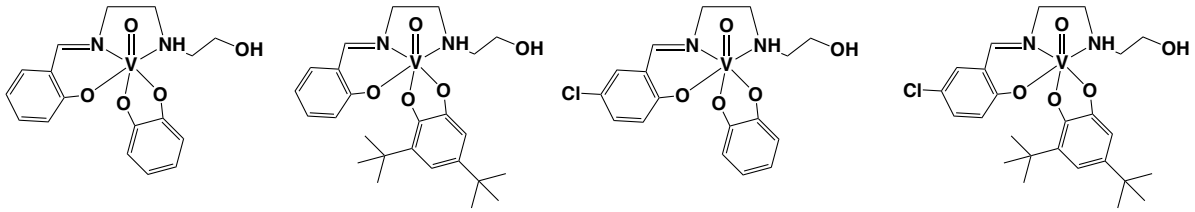

Figure 1.5. Structures of vanadium(V) catecholate complexes as potential agents for glioblastoma treatment where HSHED is N-(salicylideneaminato)-N'-(2-hydroxyethyl)-1,2-ethanediamine, CAT – catechol and DTB – di-*tert*-butylcatechol [74, 85-87].

and cytotoxicities of several non-halogenated and halogenated complexes abbreviated VO(HSHED) where HSHED stands for N-(salicylideneaminato)-N'-(2-hydroxyethyl)-1,2-ethanediamine have been reported in addition to their anticancer properties in T98g (glioblastoma multiforme), A549 (lung), PANC-1 (pancreatic) and SW1353 (bone chondrosarcoma) cell lines. The [VO(HSHED)(DTB)] and [VO(Cl-HSHED) (DTB)] complexes where DTB stands for di-*tert*-butylcatechol (IC_{50} =2.5 ± 0.1 μM and 4.1± 0.5 μM, respectively) have been found to be most cytotoxic toward cancer cells, but less toxic toward normal cells and most hydrolytically stable due to the steric bulk of the *tert*-butyl substituents on the catecholate ligand (Crans et al., 2019b, Levina et al., 2020, Murakami et al., 2022).

Dioxovanadium Schiff base complexes, a much smaller subclass of vanadium Schiff base complexes, have two oxo groups and have also been reported. *A cis*-dioxovanadium species with the formula $(HNEt_3)[V^VO_2L]$ was reported to be highly cytotoxic in colon cancer cell lines (HT-29 cells, IC_{50} = 8.56 ± 0.62 μM) while being non-toxic to normal cell lines (NIH-3T3 cells) IC_{50} = 67.8± 5.48 μM, making it a promising treatment for colon cancer (Sahu et al., 2021). Another dioxovanadium species, with a dimeric structure and the formula $[(V^VO_2)_2(pedf)_2]$, is a promising multitargeted anticancer treatment with relatively low cytotoxicity in lung cancer (A549 cells, IC_{50} = 64.2 μM) and in human skin carcinoma (A431 cells, IC_{50} = 56.3 μM) cell lines (Biswas et al., 2022).

Overall, this section summarizes the diversity of structures and applications of vanadium(IV/V) Schiff base complexes for different types of cancer. Rigorous assay studies are much needed to evaluate whether the toxicity of newly synthesized vanadium(IV/V) Schiff base complexes is attributed to the complex or the free ligand.

1.2.1.3 V^V dioxo complexes

Vanadium(V) dipicolinates contain the *cis*-dioxo moiety and have the general formula $[VO_2dipic\text{-}X]^-$. Vanadium(V) dipicolinates are well-known coordination complexes with antidiabetic properties (Crans et al., 2003, Crans et al., 2000, Willsky et al., 2011) and are also reported to exert anticancer properties by enhancing the effects of oncolytic viruses, **Figure 1.6** (Bergeron et

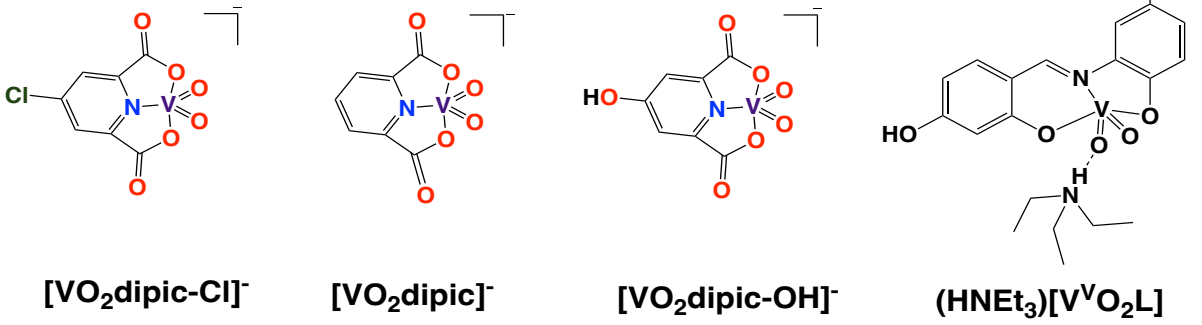

Figure 1.6. Representative dioxovanadium anticancer complexes [13,81,90].

al., 2019, Crans et al., 2003, Crans et al., 2000). Oncolytic viruses are FDA-approved for the treatment of advanced melanoma in both U.S. and Europe (McAusland et al., 2021). Vanadium salts and complexes have been chosen due to their reported immunostimulatory and anticancer effects. Three vanadium(V) dipicolinate derivatives, $[VO_2dipic\text{-}X]^-$ where X = H, Cl, OH, were tested in combination with oncolytic viruses, non-pathogenic DNA rhabidoviruses that preferentially infect and kill cancer cells by inducing antitumor immunity (Bergeron et al., 2019). Vanadium(V) dipicolinates enhance the viral spread in 786-0 cells at the same magnitude of viral enhancement, as is reported for vanadium salts and vanadium(V) dipicolinates. Similarly, vanadium citrate complexes were investigated and also found to enhance oncolytic viruses (Diallo et al., 2022). The immunomodulatory mechanism of vanadate has been recently reported by Wong and coworkers (Wong et al., 2022) which indicates that vanadate regulates STAT1 and STAT2 heterodimers through EGFR to modulate the IFN response, which consequentially, results in the replication of oncolytic viruses (Wong et al., 2022). The reports of vanadium coordination

complexes enhancing the effects of oncolytic viruses open the possibilities of a promising efficient anticancer treatment.

1.2.1.4 Non-oxovanadium complexes

As described earlier, non-oxovanadium complexes include vanadocenes, a class of organometallic compounds that have a vanadium ion sandwiched between two cyclopentadienyl rings (Köpf-Maier and Köpf, 1986). Vanadocene is the first non-oxo organovanadium species to have reported anticancer effects (Pessoa et al., 2015). Vanadocene has shown to induce apoptosis in HepG2 (human liver) cells, yet its mechanism of action remains unknown. Recent studies indicate that vanadocene does not cause primary DNA damage, meaning that its mechanism of action is different from cisplatin (Mahanty et al., 2021).

A recent study has reported non-oxovanadium tridentate ONO Schiff base complexes with promising inhibitory activities (IC_{50} = 19.0 μM) of lysine specific demethylase (LSD1), an enzyme associated with the progress and oncogenesis of multiple human cancers (**Figure 1.7)** (Lu et al.,

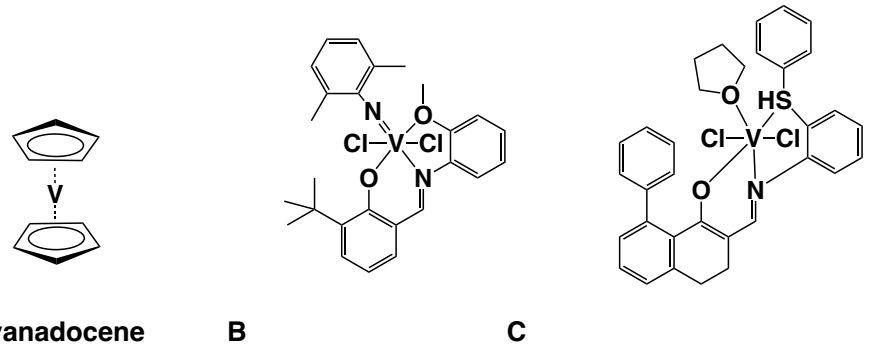

A vanadocene **B** **C**

Figure 1.7. Representative non-oxovanadium anticancer complexes.

2019a). A series of structurally similar complexes has been reported shortly thereafter with the lead complex of the series being highly cytotoxic in gastric (MCG803, IC_{50} = 2.69 ± 0.56 μM), breast (MCF7, IC_{50} = 4.52 ± 0.65 μM), and liver (HepG2, IC_{50} = 5.50 ± 0.74 μM) cancer cell lines, and drug-resistant esophageal squamous cell carcinoma (EC109, IC_{50} = 7.21 ± 0.85 μM) (Lu et al., 2019b).

1.2.2 Vanadium salts

Vanadium salts are well-known and well-studied antidiabetic agents, some of which have been studied in phase I and II clinical trials ($VOSO_4$ and $NaVO_3$) (Thompson et al., 2009, Crans et al., 2019a). Consequently, the research focus has recently shifted towards anticancer applications of vanadium salts (**Figure 1.8)** (Tian et al., 2021, Wu et al., 2016, McAusland et al., 2021).

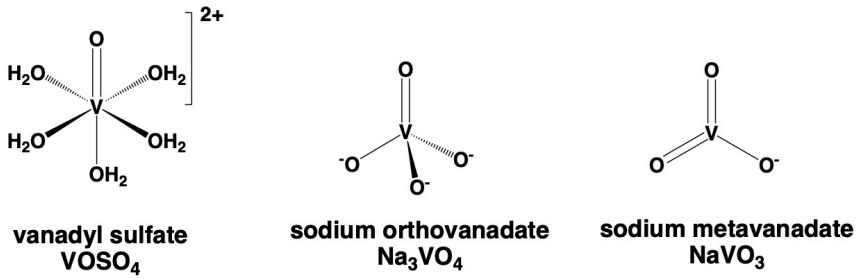

Figure 1.8. Structures of vanadium(IV/V) salts studied for their anticancer applications. These structures represent the anionic forms of the respective oxovanadates.

Vanadium(IV/V) salts, such as vanadyl sulfate ($VOSO_4$), sodium orthovanadate (Na_3VO_4), and sodium metavanadate ($NaVO_3$) are being used in several anticancer studies (**Figure 1.8**). $VOSO_4$ is often a positive control that is used frequently. Recently, $VOSO_4$ and $NaVO_3$ have been tested in combination with oncolytic viruses (Diallo et al., 2022). The first study has documented that all salts robustly enhance the spread of oncolytic viruses, which led to subsequent studies with vanadium coordination complexes (Bergeron et al., 2019, Selman et al., 2018). The combination of vanadyl sulfate and Newcastle disease virus has been administered via intratumoral injections and has proven effective in melanoma and murine prostate cancer models (McAusland et al., 2021). $NaVO_3$ has been reported to exhibit antiproliferative effects in human pancreatic cancer cell line AsPC-1 by inducing the activation of both PI3K/AKT and MAPK/ERK signaling pathways dose and time dependently (Wu et al., 2016). Sodium metavanadate has also been tested in murine breast cancer model both *in vitro* and *in vivo*. The data have shown that $NaVO_3$ inhibits proliferation of murine breast cancer cells 4T1 with the IC_{50} value of 8.19 μM and

1.92 μM at 24 h and 48 h, respectively (Tian et al., 2021). The study has also reported the underlying mechanism of the inhibition activity where $NaVO_3$ increases the ROS levels in a concentration-dependent way, arrests cells at G2/M phase, diminishes the mitochondrial membrane potential, and promotes the progress of apoptosis (Tian et al., 2021). $NaVO_3$ has also exhibited a dose-dependent anticancer activity in breast cancer-bearing mice that led to the shrinkage of tumor volume by about 50% (Tian et al., 2021). Overall, the studies with vanadium salts have established a foundation to the development of more efficient vanadium-based anticancer therapeutics.

1.2.3 Polyoxidovanadates

Polyoxidovanadates (POVs) are polyanionic vanadium-oxygen clusters and a subclass of polyoxidometalates (POMs), which is a class of compounds consisting of group V and VI metal-oxide clusters (Aureliano et al., 2021). The first report of anticancer activity of a POM was published in 1965 and the field has grown significantly since then (Aureliano et al., 2021). The number of papers regarding the use of POMs for anticancer applications has increased 7-fold over the last decade, with about 10% of publications covering anticancer applications of POVs. POVs have been reported to demonstrate biological activities against diabetes, cancer, bacteria,l and viral diseases (Aureliano et al., 2021, Nunes et al., 2012, Samart et al., 2018). Two decavanadate derivatives, $(H_2tmen)_3[V_{10}O_{28}]$ (tmen = N,N,N^0,N^0-tetramethylethylenediamine) and $(H_2en)_3[V_{10}O_{28}]$ (en = ethylenediamine), have been found highly effective against human lung carcinoma (A549; IC_{50} = 4.3±0.3 μM and 1.5±0.1 μM, respectively) (Li et al., 2010). The clusters, however, have been found to be highly cytotoxic to normal hepatocytes (IC_{50} = 6.5±0.6 μM and 7.2±0.7 μM, respectively) (Li et al., 2010). For more information regarding anticancer applications of POMs and POV, refer to the following recent reviews: (Aureliano et al., 2021, Aureliano et al., 2022).

1.2.4 Novel Modes of Administration of Vanadium Anticancer Compounds

The mode of administration is highly dependent on the compound and its potential application. Due to its non-invasive nature, cost effectiveness, and patient convenience and compliance, oral administration has traditionally been the most preferred method to administer vanadium compounds (Alqahtani et al., 2021). The compounds are often added to food in animal studies or some carrier that generally improve the absorption of the drug significantly. Oral administration of vanadium complexes and salts, such as BMOV, $VOSO_4$ and $NaVO_3$, has been most extensively investigated in phase I and II clinical trials for diabetes treatment (Thompson et al., 2009, Thompson and Orvig, 2006). The oral administration of organovanadium species such as BMOV and BEOV is advantageous as the bioavailability of vanadium increases threefold compared to the vanadium salts (Thompson et al., 2009, Thompson and Orvig, 2006). However, the distribution and cell uptake are much lower than desired, causing a higher systemic concentration needed for treatment. BEOV, an organovanadium(IV) antidiabetic drug studied in phase I and II clinical trials, went off patent in 2011 which, unfortunately, put the studies exploring the safety of oral administration of vanadium compounds on a halt (Thompson and Orvig, 2006)..

Different methods of administration of vanadium compounds are used for the treatment of cancer. Since cancer can be terminal, more aggressive methods of administration are generally developed and used in the clinic. The following section describes modes of administration of vanadium anticancer compounds, such as nanoparticles and intratumoral injections. These methods provide targeted delivery and show significant reduction of cancerous tumors. The resulting reduced systemic toxicity to normal tissues is particularly desirable.

1.2.4.1 Oral Administration via Lipid Nanoparticles (LNPs)

Lipid nanoparticles are used both as a diagnostic tool and a drug carrier to specific organs and tissues. Among different types of nanotransporters, lipid nanotransporters are most frequently used in medicine due to their high biocompatibility, controlled release, and ability to encapsulate

both hydrophilic and hydrophobic species (Hallan et al., 2022). Lipid nanotransporters are increasingly used for the delivery of highly cytotoxic platinum metallodrugs to reduce overall systemic toxicity (Hallan et al., 2022, Boztepe et al., 2021). Several delivery methods have been reported for vanadium anticancer agents, including micelles, liposomes, inorganic nanoparticles, polymeric nanoparticles, and proteins (albumin, ferritin) (Levina et al., 2022, Gou et al., 2021). A recent study has reported using four different LNP formulations to encapsulate metvan, one of the most well-known vanadium(IV) anticancer complexes (Cacicedo et al., 2019). An optimization process concluded that the desirable formulation consisted of 505.0 mg of myristyl myristate, 4.0% p/v of Pluronic F128 surfactant in an aqueous medium. The biological studies have shown that the LNP formulation decreases cell viability of osteosarcoma (MG-63 cells) in the MTT assay from 90% (metvan at 25 μM loading) to 30% (metvan-LNP formulation at 25 μM metvan loading) (Cacicedo et al., 2019). There is no doubt that such approaches will significantly enhance the efficacy of the potential anticancer agents and allow for reduction of the systemic concentration needed for treatment.

1.2.4.2 Intratumoral injections

Intratumoral injections (ITIs) provide a method of procedure that is increasingly applied in the clinic due to its novel mode of delivery of highly cytotoxic metal-based anticancer complexes (**Figure 1.9**) (Levina et al., 2022). Currently, the ongoing and recent clinical trials with ITIs use established Pt-based anticancer drugs, such as cisplatin, carboplatin, and oxaliplatin (Levina et al., 2022). Two related techniques, convection enhanced delivery (CED) (D'Amico et al., 2021, Nwagwu et al., 2021, Kang and Desjardins, 2021) and pressurized intraperitoneal aerosolized chemotherapy (PIPAC) (Alyami et al., 2019, de Jong et al., 2021), are being developed to increase the cytotoxic drug concentration within the tumor and to decrease the concentration outside the tumor and in the blood. The concept of using ITIs has been recently proposed for relatively unstable non-innocent oxidovanadium(V) catecholate complexes. The complexes consist of a

tridentate Schiff base and a redox-active catecholate ligand (**Figure 1.9**). Previous studies have

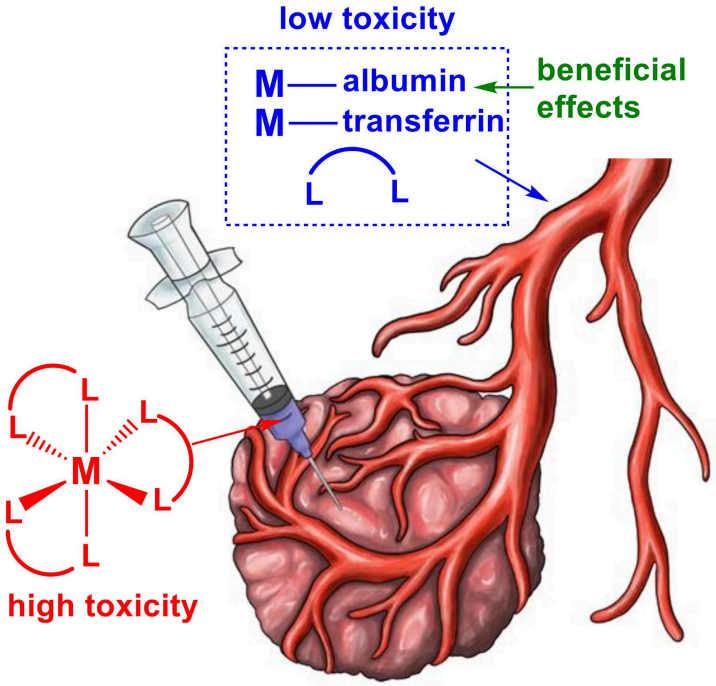

Figure 1.9. The principle of the use of reactive and unstable metal complexes in intratumoral injections. Designations: M is the metal ion; and L are the ligands. The image was reproduced from Levina et. al 2022 [74] under the Creative Commons Attribution-Share Alike 4.0 Unported license (https://creativecommons.org/licenses/by- sa/4.0/deed.en).

shown that the catecholate complexes with bulky hydrophobic substituents on the catecholate ligand are the most suitable agents for ITIs due to their high cytotoxicity and relatively short lifetimes in media (half-life = 30 s at 37°C). The hydrophobic bulk on the catecholate ligand increases hydrolytic stability in media and uptake into cancer cell monolayers. Consequently, this causes high cytotoxicity in cancer cell monolayers which has been reported for the lead complex of the catecholate series, [VO(HSHED)(DTB)] (IC_{50} 1-4 μM in 72 h treatments). Additionally, previous studies have shown that decomposition side products of the catecholate complexes, such as V-Tf adducts, are non-toxic and in some cases can have neuroprotective and neurostimulatory effects (Levina et al., 2022).

ITIs have also been proposed for other vanadium(V) complexes and vanadium salts. One of the recent studies has reported using intratumoral injections of $VOSO_4$ and

Newcastle disease virus (NDV) (McAusland et al., 2021). This combination therapy was effective in melanoma and murine prostate cancer models (McAusland et al., 2021). Another study has reported using intratumoral injections of a novel vanadium(V) nanocomplex for photodynamic therapy (PDT) (Hu et al., 2021). The complex consists of vanadyl ions chelated with tannic acid and silk sericin, a biocompatible protein. The vanadyl(V) nanocomplex has been injected into tumors 7 and 10 days after tumor inoculation, followed by PDT treatment. The results have demonstrated the enhancement of photothermal-induced cancer immunotherapy to inhibit primary tumor metastasis and recurrence by the novel vanadyl(V) nanocomplex (Hu et al., 2021).

In summary, ITIs and related methods are a new and promising avenue of vanadium anticancer research that are currently used as palliative methods for late-stage cancers. The evidence from the ongoing clinical trials shows that these administration methods will soon be employed in modern medicine. Importantly, these methods allow the administration of hydrolytically unstable and cytotoxic hydrophobic complexes, as well as vanadium salts. When optimized, the ITIs maximize the concentration of cytotoxic species in the target tumor and reduce the concentrations outside the tumor and in the blood. Overall, this results in the decrease systemic concentration of drug and significantly lowered toxicity.

1.3 Applications of Vanadium for Treatment of Diabetes and Cardiovascular Problems

Diabetes mellitus is a complex disease classified into Type 1 and Type 2 with distinct clinical features. Type 1 is an autoimmune disease where beta cells in the pancreas cannot produce insulin, while in Type 2 diabetes , the body is either partially or completely resistant to insulin, unable to produce sufficient amounts of insulin, or a combination of both (ElSayed et al., 2022). Both types of diabetes mellitus cause chronic hyperglycemia which, when uncontrolled, have dramatic consequences on multiple essential organs, such as the cardiovascular system and its function (Domingo and Gómez, 2016, ElSayed et al., 2022). Vanadium salts and

coordination compounds have a long history of normalizing the elevated blood glucose levels (Crans et al., 2003, Sakurai, 2002, Thompson et al., 2009). Indeed, several compounds have undergone Phase 1 and 2 clinical trials, although most of these studies were done at a time, when the requirements for such studies were more lenient and did not require as many subjects or time of the clinical trial (Thompson and Orvig, 2006, Pessoa et al., 2015, Thompson et al., 2009). However, as described below, some of the same enzymes and metabolic pathways are impacted in cancer and diabetes so some of the studies carried out on both diseases are relevant to each other (Crans et al., 2019a, Crans et al., 2018).

1.3.1 Reports of antidiabetic vanadium complexes

Recent studies demonstrating antidiabetic effects of vanadium compounds report the decrease of elevated blood glucose levels *in vivo* and *in vitro,* meaning that the recent studies (Treviño et al., 2016, Treviño and González-Vergara, 2019, Sánchez-Lara et al., 2018, Alajrawy et al., 2022, Shaik et al., 2022, Lima et al., 2021, Lima et al., 2023) confirm the studies reported previously (Crans et al., 2019a, Crans et al., 2018, Thompson et al., 2009, Thompson and Orvig, 2006, Willsky et al., 2011, Crans, 2015, Aureliano et al., 2021). The following section describes *in vitro* studies, and animal studies are described in Section 5.

Type 2 diabetic patients with hyperglycemia showed increased oxidative stress and free radical-mediated lipid peroxidation (Ceriello et al., 2002, Likidlilid et al., 2010, Davì et al., 2005) which may facilitate the development of micro- and macrovascular complications (Giacco and Brownlee, 2010, de Souza Bastos et al., 2016, Rendra et al., 2019)]. Compounds that modulate lipid peroxidation and oxidative stress and have an antioxidant potential may in part contribute to improving the metabolic health in patients with diabetes (Yanardag and Tunali, 2006). For example, oxidative stress in the liver and muscle tissues of alloxan-induced diabetic rats was treated with $(H_2Metf)_3[V_{10}O_{28}]$ (metformin-decavanadate, MV_{10}) resulting in decreased levels of SOD and CAT activity (Sánchez-Lara et al., 2018, Treviño and González-Vergara, 2019, Treviño

et al., 2016, Rusanov et al., 2022). Furthermore, lipid peroxidation markers and other effects were normalized similarly to treatment with insulin whereas metformin alone showed less effects.

Vanadium compounds were reported to activate Akt signaling and tyrosine phosphorylation through inhibition of PTPs in CHO cells containing the human insulin receptor (CHO-HIR cells) (Bhuiyan and Fukunaga, 2009). Furthermore, organovanadium complexes and vanadium salts have also been reported to stimulate glucose transport in an insulin-deficient cardiac system. These reports confirm similar earlier reports with other vanadium compounds (Crans, 2015, Crans et al., 2014).

The protein tyrosine phosphatase associated with the antidiabetic effects of vanadium compounds is protein phosphatase 1B (abbreviated PTP1B). It was found that upon cell mutation and phosphatase removal, the cells no longer are affected by vanadium compounds (Crans et al., 2014, McLauchlan et al., 2015, Crans, 2015). Recent studies were done with this phosphatase including measuring the inhibition constant of some acac-derived vanadium complexes (Shaik et al., 2022) to complement the work reviewed preciously (Crans et al., 2014, McLauchlan et al., 2015, Crans, 2015) . Prior to this work, it was expected that a similar transition state for the hydrolysis of alkyl phosphates and peptide phosphates is found for all phosphatases. The hydrolysis of a phosphate ester that is found after the S_N2 attack results in trigonal bipyramidal transition state complexes. Vanadate forms stable five coordinate trigonal bipyramidal complexes and, accordingly, inhibits most phosphatases potently. Hence, the similarities of the active site for all phosphatases have led to the expectation that it was impossible to develop an inhibitor that was specific for any phosphatase. This expectation has become a dogma. However, recently Yang and Crans developed a vanadate ester consisting of vanadate and an unnatural peptide ligand that was complementary to a cleft on PTP1B adjacent to the phosphate ester hydrolysis active site (Feng et al., 2022). This vanadate ester is found to be an effective inhibitor for PTP1B. The approach for development of this potent inhibitor is shown in **Figure 1.10 (Feng et al., 2022)**. Cell culture studies and animal studies in rats demonstrated that this inhibitor was not only specific

in studies *in vitro*, but, with the assistance of graphite quantum dots, was stabilized and able to enter cells through a lipid raft mechanism. Administration of such a system was found to be more effective than the bismaltolatoperoxovanadium(IV) complex that had been investigated in phase I and II clinical trials for treatment of STZ induced diabetic rats. These studies therefore show not only that the vanadium complex is a potent and selective inhibitor for PTP1B, but that in the combination with graphite quantum dots this vanadate ester can enter cells and normalize the diabetic animal.

Considering that the peptide analog bound to the vanadate can be readily changed, Yang and Crans replaced the initial peptide analog with a peptide that was specific for binding to the T-cell specific phosphatase. This system was indeed found to no longer bind to the PTP1B, but instead to be specific for the T-cell protein tyrosine phosphatase. This approach thus presented a new and general method for designing specific phosphatase inhibitors.

Vanadium complexes are also known to initiate signal transduction (Althumairy et al., 2020b, Kostenkova et al., 2023) and, accordingly, initiate a response in mammalian cells. Additionally, vanadium complexes are reported to mediate insulin activity and prompt the body to stabilize its insulin sensitivity. Some of these effects are due to the inhibition of protein tyrosine phosphatases (PTPs). The inhibition of the PTPase that stimulates the insulin receptor tyrosine kinase (IRTK) activity will result in some cellular uptake of glucose (Panchal et al., 2017). In another study, Iglesias-González and coworkers found that bis(maltolato)oxovanadium(IV) (BMOV) was able to mimic the function of insulin in hyperglycemic rats (Domingo and Gómez, 2016). This study, as many others prior to it, shows that vanadium compounds can result in the same response as insulin (Crans et al., 2019a, Crans et al., 2018, McLauchlan et al., 2015, Crans, 2000, Thompson et al., 2009, Thompson and Orvig, 2006).

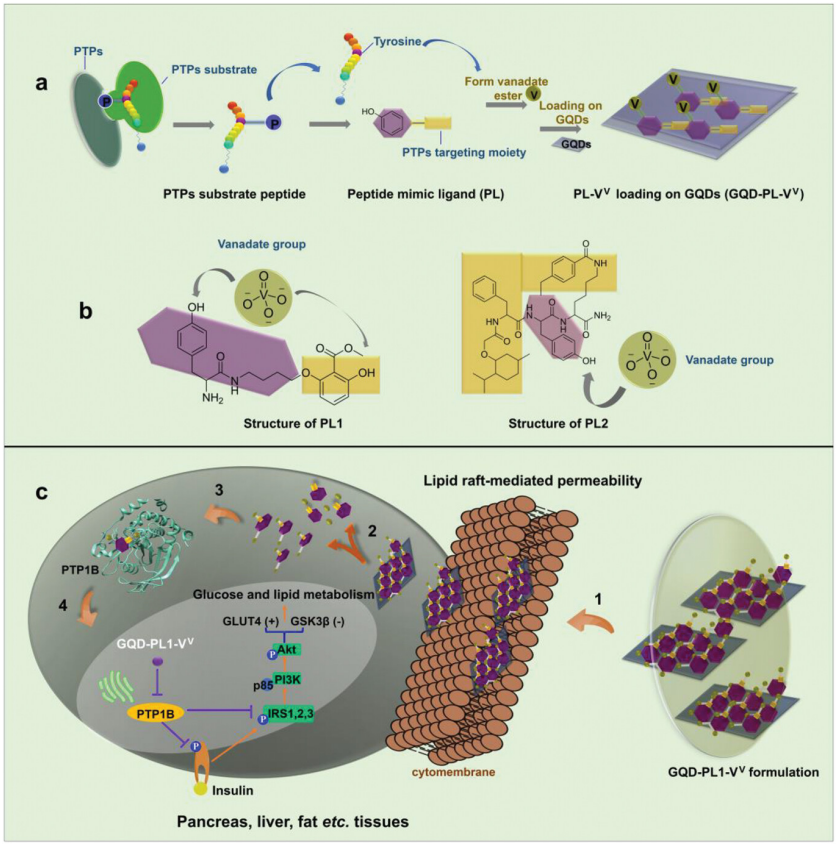

Figure 1.10. Concept and action of PTPs selective graphite quantum dot (GQD)-(peptide mimic ligand)-vanadate complex (GQD-PL1-VV). a) Schematic diagram of GQD-(peptide mimic ligand)-vanadate complex; b) Structure of the two inhibitors designed, one for PP1B (GQD-PL1-VV) and one for T-cell PTPase (GQD-PL2-VV); c) Schematic diagram of cellular uptake and PTP1B inhibition of GQD-PL1-VV that were absorbed through lipid raft-mediated permeation (step 1). Then PL1-VV was released into the cytoplasm (step 2) and selectively bound to PTP1B (step 3) causing inhibition of PTP1B which trigger insulin signal transduction and downstream effects (step 4). The figure is adapted with permission from *Adv. Funct. Mater.* 2022, 32, 2108645 [132]. Copyright © 2021 Wiley-VCH GmbH.

1.3.2 Vanadium compounds and their effects on cardiovascular system

In recent years, vanadium compounds have demonstrated efficacy in the treatment of a broad range of cardiovascular diseases including myocardial ischemia, hypertension, and myocardial hypertrophy (Domingo and Gómez, 2016, Bhuiyan and Fukunaga, 2009). More specifically, vanadium compounds have shown potential for the treatment of metabolic syndrome and for the treatment of heart attacks. The following section describes vanadium compounds as prospective treatments for these cardiovascular diseases.

The impact of vanadium salts (Na_3VO_4 and $VOSO_4$) and complexes (bis(maltolato)oxovanadium, and VO(OPT)) (Mehdi and Srivastava, 2005) on treating the effects of metabolic syndrome contributes to the improved cardiovascular function from vanadium treatment by multiple factors, including the increase of GLUT translocation to plasma membrane and glucose transport, activation of PI3K/Akt pathway in cardiomyocytes, and endothelial NO synthase. The function is further improved by the decrease of hepatic triglyceride glucose intolerance, and pre-adipocyte differentiation through PPAR-γ and C/EBPs expression. The primary result of these effects is improved smooth muscle contractility and lowered blood pressure (Panchal et al., 2017). The impact of vanadium complexes on metabolic syndrome is also linked to the effect of vanadium on vascular muscles and blood vessels.

1.3.3 The effects of vanadium on myocardial infarction (heart attacks)

The ability of vanadium compounds to inhibit PTPases has the potential to be cardioprotective and to also treat metabolic syndrome. The inhibition of a PTP by vanadate may result in the upregulation of protein kinase B (akt) which is important in cardiac growth. Upregulating protein kinase B can prevent a heart attack and support recovery during the post-heart-attack period. Specifically, a pyridinethiolato complex and a picolinato-bis(peroxide)vanadium(V) complex have been reported to have significant cardioprotective effects in animal studies (Rehder, 2013).

Furthermore, vanadium complexes have recently been used to determine their efficacy on cardio protection, especially for the prevention of myocardial infarction (heart attacks). Vanadium complexes present potential as key inhibitors of lipid phosphatase and tensin homolog on chromosome ten (PTEN). The inhibition of this enzyme plays a significant role in limiting heart attack size and improving heart function after a heart attack episode (Keyes et al., 2010). For example, Keyes and coworkers examined how bisperoxovanadium [BpV(HOpic)] can inhibit PTEN genes to improve ventricular function after a heart attack [137]. Bisperoxovanadium [BpV(HOpic)] was found to reduce the size of the heart attack and the accompanying side effects.

The study found that BpV protects cardiomyocytes against simulated ischemia and ischemia-reperfusion injury, presumably through inhibition of PTEN (Keyes et al., 2010).

1.4 Reactive Oxygen Species, Lipid Peroxidation in Disease and Oxidative Stress

Vanadium is known to impact the formation of reactive oxygen species (ROS), lipid peroxidation, and oxidative stress (Aureliano et al., 2023). Depending on conditions and the nature of the vanadium species, vanadium compounds have been found to induce (Gândara et al., 2005, Soares et al., 2007, Aureliano et al., 2023, Cheeseman, 1993) or decrease (Zhang et al., 2003, Capella et al., 2002, Yang et al., 2004, Aureliano et al., 2023) ROS. The effects are observed when using lipid peroxidation markers such as malondialdehyde (MDA), thiobarbituric acid (TBA) or 4-hydroxy-2-nonenal (4-HNE) (Lapenna et al., 2001, Taso et al., 2019, Dalle-Donne et al., 2006). However, the mode of action is complex, and vanadium can directly or indirectly have effects on reactive oxygen species via Fenton reactions (Shi and Dalal, 1993) or Haber-Weiss mechanisms (Shi and Dalal, 1993, Cheeseman, 1993). For example, $VOSO_4$ is known to increase ROS formation faster than the effects of vanadate consistent with the conversion of vanadate to vanadyl before initiation of ROS. Furthermore, vanadate monomer and decavanadate are known to impact ROS differently (Gândara et al., 2005, Soares et al., 2007). Little has been done with exploring the effects of speciation of vanadium complexes on ROS levels (Aureliano et al., 2023). The difference in responses to simple salts and oxidovanadates suggest that the differences will be observed with vanadium complexes, particularly if speciation of the complexes is considered.

Oxidative stress, ROS, and lipid peroxidation have been implicated in diseases such as cancer, diabetes, and neurogenerative diseases (Aureliano et al., 2023). Recent reports document similar effects caused by vanadium compounds both in cellular studies and in animal model systems, and future studies might reveal that those similar effects are not accidental. For example, coadministration of $VOSO_4$ with selenium tetrachloride ($SeCl_4$) significantly reduces the oxidative stress and lipid peroxidation levels obtained in studies with only administration of $VOSO_4$

(Al-Salmi and Hamza, 2022). A better understanding of the impact of vanadium on lipid peroxidation and ROS formation will consequentially help design better anticancer and antidiabetic treatments.

1.5. Animal Studies with Vanadium Anticancer and Antidiabetic Complexes

The efficacy of several vanadium coordination complexes and salts have been tested in human studies some time ago, mainly for the treatment of diabetes (Ghalichi et al., 2022). More recent analyses require longer studies and more subjects in the studies (Pessoa et al., 2015, Ghalichi et al., 2022). Several human studies have been recently reported to test the efficacy of vanadium. One large human study, involving approximately 1,500 human patients, demonstrated that low levels of vanadium in their diet are protective against the development of a metabolic disease, such as diabetes (Ji et al., 2013). In a different study, higher vanadium content was observed in rejected kidneys and in cancerous kidneys (Wilk et al., 2017). In another study, vanadium coordination chemistry explained pharmacokinetics and clinical response of administered vanadyl sulfate in type 2 diabetic patients (Willsky et al., 2013). The study with 7,359 pregnant women enrolled from Wuhan Medical and Health Center, however, demonstrated that the exposure to vanadium causes the highest risk of preterm births (defined as 37 weeks of completed gestation or less according to the World Health Organization) (Liu et al., 2022). Of 18 transition-metal ions measured in the urine vanadium, chromium and zinc cause the highest risk of preterm births (Liu et al., 2022).

Numerous animal studies with vanadium compounds have been carried out over the years. The studies demonstrated the blood glucose lowering effects of vanadium compounds (Crans et al., 2019a, Crans et al., 2018, Willsky et al., 2011, Crans, 2015, Aureliano et al., 2021, Thompson and Orvig, 2006, Thompson et al., 2009). Several complexes with blood glucose lowering effects have been reported recently, including both known compounds (Treviño and González-Vergara, 2019, Treviño et al., 2016, Sánchez-Lara et al., 2018) and novel complexes (Alajrawy et al., 2022, Shaik et al., 2022, Lima et al., 2021, Lima et al., 2023). These studies

showed that known complexes can be improved by modification and applications of structure-activity relationships as the novel vanadium complexes are continuously developed. Specifically, studies with the combination of decavanadate and metformin continue to show that the effect of the combination of these compounds is better than each compound separately in animal models other than the STZ-induced diabetic rats (Sánchez-Lara et al., 2018, Treviño and González-Vergara, 2019, Treviño et al., 2016). The new complexes included oxovanadium(IV) acac derivatives. One study of these derivatives showed that methyl imidazole complexes were *in vitro* inhibitors for PTP1B, and one of them was shown to normalize elevated blood glucose levels. A second study showed an oxovanadium(IV) acac derivative with a 3,4-diaminobenzoic acid complex had insulin enhancing properties albeit although at a lower level than $VOSO_4$. Two studies with oxovanadium(IV) complexes administered oral gavage animal studies with a nitrogen-oxidovanadium(IV) and a sulfur-oxidovanadium(IV) complex, both showing improved effects compared to $VOSO_4$ and insulin. The results with these compounds are particularly noteworthy because both complexes have limited stability under aqueous solutions. Since the effects of the complexes were investigated using oral gavage administration, the complexes were intact when administered and for about 30 min after the administration.

Recently, two systematic reviews of vanadium were reported (Ghalichi et al., 2022, Feng et al., 2022). One of the reviews dealt with the analysis of publications on vanadium and diabetic dyslipidemia. Lipid levels are very sensitive to the diabetic condition. The electronic search identified 1667 publications of which 252 studies were considered further. The studies that were unable to meet inclusion criteria, including human studies and review articles, were excluded from the search. The search resulted in 124 articles for the analysis, 48 of which covered the studies carried out from 1989 to 2021. The studies were analyzed based on the vanadium compounds studied separating out treatments with $VOSO_4$, vanadate (which include orthovanadate, metavanadate, and peroxovanadate), and coordination complexes. The systematic review of the 48 studies concluded that different forms of vanadium compounds do normalize the diabetes-

induced alterations in lipid profile (Ghalichi et al., 2022). Considering that minor risk bias was found for most analyzed studies, it was confirmed that administration of both vanadium salts and coordination complexes could be beneficial in ameliorating lipid profile in diabetic animals and preventing vascular complications due to diabetes.

The second systematic review aimed to assess the effects of vanadium supplementation on inflammation and oxidative stress biomarkers in diabetes-induced animals covering the period of 1990 to 2021. A total of 341 articles were evaluated, 42 of which were selected for inclusion. The vanadium compounds studied include $VOSO_4$, vanadate (which include orthovanadate, metavanadate, and peroxovanadate), and several coordination complexes. The enzymatic activity of inflammatory biomarkers measured include TNF-α, Il-6, hs-CRP, caspase 3, as well as oxidative stress biomarkers including GSH, SOD, GPx, GST, and GR. A minor risk of bias was reported, based on the SYRCLE's tool. Most of the studies confirmed the desirable properties of vanadium treatment on inflammatory and oxidative stress biomarkers in animals with Type 2 diabetes mellitus.

Much less has been done to explore vanadium treatments of animals with various types of cancers. Most of the reports involve tissue culture studies of primary cultures rather than animal experiments. Not only different assays were performed *in vitro,* or *in vivo* but also different results were obtained (Ferretti and León, 2022, Kostenkova et al., 2023). Vanadium compounds can activate different cancer signaling pathways and exert their antitumoral action. The MAPK/Erk, PI3K/Akt, and caspase family and JAK/Stat signaling pathways were stimulated by the vanadium compounds, prompting a cell cycle arrest, ROS production and apoptosis towards different types of cancer cells. The Nrf-2 was also activated by vanadium; however, in this case, it seemed to enhance the defense system and functioned as chemoprotective. The MAPK/Erk, PI3K/Akt, and caspase family and JAK/Stat signal and apoptosis towards different types of cancer cells (Ferretti and León, 2022, Althumairy et al., 2020b).

The 33 investigations of therapeutic applications of vanadium compounds must consider toxicity of corresponding compounds and some publications were recently reported (Assem and Oskarsson, 2015, Scalese et al., 2022a, Crans et al., 2020). One vanadium(V) catecholate complex, [VO(HSHED)(DTB)], which is currently investigated for cancer intratumoral cancer treatment (Levina et al., 2020, Murakami et al., 2022) was investigated in a recent animal study where the complex was administered at 300 mg/kg for 14 days (Lima et al., 2021). The complex exhibited low oral acute toxicity and less than vanadate (Lima et al., 2021).

1.6. Conclusions and Outlook

Vanadium salts and complexes have been considered extensively as potential therapeutic agents for the past three decades. Initially, vanadium was considered as an antidiabetic agent; however, more recent studies focused on other effects of vanadium, particularly its anticancer effects. Vanadium(IV/V) coordination complexes, vanadium salts, and polyoxidovanadates gained attention for their antidiabetic applications, normalizing elevated blood glucose and lipid levels in diabetic mammals and humans. The ability of vanadium compounds to inhibit protein tyrosine phosphatases has been attributed to protein phosphatase 1B (PTP1B); mutation of this PTPase eliminate the response of vanadium compounds. However, other mechanisms have been extensively investigated including the interaction with blood proteins (transferrin, serum albumin and immunoglobins), redox state of the cells, and other metabolic pathways. Some of these metabolic pathways are also important for understanding the anticancer effects of vanadium. Thus, the studies that explored the antidiabetic pathways are now important for studies with vanadium anticancer agents.

Vanadium(IV/V) coordination complexes, vanadium salts and polyoxidovanadates have gained increasing attention for anticancer applications in the past decade. Several metabolic and signaling pathways have been identified as targets and implicated in the mode of action of the vanadium compounds. Signaling pathways specific for vanadium compounds include signaling

pathways involving Protein Tyrosine Kinases and G-protein coupled receptors, of which the effects of vanadium on the luteinizing hormone receptor (LHR) having been studied most extensively. Vanadium also induces ROS formation and lipid peroxidation and affects signal transduction. Vanadium compounds can also activate different cancer signaling pathways and exert their antitumoral action. The MAPK/Erk, PI3K/Akt, and caspase family and JAK/Stat signaling pathways were stimulated by the vanadium compounds, prompting a cell cycle arrest, ROS production and apoptosis towards different types of cancer cells. The Nrf-2 was also activated by vanadium; however, in this case, it seemed to enhance the defense system and functioned as chemoprotective. The MAPK/Erk, PI3K/Akt, and caspase family and JAK/Stat signal and apoptosis towards different types of cancer cells (Ferretti and León, 2022, Althumairy et al., 2020b). Some signaling pathways are inactivated by vanadium compounds and include the FAK, TGF-B/EMT, Notch-1, and autophagy signaling pathways. This inhibition could potentially result in cell arrest and apoptosis, decrease in cellular migration and adhesions, FAK Signaling pathway, autophagy signaling pathway, transforming growth factor-beta (TGFbeta) - Epithelial to Mesenchymal Transition (EMT) signaling pathway, and Notch-1-signaling pathway. These processes are important to cellular processes and a believed to exhibit tumor suppressor effects.

Vanadium anticancer complexes are structurally diverse and can be used to treat different types of cancer. Oxovanadium(IV/V) and dioxovanadium(IV/V) Schiff base complexes, in particular, have been the most growing classes of vanadium anticancer complexes for the past five years. These complexes support structural diversity and the ability to stabilize vanadium in physiologically relevant oxidation states IV and V. Oxovanadium(IV) complexes have also been investigated for photodynamic therapy applications due to their photocytotoxicity in several cancer cells lines. The coordination complexes oxovanadium(V) dipicolinate and chlorodipicolinate complexes have been reported as oncolytic virotherapeutic agents, that combat cancer cell growth. VOSO4 is similarly a potent agent in this regard.

The development of modes of delivery of cytotoxic anticancer compounds, including vanadium(IV/V) complexes and salts, is important, and here we describe such applications of lipid nanoparticle carriers and intratumoral injections which allow the delivery of the complexes to cancerous tissues that causes minimal damage to normal cells. Vanadium complexes continue to be explored for their antidiabetic applications and prevention of cardiovascular complications. Future development of vanadium-based therapeutics should also include considerations about their administration and stability, overall toxicity, and modes of action in early stages of development.

1.7 References

Al-Quatati, A., Fontes, F. L., Barisas, G. B., Zhang, D., Roess, D. A. & Crans, D. C. 2013. Raft localization of Type I Fcε receptor and degranulation of RBL-2H3 cells exposed to decavanadate, a structural model for V2O5. *Dalton Trans.,* 42**,** 11912-11920

Al-Salmi, F. A. & Hamza, R. Z. 2022. Efficacy of Vanadyl Sulfate and Selenium Tetrachloride as Anti-Diabetic Agents against Hyperglycemia and Oxidative Stress Induced by Diabetes Mellitus in Male Rats. *Curr. Issues Mol. Biol.,* 44**,** 94-104.

Alajrawy, O. I., Tuleab, S. F. & Alshammary, E. T. 2022. Vanadium(IV) and vanadium(V) complexes: Syntheses, structural characterization, DFT studies and impact of oral uptake on enhancing insulin activity of diabetic albino rats. *J. Mol. Struct.,* 1269**,** 133821.

Alqahtani, M. S., Kazi, M., Alsenaidy, M. A. & Ahmad, M. Z. 2021. Advances in Oral Drug Delivery. *Front. Pharmacol.,* 12.

Althumairy, D., Murakami, H. A., Zhang, D., Barisas, B. G., Roess, D. A. & Crans, D. C. 2020a. Effects of vanadium(IV) compounds on plasma membrane lipids lead to G protein-coupled receptor signal transduction. *J. Inorg. Biochem.,* 203**,** 110873.

Althumairy, D., Postal, K., Barisas, B. G., Nunes, G. G., Roess, D. A. & Crans, D. C. 2020b. Polyoxometalates function as indirect activators of a G protein-coupled receptor†. *Metallomics,* 12**,** 1044-1061.

Alyami, M., Hübner, M., Grass, F., Bakrin, N., Villeneuve, L., Laplace, N., Passot, G., Glehen, O. & Kepenekian, V. 2019. Pressurised intraperitoneal aerosol chemotherapy: rationale, evidence, and potential indications. *Lancet Oncol.,* 20**,** e368-e377.

Assem, F. L. & Oskarsson, A. 2015. *Vanadium*.

Aureliano, M. & Crans, D. C. 2009. Decavanadate (V10O286-) and oxovanadates: Oxometalates with many biological activities. *J. Inorg. Biochem.,* 103**,** 536-546.

Aureliano, M., Gumerova, N. I., Sciortino, G., Garribba, E., Mclauchlan, C. C., Rompel, A. & Crans, D. C. 2022. Polyoxidovanadates' interactions with proteins: An overview. *Coord. Chem. Rev.,* 454**,** 214344.

Aureliano, M., Gumerova, N. I., Sciortino, G., Garribba, E., Rompel, A. & Crans, D. C. 2021. Polyoxovanadates with emerging biomedical activities. *Coord. Chem. Rev.,* 447**,** 214143.

Aureliano, M., Sousa-Coelho, A. L. D., Dolan, C. C., Roess, D. A. & Crans, D. C. 2023. Biological Consequences of Vanadium Effects on Formation of Reactive Oxygen Species and Lipid Peroxidation. *Int. J. Mol. Sci.,* 24**,** 5382.

Bai, Y., Zhang, H., Wang, Y., Zhu, L., Shi, T., Wei, H., Xiao, J., Zhang, Y. & Wang, Z. 2021. Novel Oxovanadium Complex VO(hntdtsc)(NPIP): Anticancer Activity and Mechanism of Action on HeLa Cells. *Front. Pharmacol.,* 11.

Balaji, B., Balakrishnan, B., Perumalla, S., Karande, A. A. & Chakravarty, A. R. 2014. Photoactivated cytotoxicity of ferrocenyl-terpyridine oxovanadium(IV) complexes of curcuminoids. *Eur. J. Med. Chem.,* 85**,** 458-467.

Banik, B., Somyajit, K., Nagaraju, G. & Chakravarty, A. R. 2014. Oxovanadium(iv) complexes of curcumin for cellular imaging and mitochondria targeted photocytotoxicity. *Dalton Trans.,* 43**,** 13358-13369.

Bergeron, A., Kostenkova, K., Selman, M., Murakami, H. A., Owens, E., Haribabu, N., Arulanandam, R., Diallo, J.-S. & Crans, D. C. 2019. Enhancement of oncolytic virotherapy by vanadium(V) dipicolinates. *BioMetals,* 32**,** 545-561.

Bhuiyan, M. S. & Fukunaga, K. 2009. Cardioprotection by Vanadium Compounds Targeting Akt-Mediated Signaling. *J. Pharmacol. Sci.,* 110**,** 1-13.

Biswas, B. K., Biswas, N., Saha, S., Rahaman, A., Mandal, D. P., Bhattacharjee, S., Sepay, N., Zangrando, E., Garribba, E. & Roy Choudhury, C. 2022. Interaction with bioligands and

in vitro cytotoxicity of a new dinuclear dioxido vanadium(V) complex. *J. Inorg. Biochem.,* 237**,** 111980.
Boztepe, T., Scioli-Montoto, S., Ruiz, M. E., Alvarez, V. A., Castro, G. R. & León, I. E. 2021. 8-Hydroxyquinoline platinum(ii) loaded nanostructured lipid carriers: synthesis, physicochemical characterization and evaluation of antitumor activity. *New J. Chem.,* 45**,** 821-830.
Cacicedo, M. L., Ruiz, M. C., Scioli-Montoto, S., Ruiz, M. E., Fernández, M. A., Torres-Sanchez, R. M., Baran, E. J., Castro, G. R. & León, I. E. 2019. Lipid nanoparticles – Metvan: revealing a novel way to deliver a vanadium compound to bone cancer cells. *New J. Chem.,* 43**,** 17726-17734.
Capella, L. S., Gefé, M. R., Silva, E. F., Affonso-Mitidieri, O., Lopes, A. G., Rumjanek, V. M. & Capella, M. a. M. 2002. Mechanisms of vanadate-induced cellular toxicity: role of cellular glutathione and NADPH. *Arch. Biochem. Biophys.,* 406**,** 65-72.
Ceriello, A., Quagliaro, L., Catone, B., Pascon, R., Piazzola, M., Bais, B., Marra, G., Tonutti, L., Taboga, C. & Motz, E. 2002. Role of Hyperglycemia in Nitrotyrosine Postprandial Generation. *Diabetes Care,* 25**,** 1439-1443.
Chasteen, N. D. 1983. *Struct. Bonding,* 53**,** 107-138.
Cheeseman, K. H. 1993. Mechanisms and effects of lipid peroxidation. *Mol. Aspects Med.,* 14**,** 191-197.
Costa Pessoa, J. & Tomaz, I. 2010. Transport of Therapeutic Vanadium and Ruthenium Complexes by Blood Plasma Components. *Curr. Med. Chem.,* 17**,** 3701-3738.
Crans, D., Yang, L., Jakusch, T. & Kiss, T. 2000. Aqueous Chemistry of Ammonium (Dipicolinato)oxovanadate(V): The First Organic Vanadium(V) Insulin-Mimetic Compound. *Inorg. Chem.,* 39**,** 4409-4416.
Crans, D. C. 2000. Chemistry and insulin-like properties of vanadium(IV) and vanadium(V) compounds1This manuscript summarizes the presentation given at the symposium 'Biological Aspects of Vanadium Chemistry — Chemistry, Biochemistry and Therapeutic Applications of Vanadium Compounds' and recently communicated in original research articles. The original research articles describing the experimental details of this work are given in Refs: [1], [2], [3], [4], [5].1. *J. Inorg. Biochem.,* 80**,** 123-131.
Crans, D. C. 2015. Antidiabetic, Chemical, and Physical Properties of Organic Vanadates as Presumed Transition-State Inhibitors for Phosphatases. *J. Org. Chem.,* 80**,** 11899-11915.
Crans, D. C., Henry, L., Cardiff, G. & Posner, B. I. 2019a. 8. DEVELOPING VANADIUM AS AN ANTIDIABETIC OR ANTICANCER DRUG: A CLINICAL AND HISTORICAL PERSPECTIVE. *In:* PEGGY, L. C. (ed.) *Essential Metals in Medicine: Therapeutic Use and Toxicity of Metal Ions in the Clinic.* Berlin, Boston: De Gruyter.
Crans, D. C., Koehn, J. T., Petry, S. M., Glover, C. M., Wijetunga, A., Kaur, R., Levina, A. & Lay, P. A. 2019b. Hydrophobicity may enhance membrane affinity and anti-cancer effects of Schiff base vanadium(v) catecholate complexes. *Dalton Trans.,* 48**,** 6383-6395.
Crans, D. C. & Kostenkova, K. 2020. Open questions on the biological roles of first-row transition metals. *Commun. Chem.,* 3**,** 104.
Crans, D. C., Mahroof-Tahir, M., Johnson, M. D., Wilkins, P. C., Yang, L., Robbins, K., Johnson, A., Alfano, J. A., Godzala, M. E., Austin, L. T. & Willsky, G. R. 2003. Vanadium(IV) and vanadium(V) complexes of dipicolinic acid and derivatives. Synthesis, X-ray structure, solution state properties: and effects in rats with STZ-induced diabetes. *Inorg. Chim. Acta,* 356**,** 365-378.
Crans, D. C., Peters, B. J., Wu, X. & Mclauchlan, C. C. 2017. Does anion-cation organization in Na+-containing X-ray crystal structures relate to solution interactions in inhomogeneous nanoscale environments: Sodium-decavanadate in solid state materials, minerals, and microemulsions. *Coord. Chem. Rev.,* 344**,** 115-130.

Crans, D. C., Postal, K. & Macgregor, J. A. 2020. Vanadium—Speciation Chemistry Can Be Important When Assessing Health Effects on Living Systems. *Metal Toxicology Handbook.* CRC Press.
Crans, D. C., Smee, J. J., Gaidamauskas, E. & Yang, L. 2004. The Chemistry and Biochemistry of Vanadium and the Biological Activities Exerted by Vanadium Compounds. *Chem. Rev.,* 104**,** 849-902.
Crans, D. C., Tarlton, M. L. & Mclauchlan, C. C. 2014. Trigonal Bipyramidal or Square Pyramidal Coordination Geometry? Investigating the Most Potent Geometry for Vanadium Phosphatase Inhibitors. *Eur. J. Inorg. Chem.,* 2014**,** 4450-4468.
Crans, D. C., Woll, K. A., Prusinskas, K., Johnson, M. D. & Norkus, E. 2013. Metal Speciation in Health and Medicine Represented by Iron and Vanadium. *Inorg. Chem.,* 52**,** 12262-12275.
Crans, D. C., Yang, L., Haase, A. & Yang, X. 2018. 9. HEALTH BENEFITS OF VANADIUM AND ITS POTENTIAL AS AN ANTICANCER AGENT. *In:* ASTRID, S., HELMUT, S., EVA, F. & ROLAND, K. O. S. (eds.) *Metallo-Drugs: Development and Action of Anticancer Agents.* Berlin, Boston: De Gruyter.
D'amico, R. S., Aghi, M. K., Vogelbaum, M. A. & Bruce, J. N. 2021. Convection-enhanced drug delivery for glioblastoma: a review. *Journal of Neuro-Oncology,* 151**,** 415-427.
D'cruz, O. J. & Uckun, F. M. 2002. Metvan: a novel oxovanadium(IV) complex with broad spectrum anticancer activity. *Expert Opin. Invest. Drugs,* 11**,** 1829-1836.
Dalle-Donne, I., Rossi, R., Colombo, R., Giustarini, D. & Milzani, A. 2006. Biomarkers of Oxidative Damage in Human Disease. *Clin. Chem.,* 52**,** 601-623.
Davì, G., Falco, A. & Patrono, C. 2005. Lipid peroxidation in diabetes mellitus. *Antioxid. Redox Signal.,* 7**,** 256-68.
De Jong, L. a. W., Van Erp, N. P. & Bijelic, L. 2021. Pressurized Intraperitoneal Aerosol Chemotherapy: The Road from Promise to Proof. *Clin. Cancer Res.,* 27**,** 1830-1832.
De Souza Bastos, A., Graves, D. T., De Melo Loureiro, A. P., Júnior, C. R., Corbi, S. C. T., Frizzera, F., Scarel-Caminaga, R. M., Câmara, N. O., Andriankaja, O. M., Hiyane, M. I. & Orrico, S. R. P. 2016. Diabetes and increased lipid peroxidation are associated with systemic inflammation even in well-controlled patients. *J. Diabetes Complications,* 30**,** 1593-1599.
Diallo, J.-S., Crans, D. C. & Arulanandam, R. 2022. *Pharmaceutical compositions comprising vanadium salts*. Canada, United States patent application.
Domingo, J. L. & Gómez, M. 2016. Vanadium compounds for the treatment of human diabetes mellitus: A scientific curiosity? A review of thirty years of research. *Food Chem. Toxicol.,* 95**,** 137-141.
Drewry, J. A. & Gunning, P. T. 2011. Recent advances in biosensory and medicinal therapeutic applications of zinc(II) and copper(II) coordination complexes. *Coord. Chem. Rev.,* 255**,** 459-472.
Elsayed, N. A., Aleppo, G., Aroda, V. R., Bannuru, R. R., Brown, F. M., Bruemmer, D., Collins, B. S., Hilliard, M. E., Isaacs, D., Johnson, E. L., Kahan, S., Khunti, K., Leon, J., Lyons, S. K., Perry, M. L., Prahalad, P., Pratley, R. E., Seley, J. J., Stanton, R. C., Gabbay, R. A. & Association, O. B. O. T. a. D. 2022. 2. Classification and Diagnosis of Diabetes: Standards of Care in Diabetes—2023. *Diabetes Care,* 46**,** S19-S40.
Etcheverry, S. B., Ferrer, E. G., Naso, L., Rivadeneira, J., Salinas, V. & Williams, P. a. M. 2008. Antioxidant effects of the VO(IV) hesperidin complex and its role in cancer chemoprevention. *JBIC, J. Biol. Inorg. Chem.,* 13**,** 435-447.
Feng, B., Dong, Y., Shang, B., Zhang, B., Crans, D. C. & Yang, X. 2022. Convergent Protein Phosphatase Inhibitor Design for PTP1B and TCPTP: Exchangeable Vanadium Coordination Complexes on Graphene Quantum Dots. *Adv. Funct. Mater.,* 32**,** 2108645.

Ferrer, E. G., Salinas, M. V., Correa, M. J., Naso, L., Barrio, D. A., Etcheverry, S. B., Lezama, L., Rojo, T. & Williams, P. a. M. 2006. Synthesis, characterization, antitumoral and osteogenic activities of quercetin vanadyl(IV) complexes. *JBIC, J. Biol. Inorg. Chem.,* 11**,** 791-801.

Ferretti, V. A. & León, I. E. 2022. An Overview of Vanadium and Cell Signaling in Potential Cancer Treatments. *Inorganics,* 10**,** 47.

Gândara, R. M. C., Soares, S. S., Martins, H., Gutiérrez-Merino, C. & Aureliano, M. 2005. Vanadate oligomers: In vivo effects in hepatic vanadium accumulation and stress markers. *J. Inorg. Biochem.,* 99**,** 1238-1244.

Ghalichi, F., Ostadrahimi, A. & Saghafi-Asl, M. 2022. Vanadium and diabetic dyslipidemia: A systematic review of animal studies. *J. Trace Elem. Med. Biol.,* 71**,** 126955.

Giacco, F. & Brownlee, M. 2010. Oxidative stress and diabetic complications. *Circ. Res.,* 107**,** 1058-70.

Gou, Y., Huang, G., Li, J., Yang, F. & Liang, H. 2021. Versatile delivery systems for non-platinum metal-based anticancer therapeutic agents. *Coord. Chem. Rev.,* 441**,** 213975.

Gourdon, L., Cariou, K. & Gasser, G. 2022. Phototherapeutic anticancer strategies with first-row transition metal complexes: a critical review. *Chem. Soc. Rev.,* 51**,** 1167-1195.

Hallan, S. S., Amirian, J., Brangule, A. & Bandere, D. 2022. Lipid-Based Nano-Sized Cargos as a Promising Strategy in Bone Complications: A Review. *Nanomaterials,* 12**,** 1146.

Hassan, S. S., Bedir, E. A., Hamza, A. E.-R. M., Ahmed, A. M., Ibrahim, N. M., Abd El-Ghany, M. S., Khattab, N. N., Emeira, B. M., Salama, M. M., Mohamed, E. F. & Fayed, D. B. 2022. The dual therapeutic effect of metformin nuclei-based drugs modified with one of Tulbaghia violacea extract compounds. *Appl. Organomet. Chem.,* 36**,** e6804.

Hernández, L., Araujo, M. L., Madden, W., Del Carpio, E., Lubes, V. & Lubes, G. 2022. Vanadium complexes with polypyridyl ligands: Speciation, structure and potential medicinal activity. *J. Inorg. Bioch.,* 229**,** 111712.

Hou, R., He, Y., Yan, G., Hou, S., Xie, Z. & Liao, C. 2021. Zinc enzymes in medicinal chemistry. *Eur. J. Med. Chem.,* 226**,** 113877.

Hu, D., Xu, H., Zhang, W., Xu, X., Xiao, B., Shi, X., Zhou, Z., Slater, N. K. H., Shen, Y. & Tang, J. 2021. Vanadyl nanocomplexes enhance photothermia-induced cancer immunotherapy to inhibit tumor metastasis and recurrence. *Biomaterials,* 277**,** 121130.

Islas, M. S., Naso, L. G., Lezama, L., Valcarcel, M., Salado, C., Roura-Ferrer, M., Ferrer, E. G. & Williams, P. a. M. 2015. Insights into the mechanisms underlying the antitumor activity of an oxidovanadium(IV) compound with the antioxidant naringenin. Albumin binding studies. *J. Inorg. Biochem.,* 149**,** 12-24.

Ji, L., Hu, D., Pan, C., Weng, J., Huo, Y., Ma, C., Mu, Y., Hao, C., Ji, Q., Ran, X., Su, B., Zhuo, H., Fox, K. A., Weber, M. & Zhang, D. 2013. Primacy of the 3B approach to control risk factors for cardiovascular disease in type 2 diabetes patients. *Am. J. Med.,* 126**,** 925.e11-22.

Kamta, J., Chaar, M., Ande, A., Altomare, D. A. & Ait-Oudhia, S. 2017. Advancing Cancer Therapy with Present and Emerging Immuno-Oncology Approaches. *Front. Oncol.,* 7.

Kang, J. H. & Desjardins, A. 2021. Convection-enhanced delivery for high-grade glioma. *Neuro-Oncology Practice,* 9**,** 24-34.

Keyes, K. T., Xu, J., Long, B., Zhang, C., Hu, Z. & Ye, Y. 2010. Pharmacological inhibition of PTEN limits myocardial infarct size and improves left ventricular function postinfarction. *Am. J. Physiol.: Heart Circ. Physiol. ,* 298**,** H1198-H1208.

Kieler, J., Gromek, A. & Nissen, N. I. 1965. Studies on the antineoplastic effect of vanadium salts. *Acta Chir. Scand. Suppl.,* 343**,** 154-64.

Kioseoglou, E., Petanidis, S., Gabriel, C. & Salifoglou, A. 2015. The chemistry and biology of vanadium compounds in cancer therapeutics. *Coord. Chem. Rev.,* 301-302**,** 87-105.

Kongot, M., Dohare, N., Reddy, D. S., Pereira, N., Patel, R., Subramanian, M. & Kumar, A. 2019. In vitro apoptosis-induction, antiproliferative and BSA binding studies of a oxidovanadium(V) complex. *J. Trace Elem. Med. Biol.,* 51**,** 176-190.

Köpf-Maier, P. & Köpf, H. 1986. Metallocene complexes: organometallic antitumor agents. *Drugs Future,* 11**,** 297–319.

Kostenkova, K., Althumairy, D., Rajan, A., Kortz, U., Barisas, B. G., Roess, D. A. & Crans, D. C. 2023. Polyoxidovanadates [MoVIVV9O28]5- and [H2PtIVVV9O28]5- interact with CHO cell plasma membrane lipids causing aggregation and activation of a G protein-coupled receptor. *Front. Chem. Biol.,* 2.

Kostenkova, K., Scalese, G., Gambino, D. & Crans, D. C. 2022. Highlighting the roles of transition metals and speciation in chemical biology. *Curr. Opin. Chem. Biol.,* 69**,** 102155.

Kumar, A., Dixit, A., Banerjee, S., Bhattacharyya, A., Garai, A., Karande, A. A. & Chakravarty, A. R. 2016. Cellular imaging and mitochondria targeted photo-cytotoxicity in visible light by singlet oxygen using a BODIPY-appended oxovanadium(iv) DNA crosslinking agent. *Med. Chem. Comm.,* 7**,** 1398-1404.

Kumar, A., Dixit, A., Sahoo, S., Banerjee, S., Bhattacharyya, A., Garai, A., Karande, A. A. & Chakravarty, A. R. 2020. Crystal structure, DNA crosslinking and photo-induced cytotoxicity of oxovanadium(IV) conjugates of boron-dipyrromethene. *J. Inorg. Biochem.,* 202**,** 110817.

Lapenna, D., Ciofani, G., Pierdomenico, S. D., Giamberardino, M. A. & Cuccurullo, F. 2001. Reaction conditions affecting the relationship between thiobarbituric acid reactivity and lipid peroxidesin human plasma. *Free Radical Biol. Med.,* 31**,** 331-335.

Leon, I. E., Di Virgilio, A. L., Porro, V., Muglia, C. I., Naso, L. G., Williams, P. a. M., Bollati-Fogolin, M. & Etcheverry, S. B. 2013. Antitumor properties of a vanadyl(iv) complex with the flavonoid chrysin [VO(chrysin)2EtOH]2 in a human osteosarcoma model: the role of oxidative stress and apoptosis. *Dalton Trans.,* 42**,** 11868-11880.

León, I. E., Díez, P., Etcheverry, S. B. & Fuentes, M. 2016. Deciphering the effect of an oxovanadium(iv) complex with the flavonoid chrysin (VOChrys) on intracellular cell signalling pathways in an osteosarcoma cell line†. *Metallomics,* 8**,** 739-749.

Levina, A., Crans, D. C. & Lay, P. A. 2017. Speciation of metal drugs, supplements and toxins in media and bodily fluids controls in vitro activities. *Coord. Chem. Rev.,* 352**,** 473-498.

Levina, A., Crans, D. C. & Lay, P. A. 2022. Advantageous Reactivity of Unstable Metal Complexes: Potential Applications of Metal-Based Anticancer Drugs for Intratumoral Injections. *Pharmaceutics,* 14**,** 790.

Levina, A., Pires Vieira, A., Wijetunga, A., Kaur, R., Koehn, J. T., Crans, D. C. & Lay, P. A. 2020. A Short-Lived but Highly Cytotoxic Vanadium(V) Complex as a Potential Drug Lead for Brain Cancer Treatment by Intratumoral Injections. *Angew. Chem., Int. Ed.,* 59**,** 15834-15838.

Li, Y.-T., Zhu, C.-Y., Wu, Z.-Y., Jiang, M. & Yan, C.-W. 2010. Synthesis, crystal structures and anticancer activities of two decavanadate compounds. *Transition Metal Chem.,* 35**,** 597-603.

Likidlilid, A., Patchanans, N., Peerapatdit, T. & Sriratanasathavorn, C. 2010. Lipid peroxidation and antioxidant enzyme activities in erythrocytes of type 2 diabetic patients. *J. Med. Assoc. Thai.,* 93**,** 682-93.

Lima, L. M. A., Da Silva, A. K. J. P. F., Batista, E. K., Postal, K., Kostenkova, K., Fenton, A., Crans, D. C., Silva, W. E., Belian, M. F. & Lira, E. C. 2023. The antihyperglycemic and hypolipidemic activities of a sulfur-oxidovanadium(IV) complex. *J. Inorg. Bioch.,* 241**,** 112127.

Lima, L. M. A., Murakami, H., Gaebler, D. J., Silva, W. E., Belian, M. F., Lira, E. C. & Crans, D. C. 2021. Acute Toxicity Evaluation of Non-Innocent Oxidovanadium(V) Schiff Base Complex. *Inorganics,* 9**,** 42.

Liu, X.-C., Strodl, E., Huang, L.-H., Hu, B.-J. & Chen, W.-Q. 2022. Effect of Prenatal Exposure to Household Air Pollution from Multiple Sources on Risk of Preterm Birth. *Atmosphere,* 13**,** 2022.

Lu, L.-P., Liu, J.-H., Cen, S.-H., Jiang, Y.-L. & Hu, G.-Q. 2019a. Discovery of vanadium complexes bearing tridentate schiff base ligands as novel LSD1 inhibitors. *Bioorg. Med. Chem. Lett.,* 29**,** 681-683.

Lu, L.-P., Suo, F.-Z., Feng, Y.-L., Song, L.-L., Li, Y., Li, Y.-J. & Wang, K.-T. 2019b. Synthesis and biological evaluation of vanadium complexes as novel anti-tumor agents. *Eur. J. Med. Chem.,* 176**,** 1-10.

Mahanty, S., Raghav, D. & Rathinasamy, K. 2021. Vanadocene dichloride induces apoptosis in HeLa cells through depolymerization of microtubules and inhibition of Eg5. *JBIC, J. Biol. Inorg. Chem.,* 26**,** 511-531.

Martínez Medina, J. J., Naso, L. G., Pérez, A. L., Rizzi, A., Okulik, N. B., Ferrer, E. G. & Williams, P. a. M. 2017. Apigenin oxidovanadium(IV) cation interactions. Synthesis, spectral, bovine serum albumin binding, antioxidant and anticancer studies. *J. Photochem. Photobiol., A,* 344**,** 84-100.

Mcausland, T. M., Van Vloten, J. P., Santry, L. A., Guilleman, M. M., Rghei, A. D., Ferreira, E. M., Ingrao, J. C., Arulanandam, R., Major, P. P., Susta, L., Karimi, K., Diallo, J.-S., Bridle, B. W. & Wootton, S. K. 2021. Combining vanadyl sulfate with Newcastle disease virus potentiates rapid innate immune-mediated regression with curative potential in murine cancer models. *Mol. Ther.--Oncolytics,* 20**,** 306-324.

Mclauchlan, C. C., Peters, B. J., Willsky, G. R. & Crans, D. C. 2015. Vanadium–phosphatase complexes: Phosphatase inhibitors favor the trigonal bipyramidal transition state geometries. *Coord. Chem. Rev.,* 301-302**,** 163-199.

Mehdi, M. Z. & Srivastava, A. K. 2005. Organo-vanadium compounds are potent activators of the protein kinase B signaling pathway and protein tyrosine phosphorylation: Mechanism of insulinomimesis. *Arch. Biochem. Biophys.,* 440**,** 158-164.

Mokhtari, P. & Mohammadnezhad, G. 2022. Anti-cancer properties and catalytic oxidation of sulfides based on vanadium(V) complexes of unprotected sugar-based Schiff-base ligands. *Polyhedron,* 215**,** 115655.

Murakami, H. A., Uslan, C., Haase, A. A., Koehn, J. T., Vieira, A. P., Gaebler, D. J., Hagan, J., Beuning, C. N., Proschogo, N., Levina, A., Lay, P. A. & Crans, D. C. 2022. Vanadium Chloro-Substituted Schiff Base Catecholate Complexes are Reducible, Lipophilic, Water Stable, and Have Anticancer Activities. *Inorg. Chem.,* 61**,** 20757-20773.

Naso, L., Martínez, V. R., Lezama, L., Salado, C., Valcarcel, M., Ferrer, E. G. & Williams, P. a. M. 2016. Antioxidant, anticancer activities and mechanistic studies of the flavone glycoside diosmin and its oxidovanadium(IV) complex. Interactions with bovine serum albumin. *Bioorg. Med. Chem. Lett.,* 24**,** 4108-4119.

Naso, L. G., Lezama, L., Rojo, T., Etcheverry, S. B., Valcarcel, M., Roura, M., Salado, C., Ferrer, E. G. & Williams, P. a. M. 2013. Biological evaluation of morin and its new oxovanadium(IV) complex as antio-xidant and specific anti-cancer agents. *Chem.-Biol. Interact.,* 206**,** 289-301.

Nie, Y., Zhang, W., Xiao, W., Zeng, W., Chen, T., Huang, W., Wu, X., Kang, Y., Dong, J., Luo, W. & Ji, X. 2022. Novel biodegradable two-dimensional vanadene augmented photoelectro-fenton process for cancer catalytic therapy. *Biomaterials,* 289**,** 121791.

Noriega, L., Castro, M. E., Perez-Aguilar, J. M., Caballero, N. A., Sanchez-Gaytan, B. L., González-Vergara, E. & Melendez, F. J. 2020. Oxidovanadium(V) complexes as promising anticancer photosensitizers. *J. Inorg. Biochem.,* 203**,** 110862.

Nunes, G. G., Bonatto, A. C., De Albuquerque, C. G., Barison, A., Ribeiro, R. R., Back, D. F., Andrade, A. V. C., De Sá, E. L., Pedrosa, F. D. O., Soares, J. F. & De Souza, E. M. 2012. Synthesis, characterization and chemoprotective activity of polyoxovanadates against DNA alkylation. *J. Inorg. Biochem.,* 108**,** 36-46.

Nunes, P., Correia, I., Cavaco, I., Marques, F., Pinheiro, T., Avecilla, F. & Pessoa, J. C. 2021. Therapeutic potential of vanadium complexes with 1,10-phenanthroline ligands, quo vadis? Fate of complexes in cell media and cancer cells. *J. Inorg. Biochem.,* 217**,** 111350.

Nwagwu, C. D., Immidisetti, A. V., Jiang, M. Y., Adeagbo, O., Adamson, D. C. & Carbonell, A.-M. 2021. Convection Enhanced Delivery in the Setting of High-Grade Gliomas. *Pharmaceutics,* 13**,** 561.

Panchal, S. K., Wanyonyi, S. & Brown, L. 2017. Selenium, Vanadium, and Chromium as Micronutrients to Improve Metabolic Syndrome. *Curr. Hypertens. Rep.,* 19**,** 10.

Pellei, M., Del Bello, F., Porchia, M. & Santini, C. 2021. Zinc coordination complexes as anticancer agents. *Coord. Chem. Rev.,* 445**,** 214088.

Pessoa, J. C., Etcheverry, S. & Gambino, D. 2015. Vanadium compounds in medicine. *Coord. Chem. Rev.,* 301-302**,** 24-48.

Pessoa, J. C., Santos, M. F. A., Correia, I., Sanna, D., Sciortino, G. & Garribba, E. 2021. Binding of vanadium ions and complexes to proteins and enzymes in aqueous solution. *Coord. Chem. Rev.,* 449**,** 214192.

Rehder, D. 2012. The potentiality of vanadium in medicinal applications. *Future Med. Chem.,* 4**,** 1823-1837.

Rehder, D. 2013. Vanadium. Its Role for Humans. *In:* SIGEL, A., SIGEL, H. & SIGEL, R. K. O. (eds.) *Interrelations between Essential Metal Ions and Human Diseases.* Dordrecht: Springer Netherlands.

Rendra, E., Riabov, V., Mossel, D. M., Sevastyanova, T., Harmsen, M. C. & Kzhyshkowska, J. 2019. Reactive oxygen species (ROS) in macrophage activation and function in diabetes. *Immunobiology,* 224**,** 242-253.

Ribeiro, N., Galvão, A. M., Gomes, C. S. B., Ramos, H., Pinheiro, R., Saraiva, L., Ntungwe, E., Isca, V., Rijo, P., Cavaco, I., Ramilo-Gomes, F., Guedes, R. C., Pessoa, J. C. & Correia, I. 2019. Naphthoylhydrazones: coordination to metal ions and biological screening. *New J. Chem.,* 43**,** 17801-17818.

Rodríguez, M. R., Balsa, L. M., Del Plá, J., García-Tojal, J., Pis-Diez, R., Parajón-Costa, B. S., León, I. E. & González-Baró, A. C. 2019. Synthesis, characterization, DFT calculations and anticancer activity of a new oxidovanadium(iv) complex with a ligand derived from o-vanillin and thiophene. *New J. Chem.,* 43**,** 11784-11794.

Roy, S., Majumdar, S., Singh, A. K., Ghosh, B., Ghosh, N., Manna, S., Chakraborty, T. & Mallick, S. 2015a. Synthesis, Characterization, Antioxidant Status, and Toxicity Study of Vanadium–Rutin Complex in Balb/c Mice. *Biol. Trace Elem. Res.,* 166**,** 183-200.

Roy, S., Mallick, S., Chakraborty, T., Ghosh, N., Singh, A. K., Manna, S. & Majumdar, S. 2015b. Synthesis, characterisation and antioxidant activity of luteolin–vanadium(II) complex. *Food Chem.,* 173**,** 1172-1178.

Rudbari, H. A., Saadati, A., Aryaeifar, M., Correia, I., Marques, F., Blacque, O. & Micale, N. 2021. Cytotoxic oxidovanadium(IV) complexes of tridentate halogen-substituted Schiff bases: First dinuclear V(IV) complexes with O → VIV = O → VIV = O core. *Bioorg. Med. Chem. Lett.,* 49**,** 128285.

Rusanov, D. A., Zou, J. & Babak, M. V. 2022. Biological Properties of Transition Metal Complexes with Metformin and Its Analogues. *Pharmaceuticals,* 15**,** 453.

Sahu, G., Patra, S. A., Pattanayak, P. D., Kaminsky, W. & Dinda, R. 2023. LVVO-Ethyl Maltol-Based Metallodrugs (L2– = Tridentate ONO Ligands): Hydrophobicity, Hydrolytic Stability, and Cytotoxicity via ROS-Mediated Apoptosis. *Inorg. Chem.,* 62**,** 6722-6739.

Sahu, G., Tiekink, E. R. T. & Dinda, R. 2021. Study of DNA Interaction and Cytotoxicity Activity of Oxidovanadium(V) Complexes with ONO Donor Schiff Base Ligands. *Inorganics,* 9**,** 66.

Sakurai, H. 2002. A New Concept: The Use of Vanadium Complexes in the Treatment of Diabetes Mellitus. *The Chemical Record,* 2**,** 237-248.

Samart, N., Althumairy, D., Zhang, D., Roess, D. A. & Crans, D. C. 2020. Initiation of a novel mode of membrane signaling: Vanadium facilitated signal transduction. *Coord. Chem. Rev.,* 416**,** 213286.

Samart, N., Arhouma, Z., Kumar, S., Murakami, H. A., Crick, D. C. & Crans, D. C. 2018. Decavanadate Inhibits Mycobacterial Growth More Potently Than Other Oxovanadates. *Front. Chem.,* 6.

Sanasam, B., Raza, M. K., Musib, D., Pal, M., Pal, M. & Roy, M. 2020. Photodynamic Applications of New Imidazo[4,5-f][1,10]phenanthroline Oxidovanadium(IV) Complexes: Synthesis, Photochemical, and Cytotoxic Evaluation. *ChemistrySelect,* 5**,** 13824-13830.

Sánchez-Lara, E., Treviño, S., Sánchez-Gaytán, B. L., Sánchez-Mora, E., Eugenia Castro, M., Meléndez-Bustamante, F. J., Méndez-Rojas, M. A. & González-Vergara, E. 2018. Decavanadate Salts of Cytosine and Metformin: A Combined Experimental-Theoretical Study of Potential Metallodrugs Against Diabetes and Cancer. *Front. Chem.,* 6.

Sasmal, P. K., Patra, A. K., Nethaji, M. & Chakravarty, A. R. 2007. DNA Cleavage by New Oxovanadium(IV) Complexes of N-Salicylidene α-Amino Acids and Phenanthroline Bases in the Photodynamic Therapy Window. *Inorg. Chem.,* 46**,** 11112-11121.

Scalese, G., Arhouma, Z., Kostenkova, K., Pérez-Díaz, L., Crick, D. C., Gambino, D. & Crans, D. C. 2022a. Do bioactive 8-hydroxyquinolines oxidovanadium(IV) and (V) complexes inhibit the growth of M. smegmatis? *J. Inorg. Biochem.,* 237**,** 111984.

Scalese, G., Kostenkova, K., Crans, D. C. & Gambino, D. 2022b. Metallomics and other omics approaches in antiparasitic metal-based drug research. *Curr. Opin. Chem. Biol.,* 67**,** 102127.

Scior, T., Abdallah, H. H., Mustafa, S. F. Z., Guevara-García, J. A. & Rehder, D. 2021. Are vanadium complexes druggable against the main protease Mpro of SARS-CoV-2? – A computational approach. *Inorg. Chim. Acta,* 519**,** 120287.

Scior, T., Guevara-Garcia, A. J., Do, Q.-T., Bernard, P. & Laufer, S. 2016. Why Antidiabetic Vanadium Complexes are Not in the Pipeline of “Big Pharma” Drug Research? A Critical Review. *Curr. Med. Chem.,* 23**,** 2874-2891.

Selman, M., Rousso, C., Bergeron, A., Son, H. H., Krishnan, R., El-Sayes, N. A., Varette, O., Chen, A., Le Boeuf, F., Tzelepis, F., Bell, J. C., Crans, D. C. & Diallo, J.-S. 2018. Multi-modal Potentiation of Oncolytic Virotherapy by Vanadium Compounds. *Mol. Ther.,* 26**,** 56-69.

Selvaraj, S. & Krishnan, U. M. 2021. Vanadium–Flavonoid Complexes: A Promising Class of Molecules for Therapeutic Applications. *J. Med. Chem.,* 64**,** 12435-12452.

Semiz, S. 2022. Vanadium as potential therapeutic agent for COVID-19: A focus on its antiviral, antiinflamatory, and antihyperglycemic effects. *J. Trace Elem. Med. Biol.,* 69**,** 126887.

Shaik, A., Kondaparthy, V., Aveli, R., Vemulapalli, L. & Manwal, D. D. 2022. Vanadium metal complexes' inhibition studies on enzyme PTP-1B and antidiabetic activity studies on Wistar rats. *Appl. Organomet. Chem.,* 36**,** e6710.

Sharfalddin, A. A., Al-Younis, I. M., Mohammed, H. A., Dhahri, M., Mouffouk, F., Abu Ali, H., Anwar, M. J., Qureshi, K. A., Hussien, M. A., Alghrably, M., Jaremko, M., Alasmael, N., Lachowicz, J. I. & Emwas, A.-H. 2022. Therapeutic Properties of Vanadium Complexes. *Inorganics,* 10**,** 244.

Shaw, C. A., Li, D. & Tomljenovic, L. 2014. Are there negative CNS impacts of aluminum adjuvants used in vaccines and immunotherapy? *Immunotherapy,* 6**,** 1055-1071.

Shi, X. L. & Dalal, N. S. 1993. Vanadate-Mediated Hydroxyl Radical Generation from Superoxide Radical in the Presence of NADH: Haber-Weiss vs Fenton Mechanism. *Arch. Biochem. Biophys.,* 307**,** 336-341.

Soares, S. S., Martins, H., Duarte, R. O., Moura, J. J. G., Coucelo, J., Gutiérrez-Merino, C. & Aureliano, M. 2007. Vanadium distribution, lipid peroxidation and oxidative stress markers upon decavanadate in vivo administration. *J. Inorg. Biochem.,* 101**,** 80-88.

Taso, O. V., Philippou, A., Moustogiannis, A., Zevolis, E. & Koutsilieris, M. 2019. Lipid peroxidation products and their role in neurodegenerative diseases. *Annals of Research Hospitals,* 3.

Thompson, K. H., Lichter, J., Lebel, C., Scaife, M. C., Mcneill, J. H. & Orvig, C. 2009. Vanadium treatment of type 2 diabetes: A view to the future. *J. Inorg. Biochem.,* 103**,** 554-558.

Thompson, K. H. & Orvig, C. 2006. Vanadium in diabetes: 100 years from Phase 0 to Phase I. *J. Inorg. Biochem.,* 100**,** 1925-1935.

Tian, Y., Qi, H., Wang, G., Li, L. & Zhou, D. 2021. Anticancer effect of sodium metavanadate on murine breast cancer both in vitro and in vivo. *BioMetals,* 34**,** 557-571.

Treviño, S., Díaz, A., Sánchez-Lara, E., Sanchez-Gaytan, B. L., Perez-Aguilar, J. M. & González-Vergara, E. 2019. Vanadium in Biological Action: Chemical, Pharmacological Aspects, and Metabolic Implications in Diabetes Mellitus. *Biol. Trace Elem. Res.,* 188**,** 68-98.

Treviño, S. & González-Vergara, E. 2019. Metformin-decavanadate treatment ameliorates hyperglycemia and redox balance of the liver and muscle in a rat model of alloxan-induced diabetes. *New J. Chem.,* 43**,** 17850-17862.

Treviño, S., Velázquez-Vázquez, D., Sánchez-Lara, E., Diaz-Fonseca, A., Flores-Hernandez, J. Á., Pérez-Benítez, A., Brambila-Colombres, E. & González-Vergara, E. 2016. Metforminium Decavanadate as a Potential Metallopharmaceutical Drug for the Treatment of Diabetes Mellitus. *Oxid. Med. Cell. Longevity,* 2016**,** 6058705.

Valko, M., Morris, H. & Cronin, T. D. M. 2005. Metals, Toxicity and Oxidative Stress. *Curr. Med. Chem.,* 12**,** 1161-1208.

Valko, M., Rhodes, C. J., Moncol, J., Izakovic, M. & Mazur, M. 2006. Free radicals, metals and antioxidants in oxidative stress-induced cancer. *Chem.-Biol. Interact.,* 160**,** 1-40.

Van Cleave, C. & Crans, D. C. 2019. The First-Row Transition Metals in the Periodic Table of Medicine. *Inorganics,* 7**,** 111.

Vlasiou, M. C. & Pafiti, K. S. 2021. Cell Arrest and Apoptosis Induced by the Next Generation of Vanadium Based Drugs: Action Mechanism to Structure Relation and Future Perspectives. *Anti-Cancer Agents Med. Chem.,* 21**,** 2111-2116.

Wilk, A., Wiszniewska, B., Szypulska-Koziarska, D., Kaczmarek, P., Romanowski, M., Różański, J., Słojewski, M., Ciechanowski, K., Marchelek-Myśliwiec, M. & Kalisińska, E. 2017. The Concentration of Vanadium in Pathologically Altered Human Kidneys. *Biol. Trace Elem. Res.,* 180**,** 1-5.

Willsky, G. R., Chi, L.-H., Godzala, M., Kostyniak, P. J., Smee, J. J., Trujillo, A. M., Alfano, J. A., Ding, W., Hu, Z. & Crans, D. C. 2011. Anti-diabetic effects of a series of vanadium dipicolinate complexes in rats with streptozotocin-induced diabetes. *Coord. Chem. Rev.,* 255**,** 2258-2269.

Willsky, G. R., Halvorsen, K., Godzala Iii, M. E., Chi, L.-H., Most, M. J., Kaszynski, P., Crans, D. C., Goldfine, A. B. & Kostyniak, P. J. 2013. Coordination chemistry may explain pharmacokinetics and clinical response of vanadyl sulfate in type 2 diabetic patients. *Metallomics,* 5**,** 1491-1502.

Winter, P. W., Al-Qatati, A., Wolf-Ringwall, A. L., Schoeberl, S., Chatterjee, P. B., Barisas, B. G., Roess, D. A. & Crans, D. C. 2012. The anti-diabetic bis(maltolato)oxovanadium(iv) decreases lipid order while increasing insulin receptor localization in membrane microdomains. *Dalton Trans.,* 41**,** 6419-6430.

Wong, B., Bergeron, A., Alluqmani, N., Maznyi, G., Chen, A., Arulanandam, R. & Diallo, J.-S. 2022. Dependency of EGFR activation in vanadium-based sensitization to oncolytic virotherapy. *Mol. Ther. - Oncolytics,* 25**,** 146-159.

Wu, J.-X., Hong, Y.-H. & Yang, X.-G. 2016. Bis(acetylacetonato)-oxidovanadium(IV) and sodium metavanadate inhibit cell proliferation via ROS-induced sustained MAPK/ERK activation but with elevated AKT activity in human pancreatic cancer AsPC-1 cells. *JBIC, J. Biol. Inorg. Chem.,* 21**,** 919-929.

Yanardag, R. & Tunali, S. 2006. Vanadyl Sulfate Administration Protects the Streptozotocin-Induced Oxidative Damage to Brain Tissue in Rats. *Mol. Cell. Biochem.,* 286**,** 153-159.

Yang, X.-G., Yang, X.-D., Yuan, L., Wang, K. & Crans, D. C. 2004. The Permeability and Cytotoxicity of Insulin-Mimetic Vanadium Compounds. *Pharm. Res.,* 21**,** 1026-1033.

Zhang, Z., Leonard, S. S., Huang, C., Vallyathan, V., Castranova, V. & Shi, X. 2003. Role of reactive oxygen species and MAPKs in vanadate-induced G2/M phase arrest. *Free Radical Biol. Med.,* 34**,** 1333-1342.

Chapter 2 Vanadium(V) pyridine-containing Schiff base catecholate complexes are novel lipophilic, redox-active and selectively cytotoxic in glioblastoma (T98g) cells

2.1 Introduction

Aggressive cancers that include brain and pancreatic cancers are difficult to treat and continue to pose a challenge to develop novel antitumor therapies (Hirooka et al., 2018, Mohan et al., 2018, Newman et al., 2020). Glioblastoma is by far the most common and aggressive form of glioma (brain tumor) with an average incidence of three cases per 100,000 individuals (Fakhoury, 2016). Glioblastoma (previously known as glioblastoma multiforme, GBM) is characterized by a highly proliferative population of cells that invade surrounding tissue and that frequently recur after surgical intervention and chemotherapy (Fakhoury, 2016). Traditional methods to treat glioblastoma include surgical intervention and/or chemotherapy. Due to the very high rate of recurring, new treatment methods for glioblastoma are of high interest. One of the main challenges for glioblastoma drug development is the design of drug candidates that can cross the blood brain barrier (BBB), which normally requires them to be small and lipophilic (Fakhoury, 2016, Thakur et al., 2022). A promising approach to circumvent the impediment of the BBB is to use intratumoral injections of highly cytotoxic or immunomodulating drugs directly into the inoperable tumor, which represents the next generation of glioblastoma treatments. Such intratumoral injections are currently in Phase I and II human clinical trials (Levina et al., 2022, Hamid et al., 2019) for other drugs and injections of T-Vec, a drug used to treat advanced melanoma, are currently studied in the clinic (Levina et al., 2022, Hamid et al., 2019). Additionally, intratumoral injections of vanadyl sulfate and Newcastle disease virus have been reported recently and shown to be highly effective in murine cancer models (McAusland et al., 2021).

Recently, intratumoral injections of cytotoxic, non-innocent vanadium(V) catecholates with hydrophobic substituents have been proposed as potential drugs for difficult-to-treat cancers (Crans et al., 2019b, Levina et al., 2020, Murakami et al., 2022). Vanadium is a well-known and studied first row transition metal with reported anticancer, antidiabetic, antimutagenic, antituberculosis and antiviral properties (Pessoa et al., 2015, Pessoa and Correia, 2019, Bergeron et al., 2019, Scalese et al., 2017, Samart et al., 2018, Gourdon et al., 2022, Barr-David et al., 1992, Levina and Lay, 2017). The beneficial properties are attributed to vanadate, a six-coordinate species and a structural and electronic phosphate analog, which can regulate phosphatases, kinases and mammalian signal transduction (Crans et al., 2017, Crans, 2015, Kostenkova et al., 2023, Levina and Lay, 2017, Mulyani et al., 2004, Safitri et al., 2017). Vanadium(V) catecholate complexes have rather unique properties compared to the reported vanadium Schiff base complexes (Lu et al., 2019, Noriega et al., 2020). Their distinct feature is the short hydrolytic stability under physiological conditions, which enables them to remain intact during cellular uptake in vitro and the potential to cause localized systemic toxicity in cancerous tissues. By contrast, upon hydrolysis the decomposition products that diffuse away would not cause systemic toxicity and indeed can be neuroprotective (Crans et al., 2019b, Levina et al., 2020, Murakami et al., 2022). The lack of systemic toxicity on the hydrolysis products has been confirmed in vivo in an animal model (Lima et al., 2021). The design of V(V)-based drugs has been inspired by the early work by the Pecoraro group in which the structures and spectroscopic signatures of the catecholates of different parent Schiff base and substituted systems,(Cornman et al., 1992b, Cornman et al., 1992a) and the stability and biological activity of the $[V(dtb)_n]^-$ and its decomposition product $[VO(dtb)_2]^-$ (dtb = 3,5-di-*tert*-butylcatecholato(2-)) studied by the Lay group (Griffin et al., 2019). In the catecholate complexes, Schiff base ligands are used to stabilize the vanadium center in the vanadium(V) oxidation state (Cornman et al., 1992a). The lead analog [VO(HSHED)(DTB)] (HSHED = *N*-(salicylideneaminato)-*N*'-(2-hydroxyethyl)ethane-1,2-diamine) was 12-fold more cytotoxic than cisplatin in T98g (glioblastoma) cells. It is also highly cytotoxic in

A549 (lung), PANC-1 (pancreatic) and SW1353 (bone chondrosarcoma) cell lines,(Crans et al., 2019b) and non-toxic in normal cells and mice (Lima et al., 2021, Levina et al., 2022). The stability and superior cytotoxicity of the lead analog are attributed to the hydrophobic *tert*-butyl substituents on the catecholate ligand, which increased cell permeability and provided steric effects that increased the overall stability to hydrolysis (Crans et al., 2019b, Levina et al., 2020). Additionally, the HSHED Schiff base hydrolyzes into non-toxic decomposition side products under physiological conditions. Another promising agent for intratumoral injections, [VO(Cl-HSHED)(DTB)] Cl-HSHED = *N*-(5-chlorosalicylideneaminato)-*N*'-(2- hydroxyethyl)ethane-1,2-diamine) has been reported recently. The chloro substituent on the Schiff base of parent complex increases hydrophobicity and tripled the half-life for hydrolysis under physiological conditions, making the [VO(Cl-HSHED)(DTB)] complex another promising agent for intratumoral injections (Murakami et al., 2022).

The [VO(HSHED)(DTB)] and [VO(Cl-HSHED)(DTB)] complexes have complex dynamic isomer speciation with up to four geometric isomers in solution (Murakami et al., 2022). This makes it impossible to determine which isomer(s) is(are) responsible for the high cytotoxicity and have the most influence on hydrolytic stability. Thus, we have investigated novel vanadium(V) catecholates with aromatic Schiff bases to limit the potential number of geometric isomers to two depending on the coordination of the catecholate ligand. In the following study, we report two new series of vanadium(V) catecholate complexes with pyridine-containing Schiff bases, [VO(SALIEP)X] and [VO(Cl-SALIEP)X], (SALIEP = *N*-(salicydeneaminato)-2-(2-aminoethylpyridine); Cl-SALIEP = *N*-(5-chlorosalicydeneaminato)-2-(2-aminoethylpyridine); X = a catecholato(2-); **Figure 2.1**). The compound design was derived from the previously reported [VO(HSHED)(DTB)] and [VO(Cl-HSHED)(DTB)] analogs (**Figure 2.1**) (Cornman et al., 1992b, Crans et al., 2019b). Interestingly, a structurally similar Schiff base with a methyl linker

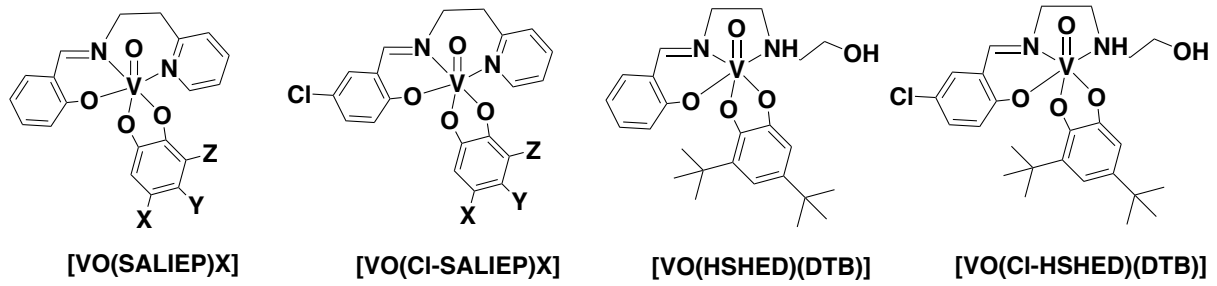

Figure. 2.1. General structures of the [VO(SALIEP)X] and [VO(Cl-SALIEP)X] analogs where X represents a catecholate ligand, and the reported analogs with best anticancer properties, [VO(HSHED)(DTB)] and [VO(Cl-HSHED)(DTB)]. In the schematic above, protons labeled X, Y, and Z stand for the following: X = H or *tert*-butyl, Y = H or *tert*-butyl, Z = H or *tert*-butyl.

abbreviated [VO(SALIMP)] = *N*-(salicydeneaminato)-2-(2-aminoethylpyridine) has been reported previously (Tandon et al., 2000). We have chosen the complexes with pyridine-containing Schiff bases to see how the lack of H-bonding on the Schiff base affects hydrolytic stability and cytotoxicity of the complexes. The pyridine moiety also improves permeability through membranes and increases metabolic stability of many pharmaceuticals (Richaud et al., 2011, Ling et al., 2021). The structure of the $[V(O)_2(SALIEP)]$ complex was first reported by the Pessoa group (Tandon et al., 2000, Maurya et al., 2009). This dioxido complex has catalytic properties in the hydroamination of styrene and vinyl pyridine with amines (aniline and diethylamine) where the anti-Markovnikov hydroamination product is favored (Maurya et al., 2009). The $[VO_2(SALIEP)]$ complex, however, has not been tested in any biological systems or used for the preparation of any biologically relevant vanadium complexes.

Vanadium(V) catecholate complexes are redox-active, and the electrochemical properties of the VOHSHED and VOCl-HSHED complexes have been reported previously (Manganaro et al., 2022, Li et al., 1988, Chatterjee et al., 2011). Solid tumors generally have highly reducing environments due to the presence of intracellular reductants, mainly glutathione and ascorbate and hypoxic regions within the tumor (Areias et al., 2016, Harfield et al., 2012). Thus, studying the redox chemistry of vanadium(V) catecholates is of interest, particularly since the cytotoxicity

of the complexes can result, in part, from ROS activity from the ROS formation (Milsmann et al., 2006, Crans et al., 2019a, Shul'pin et al., 2019, More et al., 2019, Crans, 2015, Thompson and Orvig, 2006, Treviño and Diaz, 2020, Arhouma et al., 2022). Little is known about the effects of the Schiff base structure and the substitution pattern on the catecholate ligand on the observed redox properties, and establishing those relationships is also of interest. The VOHSHED and VOCl-HSHED complexes show reversible couples in organic solvents (Murakami et al., 2022). The stability of the reduced V(IV) species is attributed to the bulky hydrophobic substituents on the catecholate ligand and the stability of the five-membered ring core between NN coordination sites of the Schiff base, the ethyl arm and V center (Murakami et al., 2022). This may not be the case for the VOSALIEP and VOCl-SALIEP complexes, since the pyridine ring on the Schiff base results in a six-membered core between NN coordination sites of the Schiff base, the ethyl arm and V center. In this work, we have further explored the impact of different structural motifs on the observed redox chemistry of vanadium(V) catecholates.

Herein, we report the syntheses and spectroscopic characterization of two vanadium(V) catecholate series abbreviated [VO(SALIEP)X] and [VO(Cl-SALIEP)X] (X = catecholato(2-), 4-*tert*-butylcatecholato(2-) and di-*tert*-butyl-catecholato(2-). Specifically, we examined whether: 1) the removal of the H bonding on the aromatic Schiff base affected the redox chemistry and the hydrolytic stability; 2) the increased hydrophobicity due to the pyridine ring improved cellular uptake and cytotoxicity; and 3) different structural motifs impacted redox chemistry of the complexes. Antiproliferative properties of the [VO(SALIEP)X] and [VO(Cl-SALIEP)X] complexes were also studied in T98g (human glioblastoma) and HFF-1 (human normal skin fibroblasts) cell lines. We have established the relationships between the structure, spectroscopic properties and observed cytotoxicity, and compared them with those of the previously reported [VO(HSHED)X] and [VO(Cl-HSHED)X] analogs.

2.2 Materials and Methods

2.2.1 General Materials

Salicylaldehyde (98%), 5-chlorosalicylaldehyde (98%), [$VO(acac)_2$] (acac = acetylacetonatonato(1-)) (98%) and aqueous H_2O_2 (30%) were purchased from Sigma Aldrich and used as received. 2-(2-Aminoethyl)pyridine (98%) was purchased from Oakwood Chemical and used as received. Catechol (≥99.0%), 4-*tert*-butyl-catechol (≥99.0%) and di-*tert*-butyl-catechol (98%) were purchased from Sigma Aldrich and recrystallized from toluene, pentane and petroleum ether, respectively, prior to use. The purity of recrystallized ligands was confirmed by ^{1}H NMR in d_6-DMSO. d_3-Acetonitrile (≥99.8 atom % D) and d_6-DMSO (≥99.9 atom % D) were purchased from Cambridge Isotope Laboratories and used as received. Silver nitrate, ferrocene and tetra-*n*-butylammonium perchlorate (TBAP) were purchased from Merck Millipore for electrochemistry experiments and used as received.

2.2.2 General Methods

All syntheses were carried out under an Ar atmosphere unless noted otherwise.

2.2.3 Synthesis of the [V^VO_2(SALIEP)] precursor

The [$V(O)_2$(SALIEP)] precursor was synthesized by using modified procedures from the literature.(Tandon et al., 2000, Maurya et al., 2009)

Step 1. Synthesis of 2-[[[2-(2-*pyridinyl*)*ethyl*]*imino*]*methyl*]*phenol* (*HSALIEP*)

To 10 mL of absolute EtOH, salicylaldehyde (0.611 g, 5.00 mmol) and 2-(2-aminoethyl)pyridine (0.611 g, 5.00 mmol), were added and then stirred under reflux for about 30 min. The resulting Schiff base was used immediately in the second step to avoid noticeable degradation.

Step 2. Preparation of [V^{IV}O(SALIEP)(acac)] To 25 mL of absolute EtOH, [$V^{IV}O(acac)_2$] (1.33 g, 5.00 mmol) was added and stirred at 60 ^oC to enable the complex to dissolve. Subsequently, this solution was added to the ethanolic Schiff base solution from Step 1, and the resulting reaction mixture was stirred under reflux for 3 h. The resulting red solid was filtered off, washed with 50 mL cold (0 ^oC) diethyl ether and dried *in vacuo*. **Yield 60%.** FT-IR: 3100 (sp^2 C-H stretch), 2916 (sp^3 C-H stretch), 1590-1416 (aromatic C-C and C-N and imine C=N stretches), 1383 (sp^3 C-H bend), 1342 (aromatic C – N stretch), 929 (V=O stretch) cm^{-1}.

Step 3. Preparation of $[V^{V}(O)_2(SALIEP)]$ The **$[V^{IV}O(SALIEP)(acac)]$ complex** (0.391 g, 1.00 mmol) was dissolved in 20 mL of methanol and after the addition of aqueous 30% H_2O_2 (0.2 mL, 2.00 mmol), the solution was exposed to aerial oxidization for 10 min. The resulting yellow solid was filtered, washed with 50 mL cold (0 °C) diethyl ether and dried *in vacuo*. **Yield 59%.** NMR: ^{1}H (d_6-DMSO): 8.52 (d, 1H), 8.34 (s, 1H), 7.66 (t, 1H), 7.46 (t, 1H), 7.33 (d, 1H), 7.22 (t, 1H), 7.18 (d, 1H), 4.04 (t, 2H), 3.32 (t, 2H). ^{1}H (d_3-MeCN): 8.90 (d, 1H), 8.69 (s, 1H), 7.99 (t, 1H), 7.49 (t, 2H), 7.43 (t, 1H), 6.87 (m, 2H), 4.03 (t, 2H), 3.39 (t, 1H), 3.29 (d, 1H). ^{51}V NMR (d_6-DMSO): -507, -539 ppm; (d_3-MeCN): - 511 ppm. FT-IR: 3057 (sp^2 C-H stretch), 1623-1473 (aromatic C-C and C-N and imine C=N stretches), 1305 (aromatic C–N stretch), 917 (V=O stretch), 761 (sp^2 C-H bend, 1,2-disubstituted) cm^{-1}. HRMS (ESI) calc. for $C_{19}H_{20}N_2O_4V$ $[M]^+$ = 391.08572, found 391.08557.

2.2.4 Synthesis of the [VO(SALIEP)(Cat)] complex

To 25.0 mL of degassed methanol, $[V^{V}(O)_2(SALIEP)]$ (0.308 g, 1.00 mmol) was added, followed by the addition of catechol (0.132 g, 1.20 mmol). The reaction mixture was stirred for 20 h at room temperature (~20 °C) under Ar. The resulting product was vacuum filtered, washed with cold (0 °C) diethyl ether (30 mL) and dried under high vacuum for 24 h. Yield: 58%. NMR: ^{1}H (d_3-MeCN, 400 MHz): 8.80 (d, 1H), 8.54 (s, 1H), 7.91 (t, 1H), 7.47 (d, 1H), 7.44 (s, 1H), 7.43 (s, 1H), 7.41 (dd, 1H), 6.78 (t, 1H), 6.69 (d, 2H), 6.45 (d, 1H), 6.04 (d, 1H).; ^{51}V (d_3-MeCN, 105.2 MHz): - 508 ppm (broad). FT-IR: 3060 (sp^2 C-H stretch), 1618-1447 (aromatic C-C and C-N and imine C=N stretches), 1308-1206 (aromatic C – N stretch), 1150 (C–O stretch), 965 (V=O stretch) cm^{-1}. UV/Vis λ_{max} (0.10 mM in MeCN) = 561 nm. HRMS (ESI) calc. for $C_{20}H_{17}N_2O_4V$ $[M+H]^+$ = 401.07007, found 401.07015.

2.2.5 Synthesis of the [VO(SALIEP)(4TB)] complex

To 50.0 mL of degassed methanol, $[V^{V}(O)_2(SALIEP)]$ (0.308 g, 1.00 mmol) was added, followed by the addition of 4-*tert*-butyl-catechol (0.199 g, 1.20 mmol). The reaction mixture was stirred for 20 h at room temperature under Ar. The resulting product was vacuum filtered, washed with cold

(0 °C) diethyl ether (30 mL) and dried under high vacuum for 24 h. Yield: 39%. NMR: ^{1}H (d_3-MeCN, 400 MHz): 8.85 (d, 1H), 8.51 (s, 1H), 7.90 (t, 1H), 7.52 (d, 1H), 7.43 (t, 1H), 7.41 (t, 1H), 6.78 (t, 1H), 6.69 (d, 1H), 6.67 (d, 1H), 6.54 (d, 1H), 6.40 (d, 1H), 6.10 (s, 1H), 4.01 (dd, 2H), 3.52 (dd, 2H) 1.21 (s, 9H); ^{51}V (d_3-MeCN, 105.2 MHz): -511 ppm. FT-IR: 3054 (sp^2 C-H stretch), 2951 (sp^3 C-H stretch), 1621-1451 (aromatic C-C and C-N and imine C=N stretches), 1339 (aromatic C – N stretch), 952.45 (V = O stretch) cm^{-1}. $\boldsymbol{\lambda_{max}}$ (0.10 mM in MeCN) = 551 nm. HRMS (ESI) calc. for $C_{24}H_{25}N_2O_4V$ $[M+H]^+$ = 457.13267, found 457.13274.

2.2.6 Synthesis of the [VO(SALIEP)(DTB)] complex

To 50.0 mL of degassed methanol, [$V^{V}O_2$(SALIEP)] (0.308 g, 1.00 mmol) was added, followed by the addition of di-*tert*-butyl-catechol (0.267 g, 1.20 mmol). The reaction mixture was let stirred for 20 h at room temperature under Ar. The resulting product was vacuum filtered, washed with cold (0 °C) diethyl ether (30 mL) and dried under high vacuum for 24 h. Yield: 58%. NMR: ^{1}H (d_3-MeCN, 400 MHz): 8.98 (d, 1H), 8.50 (d, 1H), 7.90 (q, 1H); 7.46 (t, 1H), 7.42 (d, 1H), 7.40 (d, 1H), 7.38 (d, 1H), 6.75 (m, 1H), 6.65 (m, 1H), 6.46 (s, 1H), 6.03 (s, 1H), 4.07 (m, 2H), 3.55 (m, 1H), 3.42 (m, 1H), 1.40 (s, 6H), 1.27 (s, 3H), 1.21 (s, 6H), 0.98 (s, 3H).; ^{51}V (d_3-MeCN, 105.2 MHz): -511 ppm. FT-IR: 3054 (sp^2 C-H stretch), 2951 (sp^3 C-H stretch), 1618-1446 (aromatic C-C and C-N and imine C=N stretches), 132 (aromatic C – N stretch), 940 (V=O stretch) cm^{-1}. $\boldsymbol{\lambda_{max}}$ (0.10 mM in MeCN) = 555 nm. HRMS (ESI) calc. for $C_{28}H_{33}N_2O_4V$ $[M+H]^+$ = 513.19527, found 513.19520.

2.2.7 Synthesis of the [$V^{V}O_2$ (Cl-SALIEP)] precursor

Step 1. Synthesis of 2-[[[2-(2-*pyridinyl*)*ethyl*]*imino*] *methyl*]chloro*phenol* (*H-ClSALIEP*) To 10 mL of absolute EtOH, 5-chlorosalicylaldehyde (0.783 g, 5.00 mmol) and 2-(2-aminoethyl)pyridine (0.611 g, 5.00 mmol), were added and then stirred under reflux for about 30 min. The ligand was used immediately in the second step to avoid noticeable degradation.

Step 2. Preparation of [$V^{IV}O$(Cl-SALIEP)(acac)] To 25 mL of absolute EtOH, [$V^{IV}O(acac)_2$] (1.33 g, 5.00 mmol) was added and the mixture wasstirred at 60 °C until the complex dissolved. Subsequently, this solution was added to the ethanolic Schiff base solution from Step 1, and the resulting reaction mixture was stirred under reflux for 3 h. The resulting shiny brown solid was filtered off, washed with 50 mL cold (0 °C) diethyl ether, and dried *in vacuo*. **Yield 57%.** FT-IR: 3049 (sp^2 C-H stretch), 2953-2922 (sp^3 C-H stretch), 1586-1463 (aromatic stretch C-C and C-N and imine C=N stretches), 1376 (sp^3 C-H bend), 1308 (aromatic C – N stretch), 1183 (C–O stretch), 929 (V=O stretch), 703 (C–Cl stretch) cm^{-1}. HRMS (ESI) calc. for $C_{19}H_{19}ClN_2O_4V$ $[M]^+$ = 425.04674, found 425.04649.

Step 3. Preparation of [$V^{V}(O)_2$(Cl-SALIEP). [$V^{IV}O$(Cl-SALIEP)(acac)] (0.426 g, 1.00 mmol) was dissolved in 20 mL of methanol and after the addition of aqueous 30% H_2O_2 (0.2 mL, 2.00 mmol), the solution underwent aerial oxidation for 10 min. The resulting brown solid was filtered, washed with 50 mL of cold (0 °C) diethyl ether and dried *in vacuo*. **Yield 75%.** ^{51}V NMR (d_3-MeCN, 10.0 mM): -512 ppm. FT-IR: 3057 (sp^2 C-H stretch), 1626-1485 (aromatic C-C and C-N and imine C=N stretches), 1298 (aromatic C – N stretch), 927 (V=O stretch), 78 (C–Cl stretch) cm^{-1}. HRMS (ESI) calc. for $C_{14}H_{12}ClN_2O_3V$ $[M+H]^+$ = 343.00488, found 343.00487.

2.2.8 Synthesis of the [VO(Cl-SALIEP)(Cat)] complex

To 12.5 mL of degassed methanol, [$V^{V}(O)_2$(Cl-SALIEP)] (0.343 g, 1.00 mmol) was added, followed by the addition of catechol (0.132 g, 1.20 mmol). The reaction mixture was stirred for 20 h at room temperature under Ar. The resulting product was vacuum filtered, washed with cold (0 °C) diethyl ether (30 mL) and dried under high vacuum for 24 h. Yield: 44%. NMR: ^1H (d_3-MeCN, 400 MHz): 8.76 (d, 1H), 8.49 (s, 1H), 7.92 (t, 1H), 7.48 (d, 1H), 7.43 (s, 1H), 7.42 (s, 1H), 7.36 (dd, 1H), 6.69 (d, 2H), 6.43 (d, 1H), 6.03 (d, 1H).; ^{51}V (d_3-MeCN, 105.2 MHz): N/A. ^{51}V (d_6-DMSO, 105.2 MHz): -508 ppm. FT-IR: 3100 (sp^2 C-H stretch), 2958 (sp^3 C-H stretch), 1625-1461 (aromatic C-C and C-N and imine C=N stretches), 1388 (sp^3 C-H bend), 1384 (aromatic C – N

stretch), 921 (V=O stretch), 786 (C–Cl stretch) cm^{-1}. $\boldsymbol{\lambda_{max}}$ (0.10 mM in MeCN) = 555 nm. HRMS (ESI) calc. for $C_{20}H_{16}ClN_2O_4V$ $[M+H]^+$ = 457.01304, found 457.01323.

2.2.9 Synthesis of the [VO(Cl-SALIEP)(4TB)] complex

To 12.5 mL of degassed methanol, $[V^V(O)_2$(Cl-SALIEP)] (0.171 g, 0.500 mmol) was added, followed by the addition of 4-*tert*-butylcatechol (0.100 g, 0.600 mmol). The reaction mixture was stirred for 20 h at room temperature under Ar. The resulting product was vacuum filtered, washed with cold (0 °C) diethyl ether (30 mL) and dried under high vacuum for 24 h. Yield: 57%. NMR: ^{1}H (d_3-MeCN, 400 MHz): 8.81 (d, 1H), 8.46 (s, 1H), 7.91 (t, 1H), 7.47 (t, 1H), 7.42 (d, 1H), 7.41 (s, 1H), 7.36 (d, 1H), 6.67 (d, 1H), 6.50 (s, 1H), 6.40 (d, 1H), 6.09 (s, 1H), 4.04 (dt, 2H), 3.40 (dt, 2H), 1.26 (s, 3H), 1.21 (s, 6H); ^{51}V (d_3-MeCN, 105.2 MHz): -536 ppm. FT-IR: 3100 (sp^2 C-H stretch), 2958 (sp^3 C-H stretch), 1625-1461 (aromatic C-C and C-N and imine C=N stretches), 1388 (sp^3 C-H bend), 1309 (aromatic C – N stretch), 951 (V=O stretch), 786 (C–Cl stretch) cm^{-1}. $\boldsymbol{\lambda_{max}}$ (0.10 mM in MeCN) = 551 nm. HRMS (ESI) calc. for $C_{24}H_{24}ClN_2O_4V$ $[M+H]^+$ = 491.09369, found 491.09322.

2.2.10 Synthesis of the [VO(Cl-SALIEP)(DTB)] complex

To 50.0 mL of degassed methanol, $[V^V(O)_2$(Cl-SALIEP)] (0.343 g, 1.00 mmol) was added, followed by the addition of 3,5-di-*tert*-butylcatechol (0.267 g, 1.20 mmol). The reaction mixture was stirred for 20 h at room temperature under Ar. The resulting product was vacuum filtered, washed with cold (0 °C) diethyl ether (30 mL) and dried under high vacuum for 24 h. Yield: 54%. NMR: ^{1}H (d_3-MeCN, 400 MHz): 8.94 (d, 1H), 8.45 (d, 1H), 7.89 (q, 1H); 7.47 (t, 1H), 7.40 (s, 1H), 7.37 (dd, 1H), 7.33 (dd, 1H), 6.46 (s, 1H), 6.03 (s, 1H), 4.07 (m, 2H), 3.55 (m, 1H), 3.44 (m, 1H), 1.39 (s, 6H), 1.27 (s, 3H), 1.21 (s, 6H), 0.97 (s, 3H). ^{51}V (d_3-MeCN, 105.2 MHz): -531 ppm. FT-IR: 3100 (sp^2 C-H stretch), 2958 (sp^3 C-H stretch), 1625-1461 (aromatic C-C and C-N and imine C=N stretches), 1388 (sp^3 C-H bend), 1384 (aromatic C – N stretch), 923-921 (V=O stretch), 786 (C–Cl stretch) cm^{-1}. $\boldsymbol{\lambda_{max}}$ (0.10 mM in MeCN) = 551 nm. HRMS (ESI) calc. for $C_{28}H_{32}ClN_2O_4V$ $[M+H]^+$ = 547.15629, found 547.15550.

2.2.11 1D NMR Spectroscopy Experiments

The complexes were characterized using ^{51}V NMR spectroscopy recorded on a Bruker NEO400 spectrometer equipped with an automated tuning module operating at 105.2 MHz at an ambient temperature. The ^{51}V NMR spectra were acquired with a spectral window of 800 ppm, 4096 scans, a 90° pulse, an acquisition time of 0.08 s, and a 0.01 s relaxation delay, as reported previously.[ref] 1D ^{51}V NMR studies were referenced against $[V(O)_2(HSHED)]$ at -529 ppm as a standard and reported in reference to $VOCl_3$ (0 ppm).(Murakami et al., 2022, Kostenkova et al., 2021) 1D and 2D ^{1}H NMR studies were carried out in deuterated organic solvents using a Bruker NEO400 spectrometer operating at 400 MHz at an ambient temperature. Chemical shift values (δ) are reported in ppm and referenced against TMS using the internal solvent peaks in ^{1}H NMR spectra (d_3-MeCN, δ at 1.94 ppm; d_6-DMSO, δ at 2.50 ppm) as internal standards. All complexes (10 mM) were dissolved in either d_3-MeCN or d_6-DMSO at 10 mM for spectral comparison. Spectroscopic studies were carried out using solutions of isolated complexes, and both ^{1}H and ^{51}V NMR spectra were recorded on the same samples. 1D samples were run within 30 min. of preparation, and no significant differences were observed in spectra recorded within 24 h.

2.2.12 2D NMR Spectroscopy Experiments

^{1}H-^{1}H gCOSY experiments were carried out on a Bruker NEO400 spectrometer using the following parameters: 8 scans, 13 ppm spectral window, a 2.0 s relaxation delay, a 0.19 s acquisition time and a 12 μs pulse.

^{1}H-^{1}H NOESY experiments were carried out on a Bruker NEO400 spectrometer using the following parameters: 256 scans, 1.5 s relaxation delay, 500 ms mixing time.

1H-^{1}H ROESY experiments were carried out on a Bruker NEO400 spectrometer using the following parameters: 256 scans, 2.0 s relaxation delay, 400 ms mixing time.

2.2.13 EPR Spectroscopy

Instrumentation:

Electron paramagnetic resonance (EPR) spectra were recorded at 298 K using a Bruker X-Band EPR Spectrometer (9.84 GHz). The X-band EPR spectra were recorded in 1 mm quartz capillary tubes that were placed in 4- or 5-mm quartz tubes at ambient temperature. The spectra were referenced to a DPPH external standard (g = 2.0037). The spectra were collected using the following parameters: 16 scans, 1600 G sweep width, 22 dB attenuation, 10 modulation amplitude, 60 s sweep time, 60 s conversion time. The EPR spectra were collected at 0, 1, 2, 6 and 24 h. The g_{iso} and A_{iso} values were calculated using "garlic" simulation in EasySpin (version 5.2.35) open-source MatLab toolbox (version R2022b). The calculations of g_{iso} and A_{iso} values did not involve second-order corrections. The stacked EPR spectra were plotted using OriginLab software (2022 version, Northampton, MA, USA).

Sample preparation: [VO(SALIEP)(CAT)] and [VO(Cl-SALIEP)(CAT)] (10.0 mM) in 2.0 mL of DMSO dried over 3 Å activated molecular sieves for 2 d prior was used to collect the EPR spectra. To check for the presence of semi-quinone radicals,(Reszka and Chignell, 1993) solutions of [VO(SALIEP)(CAT)] and [VO(Cl-SALIEP)(CAT)] (10.0 mM in 2.0 mL of dry DMSO to which 100 μL of 50.0 mM DMSO solution of $Zn(OAc)_2$ was added), EPR spectra were collected at 0, 1, 2, 6 and 24 h.

2.2.14 Cyclic Voltammetry

Instrumentation: Cyclic voltammetry was undertaken using a WaveDriver 40 DC Bipotentiostat/Galvanostat and a Low Volume Three Electrode Cell Basic Kit (AF01CKT1006) purchased from Pine Research Instrumentation (AfterMath v 1.5.9807 data acquisition). The working electrode was a glassy carbon electrode with a 3.0 mm diameter (2.997−2.972 mm) and an area of approximately 9 mm^2, and polished using silica pad wetted with a small amount of DDI water. The software used during was with the *iR* Compensation option turned off, while eL-Chem Viewer and Microsoft Excel were used for post-acquisition processing. All cyclic voltammograms were externally referenced to the ferrocenium/ferrocene ($Fc^{+/0}$ couple. Normal cyclic

voltammograms were recorded at a scan rate of 100 mV s^{-1} and two segments using the following parameters:

ferrocene, initial potential 1.0 V, vertex potential -1.5 V, final potential 1.0 V; [VO(SALIEP)(4TB)], initial potential -0.10 V, vertex potential -1.65 V, final potential -0.10 V; [VO(SALIEP)(DTB)], initial potential -0.45 V, vertex potential -1.65 V, final potential -0.45 V; [VO(Cl-SALIEP)(4TB)], initial potential 0.25 V, vertex potential -1.5 V, final potential 0.25 V; and [VO(Cl-SALIEP)(DTB)], initial potential -0.55 V, vertex potential -1.85 V, final potential -0.55 V.

Sample preparation: Complexes (2.0 mM) or ferrocene (10 mM) were dissolved in 100 mM TBAP in dry acetonitrile solution. A 2.0 mM silver nitrite solution was used to fill a refillable Ag reference electrode. All samples were degassed using Ar for 10 min prior to cyclic voltammogram collection.

2.2.15 Electrospray mass spectrometry (ESI-MS)

Low-resolution ESI-MS data were collected on a Bruker amaZon SL spectrometer, using the following parameters: nebulizer pressure, 27.3 psi; spray voltage, 4.5 kV; capillary temperature, 453 K; N_2 flow rate, 4 L min□1; *m*/*z* range, 100-1000 (alternating positive- and negative-ion modes). Analyzed solutions (5.0 □L) were injected into a flow of MeOH (flow rate, 0.30 mL min^{-1}). Acquired spectra were the averages of 100-200 scans (scan time, 10 ms). Solutions for mass spectrometry were prepared by dissolving ~0.1 mg of complexes in 0.50 mL MeOH (~100 mM V) immediately before the experiments. Simulations of the mass spectra were performed using IsoPro software (version 3.0, M. Senko, Sunnyvale, CA, USA, 1998).

High resolution positive ion ESI-MS was performed on a Bruker Solarix 2XR 7T Fourier transform ion cyclotron resonance mass spectrometer via syringe infusion at 120 □L per hour. The transient length was 2 M and acquired in 2-ω mode and the Fourier transform was performed in adsorption mode. The instrument was externally calibrated from 300-2000 *m*/*z* prior to analysis, and the isotopic patterns were simulated using Bruker Compass Data Analysis 5.0 software.

2.2.16 UV-Vis Spectroscopy experiments

All complexes have been characterized by UV-Vis spectroscopy in 0.10 mM solutions in dry acetonitrile. The hydrolytic stability studies of the DTB analogs have been carried out in 0.10 mM solutions in PBS 1x buffer (pH 7.4) at t = 0 h, 15 min., 30 min., 45 min., 1 h, 2 h, 4 h, 24 h and 48 h. Due to the hydrophobic nature of the complexes, 10.0 mM stocks solutions in acetonitrile were prepared, and then dilute to the 0.10 mM with the buffer solution immediately before recording the spectra..

2.2.17 Cell culture, proliferation and V uptake assays

Pre-sterilized media and sterile plasticware used in cell culture were purchased from Thermo Fisher Scientific Australia. High purity Na_3VO_4 (99.98%, Cat. No. 450243) and $DTBH_2$ (98% Car. No. D45800) for cell experiments were purchased from Merck. The well-established human cancer cell lines: T98g (glioblastoma multiforme, Cat. No. CRL-1690; and HFF-1 (normal human foreskin fibroblasts, Cat. No. SCRC-1041) were purchased from ATCC and used at passages 4-6. The cells were cultured in Advanced DMEM (Thermo Fisher Scientific Cat. No. 12491-015), supplemented with L-glutamine (2.0 mM), antibiotic-antimycotic mixture (100 U mL^{-1} penicillin, 100 mg mL^{-1} streptomycin and 0.25 mg mL^{-1} amphotericin B) and foetal calf serum (FCS; Thermo Fisher Scientific Cat. No. 10100147, heat-inactivated; 2% vol). For proliferation and cytotoxicity experiments, cells were seeded in 96-well plates at an initial density of $(1\text{-}2)\times10^3$ viable cells per well in 0.10 mL medium and left to attach overnight.

Anti-proliferative activities of V(V/IV) complexes and their model decomposition products were measured using the standard MTT assay.(Sylvester, 2011) Freshly prepared stock solutions of V(V/IV) complexes, $DTBH_2$ (all 10 mM in DMSO) and Na_3VO_4 (10 mM in Milli-Q H_2O) were used for cell assays. These solutions were further diluted so that all the cell treatments, including controls, contained 1.0% (vol.) of DMSO (for the treatments that included Na_3VO_4 only, DMSO was added separately into cell culture medium). Stock solutions of the treatment compounds were diluted with fully supplemented cell culture media to the required final concentrations, and the resultant media were either added to the cells within 1 min (fresh solutions), or left in cell culture

incubator (310 K, 5% CO_2) for 24 h prior to the cell treatments (aged solutions). Each treatment included six replicate wells and two background wells that contained the same components except the cells. After the addition of treatment compounds, the plates were incubated for 72 h at 310 K and 5% CO_2, then the treatment medium was removed and MTT reagent (1-(4,5-dimethylthiazol-2-yl)-3,5-diphenylformazan, Merck M5655) was added (1.0 mg mL^{-1} solution in complete medium), and incubation was continued for 4-6 h. After that, the medium was removed, the blue formazan crystals were dissolved in 0.10 mL per well of DMSO, and the absorbance at 600 nm was measured using Victor V3 plate reader. Typically, the treatment compounds were applied in a series of nine two-fold dilutions, starting from 100 μM V, plus the vehicle control. Fitting of the experimental data and calculations of the IC_{50} values were performed using Origin Pro software (2022 version, OriginLab, Northampton, MA, USA).

For V uptake experiments, T98g cells were grown to ~80% confluence in twelve-well plates (three replicates per treatment). Incubations with the treatment compounds (100 μM V; freshly added to fully supplemented medium) were performed for 30 min at 310 K, 5% CO_2. After that, V-containing media were removed, the cell layers were washed twice with phosphate buffered saline (PBS), detached with TrypLE solution (Thermo Fisher Scientific Cat. No. 12605028), pelleted, and washed again with PBS. Detachment and washing of cell pellets were used to remove V that was absorbed on the culture plates and on the cell surface.(Jensen et al., 2011) Cell numbers in each pellet were counted with Countess automatic counter, typical numbers were $(5 \pm 1)\times10^5$ cells/well, cell viability was >95% (Trypan blue staining). Cell pellets were digested with 0.20 mL of 65% HNO_3 (trace pure, Merck 225711) for 3 d at 295 K, then diluted with Milli-Q water to 1.0 mL for ICP-MS analysis. The analysis was performed with a Perkin-Elmer Nexion 350X spectrometer, using a standard V(IV) solution (Choice Analytical, Australia) and ^{193}Ir peak as an internal standard. The measurements were performed in kinetic energy discrimination (KED) mode to

eliminate the interference of $[^{35}Cl^{16}O]^+$ ions with the determination of $^{51}V^+$.(Sarmiento-González et al., 2005) Cellular V concentrations were expressed in atoms V per cell.

For all the cell assays, consistent results were obtained in at least two independent experiments, using different passages of cells and different stock solutions of the treatment compounds.

2.3 Results and Discussion

2.3.1 Design of new vanadium Schiff base complexes

The complex design was inspired by the promising anti-cancer activity of the [VO(HSHED)(DTB)] analog, the lead compound that has been found to be 12-fold more potent than cisplatin (Levina et al., 2020). The synthesis of [VO(HSHED)(DTB)] was first reported by the Pecoraro group in 1992 along with the catecholates containing other Schiff bases (Cornman et al., 1992a, Cornman et al., 2002). The Pessoa group then reported the synthesis and characterization of $[V^V(O)_2(SALIEP)]$ in 2009 as a catalyst for hydroamination of olefins where the anti-Markovnikov product is favored (Tandon et al., 2000, Maurya et al., 2009). Vanadium(V) pyridine-containing Schiff base catecholates, however, have not been previously reported and studied for anticancer applications. We have decided to explore pyridine-containing Schiff base complexes due to their catalytic properties which, consequentially, result in different reactivities that the corresponding HSHED complexes. Our goal has been to investigate how the removal of the hydrogen bond on the Schiff base affects anticancer properties of the two series of catecholato V(V) complexes (**Figure 2.1**).

2.3.2 Syntheses of the complexes

The $[V^{V}(O)_2(SALIEP)]$ precursor was synthesized by using a modified procedure from the literature (**Figure 2.2**) (Maurya et al., 2009, Tandon et al., 2000). The Schiff base was first formed

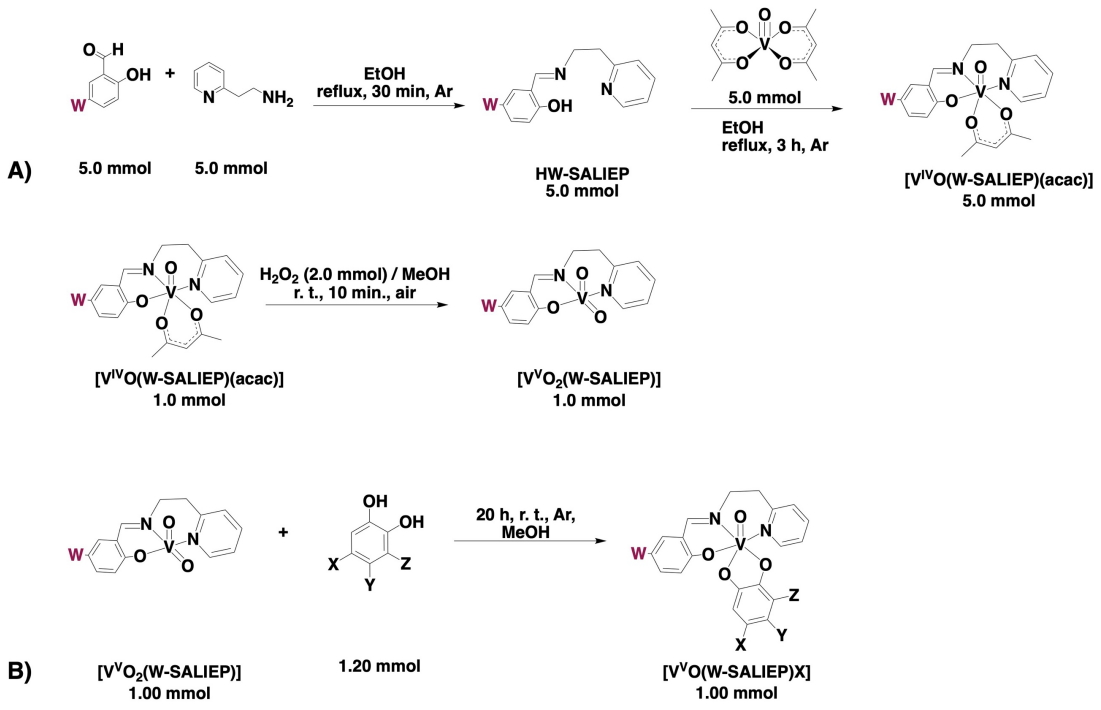

Figure 2.2. A) Syntheses of the $[V(O)_2(X\text{-}SALIEP)]$ precursors using modified procedures from the literature where W = H, Cl. B) Syntheses of the [VO(W-SALIEP)X] complexes where W = H, Cl and X, Y and Z represent H *or t*-Bu substituents on the catecholato ligand.

from a condensation reaction between salicylaldehyde and 2-(2-aminoethyl)pyridine in ethanol for 30 min, followed by the addition of the ethanolic solution of $[VO(acac)_2]$. The isolated [VO(SALIEP)(acac)] complex was oxidized by 30% aqueous H_2O_2 in air for 10 min, yielding the $[V(O)_2(SALIEP)]$ precursor in a 59% yield. The catecholato complexes were synthesized using 1.0 equivalent of $[V(O)_2(SALIEP)]$ and 1.2 equivalents of the catecholate ligand. The start of the reaction was evident by an immediate color change from mustard-yellow to deep purple. The reaction mixture was let stirred for 20 hr at room temperature (20 ^{o}C) under Ar. The yields of the isolated complexes were calculated after drying the complexes under high vacuum and are tabulated in **Table 2.1**. The $[V(O)_2(Cl\text{-}SALIEP)]$ precursor and the [VO(Cl-SALIEP)X] series were synthesized using similar methods using 5-chlorosalicylaldehyde for the Schiff base condensation

reaction (**Figure 2.2**). The yields of the isolated complexes after drying the complexes under high vacuum for 24 h and are also tabulated in **Table 2.1**. The methods reported herein have not been optimized and can be further improved.

The syntheses of the catecholate complexes reported here were inspired by the previous work (**Figure 2.2**) (Cornman et al., 1992a, Cornman et al., 1992b). The synthesis of the first structurally similar analog, [VO(HSHED)(CAT)], was reported in 1992 by the Pecoraro group. Using equimolar ratios of the [$V(O)_2$(HSHED)] precursor and the catecholate ligand the complex was prepared in a 40% yield. The stoichiometric ratio of the precursor and the ligand was adjusted to 1:1.2 by the Crans and Lay groups in previous studies and this ratio was used herein. Unlike other reported V(V) catecholate series, the pyridine series have different isolation methods, as the complexes readily precipitate from solution upon reaction completion. The complexes were isolated using vacuum filtration and washed with cold methanol, and their yields are tabulated below (**Table 2.1**). The yields of both parent and chloro analogs are comparable, which showed that the presence of the chloro substituent on the Schiff base did not affect the coordination of the catecholate ligand to the dioxide precursors.

Table 2.1. Percent yields and appearances of the isolated complexes.

Complex	% Yield	Appearance
[$V(O)_2$(SALIEP)]	59%	Dark mustard yellow solid
[VO(SALIEP)(Cat]	61%	Deep purple solid
[VO(SALIEP)(4TB)]	25%	Purple solid
[VO(SALIEP)(DTB)]	31%	Deep purple solid
[$V(O)_2$(Cl-SALIEP)]	75%	Dark mustard yellow solid
[VO(Cl-SALIEP)(Cat)]	44%	Purple solid
[VO(Cl-SALIEP)(4TB)]	57%	Deep purple solid
[VO(Cl-SALIEP)(DTB)]	22%	Deep purple solid

2.3.3 Lipophilicity of the Complexes

Lipophilicity, or log*P*, is a partition between a lipophilic organic phase, generally *n*-octanol, and a polar aqueous phase, as reported previously (Ren et al., 2002, Weekes et al., 2016). While log*P* values help to understand the cell uptake of the complexes and hence, provide useful

information with regard to the antiproliferative activities of these complexes, such measurements are only accurate with hydrolytically stable compounds. In the case of the VOSALIEP complexes, the experiment is difficult to conduct because most of these analogs hydrolyze within a few minutes, as evidenced by the hydrolytic stability data (**Figure A2.14**). Because such experiments would produce results that are not accurate, we used computational methods (Chemicalize) to estimate the log*P* values (**Table 2.2**), to understand the effects of lipophilicity of the complexes

Table 2.2. Estimated log*P* values of the VOSALIEP complexes from Chemicalize calculations *

Complex	log*P*	Complex	log*P*
[VO(SALIEP)(Cat)]	4.112	[VO(Cl-SALIEP)(Cat)]	4.630
[VO(SALIEP)(4TB)]	5.739	[VO(Cl-SALIEP)(4TB)]	6.257
[VO(SALIEP)(DTB)]	7.366	[VO(Cl-SALIEP)(DTB)]	7.884
* The calculations required the assumption that a covalent bond description can approximate a V-N coordinate bond in these metal complexes.			

on their uptake by the glioblastoma cells. Since this program was developed for organic molecules, its use requires the assumption that a covalent bond can approximate a V-N coordinate bond description in these metal complexes. Since any systematic errors introduced by this assumption will be consistent throughout the series, this method is only used to estimate relative lipophilicity amongst these metal complexes. The results showed that increasing the number of *tert*-butyl substituents increased lipophilicity of the complexes. Additionally, the presence of the chloro group on the Schiff base increased lipophilicity due to the electron-donating effects of the chloro group on the π aromatic system. The log*P* values of the VOSALIEP complexes were also compared to those of the VOHSHED analogs (Murakami et al., 2022). The VOSALIEP analogs were significantly more hydrophobic due to the presence of the pyridine ring on the Schiff base. The VOSALIEP complexes do not follow under the Lipinski's rule of five, as most of their log*P* values exceed 4.5, yet they have promising anticancer properties against glioblastoma. This may be due to the inaccuracies of the absolute values as described above.

2.3.4 ^{51}V NMR Characterization

The [VO(SALIEP)X] and [VO(Cl-SALIEP)X] complexes were characterized by ^{51}V NMR in 10.0 mM solutions of d_3-MeCN and d_6-DMSO. Most parent and chloro complexes had one peak in d_3-, which indicated the formation of one geometric isomer in solution (**Figure 2.3**). The

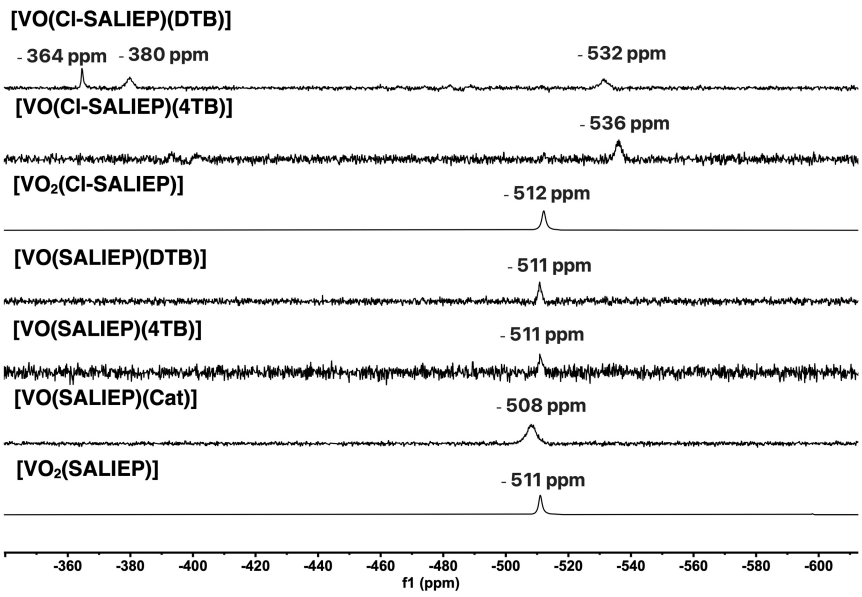

Figure 2.3 Stacked ^{51}V NMR plots of the [VO(SALIEP)X] and [VO(Cl-SALIEP)X] series in 10.0 mM d_3-MeCN solutions.

electron-donating nature of the Cl substituent on the π system caused a downfield shift of the peaks for the [VO(Cl-SALIEP)(4TB)] and [VO(Cl-SALIEP)(DTB)] complexes (**Figure 2.3**). The chlorinated DTB analog, [VO(Cl-SALIEP)(DTB)], had a peak corresponding to a major isomer at -532 ppm and two peaks at -380 and -364 ppm corresponding to minor geometric isomers. All parent and chloro analogs showed one peak in d_6-DMSO, indicating the formation of one geometric isomer in this solvent. The similarity of the chemical shifts in both solvents indicated that the solution environments were similar, which could be explained by similar dielectric constants of MeCN and DMSO (35.9 and 47.1, respectively) (Shcherbakov et al., 2021). Thus, the isomer distribution was similar in MeCN and DMSO for both parent and chloro series.

Most ^{51}V NMR had a relatively high signal-to-noise ratio, indicating some potential reduction of the complexes to V(IV). The observations could be explained by the fact that the six-membered core connecting coordination sites of the Schiff base, which causes the ethylene connector of the Schiff base and the vanadium to canter significantly. Such distortions would decrease the stability of the V(V) complex and increase the likelihood of reduction to V(IV), compared to the VOHSHED complexes that have a five-membered core structure. In addition, pyridine group also has weak pi-acceptor properties that tends to stabilize lower oxidation states, such as V(IV). In some cases, different solvent environments can facilitate (or slow down) the reduction to V(IV). For example, the [VO(Cl-SALIEP)(Cat)] analog was immediately reduced to V(IV) in d_3-MeCN but was relatively stable in d_6-DMSO. The observation could also be explained by the sensitivity of the analogs to trace moisture in the organic solvent. Overall, the ^{51}V NMR data showed the presence of one geometric isomer for most complexes and their rather unstable nature in organic solvent compared to the reported VO(HSHED) and VO(Cl-HSHED) analogs.

2.3.5 2D NMR Characterization

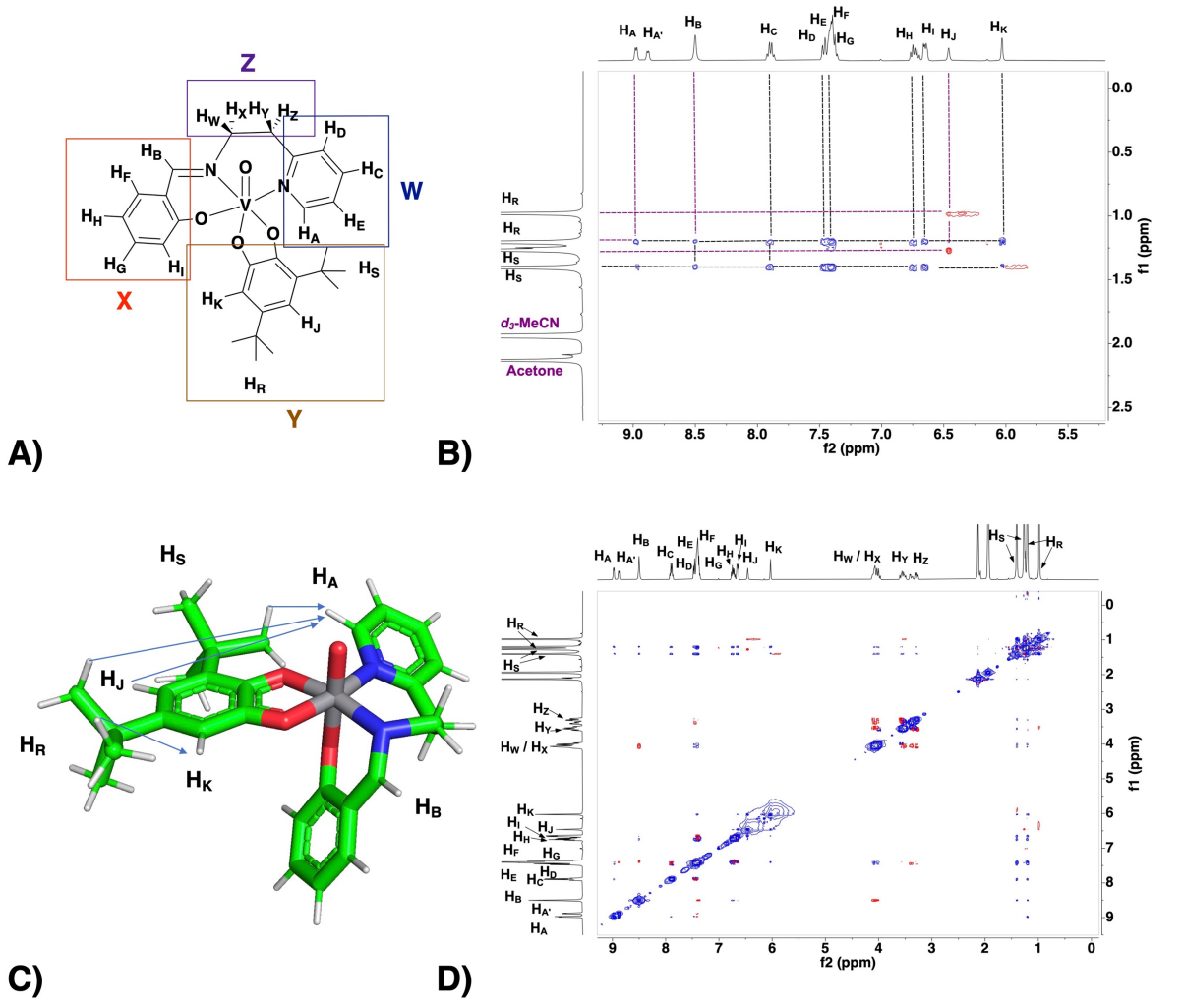

Figure 2.4 A) ^{1}H NMR assignments of the [VO(SALIEP)(DTB)] complex. B) Partial ^{1}H-^{1}H 2D NOESY NMR spectrum of the of the [VO(SALIEP)(DTB)] complex. C) 3D model of the major isomer of the [VO(SALIEP)(DTB)] complex, as evidenced by the ^{1}H-^{1}H 2D NOESY NMR spectrum. D) Full ^{1}H-^{1}H 2D NOESY NMR spectrum of the of the [VO(SALIEP)(DTB)] complex.

2D NMR experiments were undertaken to determine isomer distribution of the parent DTB complex, [VO(SALIEP)(DTB)], and the 3D structure of its major isomer. Unlike previously reported HSHED and Cl-HSHED Schiff bases, the SALIEP Schiff base consists of two rigid π systems (salicydene and pyridine; **Figure 2.4**), which limit the number of potential geometric isomers in

solution to two (on the assumption that the Schiff base is constrained to the equatorial plane), depending on the coordination of the asymmetric DTB ligand.

The [VO(SALIEP)(DTB)] complex has four distinctly different nuclear spin systems, abbreviated *X* – *Z* where W corresponds to the pyridine ring, *X* – to the Schiff base, *Y* – to the catecholate ring and *Z* – to the ethyl arm (**Figure 2.4A**). Since *W*, *X* and *Y* spin systems exclusively consist of the aromatic protons, their chemical shifts were determined using ^{1}H-^{1}H gCOSY NMR. The deduced assignments are shown in **Figures 2.4A and A2.7-A2.8**. The most upfield peak at 8.98 ppm was assigned to the H at the C2 position on the pyridine ring (H_A), in addition to the peak at 8.88 ppm, which corresponds to the H_A proton of the minor isomer. The singlet at 8.50 pm was assigned to the imine proton (H_B). The protons on the ethyl arm (H_Y and H_Z) are non-equivalent, which is evidenced by the presence of the multiplets at 3.54 and 3.30 ppm, respectively. The DTB groups have different electronic environments, resulting in a distinct set of peaks abbreviated H_R and H_S. The protons on the DTB groups are non-equivalent, which is evidenced by the presence of two peaks with the integrations of 6H and 3H for both H_R (1.21 and 0.98 ppm) and H_S (1.40 and 1.27 ppm).

The ^{1}H-^{1}H NOESY NMR experiments enabled the major geometric isomer of [VO(SALIEP)(DTB)] to be determined based on the crosstalk between protons. The data showed that both DTB groups couple with both salicylidene and pyridine spin systems (**Figure 2.4B-2.4D**). Specifically, both DTB groups have medium to weak cross-peaks with H_C, H_D and H_E protons on the pyridine ring, and H_H and H_I protons on the salicylidene. H_R is the only DTB group to have a crosstalk with the pyridine proton H_A, which indicated the closer proximity of the H_R protons on the DTB group to the pyridine ring. The interproton distance measurement from the 3D model is 2 Å, which confirmed the presence of the cross-peak with the medium intensity. Both H_R and H_S have a weak cross-peak with H_B. The interproton distance measurements from the 3D model confirm a stronger H_B-H_S cross-peak due to a shorter interproton distance (6.7 Å, 7.9 Å for H_B-H_R). the presence of the cross-peak with the medium intensity. The remaining interproton

distances are shown in **Table A2.1**. Crosstalk was also observed between the imine proton H_B and two nonequivalent protons on the ethyl arm, H_W and H_X, confirming the proximity of the *X* and *Z* spin systems.

2.3.6 EPR Spectroscopy

EPR studies confirmed that the complexes with unsubstituted catecholate ligands existed predominantly as the reduced V(IV) species in solution. Initially, EPR spectra in 10.0 mM DMSO solutions were collected to demonstrate the formation of V(IV) species and calculate the g_{iso} and A_{iso} values of the complexes (**Figure 2.5A-2.5B**). Additional experiments were performed to

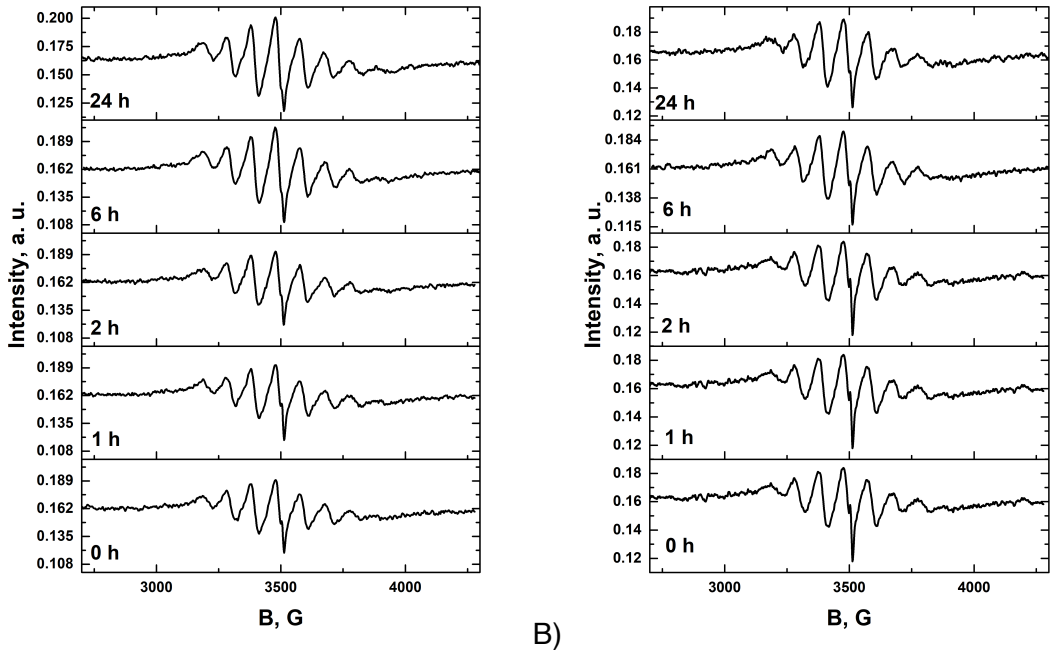

Figure 2.5 Room temperature stacked EPR spectra of A) [$V^{IV}O$(SALIEP)(Cat)] and B) [$V^{IV}O$(Cl-SALIEP)(Cat)] in 10.0 mM DMSO solutions with added $Zn(OAc)_2$ to trap the resulting semiquinone radicals.

demonstrate the formation of the semiquinone ligands in DMSO solutions, which is referred to as the metal ion-stabilization technique (Reszka and Chignell, 1993). A solution of $Zn(OAc)_2$: 1) trapped the resulting semiquinone radicals; and 2) dissolved in several organic solvents, including DMSO and MeCN. The data showed an increased concentration of [$V^{IV}O$(SALIEP)(Cat)] starting

at 0 h, as evidenced by the increasing intensities of the peaks (**Figure 2.5A**). Additionally, the formation of semiquinone radicals was observed at all time points, which confirmed the hypotheses that the formation of semiquinone radicals occurred upon reduction of the catecholates. We also carried out EPR experiments using a 3,400-3,600 G window to confirm the formation of semiquinone radicals over time (Supplemental Material, **Figure A2.26-A2.27**). The EPR spectra of the [$V^{IV}O$(Cl-SALIEP)(Cat)] complex showed a different trend where the amount of the reduced species remains approximately the same but slightly increases at *t* = 6 h (**Figure 2.5B**). The formation of the semiquinone radicals was also observed at all time points, which confirmed that the chloro analogs also form semiquinone radicals upon reduction in solution.

This is the first EPR spectroscopic study with V(IV) mixed-ligand Schiff base/catecholato complexes. Our data showed that the six-membered core resulting from the NON coordination sites of the Schiff base, the ethyl arm of the Schiff base and the vanadium canter significantly decreased the stability of the V(V) precursor with respect to V(IV) and, hence, increased the ease of reduction, compared to the VOHSHED analogs. This is because the VOHSHED complexes have a five-membered ring from the NON coordination sites of the Schiff base, the ethylene arm of the Schiff base and the vanadium canter which, consequentially, significantly increased their stability and decreased the ease of reduction to the corresponding V(IV) species. The EPR spectroscopic data confirmed that both [VO(SALIEP)(Cat)] and [VO(Cl-SALIEP)(Cat)] predominantly exist as the reduced V(IV) species, when the product of the reaction of the [$V(O)_2$(X-SALIEP)] with catechol is dissolved in the organic solvents, DMSO and MeCN. This observation was consistent with our hypothesis that the weak ^{51}V NMR signals of the V(V) complexes in these organic solvents was due to substantial reduction to V(IV). This showed that this series of V(V) complexes with pyridine-containing Schiff bases substantially reduced to the corresponding V(IV) species, particularly in the absence of bulky hydrophobic substituents on the catecholate ligand.

2.3.7 Cyclic voltammetry

Given the EPR spectroscopic results, the redox chemistry of pyridine Schiff base-containing catecholates was particularly interesting given that the reduction can happen at either the vanadium center, or the catecholate ligand or be delocalized over both. The extent of the redox delocalization can be probed by XAS studies using XANES to determine the metal oxidation state and bond lengths combined with DFT calculations. Dry acetonitrile was chosen as a solvent due to its wide potential window (-3.1 to +1.5 V) (Schotten et al., 2020) and excellent solubility of the vanadium complexes with 0.1 M tetrabutylammonium perchlorate (TBAP) as the supporting electrolyte. The $E_{1/2}$ values were reported against an external ferrocene standard (Fc^+/Fc) in

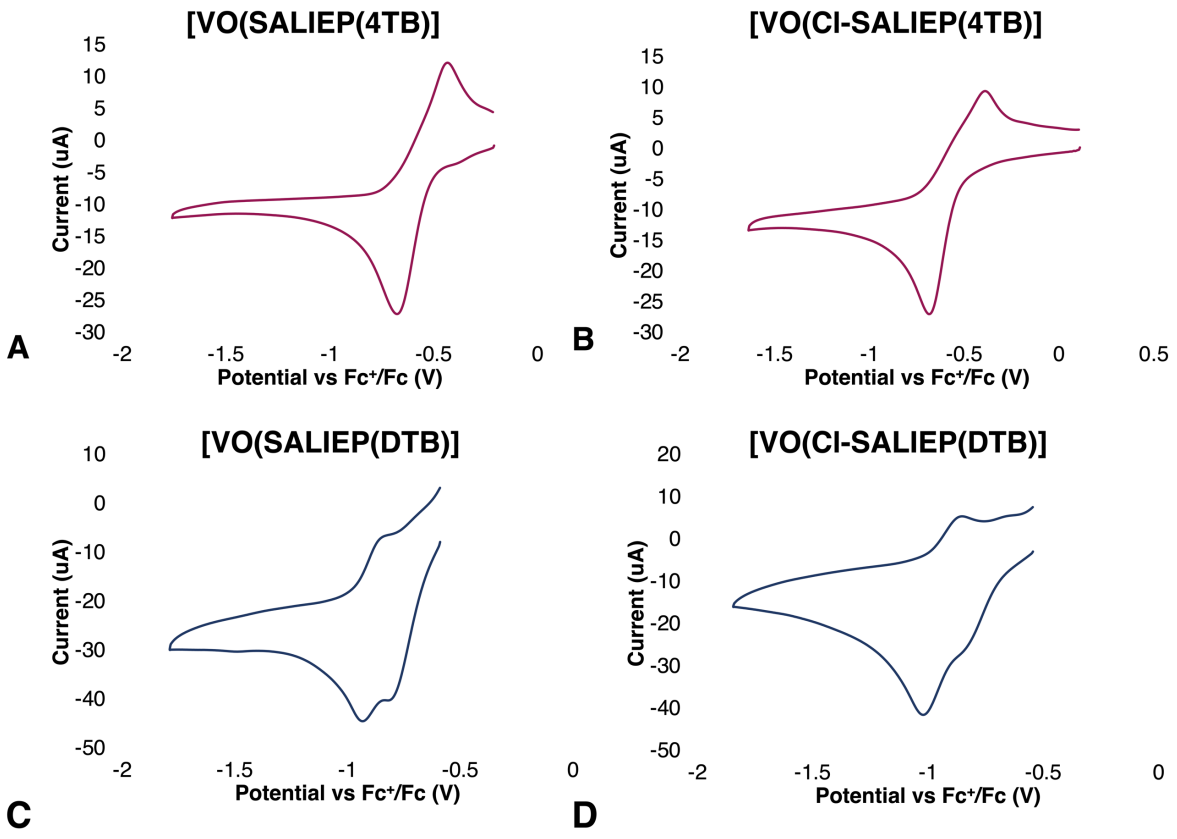

Figure 2.6. Cyclic voltammograms of 2.0 mM dry and degassed MeCN solutions of [VO(SALIEP)(4TB)] (A), [VO(SALIEP)(DTB)] (B), [VO(Cl-SALIEP)(4TB)] (C) and [VO(Cl-SALIEP)(DTB)] (D) analogs run at 100 mV s^{-1}.

acetonitrile. Solutions of 2.0 mM vanadium complexes in 0.1 M TBAP acetonitrile solution were prepared and their cyclic voltammograms (CVs) have recorded at 100 mV s^{-1}.

The complexes with 4TB and DTB ligands had quasi-reversible redox couples (**Figure 2.6)** for the V(V/IV) couples vs Fc^{+}/Fc for all four complexes. The observed chemically reversible redox couples corresponded to the reduction occurring at the vanadium center and not the catecholate ligand (**Figure 2.6**). The results were consistent with the reported cyclic voltammetry data for VO(Cl-HSHED) catecholate complexes, where the observed chemically reversible redox couples corresponded to the reduction at the vanadium center.

The substitution pattern on the catecholate ligand affected the observed $E_{1/2}$ values. Both VO(SALIEP) and VO(Cl-SALIEP) complexes with sterically hindered di-*tert*-butyl catechol ligands had most negative $E_{1/2}$ values (**Table 2.3**) and, hence, were the most difficult to reduce.

Table 2.3. Half-way potentials of the parent and chloro VOSALIEP and VOHSHED analogs. The CV were collected in 2.0 mM dry acetonitrile solutions at ambient temperature.

Compound	$E_{1/2}$ (1st isomer) vs Fc^{+}/Fc (V)	$E_{1/2}$ (2nd isomer) vs Fc^{+}/Fc (V)	References
[VO(SALIEP)(4TB)]	-0.548	N/A	This work
[VO(SALIEP)(DTB)]	-0.890	-0.827	This work
[VO(Cl-SALIEP)(4TB)]	-0.527	N/A	This work
[VO(Cl-SALIEP)(DTB)]	-0.936	-0.848	This work
[VO(HSHED)(Cat)]	−0.698	N/A	Murakami *et. al.* 2022 (Murakami et al., 2022)
[VO(HSHED)(DTB)]	−0.802	N/A	Murakami *et. al.* 2022 (Murakami et al., 2022)
[VO(Cl-HSHED)(Cat)]	−0.679	N/A	Murakami *et. al.* 2022 (Murakami et al., 2022)
[VO(Cl-HSHED)(DTB)]	−0.782	N/A	Murakami *et. al.* 2022 (Murakami et al., 2022)

The CVs for those complexes indicated that two V(V) isomers were in equilibrium with one V(IV) reduced species. Additionally, the [VO(Cl-SALIEP)(DTB)] complex had the most negative $E_{1/2}$ values (-0.936 V and -0.848 V, respectively) due to the electron-donating nature of the Cl group

to the aromatic system. The complexes with 4-*tert*-butyl-catechol ligands reduced more easily to V(IV), which is evidenced by more positive $E_{1/2}$ values (**Table 2.3**). The electron-donating effect of the Cl group had little effect on the redox properties of the [VO(SALIEP)(4TB)] and [VO(Cl-SALIEP)(4TB)] complexes, since their $E_{1/2}$ values were similar.

Little to no redox activity was observed for the [VO(SALIEP)(Cat)] and [VO(Cl-SALIEP)(Cat)] complexes, meaning that the complexes immediately and irreversibly reduced to V(IV). The findings were confirmed by the ^{51}V NMR of the complexes in acetonitrile, as those spectra have high signal-to-noise ratio and are very challenging to collect. Thus, the [VO(SALIEP)(Cat)] and [VO(Cl-SALIEP)(Cat)] predominantly exist as V(IV) species, which requires detailed EPR studies of those complexes in the future.

With increased hydrophobicity of the complexes, they were less easily reduced. In particular, the presence of the pyridine rind in the VOSALIEP complexes is the main contributor to increased hydrophobicity and changes in half-wave potential values, compared to the VOHSHED complexes. Since the cellular environment is reducing and has high concentrations of glutathione, most abundant intracellular reductant (Areias et al., 2016, Harfield et al., 2012), future electrochemical characterization will be carried out in the presence of glutathione to probe how it affects the redox properties of the complexes under conditions appropriate for the biological assays and physiological conditions.

2.3.8 UV-Vis Characterization

The [VO(SALIEP)X] and [VO(Cl-SALIEP)X] complexes were characterized by UV-Vis spectroscopy to probe how structural changes of both the Schiff base and the catecholate ligand contributed to the changes of the HOMO-LUMO gap. The UV-Vis spectra were collected in dry acetonitrile because all complexes are sensitive to trace moisture in the organic solvents. The UV-Vis spectra of all complexes (0.10 mM, dry MeCN) exhibited maxima at around 335 nm, 550 nm and 899 nm (**Figure 2.7**) with λ_{max} and ε_{max} values listed in **Table 2.4**. The maxima around 500

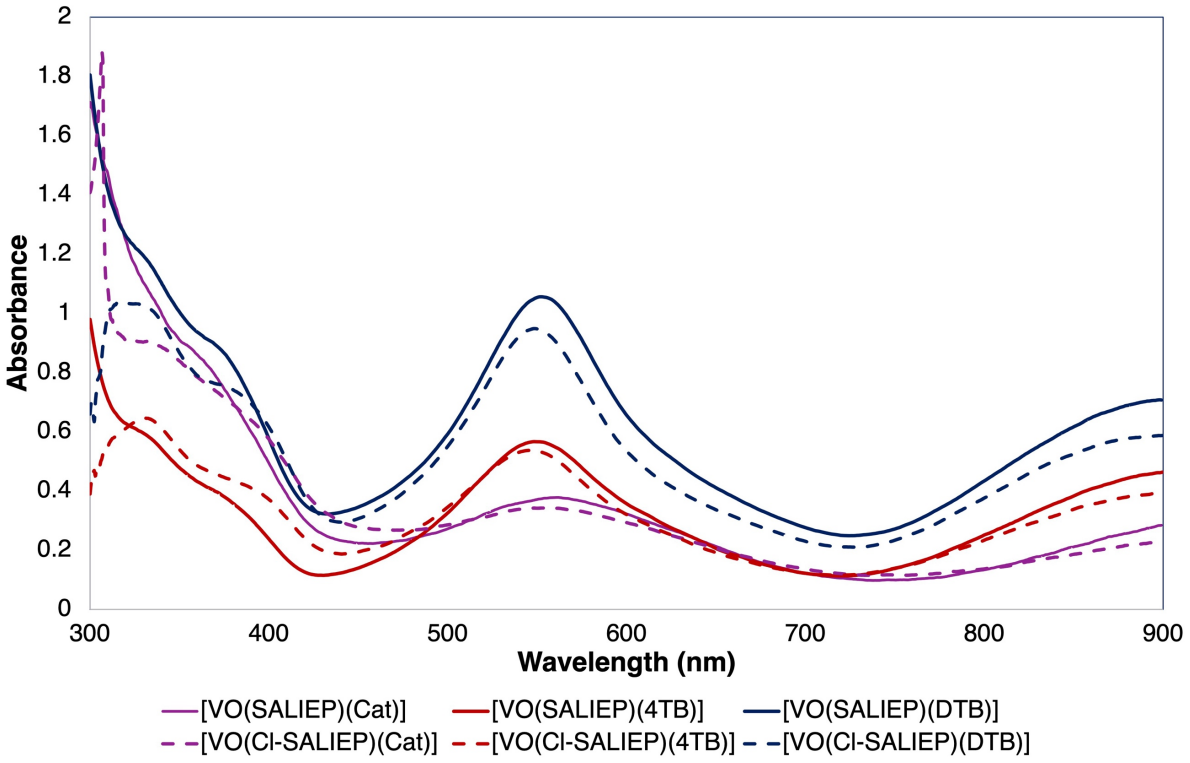

Figure 2.7. UV-Vis spectra of the parent complexes [VO(SALIEP)(X)] and the halogenated complexes [VO(Cl-SALIEP)(X)] recorded in 0.10 mM solutions of dry MeCN.

nm and 900 nm were ligand-to-metal charge transfer (LCMT) bands, confirming the presence of the catecholate ligand coordinated to the vanadium center and obscured the d-d transitions, which are an order of magnitude less intense. The maxima around 899 nm corresponded to the lower energy LMCT transition bands of the vanadium. Generally, the presence of hydrophobic substituents increased the molar absorptivity of the complexes. These data reflected that the

halogen substituent decreased the stability of the alkyl substituted catecholate complexes and, thus, increased the gap between the HOMO - LUMO orbitals. The changes in maxima and decreased intensity of the bands for the Cat complexes are consistent with their substantial reduction to V(IV) in solution.

Table 2.4. Band Positions and Corresponding Molar Extinction Coefficients of the [VOSALIEP)] and [VO(Cl-SALIEP)] compound series. The UV-Vis spectra were recorded in 0.1 mM solutions of dry acetonitrile.

Compound	λ_{max}, nm	ε (M^{-1} cm^{-1})	λ_{max}, nm	ε (M^{-1} cm^{-1})
[VO(SALIEP)(Cat)]	561	3.8×10^3	899	2.8×10^3
[VO(SALIEP)(4TB)]	551	5.6×10^3	899	4.6×10^3
[VO(SALIEP)(DTB)]	551	1.1×10^4	899	7.1×10^3
[VO(Cl-SALIEP)(Cat)]	560	3.4×10^3	899	2.3×10^3
[VO(Cl-SALIEP)(4TB)]	548	5.4×10^3	899	3.9×10^3
[VO(Cl-SALIEP)(DTB)]	549	9.5×10^3	899	5.9×10^3

2.3.9 Stabilities and *In Vitro* Anti-Proliferative Activities of V(V) Complexes

As for the previously studied V(V)-(Cl)HSHED-catecholato complexes,(Crans et al., 2019b, Levina et al., 2020, Murakami et al., 2022) V(V)-(Cl)SALIEP-catecholato complexes decomposed within seconds or minutes under the conditions matching those of cell culture assays (100 mM V, 310 K, fully supplemented cell culture medium with added 10 mM HEPES buffer to maintain the pH value at 7.4 in the absence of 5% CO_2).(Levina et al., 2017) The decomposition kinetics were followed by the disappearance of characteristic absorbance bands in the visible and near-IR range (see **Figure 2.7**), as shown in **Figure A2.14** (Supporting Information). In agreement with the earlier data,(Crans et al., 2019b, Murakami et al., 2022) the presence of DTB ligands greatly increased the stability of V(V) complexes under biologically relevant conditions. Stabilities

of V(V) complexes containing DTB ligands decreased in the series [V^{V}O(Cl-SALIEP)(DTB)] > [V^{V}O(SALIEP)(DTB)] > [V^{V}O(HSHED)(DTB)] (**Figure A2.14**); the corresponding half-life-time ($t_{1/2}$) values are listed in Table 4. Decomposition of all three complexes resulted in the formation of a new absorbance band at ~650 nm, which corresponded to [$V^{V}(DTB)_3]^-$.(Milsmann et al., 2006, Griffin et al., 2019) Mixed-ligand V(V) complexes with 4TB and CAT ligands decomposed immediately after the addition of their stock solutions in DMSO to cell culture medium ($t_{1/2}$ < 5 s, **Table 2.5**). Decomposition products of these complexes showed an absorbance band at ~390 nm, which is similar to that observed for [$V^{V}(O)_2$(SALIEP)] and [$V^{V}(O)_2$(Cl-SALIEP)] complexes (**Figure A2.14**). Kinetic studies of decomposition of the other V complexes listed in Table 4 were not performed due the absence of characteristic absorbance bands in the visible range. Low-resolution ESI-MS data (~10 mM V in MeOH solutions; **Figure A2.25)** suggest that all the studied V(V/IV)-(Cl)SALIEP complexes decomposed with the formation of free (Cl)SALIEPH ligands, which is consistent with the generation of [$V^{V}(DTB)_3]^-$ as one of the products.

Of all the studied V-(Cl)SALIEP complexes, [V^{V}(O)(SALIEP)(DTB)] showed the highest anti-proliferative activity of freshly diluted solutions in T98g cells (IC_{50} = 6.7 ± 0.9 mM at 72 h treatment, condition A in **Table 2.5** and **Figure A2.28**). The activity decreased ~two-fold after the decomposition of the complex for 30 min at 310 K and 5% CO_2 (condition B in **Table 2.5** and **Figure A2.28**). The activities of all the other V(V/IV) complexes with (Cl)SALIEP ligands were similar or lower than those of the modelled decomposition products, such as Na_3VO_4, $DTBH_2$ or their combination (all pre-incubated with the medium for 30 min, **Table 2.5** and **Figure A2.28**). Notably, [V^{V}(O)(SALIEP)(DTB)] and [V^{V}(O)(Cl-SALIEP)(DTB)] complexes showed lower anti-proliferative activities and 5-10-fold lower cellular V content compared with [V^{V}O(HSHED)(DTB)] (**Table 2.5**), despite being more stable in cell culture medium (**Figure A2.28**). These results confirm the previous data[10,11] that the anti-proliferative activities of V(V)-Schiff base-catecholato complexes in cancer cells are determined by a combination of factors, including stabilities in

extracellular media, redox properties, and penetration rates through the cell membranes. On the other hand, cellular V contents in T98g cells after the 30 min treatments with 100 mM [V^{V}(O)(SALIEP)(DTB)] and [V^{V}(O)(Cl-SALIEP)(DTB)] were 15-30-fold higher than that for the cells treated with Na_3VO_4 under the same conditions, and ~three-fold higher than for the cells treated with [V^{IV}O(SALIEP)(acac)] (**Table 2.5**). These data indicate that the former two complexes are at least partially taken by cells intact via passive diffusion through the cell membranes.[9-11] The lower uptake of the X-SALIEP complexes compared with their HSHED counterparts is consistent with the increased lipophilicity moving them out of the range of optimal drug uptake and efficacy.

However, on the positive side for therapeutic applications, unlike for [V^{V}O(HSHED)(DTB)],(Murakami et al., 2022) V(V) complexes with (Cl)SALIEP ligands were consistently less toxic to non-cancer HFF-1 (human skin fibroblast) cells compared with T98g (human glioblastoma) cells (**Table 2.5** and **Figure A2.28**). In particular, freshly diluted solutions of [V^{V}O(SALIEP)(DTB)] were five-fold less toxic in HFF-1 compared with T98g cells. In addition, subtoxic concentrations of V(V)-(Cl)SALIEP complexes, as well as of Na_3VO_4, increased the viability of HFF-1, but not of T98g, cells by 120-140% compared with the vehicle control (**Figure A2.28**). Similar selective stimulating effect of V(V)-(Cl)HSHED complexes on non-cancer HFF-1 cells has been recently reported.(Murakami et al., 2022) Stimulation of growth of cultured cells by low concentrations of V(V/IV) complexes (Barrio and Etcheverry, 2006, Molinuevo et al., 2004) is likely due to their phosphatase-inhibiting properties(Crans et al., 2018, Ferretti and León, 2022) and can contribute to the potential beneficial effects of decomposition products of cytotoxic V(V) complexes used in cancer treatment. (Levina et al., 2020, Levina et al., 2022, Manganaro et al., 2022)

Table 2.5. Stabilities in cell culture medium, anti-proliferative activities and cellular uptakes of [VO(SALIEP)(L)], [VO(Cl-SALIEP)(L)] complexes and reference compounds

Compound	$t_{1/2}$,[a]	IC_{50} (T98g)[b]	IC_{50} (HFF-1)[b]	Uptake (T98g)[c]
$[V^{V}(O)_2(SALIEP)]$	ND	50 ± 4 (A)	ND[d]	ND
$[V^{IV}O(SALIEP)(acac)]$	ND	50 ± 4 (A)	ND	$(1.7 \pm 0.3)\times10^{8}$
$[V^{V}O(SALIEP)(Cat)]$	<5 s	39 ± 4 (A)	ND	ND
$[V^{V}O(SALIEP)(4TB)]$	<5 s	28 ± 3 (A)	ND	ND
$[V^{V}O(SALIEP)(DTB)]$	~100 s	6.7 ± 0.9 (A) 11.3 ± 0.8 (B)	34 ± 10 (A) 32 ± 8 (B)	$(9 \pm 2)\times10^{8}$
$[V^{V}(O)_2(Cl\text{-}SALIEP)]$	ND	45 ± 4 (A)	ND	ND
$[V^{IV}O(Cl\text{-}SALIEP)(acac)]$	ND	34 ± 6 (A)	ND	ND
$[V^{V}O(Cl\text{-}SALIEP)(Cat)]$	<5 s	33 ± 5 (A)	ND	ND
$[V^{V}O(Cl\text{-}SALIEP)(4TB)]$	<5 s	30 ± 3 (A)	ND	ND
$[V^{V}O(Cl\text{-}SALIEP)(DTB)]$	~180 s	18 ± 3 (A) 33 ± 12 (B)	47 ± 5 (A) 47 ± 4 (B)	$(5.3 \pm 0.6)\times10^{8}$
$[V^{V}O(HSHED)(DTB)]$[e]	~50 s	1.9 ± 0.2 (A)	1.9 ± 0.4 (A)	$(4.9 \pm 0.9)\times10^{9}$
Na_3VO_4 + $DTBH_2$	ND	9 ± 1 (B)	28 ± 3 (B)	ND
Na_3VO_4	ND	18 ± 3 (B)	35 ± 3 (B)	$(3.3 \pm 0.8)\times10^{7}$
$DTBH_2$	ND	15 ± 3 (B)	24 ± 2 (B)	ND

[a] Half-life time of the complex in fully supplemented cell culture medium at 310 K, determined by UV-vis spectroscopy (see **Figure A2.14**) in SI. [b] Typical IC_{50} values (mM; means and standard deviations of six replicate wells) in T98g (human glioblastoma cells) and HFF-1 (non-cancer human fibroblasts). Designations of assay conditions: in (A), freshly diluted compounds were applied to cells for 72 h; and in (B), compounds were pre-incubated with cell culture medium for 30 min at 310 K and 5% CO_2, then applied to cells for 72 h. The corresponding concentration-viability curves are shown in **Figure A2.28**. [c] Uptake of V (atoms per cell; means and standard deviations of four replicate wells) by T98g cells after 30 min treatments with 100 mM of freshly diluted V complexes. [d] ND = not determined. [e] HSHED = *N*-(salicylideneaminato)-*N'*-(2-hydroxyethyl)-1,2-ethanediamine; the data for this complex have been published previously.[9,10]

2.4 Conclusions

In this study, we have developed the syntheses of novel non-innocent pyridine containing Schiff base vanadium(V) catecholates and carried out their characterization by a variety of spectroscopic (NMR, EPR, UV-Vis) and electrochemical methods. The presence of the pyridine ring on the Schiff base has resulted in the increase of hydrophobicity, as evidenced by the increase of the logP values. Additionally, the increase in hydrophobicity made the complexes harder to reduce to V(IV), according to the cyclic voltammetry data. According to the ^{51}V NMR and cyclic voltammetry studies, the presence of the pyridine ring increases the tendency for the

reduction to V(IV), as pyridine tends to stabilize the species in lower oxidation states. The EPR studies have shown that the complexes with unsubstituted catecholate ligands are most likely to reduce to V(IV) and form semiquinone radicals in the organic solvent.

Similar to previous work, the presence of bulky aliphatic substituents increases the stability of the V(V) catecholate complexes in both organic solvent and under the assay conditions. The UV-Vis hydrolytic stability study has demonstrated that both [V^{V}O(SALIEP)(DTB)] and [V^{V}O(Cl-SALIEP)(DTB)] are stable for 5 min. under the assay conditions, followed by the decomposition to the $[VO(DTB)_3]^-$ intermediate.

One of the newly synthesized mixed-ligand V(V) complexes, [V^{V}O(SALIEP)(DTB)], has shown moderate stability in cell culture media, significant cellular uptake of the intact complex by T98g (human glioblastoma) cells and high anti-proliferative activity (IC_{50} < 10 mM at 72 h treatment) in this cell line, which was ~5-fold higher than that for a non-cancerous human cell line, HFF-1. The increased hydrophobicity of the , [V^{V}O(SALIEP)(DTB)] complex, compared to the lead [VO(HSHED)(DTB)] analog, resulted in the lower uptake by T98g cells and also introduced increased selectivity for T98g cells. Decomposition of [V^{V}O(SALIEP)(DTB)] in cell culture medium decreased its anti-proliferative activity in T98g cells ~2-fold, while the activities of the fresh complex and its decomposition products in HFF-1 cells were equally low. These properties make [V^{V}O(SALIEP)(DTB)] a potential drug candidate for the treatment of advanced glioblastomas by intracranial injections, as was suggested previously for a related V(V) complex, [V^{V}O(HSHED)(DTB)].

The structure-activity relationships have demonstrated that the presence of the pyridine ring on the Schiff base results in the selective uptake of the complexes by T98g cells compared to the non-cancerous HFF cells. Additionally, pyridine significantly improves hydrolytic stability of the DTB analogs, as evidenced by the UV-Vis data. The complex redox chemistry of the

[VO(SALIEP)X] complexes, however, requires further spectroscopic and cyclic voltammetry studies in the presence of intracellular reductants, such as ascorbate and glutathione. Those studies would be necessary to understand the effects of intracellular reductants on the redox properties and redox reaction mechanism of the [VO(SALIEP)X] complexes. The knowledge of the chemical properties, cytotoxicity, and metal uptake of the VOHSHED and the VOSALIEP series will be crucial to optimizing the chemical properties of potential candidates for intratumoral injections to treat glioblastoma.

2.5 References

Areias, M. C. C., Shimizu, K. & Compton, R. G. 2016. Voltammetric detection of glutathione: an adsorptive stripping voltammetry approach. *Analyst,* 141**,** 2904-2910.

Arhouma, Z., Murakami, H. A., Koehn, J. T., Li, X., Roess, D. A., Crick, D. C. & Crans, D. C. 2022. Exploring Growth of Mycobacterium smegmatis Treated with Anticarcinogenic Vanadium Compounds. *Inorganics,* 10**,** 50.

Barr-David, G., Hambley, T. W., Irwin, J. A., Judd, R. J., Lay, P. A., Martin, B. D., Bramley, R., Dixon, N. E. & Hendry, P. 1992. Suppression by vanadium(IV) of chromium(V)-mediated DNA cleavage and chromium(VI/V)-induced mutagenesis. Synthesis and crystal structure of the vanadium(IV) complex (NH4)[V(O){HOC(Et)2COO}{OC(Et)2COO}]. *Inorg. Chem.,* 31**,** 4906-4908.

Barrio, D. A. & Etcheverry, S. B. 2006. Vanadium and bone development: putative signaling pathwaysThis paper is one of a selection of papers published in this Special issue, entitled Second Messengers and Phosphoproteins—12th International Conference. *Can. J. Physiol. Pharmacol.,* 84**,** 677-686.

Bergeron, A., Kostenkova, K., Selman, M., Murakami, H. A., Owens, E., Haribabu, N., Arulanandam, R., Diallo, J.-S. & Crans, D. C. 2019. Enhancement of oncolytic virotherapy by vanadium(V) dipicolinates. *BioMetals,* 32**,** 545-561.

Chatterjee, P. B., Goncharov-Zapata, O., Quinn, L. L., Hou, G., Hamaed, H., Schurko, R. W., Polenova, T. & Crans, D. C. 2011. Characterization of Noninnocent Metal Complexes Using Solid-State NMR Spectroscopy: o-Dioxolene Vanadium Complexes. *Inorg. Chem.,* 50**,** 9794-9803.

Cornman, C. R., Colpas, G. J., Hoeschele, J. D., Kampf, J. & Pecoraro, V. L. 1992a. Implications for the spectroscopic assignment of vanadium biomolecules: structural and spectroscopic characterization of monooxovanadium(V) complexes containing catecholate and hydroximate based noninnocent ligands. *J. Am. Chem. Soc.,* 114**,** 9925-9933.

Cornman, C. R., Kampf, J. & Pecoraro, V. L. 1992b. Structural and spectroscopic characterization of vanadium(V)-oxoimidazole complexes. *Inorg. Chem.,* 31**,** 1981–1983.

Cornman, C. R., Kampf, J. & Pecoraro, V. L. 2002. Structural and spectroscopic characterization of vanadium(V)-oxoimidazole complexes. *Inorg. Chem.,* 31**,** 1981-1983.

Crans, D. C. 2015. Antidiabetic, Chemical, and Physical Properties of Organic Vanadates as Presumed Transition-State Inhibitors for Phosphatases. *J. Org. Chem.,* 80**,** 11899-11915.

Crans, D. C., Henry, L., Cardiff, G. & Posner, B. I. 2019a. 8. DEVELOPING VANADIUM AS AN ANTIDIABETIC OR ANTICANCER DRUG: A CLINICAL AND HISTORICAL PERSPECTIVE. *In:* PEGGY, L. C. (ed.) *Essential Metals in Medicine: Therapeutic Use and Toxicity of Metal Ions in the Clinic.* Berlin, Boston: De Gruyter.

Crans, D. C., Koehn, J. T., Petry, S. M., Glover, C. M., Wijetunga, A., Kaur, R., Levina, A. & Lay, P. A. 2019b. Hydrophobicity may enhance membrane affinity and anti-cancer effects of Schiff base vanadium(v) catecholate complexes. *Dalton Trans.,* 48**,** 6383-6395.

Crans, D. C., Peters, B. J., Wu, X. & Mclauchlan, C. C. 2017. Does anion-cation organization in Na+-containing X-ray crystal structures relate to solution interactions in inhomogeneous nanoscale environments: Sodium-decavanadate in solid state materials, minerals, and microemulsions. *Coord. Chem. Rev.,* 344**,** 115-130.

Crans, D. C., Yang, L., Haase, A. & Yang, X. 2018. 9. HEALTH BENEFITS OF VANADIUM AND ITS POTENTIAL AS AN ANTICANCER AGENT. *In:* ASTRID, S., HELMUT, S., EVA, F. & ROLAND, K. O. S. (eds.) *Metallo-Drugs: Development and Action of Anticancer Agents.* Berlin, Boston: De Gruyter.

Fakhoury, M. 2016. Drug delivery approaches for the treatment of glioblastoma multiforme. *Artif. Cells, Nanomed., Biotechnol.,* 44**,** 1365-1373.
Ferretti, V. A. & León, I. E. 2022. An Overview of Vanadium and Cell Signaling in Potential Cancer Treatments. *Inorganics,* 10**,** 47.
Gourdon, L., Cariou, K. & Gasser, G. 2022. Phototherapeutic anticancer strategies with first-row transition metal complexes: a critical review. *Chem. Soc. Rev.,* 51**,** 1167-1195.
Griffin, E., Levina, A. & Lay, P. A. 2019. Vanadium(V) tris-3,5-di-tert-butylcatecholato complex: Links between speciation and anti-proliferative activity in human pancreatic cancer cells. *J. Inorg. Biochem.,* 201**,** 110815.
Hamid, O., Ismail, R. & Puzanov, I. 2019. Intratumoral Immunotherapy—Update 2019. *The Oncologist,* 25**,** e423-e438.
Harfield, J. C., Batchelor-Mcauley, C. & Compton, R. G. 2012. Electrochemical determination of glutathione: a review. *Analyst,* 137**,** 2285-2296.
Hirooka, Y., Kasuya, H., Ishikawa, T., Kawashima, H., Ohno, E., Villalobos, I. B., Naoe, Y., Ichinose, T., Koyama, N., Tanaka, M., Kodera, Y. & Goto, H. 2018. A Phase I clinical trial of EUS-guided intratumoral injection of the oncolytic virus, HF10 for unresectable locally advanced pancreatic cancer. *BMC Cancer,* 18**,** 596.
Jensen, M. P., Gorman-Lewis, D., Aryal, B., Paunesku, T., Vogt, S., Rickert, P. G., Seifert, S., Lai, B., Woloschak, G. E. & Soderholm, L. 2011. An iron-dependent and transferrin-mediated cellular uptake pathway for plutonium. *Nat. Chem. Biol.,* 7**,** 560-565.
Kostenkova, K., Althumairy, D., Rajan, A., Kortz, U., Barisas, B. G., Roess, D. A. & Crans, D. C. 2023. Polyoxidovanadates [MoVIVV9O28]5- and [H2PtIVVV9O28]5- interact with CHO cell plasma membrane lipids causing aggregation and activation of a G protein-coupled receptor. *Front. Chem. Biol.,* 2.
Kostenkova, K., Arhouma, Z., Postal, K., Rajan, A., Kortz, U., Nunes, G. G., Crick, D. C. & Crans, D. C. 2021. PtIV- or MoVI-substituted decavanadates inhibit the growth of Mycobacterium smegmatis. *J. Inorg. Biochem.,* 217**,** 111356.
Levina, A., Crans, D. C. & Lay, P. A. 2017. Speciation of metal drugs, supplements and toxins in media and bodily fluids controls in vitro activities. *Coord. Chem. Rev.,* 352**,** 473-498.
Levina, A., Crans, D. C. & Lay, P. A. 2022. Advantageous Reactivity of Unstable Metal Complexes: Potential Applications of Metal-Based Anticancer Drugs for Intratumoral Injections. *Pharmaceutics,* 14.
Levina, A. & Lay, P. A. 2017. Stabilities and Biological Activities of Vanadium Drugs: What is the Nature of the Active Species? *Chem. - Asian J.,* 12**,** 1692-1699.
Levina, A., Pires Vieira, A., Wijetunga, A., Kaur, R., Koehn, J. T., Crans, D. C. & Lay, P. A. 2020. A Short-Lived but Highly Cytotoxic Vanadium(V) Complex as a Potential Drug Lead for Brain Cancer Treatment by Intratumoral Injections. *Angew. Chem. Int. Ed. ,* 59**,** 15834-15838.
Li, X., Lah, M. S. & Pecoraro, V. L. 1988. Vanadium complexes of the tridentate Schiff base ligand N-salicylidene-N'-(2-hydroxyethyl)ethylenediamine: acid-base and redox conversion between vanadium(IV) and vanadium(V) imino phenolates. *Inorg. Chem.,* 27**,** 4657-4664.
Lima, L. M. A., Murakami, H., Gaebler, D. J., Silva, W. E., Belian, M. F., Lira, E. C. & Crans, D. C. 2021. Acute Toxicity Evaluation of Non-Innocent Oxidovanadium(V) Schiff Base Complex. *Inorganics,* 9**,** 42.
Ling, Y., Hao, Z.-Y., Liang, D., Zhang, C.-L., Liu, Y.-F. & Wang, Y. 2021. The Expanding Role of Pyridine and Dihydropyridine Scaffolds in Drug Design. *Drug Des. Devel. Ther.,* 15**,** 4289–4338.
Lu, L.-P., Liu, J.-H., Cen, S.-H., Jiang, Y.-L. & Hu, G.-Q. 2019. Discovery of vanadium complexes bearing tridentate schiff base ligands as novel LSD1 inhibitors. *Bioorg. Med. Chem. Lett.,* 29**,** 681-683.

Manganaro, J., Levina, A., Lay, P. A. & Crans, D. C. 2022. Potential Applications of Vanadium-Based Anticancer Drugs for Intratumoral Injections. *Medical Sciences Forum,* 11**,** 10.

Maurya, M. R., Arya, A., Kumar, U., Kumar, A., Avecilla, F. & Pessoa, J. C. 2009. Polymer-bound oxidovanadium(IV) and dioxidovanadium(V) complexes: synthesis, characterization and catalytic application for the hydroamination of styrene and vinyl pyridine. *Dalton Trans.***,** 9555–9566.

Mcausland, T. M., Van Vloten, J. P., Santry, L. A., Guilleman, M. M., Rghei, A. D., Ferreira, E. M., Ingrao, J. C., Arulanandam, R., Major, P. P., Susta, L., Karimi, K., Diallo, J.-S., Bridle, B. W. & Wootton, S. K. 2021. Combining vanadyl sulfate with Newcastle disease virus potentiates rapid innate immune-mediated regression with curative potential in murine cancer models. *Mol. Ther.--Oncolytics,* 20**,** 306-324.

Milsmann, C., Levina, A., Harris, H. H., Foran, G. J., Turner, P. & Lay, P. A. 2006. Charge Distribution in Chromium and Vanadium Catecholato Complexes: X-ray Absorption Spectroscopic and Computational Studies. *Inorg. Chem.,* 45**,** 4743-4754.

Mohan, A., Harris, K., Bowling, M. R., Brown, C. & Hohenforst-Schmidt, W. 2018. Therapeutic bronchoscopy in the era of genotype directed lung cancer management. *J. Thorac. Dis.,* 10**,** 6298-6309.

Molinuevo, M. S., Barrio, D. A., Cortizo, A. M. & Etcheverry, S. B. 2004. Antitumoral properties of two new vanadyl(IV) complexes in osteoblasts in culture: role of apoptosis and oxidative stress. *Cancer Chemother. Pharmacol.,* 53**,** 163-172.

More, M. S., Joshi, P. G., Mishra, Y. K. & Khanna, P. K. 2019. Metal complexes driven from Schiff bases and semicarbazones for biomedical and allied applications: a review. *Mater. Today Chem.,* 14**,** 100195.

Mulyani, I., Levina, A. & Lay, P. A. 2004. Biomimetic Oxidation of Chromium(III): Does the Antidiabetic Activity of Chromium(III) Involve Carcinogenic Chromium(VI)? *Angew. Chem. Int. Ed.,* 43**,** 4504-4507.

Murakami, H. A., Uslan, C., Haase, A. A., Koehn, J. T., Vieira, A. P., Gaebler, D. J., Hagan, J., Beuning, C. N., Proschogo, N., Levina, A., Lay, P. A. & Crans, D. C. 2022. Vanadium Chloro-Substituted Schiff Base Catecholate Complexes are Reducible, Lipophilic, Water Stable, and Have Anticancer Activities. *Inorg. Chem.,* 61**,** 20757-20773.

Newman, J. H., Chesson, C. B., Herzog, N. L., Bommareddy, P. K., Aspromonte, S. M., Pepe, R., Estupinian, R., Aboelatta, M. M., Buddhadev, S., Tarabichi, S., Lee, M., Li, S., Medina, D. J., Giurini, E. F., Gupta, K. H., Guevara-Aleman, G., Rossi, M., Nowicki, C., Abed, A., Goldufsky, J. W., Broucek, J. R., Redondo, R. E., Rotter, D., Jhawar, S. R., Wang, S.-J., Kohlhapp, F. J., Kaufman, H. L., Thomas, P. G., Gupta, V., Kuzel, T. M., Reiser, J., Paras, J., Kane, M. P., Singer, E. A., Malhotra, J., Denzin, L. K., Sant'angelo, D. B., Rabson, A. B., Lee, L. Y., Lasfar, A., Langenfeld, J., Schenkel, J. M., Fidler, M. J., Ruiz, E. S., Marzo, A. L., Rudra, J. S., Silk, A. W. & Zloza, A. 2020. Intratumoral injection of the seasonal flu shot converts immunologically cold tumors to hot and serves as an immunotherapy for cancer. *Proc. Natl. Acad. Sci.,* 117**,** 1119-1128.

Noriega, L., Castro, M. E., Perez-Aguilar, J. M., Caballero, N. A., Sanchez-Gaytan, B. L., González-Vergara, E. & Melendez, F. J. 2020. Oxidovanadium(V) complexes as promising anticancer photosensitizers. *J. Inorg. Biochem.,* 203**,** 110862.

Pessoa, J. C. & Correia, I. 2019. Salan vs. salen metal complexes in catalysis and medicinal applications: Virtues and pitfalls. *Coord. Chem. Rev.,* 388**,** 227-247.

Pessoa, J. C., Etcheverry, S. & Gambino, D. 2015. Vanadium compounds in medicine. *Coord. Chem. Rev.,* 301-302**,** 24-48.

Ren, S., Wang, R., Komatsu, K., Bonaz-Krause, P., Zyrianov, Y., Mckenna, C. E., Csipke, C., Tokes, Z. A. & Lien, E. J. 2002. Synthesis, Biological Evaluation, and Quantitative Structure−Activity Relationship Analysis of New Schiff Bases of Hydroxysemicarbazide as Potential Antitumor Agents. *J. Med. Chem.,* 45**,** 410-419.

Reszka, K. J. & Chignell, C. F. 1993. EPR and spin-trapping investigation of free radicals from the reaction of 4-methoxybenzenediazonium tetrafluoroborate with melanin and melanin precursors. *J. Am. Chem. Soc.,* 115**,** 7752-7760.

Richaud, A., Barba-Behrens, N. & M 2011. Chemical Reactivity of the Imidazole: A Semblance of Pyridine and Pyrrole? *Org. Lett.,* 13**,** 972-975.

Safitri, A., Levina, A., Lee, J., Carter, E. A. & Lay, P. A. 2017. Biospectroscopy for studying the influences of anti-diabetic metals (V, Cr, Mo, and W) to the insulin signaling pathway. *AIP Conference Proceedings,* 1823.

Samart, N., Arhouma, Z., Kumar, S., Murakami, H. A., Crick, D. C. & Crans, D. C. 2018. Decavanadate Inhibits Mycobacterial Growth More Potently Than Other Oxovanadates. *Front. Chem.,* 6.

Sarmiento-González, A., Marchante-Gayón, J. M., Tejerina-Lobo, J. M., Paz-Jiménez, J. & Sanz-Medel, A. 2005. ICP-MS multielemental determination of metals potentially released from dental implants and articular prostheses in human biological fluids. *Anal. Bioanal. Chem.,* 382**,** 1001-1009.

Scalese, G., Correia, I., Benítez, J., Rostán, S., Marques, F., Mendes, F., Matos, A. P., Costa Pessoa, J. & Gambino, D. 2017. Evaluation of cellular uptake, cytotoxicity and cellular ultrastructural effects of heteroleptic oxidovanadium(IV) complexes of salicylaldimines and polypyridyl ligands. *J. Inorg. Biochem.,* 166**,** 162-172.

Schotten, C., Nicholls, T. P., Bourne, R. A., Kapur, N., Nguyen, B. N. & Willans, C. E. 2020. Making electrochemistry easily accessible to the synthetic chemist. *Green Chem.,* 22**,** 3358-3375.

Shcherbakov, V. V., Artemkina, Y. M., Akimova, I. A. & Artemkina, I. M. 2021. Dielectric Characteristics, Electrical Conductivity and Solvation of Ions in Electrolyte Solutions. *Materials,* 14**,** 5617.

Shul'pin, G. B., Kozlov, Y. N. & Shul'pina, L. S. 2019. Metal Complexes Containing Redox-Active Ligands in Oxidation of Hydrocarbons and Alcohols: A Review. *Catalysts,* 9**,** 1046.

Sylvester, P. W. 2011. Optimization of the Tetrazolium Dye (MTT) Colorimetric Assay for Cellular Growth and Viability. *In:* SATYANARAYANAJOIS, S. D. (ed.) *Drug Design and Discovery: Methods and Protocols.* Totowa, NJ: Humana Press.

Tandon, S. S., Chander, S. & Thompson, L. K. 2000. Ligating properties of tridentate Schiff base ligands, 2-[[(2-pyridinylmethyl)imino]methyl] phenol (HSALIMP) and 2-[[[2-(2-pyridinyl)ethyl]imino]methyl]phenol (HSALIEP) with zinc(II), cadmium(II), nickel(II) and manganese(III) ions. X-ray crystal structures of the [Zn(SALIEP)(NO3)]2 dimer, [Mn(SALIEP)2](ClO4), and [Zn(AMP)2(NO3)2]. *Inorg. Chim. Acta,* 300-302**,** 683-692.

Thakur, A., Faujdar, C., Sharma, R., Sharma, S., Malik, B., Nepali, K. & Liou, J. P. 2022. Glioblastoma: Current Status, Emerging Targets, and Recent Advances. *J. Med. Chem.,* 65**,** 8596-8685.

Thompson, K. H. & Orvig, C. 2006. Vanadium in diabetes: 100 years from Phase 0 to Phase I. *J. Inorg. Biochem.,* 100**,** 1925-1935.

Treviño, S. & Diaz, A. 2020. Vanadium and insulin: Partners in metabolic regulation. *J. Inorg. Biochem.,* 208**,** 111094.

Weekes, D. M., Ramogida, C. F., Jaraquemada-Peláez, M. D. G., Patrick, B. O., Apte, C., Kostelnik, T. I., Cawthray, J. F., Murphy, L. & Orvig, C. 2016. Dipicolinate Complexes of Gallium(III) and Lanthanum(III). *Inorg. Chem.,* 55**,** 12544-12558.

Chapter 3 Redox mechanism determination of vanadium(V) pyridine Schiff base catecholate complexes using non-aqueous cyclic voltammetry

3.1 The redox properties of vanadium(V) catecholates contribute to their cytotoxicity in glioblastoma cells

Over the last two decades, many classes of vanadium(IV/V) complexes have been investigated for their anticancer applications (Aureliano et al., 2022, Cacicedo et al., 2019, Pessoa and Correia, 2019, Crans et al., 2019a, Pessoa et al., 2015, Sanasam et al., 2020, Bergeron et al., 2019, Lima et al., 2021). Vanadium complexes prevent cancer cell proliferation through their effects on signal transduction and protein transport, and interactions with protein phosphatases and kinases (Pessoa et al., 2015, Pessoa et al., 2021, Crans et al., 2017, Rehder, 2012, Kostenkova et al., 2023a). Recently, vanadium(V) catecholate complexes have been reported to be promising agents for the treatment of glioblastoma, an aggressive form of brain cancer (Crans et al., 2019b, Levina et al., 2020, Murakami et al., 2022, Kostenkova et al., 2023b). Vanadium(V) catecholate complexes offer a unique approach to glioblastoma treatment due to their hydrophobicity which increases their overall stability before uptake by the cells (Crans et al., 2019b, Levina et al., 2020, Murakami et al., 2022). The improved hydrolytic stability and increased cytotoxicity of the complexes due to the presence of bulky hydrophobic substituents on the catecholate ligand has been reported recently. Specifically, the vanadium(V) catecholate complex, abbreviated [VO(HSHED)(DTB)] where HSHED stands for N-(salicylideneaminato)-N´-(2-hydroxyethyl)-1,2-ethanediamine and DTB stands for di-*tert*-butylcatechol has been found to be 12 times more potent than cisplatin in glioblastoma (T98g) cells and highly effective in other

difficult-to-treat cancers, such as A549 (lung), PANC-1 (pancreatic), and SW1353 (bone

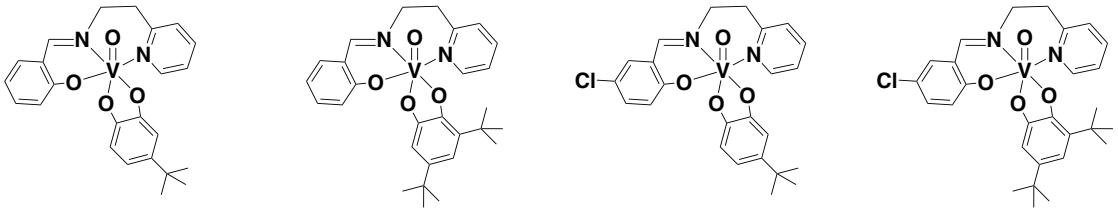

[VO(SALIEP)(4TB)] **[VO(SALIEP)(DTB)]** **[VO(Cl-SALIEP)(4TB)]** **[VO(Cl-SALIEP)(DTB)]**

Figure 3.1. Structures of the [VO(SALIEP)X] and [VO(Cl-SALIEP)X] analogs where X = H or *tert*-butyl, Y = H or *tert*-butyl, Z = H or *tert*-butyl investigated in this work.

chondrosarcoma) cells (**Figure 3.1**) (Levina et al., 2020, Crans et al., 2019b). Since the complexes have relatively short hydrolytic stability, their cytotoxic solutions are suitable candidates for intratumoral injections, a treatment currently investigated in the clinic in nearly 100 studies (Levina et al., 2022, Levina et al., 2020, Manganaro et al., 2022, Murakami et al., 2022).

Three vanadium(V) catecholate complexes have been reported as potential drug candidates for advanced glioblastoma between 2019-2023 (Crans et al., 2019b, Levina et al., 2020, Murakami et al., 2022). As mentioned previously, the [VO(HSHED)(DTB)] complex is a lead analog with superior anti-proliferative activity (IC_{50} < 10 μM at 72 h treatment) in T98g cells and high hydrolytic stability (**Figure 3.1**). The second analog, [VO(Cl-HSHED)(DTB)], is another potential drug candidate due to its exceptional hydrolytic stability ([$t_{1/2}$ (298 K) = 15 min in cell medium] and high cytotoxicity (IC_{50} = 4.1 μM, **Figure 3.1**) (Murakami et al., 2022). The third analog abbreviated [V^{V}O(SALIEP)(DTB)] where SALIEP stands for N-(salicydeneaminato)-2-(2-aminoethylpyridine) is a newly reported drug candidate (Kostenkova et al., 2023b). [V^{V}O(SALIEP)(DTB)], has shown moderate stability in cell culture media, significant cellular uptake of the intact complex by T98g (human glioblastoma) cells and high anti-proliferative activity (IC_{50} < 10 mM at 72 h treatment) in this cell line, which was ~5-fold higher than that for a non-cancerous human cell line, HFF-1 (**Figure 3.1**) (Kostenkova et al., 2023b). The hydrophobicity of

the DTB ligand attributes to superior hydrolytic stability and, thus, high cytotoxicity of the complexes. The [V^{V}O(SALIEP)(DTB)] is the also first catecholate complex with selective cytotoxicity against T98g cells.

The observed cytotoxic properties of vanadium(V) catecholates are also attributed to their redox properties, as both the vanadium(V) center and the catecholate ligand are redox-active (Murakami et al., 2022, Li et al., 1988, Cornman et al., 1992b). Thus, vanadium(V) catecholates undergo a one-electron redox reaction where the complexes reduce to vanadium(IV). According to previous reports, the redox reaction of vanadium(V) catecholates is delocalized over their vanadium center and the catecholate ligand (Cornman et al., 1992a, Cornman et al., 1992b, Li et al., 1988). Previous electrochemical characterization of [VO(HSHED)X] and [VO(SALIEP)X] complexes has shown that the hydrophobic substituents on the catecholate ligand stabilizes the reduced V(IV) species (Murakami et al., 2022, Kostenkova et al., 2023b). The cellular environment is highly reducing due to the presence of several intracellular reductants, including ascorbate and glutathione, thus, vanadium(V) catecholates likely reduce to the respective V(IV) species (Forman et al., 2009). The complexes with bulky aliphatic substituents are more cytotoxic because of the increased stability of the reduced V(IV) species. Previous work has also established that differences between the amines of the SALIEP and HSHED Schiff bases affect the observed redox properties and, consequentially, cytotoxicity in T98g cells (Murakami et al., 2022, Kostenkova et al., 2023b). The SALIEP Schiff base contains a pyridine ring which significantly increases the hydrophobicity of the resulting V(V) complexes, thus, making them harder to reduce (**Figure 3.1**). The presence of the pyridine ring, however, results in the formation of the six-membered core between the V center, the ethanol linker and the pyridine ring which reduces the stability of the V(V) species in the absence of aliphatic substituents on the catecholate ligand (Kostenkova et al., 2023b). The aliphatic DTB substituents and the pyridine ring of the Schiff base increase the stability of the reduced V(IV) species and, thus, cytotoxicity of the

[VO(SALIEP)(DTB)] and [VO(Cl-SALIEP)(DTB)] overall. The VOHSHED complexes, on the other hand, remain as V^{V} species due to their five-membered ring core which is evidenced by both ^{51}V NMR and non-aqueous cyclic voltammetry (Murakami et al., 2022, Crans et al., 2019b). This leads to even higher cytotoxicity than that of the VOSALIEP complexes.

Despite extensive electrochemical characterization of the complexes, no studies have investigated the effects of the redox properties of V(V) catecholates on their observed cytotoxicity. The complexes likely undergo redox under the assay conditions, as the cellular environment is highly reducing due to the presence of glutathione (GSH), an antioxidant and the most abundant intracellular reducing agent (Levina et al., 2020). GSH is a thiol-containing tripeptide and most common low molecular weight thiol present in animal cells (0.5-10 mM) and is found at a concentration of 2-12 uM in healthy humans (Areias et al., 2016). GSH is redox-active and readily oxidizes to glutathione disulfIde (GSSG). GSH also undergoes two-electron redox reactions with catecholate moieties which is shown in **Figure 3.2**. Catechol is oxidized to *o*-quinone which then

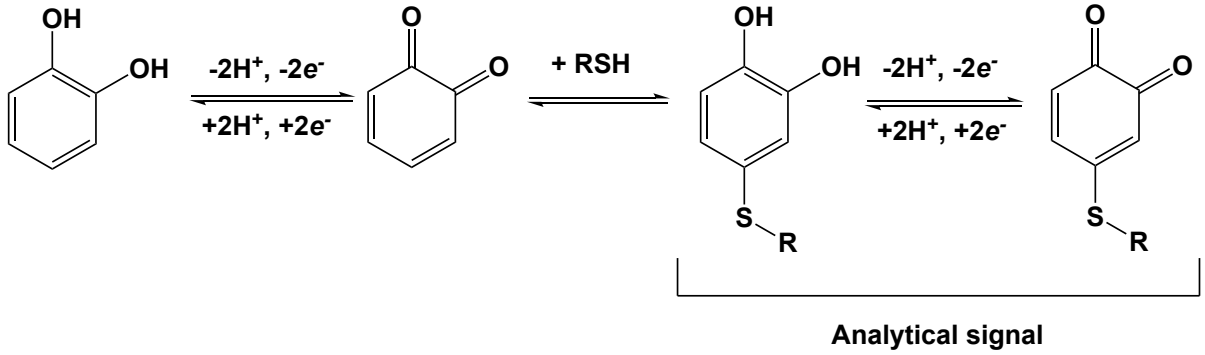

Figure 3.2. A two-electron redox reaction of glutathione (GSH; RSH in the diagram) and catechol.

reacts with GSH via 1,4 Michael addition to generate a catechol-like entity which is observable by cyclic voltammetry (Harfield et al., 2012). The redox reaction between catechol and GSH is a four-electron process which results in an enhanced CV signal (Harfield et al., 2012).

In this study, we have investigated the reversibility of the redox reactions and the redox mechanism of the VOSALIEP complexes with 4TB and DTB ligands using variable scan non-aqueous cyclic voltammetry (**Figure 3.1**). Additionally, we have carried out electrochemical characterization with an intracellular reductant GSH to see whether it affects the redox properties of the complexes.

3.2 Materials and Methods

3.2.1 General Materials

The [VO(SALIEP)X] and [VO(Cl-SALIEP)X] complexes were synthesized using reported methods from the literature (Kostenkova et al., 2023b). Silver nitrate, ferrocene and tetra-*n*-butylammonium perchlorate (TBAP) were purchased from Merck Millipore for electrochemistry experiments and used as received. Acetonitrile (HPLC grade) was dried using 3 Å molecular sieves for at least 48 h prior to use.

3.2.2 General Methods: Cyclic Voltammetry

Instrumentation: Cyclic voltammetry experiments were carried out using a WaveDriver 40 DC Bipotentiostat/Galvanostat and a Low Volume Three Electrode Cell Basic Kit (AF01CKT1006) purchased from Pine Research Instrumentation. AfterMath v 1.5.9807 data acquisition The software used during was with the iR Compensation option turned off, while eL-Chem Viewer and Microsoft Excel were used for post-acquisition processing. All cyclic voltammograms (CVs) were externally referenced to ferrocene.

3.2.3 Variable scan rate cyclic voltammetry experiments

Sample preparation: The solutions of all complexes had a final concentration of 2.0 mM in 100 mM TBAP in dry acetonitrile solution. A 10.0 mM ferrocene solution (in 100 mM TBAP in dry acetonitrile solution) was used as an external reference. A 2.0 mM silver nitrite solution was used

to fill a refillable Ag reference electrode. All samples were degassed using Ar for 10 minutes prior to cyclic voltammogram collection.

Experimental parameters: The CVs were recorded using the following scan rates for all samples: 25 mV/s, 50 mV/s, 75 mV/s, 100 mV/s, 125 mV/s, 150 mV/s, 175 mV/s, 200 mV/s and 225 mV/s. The CVs were externally referenced to ferrocene collected at the appropriate scan rates. The parameters used to collect the CVs are tabulated below (**Table 3.1**).

Table 3.1. Experimental parameters for variable scan rate cyclic voltammetry studies.

Compound	Concentration	Segments	Initial Potential	Vertex Potential	Final Potential
Ferrocene (external standard)	2.0 mM	2	1.0 V	-1.5 V	1.0 V
[VO(SALIEP)(4TB)]	2.0 mM	2	-0.10 V	-1.65 V	-0.10 V
[VO(SALIEP)(DTB)]	2.0 mM	2	-0.45 V	-1.65 V	-0.45 V
[VO(Cl-SALIEP)(4TB)]	2.0 mM	2	0.25 V	-1.5 V	0.25 V
[VO(Cl-SALIEP)(DTB)]	2.0 mM	2	-0.55 V	-0.85 V	-0.55 V

3.2.4 Cyclic voltammetry experiments with glutathione

Sample preparation: The solutions of all complexes had a final concentration of 2.0 mM in 100 mM TBAP in dry acetonitrile solution (5 mL). Additionally, all samples had a 2.0 mM concentration of glutathione (GSH). A 10.0 mM ferrocene solution (in 100 mM TBAP in dry acetonitrile solution) was used as an external reference. A 2.0 mM silver nitrite solution was used to fill a refillable Ag reference electrode. All samples were degassed using Ar for 10 minutes prior to cyclic voltammogram collection.

Experimental parameters: The CVs were recorded using the following scan rates for all samples: 100 mV/s and 150 mV/s. The CVs were externally referenced to ferrocene collected at the appropriate scan rates. The parameters used to collect the CVs are tabulated below (**Table 3.2**).

Table 3.2. Experimental parameters for cyclic voltammetry studies in the presence of glutathione.

Compound	Concentration	Segments	Initial Potential	Vertex Potential	Final Potential
Ferrocene (external standard)	2.0 mM	2	1.0 V	-1.5 V	1.0 V
[VO(SALIEP)(4TB)]	2.0 mM	2	-0.10 V	-1.65 V	-0.10 V
[VO(SALIEP)(DTB)]	2.0 mM	2	-0.45 V	-1.65 V	-0.45 V
[VO(Cl-SALIEP)(4TB)]	2.0 mM	2	0.25 V	-1.5 V	0.25 V
[VO(Cl-SALIEP)(DTB)]	2.0 mM	2	-0.55 V	-0.85 V	-0.55 V

3.2.5 Information of calculation of the diffusion constant (D_{CO})

The open-source Randles-Sevcik on the CalcTool website was used to calculate the D_{CO} values, with the solution assumed to be at 25 °C and standard temperature and pressure (STP) conditions.

$$D_{CO} = \left(\frac{I_P}{2.69 * 10^5 \ * n^{\frac{3}{2}} * A_E * C * \ v^{\frac{1}{2}}} \right)^2$$

I_P is the peak current from a voltammogram in amps. The number of electrons transferred is *n*, which is equal to 1 for these compounds. A_E is the area of the working electrode, 0.09 cm^2. *C* is the concentration of the analyte in the solution in mol/cm^3. The scan rate is *v*, in volts per second.

Information of establishing the reversibility of the redox reactions

To establish the reversibility of the redox reactions, the Randles-Sevcik plot was used where $v^{1/2}$ (scan rate) vs. I_P (peak current in μA) were plotted. The R^2 value of the trendline helped to establish the linearity of the $v^{1/2}$ vs. I_P relationship. Additionally, the I_{PA}/I_{PC} ratios were used to establish the reversibility of the redox reactions where I_{PA} is the peak anodic current, and I_{PC} is the peak cathodic current.

3.3 Results and Discussion

3.3.1 Variable scan experiments of [VO(SALIEP)X] Complexes

Variable scan rate experiments have carried out to investigate the redox mechanism of the VOSALIEP complexes with 4TB and DTB ligands. The CV of [VO(SALIEP)(4TB)] exhibits one major isomer peak on the cathodic side and one peak on the anodic side, corresponding to one V(V) and one V(IV) isomer that equilibrate in solution (**Figure 3.3A**). The CV also exhibits a more negative minor isomer peak on the anodic side, meaning that the [V^VO(SALIEP)(4TB)] forms two V(IV) isomers upon reduction. The second V(IV) isomer is more stable on the electrochemical

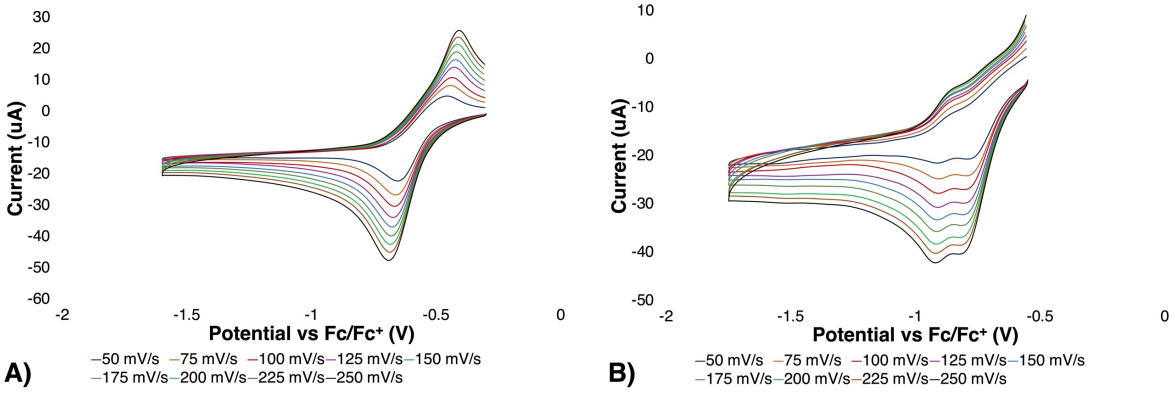

Figure 3.3. Variable scan rate cyclic voltammetry experiments of the A) [VO(SALIEP)(4TB)] and B) [VO(SALIEP)(DTB)] complexes. All cyclic voltammograms were collected in 2.0 mM solutions of dry acetonitrile.

scale, since it has a higher maximum peak current and, thus, higher concentration. The proposed

redox mechanism of the [V^{V}O(SALIEP)(4TB)] is the following: the complex reduces to two V(IV) isomers which exist equilibrate in solution. Since the second V(IV) isomer is more stable, it reoxidizes back to the V(V) species. The V(V) species can, consequentially, reduce back to the second V(IV) isomer The proposed redox mechanism is shown in **Figure 3.4**.

The complex exhibits quasi-reversible behavior at scan rates using the scan rates under 225 mV/s which is evident by the I_{PA}/I_{PC} ratios <1 (**Table 3.3**) (Frenzel et al., 2017). The higher intensity

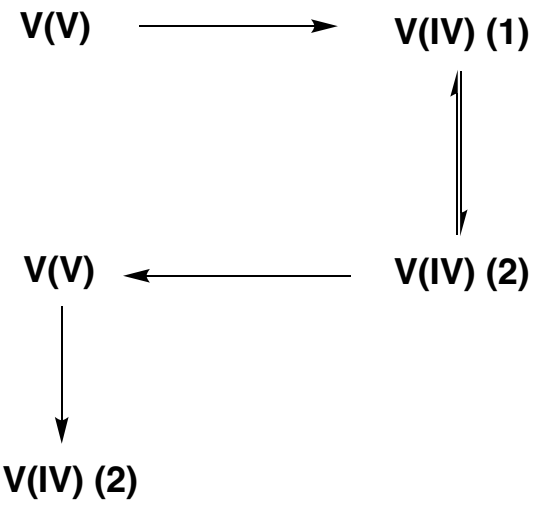

Figure 3.4. Proposed redox mechanism of the [VO(SALIEP)(4TB)] complex, based on the variable scan rate cyclic voltammetry data.

of the cathodic peaks at all scan rates and the I_{PA}/I_{PC} ratio of <1 corresponds to the higher concentration of V(V) species, compared to the reduced V(IV) species, meaning that the [V^{V}O(SALIEP)(4TB)] is more stable. The reversibility has been determined using the Randles-Sevcik plot (**Figure 3.5A**) where the square root of the scan rate ($v^{1/2}$) has been plotted against maximum peak current (I_P). The Randles-Sevcik plot shows that $v^{1/2}$ vs I_P show a linear relationship, meaning that the redox reaction of the [V^{V}O(SALIEP)(4TB)] complex follows a

diffusion mechanism. In a diffusion-controlled redox mechanism, V(IV/V) species are stable and equilibrate in solution.

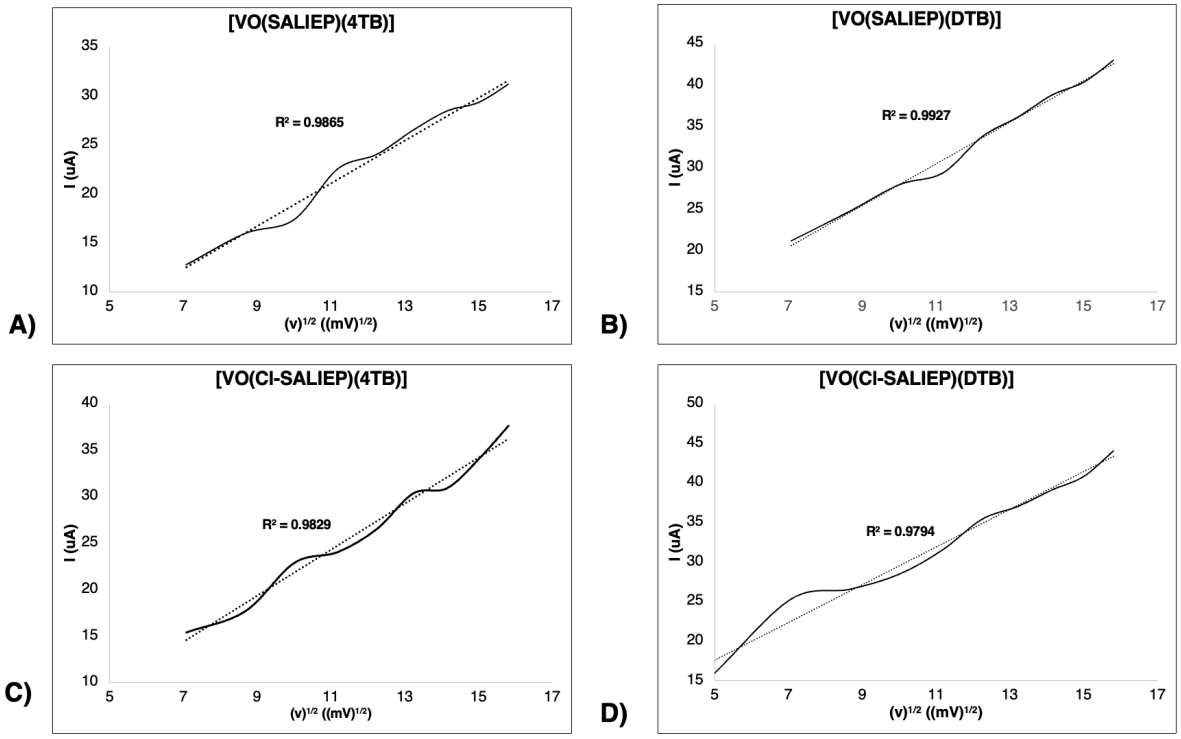

Figure 3.5. Randles-Sevcik plots of the A) [VO(SALIEP)(4TB)], B) [VO(SALIEP)(DTB)], C) [VO(Cl-SALIEP)(4TB)] and D) [VO(Cl-SALIEP)(DTB)] complexes where the square root of the scan rate (in mV/s) was plotted against the maximum current (in uA).

Table 3.3. Data from the CV scan rate study of the [VO(SALIEP)(4TB)] complex.

Scan Rate, mV/s	$E_{1/2}$ vs Fc^+/Fc (V)	I_{PA} (uA)	I_{PC} (uA)	I_{PA} / I_{PC} (uA)	D_{CO} x 10^{-6} (cm^2/s)
50	-0.555	9	13	0.67	1.4
75	-0.552	12	16	0.76	1.5
100	-0.552	14	17	0.83	1.3
125	-0.550	18	23	0.78	1.7
150	-0.547	20	24	0.82	1.7
175	-0.550	23	27	0.86	1.7
200	-0.550	25	28	0.88	2.0
225	-0.550	27	29	0.93	1.6
250	-0.550	29	31	0.94	1.7

The [VO(SALIEP)(DTB)] complex exhibits reversible redox behavior at all scan rates, as indicated by the I_{PA} / $I_{PC\ 1}$ = I_{PA} / $I_{PC\ 2}$ = 1 ratios (**Table 3.4**) (Frenzel et al., 2017). The CVs of the

Table 3.4. Data from the CV scan rate study of the [VO(SALIEP)(DTB)] complex.

Scan Rate, mV/s	$E_{1/2\ 1}$ vs Fc^+/Fc (V)	I_{PA} (uA)	$I_{PC\ 1}$ (uA)	I_{PA} / $I_{PC\ 1}$ (uA)	$D_{CO\ 1}$ x 10^{-6} (cm^2/s)
50	-0.812	21	20	1.04	3.5
75	-0.816	25	24	1.04	3.2
100	-0.847	28	27	1.05	3.0
125	-0.827	29	31	0.95	3.3
150	-0.832	34	32	1.07	2.9
175	-0.832	36	34	1.00	2.8
200	-0.834	39	36	1.07	2.9
225	-0.831	40	38	1.06	2.7
250	-0.844	43	40	1.08	2.7
Scan Rate, mV/s	**$E_{1/2\ 2}$ vs Fc^+/Fc (V)**	**I_{PA} (uA)**	**$I_{PC\ 2}$ (uA)**	**I_{PA} / $I_{PC\ 2}$ (uA)**	**$D_{CO\ 2}$ x 10^{-6} (cm^2/s)**
50	-0.877	21	22	0.98	4.0
75	-0.879	25	25	0.99	3.6
100	-0.884	28	28	1.00	3.4
125	-0.889	29	31	0.95	3.3
150	-0.892	34	34	1.01	3.2
175	-0.892	36	36	1.07	3.2
200	-0.892	39	39	1.00	3.2
225	-0.891	40	41	0.99	3.1
250	-0.899	43	43	1.00	3.1

[VO(SALIEP)(DTB)] complex have two peaks on the cathodic side, corresponding to two V(V) species that are in equilibrium with the reduced V(IV) species in solution and exchange slowly on the electrochemical scale (**Figure 3.3B**). The presence of two isomers in solution and the structure of the major isomer have been confirmed in earlier work by Kostenkova *et. al*. According to previous reports, two [VO(SALIEP)(DTB)] isomers form in solution depending on the coordination of the DTB ligand relative to the SALIEP Schiff base. V(V) isomers reduce to one V(IV) species, as evidenced by one peak on the anodic side of the CV. The slightly higher peak maximum current on the cathodic side (I_{PC}) indicates that the concentration of V(V) species in solution is higher, as the maximum current is directly proportional to concentration (**Table 3.4, Figure 3.3B**). Thus, the reversibility of this redox process indicates that two V(V) isomers and the reduced V(IV) species are stable and equilibrate in solution, although the concentration of the

V(V) species in solution is slightly higher. The formation of the second V(IV) species, however, is observed at the scan rate of 250 mV/s which, most likely, corresponds to the second V(IV) isomer.

The reversibility of the [VO(SALIEP)(DTB)] redox mechanism has been determined using the Randles-Sevcik plot (**Figure 3.5B**) where the square root of the scan rate ($v^{1/2}$) has been plotted against maximum peak current (I_P). The [VO(SALIEP)(DTB)] complex exhibits a linear relationship between $v^{1/2}$ and I_P which corresponds to a reversible redox reaction (**Figure 3.5B**). The reversible redox reaction of the [VO(SALIEP)(DTB)] is also indicative of the diffusion-controlled redox process where V(IV/V) species are stable and equilibrate in solution.

3.3.2 Variable scan experiments of [VO(Cl-SALIEP)X] Complexes

Variable scan rate experiments have also been carried out with the [VO(Cl-SALIEP)X] analogs to investigate their redox mechanism and establish how it affects the relative stability of the V(IV/V) species. Previous electrochemical characterization of the [VO(Cl-SALIEP)X] has shown that the complexes are more hydrophobic due to the electron-donating Cl group in the π aromatic system, making the complexes harder to reduce (Kostenkova et al., 2023b). The [VO(Cl-

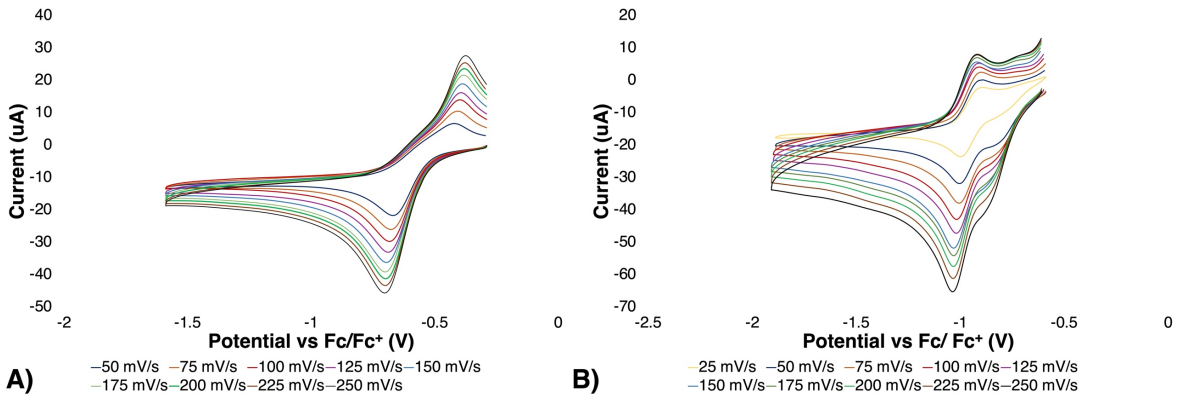

Figure 3.6. Variable scan rate cyclic voltammetry experiments of the A) [VO(Cl-SALIEP)(4TB)] and B) [VO(Cl-SALIEP)(DTB)] complexes. All cyclic voltammograms were collected in 2.0 mM solutions of dry acetonitrile.

SALIEP)(4TB)] complex exhibits quasi-reversible redox behavior at all scan rates, as indicated by the I_{PA} / $I_{PC\ 1}$ = I_{PA} / $I_{PC\ 2}$ < 1 ratios (**Figure 3.6A**) (Frenzel et al., 2017). The higher peak maximum current on the cathodic side (I_{PC}) indicates that the concentration of V(V) species in solution is higher, as the maximum current is directly proportional to concentration. Similar to the [VO(SALIEP)(4TB)], the [VO(Cl-SALIEP)(4TB)] forms a minor isomer which has a more negative $E_{1/2}$ than the major isomer (**Figure 3.6A**). Thus, the [VO(Cl-SALIEP)(4TB)] follows a similar redox mechanism to [VO(SALIEP)(4TB)] where the complex reduces to two V(IV) isomers that exist at equilibrium. The more stable second V(IV) isomer readily reoxidizes back to the V(V) species which then reduces to the second V(IV) isomer.

The Randles-Sevcik plot of the square root of the scan rate ($v^{1/2}$) against maximum peak current (I_P) showed an off-linear relationship between $v^{1/2}$ and I_P and, thus, has confirmed the quasi-reversible and diffusion-controlled nature of the redox reaction (**Figure 3.5C**). Similar to the [VO(SALIEP)(4TB)] complex, the [V^VO(Cl-SALIEP)(4TB)] species is more stable due to the higher maximum current on the cathodic side (I_{PC}) (**Table 3.5**). The data demonstrated that both the V(V) and V(IV) species were stable and equilibrated in solution, although the V(V) species were present in a slightly higher concentration.

Table 3.5. Data from the CV scan rate study of the [VO(Cl-SALIEP)(4TB)] complex.

Scan Rate, mV/s	$E_{1/2}$ vs Fc^+/Fc (V)	I_{PA} (uA)	I_{PC} (uA)	I_{PA} / I_{PC} (uA)	D_{CO} x 10^{-6} (cm^2/s)
50	-0.538	12	15	0.80	2.0
75	-0.542	12	18	0.70	1.8
100	-0.542	16	23	0.70	2.2
125	-0.542	18	24	0.76	2.0
150	-0.542	21	27	0.80	2.0
175	-0.542	24	30	0.78	2.2
200	-0.540	26	31	0.83	2.0
225	-0.540	28	34	0.81	2.2
250	-0.540	30	38	0.79	2.4

The addition of the electron-donating Cl group to the π aromatic system drastically changed the observed redox behavior of the [VO(Cl-SALIEP)(DTB)] complex. The cathodic side exhibited two distinct peaks, corresponding to two V(V) isomers that are at equilibrium (**Figure 3.6B**). Similar to the [VO(SALIEP)(DTB)] complex, both of the [VO(Cl-SALIEP)(DTB)] isomers reduce to one V(IV) isomer in solution. Further electrochemical analysis, however, confirmed the quasi-reversible nature of the [VO(Cl-SALIEP)(DTB)] redox reaction. The quasi-reversible process was evident by the I_{PA} / I_{PC} > >1 (**Table 3.6**) (Frenzel et al., 2017). The maximum peak current measurements demonstrated that the V(IV) species were present in a much higher concentration, compared to both V(V) species, which was evidenced by higher maximum current on the anodic side (**Table 3.6**). The formation of the second V(IV) species, however, was observed at the scan rate of 250 mV/s which, most likely, corresponded to the second V(IV) isomer. The reversibility of the [VO(Cl-SALIEP)(DTB)] redox mechanism was determined using the Randles-Sevcik plot where the square root of the scan rate ($v^{1/2}$) has been plotted against maximum peak current (I_P) (**Figure 3.5D**). The [VO(Cl-SALIEP)(DTB)] complex exhibited a linear relationship between $v^{1/2}$ and I_P which corresponds to a reversible redox reaction (**Figure 3.5D**).. The reversible redox reaction of the [VO(SALIEP)(DTB)] was also indicative of the diffusion-controlled redox process where V(IV/V) were stable and equilibrated in solution.

Table 3.6. Data from the CV scan rate study of the [VO(Cl-SALIEP)(DTB)] complex.

Scan Rate, mV/s	$E_{1/2\,1}$ vs Fc^+/Fc (V)	I_{PA} (uA)	$I_{PC\,1}$ (uA)	I_{PA} / $I_{PC\,1}$ (uA)	$D_{CO\,1}$ x 10^{-6} (cm^2/s)
25	-0.954	16	6	3	0.6
50	-0.959	25	6	4	0.3
75	-0.964	27	9	3	0.5
100	-0.964	28	9	3	0.3
125	-0.977	32	9	3	0.3
150	-0.984	35	9	4	0.2
175	-0.982	37	13	3	0.4
200	-0.984	39	12	3	0.3

Table 3.6. Data from the CV scan rate study of the [VO(Cl-SALIEP)(DTB)] complex.

225	-0.984	41	12	3	0.3
250	-0.984	44	11	4	0.2
Scan Rate, mV/s	**$E_{1/2\ 2}$ vs Fc^+/Fc (V)**	**I_{PA} (uA)**	**$I_{PC\ 2}$ (uA)**	**I_{PA} / $I_{PC\ 2}$ (uA)**	**$D_{CO\ 2}$ x 10^{-6} (cm^2/s)**
25	-0.844	16	1	13	0.02
50	-0.854	25	3	8	0.08
75	-0.856	27	3	9	0.05
100	-0.872	28	7	4	0.2
125	-0.869	32	4	8	0.05
150	-0.886	35	4	8	0.05
175	-0.882	37	4	9	0.04
200	-0.884	39	4	9	0.03
225	-0.889	41	5	9	0.05
250	-0.891	44	5	9	0.04

Herein, we describe the first detailed electrochemical characterization of vanadium(V) catecholate complexes. Previous reports characterized VOHSHED and VOCl-HSHED complexes and demonstrated that the complexes exhibit reversible redox behavior (Murakami et al., 2022, Crans et al., 2019b). The studies, however, did not investigate whether the processes are diffusion-controlled using Randles-Sevcik plots. The VOSALIEP and VOCl-SALIEP complexes exhibit a different and a more complex redox chemistry due to the presence of pyridine in their Schiff base ligands. The presence of the pyridine ring results in the formation of the six-membered ring core between the V center, the ethyl arm of the SALIEP ligand, and the imine of the Schiff base which significantly decreases the stability of V(V) species (**Figure 3.1**). According to previous spectroscopic studies with VOSALIEP and VOCl-SALIEP complexes readily reduce to V(IV), particularly when catecholate ligand lack bulky aliphatic substituents (Kostenkova et al., 2023b). This study showed that some complexes form two isomers, meaning that the VOSALIEP and VOCl-SALIEP complexes exchange slower on the electrochemical scale, compared to the VOHSHED complexes (Kostenkova et al., 2023b, Murakami et al., 2022). Interestingly, those isomers are not in ^{51}V NMR, according to previous study with VOSALIEP and VOCl-SALIEP

complexes (Kostenkova et al., 2023b). All three electrochemical studies have established that the presence of bulky aliphatic substituents on the catecholate ring contributes to the stability of the reduced V(IV/V) species. Future electrochemical studies with novel vanadium(V) catecholate complexes are needed to further establish which motifs contribute to the stability of the reduced V(IV/V) species.

3.3.3 Cyclic voltammetry experiments with glutathione

Cyclic voltammograms in the presence of glutathione (GSH) were collected to see whether this intracellular reductant affected the redox properties of the VOSALIEP complexes. GSH is the most abundant reductant in the cytoplasm, making the cellular environment highly reducing (Forman et al., 2009). In this study, all dry acetonitrile solutions contained identical concentrations of the VOSALIEP complexes and the glutathione reductant (2.0 mM of each). The data showed that the presence of GSH increased the peak current on both anodic and cathodic sides for the [VO(SALIEP)(4TB)] complex (**Figure 3.7A**). The I_{PA}/I_{PC} ratio of ≈ 1 indicated that the complex

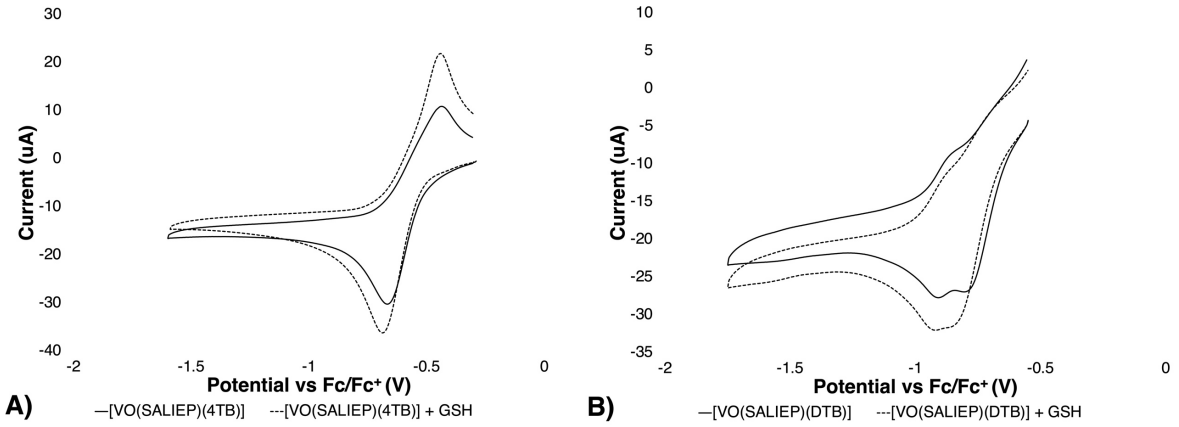

Figure 3.7. Cyclic voltammetry experiments with the A) [VO(SALIEP)(4TB)] and B) [VO(SALIEP)(DTB)] complexes in the presence of glutathione (GSH). All cyclic voltammograms were collected in 2.0 mM solutions of dry acetonitrile.

underwent a reversible redox reaction in the presence of GSH. The increase maximum current can be explained by the complexation of GSH to the 4TB ligand, resulting in the

[VO(SALIEP)(4TB)] – GSH complex which is evidenced by more negative half-way potential values. After the complexation of GSH, the [V^{V}O(SALIEP)(4TB)] was reduced to the [V^{IV}O(SALIEP)(4TB)] and GSH was oxidized to GSSG, an oxidized form of GSH. The [V^{V}O(SALIEP)(4TB)], however, formed only one V(IV) isomer in the presence of GSH, meaning that the second V(IV) isomer observed in acetonitrile is unstable in the presence of GSH. The data have shown that the presence of GSH also increases the peak current on both anodic and cathodic sides for the [VO(SALIEP)(DTB)] complex (**Figure 3.7B**). The I_{PA}/I_{PC} ratio of ≈ 1 indicates that the complex undergoes a reversible redox reaction in the presence of GSH. The increase maximum current can be explained by the complexation of GSH to the DTB ligand, resulting in the [VO(SALIEP)(DTB)] – GSH complex which is evidenced by more negative half-way potential values. After the complexation of GSH, the [V^{V}O(SALIEP)(DTB)] complex is reduced to the [V^{IV}O(SALIEP)(DTB)] and GSH is oxidized to GSSG, an oxidized form of GSH. Thus, the redox chemistry of both [VO(SALIEP)(4TB)] and [VO(SALIEP)(DTB)] is unaffected by the presence of GSH. In fact, the increased stability of the reduced V(IV) species would likely result in higher cytotoxicity in cellular assays.

Table 3.7. Data from the CV scan rate study of the [VO(SALIEP)(DTB)] complex.

Species	**Scan Rate, mV/s**	**$E_{1/2}$ vs Fc^{+}/Fc (V)**	**I_{PA} (uA)**	**I_{PC} (uA)**	**I_{PA} / I_{PC} (uA)**	**D_{CO} x 10^{-6} (cm^2/s)**
[VO(SALIEP)(4TB)]	100	-0.552	14	17	0.83	1.3
[VO(SALIEP)(4TB)] + GSH	100	-0.565	25	27	0.91	3.1
[VO(SALIEP)(DTB)]	100	-0.884, -0.847	28	28,27	1.05, 1.00	3.4, 3.0
[VO(SALIEP)(DTB)] + GSH	100	-0.879, -0.864	31	32,32	0.97, 0.99	4.4
[VO(Cl-SALIEP)(4TB)]	100	-0.542	16	23	0.70	2.2
[VO(Cl-SALIEP)(4TB)] + GSH	100	-0.542	11	22	0.52	2.1

Table 3.7. Data from the CV scan rate study of the [VO(SALIEP)(DTB)] complex.

[VO(Cl-SALIEP)(DTB)]	100	-0.964, -0.872	28	9, 7	3,4	0.3, 0.2
[VO(Cl-SALIEP)(DTB)] + GSH	100	-0.964, -0.872	28	9, 7	3,4	0.3, 0.2

The redox chemistry of the chloro analogs was also investigated in the presence of GSH. The data showed that the [VO(Cl-SALIEP)(4TB)] complex forms the thiol bond with GSH which is indicative by the increased maximum current on the cathodic side (**Figure 3.8A, Table 3.7**).

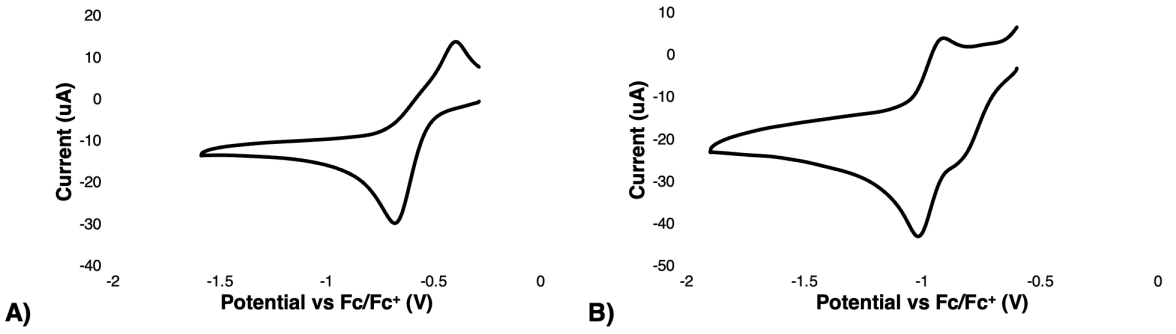

Figure 3.8. Cyclic voltammetry experiments with the A) [VO(Cl-SALIEP)(4TB)] and B) [VO(Cl-SALIEP)(DTB)] complexes in the presence of glutathione (GSH). All cyclic voltammograms were collected in 2.0 mM solutions of dry acetonitrile.

The I_{PA}/I_{PC} ratio of < 1 indicates that the complex undergoes a quasi-reversible redox reaction in the presence of GSH where the oxidizes [V^{V}O(Cl-SALIEP)(4TB)] is present in a much higher concentration. The resulting [VO(Cl-SALIEP)(4TB)] – GSH, however, has the identical half-wave potential as the [VO(Cl-SALIEP)(4TB)] complex. The peak current on the anodic side, however, decreased in the presence of GSH which corresponds to the lower concentration and, thus, a decreased stability of the [V^{IV}O(Cl-SALIEP)(4TB)] species.

The redox chemistry of the [VO(Cl-SALIEP)(DTB)] complex, however, is unaffected by the presence of GSH which is indicative by identical maximum current in the presence or absence of GSH (**Figure 3.8B, Table 3.7**). The I_{PA}/I_{PC} ratio of > 1 indicates that the complex undergoes a

quasi-reversible redox reaction in the presence of GSH where the reduced V(IV) species are present in a much higher concentration. Thus, the reduced [VO(Cl-SALIEP)(DTB)] complex is much stable in solution which is evidenced by the CV data. The experiments with GSH, however, demonstrated that the parent VOSALIEP complexes are more likely to undergo a complexation reaction with GSH which is evidenced by greater increase of the maximum peak current.

Herein, we describe the first electrochemical study of vanadium complexes with GSH, most abundant intracellular reductant. GSH supports metabolism of both healthy and cancerous cells which is why we are interested in interaction of GSH with vanadium(V) catecholate complexes. GSH is redox active; however, it cannot be detected my cyclic voltammetry, unless added to a solution containing a redox-active transition metal, according to previous reports (Harfield et al., 2012). The data have shown that the presence of GSH doesn't disrupt the stability of the redox-active V(IV/V) species in the organic solvent. Presumably, GSH does not disrupt the stability of the redox-active V(IV/V) under the assay conditions. The caveat is that the electrochemical studies with GSH described here were carried out in the organic solvent which doesn't accurately represent the assay conditions. Previous reports demonstrated that under aqueous conditions, the complexation of vanadium to thiols is favored which suppresses redox reactions in aqueous solution (Crans et al., 2010). The distribution of V(IV/V) thiol complexes is highly dependent on the pH and concentrations of the vanadate species (Crans et al., 2010) which would make the aqueous electrochemical studies very challenging. Electrochemical studies under the assay conditions would be of interest; however, the proposed experiments are beyond the scope of this study.

3.4 Conclusions

In this study, we carried out detailed electrochemical characterization of the VOSALIEP and VOCl-SALIEP complexes. The data have shown that most redox processes exhibit a quasi-

reversible mechanism, except for the [VO(SALIEP)(DTB)] complex which exhibits a reversible redox mechanism at variable scan rates. The complexes with 4TB ligands exhibit two V(IV) isomers, one of which is much more stable and readily reoxidizes back to the V(V) species. The Randles-Sevcik plot of all four redox reactions showed a linear relationship between the square-root of the scan rate and the maximum current which corresponded to the diffusion-controlled reaction mechanisms. In the diffusion-controlled redox mechanisms, all V(IV/V) isomers are stable and equilibrate in the organic solution. All complexes form complexes in the presence of GSH which means that the stability of the V(IV/V) species is unaffected. The formation of the catecholate – GSH complex is evidenced by the maximum anodic current and more negative half-way potential values. Overall, the study contributed to better understanding of the redox chemistry of the VOSALIEP and VOCl-SALIEP complexes.

3.5 References

Areias, M. C. C., Shimizu, K. & Compton, R. G. 2016. Voltammetric detection of glutathione: an adsorptive stripping voltammetry approach. *Analyst,* 141**,** 2904-2910.

Aureliano, M., Gumerova, N. I., Sciortino, G., Garribba, E., Mclauchlan, C. C., Rompel, A. & Crans, D. C. 2022. Polyoxidovanadates' interactions with proteins: An overview. *Coordination Chemistry Reviews,* 454**,** 214344.

Bergeron, A., Kostenkova, K., Selman, M., Murakami, H. A., Owens, E., Haribabu, N., Arulanandam, R., Diallo, J.-S. & Crans, D. C. 2019. Enhancement of oncolytic virotherapy by vanadium(V) dipicolinates. *BioMetals,* 32**,** 545-561.

Cacicedo, M. L., Ruiz, M. C., Scioli-Montoto, S., Ruiz, M. E., Fernández, M. A., Torres-Sanchez, R. M., Baran, E. J., Castro, G. R. & León, I. E. 2019. Lipid nanoparticles – Metvan: revealing a novel way to deliver a vanadium compound to bone cancer cells. *New Journal of Chemistry,* 43**,** 17726-17734.

Cornman, C. R., Colpas, G. J., Hoeschele, J. D., Kampf, J. & Pecoraro, V. L. 1992a. Implications for the spectroscopic assignment of vanadium biomolecules: structural and spectroscopic characterization of monooxovanadium(V) complexes containing catecholate and hydroximate based noninnocent ligands. *J. Am. Chem. Soc.,* 114**,** 9925-9933.

Cornman, C. R., Kampf, J. & Pecoraro, V. L. 1992b. Structural and spectroscopic characterization of vanadium(V)-oxoimidazole complexes. *Inorg. Chem.,* 31**,** 1981–1983.

Crans, D. C., Henry, L., Cardiff, G. & Posner, B. I. 2019a. 8. DEVELOPING VANADIUM AS AN ANTIDIABETIC OR ANTICANCER DRUG: A CLINICAL AND HISTORICAL PERSPECTIVE. *In:* PEGGY, L. C. (ed.) *Essential Metals in Medicine: Therapeutic Use and Toxicity of Metal Ions in the Clinic.* Berlin, Boston: De Gruyter.

Crans, D. C., Koehn, J. T., Petry, S. M., Glover, C. M., Wijetunga, A., Kaur, R., Levina, A. & Lay, P. A. 2019b. Hydrophobicity may enhance membrane affinity and anti-cancer effects of Schiff base vanadium(v) catecholate complexes. *Dalton Trans.,* 48**,** 6383-6395.

Crans, D. C., Peters, B. J., Wu, X. & Mclauchlan, C. C. 2017. Does anion-cation organization in Na+-containing X-ray crystal structures relate to solution interactions in inhomogeneous nanoscale environments: Sodium-decavanadate in solid state materials, minerals, and microemulsions. *Coord. Chem. Rev.,* 344**,** 115-130.

Crans, D. C., Zhang, B., Gaidamauskas, E., Keramidas, A. D., Willsky, G. R. & Roberts, C. R. 2010. Is Vanadate Reduced by Thiols under Biological Conditions? Changing the Redox Potential of V(V)/V(IV) by Complexation in Aqueous Solution. *Inorg. Chem.,* 49**,** 4245-4256.

Forman, H. J., Zhang, H. & Rinna, A. 2009. Glutathione: Overview of its protective roles, measurement, and biosynthesis. *Mol. Aspects Med.,* 30**,** 1-12.

Frenzel, N., Hartley, J. & Frisch, G. 2017. Voltammetric and spectroscopic study of ferrocene and hexacyanoferrate and the suitability of their redox couples as internal standards in ionic liquids. *Phys. Chem. Chem. Phys.,* 19**,** 28841-28852.

Harfield, J. C., Batchelor-Mcauley, C. & Compton, R. G. 2012. Electrochemical determination of glutathione: a review. *Analyst,* 137**,** 2285-2296.

Kostenkova, K., Althumairy, D., Rajan, A., Kortz, U., Barisas, B. G., Roess, D. A. & Crans, D. C. 2023a. Polyoxidovanadates [MoVIVV9O28]5- and [H2PtIVVV9O28]5- interact with CHO cell plasma membrane lipids causing aggregation and activation of a G protein-coupled receptor. *Front. Chem. Biol.,* 2.

Kostenkova, K., Levina, A., Walters, D. A., Murakami, H. A., Lay, P. A. & Crans, D. C. 2023b. Vanadium(V) pyridine-containing Schiff base catecholate complexes are novel lipophilic, redox-active and selectively cytotoxic in glioblastoma (T98g) cells. *Inorg. Chem.,* In preparation.

Levina, A., Crans, D. C. & Lay, P. A. 2022. Advantageous Reactivity of Unstable Metal Complexes: Potential Applications of Metal-Based Anticancer Drugs for Intratumoral Injections. *Pharmaceutics,* 14.

Levina, A., Pires Vieira, A., Wijetunga, A., Kaur, R., Koehn, J. T., Crans, D. C. & Lay, P. A. 2020. A Short-Lived but Highly Cytotoxic Vanadium(V) Complex as a Potential Drug Lead for Brain Cancer Treatment by Intratumoral Injections. *Angew. Chem. Int. Ed. ,* 59**,** 15834-15838.

Li, X., Lah, M. S. & Pecoraro, V. L. 1988. Vanadium complexes of the tridentate Schiff base ligand N-salicylidene-N'-(2-hydroxyethyl)ethylenediamine: acid-base and redox conversion between vanadium(IV) and vanadium(V) imino phenolates. *Inorg. Chem.,* 27**,** 4657-4664.

Lima, L. M. A., Murakami, H., Gaebler, D. J., Silva, W. E., Belian, M. F., Lira, E. C. & Crans, D. C. 2021. Acute Toxicity Evaluation of Non-Innocent Oxidovanadium(V) Schiff Base Complex. *Inorganics,* 9**,** 42.

Manganaro, J., Levina, A., Lay, P. A. & Crans, D. C. 2022. Potential Applications of Vanadium-Based Anticancer Drugs for Intratumoral Injections. *Medical Sciences Forum,* 11**,** 10.

Murakami, H. A., Uslan, C., Haase, A. A., Koehn, J. T., Vieira, A. P., Gaebler, D. J., Hagan, J., Beuning, C. N., Proschogo, N., Levina, A., Lay, P. A. & Crans, D. C. 2022. Vanadium Chloro-Substituted Schiff Base Catecholate Complexes are Reducible, Lipophilic, Water Stable, and Have Anticancer Activities. *Inorg. Chem.,* 61**,** 20757-20773.

Pessoa, J. C. & Correia, I. 2019. Salan vs. salen metal complexes in catalysis and medicinal applications: Virtues and pitfalls. *Coord. Chem. Rev.,* 388**,** 227-247.

Pessoa, J. C., Etcheverry, S. & Gambino, D. 2015. Vanadium compounds in medicine. *Coord. Chem. Rev.,* 301-302**,** 24-48.

Pessoa, J. C., Santos, M. F. A., Correia, I., Sanna, D., Sciortino, G. & Garribba, E. 2021. Binding of vanadium ions and complexes to proteins and enzymes in aqueous solution. *Coord. Chem. Rev.,* 449**,** 214192.

Rehder, D. 2012. The potentiality of vanadium in medicinal applications. *Future Med. Chem.,* 4**,** 1823-1837.

Sanasam, B., Raza, M. K., Musib, D., Pal, M., Pal, M. & Roy, M. 2020. Photodynamic Applications of New Imidazo[4,5-f][1,10]phenanthroline Oxidovanadium(IV) Complexes: Synthesis, Photochemical, and Cytotoxic Evaluation. *ChemistrySelect,* 5**,** 13824-13830.

Chapter 4: Enhancement of oncolytic virotherapy by vanadium(V) dipicolinates

4.1 Introduction: vanadium(V) dipicolinates - first coordination complexes to enhance oncolytic viruses

For over a century, vanadium compounds have been studied for their various health benefits (Lyonnet et al., 1899, Kieler et al., 1965, Kopfmaier et al., 1981, Murthy et al., 1986, D'Cruz and Uckun, 2002, Evangelou et al., 2002, Etcheverry et al., 2008, Bishayee et al., 2010, Wang et al., 2010, Petanidis et al., 2013, Willsky et al., 2013, Yoshikawa et al., 2014, Kioseoglou et al., 2015, Pessoa et al., 2015b, León et al., 2015, Kowalski et al., 2017, Leon et al., 2017, Crans et al., 2018, Crans et al., 2019a, Storr et al., 2006, Thompson et al., 2009, Scior et al., 2016). For instance, several classes of vanadium compounds such as vanadium salts (Lyonnet et al., 1899, Kieler et al., 1965), organometallic vanadium compounds (Kopfmaier et al., 1981, Murthy et al., 1986) and coordination complexes (D'Cruz and Uckun, 2002, Etcheverry et al., 2008, Wang et al., 2010, Petanidis et al., 2013, Yoshikawa et al., 2014, León et al., 2015, Kowalski et al., 2017, Sanna et al., 2017) are effective in the treatment of diabetes, cancer and other illnesses. Several vanadium compounds and salts have been subject to animal studies and progressed to human Phase 1 and 2 clinical trials (Goldfine et al., 2000, Willsky et al., 2013,

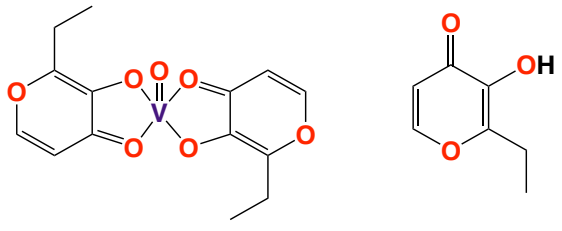

BEOV **ethyl-maltol**

Fig. 4.1 The structures of bis-ethylmaltolatooxovanadium(IV) (BEOV) and the free ethyl-maltol ligand, 2-ethyl-3-hydroxy-4H-pyran-4-one.

Crans, 2015, Storr et al., 2006). In the past decades, the major focus has been on anti-diabetic investigations until recently when the front runner drug bis-ethylmaltolatooxovanadium(IV) BEOV (**Fig. 4.1**) went off patent in 2011 (Thompson and Orvig, 2006a, Thompson et al., 2009, Crans, 2015). Phase 2 studies were completed with BEOV but funding for Phase 3 studies was not raised before the patent expired, thereby bringing clinical investigation to a halt. As a result, novel applications have been explored for vanadium compounds – their antineoplastic actions and potential as orphan drugs or food additives have been the focus of growing scientific efforts (Pessoa et al., 2015b, Leon et al., 2017, Crans et al., 2018). Structural studies have been conducted exploring the interactions with phosphatases and the molecular details in this process (McLauchlan et al., 2015a, Davies and Hol, 2004, Wu et al., 2016a). In addition, studies have shown a correlation between the anti-cancer and anti-diabetic effects of some coordination complexes (Yang and Wang, 2016, Crans et al., 2018, Wu et al., 2016a).

Oncolytic viruses (OVs) are nonpathogenic viruses with natural or engineered tropism for cancer cells (**Fig. 4.2**). They stimulate an antitumor immune response through direct oncolysis,

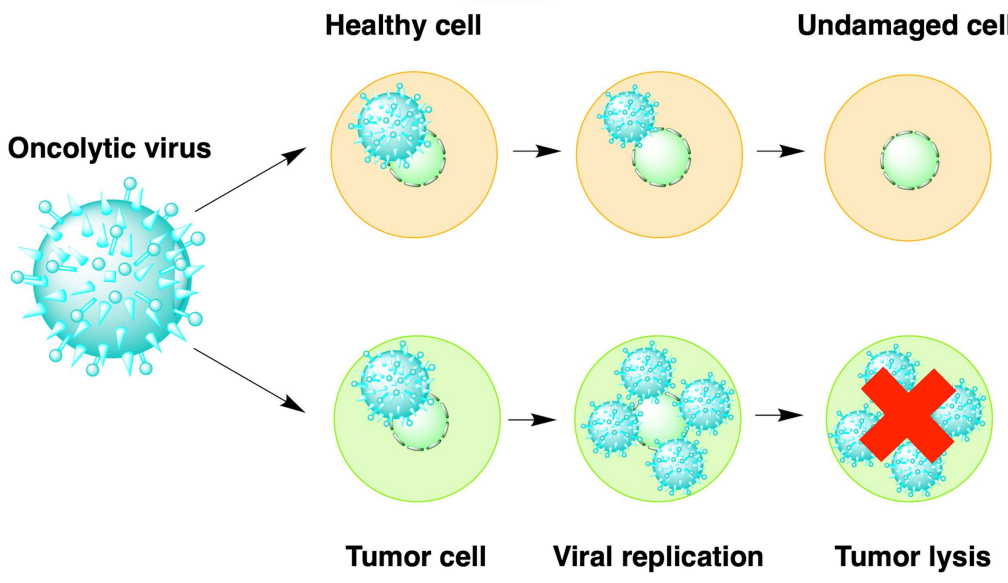

Fig. 4.2 Schematic illustrating the effects on oncolytic viruses on healthy and tumor cells.

by disrupting tumor vasculature and by recruiting the immune system thereby converting an immunosuppressive tumor microenvironment into a pro-immune ecosystem (Achard et al., 2018). These immune responses mediated by both the innate and adaptive arms confer durable and systemic protection against malignancies and prevent recurrence. In recent years, the number of clinical trials involving OVs has significantly increased, and Talimogene laherparepvec (T-VEC), a modified herpes simplex virus type 1, was approved by the Food and Drug Administration for the treatment of advanced melanoma (Rehman et al., 2016). The therapeutic potential of OVs is widely recognized, but thus far, OV monotherapies have only been successful in a subset of patients in the clinic. Recently, efforts have been geared towards the development of multimodal therapeutic strategies to increase efficacy. Combinations involving chemotherapies, immune checkpoint inhibitors or small molecule modulators of cellular innate immunity with various OV platforms are being investigated (reviewed in (Phan et al., 2018).

Recently, vanadium compounds were tested and found to be highly effective in combination with oncolytic viruses (Selman et al., 2018). Multiple vanadium compounds improved the infection of cancer cell lines by oncolytic RNA viruses and killing of both infected and surrounding uninfected cells in vitro (Selman et al., 2018). Most importantly, in immune-competent murine models of cancer, a therapy regimen consisting of vanadate and oncolytic vesicular stomatitis virus (VSVΔ51) improved survival, in some instances leading to complete tumor remission associate with an increase in T cell infiltration in the tumor microenvironment (Selman et al., 2018)., and it is supporting previous studies that suggest an impact of vanadate on immune cell function through IL2 secretion (Secrist et al., 1993; O'Shea et al., 1992) treated with pervanadate increased interleukin-2 secretion and T cell activation.

Many effects of vanadium compounds including but not limited to their anti-diabetic properties have been documented in cells, animals and humans, (Evangelou et al., 2002, Etcheverry et al., 2008, Bishayee et al., 2010, Willsky et al., 2013, Kioseoglou et al., 2015, Pessoa et al., 2015b, Leon et al., 2017, Crans et al., 2018, Crans et al., 2019a) and some effects including

their insulin mimetic effects are attributed to the inhibition of phosphatases (McLauchlan et al., 2015a). Potent inhibition has been reported with protein tyrosine phosphatases; however, less inhibition is observed for protein serine/threonine phosphatases and other phosphorylases (Pessoa et al., 2015a, McLauchlan et al., 2015a, Scior et al., 2016). X-ray structures of several vanadium-phosphatases have been described, and many vanadium-protein crystals contained a vanadate (McLauchlan et al., 2015a). Thus, those molecular studies support the possibility that some vanadium compounds act through vanadate and that the complex is simply a vehicle delivering the vanadium to the phosphatase (McLauchlan et al., 2015a). For example, in vivo studies have confirmed that bis-maltolatooxovanadium(IV) (BMOV) loses the ligand upon cell absorption, and that cellular membranes may assist in dissociating the ligand from the metal ion (Thompson et al., 2003).

In this study, we have preselected one class of vanadium coordination complexes, dioxovanadium(V) dipicolinates (**Fig. 4.3**) as a first series of compounds for structure-activity

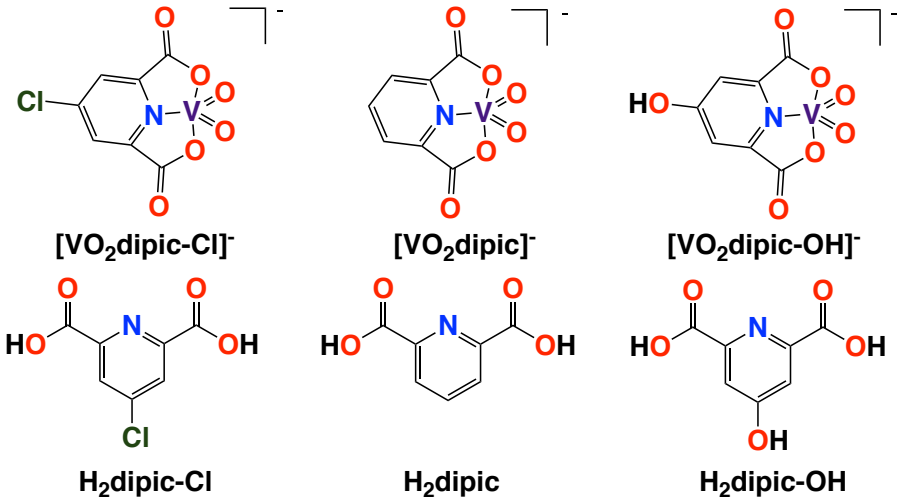

Fig. 4.3. The structures of V(V)-dipicolinate complexes (top row) and the corresponding free ligands shown in the protonated state (bottom row) investigated in this study. Compounds are identified by abbreviations and full names, provided in the abbreviations list.

relationship studies based on their chemical and antidiabetic properties (Crans et al., 2003b, Buglyo et al., 2005, Li et al., 2009, Willsky et al., 2011) and to further explore their predicted

effects in enhancing RNA oncolytic viruses like VSVΔ51 (Selman et al., 2018). Specifically, we examine three vanadium(V) dipicolinate complexes: ([VO_2dipic]$^-$, [VO_2dipic-OH]$^-$ and [VO_2dipic-Cl]$^-$) where the dipicolinate was substituted with –OH or –Cl in the para position (**Fig. 4.3**). The substituent changes the properties of the compounds, their stability in aqueous solution and their ability to penetrate cells (Willsky et al., 2011, Yang et al., 2003a, Crans, 2000). The chemistry of the vanadium(V) dipicolinate complexes has been described, and the pH stability shows that the complexes are more stable at acidic pH values (Crans, 2015, Willsky et al., 2011, Buglyo et al., 2005). The parent dioxovanadium(V) dipicolinate complex is known to lose its ligand at a neutral pH, although this complex readily penetrates interfaces and is thus presumed to enter cells (Crans et al., 2006, Crans et al., 2000, Crans et al., 2003b). When the complexes decompose, not only the free ligand but also the vanadate forms. As a result, the effects of the vanadium-dipicolinate compounds should be compared to the vanadate salt alone (Buglyo et al., 2005, Li et al., 2009, Willsky et al., 2011). Furthermore, since vanadium undergoes redox chemistry under physiological conditions, the effects should be compared to the effects of vanadyl cation as well (Buglyo et al., 2005, Li et al., 2009, Willsky et al., 2011). We present herein the biological responses of three vanadium(V) dipicolinate complexes upon oncolytic virus infection of cancer cells. These studies are further complemented with an analysis of the stability of the compounds under physiological conditions.

4.2 Reverse micelles as a model to determine relative locations and interactions of the complexes with eukaryotic membranes

Reverse micelles (RMs), or model membrane interfaces, are self-assembled lipid structures that form in nonpolar media with an aqueous center (Baruah et al., 2007). They are used as vehicles for various reactions and model systems in chemical biology to study interactions of different compounds with biological membranes. The RMs consist of a non-polar solvent, typically isooctane, an aqueous center, and a surfactant, typically sodium-OT (AOT) (Baruah et al., 2007). The nonpolar tails of the surfactant contact the nonpolar solvent while the polar

headgroups assemble near the aqueous pool, forming microdroplets. The size of those particles is characterized using the parameter w_0 which describes the molar ratio of water to the surfactant molecules, w_0 = [water] / [surfactant]. For near-spherical RMs, w_0 is directly proportional to the RM radius. Herein, the NMR studies in the RMs have been carried out to further understand membrane interactions and speciation of vanadium(V) dipicolinates.

4.3 Materials and Methods

4.3.1 General Materials

$[VO_2dipic\text{-}X]^-$ derivatives were prepared from corresponding ligand and vanadate as described previously for $NH_4[VO_2dipic]$ (Crans et al., 2000), $NH_4[VO_2dipic\text{-}OH]$ (Crans et al., 2003b) and $Na[VO_2dipic\text{-}Cl]$ (Li et al., 2009). The relevant chemicals were purchased from Sigma Aldrich and used without purification. Isooctane (2,2,4-trimethylpentane, 99.8%), activated charcoal (99.5%), deuterium oxide (99.9%), sodium hydroxide (≥98%) and hydrochloric acid (37%) were purchased from Sigma Aldrich and used without further purification.

Sodium aerosol-OT (AOT) (sodium salt of bis(2-ethylhexyl)sulfosuccinate, ≥99.0%) was purchased from Sigma Aldrich and further purified, as has been reported previously, to remove acidic impurities (Crans et al., 2006). To do so, 50.0 g AOT was dissolved into 150 mL of methanol to which 15 g of activated charcoal was added. This suspension was stirred on a shaker for 2 weeks and then filtered to remove the activated charcoal. The filtrate was dried under rotary evaporation at 50°C until the water content was below 0.2 molecules of water per AOT, as determined by ^{1}H NMR spectroscopy. The pH was adjusted throughout this study using solutions of NaOH or HCl mixed in D_2O to reach the final concentrations of 0.1 M. NaOH and HCl dissolved in D_2O are referred to as NaOD and DCl, respectively.

4.3.2 Cell Culture Treatments and Infection

The 786-0 cells were grown in supplemented Dulbecco's modification of Eagle's medium as specified above. Incubators were kept at 37°C with 5% CO2. The recombinant vesicular

stomatitis virus (VSV, Indiana serotype) with a deletion in the M protein (methionine 51) and expressing GFP was grown and purified as previously described (Diallo et al. 2012).

For evaluation of compounds in our cell culture system, 786-0 cells were grown to confluency and treated with vanadium compounds or ligand controls (0.002-400μM) using the Biotek Precision XS pipetting system. Four hours later, cells were infected with VSVΔ51 expressing green fluorescent protein (GFP) at a multiplicity of infection (MOI) of 0.05 or mock infected with media alone. At 24 hours post infection (HPI), GFP images were captured by fluorescence microscopy (ArrayScan, ThermoFisher Scientific) and GFP foci quantified. Cell viability was assessed using the metabolic dye AlamarBlue® by measuring fluorescence (530nm excitation, 590nm emission) at 48HPI using the BioTek Microplate Reader (BioTek Instruments Inc.) after a 2.5hr incubation.

4.3.3 Generation of $[VO_2dipic]^-$ and $[VO_2dipic\text{-}Cl]^-$ Speciation Profiles

4.3.3.1 Speciation Calculations and Analysis

Solution speciation are measured using potentiometry and spectroscopic methods resulting in quantification of species with defined stoichiometry (Kiss et al., 2008, Crans et al., 2013). Details in the speciation of $[VO_2dipic]^-$ has been reported, and information on other V-dipic derivatives have been described as well albeit in less detail. The complexes are defined by the notation (p, q, r). Equation (1) shows H^+, a metal ion (M), and a ligand (L) forming a complex with the stoichiometry defined by p, q, and r in an equilibrium reaction, respectively. The resulting formation constant β (p, q, r) is shown in equation (2), where the concentrations of H^+, M, and L (which are the dipic derivatives investigated here) are multiplied with each other and divided by the concentration of the complex. Speciation chemistry is defined by a series of constants that represent the system (Kiss et al., 2008, Crans et al., 2013). Using these constants will allow for prediction of species distribution at defined parameters.

$$pH^+ + qM + rL \rightleftharpoons (H^+)_p(M)_q(L)_r \qquad (1)$$

$$\beta\ (p,q,r) = \frac{(H^+)_p(M)_q(L)_r}{(H^+)^p + (M)^q + (L)^r} \qquad (2)$$

Formation constants are reported in the literature values at a 0.40 ionic strength for $[VO_2dipic]^-$ and $[VO_2dipic\text{-}OH]^-$ (Crans et al., 2003a, Crans et al., 2003b). However, a comparison of more derivatives was done at a lower ionic strength (Willsky et al., 2011). The vanadate oligomeric speciation constants are reported at several ionic strengths including 0.15 (Elvingson et al., 1996), 0.40 (Crans et al., 2000), 0.60 (Pettersson et al., 1983) and 3.00 (Pettersson et al., 1985). We carried out NMR studies quantitating $[VO_2dipic]^-$ both at low ionic strength (no salts added), at 0.15 and at 0.40 to evaluate the effects of ionic strength on intact complexes. Since the concentrations of intact complexes are dependent on ionic strengths, we modelled the speciation profiles to accurately estimate the amounts of intact complexes during the biological treatment (see the Supplemental Material).

4.3.3.2 Generation of $[VO_2dipic]^-$ and $[VO_2dipic\text{-}Cl]^-$ Speciation Profiles

The formation constants are known for some ionic strengths, and speciation profiles can be calculated for these conditions using the known pH-dependent apparent equilibrium constants, see equations (3) and (4) (Alberty, 2000). NMR measurements were done to determine the amounts of the parent $[VO_2dipic]^-$ complex at 0.40 ionic strength to confirm the reported values (Crans et al., 2000). Then, NMR studies were performed at other ionic strengths to verify the known $[VO_2dipic]^-$. These studies confirmed the amounts of both $[VO_2dipic]^-$ and $[VO_2dipic\text{-}Cl]^-$ present to quantify the amounts of $[VO_2dipic]^-$ and $[VO_2dipic\text{-}Cl]^-$ under varying conditions. Using the formation constants, speciation profiles could be calculated using the HySS2009 program (Alderighi et al., 1999), and were used to predict the parent $[VO_2dipic]^-$ complex at the ionic strength 0.40 at which the formation constants have been reported for both vanadate oligomers and the $[VO_2dipic]^-$ complex (Crans et al., 2000). These calculations allow comparisons between calculated and experimentally measured $[VO_2dipic]^-$ to verify the approach.

$$dipic^{2-}(or\ dipic - Cl^{2-}) + H_2VO_4^- \rightleftharpoons [VO_2dipic]^- + 2OH^- \quad (3)$$

$$K_{eq} = \frac{[VO_2dipic]^-}{[dipic^{2-}][H_2VO_4^-]} \quad (4)$$

$$\mu = {}^1/_2 \sum_1^n c_i z_i^2 \quad (5)$$

The speciation profiles should be calculated at the ionic strength of the cell culture media, and this ionic strength is calculated using equation (5). The details of the calculation are shown in the Supplemental Material, and the result was found to be 0.17. Accordingly, the speciation evaluations in this manuscript were continued using an ionic strength of 0.15. NMR measurements were done at ionic strength I = 0.15. This was followed by calculations carried out using the oxovanadate formation constants determined at ionic strength I = 0.15. We also investigated Na[VO_2dipic-OH]. Studies were carried out in detail with this system (Crans et al., 2000), however the medium that has an ionic strength of 0.20 or 0.15 is similar to investigate the system in a more convenient way.

4.3.4 Preparation of Aqueous [VO_2dipic]$^-$ Stock Solution to Verify Formation Constants

A solution of [VO_2dipic]$^-$ was prepared by dissolving 5.00 mM [VO_2dipic]$^-$ (6.20 mg, 0.0250 mmol) or 25.0 mM [VO_2dipic]$^-$ (31.0 mg, 0.125 mmol) in D_2O (5.00 mL) containing appropriate KCl to make up an ionic strength of 0.40. This 5.00 mM solution was then pipetted into appropriate aliquots, and the pD (pD = pH + 0.4) (Peters et al., 2016) of each was adjusted by a dropwise addition of NaOD or DCl (both 0.10 M). Solutions of [VO_2dipic]$^-$ were similarly prepared containing appropriate NaCl to make up an ionic strength of 0.15.

^{51}V and ^1H NMR measurements were done to determine the amounts of [VO_2dipic]$^-$ complex and [VO_2dipic-Cl]$^-$ complexes, the corresponding free ligands and V_1 concentrations in these samples to confirm that the calculations are in agreement with previous reports on these

systems (see Table S1) (Crans et al., 2000). Then HySS calculations were done using the parameters obtained for 0.15 ionic strength, showing speciation profiles.

4.3.5 Preparation of Aqueous $[VO_2dipic\text{-}Cl]^-$ Stock Solution for Membrane Model Studies

A stock solution of $[VO_2dipic\text{-}Cl]^-$ was prepared by dissolving $[VO_2dipic\text{-}Cl]^-$ (7.06 mg, 0.0250 mmol) in D_2O (1.00 mL). This 25.0 mM solution was then pipetted into appropriate aliquots, and the pD (pD = pH + 0.4) of each was adjusted by a dropwise addition of NaOD or DCl (each 0.10 M).

4.3.6 Preparation of AOT-Isooctane Stock Solution and Reverse Micelles

A 750 mM AOT-isooctane stock solution was prepared by dissolving the sodium salt of AOT (8.34 g, 18.8 mmol) in 25.0 mL isooctane; the solution was vortexed until clear (Stahla et al., 2008). The w_0 ($[D_2O]/[AOT]$) values of 8, 12 and 20 were prepared by adding calculated volumes of an aqueous $[VO_2dipic\text{-}Cl]^-$ and an AOT - isooctane stock solutions. For the varying pH studies, the pD (pD = pH + 0.4) of the w_0 12 samples was adjusted by a dropwise addition of 0.1 M NaOD and 0.1 M DCl (each 0.10 M) until the desired pH was reached.

4.3.7 ^1H and ^{51}V NMR Studies on Reverse Micelles

The ^1H and ^{51}V NMR experiments were recorded on a 400 MHz Bruker NMR spectrometer at 400 MHz and 105.2 MHz. The ^1H NMR parameters were as follows: 16 scans in the F1 domain, 1.0 s relaxation delay, 45° pulse angle, and 11μs pulse. The ^1H NMR spectra were reported against an external reference, DSS at 0 ppm, and the reverse micelle samples were referenced using the septet at 1.67 ppm for AOT. The ^{51}V NMR parameters were as follows: 4096 scans in the F1 domain, 0.01 sec relaxation delay, 45° pulse angle, and 16μs pulse. The ^{51}V NMR of reverse micelle samples were reported relatively to $VOCl_3$ at 0 ppm and spectra were referenced against an external reference of an aqueous $NaHVO_4$ solution at pH 12 (two signals at 535.7 ppm and 560.4 ppm) (Wu et al., 2016b, Zizic et al., 2016). The data was processed using MestreNova NMR processing software (Version 10.0.1).

4.4 Results and Discussion

4.4.1 High-throughput screen

A screen was undertaken to test the ability of vanadium(V)-dipic compounds and free

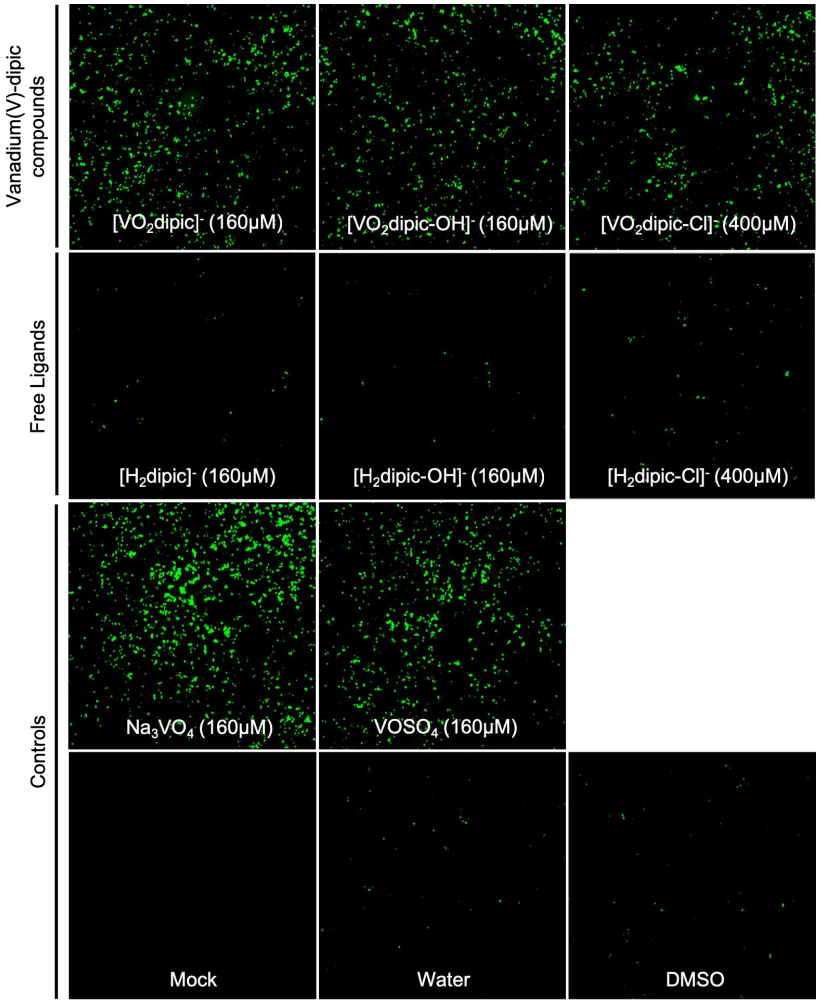

Fig. 4.4. Resistant human renal cell adenocarcinoma (786-0 cells) were pre-treated with dioxovanadium(V) dipicolinate complexes and ligand controls at indicated concentrations for 4 hours. The cells were then infected with VSVΔ51 expressing GFP (MOI 0.05, [750 γM]). Representative fluorescence images at peak GFP count are shown (n=2-4, 24HPI). As a control, images of untreated uninfected ('Mock'), solvent-treated and ligand treated cells are presented.

ligands to enhance VSVΔ51 infection in cancer cells (**Fig. 4.4**). The 786-0 cells were chosen as a model because they are inherently resistant to VSVΔ51 infection compared to other cancer cell lines. The parent complex, $[VO_2dipic]^-$ and its ligand 2,6-dicarboxylatopyridine, a second complex,

[VO_2dipic-Cl]$^-$ and its free ligand 4-hydroxy-2,6-dicarboxylatopyridine, as well as the [VO_2(dipic-Cl)]$^-$ complex, which was recently investigated in detail as an insulin-enhancing agent (Li et al., 2009) and corresponding ligand 4-chloro-2,6-dicarboxylatopyridine (H_2dipic-Cl) were each synthesized and reconstituted in DMSO. Complexes, free ligands, as well as sodium vanadate (Na_3VO_4) and vanadyl sulfate ($VOSO_4$) control compounds were then serially diluted and transferred onto 786-0 cells at final concentrations of 0.002-400uM. After 4h, cells were infected with recombinant VSVΔ51 encoding the GFP protein, as a measure of viral infection. 24 hours later, when GFP transgene expression was maximal, fluorescence microscopy images were

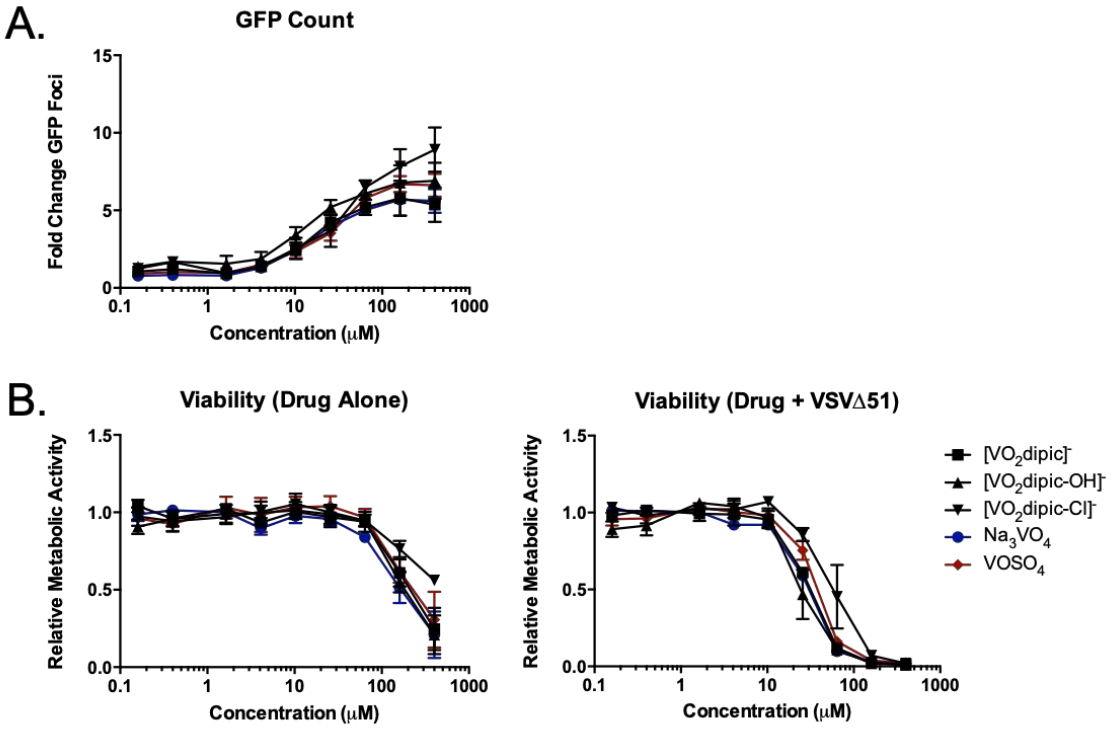

Fig. 4.5. Viability and GFP count. The 786-0 cells were treated with V-dipicolinate compounds or respective free-ligand controls (see supplemental material Fig. 2S) for 4hrs. As a reference, cells were treated with vanadate (Na_3VO_4) and vanadyl sulfate ($VOSO_4$) in parallel. After treatment, cells were infected with VSVΔ51 expressing GFP at a MOI of 0.05. GFP images were captured 24 hours post infection (24 HPI) as an indicator of viral replication. GFP foci were quantified and normalized to untreated infected baseline values (A). At 48 HPI, the relative metabolic activity, an indicator of cell viability, was quantified using the metabolic dye AlamarBlue® (fluorescence 530 nm excitation; 590 nm emission). Values are blank-controlled and normalized to untreated uninfected controls. The drug concentration at which half the cell population is killed (lethal dose; LD_{50}) is calculated for each compound (n = 2-4), error bars represent SEM.

collected for each compound and GFP foci quantified (**Fig. 4.5**). The results for $[VO_2dipic\text{-}Cl]^-$, $H_2dipic\text{-}Cl$, $[VO_2dipic]^-$, $[VO_2dipic\text{-}OH]^-$, $H_2dipic\text{-}OH$, vanadyl sulfate ($VOSO_4$) and sodium vanadate (prepared from $Na_3VO_4^{2-}$) are presented at the respective concentration for each compound yielding maximum GFP counts, and are compared to water, media or solvent (DMSO) controls (**Fig. 4.4**). Images of the full dose range are presented in the Supplemental Material. As shown in **Figs. A3.3-A3.4** and **Fig. 4.4**, all three dipic complexes show effects identical to that of vanadate and vanadyl sulfate in enhancing VSVΔ51-GFP infection of 786-0 cells while the three dipic ligands show no effects on viral infection. Since neither of the ligands tested were able to impact GFP counts in VSVΔ51 infected cells compared to vehicle controls, the observed enhancement in GFP expression and thus viral replication upon treatment with our complexes can therefore be attributed to the presence of the vanadium complex. Indeed, treatment with $[VO_2dipic]^-$ and $[VO_2dipic\text{-}OH]^-$ resulted in increased VSVΔ51 infection in 786-0 cells at concentrations ranging between 10-400μM as shown by fluorescence images and GFP counts (**Figs. 4.4-4.5**). Since the complexes are likely to decompose under the biological conditions used, vanadate and vanadyl cations will form and biological responses should be compared with the effects of these salts. From **Fig. 4.4-4.5** it is seen that both the vanadium(V) and vanadium(IV) salts are effective virus enhancers (as previously reported in Selman et al. 2018) and that the three V-dipicolinate complexes have similar effects as the vanadate and vanadyl cations.

4.4.2 Cell Viability

The effects of vanadium(V) complexes, ligands and vanadate on cell viability were measured 48h after addition of VSVΔ51 or mock infection using the metabolic dye AlamarBlue® (Rampersad, 2012). When cells were treated with vanadium compounds alone (**Fig. 4.4B and Table 4.1**), some reduction in viability was observed at concentrations exceeding about 100μM, with the chloro-dipicolinate being the least cytotoxic complex. However, the reduction by the vanadate salts takes place at higher concentrations for both $[VO_2dipic]^-$ and $[VO_2dipic\text{-}OH]^-$ and is around 30-50% of that observed in the presence of vanadium salts (or compounds and virus).

The combination of vanadium compounds and VSVΔ51 results in a synergistic decline in cancer cell viability. As expected, the vanadium compound concentration which results in maximal GFP foci counts (**Fig. 4.5A and Fig. A3.2**) also corresponds to the concentration at which the viability of the 786-0 cells treated with the combination therapy drops sharply (**Fig. 4.5B and Fig. A3.2**). Notably, the LD_{50} of the V-dipicolinate complexes drops approximately 10-fold in the presence of VSVΔ51 (**Table 4.1**). The chloro-dipicolinate shows the highest LD_{50} in the combination treatment and correlates well with the toxicity of the compounds alone. No effects on cell viability are observed with free ligands as shown in **Fig. A3.2** suggesting that the synergistic increase in cytotoxicity upon infection is dependent on the presence of the vanadium.

Table 4.1. The LD_{50} values for $[VO_2dipic\text{-}Cl]^-$, $[VO_2dipic]^-$, $[VO_2dipic\text{-}OH]^-$, and sodium vanadate ($H_2VO_4^{2-}$).[a]

Compound	LD_{50} values of Drug alone (μM)	LD_{50} values of Drug+ VSVΔ51 (μM)
$[VO_2dipic]^-$	250	31
$[VO_2dipic\text{-}OH]^-$	220	28
$[VO_2dipic\text{-}Cl]^-$	560	62
NaH_2VO_4	180	29
$VOSO_4$	290	39

See supplemental material for corresponding the LD_{50} values for deprotonated ligands of H_2dipic, H_2dipic-Cl and H_2dipic-OH observed at neutral pH (n = 2-4).

These results show convincingly that the V-dipicolinate complexes have similar viral sensitizing and cytotoxic effects as the V-salts. However, the oncolytic activity of the combination of V-compound and VSVΔ51 was dramatically more profound than the compound or virus alone. Building on these findings, we next sought to investigate the forms of the vanadium compounds under conditions representative of the cell culture media.

4.4.3 Verification of the Known Speciation Constant at pH 6.60

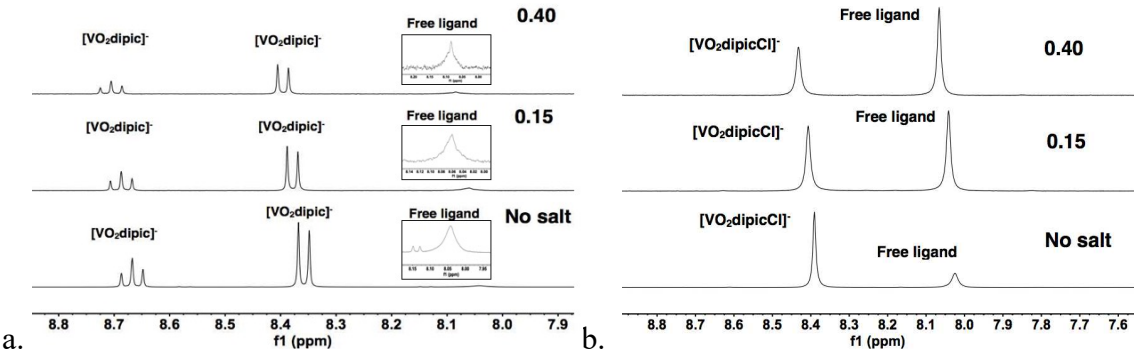

Fig. 4.6. The ^{1}H NMR spectra recorded in solutions of $[VO_2dipic]^-$ at pH 6.00 (a) and $[VO_2dipicCl]^-$ at pH 6.00 (b) at no added salt (bottom), 0.15 M KCl and at 0.40 M KCl.

First, the ^{51}V and ^{1}H NMR spectra were recorded at pH 6.00 at ionic strength of 0.40, 0.15 and without any addition of salt. As shown in **Fig. 4.6,** there are large differences in how much complex is formed at these different ionic strengths, as is evidenced by the ratio of the complex and free ligand peaks. These differences show that it is critical to select proper ionic strength to predict speciation under the conditions that the compounds interact with the host. The calculation of ionic strength of the media was done using equation (5). As detailed in the Supplemental Material, more than 40 components in the media were evaluated regarding the charge and their respective contribution to the ionic strength. Assuming that the contributions of serum albumin and other minor component were negligible, the total ionic strength was found to be 0.17. This ionic strength is similar to the speciation studies reported generated in aqueous solutions with NaCl up to an ionic strength of 0.15 (Elvingson et al., 1996). The constants were determined in these studies for vanadate oligomers and were chosen to be used for prediction of speciation in media described in this work. The ionic strength of the growth medium was calculated using equation (5). The known pH-dependent apparent equilibrium constants were calculated by using the concentrations obtained by ^{1}H and ^{51}V NMR spectroscopies, see equations (4) and (5). Then, NMR studies were performed to verify the known fits with $[VO_2dipic]^-$ to then carry out studies with both $[VO_2dipic]^-$ and $[VO_2dipic\text{-}Cl]^-$ compounds to quantify the amounts of $[VO_2dipic]^-$ and $[VO_2dipic\text{-}Cl]^-$ at the ionic strength of the cell culture media (**Fig. 4.6).**

Spectra of the $[VO_2dipic]^-$ complex and the free ligand are reported at 0.40 ionic strength were repeated at pH 6.60 to verify that ^{51}V and ^{l}H NMR spectroscopies accurately describe the stability of the $[VO_2dipic]^-$ complex. These NMR spectra were done at several pH values, but specifically compared to the pH 6.60 data with the apparent formation constant reported previously (Crans et al., 2000). Using the data at pH 6.60, the apparent formation constant for $[VO_2dipic]^-$ was determined to be 3.9×10^{-2} M^{-1} reported previously (Crans et al., 2000), and thus verifying this approach to obtain parameters needed to do the speciation profile calculations (**Fig. A3.4** and **Table A3.1**).

4.4.4 Speciation Constants Developed to Estimate Intact Vanadium(V) Dipicolinate Complex in Cell Culture Media

Spectra of the $[VO_2dipic]^-$ complex, the free dipic ligand and the corresponding $[VO_2dipic\text{-}Cl]^-$ complex and its free ligand at 0.15 ionic strength were recorded using ^1H and ^{51}V NMR spectroscopies. These NMR spectra are shown in the Supplemental Material (**Figs. A3.4 – A3.7**). Using the measured pKa value for H_2dipic and $H_2dipic\text{-}Cl$ and the apparent formation constants for $[VO_2(dipic)]^-$ and $[VO_2dipic\text{-}Cl]^-$ allowed for the calculation of speciation profiles for both complexes. The speciation of these systems is shown in **Fig. A3.8** from pH 5 though 9 at the concentration that the NMR spectra were recorded at. However, for the studies described here, the speciation profiles were calculated for 0.16 mM which is near or at the concentration where the greatest amount of virus enhancement was observed for $[VO_2(dipic)]^-$ and $[VO_2dipic\text{-}OH]^-$.

According to the speciation profiles for the low end of the dose response range (0.002 μM), there is a little of the intact $[VO_2dipic]^-$, $[VO_2dipic\text{-}OH]^-$ and $VO_2dipic\text{-}Cl]^-$ complexes, whereas at the high end of the dose response range (0.4 mM) observable amounts of both complexes are present. The speciation profiles of the $[VO_2dipic]^-$ and $[VO_2dipic\text{-}Cl]^-$ complexes illustrated in **Fig. 4.7** are shown at the limiting concentrations which results in maximal GFP foci counts (**Fig. 4.5A and Fig. A3.2**) which is also the concentration where the viability of the 786-0 cells treated with the combination therapy drops sharply (**Fig. 4.5B and Fig. A3.2).** The concentration at the peak

GFP count was observed at 160 μM for both $[VO_2dipic]^-$ and $[VO_2dipic\text{-}OH]^-$ complexes and at 400 μM for the $[VO_2dipic\text{-}Cl]^-$ complex. Viability and GFP data for the $[VO_2dipic]^-$, $[VO_2dipic\text{-}OH]^-$ and $[VO_2dipic\text{-}Cl]^-$ complexes are indistinguishable from the effects observed with vanadate at 160 μM. The LD_{50} of the $[VO_2dipic\text{-}Cl]^-$ complex when combined with VSVΔ51 is twice that of the $[VO_2dipic]^-$ compound combined with virus (**Fig. 4.5**). These observations show that the

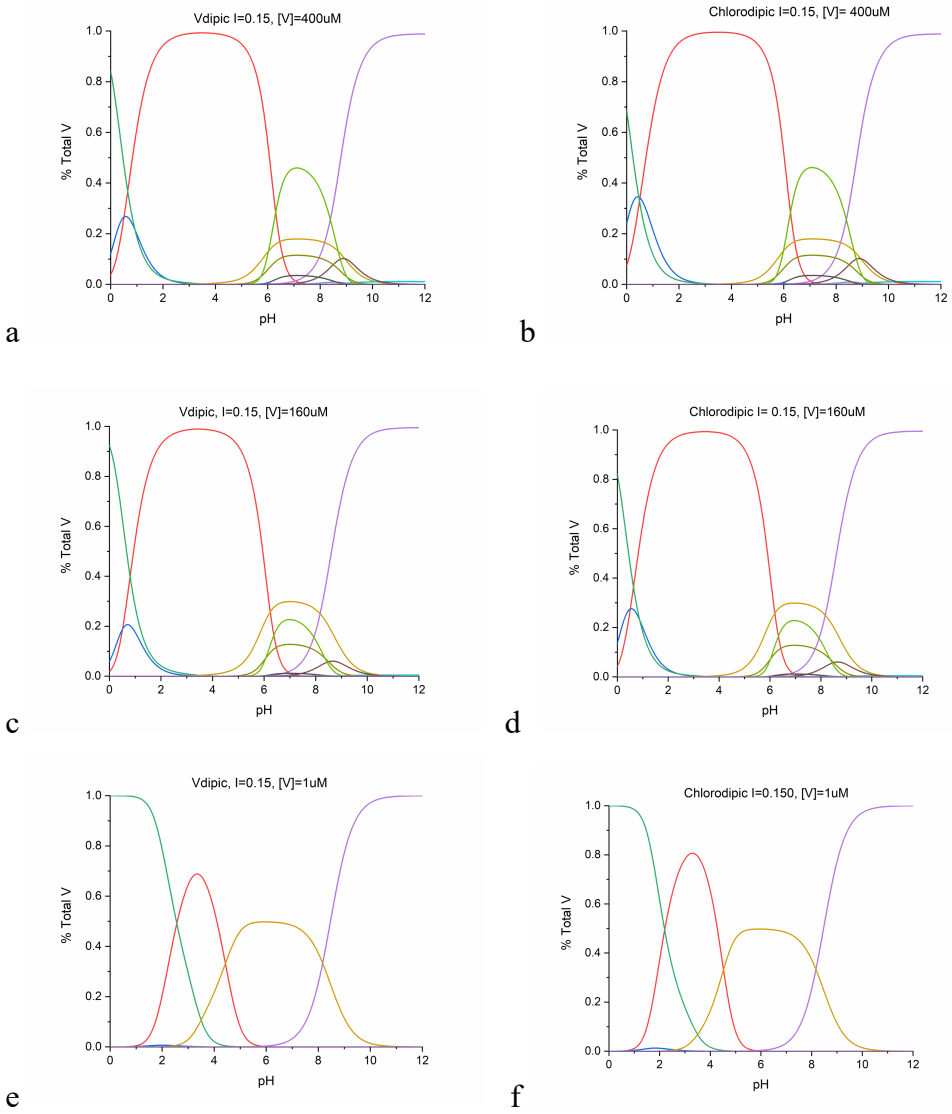

Fig. 4.7. The speciation profiles for $[VO_2dipic]^-$ (a, c, e) and $[VO_2dipic\text{-}Cl]^-$ (b, d, f) are shown using total V-concentrations of 400 μM mM (a, b), 160 μM (c, d) and 1.0 **μ**M (e, f). The calculations were done using the vanadate oligomerization constants for 0.15 M NaCl (Elvingson et al., 1996). Key for the curves: red $[VO_2dipic]^-$ or $[VO_2dipic\text{-}Cl]^-$; blue $H[VO_2dipic]$ or $H[VO_2dipic\text{-}Cl]$; purple V_1 ($H_2VO_4^{2-}$); green VO^{2+}; light green and beige V_4 ($V_4O_{12}^{4-}$).

$[VO_2dipic]^-$ and the $[VO_2dipic\text{-}OH]^-$ complexes may be slightly more effective although it is not statistically significant. This interpretation is supported since the speciation shows similar amount of complex present in solutions when the virus enhancement takes place. This would suggest that regardless of whether some of these coordination complexes are intact or hydrolyzed in the incubation media, similar responses may facilitate the uptake of the compounds by cancer cells so the interactions of the $[VO_2dipic\text{-}Cl]^-$ complex was explored by studies in the microemulsion cellular system for comparison with similar studies done with $[VO_2dipic]^-$.

4.4.5 Interactions of $[VO_2dipic\text{-}Cl]^-$ Complex with Model Membrane Interfaces

The interaction of the $[VO_2dipic\text{-}Cl]^-$ complex with model membrane interfaces was investigated using a microemulsion system, specifically in 750 mM AOT/isooctane reverse micelles. Microelmulsions are useful in the investigation of molecular placement of molecules at the interface, and the aforementioned system has been well-studied and characterized in detail (Baruah et al., 2006, Correa et al., 2012). Studies were done at different pH values of the aqueous solution containing $[VO_2dipic\text{-}Cl]^-$ complex prior to addition to the AOT/isooctane suspension, but no changes were observed in the chemical shifts for the complex indicative of no changes in the protonation state near the physiological pH range (**Fig. A3.6-A3.7**). Studies were then done at pH 5.50 and 6.00 (see the Supplemental Material (**Fig. A3.6-A3.7**)) demonstrating that these complexes tend to be more stable in acidic media. The $[VO_2dipic\text{-}Cl]^-$ complex was found to be less stable than either $[VO_2dipic\text{-}OH]^-$ or $[VO_2dipic]^-$ complexes which is consistent with previous report (Smee et al., 2009, Li et al., 2009, Willsky et al., 2011), and may explain the observed inferior potency and cytotoxicity of the chloro-dipicolinate complex (**Fig. 4.5**).

To examine the possibility that the complexes reside in the water pool or near the interface, the size of the reverse micelles was changed, and the system was observed using both ^1H and ^{51}V NMR spectroscopies, **Fig. 4.6**. It has previously been documented that complexes penetrating the interface show no differences in ^{51}V NMR chemical shifts upon placement into the reverse micelle (Crans et al., 2006, Sostarecz et al., 2014). If the compound associates with the

interface as well as the water pool, then there is an observed change in the ^{1}H NMR chemical shifts defined by the particular location of the compound as the size of the reverse micelle changes; this is caused by the decrease of the size of the water pool and the change of the interface-water layer (Crans et al., 2011, Sostarecz et al., 2014). A solution of $[VO_2dipic\text{-}Cl]^-$ was added to reverse micelles ranging from sizes 8 to 20. As shown in **Fig. 4.8**, there are two signals

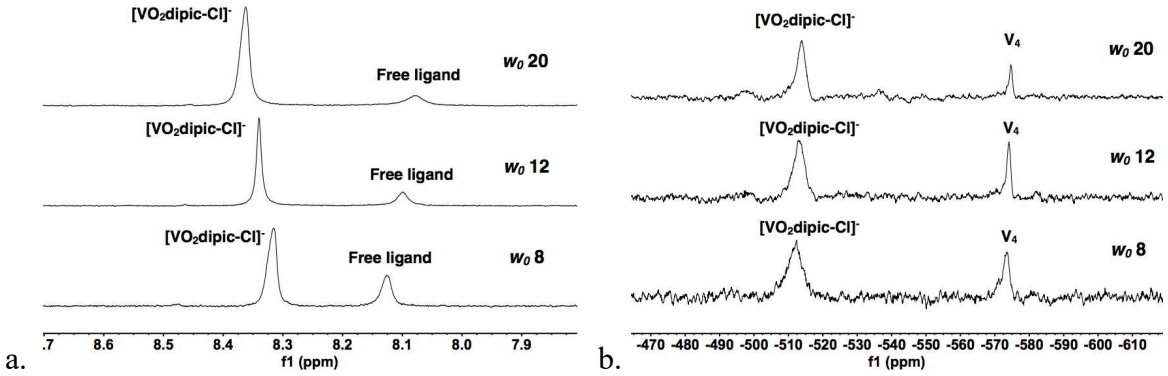

Fig. 4.8. ^{1}H (a) and ^{51}V (b) NMR spectra of 750 mM AOT/isooctane suspensions containing $[VO_2dipic\text{-}Cl]^-$ complex (concentrations ranging from 2.25 to 5.25 mM) in sizes w_0 8 - 20.

observed above 8 ppm; the signal near 8.1 ppm is due to the free ligand and the signal at 8.3 ppm is due to the $[VO_2dipic\text{-}Cl]^-$ complex. The observed downfield shift of the ^{1}H NMR peaks as the reverse micelle increased in size is consistent with the complex penetrating the interface albeit perhaps not as deeply as the parent complex (Crans et al., 2006, Sostarecz et al., 2014).

In contrast, the ^{1}H peaks corresponding to the free ligand were found to shift upfield. This shift is generally associated with interactions of the solute with the interface near the water pool which are different than that of the corresponding complex (Crans et al., 2011). The visual representation of the suggested average locations of the $[VO_2dipic\text{-}Cl]^-$ complex and the free chlorodipic ligand is shown in **Fig. 4.9**. The location suggested previously for the $[VO_2dipic]^-$ complex is high up in the tails which is not quite accurate for the $[VO_2dipic]^-$ complex (Crans et al., 2006, Sostarecz et al., 2014). The dipic ligand is more mobile and moves up and down ranging from the deep tails to the headgroup; however, the chemical shift varies from 8.1 ppm for

w_0 6 to 7.9 ppm for w_0 12 which is similar to the changes in chemical shift of the chlorodipic-ligand, shown in the schematic representation in **Fig. 2.9**.

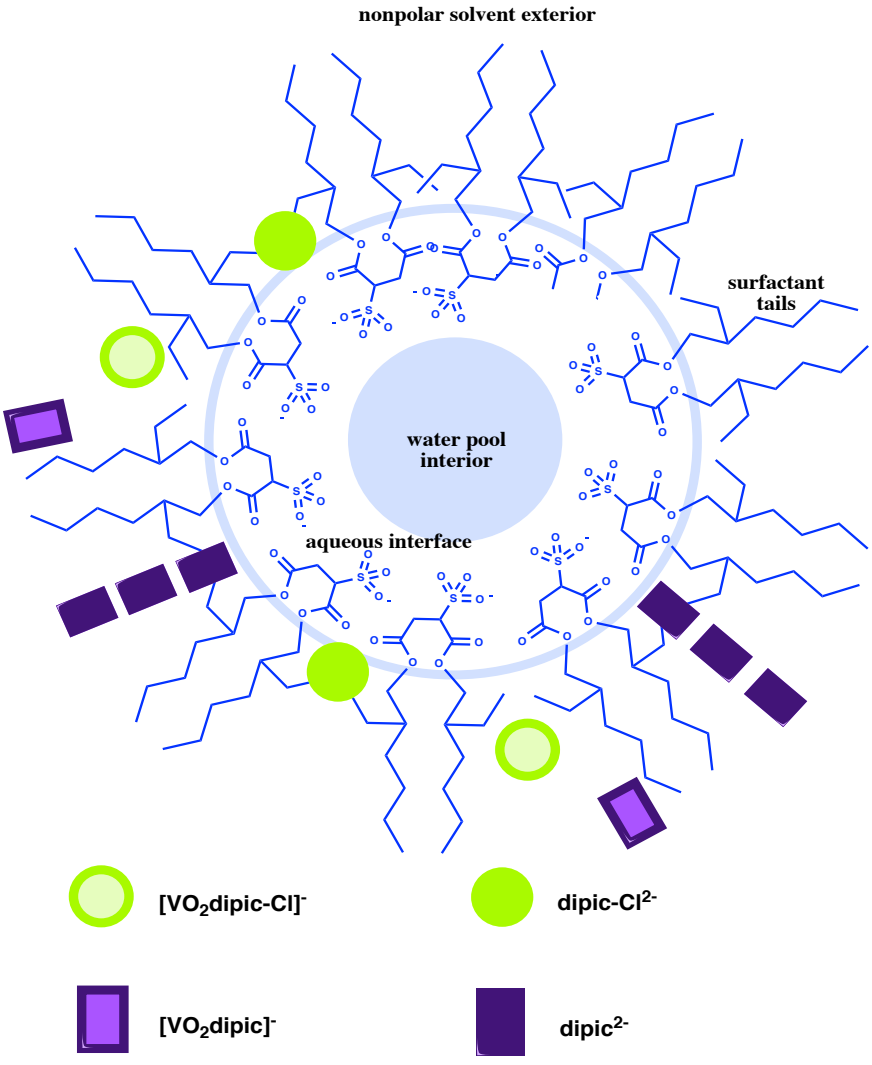

Fig. 2.9. Schematic representation of the average locations of the $[VO_2dipic\text{-}Cl]^-$ complex and the free chlorodipic ligand in a reverse micelle compared to the $[VO_2dipic]^-$ complex and the free dipic ligand.

4.5 Discussion

In this study, we have investigated the capacity of one class of vanadium coordination complexes, dioxovanadium(V) dipicolinates, to enhance oncolytic virus infection. These complexes have been selected as the first series of compounds to evaluate because of their five-coordinate geometry (Willsky et al. 2011; (Crans et al., 1996), chemical ((Crans, 2000, Crans et

al., 2003b, Smee et al., 2009, Li et al., 2009) and antidiabetic properties which have been investigated extensively (Crans et al., 2003b, Willsky et al., 2011)). Therefore, the breadth of previous work has made it possible to investigate the pharmacochemical properties of vanadium complexes in enhancing OV activity. The studies described in this work are conducted using speciation analysis with the intent to examine the nature of the active form. The complexes selected have a well-known chemistry, and some biological responses of these vanadium coordination complexes have been reported (Crans et al., 2003b, Smee et al., 2009, Li et al., 2009, Willsky et al., 2011). Because several classes of vanadium compounds have been reported to have both anti-cancer and anti-diabetic effects, it is of interest to learn the similarity of how the enhancement of oncolytic viruses compares with the anti-diabetic and anti-cancer effects with different classes of vanadium compounds, such as the vanadium(V) dipicolinates tested in this study.

The hydrolytic chemistry of V-dipicolinate compounds has been studied extensively (Crans, 2000, Crans et al., 2003b, Smee et al., 2009, Li et al., 2009), and thus facilitates the analysis of the observed oncolytic effects of these vanadium compounds. All the vanadium(V) dipicolinate compounds were found to be more stable at the acidic pH values, with the parent $[VO_2dipic]^-$ complex showing the highest stability (Crans, 2000, Crans et al., 2003b, Smee et al., 2009, Li et al., 2009, Willsky et al., 2011). However, the difference in stability was modest, and unlikely to impact biological activity. It is therefore important that the effects of these complexes should be compared to that of the simple salts, the vanadate anion and the vanadyl cation. In this work we modeled the expected speciation under the condition of the virus infection for both the $[VO_2dipic\text{-}Cl]^-$ and the parent $[VO_2dipic]^-$ complex. Much work has been done on the speciation and binding of the complexes to transferrin and serum albumin (Sanna et al., 2009a); (Sanna et al., 2009b); (Sanna et al., 2012), however, since these studies were exclusively done in cell culture, such considerations are not appropriate for the studies reported here. We find that the

anticipated concentrations of the intact complexes are within a factor of two, and that this is consistent with the observed differences in the LD_{50} values.

No statistically distinguishable differences could be observed in the normalization of blood glucose levels between all the different vanadium(V)-dipicolinates tested (the parent, -OH, -Cl, -NH_2, -NO_2 substituted vanadium(V) dipicolinates) (Willsky et al., 2011). Trends of improved activity were, however, reported for the parent $[VO_2dipic]^-$ complex (Crans et al., 2003b, Li et al., 2009, Willsky et al., 2011). These results are consistent with the interpretation that the action of the vanadium compounds is a result of the vanadate after it dissociates from the coordination complex. It was, therefore, of interest to investigate if compound degradation was observed during viral sensitization. The fact that all three vanadium(V)-dipicolinate complexes show similar enhancement of virus infection compared to vanadate and vanadyl cation confirms that for these three complexes and the two salts the effects are likely to be caused by the vanadium.

The possibility that the dipicolinate ligands may mainly serve to assist with absorption of the compounds was examined both in a simple membrane model study with $[VO_2dipic\text{-}Cl]^-$ and microemulsions, thereby testing how the complex responds as it approaches interfaces. The studies showed that the $[VO_2dipic\text{-}Cl]^-$ complex, as well as that of $[VO_2dipic]^-$, associates with the interface. However, whereas the parent complex can penetrate the interface (Crans et al., 2006), the $[VO_2dipic\text{-}Cl]^-$ is likely to associate more with the interface, and is not able to overcome the hydrolysis as much as the parent complex. The biological studies show no statistically significant difference between the complexes (Crans et al., 2003b, Li et al., 2009, Willsky et al., 2011), thereby suggesting that the ligands are not different to the point of exerting a robust biological effect.

Oncolytic virotherapy has led to durable responses in only a small portion of patients when used as single agents. To improve therapeutic outcomes, several pharmaco-viral strategies are currently being explored. For example, the JAK inhibitor ruxolitinib, dimethyl fumarate, histone deacetylase inhibitor, mTOR inhibitors and other novel synthetic compounds have all been tested

preclinically in combination with oncolytic rhabdoviruses like VSVΔ51 (reviewed in Phan et al., 2018). Adding to this list, our group has shown that vanadate improves oncolytic VSVΔ51 spread, bystander killing, and the combination therapy can lead to robust anti-tumor immunity in murine models (Selman et al., 2018). Herein, we further demonstrate that vanadium(V)-dipicolinate complexes enhance OVs in a fashion consistent with the hydrolysis of the complexes into active vanadate as reported in anti-diabetic studies. The results of the current study suggest that improving vanadium compound stability and their ability to traverse lipid membranes could lead to improvements in potency. This is an important pursuit when contemplating vanadium compounds as adjuvants specifically catered to oncolytic viruses, much like aluminum oxides (Li et al., 2008) have and continue to be used as adjuvants for vaccines for infectious disease. Further studies will be required to better understand the implication of the observed lipid association of dipicolinate compounds in terms of the previously reported mechanism of action in the context of OV therapy, which involves a shift in the phosphorylation pattern of STAT1 and STAT2 (Selman et al., 2018), as well as the role of cellular phosphatases.

4.6 Conclusions

In this project, we have investigated the chemistries of two classes of vanadium(IV/V) coordination complexes that enhance the oncolytic viruses. The first study has investigated speciation and relative location of vanadium(V) dipicolinates, known antidiabetic agents, in model membranes. The ^{1}H and ^{51}V NMR speciation studies at physiological conditions have shown that the complexes readily hydrolyze into active vanadate, as previously reported in anti-diabetic studies. Consequentially, vanadate is responsible for the oncolytic viral enhancement. The results of the first speciation study suggest that improving vanadium compounds' stability and their ability to traverse lipid membranes could lead to improvements in potency of oncolytic viral enhancement.

4.7 References

Achard, C., Surendran, A., Wedge, M., Ungerechts, G., Bell, J. & Ilkow, C. 2018. Lighting a Fire in the Tumor Microenvironment Using Oncolytic Immunotherapy. *EBioMedicine,* 31**,** 17-24.

Alberty, R. 2000. Calculating apparent equilibrium constants of enzyme-catalyzed reactions at pH 7. *Biochem Educ,* 28**,** 12-17.

Alderighi, L., Gans, P., Ienco, A., Peters, D., Sabatini, A. & Vacca, A. 1999. Hyperquad simulation and speciation (HySS): a utility program for the investigation of equilibria involving soluble and partially soluble species. *Coord Chem Rev,* 184**,** 311-318.

Baruah, B., Crans, D. C. & Levinger, N. E. 2007. Simple Oxovanadates as Multiparameter Probes of Reverse Micelles. *Langmuir,* 23**,** 6510-6518.

Baruah, B., Roden, J., Sedgwick, M., Correa, N., Crans, D. & Levinger, N. 2006. When Is Water Not Water? Exploring Water Confined in Large Reverse Micelles Using a Highly Charged Inorganic Molecular Probe. *J Am Chem Soc,* 128**,** 12758-12765.

Bishayee, A., Waghray, A., Patel, M. & Chatterjee, M. 2010. Vanadium in the detection, prevention and treatment of cancer: The in vivo evidence. *Cancer Letters,* 294**,** 1-12.

Buglyo, P., Crans, D., Nagy, E., Lindo, R., Yang, L., Smee, J., Jin, W., Chi, L., Godzala, M. & Willsky, G. 2005. Aqueous chemistry of the vanadium(III) (V-III) and the V-III-dipicolinate systems and a comparison of the effect of three oxidation states of vanadium compounds on diabetic hyperglycemia in rats. *Inorg Chem,* 44**,** 5416-5427.

Correa, N., Suilber, J., Riter, R. & Levinger, N. 2012. Nonaqueous Polar Solvents in Reverse Micelle Systems. *Chem Rev,* 112**,** 4569-4602.

Crans, D. 2000. Chemistry and insulin-like properties of vanadium(IV) and vanadium(V) compounds. *J Inorg Biochem,* 80**,** 123-131.

Crans, D. 2015. Antidiabetic, Chemical, and Physical Properties of Organic Vanadates as Presumed Transition-State Inhibitors for Phosphatases. *J Org Chem,* 80**,** 11899-11915.

Crans, D., Barkley, N., Montezinho, L. & Castro, M. 2019. Vanadium Compounds as enzyme inhibitors with a focus on anticancer effects. *In:* ANGELA CASINI, A. V. A. S. M. M. (ed.) *Metal-based Anticancer Agents.* RSC.

Crans, D., Keramidas, A. & Drouza, C. 1996. Organic vanadium compounds - Transition state analogy with organic phosphorus compounds. *Phosphorus, Sulfur Silicon Relat Elem,* 109-110**,** 245-248.

Crans, D., Mahroof-Tahir, M., Johnson, M., Wilkins, P., Yang, L., Robbins, K., Johnson, A., Alfano, J., Godzala, M., Austin, L. & Willsky, G. 2003a. Vanadium(IV) and vanadium(V) complexes of dipicolinic acid and derivatives. Synthesis, X-ray structure, solution state properties and effects in rats with STZ-induced diabetes. *Inorg Chim Acta,* 356**,** 365-378.

Crans, D., Rithner, C., Baruah, B., Gourley, B. & Levinger, N. 2006. Molecular probe location in reverse micelles determined by NMR dipolar interactions. *J Am Chem Soc,* 128**,** 4437-4445.

Crans, D., Trujillo, A., Pharazyn, P. & Cohen, M. 2011. How environment affects drug activity: Localization, compartmentalization and reactions of a vanadium insulin-enhancing compound, dipicolinatooxovanadium(V). *Coord Chem Rev,* 255**,** 2178-2192.

Crans, D., Woll, K., Prusinskas, K., Johnson, M. & Norkus, E. 2013. Metal Speciation in Health and Medicine Represented by Iron and Vanadium. *Inorg Chem,* 52**,** 12262-12275.

Crans, D., Yang, L., Alfano, J., Chi, L., Jin, W., Mahroof-Tahir, M., Robbins, K., Toloue, M., Chan, L., Plante, A., Grayson, R. & Willsky, G. 2003b. (4-Hydroxypyridine-2,6-dicarboxylato)oxovanadate(V)-a new insulin-like compound: chemistry, effects on myoblast and yeast cell growth and effects on hyperglycemia in rats with STZ-induced diabetes. *Coord Chem Rev,* 237**,** 13-22.

Crans, D., Yang, L., Haase, A. & Yang, X. 2018. Health Benefits of Vanadium and Its Potential as an Anticancer Agent. *Met Ions Life Sci,* 18**,** 251-279.
Crans, D., Yang, L., Jakusch, T. & Kiss, T. 2000. Aqueous chemistry of ammonium (dipicolinato)oxovanadate(V): The first organic vanadium(V) insulin-mimetic compound. *Inorg Chem,* 39**,** 4409-4416.
D'cruz, O. & Uckun, F. 2002. Metvan: a novel oxovanadium(IV) complex with broad spectrum anticancer activity. *Expert Opin Invest. Drugs,* 11**,** 1829-36.
Davies, D. & Hol, W. 2004. The power of vanadate in crystallographic investigations of phosphoryl transfer enzymes. *FEBS Lett,* 577**,** 315-321.
Elvingson, K., Gonzalez Baro, A. & Pettersson, L. 1996. Speciation in Vanadium Bioinorganic Systems. 2. An NMR, ESR, and Potentiometric Study of the Aqueous H+-Vanadate-Maltol System. *Inorg Chem,* 35**,** 3388-3393.
Etcheverry, S., Ferrer, E., Naso, L., Rivadeneira, J., Salinas, V. & Williams, P. 2008. Antioxidant effects of the VO(IV) hesperidin complex and its role in cancer chemoprevention. *J Biol Inorg Chem,* 13**,** 435-47.
Evangelou, A., Kolettas, E., Tenopoulou, M., Galaris, D., Gonos, E. & Manos, G. 2002. Vanadium inhibits HaCaT cell proliferation but does not cause apoptosis. *Met Ions Biol Med,* 7**,** 154-158.
Goldfine, A., Patti, M., Zuberi, L., Goldstein, B., Leblanc, R., Landaker, E., Jiang, Z., Willsky, G. & Kahn, C. 2000. Metabolic effects of vanadyl sulfate in humans with non—insulin-dependent diabetes mellitus: In vivo and in vitro studies. *Metabolism,* 49**,** 400-410.
Kieler, J., Gromek, A. & Nissen, N. 1965. Studies on the antineoplastic effect of vanadium salts. *Acta Chir Scand Suppl,* 343**,** 154-64.
Kioseoglou, E., Petanidis, S., Gabriel, C. & Salifoglou, A. 2015. The chemistry and biology of vanadium compounds in cancer therapeutics. *Coord Chem Rev,* 301–302**,** 87–105.
Kiss, T., Jakusch, T., Hollender, D., Dornyei, A., Enyedy, E., Pessoa, J., Sakurai, H. & Sanz-Medel, A. 2008. Biospeciation of antidiabetic VO(IV) complexes. *Coord Chem Rev,* 252**,** 1153-1162.
Kopfmaier, P., Wagner, W., Hesse, B. & Köpf, H. 1981. Tumor inhibition by metallocenes: Activity against leukemias and detection of the systemic effect. *Europ J Cancer,* 17**,** 665-669.
Kowalski, S., Hac, S., Wyrzykowski, D., Zauszkiewicz-Pawlak, A. & Inkielewicz-Stepniak, I. 2017. Selective cytotoxicity of vanadium complexes on human pancreatic ductal adenocarcinoma cell line by inducing necroptosis, apoptosis and mitotic catastrophe process. *Oncotarget,* 8**,** 60324-60341.
León, I., Cadavid-Vargas, J., Tiscornia, I., Porro, V., Castelli, S., Katkar, P., Desideri, A., Bollati-Fogolin, M. & Etcheverry, S. 2015. Oxidovanadium (IV) complexes with chrysin and silibinin: anticancer activity and mechanisms of action in a human colon adenocarcinoma model. *J Biol Inorg Chem,* 20**,** 1175-1191.
Leon, I., Diez, P., Baran, E., Etcheverry, S. & Fuentes, M. 2017. Decoding the anticancer activity of VO-clioquinol compound: the mechanism of action and cell death pathways in human osteosarcoma cells. *Metallomics,* 9**,** 891-901.
Li, H., Willingham, S., Ting, J. & Re, F. 2008. Cutting Edge: Inflammasome Activation by Alum and Alum's Adjuvant Effet Are Mediated by NLRP3. *J Immunol,* 181**,** 17-21.
Li, M., Ding, W., Smee, J., Baruah, B., Willsky, G. & Crans, D. 2009. Anti-diabetic effects of vanadium(III, IV, V)-chlorodipicolinate complexes in streptozotocin-induced diabetic rats. *Biometals,* 22**,** 895-905.
Lyonnet, B., Martz, S. & Martin, E. 1899. L'emploi therapeutique des derives du vanadium. *La Presse Méd,* 1**,** 191-192.

Mclauchlan, C., Peters, B., Willsky, G. & Crans, D. 2015. Vanadium-phosphatase complexes: Phosphatase inhibitors favor the trignonal bipyramidal transition state geometries. *Coord Chem Rev,* 301-302**,** 163-199.
Murthy, M., Toney, J., Rao, L., Kuo, L. & Marks, T. 1986. Pharmacologic studies on the new antitumor agent vanadocene dichloride (VDC). *Proc Am Assoc Cancer Res,* 27**,** 279-279.
Pessoa, J., Etcheverry, S. & Gambino, D. 2015a. Vanadium compounds in medicine. *Coord Chem Rev,* 301**,** 24-48.
Pessoa, J., Etcheverry, S. & Gambino, D. 2015b. Vanadium compounds in medicine. *In:* CONTE, V. & GIULIA, L. (eds.) *The Ninth International Symposium on the Chemistry and Biological Chemistry of Vanadium.* Padova, Italy.
Petanidis, S., Kioseoglou, E., Hadzopoulou-Cladaras, M. & Salifoglou, A. 2013. Novel ternary vanadium-betaine-peroxido species suppresses H-ras and matrix metalloproteinase-2 expression by increasing reactive oxygen species-mediated apoptosis in cancer cells. *Cancer Lett,* 335**,** 387-96.
Peters, B., Groninger, A., Fontes, F., Crick, D. & Crans, D. 2016. Differences in Interactions of Benzoic Acid and Benzoate with Interfaces. *Langmuir,* 32**,** 9451-9459.
Pettersson, L., Andersson, I. & Hedman, B. 1985. Multicomponent polyanions. 37. A potentiometric and 51V-NMR study of equilibria in the H+-HVO42- system in 3.0 M-Na(ClO4) medium covering the range 1£-1g[H+]£10. *Chem Scr,* 25**,** 309-317.
Pettersson, L., Hedman, B., Andersson, I. & Ingri, N. 1983. Multicomponent polyanions. 34. P potentiometric and 51V NMR study of equilibria in the H+-HVO42- system in the 0.6 M Na(Cl) medium covering the range 1£-1g[H+]£10. *Chem Scrip,* 22**,** 254-264.
Phan, M., Watson, M., Alain, T. & Diallo, J. 2018. Oncolytic Viruses on Drugs: Achieving Higher Therapeutic Efficacy. *ACS Infect Dis,* 4**,** 1448-1467.
Rampersad, S. 2012. Multiple Applications of Alamar Blue as an Indicator of Metabolic Function and Cellular Health in Cell Viability Bioassays. *Sensors,* 12**,** 12347-12360.
Rehman, H., Silk, A., Kane, M. & Kaufman, H. 2016. Into the clinic: Talimogene laherparepvec (T-VEC), a first-in-class intratumoral oncolytic viral therapy. *J ImmunoTher Canc,* 4.
Sanna, D., Buglyo, P., Micera, G. & Garribba, E. 2012. Biotransformation of BMOV in the presence of blood serum proteins. *Metabolomics,* 4**,** 33-36.
Sanna, D., Garribba, E. & Micera, G. 2009a. Interaction of VO2+ ion with human serum transferrin and albumin. *J Inorg Biochem,* 103**,** 648-655.
Sanna, D., Micera, G. & Garribba, E. 2009b. On the Transport of Vanadium in Blood Serum. *Inorg Chem,* 48**,** 5747-5757.
Sanna, D., Ugone, V., Micera, G., Buglyo, P., Biro, L. & Garribba, E. 2017. Speciation in human blood of Metvan, a vanadium based potential anti-tumor drug. *Dalton Trans,* 46**,** 8950-8967.
Scior, T., Guevara-Garcia, J., Do, Q., Bernard, P. & Laufer, S. 2016. Why Antidiabetic Vanadium Complexes are Not in the Pipeline of “Big pharma” Drug Research? A Critical Review. *Curr Med Chem,* 23**,** 2874-2891.
Selman, M., Rousso, C., Bergeron, A., Son, H., Krishnan, R., El-Sayes, N., Varette, O., Chen, A., Le Boeuf, F., Tzelepis, F., Bell, J., Crans, D. & Diallo, J. 2018. Multi-modal Potentiation of Oncolytic Virotherapy by Vanadium Compounds. *Mol Ther,* 26**,** 56-69.
Smee , J., Epps, J., Ooms, K., Bolte, S., Polenova, T., Baruah, B., Yang, L., Ding, W., Li, M., Willsky, G., La Cour, A., Anderson, O. & Crans, D. 2009. Chloro-substituted dipicolinate vanadium complexes: Synthesis, solution, solid-state, and insulin-enhancing properties. *J Inorg Biochem,* 103**,** 575–584.
Sostarecz, A., Gaidamauskas, E., Distin, S., Bonetti, S., Levinger, N. & Crans, D. 2014. Correlation of Insulin-Enhancing Properties of Vanadium-Dipicolinate Complexes in

Model Membrane Systems: Phospholipid Langmuir Monolayers and AOT Reverse Micelles. *Chemistry-a European Journal,* 20**,** 5149-5159.
Stahla, M., Baruah, B., James, D., Johnson, M., Levinger, N. & Crans, D. 2008. 1H NMR studies of aerosol-OT reverse micelles with alkali and magnesium counterions: preparation and analysis of MAOTs. *Langmuir,* 24**,** 6027-6035.
Storr, T., Thompson, K. & Orvig, C. 2006. Design of targeting ligands in medicinal inorganic chemistry. *Chem Soc Rev,* 36**,** 534-544.
Thompson, K., Liboiron, B., Sun, Y., Bellman, K., Setyawati, I., Patrick, B., Karunaratne, V., Rawji, G., Wheeler, J., Sutton, K., Bhanot, S., Cassidy, C., Mcneill, J., Yuen, V. & Orvig, C. 2003. Preparation and characterization of vanadyl complexes with bidentate maltol-type ligands; in vivo comparisons of anti-diabetic therapeutic potential. *J Biol Inorg Chem,* 8**,** 66-74.
Thompson, K., Lichter, J., Lebel, C., Scaife, M., Mcneill, J. & Orvig, C. 2009. Vanadium treatment of type 2 diabetes: a view to the future. *J Inorg Biochem,* 103**,** 554-8.
Thompson, K. & Orvig, C. 2006. Vanadium in diabetes: 100 years from Phase 0 to Phase I. *J Inorg Biochem,* 100**,** 1925-1935.
Wang, Q., Liu, T., Fu, Y., Wang, K. & Yang, X. 2010. Vanadium compounds discriminate hepatoma and normal hepatic cells by differential regulation of reactive oxygen species. *J Biol Inorg Chem,* 15**,** 1087-97.
Willsky, G., Chi, L., Godzala, M., Kostyniak, P., Smee, J., Trujillo, A., Alfano, J., Ding, W., Hu, Z. & Crans, D. 2011. Anti-diabetic effects of a series of vanadium dipicolinate complexes in rats with streptozotocin-induced diabetes. *Coord Chem Rev,* 255**,** 2258-2269.
Willsky, G., Halvorsen, K., Godzala, M., Chi, L., Most, M., Kaszynski, P., Crans, D., Goldfine, A. & Kostyniak, P. 2013. Coordination chemistry may explain pharmacokinetics and clinical response of vanadyl sulfate in type 2 diabetic patients. *Metallomics,* 5**,** 1491-1502.
Wu, J., Hong, Y. & Xg, X. Y. 2016a. Bis(acetylacetonato)-oxidovanadium(IV) and sodium metavanadate inhibit cell proliferation via ROS-induced sustained MAPK/ERK activation but with elevated AKT activity in human pancreatic cancer AsPC-1 cells. *J Biol Inorg Chem***,** 1-11.
Wu, X., Peters, B., Rithner, C. & Crans, D. 2016b. Multinuclear NMR studies of aqueous Vanadium-HEDTA Complexes. *Polyhedron,* 114**,** 325–332.
Yang, X. & Wang, K. 2016. Focusing on the Link between Diabetes, Alzheimer's Disease and Cancer for the Discovery of New Medicines. *Curr Top Med Chem,* 16**,** 675.
Yang, X., Wang, K., Lu, J. & Crans, D. 2003. Membrane transport of vanadium compounds and the interaction with the erythrocyte membrane. *Coord Chem Rev,* 237**,** 103-111.
Yoshikawa, Y., Sakurai, H., Crans, D., Micera, G. & Garribba, E. 2014. Structural and redox requirements for the action of anti-diabetic vanadium compounds. *Dalton Trans,* 43**,** 6965-6972.
Zizic, Z., Miladinovic, M., Stanic, M., Hadzibrahimovic, M., Zivic, M. & Zakrzekska, J. 2016. (51)V NMR investigation of cell-associated vanadate species in Phycomyces blakesleeanus mycelium. *Res Microbiol,* 167**,** 521-528.

Chapter 5: Polyoxidovanadates $[Mo^{VI}V^{V}_{9}O_{28}]^{5-}$ and $[H_2Pt^{IV}V^{V}_{9}O_{28}]^{5-}$ interact with CHO cell plasma membrane lipids causing aggregation and activation of a G protein-coupled receptor

5.1 Introduction

Polyoxidovanadates (POVs) are oxo-clusters containing octahedral vanadium metal ions vanadium oxo-cluster building blocks. These clusters are classified as homo- or heteropolyoxovanadates now also known as heteropolyoxidovanadates depending on whether their metal ion content is solely vanadium or vanadium with other metal ions. Isopolyoxidovanadates have specific nuclearities such as one, two, four, five, ten, 12 and 18 (Pope, 1983, Pope and Müller, 1991, Hayashi, 2011, Crans, 1994, Hill, 1998, Crans et al., 2004, Bijelic et al., 2019, Treviño and Diaz, 2020, Pessoa et al., 2021) and properties such as stability and redox potential that vary depending on their structures. Replacement of one of the metal ion with another metal provides number of novel heteropolyoxidovanadate molecules with a wide range of properties. Recently studies of POVs (Aureliano et al., 2022, Aureliano et al., 2021, Treviño and Diaz, 2020, Treviño and González-Vergara, 2019, Sánchez-Lara et al., 2018; (Samart et al., 2018, Mutlu et al., 2017) have shown that the anions were highly active and had biological properties that differed from the parent homopolyoxometallate. Although some information is available on the interactions of isopolyoxidometallates with enzymes with distinct selectivity, there is little information comparing the biological effects of the POVs with novel heteropolyoxidovanadates and no consistent patterns identified for their effects (Crans, 1994). As examples, isopolyoxidovanadates have effects on glycerol-3-phosphate dehydrogenase and 6-phosphogluconate dehydrogenase activity (Crans, 1994), isopolyoxidomolybdates are most

potent in their effects on glucose-6-phosphate dehydrogenase (Crans, 1993) and the heteropolyoxidovanadates are most potent in affecting recombinant and native reverse transcriptase activity (Yamamoto et al., 1992).

In this manuscript, we compare the effects of two monosubstituted isopolymetalates, two (POVs), monomolybdo(VI)nonavanadate ($[V_9MoO_{28}]^{5-}$, abbreviated V_9Mo) and monoplatino(IV)nonavanadate ($[H_2PtV_9O_{28}]^{5-}$, abbreviated V_9Pt), with those of decavanadate ($[V_{10}O_{28}]^{6-}$, abbreviated V_{10}) on activation of luteinizing hormone receptors (LHR) expressed in Chinese hamster ovary (CHO) cells, a eukaryotic cell line. Comparing polyoxidometalates V_9Pt and V_9Mo effects on a eukaryotic cell membrane with V_{10} is important because it begins to address structural features of these molecules necessary for their selective interaction with cell membranes. Decavanadate is an isopolyoxidometalate that consists of ten octahedral vanadium(V) atoms, eight of which are bound to one terminal oxo ligand and five of those share oxygens in their octahedra (**Figure 5.1**) (Aureliano and Crans, 2009, Crans et al., 1994, Crans

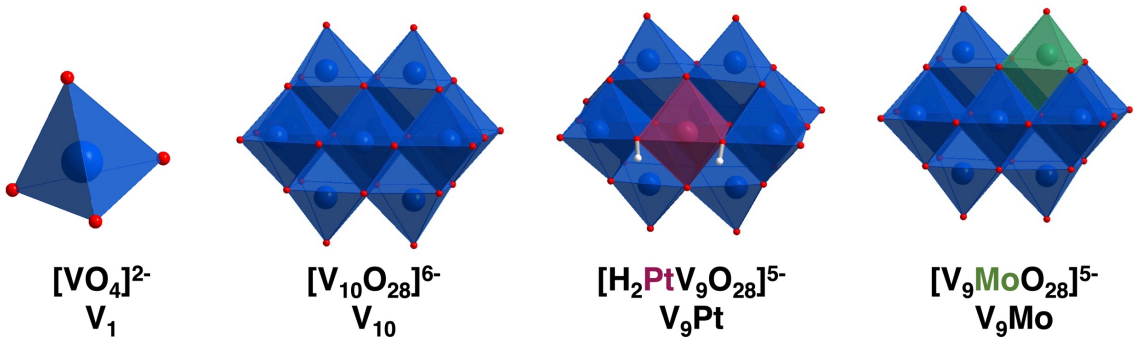

Figure 5.1. Polyhedral representations of $[VO_4]^{2-}$ (V_1), $[V_{10}O_{28}]^{6-}$ (V_{10}), $[H_2PtV_9O_{28}]^{5-}$ (V_9Pt) and $[Mo^{VI}V_9O_{28}]^{5-}$ (V_9Mo) illustrating the differences between the simple vanadate ion and the polyanions investigated in this work at pH 7.4. For illustrative purposes, Pt is depicted in maroon and Mo is depicted in green.

and Willsky, 1997). The last two vanadium atoms are internal and have six bridging oxygens in their octahedra. The V_{10} structure is a compact ion and has the dimensions of 5.8 Å × 7.8 Å × 8.4 Å (Crans et al., 1994). Although the two POVs used in these studies are structurally similar to V_{10}, the replacement of one vanadium atom with either Pt^{IV} and Mo^{VI} results in a molecule with a

different charge distribution and lower symmetry compared to the all-V-containing V_{10} (**Figure 5.1**). In the V_9Pt cluster, one of the two internal vanadium atoms is replaced by a platinum(IV) atom (**Figure 5.1**) and the charge on the V_9Pt ion is minus 5 due to the exchange of one central addenda site by a Pt^{IV} ion. The dimensions of V_9Pt (5.5 Å × 7.7 Å × 8.5 Å) are similar to those of the V_{10}, calculated from XRD data (Uk Lee et al., 2008, Crans et al., 1994). The crystal structure shows the complex with a C_{2v} point group symmetry, with two protons found on the polyanion located on oxygens bridging Pt and V (Uk Lee et al., 2008). These protons are key for the formation of a dimer, $[H_4(Pt^{IV}V_9O_{28})_2]^{10-}$, through four O-H···O hydrogen bonds. Although hydrogen bonds between two V_9Pt ions persist at ambient temperature after dissolving the polyanion salt in water, heating result in discrete V_9Pt ions (Uk Lee et al., 2008, Dugar et al., 2016). In the V_9Mo cluster, one of the surface vanadium atoms on the cluster is replaced by molybdenum (Sánchez-Lombardo et al., 2016). Single-crystal X-ray analysis of the polyoxidometalate $[(CH_3)_4N]_4[H_2MoV_9O_{28}]Cl{\cdot}6H_2O$ has indicated that the molybdenum atom can occupy four different “capping” metal atom positions (Strukan et al., 1997). Although this structure is not deposited in the Cambridge Crystal Structure Database, we assume that the POM dimensions are very similar, because the Mo–O and V–O bond lengths are close in size. Despite the different molecular composition, the spectroscopic properties of V_9Pt, V_9Mo and V_{10} vary as do their solubility and stability in the cell growth medium used in these studies.

Vanadium coordination complexes (Hernández et al., 2022, Ferretti and León, 2022, Semiz, 2022, Biswas et al., 2022, Ribeiro et al., 2022, Nunes et al., 2022, Pessoa et al., 2021, Rudbari et al., 2021, Sahu et al., 2022, Thompson and Orvig, 2006b, Treviño and Diaz, 2020, Scalese et al., 2019, Mosquillo et al., 2020, More et al., 2019, Loizou et al., 2021, Banerjee et al., 2020, He et al., 2020, Levina and Lay, 2011, Patel et al., 2020, Favre et al., 2022) such as bismaltolatodioxovanadium(IV) (BMOV) and polyoxidovanadates have recently been shown to initiate signaling by the luteinizing hormone receptor (LHR), a G-protein coupled receptor (GPCR) (Althumairy et al., 2020c, Althumairy et al., 2020e, Althumairy et al., 2020b, Samart et al., 2020,

Winter et al., 2012, Al-Quatati et al., 2013, Althumairy et al., 2020a, Roess et al., 2008, Crans et al., 2011).

Vanadium coordination complexes have been the focus of recent work in cell systems (Hernández et al., 2022, Ferretti and León, 2022, Semiz, 2022, Damena et al., 2022, Biswas et al., 2022, Ribeiro et al., 2022, Santos et al., 2022, Nunes et al., 2022, Pessoa et al., 2021, Rudbari et al., 2021, Patra et al., 2022, Sahu et al., 2022, Thompson and Orvig, 2006b, Treviño and Diaz, 2020, Scalese et al., 2019, Mosquillo et al., 2020, More et al., 2019, Loizou et al., 2021, Banerjee et al., 2020, He et al., 2020, Levina and Lay, 2011, Patel et al., 2020). Our group has shown that bismaltolatodioxovanadium(IV) (BMOV) and polyoxidovanadates are able to initiate signaling by the luteinizing hormone receptor (LHR), a G-protein coupled receptor (GPCR) (Althumairy et al., 2020c, Althumairy et al., 2020e, Althumairy et al., 2020b, Samart et al., 2020, Winter et al., 2012, Al-Quatati et al., 2013, Althumairy et al., 2020a, Roess et al., 2008, Crans et al., 2011).

The hydrophobic coordination complexes appear to initiate LHR signaling through interactions of the coordination complex with the external surface of the cell membrane and potential penetration of the complex into the lipid bilayer (Samart et al., 2020, Winter et al., 2012, Althumairy et al., 2020a, Crans et al., 2022). V_{10} is one of the POVs that have been found to be particularly potent in activation of LHR (Althumairy et al., 2020c) and the Type I Fcε receptor (Fc εRI) (Al-Quatati et al., 2013, Winter et al., 2012). V_{10} , part of a class of polyoxometalates also referred to as polyoxidometalates (POMs) which are anionic metal-oxo clusters, has potential applications in the field of medicine (Pope and Müller, 1994, Rhule et al., 1998, Hasenknopf, 2005, Bijelic et al., 2018, Bijelic et al., 2019). Decametalates have anticancer and antidiabetic effects in eukaryotic cell lines and tissues and inhibit the growth of prokaryotic *Mycobacterium tuberculosis* mc2 6230 (*M. tb*) and *Mycobacterium smegmatis* mc2 155 (*M. smeg* is now reclassified as a *Mycolicibacterium*) (Aureliano et al., 2021, Aureliano et al., 2022). Interestingly, in bacterial cell lines, inhibitory growth effects of V_{10} were greater that the effects of the known potent phosphatase inhibitor monovanadate (V_1) **(Figure 5.1**) (Samart et al., 2018, Kostenkova

et al., 2021). The wide range of biological effects of decametalates in prokaryotic and eukaryotic cells motivates further work with these compounds given their potential pharmacologic value.

One mechanism of action used by several reported V-compounds is initiated through interactions of vanadium compounds with eukaryotic cell membranes either through intercalation or interactions at the membrane interface to alter the packing of plasma membrane lipids. Changes in lipid packing, in turn, drive the reorganization of the LHR in the membrane with receptors becoming concentrated in plasma membrane microdomains which function as signaling platforms for the receptor (Samart et al., 2020, Samart et al., 2018). Upon LHR aggregation, necessary for signal transduction by functional LHR, the receptor initiates intracellular signaling, producing elevated intracellular levels of cAMP (Smith et al., 2006, Wolf-Ringwall et al., 2011). In the case of $V_{10,}$ the mechanism of action is not likely to involve penetration or direct interaction of V_{10} at the membrane interface because the highly charged V_{10} polyanion remains outside the membrane. Of interest here are the biological effects of similar decametalates and, importantly, whether the lower charged V_9Mo and V_9Pt are capable of initiating through, albeit indirectly, LHR activation despite reduced stability compared to V_{10} in the eukaryotic cell medium.

5.2 Materials and Methods

5.2.1 General materials

CHO-K1 cells were a kind gift from Dr. Takamitsu Kato at Colorado State University. Dulbecco's Modified Eagle medium (DMEM) with added geneticin was purchased from Corning Cellgro. Cell medium also contained penicillin/streptomycin and L-glutamine purchased from Gemini Bio-Products (West Sacramento, CA) and fetal bovine serum (FBS) purchased from Atlas Biologicals (Fort Collins, CO). The 100X MEM non-essential amino acid solution, sodium metavanadate ($NaVO_3$) and bovine albumin were from Sigma-Aldrich (St. Louis, MO). Trypsin-EDTA (0.25%) was supplied by Fisher Scientific Co (Pittsburgh, PA), Optimal-MEM was obtained

from Life Technologies (Carlsbad, CA). Glass-bottom cell culture dishes (CA35 mm diameter) used for optical measurements were obtained from In Vitro Scientific (Sunnyvale, CA).

$NaVO_3$ and sodium molybdate (Na_2MoO_4) were purchased from Sigma Aldrich and used without purification. Monoplatinononavanadate ($[H_2PtV_9O_{28}]^{5-}$, abbreviated V_9Pt) the sodium salt was prepared as reported previously (Uk Lee et al., 2008, Kostenkova et al., 2021). The peaks observed at in ^{51}V NMR confirm the synthesis of the compound and are identical to those reported in the literature (**Figures A4.1-A4.2**) (Uk Lee et al., 2008, Kostenkova et al., 2021). Monomolybdononavanadate ($[MoV_9O_{28}]^{5-}$) abbreviated V_9Mo) solution was freshly prepared following the reported procedure for the sodium salt ($Na_5[MoV_9O_{28}]\cdot 10H_2O$) (Sánchez-Lombardo et al., 2016, Kostenkova et al., 2021). The peaks observed at in ^{51}V NMR confirm the synthesis of the compound and were identical to those reported in the literature (**Figures A4.3-A4.4**) (Sánchez-Lombardo et al., 2016, Kostenkova et al., 2021). The pH in NMR speciation experiments was adjusted by using either 0.1 M HCl or 0.1 M NaOH prepared in doubly deionized water (DDI) water.

5.2.2 General Methods: NMR

All NMR spectra were recorded using a Bruker NMR spectrometer at 105.2 MHz for ^{51}V, and a Varian NMR spectrometer at 131.5 MHz for ^{51}V at ambient temperature. Varian 500 MHz NMR spectrometer was manually calibrated by using a 5 mm broadband probe. The ^{51}V NMR spectra were recorded in DDI water (controls) and DMEM medium to determine speciation of V_9Mo and V_9Pt at several time-points (0, 1, 5, 24, 30 and 48 h) during the experiment. The ^{51}V NMR spectra were recorded using the following parameters: 4096 scans in the f1 domain, 0.01 s relaxation delay, O1P = –500 ppm, SW = 900 ppm, and a 16 μs pulse in a 45° pulse angle without lock and shimming turned on. The ^{51}V NMR spectra were reported relative to a neat $VOCl_3$ at 0 ppm but experimentally referenced against an $NaVO_4$ solution at pH 12 (two signals one for V_1 at –535.7 ppm and the other for V_2 at –560.4 ppm) as an external reference) (Althumairy et al.,

2020c, Samart et al., 2018). The MestreNova NMR processing software (version 14.0.1) was used for data processing.

5.2.3 Preparation of the stock solutions for speciation studies

The stock solution of V_9Pt (2.0 mM) was prepared by dissolving solid (0.0140 g, 0.0100 mmol) $Na_5[H_2PtV_9O_{28}]\cdot 21H_2O$ in 5.00 mL DDI water. The stock solution of V_9Mo (2.0 mM) was prepared by using the desired volumes of DDI water and a 100 mM V_9Mo stock solution; the pH was adjusted to 5.0 by a dropwise addition of 0.1 M NaOH and 0.1 M HCl. The 1.0 mM control solutions of V_9Mo and V_9Pt were prepared by mixing 1,000 µL of the appropriate 2.0 mM stock solution with 1,000 µL of DDI H_2O. The 1.0 mM solutions of V_9Mo and V_9Pt in serum-free media prepared using the same method from 500 mL of DMEM, 5.0 mL of each penicillin/streptomycin, 100x non-essential amino acid solution, and L-glutamine solution). The pH of all solutions was measured at each indicated time-points (0, 1, 5, 24, 30 and 48 h) to determine possible changes in vanadium speciation during the 48 h period of the experiment.

5.2.4 Preparation of the 1.0 mM V_9Pt solution with 0.11 M NaCl and 0.0054 M KCl for speciation studies

The 1.0 mM stock solution of V_9Pt with 0.11 M NaCl and 0.0054 M KCl was prepared by dissolving solid $Na_5[H_2PtV_9O_{28}]\cdot 21H_2O$ (0.0070 g, 5.0 mmol), NaCl (0.032 g, 0.55 mmol) and KCl (0.0020 g, 0.027 mmol) in 90% H_2O / 10% D_2O (4.5 mL DDI H_2O / 0.5 mL D_2O). The pH of the solution was adjusted to 7 (pH = 7.4) with 0.05 M NaOH. The pH of the sample was measured at several time-points (0, 1, 5, 24, 30 and 48 h) to determine the changes in vanadium speciation over 48 h.

5.2.5 Effects of V_9Pt and V_9Mo on CHO cell viability

Cell growth was assessed used a resazurin-based fluorometric assay and serial diluted stock solutions of V_9Pt and V_9Mo into DMEM cell media as previously described (Althumairy et al., 2020c). Approximately 20,000 cells/well were seeded in 96-well plates in 100 µL free serum

media. Cells were allowed to attach to plate surfaces for 3 h and then treated with solutions of 1.0, 5.0, 10, 50 or 100 μM of V_9Pt or V_9Mo together with 10% resazurin for 3h to obtain a baseline value for cell viability (t = 0). A separate population of cells in 96 well plates were similarly treated for 12 h before the addition of 10% resazurin followed by an additional 3 h incubation (t = 15 h). Fluorescence measurements at t = 0 and t= 15 h were made using an excitation wavelength of 530 nm and measurement of fluorescence emission at 590 nm. The compound concentration where cell viability was 50% of the cell number at t = 0 was designated as the IC_{50} and was estimated by curve fitting to log values for both V_9Pt and V_9Mo (data not shown) to be 12.9 μM for V_9Pt and 10.8 μM for V_9Mo. The concentrations of V_9Pt and V_9Mo used in subsequent cell experiments, 10 μM and 8 μM, respectively, were less than the IC_{50} values for each compound and were concentrations that were efficacious without causing high levels of cell death during the cell treatment.

5.2.6 V_9Pt and V_9Mo effects on CHO cell membrane lipid order

An environmentally sensitive styryl dye, di-4-ANEPPDHQ, was used to evaluate effects of V_9Pt and V_9Mo on membrane lipid order. This approach has been described in detail previously (Althumairy et al., 2020c). Briefly, CHO cells (0.5 mL) grown to at least 80% confluence in 50 mL cell culture flasks and treated with 1.0 mL trypsin-EDTA (0.25%) for 3 min were placed in a 35 mm glass-bottom petri dish. After 12 h, cells were washed twice with phosphate-buffered saline (PBS) at pH 7.3 and then incubated in cell medium alone or in medium containing 10 μM V_9Pt or 8 μM V_9Mo. At time 0, a Petri dish containing CHO cells was labeled for 15 min with 200 μL of a stock solution containing 1.5 μM di-4-ANEPPDHQ before washing cells once, covering the cell layer with PBS and imaging cells (Althumairy et al., 2020b). Remaining Petri dishes were treated with 11 mM V_9Pt or 13 mM V_9Mo in media for 10 h, washed with PBS, covered in medium free serum and imaged at times 0, 1, and 3 h after labeling with di-4-ANEPPDHQ. The Zeiss Axiovert 200 M inverted microscope used for imaging was equipped with a 63 x 1.2 NA water objective

and an Andor Du897E EMCCD camera. Cell samples were illuminated using an arc lamp with a 480/30x or 495/20x excitation filter. Fluorescence emission was collected in channel 1 using a 535/40 nm filter and in channel 2 using a 620/40 nm filter and MetaFluor software. Image J software was used for background correction calculation of the fluorescence intensity ratio at 620nm/535nm. Repeated cell washing was used in some experiments to evaluate the interactions of V_9Pt or V_9Mo with membrane lipids. As shown in Figure 2, cells at t=0 were washed two additional times designated 2x and 3x, prior to assessment of membrane lipid.

5.2.7 LHR aggregation Determined by Polarized homo-fluorescence resonance energy transfer

The extent of LHR aggregation was determined using polarized homo-transfer fluorescence resonance energy transfer methods (referred to as homo-FRET) and performed as previously described (Althumairy et al., 2020c). Cells grown as described above were plated in 35 mm glass-bottom Petri dishes and allowed to attach to the glass surface for 12 hr. Cells were then washed with PBS at pH 7.3 and treated for 10 h with solutions containing either 10μM V_9Pt or 8μM V_9Mo. After washing once to remove V_9Pt or V_9Mo, cells were covered with serum-free medium and imaged using homo-FRET protocols immediately at t = 0 or after further incubation for 1 h or 3 h, respectively (Althumairy et al., 2020c). At least 5 cells were examined from each Petri dish and a minimum of 30 cells were examined for each measured condition. Results are expressed as the mean ± SEM of individual measurements. Statistical evaluation of mean differences in untreated and treated groups were analyzed using a one-way ANOVA followed by the Tukey multiple comparison test and Student's t-test using R version 3.3.1. P values < 0.05 were considered statistically significant.

5.2.8 Intracellular cAMP levels in V_9Pt- and V_9Mo-treated cells

Fluorescence assays of intracellular cyclic adenosine mono-phosphate (cAMP) were performed using a cAMP reporter ICUE3 expressed in CHO cells from an ICUE3 plasmid provided by Dr. Jin Zhang (DiPilato and Zhang, 2009) and methods in our laboratory that have been previously described in detail (Althumairy et al., 2020c). After transfection of CHO cells with the ICUE3 plasmid, images were acquired from cells in PBS to establish baseline levels of intracellular cAMP. The cell medium was then exchanged with solutions containing 10 μM V_9Pt or 8 μM V_9Mo. Cells were incubated for 15 min and reimaged. To evaluate eYFP emission and eYFP sensitized emission (YFPSE) due to energy transfer from CFP, images were acquired used a 63x 1.2 NA water objective in a Zeiss Axiovert 200M inverted microscope with an Andor Du897E EMCCD camera, arc lamp excitation with a 436DF20 excitation filter and two emission filters, 480DF40 for CFP and 535DF30. After background subtraction from the fluorescence images, data were analyzed using Image J software to calculate the emission intensity ratio of CFP/YFPSE. For each petri dish, 2-5 cells were observed, and data were collected from a minimum of 15 cells for each treatment condition.

5.3 Results

5.3.1 Effects of V_9Mo and V_9Pt on lipid order in CHO cell plasma membranes

In initial experiments, we evaluated whether the water-soluble transition metal monosubstituted POVs, V_9Pt or V_9Mo, both less charged than V_{10}, had similar effects to those of V_{10} on membrane lipid order. We have previously shown that V_{10} decreases membrane lipid order in CHO cells for over 6 h (Althumairy et al., 2020c). Most previously investigated V-compounds are more hydrophobic coordination complexes and hence penetrate the membrane when exerting their function (Winter et al., 2012, Althumairy et al., 2020b), However, we found that in addiiton to V_{10}, V_{14} ($(K(NH_4)_4[H_6V_{14}O_{38}(PO_4)]11H_2O)$) and V_{15} ($[(CH_3)_4N]_6[V_{15}O_{36}(Cl)]$) had effects on membrane lipid order (Althumairy et al., 2020c). Initially we evaluated IC_{50} values for V_9Pt or V_9Mo

and, based on the IC_{50}, selected a lower concentration for each compound for use in subsequent experiments (**Table 5.1**). Lipid order in treated cells was decreased compared to untreated cells

Table 5.1. Calculated values for the IC_{50} in Chinese Hamster Ovary (CHO) cells treated with V_9Pt and V_9Mo

V-Compound	IC_{50} per V-compound (μM)	IC_{50} per V-atom (μM)	Selected concentration for each V-compound (μM)
V_9Pt	12.9 ± 0.5	116 ± 5	10.0
V_9Mo	10.8 ± 0.6	97 ± 6	8.0

as indicated by an increase in the ratio of emission of *di*-4-ANEPPDHQ at 640/545 nm. After one washing of cells to remove excess V_9Pt or V_9Mo, lipid packing was evaluated at 1 or 3 h. At 1 h, lipid packing had returned to baseline values which suggests that V_9Mo and V_9Pt effects on membrane lipid order were short lived. These results contrasted sharply with similar experiments with V_{10} where a single washing of V_{10} treated cells did not markedly affect membrane lipid order for at least 6 h (Althumairy et al., 2020c).

Because effects on membrane lipid order for V_9Pt and V_9Mo were short-lived, we evaluated the extent of V_9Pt and V_9Mo association with the membrane further by washing cells two additional times at time 0 as shown in **Figure 5.2**. Washing cells three times increased lipid

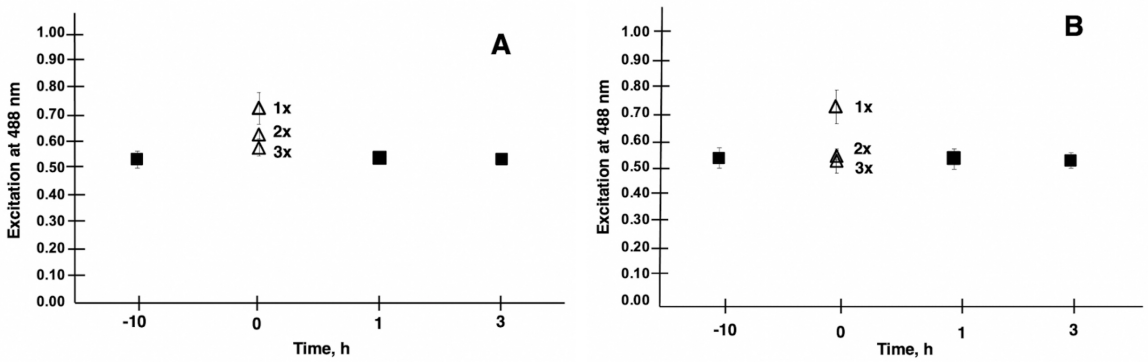

Figure 5.2: Membrane lipid order in CHO cells treated with V_9Mo (**Panel A**) and V_9Pt (**Panel B**). The extent of lipid packing as indicated by the emission ratio at 640/545 nm following excitation of the fluorophore with 488 nm light was monitored over 3 h. Increased emission at 640 nm relative to emission at 545 nm is indicative of a decrease in lipid order. The effects of repeated washing at time 0 on lipid fluidity for cells was assessed for both V_9Mo and V_9Pt. A second wash (2x) increased lipid order and three washes (3x) increased lipid order to values seen in untreated cells.

packing to baseline values for both V_9Pt- and V_9Mo-treated cells indicating that these POVs exerted effects on membrane lipids while being only weakly associated with the cell membrane.

5.3.2 Aggregation of LHR

Effects of V_9Pt and V_9Mo treatment on LHR aggregation were examined using CHO cell lines stably expressing different levels of LHR receptors in the plasma membranes: 10,000 LHR, 32,000 LHR, 122,000 LHR or 560,0000 LHR, respectively (**Figures 5.3 and A4.6**). When cells

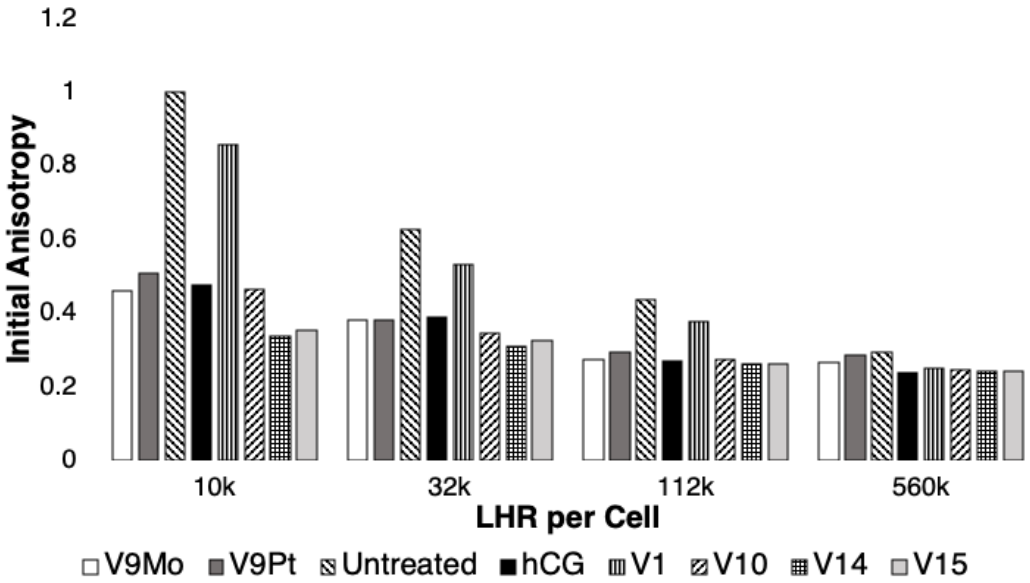

Figure 5.3. Values for the initial anisotropy measured for eYFP covalently linked to LHR using polarized homo-FRET methods was obtained by replotting data in **Figure A4.6** combined with previous reported systems (Althumairy et al., 2020c). The data is normalized relative to controls which were set to 1.0. Values for initial anisotropy less than 1.0 are indicative of LHR aggregation after treatment with V_9Pt and V_9Mo (this work) or with hCG, V_1, V_{10}, V_{14} or V_{15} as determined previously (Althumairy et al., 2020c). Pre-treatment of cells with hCG, V_1, V_9Pt, V_9Mo, V_{10}, V_{14} or V_{15} decreased values for initial anisotropy for receptors on cells expressing 10,000 or 32,000 LHR per cell. V_9Mo and V_9Pt had similar effect on LHR aggregation as did hCG and V_{10}. When cells expressed non-physiologically high numbers of LHR per cell (122,000 LHR/cell), receptors were already extensively aggregated. HCG, V_9Pt, V_9Mo, V_{10}, V_{14}, and V_{15} increased receptor aggregation while V_1 had no statistically significant effect on receptor clustering. There were no statistically significant effects of any treatment with cells with very high numbers of LHR per cell (560 000 LHR per cell) suggesting that highly over-expressed LHR are constitutively aggregated and unresponsive to any treatment.

expressed 10,000 or 32,000 LHR per cell, preincubation of cells with 10 μM V_9Pt or 8 μM V_9Mo produced significant aggregation of LHR and decreased lipid order in CHO cell membranes. As we have seen previously (Althumairy et al., 2020d), cells expressing higher, non-physiological

numbers of LHR per cell have LHRs that are extensively aggregated. For cells with 122,000 LHR per cell, V_9Mo and V_9Pt caused modest but significant effects on receptor aggregation. For cells expressing 560,000 LHR per cell, there was no further aggregation of LHR when cells were treated with either V_9Pt or V_9Mo suggesting that the constitutive LHR aggregation due to receptor overexpression on untreated cells was not affected by changes in lipid order as has been previously observed.

In **Figure 5.3** the data from **Figure A4.6** on the effects of V_9Pt and V_9Mo treatment on LHR aggregation was replotted with previously reported data for cells expressing 10,000, 32,000, 122,000 or 560,000 LHR per cell and treated with V_1, V_{10}, V_{14} ($(K(NH_4)_4[H_6V_{14}O_{38}(PO_4)]11H_2O)$) and V_{15} ($([(CH_3)_4N]_6[V_{15}O_{36}(Cl)]$) (Althumairy et al., 2020c). The control values (untreated cells) were very similar and Figure 7 shows that the initial anisotropies with V_9Pt or V_9Mo treatment were similar to those previously reported for V_{10}-treated cells. Interestingly, V_9Pt, V_9Mo and V_{10} are less effective when CHO cells express lower LHR receptor numbers per cell compared to the larger multivalent oxidometalates V_{14} and V_{15}. For CHO cells with higher LHR receptor numbers, the effects of these compounds are similar. This may be due simply to pre-existing and extensive clustering of LHR when receptor numbers are high; membrane aggregation as evaluated here or, for example, binding of human chorionic gonadotropin (hCG) to the receptor (Althumairy et al., 2020c) has no notable effects on cells where receptors were already highly aggregated.

5.3.3 Effects of V_9Mo and V_9Pt on cAMP levels in CHO cells

A low intracellular level of cAMP is indicated by a low CFP/YFPSE emission ratio. As shown in **Figure 5.4**, when examining cells expressing 10,000 LHR per cell, the increase in intracellular cAMP was most apparent with V_9Mo or V_9Pt treatment. Untreated receptors exhibit low basal levels of intracellular cAMP as indicated by the low ratio of CFP/YFPSE. However, as the number of LHR receptors increased the ratio of CFP/YFPSE increased showing that the levels of intracellular cAMP in untreated cells increases with increasing numbers of LHR per cell.

Treating cells with either V_9Mo or V_9Pt significantly increased intracellular cAMP levels in CHO cells expressing 10,000 and 32,000 LHR expressed per cell. When cells overexpressed LHR, as shown in the experiments with either 122,000 or 560,000 LHR per cell, the addition of V_9Mo and V_9Pt had little or no effect on intracellular cAMP levels which were already high. These overexpressed receptors are pre-clustered, presumably due to high expression levels in the cell membrane, and, as a result, constitutively active as indicated by high levels of intracellular cAMP in untreated cells.

As shown in **Figure 5.3**, exposing CHO cells to either V_9Mo or V_9Pt caused anisotropy values to decrease, indicating LHR aggregation. There is a relationship between receptor clustering and intracellular levels of cAMP expressed by the CFP/YFPSE emission ratio shown in **Figure 5.4.** The increasing basal levels of intracellular cAMP in untreated cells with increasing numbers of LHR per cell were associated with decreasing initial anisotropies and plotted as 1.0. The data for V_9Mo or V_9Pt was plotted as the percentage of the control. Combining the data determined in this work and shown in **Figure A4.7** and plotted in **Figure 5.4** with the data for hCG, V_1, V_{10}, V_{14} and V_{15}-treated CHO cells reported previously (Althumairy et al., 2020c) shows a similar pattern for hCG, V_1, V_9Pt and V_9Mo, V_{10}, V_{14} and V_{15}-treated cells expressing 10,000, 32,000,122,000, or 560,000 LHR per cell. In summary, receptors that were extensively clustered in response to the POVs described in this work or clustered as a result of LHR overexpression, were actively signaling as indicated by high cAMP levels. When considering cells expressing 10,000 LHR per cell, receptors needed to be activated by treatment of one of the V-anions. **Figure 5.4** shows that V_9Pt and V_9Mo treatment produces a higher level of signaling than either hCG, a naturally occurring ligand for LHR, or any of the other V-containing compounds. Considering that V_9Pt and V_9Mo hydrolyze quickly, this suggests that signaling happens very quickly after POVs are added to the assay solution. Moreover, the higher toxicity observed with V_{10} and higher multivalent POVs was not seen with V_9Pt and V_9Mo. In summary, V_9Pt and V_9Mo were both more effective in affecting membrane lipid organization and LHR-mediated cell signaling than the more

stable, higher charged V_{10} and multivalent POV. These studies document that monosubstituted isopolymetalates are more efficacious as signaling agents while causing less toxicity than corresponding unsubstituted isopolymetalates.

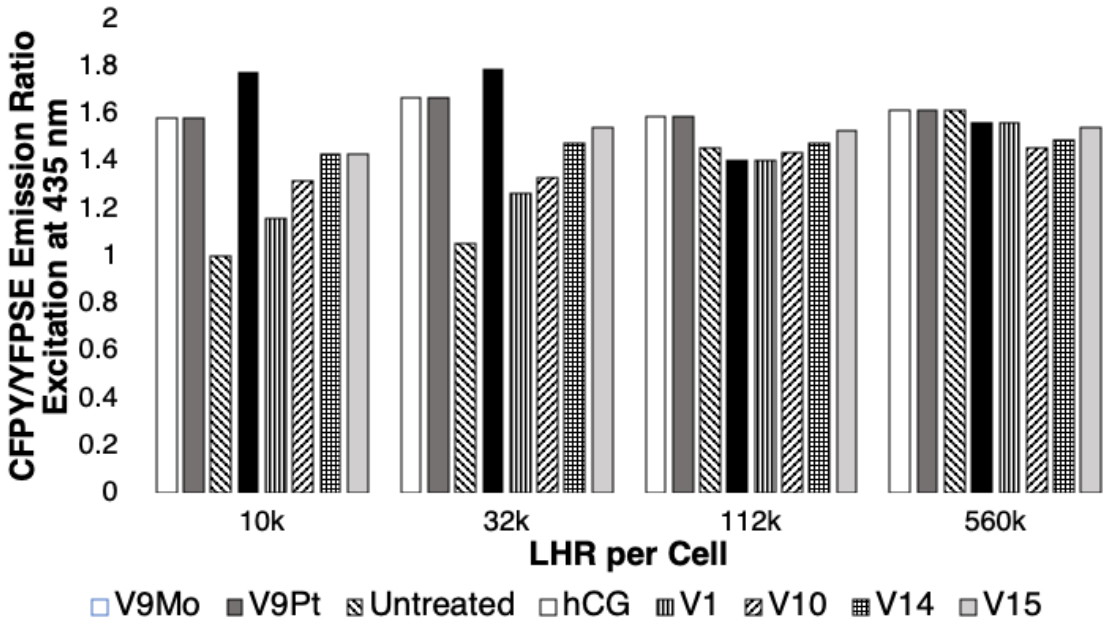

Figure 5.4. The effects of LHR numbers per cell on intracellular cAMP levels in the absence (untreated) or in the presence of cells treated with hCG, V_1, V_9Pt, V_9Mo, V_{10}, V_{10}, V_{14} or V_{15}. The data is normalized with the controls as 1.0 and the data shown as percentage of the control. ICUE3 was used as a cAMP reporter molecule. When there is an increase in intracellular cAMP, cAMP binds to ICUE3, reduces energy transfer between CFP and YFP (YFPSE) upon exposure of ICUE3 to 435 nM light and increases the CFP/YFPSE ratio. In the absence of cAMP, there is increased energy transfer from CPF to YFP, an increase in sensitized emission by YFP, and a reduction in the CFP/YFPSE ratio. Data shown are the mean of 25–43 individual measurements depending on the treatment.

5.3.4 Speciation and stability of V_9Pt and V_9Mo in H_2O and DMEM

Transition metal ion monosubstitution breaks the symmetry of V_{10}, resulting in different chemical shifts and relative signal intensities in ^{51}V NMR spectra, such as 2:4:4 in V_{10} to 1:6:2 in V_9Pt. Monosubstitution with Pt^{IV} in V_{10} results in four different types of vanadium atoms, two of which the ^{51}V NMR signals overlap, generating a total of three signals for the ^{51}V NMR spectrum of V_9Pt (V_D at -371.0, $V_{E/F}$ at -450.9, and V_G at -475.0 ppm) Figure 5. To assess V_9Pt speciation

over the time course of cell studies, time-dependent ^{51}V NMR speciation studies of both V_9Pt and V_9Mo clusters were carried out in aqueous solutions and DMEM media at pH ≈ 7.4 over 48 h. The ^{51}V NMR spectra in **Figures 5.5A and 5.5B** show that although the speciation of the V_9Pt in the aqueous solution with pH of 1.0 mM of V_9Pt maintained near pH 7.4 show limited hydrolysis of PtV_9, the addition of PtV_9 to DMEM show extensive and immediate hydrolysis (**Figure 5.5, Table 5.2**). Overall, the ^{51}V NMR data indicates that the vanadate (V_1), forms rather

Table 5.2. Speciation data of the V_9Pt and V_9Mo clusters collected at t = 0, 24, and 48 h in 1.0 mM aqueous solutions (V_9Pt and V_9Mo), aqueous solution with added chloride anions and and 1.0 mM solutions in DMEM media. No adjustments have been done to account for the polyoxidovanadates' hydrolysis.

Anions monitored	**Signals observed by ^{51}V NMR spectroscopy**								
Compound and time / conditions	V_9Pt (%)	V_9Pt minor isomers (%)	V_9Mo (%)	V_{10} (%)	V_1 (%)	V_2 (%)	V_4 (%)	V_5 (%)	Refs.
V_9Pt / 0 h Aqueous Aq. With added Cl^- Media	33.8% 7.9% 0%	1.1% 0.3% 0%	- - -	- - -	3.2% 7.5% V_1+PV 19.0%	5.4 % 7.3 % 10%	49.3% 68.0% 63.0%	7.0% 9.7% 7.0%	
V_9Pt / 24 h Aqueous Aq. with added Cl^- Media	33.0% 6.5% 0%	1.0% 0.3% 0%	- - -	- - -	3.1% 7.6% V_1+PV 20.0%	5.0 % 8.5 % 14.0 %	51.2% 69.8% 63.0%	7.0% 8.2% 4.0%	
V_9Pt / 48 h Aqueous Aq. with added Cl^- Media	33.6% 6.1% 0%	0.3% 0.2% 0%	- - -	- - -	3.1% 7.5% V_1+PV 20.0%	5.4 6.7 % 12.0	51.0% 70.4% 61.0%	5.1% 10.3 % 5.0%	
V_9Mo / 0 h Aqueous Media	- -	- -	17.5 % 16.5 %	9.5 % 7.5 %	74.0% V_1+PV 66.0%	4.0 % 1.0 %	0% 0%	0% 0%	

Table 5.2. Speciation data of the V_9Pt and V_9Mo clusters collected at t = 0, 24, and 48 h in 1.0 mM aqueous solutions (V_9Pt and V_9Mo), aqueous solution with added chloride anions and and 1.0 mM solutions in DMEM media. No adjustments have been done to account for the polyoxidovanadates' hydrolysis.

V_9Mo / 24 h Aqueous Media	- -	- -	21.5 % 0%	10.5 % 0%	74.0% V_1+PV 94.0%	0% 4.0 %	0% 3.0%	0% 0%	
V_9Mo / 48 h Aqueous Media	- -	- -	18.0 % 0%	6.0 % 0%	77.0% V_1+PV 97.0%	0% 5.0 %	0% 3.0%	0% 0%	
V_{10} / 0 h Aqueous Media	- -	- -	- -	56.9 89.3	14.6 V_1+PV 7.54	10.7 2.11	17.6 1.05	0.21 -	Althumairy, 2020
V_{10} / 24 h Aqueous Media	- -	- -	- -	47.3 5.00	13.7 V_1+PV 20.6	10.5 12.6	28.4 56.7	- 5.37	Althumairy, 2020
* PV = V(V) phosphate species ** Considering the lack of stability of some polyoxidovanadates, the values given in Table 2 have been reported without adjusting for hydrolysis under assay conditions.									

quickly after dissolution of V_9Pt cluster in the media and that V_1 is the main component found in the media by the time sample is analyzed by ^{51}V NMR spectroscopy. The lack of stability in the DMEM media could be attributed to either higher pH (pH 7.4 rather than pH 6.6 in the Middelbrook 7H9 broth media used for cultivation of mycobacteria), the higher concentrations of the chloride ions or other components in DMEM media. To determine whether the increased concentration of the chloride anions affects the stability of V_9Pt, we carried out a time-dependent ^{51}V NMR speciation experiment over 48 h with the added chloride anions (**Figure A4.5**). The concentrations of the added NaCl and KCl are identical to those in the DMEM media (0.11 M and 0.0054 M, respectively) which are significantly higher than those in 7H9 media (0.015 M NaCl and 0.0045 mM KCl). The results shows that the speciation of the V_9Pt in the aqueous solution with the added chloride anion is indistinguishable from that observed to that in the aqueous control solution (**Figures 5.5A and A4.5, Tables 5.1 and A4.1**), indicating that another component of the media causes immediate hydrolysis of V_9Pt. Overall, the ^{51}V NMR data indicates that the vanadate

oligomers (V_1+PV, V_2, V_4 NMR data indicates that the vanadate oligomers (V_1+PV, V_2, V_4, and V_5), rather than the V_9Pt cluster are the major species present in the DMEM media very quickly after dissolution of the V_9Pt.

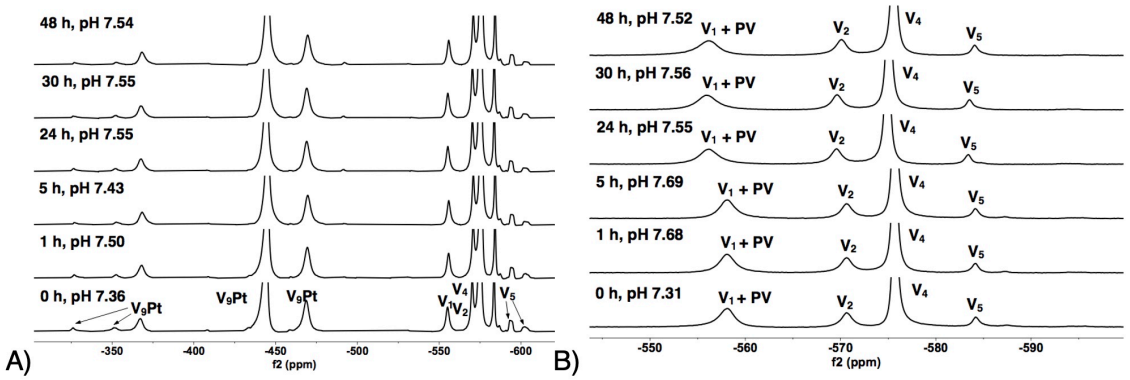

Figure 5.5. ^{51}V NMR spectra of V_9Pt in A) the 1.0 mM aqueous control solution and B) the 1.0 mM solution in DMEM as a function of time. The signals (in ppm) are assigned to the polyoxoanion V_9Pt as follows: –379 (V_D), –445 ($V_{E/F}$) and –470 (V_G), a combined V_1 + PV signal (–573), V_2 (–571), V_4 (–575) and V_5 (-584, -592 and -602). The V_9Pt peaks are identical to those reported in the literature.

To determine the speciation and stability of V_9Mo, we examine time-dependent ^{51}V NMR speciation over 48 h in H_2O and DMEM. The spectra of 1.0 mM of V_9Mo in are shown in **Figure 5.6**. Transition metal ion monosubstitution breaks the symmetry in the V_{10}, resulting in different chemical shifts and relative intensities of the signals (2:4:4 in V_{10}, and 2:2:2:1:2:1 in V_9Mo). Monosubstitution with Mo^{VI} results in six different types of vanadium atoms with the following chemical shifts: V_H at -423 ppm, V_I at -494 ppm, V_J at -503 ppm, V_K at -513 ppm, V_L at -515 ppm, and V_M at –523 ppm. Additionally, V_H, V_I and V_J contain approximately 50% of V_9Mo and 50% V_{10} which was accounted for in all concentration calculations (Kostenkova et al., 2021).

The results of the spectroscopic studies of 1.0 mM V_9Mo aqueous control and 1.0 mM V_9Mo solution in DMEM at pH ≈ 7.4 are shown in **Figures 5.6A and 5.6B**, respectively. The ^{51}V NMR speciation data show that the V_9Mo cluster partially hydrolyzes in solution into the phosphovanadate (PV) derivative and vanadium oligomers (PV, V_1, V_2, V_4 and V_5) and small

quantities of the V_9Mo isomer (-326 ppm and –352 ppm). The NMR data show that majority of the V_9Mo cluster hydrolyzes in the aqueous control solution at 0 h (17.5% of the sample), generating significant quantities of the phosphovanadate (PV) derivative and vanadate oligomers (74.0%). The amounts of both V_9Mo and V_1+PV remain unchanged during 48 h. Interestingly, a significant drop in the pH from 7.35 to 6.44 is observed after 1 h, yet it does not affect the stability of V_9Mo in an aqueous solution over time. The NMR data in DMEM has shown that most of the V_9Mo cluster hydrolyzes immediately in the media with small quantities (0.165 mM) of V_9Mo present in solution at 0 h. V_9Mo completely hydrolyzes into PV complex and vanadate oligomers (V_1 – 70.0%, V_2 – 2.0%) within 1 h (**Figure 5.6B, Table 5.2**). Overall, the results indicate that PV and vanadate (V_1), rather than the V_9Mo cluster is the major components present in the media solution; although a little V_9Mo remained in the aqueous solution, in the media it was quickly hydrolyzed.

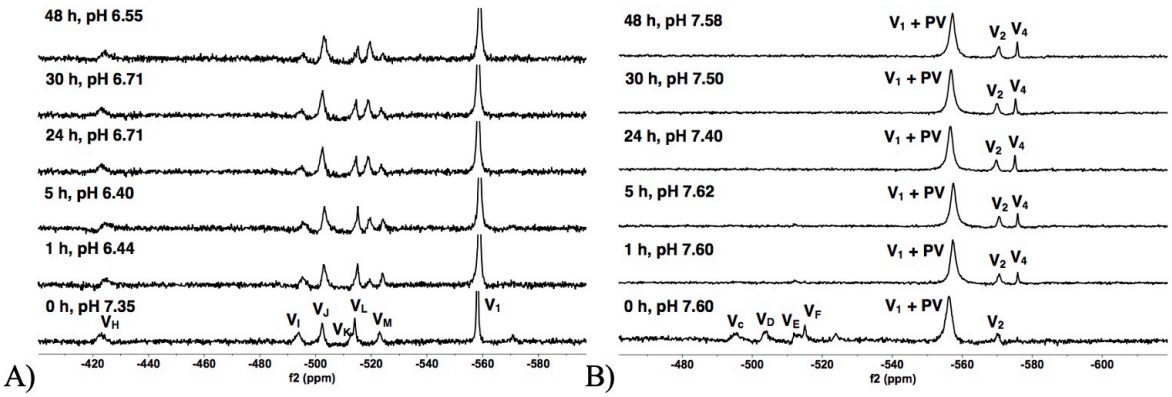

Figure 5.6. ^{51}V NMR spectra of V_9Mo in A) the 1.0 mM aqueous control solution and B) the 1.0 mM solution in DMEM as a function of time. The signals (in ppm) are assigned (V_H, V_I, V_J, V_K, V_L and V_M = -423, -494, -503, -513, -515 and –523), the combined V_1 + PV (–563) and V_2 (–570). The V_9Mo peaks are identical to those reported in the literature.

In **Table 5.2** we also list the speciation carried out and reported previously showing the stability of V_{10} both in aqueous solution and in media (Althumairy et al., 2020c). The V_{10} is initially present in both aqueous and media solution, and small amounts are present in aqueous solution and media even at 24 hrs. This is particularly relevant since some V_{10} is formed in the solution containing V_9Mo, affecting the observed effects by V_9Mo because a fraction of the active

polyoxidovanadates is not V_9Mo. Indeed, V_{10} is known to exert many different activities including antidiabetic effects (Crans et al., 2019b, Feng et al., 2022), mitochondrial function (Aureliano and Ohlin, 2014), having anticancer effects (Bijelic et al., 2018), showing activities against a range of bacteria include mycobacterial tuberculosis (Samart et al., 2018(Aureliano et al., 2022, Aureliano et al., 2021) and other bacteria (Samart et al., 2018, Bijelic et al., 2018, Aureliano and Crans, 2009, Sánchez-Lara et al., 2018, Aureliano et al., 2021, Aureliano et al., 2022). In some studies, both V_1 and V_{10} have been investigated and V_{10} was found to be much more potent than V_1 (Samart et al., 2018). In this work, we explored the responses of a G coupled-protein receptor (GCPR), LHR, to two classes of water-soluble POMs structurally related to V_{10}, hence two monosubstituted decavanadates (V_9Pt and V_9Mo). All three POVs have similar core structures but distinct chemical properties due to transition-ion monosubstitution with either Pt^{IV} or Mo^{VI} which changes formal charges, hydrolytic and redox stability of the compact decametalate. In this work, we compared the all V-atom V_{10} to monosubstituted decavanadates with potential biological applications with respect to effects on growth inhibition and signaling by a G protein-coupled receptor (Althumairy et al., 2020c, Althumairy et al., 2020a, Aureliano et al., 2021, Aureliano and Crans, 2009). In **Table 5.3** we summarize the observed growth effects of the V_9Pt and V_9Mo

Table 5.3. Calculated values for the IC_{50} in Chinese Hamster Ovary (CHO) cells treated with V_1, V_{10}, V_9Pt and V_9Mo

V-Compound	IC_{50} per V-compound (μM)	IC_{50} per V-atom (μM)	References
V_1 (Metallomics 2020)	56.7 ± 7.5	56.7 ± 7.5	**Althumairy, 2020c**
V_{10} (Metallomics 2020)	3.2 ± 0.6	32 ± 6.0	**Althumairy, 2020c**
V_9Pt	12.9 ± 0.5	129 ± 5	This work
V_9Mo	10.8 ± 0.6	108 ± 6	This work
V_{14}	6.1 ± 0.8	116 ± 5	**Althumairy, 2020c**
V_{15}	8.2 ± 3.2	97 ± 6	**Althumairy, 2020**c

determined in this work and compare them to the effects reported previously on V_1 (vanadate monomer), V_{10} (pure decavanadate), and two multivalent POVs V_{14} (((K$(NH_4)_4$[$H_6V_{14}O_{38}(PO_4)$]11H_2O)) and V_{15} ([$(CH_3)_4N]_6[V_{15}O_{36}(Cl)]$]) (Althumairy et al., 2020c).

5.4 Discussion

To attribute the effects of the two POVs and compare their effects to those of V_{10} and V_1 and the two multivalent POVs, we examined the stability and speciation of V_9Pt and V_9Mo both in aqueous stock solution and DMEM media. We monitored the speciation using ^{51}V NMR spectroscopy and the species forming under the condition of the biological studies are summarized in Table 2. The replacement of one V-atoms in the V_{10} molecule cause a difference in overall charge from -6 for V_{10} to -5 for V_9Pt and V_9Mo whereas the structure of the decametalate remains very similar. Previous work has shown that V_9Pt is stable in the acidic bacterial media (Kostenkova et al., 2021) and that V_{10} partially hydrolyzes in DMEM over 10 h so we were surprised to see that V_9Pt hydrolyzed almost immediately in these studies. Similarly, the V_9Mo was found to hydrolyze within 1 h at the neutral pH values and medium used in this work which

is faster than reported previously (Kostenkova et al., 2021). There are differences in the mediums use for bacterial 7H9 cells and eukaryotic CHO cells with higher Cl^- concentrations in 7H9 medium. To determine whether the reduced stability of V_9Pt in CHO cell growth medium could be attributed to Cl^- concentrations, we carried out time-dependent speciation experiments in an aqueous solution with added chloride anions (**Figure A4.5, Tables 5.1 and A4.1**). The concentration of the added chloride salts produced a solution that was equivalent to that found in DMEM (0.0054 M KCl and 0.11 M NaCl). Since our results have shown that the stability and speciation of V_9Pt is identical in aqueous solutions with and without added chloride anions, we conclude that the lower stability of V_9Pt in this medium is caused by other factors which may include the various additives used with mediums prepared for 7H9 and CHO cells as well as differences in the medium pH. For CHO cells studies, DMEM is supplement with penicillin, streptomycin, L-glutamine, and protein-rich fetal bovine serum as well as geneticin to maintain stable expression of LHR in CHO cells. Any one of these additives or some combination of these additives may account for observed differences in V_9Pt stability when compared to studies of this molecule in bacterial cells. However, potentially new species are not present in high enough concentrations to be observed by ^{51}V NMR spectroscopy. The presence of such species would reflect a decrease in the stability of V_9Pt and a species that was highly effective in initiating LHR signaling at very low concentrations.

Some polyoxidometalates remain intact while others hydrolyze under the conditions of the biological studies, thus, carrying out speciation experiments under biological conditions is crucial to understanding their biological activities (Levina and Lay, 2017, Pessoa and Correia, 2021, Nunes et al., 2021, Kiss et al., 2000, Levina et al., 2017, Postal et al., 2016, Bougie and Bisaillon, 2006). Interestingly, growth inhibition of CHO cells by V_9Pt and V_9Mo is weaker than the growth inhibition observed for V_{10}-treated cells. A previous study of mixed valence POVs with LHR also investigated their stability and speciation at pH 7.4 using ^{51}V NMR and EPR spectroscopies. (Althumairy et al., 2020c) V_{15} is particularly interesting in that it contains 7 V(V) and 8 V(IV) and

that part of its decomposition involves oxidation to the V_{15} – that is an all V(V) anion (Nunes et al., 2012, Postal et al., 2016). The results have therefore shown that V_{15} remains intact in DMEM at 0 and 24 h with the trace level of the reduced V(IV) species present until 24 h at ambient temperature EPR spectra (Althumairy et al., 2020c). V_{14}, in contrast, partially hydrolyzes starting at 0 h and is completely hydrolyzed at 24 h, as evidenced in the ambient temperature EPR spectra in DMEM (Althumairy et al., 2020c). The growth inhibition of V_9Pt and V_9Mo is also weaker than the growth inhibition observed for V_{14} and V_{15}. This is most readily understood if one considers that V_{10} and V_{15} are more stable than V_9Pt and V_9Mo. In the case of V_{14}, the situation is less obvious because this species easily decomposes. However, because both V_9Pt and V_9Mo are significantly more potent growth inhibitors than V_1, decomposition of these compounds to V_1 does not explain their observed effects on cell growth.

In this work, we investigated the effects on lipid order in CHO cells treated with V_9Mo and V_9Pt after repeated (three times) washings at t = 0. The lipid order was monitored measuring the emission at 640 nm relative to emission at 545 nm followed by excitation of the fluorophore with 488 nm light; decreased ratios is indicative of a decrease in lipid order. A decrease in the emission ratio after the first, the second (2x) and the third (3x) wash indicated increased lipid order compared to untreated cells (**Figure 5.2**). Because the extent of lipid packing returned to baseline values with repeated cell washing, it appears that these compounds have not penetrated the cells. Various experiments with either one cell wash or repeated cell washings were done previously for V_1, $VOSO_4$, BMOV and selected POVs-treated cells. With BMOV and $VOSO_4$ we showed that removing the V-compound with a single wash from cells that produced a low number of LHR per cell (10,000 LHR/cell) a greater increase in lipid packing was observed for the $VOSO_4$-treated cells compared to BMOV-treated cells (Althumairy et al., 2020a). After 24h the lipid packing is returned to levels near those of untreated cells suggesting that treatment with BMOV and $VOSO_4$ does not cause a significant compound internalization.

Although studies using multiple cell washes have only recently been carried out, it is possible to compare the effects of single cell washes in cells treated with oxidovanadate and POVs with variable stabilities. V_1, V_{10} and V_{15} effects on lipid packing (Althumairy et al., 2020c) can be compared with those seen for V_9Mo-treated and V_9Pt-treated cells where cell treatment is followed by washing cells once. Under these conditions, V_1, V_{10} and V_{15} did not wash off cells as readily as did V_9Mo and V_9Pt which suggests that V_1, V_{10} and V_{15} are associated more closely with the membrane interface or, alternatively, that they are being at least partially internalized. Nonetheless, V_9Mo and V_9Pt can more effectively initiate LHR signaling; the observed increase in intracellular cAMP suggests that the signaling response must be very rapid despite hydrolyzing of V_9Mo and V_9Pt and that this rapid response is at least partially distinct from the more slowing developing effects on cell growth inhibition. It is likely that termination of LHR signaling in these experiments is due to the reestablishment of reduced membrane lipid packing, disaggregation of LHR and movement of LHR out of raft domains. Previous studies of LHR activated by the receptor ligand human chorionic gonadotropin (hCG), show that LHR become aggregated in membrane rafts and actively signal upon binding of hCG (Lei reference). Chemical disruption of the raft signaling platforms through cholesterol extraction from the plasma membrane is sufficient to eliminate signaling initiated by binding of hCG to LHR and LHR aggregation (Steve Smith reference earlier). These studies led to the development of several mechanisms that are shown schematically in **Figure 5.7** but do not rule out the possibility that vanadium compounds used in these experiments are interacting with the receptor.

Figure 5.7 shows various mechanisms previous proposed for the reported vanadium compounds interactions with cells that initiate signaling by LHR or other GCPRs. Because the POVs forms multiple species in media, it is likely that more than one type of interaction is taking place. Some species may interact with cells as shown in **Figure 5.7a**, while others employ alternative mechanisms as summarized in **Figure 5.7b** or **Figure 5.7c**. For example, $VOSO_4$ and

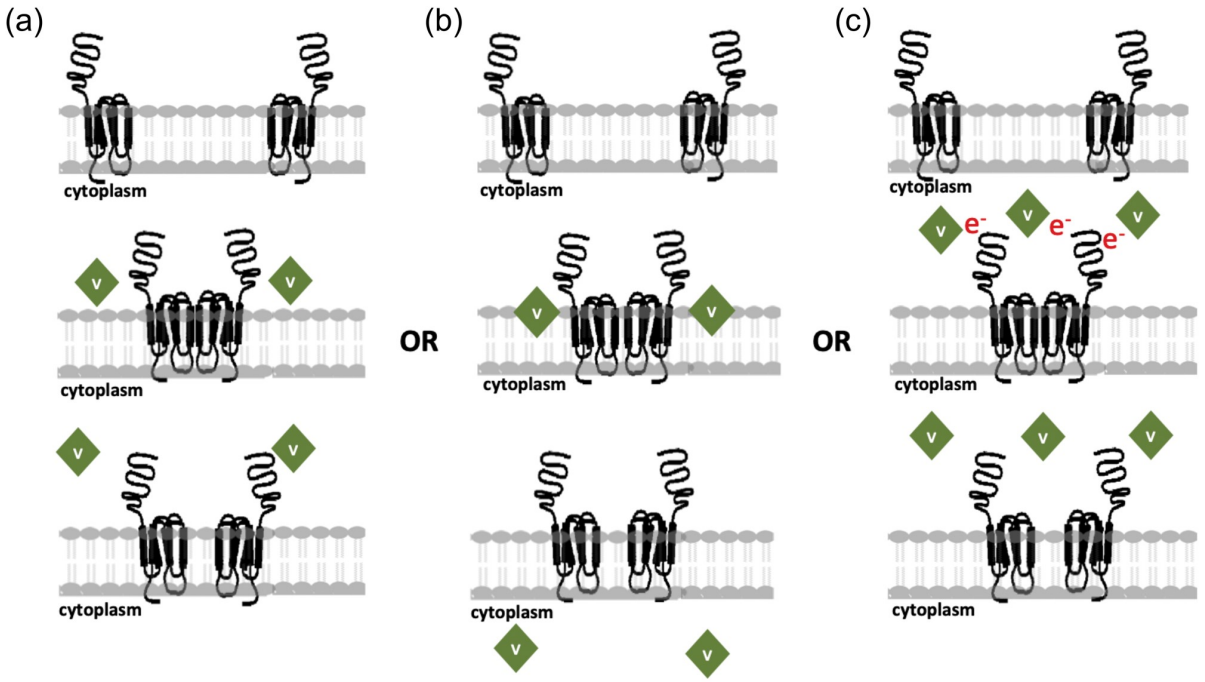

Figure 5.7. Proposed models for the modes of action of the vanadium compounds on cell membranes where cells express 10 000 LHR per cell, a comparatively low receptor density. (a) V-Compounds interact with CHO cell membranes and are not internalized; (b) V-compounds impact the lipid bilayer followed by POV hydrolysis and internalization of the resulting species; or (c) POVs exert the effects through an electron transfer process and no internalization is necessary for response. The image is adopted from (Althumairy et al., 2020c).

BMOV are likely to follow the mechanism illustrated in Figure 7b. However, washing experiments where one wash returns lipid organization to levels seen in untreated cells suggest that internalization is minimal (see (Althumairy et al., 2020a, Althumairy et al., 2020b). **Figure 5.7a** demonstrates the interactions occurring for compounds like V_{14} and V_{15} and potentially V_9Mo and V_9Pt that can interact with extracellular structures but due to their high hydrophilicity are unlikely

to insert in lipid bilayers. Whether these compounds can perturb membrane structures or, as an example, alter LHR interactions with cholesterol (reviewed by (Sarkar and Chattopadhyay, 2020), alter trafficking of this GPCR in the membrane as has been proposed for other Type A GPCRs (Weinberg and Puthenveedu, 2019) or indirectly increase homo-oligomerization of LHRs to activate signal transduction (Milligan et al., 2019) is not known. However, for hydrophilic compounds interaction with the protein is likely to be responsible for some of the cellular changes in lipid packing that are observed.

Lipid bilayer interactions with lipophilic species and internalization of these V-compounds is an attractive alternative mechanism for lipophilic compounds that can penetrate the membrane. For many compounds and drugs their action require the ability to transit the plasma membrane, enter the cell cytoplasm before targeting intracellular structures (Chen et al., 2022). Transport of many compounds across a membrane depend on suitable membrane transporters that could facilitate the transport of specific compounds (Jafurulla et al., 2011). For example, the addition of DIDS stopped the internalization of V-compounds such as $VO(acac)_2$, BMOV and vanadate across erythrocyte membrane (Yang et al., 2003b, Yang et al., 2004) but had no effect on transport of these same compounds in Caco-2 cells (Yang et al., 2004). These results demonstrate that a suitable transporter exist in erythrocytes but not in Caco-2 cells. Lipoidal diffusion is an alternative mechanism for drug movement across membrane barriers as described in detail in (McLauchlan et al., 2015b, Smith et al., 2014). The mechanism shown in **Figure 5.7c** describe compounds that can weakly associate with the membrane-protein complex and initiate signaling though possible electron transfer. These compounds would be able to exert their mode of action without requiring internalization of the derivatives. Considering these mechanisms, it is important to determine the association of the compound with the membrane as well as whether internalization is taking place. V_1, $V_{10,}$ V_{14} and $V_{15,}$ as reported previously (Althumairy et al., 2020c), are associated with the cell membrane where they modulate membrane lipid packing and are not readily removed with one cell washing. This suggests some degree of internalization of these

compounds at the membrane interface. In contrast, V_9Mo and V_9Pt are lost quickly from the cell membrane, a process that can be accelerated by washing cells repeatedly. These two compounds are examples of compounds that are not internalized and may act through mechanisms shown in **Figures 5.7a and 5.7c**.

5.5 Conclusions

These studies demonstrate that the interactions of two monosubstituted decavanadates, monoplatino(IV)nonavanadate(V) ($[H_2Pt^{IV}V^{V}_9O_{28}]^{5-}$, abbreviated V_9Pt, and monomolybdo(VI)nonavanadate(V) ($[Mo^{VI}V^{V}_9O_{28}]^{5-}$, abbreviated V_9Mo, with the eukaryotic cell plasma membrane directly decrease the packing of membrane lipids. The two monosubstituted decavanadates indirectly drive aggregation of LHR, a G protein-coupled receptor, in CHO cells when the receptor is not over-expressed in CHO cell membranes. These monosubstituted decavanadates are very effective in initiating LHR signaling, despite their hydrolytic instability and short life span under our assay conditions. This rapid signaling stands in contrast to the slower inhibitory effects on cell growth. The monosubstituted decavanadates therefore demonstrate selective signaling and lower toxicity in terms of growth inhibition and since they hydrolyze fast show less growth effects when compared to corresponding unsubstituted isopolyvanadates such as the decavanadate anion. In summary, $V_{10}O_{28}^{6-}$ is less efficient at initiating cell signaling while causing greater growth inhibition and hence cell toxicity. These studies have uncovered differences in cellular effects induced by decavanadate and monosubstituted derivatives V_9Pt and V_9Mo that may be of pharmacologic importance. Monosubstituted derivatives initiated a more rapid and greater signaling response that did V_{10}, possibly because of their structure and lower charge. Of benefit to cells, toxic effects of the monosubstituted derivatives are lessened because of their reduced stability compared to V_{10}.

5.6 References

Achard, C., Surendran, A., Wedge, M., Ungerechts, G., Bell, J. & Ilkow, C. 2018. Lighting a Fire in the Tumor Microenvironment Using Oncolytic Immunotherapy. *EBioMedicine,* 31**,** 17-24.

Al-Quatati, A., Fontes, F. L., Barisas, G. B., Zhang, D., Roess, D. A. & Crans, D. C. 2013. Raft localization of Type I Fcε receptor and degranulation of RBL-2H3 cells exposed to decavanadate, a structural model for V2O5. *Dalton Trans.,* 42**,** 11912-11920

Alberty, R. 2000. Calculating apparent equilibrium constants of enzyme-catalyzed reactions at pH 7. *Biochem Educ,* 28**,** 12-17.

Alderighi, L., Gans, P., Ienco, A., Peters, D., Sabatini, A. & Vacca, A. 1999. Hyperquad simulation and speciation (HySS): a utility program for the investigation of equilibria involving soluble and partially soluble species. *Coord Chem Rev,* 184**,** 311-318.

Althumairy, D., Murakami, H. A., Colclough, R., Barisas, B. G., Roess, D. A. & Crans, D. C. Chapter 21. Vanadium Compounds as Indirect Activators of a G Protein-coupled Receptor. 2020a.

Althumairy, D., Murakami, H. A., Zhang, D., Barisas, G. B., Roess, D. A. & Crans, D. C. 2020b. Effects of vanadium(IV) compounds on plasma membrane lipids lead to G protein-coupled receptor signal transduction. . *J. Inorg. Biochem. ,* 203**,** 110873.

Althumairy, D., Postal, K., Barisas, B. G., Nunes, G. G., Roess, D. A. & Crans, D. C. 2020c. Polyoxometalates function as indirect activators of a G protein-coupled receptor. *Metallomics,* 12**,** 1044 - 1061.

Althumairy, D., Roess, D. A. & Barisas, B. G. 2020d. Effects of Luteinizing Hormone Receptor Expression Level on Receptor Aggregation and Function. *Biophys. J.,* 118**,** 95a.

Aureliano, M. & Crans, D. C. 2009. Decavanadate (V10O628) and oxovanadates: Oxometalates with many biological activities. *J. Inorg. Biochem.,* 103**,** 536 - 546.

Aureliano, M., Gumerova, N. I., Sciortino, G., Garribba, E., Mclauchlan, C. C., Rompel, A. & Crans, D. C. 2022. Polyoxidovanadates' interactions with proteins: An overview. *Coord. Chem. Rev.,* 454**,** 214344.

Aureliano, M., Gumerova, N. I., Sciortino, G., Garribba, E., Rompel, A. & Crans, D. C. 2021. Polyoxovanadates with emerging biomedical activities. *Coord. Chem. Rev.,* 447**,** 214143.

Aureliano, M. & Ohlin, C. A. 2014. Decavanadate in vitro and in vivo effects: facts and opinions. *J. Inorg. Biochem.,* 137**,** 123-130.

Banerjee, A., Dash, S. P., Mohanty, M., Sahu, G., Sciortino, G., Garribba, E., Carvalho, M. F. N. N., Marques, F., Costa Pessoa, J., Kaminsky, W., Brzezinski, K. & Dinda, R. 2020. New VIV, VIVO, VVO, and VVO2 Systems: Exploring their Interconversion in Solution, Protein Interactions, and Cytotoxicity. *Inorg. Chem.,* 59**,** 14042-14057.

Baruah, B., Crans, D. C. & Levinger, N. E. 2007. Simple Oxovanadates as Multiparameter Probes of Reverse Micelles. *Langmuir,* 23**,** 6510-6518.

Baruah, B., Roden, J., Sedgwick, M., Correa, N., Crans, D. & Levinger, N. 2006. When Is Water Not Water? Exploring Water Confined in Large Reverse Micelles Using a Highly Charged Inorganic Molecular Probe. *J Am Chem Soc,* 128**,** 12758-12765.

Bijelic, A., Aureliano, M. & Rompel, A. 2018. The antibacterial activity of polyoxometalates: structures, antibiotic effects and future perspectives. *Chem. Commun.,* 54**,** 1153 - 1169.

Bijelic, A., Aureliano, M. & Rompel, A. 2019. Polyoxometalates as Potential Next-Generation Metallodrugs in the Combat Against Cancer. *Angew. Chem. Int. Ed.,* 58**,** 2980 –2999.

Bishayee, A., Waghray, A., Patel, M. & Chatterjee, M. 2010. Vanadium in the detection, prevention and treatment of cancer: The in vivo evidence. *Cancer Letters,* 294**,** 1-12.

Biswas, B. K., Biswas, N., Saha, S., Rahaman, A., Mandal, D. P., Bhattacharjee, S., Sepay, N., Zangrando, E., Garribba, E. & Roy Choudhury, C. 2022. Interaction with bioligands and

in vitro cytotoxicity of a new dinuclear dioxido vanadium(V) complex. *J. Inorg. Biochem.,* 237**,** 111980.
Bougie, I. & Bisaillon, M. 2006. Inhibition of a metal-dependent viral RNA triphosphatase by decavanadate. *Biochem. J.,* 398**,** 557-567.
Buglyo, P., Crans, D., Nagy, E., Lindo, R., Yang, L., Smee, J., Jin, W., Chi, L., Godzala, M. & Willsky, G. 2005. Aqueous chemistry of the vanadium(III) (V-III) and the V-III-dipicolinate systems and a comparison of the effect of three oxidation states of vanadium compounds on diabetic hyperglycemia in rats. *Inorg Chem,* 44**,** 5416-5427.
Chen, R., Kang, R. & Tang, D. 2022. The mechanism of HMGB1 secretion and release. *Experimental & Molecular Medicine,* 54**,** 91-102.
Correa, N., Suilber, J., Riter, R. & Levinger, N. 2012. Nonaqueous Polar Solvents in Reverse Micelle Systems. *Chem Rev,* 112**,** 4569-4602.
Crans, D. 2000. Chemistry and insulin-like properties of vanadium(IV) and vanadium(V) compounds. *J Inorg Biochem,* 80**,** 123-131.
Crans, D. 2015. Antidiabetic, Chemical, and Physical Properties of Organic Vanadates as Presumed Transition-State Inhibitors for Phosphatases. *J Org Chem,* 80**,** 11899-11915.
Crans, D., Barkley, N., Montezinho, L. & Castro, M. 2019a. Vanadium Compounds as enzyme inhibitors with a focus on anticancer effects. *In:* ANGELA CASINI, A. V. A. S. M. M. (ed.) *Metal-based Anticancer Agents.* RSC.
Crans, D., Keramidas, A. & Drouza, C. 1996. Organic vanadium compounds - Transition state analogy with organic phosphorus compounds. *Phosphorus, Sulfur Silicon Relat Elem,* 109-110**,** 245-248.
Crans, D., Mahroof-Tahir, M., Johnson, M., Wilkins, P., Yang, L., Robbins, K., Johnson, A., Alfano, J., Godzala, M., Austin, L. & Willsky, G. 2003a. Vanadium(IV) and vanadium(V) complexes of dipicolinic acid and derivatives. Synthesis, X-ray structure, solution state properties and effects in rats with STZ-induced diabetes. *Inorg Chim Acta,* 356**,** 365-378.
Crans, D., Rithner, C., Baruah, B., Gourley, B. & Levinger, N. 2006. Molecular probe location in reverse micelles determined by NMR dipolar interactions. *J Am Chem Soc,* 128**,** 4437-4445.
Crans, D., Trujillo, A., Pharazyn, P. & Cohen, M. 2011. How environment affects drug activity: Localization, compartmentalization and reactions of a vanadium insulin-enhancing compound, dipicolinatooxovanadium(V). *Coord Chem Rev,* 255**,** 2178-2192.
Crans, D., Woll, K., Prusinskas, K., Johnson, M. & Norkus, E. 2013. Metal Speciation in Health and Medicine Represented by Iron and Vanadium. *Inorg Chem,* 52**,** 12262-12275.
Crans, D., Yang, L., Alfano, J., Chi, L., Jin, W., Mahroof-Tahir, M., Robbins, K., Toloue, M., Chan, L., Plante, A., Grayson, R. & Willsky, G. 2003b. (4-Hydroxypyridine-2,6-dicarboxylato)oxovanadate(V)-a new insulin-like compound: chemistry, effects on myoblast and yeast cell growth and effects on hyperglycemia in rats with STZ-induced diabetes. *Coord Chem Rev,* 237**,** 13-22.
Crans, D., Yang, L., Haase, A. & Yang, X. 2018. Health Benefits of Vanadium and Its Potential as an Anticancer Agent. *Met Ions Life Sci,* 18**,** 251-279.
Crans, D., Yang, L., Jakusch, T. & Kiss, T. 2000. Aqueous chemistry of ammonium (dipicolinato)oxovanadate(V): The first organic vanadium(V) insulin-mimetic compound. *Inorg Chem,* 39**,** 4409-4416.
Crans, D. C. 1993. Interaction of polyoxovanadates and selected polyoxomolybdates with proteins *Mol. Eng.,* 3**,** 277-284.
Crans, D. C. 1994. Enzyme Interactions with Labile Oxovanadates and Other Polyoxometalates. *Comments Inorg. Chem.,* 16**,** 35-76.
Crans, D. C., Brown, M. & Roess, D. A. 2022. Vanadium compounds promote biocatalysis in cells through actions on cell membranes. *Catal. Today,* 388-389**,** 216-223.

Crans, D. C., Henry, L., Cardiff, G. & Posner, B. I. 2019b. Developing Vanadium as an Antidiabetic or Anticancer Drug: A Clinical and Historical Perspective. *Met. Ions Life Sci.,* 19.
Crans, D. C., Mahroof-Tahir, M., Anderson, O. P. & Miller, M. M. 1994. X-ray Structure of (NH4)6(Gly-Gly)2V10O28*4H2O: Model Studies for Poly oxometalate—Protein Interactions. *Inorg. Chem.,* 33**,** 5586-5590.
Crans, D. C., Smee, J. J., Gaidamauskas, E. & Yang, L. 2004. The Chemistry and Biochemistry of Vanadium and the Biological Activities Exerted by Vanadium Compounds. *Chem. Rev.,* 104**,** 849-902.
Crans, D. C. & Willsky, G. R. 1997. Oxovanadate and oxomolybdate cluster interactions with enzymes and whole cells *The Proceedings from the 25th Steenbock Symposium.* University of Wisconsin-Madison.
D'cruz, O. & Uckun, F. 2002. Metvan: a novel oxovanadium(IV) complex with broad spectrum anticancer activity. *Expert Opin Invest. Drugs,* 11**,** 1829-36.
Damena, T., Zeleke, D., Desalegn, T., Demissie, T. B. & Eswaramoorthy, R. 2022. Synthesis, Characterization, and Biological Activities of Novel Vanadium(IV) and Cobalt(II) Complexes. *ACS Omega,* 7**,** 4389-4404.
Davies, D. & Hol, W. 2004. The power of vanadate in crystallographic investigations of phosphoryl transfer enzymes. *FEBS Lett,* 577**,** 315-321.
Dipilato, L. M. & Zhang, J. 2009. The role of membrane microdomains in shaping beta2-adrenergic receptor-mediated cAMP dynamics. *Mol. BioSyst. ,* 5**,** 832-7.
Dugar, S., Izarova, N. V., Mal, S. S., Fu, R., Joo, H.-C., Lee, U., Dalal, N. S., Pope, M. T., Jameson, G. B. & Kortz, U. 2016. Characterization of PtIV-containing polyoxometalates by high-resolution solid-state 195Pt and 51V NMR spectroscopy. *New J. Chem,* 40**,** 923.
Elvingson, K., Gonzalez Baro, A. & Pettersson, L. 1996. Speciation in Vanadium Bioinorganic Systems. 2. An NMR, ESR, and Potentiometric Study of the Aqueous H+-Vanadate-Maltol System. *Inorg Chem,* 35**,** 3388-3393.
Etcheverry, S., Ferrer, E., Naso, L., Rivadeneira, J., Salinas, V. & Williams, P. 2008. Antioxidant effects of the VO(IV) hesperidin complex and its role in cancer chemoprevention. *J Biol Inorg Chem,* 13**,** 435-47.
Evangelou, A., Kolettas, E., Tenopoulou, M., Galaris, D., Gonos, E. & Manos, G. 2002. Vanadium inhibits HaCaT cell proliferation but does not cause apoptosis. *Met Ions Biol Med,* 7**,** 154-158.
Favre, D., Harmon, J. F., Zhang, A., Miller, M. S. & Kaltashov, I. A. 2022. Decavanadate interactions with the elements of the SARS-CoV-2 spike protein highlight the potential role of electrostatics in disrupting the infectivity cycle. *Journal of Inorganic Biochemistry,* 234**,** 111899.
Feng, B., Dong, Y., Shang, B., Zhang, B., Crans, D. C. & Yang, X. 2022. Convergent Protein Phosphatase Inhibitor Design for PTP1B and TCPTP: Exchangeable Vanadium Coordination Complexes on Graphene Quantum Dots. *Adv. Funct. Mater.,* 32**,** 2108645.
Ferretti, V. A. & León, I. E. 2022. An Overview of Vanadium and Cell Signaling in Potential Cancer Treatments. *Inorganics,* 10**,** 47.
Goldfine, A., Patti, M., Zuberi, L., Goldstein, B., Leblanc, R., Landaker, E., Jiang, Z., Willsky, G. & Kahn, C. 2000. Metabolic effects of vanadyl sulfate in humans with non—insulin-dependent diabetes mellitus: In vivo and in vitro studies. *Metabolism,* 49**,** 400-410.
Hasenknopf, B. 2005. Polyoxometalates: introduction to a class of inorganic compounds and their biomedical applications. *Front. Biosci.-Landmark,* 10**,** 275-287.
Hayashi, Y. 2011. Hetero and lacunary polyoxovanadate chemistry: Synthesis, reactivity and structural aspects. *Coord. Chem. Rev.,* 255**,** 2270-2280.
He, Z., Han, S., Zhu, H., Hu, X., Li, X., Hou, C., Wu, C., Xie, Q., Li, N., Du, X., Ni, J. & Liu, Q. 2020. The Protective Effect of Vanadium on Cognitive Impairment and the

Neuropathology of Alzheimer's Disease in APPSwe/PS1dE9 Mice. *Front. Mol. Neurosci.,* 13.
Hernández, L., Araujo, M. L., Madden, W., Del Carpio, E., Lubes, V. & Lubes, G. 2022. Vanadium complexes with polypyridyl ligands: Speciation, structure and potential medicinal activity. *J. Inorg. Biochem.,* 229**,** 111712.
Hill, C. L. 1998. Introduction: Polyoxometalates - Multicomponent Molecular Vehicles To Probe Fundamental Issues and Practical Problems. *Chem. Rev.,* 98**,** 1-2.
Jafurulla, M., Tiwari, S. & Chattopadhyay, A. 2011. Identification of cholesterol recognition amino acid consensus (CRAC) motif in G-protein coupled receptors. *Biochem. Biophys. Res. Commun. ,* 404**,** 569-73.
Kieler, J., Gromek, A. & Nissen, N. 1965. Studies on the antineoplastic effect of vanadium salts. *Acta Chir Scand Suppl,* 343**,** 154-64.
Kioseoglou, E., Petanidis, S., Gabriel, C. & Salifoglou, A. 2015. The chemistry and biology of vanadium compounds in cancer therapeutics. *Coord Chem Rev,* 301–302**,** 87–105.
Kiss, T., Jakusch, T., Hollender, D., Dornyei, A., Enyedy, E., Pessoa, J., Sakurai, H. & Sanz-Medel, A. 2008. Biospeciation of antidiabetic VO(IV) complexes. *Coord Chem Rev,* 252**,** 1153-1162.
Kiss, T., Kiss, E., Garribba, E. & Sakurai, H. 2000. Speciation of insulin-mimetic VO(IV)-containing drugs in blood serum. *J. Inorg. Biochem.,* 80**,** 65-73.
Kopfmaier, P., Wagner, W., Hesse, B. & Köpf, H. 1981. Tumor inhibition by metallocenes: Activity against leukemias and detection of the systemic effect. *Europ J Cancer,* 17**,** 665-669.
Kostenkova, K., Arhouma, Z., Postal, K., Rajan, A., Kortz, U., Nunes, G. G., Crick, D. C. & Crans, D. C. 2021. PtIV- or MoVI-substituted decavanadates inhibit the growth of Mycobacterium smegmatis. *J. Inorg. Biochem.,* 217**,** 1-10.
Kowalski, S., Hac, S., Wyrzykowski, D., Zauszkiewicz-Pawlak, A. & Inkielewicz-Stepniak, I. 2017. Selective cytotoxicity of vanadium complexes on human pancreatic ductal adenocarcinoma cell line by inducing necroptosis, apoptosis and mitotic catastrophe process. *Oncotarget,* 8**,** 60324-60341.
León, I., Cadavid-Vargas, J., Tiscornia, I., Porro, V., Castelli, S., Katkar, P., Desideri, A., Bollati-Fogolin, M. & Etcheverry, S. 2015. Oxidovanadium (IV) complexes with chrysin and silibinin: anticancer activity and mechanisms of action in a human colon adenocarcinoma model. *J Biol Inorg Chem,* 20**,** 1175-1191.
Leon, I., Diez, P., Baran, E., Etcheverry, S. & Fuentes, M. 2017. Decoding the anticancer activity of VO-clioquinol compound: the mechanism of action and cell death pathways in human osteosarcoma cells. *Metallomics,* 9**,** 891-901.
Levina, A., Crans, D. C. & Lay, P. A. 2017. Speciation of metal drugs, supplements and toxins in media and bodily fluids controls in vitro activities. *Coord. Chem. Rev.,* 352**,** 473-498.
Levina, A. & Lay, P. A. 2011. Metal-based anti-diabetic drugs: advances and challenges. *Dalton Trans.,* 40**,** 11675-11686.
Levina, A. & Lay, P. A. 2017. Stabilities and Biological Activities of Vanadium Drugs: What is the Nature of the Active Species? *Chem. Asian J. ,* 12**,** 1692 - 1699.
Li, H., Willingham, S., Ting, J. & Re, F. 2008. Cutting Edge: Inflammasome Activation by Alum and Alum's Adjuvant Effet Are Mediated by NLRP3. *J Immunol,* 181**,** 17-21.
Li, M., Ding, W., Smee, J., Baruah, B., Willsky, G. & Crans, D. 2009. Anti-diabetic effects of vanadium(III, IV, V)-chlorodipicolinate complexes in streptozotocin-induced diabetic rats. *Biometals,* 22**,** 895-905.
Loizou, M., Hadjiadamou, I., Drouza, C., Keramidas, A. D., Simos, Y. V. & Peschos, D. 2021. Vanadium(V) Complexes with Siderophore Vitamin E-Hydroxylamino-Triazine Ligands. *Inorganics,* 9**,** 73.

Lyonnet, B., Martz, S. & Martin, E. 1899. L'emploi therapeutique des derives du vanadium. *La Presse Méd,* 1**,** 191-192.
Mclauchlan, C., Peters, B., Willsky, G. & Crans, D. 2015a. Vanadium-phosphatase complexes: Phosphatase inhibitors favor the trignonal bipyramidal transition state geometries. *Coord Chem Rev,* 301-302**,** 163-199.
Mclauchlan, C. C., Peters, B. J., Willsky, G. R. & Crans, D. C. 2015b. Vanadium-phosphatase complexes: Phosphatase inhibitors favor the trigonal bipyramidal transition state geometries. *Coord. Chem. Rev.,* 301**,** 163-199.
Milligan, G., Ward, R. J. & Marsango, S. 2019. GPCR homo-oligomerization. *Curr. Opin. Cell Biol.,* 57**,** 40–47.
More, M. S., Joshi, P. G., Mishra, Y. K. & Khanna, P. K. 2019. Metal complexes driven from Schiff bases and semicarbazones for biomedical and allied applications: a review. *Mater. Today Chem.,* 14**,** 100195.
Mosquillo, M. F., Smircich, P., Lima, A., Gehrke, S. A., Scalese, G., Machado, I., Gambino, D., Garat, B. & Pérez-Díaz, L. 2020. High Throughput Approaches to Unravel the Mechanism of Action of a New Vanadium-Based Compound against Trypanosoma cruzi. *Bioinorg. Chem. Appl.,* 2020**,** 1634270.
Murthy, M., Toney, J., Rao, L., Kuo, L. & Marks, T. 1986. Pharmacologic studies on the new antitumor agent vanadocene dichloride (VDC). *Proc Am Assoc Cancer Res,* 27**,** 279-279.
Mutlu, E., Cristy, T., Graves, S. W., Hooth, M. J. & Waidyanatha, S. 2017. Characterization of aqueous formulations of tetra- and pentavalent forms of vanadium in support of test article selection in toxicology studies. *Environ. Sci. Pollut. Res.,* 24**,** 405-416.
Nunes, G. G., Bonatto, A. C., De Albuquerque, C. G., Barison, A., Ribeiro, R. R., Back, D. F., Andrade, A. V., De Sá, E. L., Pedrosa Fde, O., Soares, J. F. & De Souza, E. M. 2012. Synthesis, characterization and chemoprotective activity of polyoxovanadates against DNA alkylation. *J. Inorg. Biochem.,* 108**,** 36-46.
Nunes, P., Correia, I., Cavaco, I., Marques, F., Pinheiro, T., Avecilla, F. & Pessoa, J. C. 2021. Therapeutic potential of vanadium complexes with 1,10-phenanthroline ligands, quo vadis? Fate of complexes in cell media and cancer cells. *J. Inorg. Biochem.,* 217**,** 111350.
Nunes, P., Yildizhan, Y., Adiguzel, Z., Marques, F., Costa Pessoa, J., Acilan, C. & Correia, I. 2022. Copper(II) and oxidovanadium(IV) complexes of chromone Schiff bases as potential anticancer agents. *JBIC, J. Biol. Inorg. Chem.,* 27**,** 89-109.
Patel, N., Prajapati, A. K., Jadeja, R. N., Patel, R. N., Patel, S. K., Tripathi, I. P., Dwivedi, N., Gupta, V. K. & Butcher, R. J. 2020. Dioxidovanadium(V) complexes of a tridentate ONO Schiff base ligand: Structural characterization, quantum chemical calculations and in-vitro antidiabetic activity. *Polyhedron,* 180**,** 114434.
Patra, S. A., Banerjee, A., Sahu, G., Mohanty, M., Lima, S., Mohapatra, D., Görls, H., Plass, W. & Dinda, R. 2022. Evaluation of DNA/BSA interaction and in vitro cell cytotoxicity of μ2-oxido bridged divanadium(V) complexes containing ONO donor ligands. *J. Inorg. Biochem.,* 233**,** 111852.
Pessoa, J., Etcheverry, S. & Gambino, D. 2015a. Vanadium compounds in medicine. *Coord Chem Rev,* 301**,** 24-48.
Pessoa, J., Etcheverry, S. & Gambino, D. 2015b. Vanadium compounds in medicine. *In:* CONTE, V. & GIULIA, L. (eds.) *The Ninth International Symposium on the Chemistry and Biological Chemistry of Vanadium.* Padova, Italy.
Pessoa, J. C. & Correia, I. 2021. Misinterpretations in Evaluating Interactions of Vanadium Complexes with Proteins and Other Biological Targets. *Inorganics,* 9**,** 17.

Pessoa, J. C., Santos, M. F. A., Correia, I., Sanna, D., Sciortino, G. & Garribba, E. 2021. Binding of vanadium ions and complexes to proteins and enzymes in aqueous solution. *Coord. Chem. Rev.,* 449**,** 214192.
Petanidis, S., Kioseoglou, E., Hadzopoulou-Cladaras, M. & Salifoglou, A. 2013. Novel ternary vanadium-betaine-peroxido species suppresses H-ras and matrix metalloproteinase-2 expression by increasing reactive oxygen species-mediated apoptosis in cancer cells. *Cancer Lett,* 335**,** 387-96.
Peters, B., Groninger, A., Fontes, F., Crick, D. & Crans, D. 2016. Differences in Interactions of Benzoic Acid and Benzoate with Interfaces. *Langmuir,* 32**,** 9451-9459.
Pettersson, L., Andersson, I. & Hedman, B. 1985. Multicomponent polyanions. 37. A potentiometric and 51V-NMR study of equilibria in the H+-HVO42- system in 3.0 M-Na(ClO4) medium covering the range 1£-1g[H+]£10. *Chem Scr,* 25**,** 309-317.
Pettersson, L., Hedman, B., Andersson, I. & Ingri, N. 1983. Multicomponent polyanions. 34. P potentiometric and 51V NMR study of equilibria in the H+-HVO42- system in the 0.6 M Na(Cl) medium covering the range 1£-1g[H+]£10. *Chem Scrip,* 22**,** 254-264.
Phan, M., Watson, M., Alain, T. & Diallo, J. 2018. Oncolytic Viruses on Drugs: Achieving Higher Therapeutic Efficacy. *ACS Infect Dis,* 4**,** 1448-1467.
Pope, M. T. 1983. *Heteropoly and isopoly oxometalates,* Berlin, Springer-Verlag.
Pope, M. T. & Müller, A. 1991. Polyoxometalate Chemistry : An Old Field with New Dimensions in Several Disciplines. *Angew. Chem. Int. Ed.,* 30**,** 34-48.
Pope, M. T. & Müller, A. 1994. *Polyoxometalates: From Platonic Solids to Anti-Retroviral Activity*, Springer Dordrecht.
Postal, K., Maluf, D. F., Valdameri, G., R¨Udiger, A. L., Hughes, D. L., De S´A, E. L., Ribeiro, R. R., De Souza, E. M., Soaresa, J. F. & Nunes, G. G. 2016. Chemoprotective activity of mixed valence polyoxovanadates against diethylsulphate in E. coli cultures: insights from solution speciation studies. *RSC Adv.,* 6**,** 114955–114968.
Rampersad, S. 2012. Multiple Applications of Alamar Blue as an Indicator of Metabolic Function and Cellular Health in Cell Viability Bioassays. *Sensors,* 12**,** 12347-12360.
Rehman, H., Silk, A., Kane, M. & Kaufman, H. 2016. Into the clinic: Talimogene laherparepvec (T-VEC), a first-in-class intratumoral oncolytic viral therapy. *J ImmunoTher Canc,* 4.
Rhule, J. T., Hill, C. L., Judd, D. A. & Schinazi, R. F. 1998. Polyoxometalates in medicine. *Chem. Rev.,* 98**,** 327-358.
Ribeiro, N., Bulut, I., Pósa, V., Sergi, B., Sciortino, G., Pessoa, J. C., Maia, L. B., Ugone, V., Garribba, E., Enyedy, É. A., Acilan, C. & Correia, I. 2022. Solution chemical properties and anticancer potential of 8-hydroxyquinoline hydrazones and their oxidovanadium(IV) complexes. *J. Inorg. Biochem.,* 235**,** 111932.
Rudbari, H. A., Saadati, A., Aryaeifar, M., Correia, I., Marques, F., Blacque, O. & Micale, N. 2021. Cytotoxic oxidovanadium(IV) complexes of tridentate halogen-substituted Schiff bases: First dinuclear V(IV) complexes with O → VIV = O → VIV = O core. *Bioorg. Med. Chem. Lett.,* 49**,** 128285.
Sahu, G., Patra, S. A., Mohanty, M., Lima, S., Pattanayak, P. D., Kaminsky, W. & Dinda, R. 2022. Dithiocarbazate based oxidomethoxidovanadium(V) and mixed-ligand oxidovanadium(IV) complexes: Study of solution behavior, DNA binding, and anticancer activity. *J. Inorg. Biochem.,* 233**,** 111844.
Samart, N., Althumairy, D., Zhang, D., Roess, D. A. & Crans, D. C. 2020. Initiation of a novel mode of membrane signaling: Vanadium facilitated signal transduction. *Coord. Chem. Rev.,* 416**,** 213286.
Samart, N., Arhouma, Z., Kumar, S., Murakami, H. A., Crick, D. C. & Crans, D. C. 2018. Decavanadate Inhibits Mycobacterial Growth More Potently Than Other Oxovanadates. *Frontier Chem.,* 6**,** 519.

Sánchez-Lara, E., Treviño, S., Sánchez-Gaytán, B. L., Sánchez-Mora, E., Castro, M. E., Meléndez-Bustamante, F. J., Méndez-Rojas, M. A. & González-Vergara, E. 2018. Decavanadate Salts of Cytosine and Metformin: A Combined Experimental-Theoretical Study of Potential Metallodrugs Against Diabetes and Cancer. *Frontier Chem.,* 6.

Sánchez-Lombardo, I., Baruah, B., Alvarez, S., Werst, K. R., Segaline, N. A., Levinger, N. E. & Crans, D. C. 2016. Size and shape trump charge in interactions of oxovanadates with self-assembled interfaces: application of continuous shape measure analysis to the decavanadate anion. *New J. Chem.,* 40**,** 962-975.

Sanna, D., Buglyo, P., Micera, G. & Garribba, E. 2012. Biotransformation of BMOV in the presence of blood serum proteins. *Metabolomics,* 4**,** 33-36.

Sanna, D., Garribba, E. & Micera, G. 2009a. Interaction of VO2+ ion with human serum transferrin and albumin. *J Inorg Biochem,* 103**,** 648-655.

Sanna, D., Micera, G. & Garribba, E. 2009b. On the Transport of Vanadium in Blood Serum. *Inorg Chem,* 48**,** 5747-5757.

Sanna, D., Ugone, V., Micera, G., Buglyo, P., Biro, L. & Garribba, E. 2017. Speciation in human blood of Metvan, a vanadium based potential anti-tumor drug. *Dalton Trans,* 46**,** 8950-8967.

Santos, M. F. A., Sciortino, G., Correia, I., Fernandes, A. C. P., Santos-Silva, T., Pisanu, F., Garribba, E. & Costa Pessoa, J. 2022. Binding of VIVO2+, VIVOL, VIVOL2 and VVO2L Moieties to Proteins: X-ray/Theoretical Characterization and Biological Implications. *Chem. - Eur. J.,* 28**,** e202200105.

Sarkar, P. & Chattopadhyay, A. 2020. Cholesterol interaction motifs in G protein-coupled receptors: Slippery hot spots? *Syst. Biol. Med.* **,** 1-18.

Scalese, G., Machado, I., Correia, I., Pessoa, J. C., Bilbao, L., Pérez-Diaz, L. & Gambino, D. 2019. Exploring oxidovanadium(iv) homoleptic complexes with 8-hydroxyquinoline derivatives as prospective antitrypanosomal agents. *New J. Chem.,* 43**,** 17756-17773.

Scior, T., Guevara-Garcia, J., Do, Q., Bernard, P. & Laufer, S. 2016. Why Antidiabetic Vanadium Complexes are Not in the Pipeline of “Big pharma” Drug Research? A Critical Review. *Curr Med Chem,* 23**,** 2874-2891.

Selman, M., Rousso, C., Bergeron, A., Son, H., Krishnan, R., El-Sayes, N., Varette, O., Chen, A., Le Boeuf, F., Tzelepis, F., Bell, J., Crans, D. & Diallo, J. 2018. Multi-modal Potentiation of Oncolytic Virotherapy by Vanadium Compounds. *Mol Ther,* 26**,** 56-69.

Semiz, S. 2022. Vanadium as potential therapeutic agent for COVID-19: A focus on its antiviral, antiinflamatory, and antihyperglycemic effects. *J. Trace Elem. Med. Biol.,* 69**,** 126887.

Smee , J., Epps, J., Ooms, K., Bolte, S., Polenova, T., Baruah, B., Yang, L., Ding, W., Li, M., Willsky, G., La Cour, A., Anderson, O. & Crans, D. 2009. Chloro-substituted dipicolinate vanadium complexes: Synthesis, solution, solid-state, and insulin-enhancing properties. *J Inorg Biochem,* 103**,** 575–584.

Smith, D., Artursson, P., Avdeef, A., Di, L., Ecker, G. F., Faller, B., Houston, J. B., Kansy, M., Kerns, E. H., Krämer, S. D., Lennernäs, H., Van De Waterbeemd, H., Sugano, K. & Testa, B. 2014. Passive Lipoidal Diffusion and Carrier-Mediated Cell Uptake Are Both Important Mechanisms of Membrane Permeation in Drug Disposition. *Mol. Pharmaceutics,* 11**,** 1727-1738.

Smith, S. M. L., Lei, Y., Liu, J., Cahill, M. E., Hagen, G. M., Barisas, B. G. & Roess, D. A. 2006. Luteinizing Hormone Receptors Translocate to Plasma Membrane Microdomains after Binding of Human Chorionic Gonadotropin. *Endocrinology,* 147**,** 1789-1795.

Sostarecz, A., Gaidamauskas, E., Distin, S., Bonetti, S., Levinger, N. & Crans, D. 2014. Correlation of Insulin-Enhancing Properties of Vanadium-Dipicolinate Complexes in Model Membrane Systems: Phospholipid Langmuir Monolayers and AOT Reverse Micelles. *Chemistry-a European Journal,* 20**,** 5149-5159.

Stahla, M., Baruah, B., James, D., Johnson, M., Levinger, N. & Crans, D. 2008. 1H NMR studies of aerosol-OT reverse micelles with alkali and magnesium counterions: preparation and analysis of MAOTs. *Langmuir,* 24**,** 6027-6035.
Storr, T., Thompson, K. & Orvig, C. 2006. Design of targeting ligands in medicinal inorganic chemistry. *Chem Soc Rev,* 36**,** 534-544.
Strukan, N., Cindric, M. & Kamenar, B. 1997. Synthesis and structure of [(CH3) 4N] 4 [H2MoV9028] C1"6H20. *Polyhedron,* 16**,** 629 - 634.
Thompson, K., Liboiron, B., Sun, Y., Bellman, K., Setyawati, I., Patrick, B., Karunaratne, V., Rawji, G., Wheeler, J., Sutton, K., Bhanot, S., Cassidy, C., Mcneill, J., Yuen, V. & Orvig, C. 2003. Preparation and characterization of vanadyl complexes with bidentate maltol-type ligands; in vivo comparisons of anti-diabetic therapeutic potential. *J Biol Inorg Chem,* 8**,** 66-74.
Thompson, K., Lichter, J., Lebel, C., Scaife, M., Mcneill, J. & Orvig, C. 2009. Vanadium treatment of type 2 diabetes: a view to the future. *J Inorg Biochem,* 103**,** 554-8.
Thompson, K. & Orvig, C. 2006a. Vanadium in diabetes: 100 years from Phase 0 to Phase I. *J Inorg Biochem,* 100**,** 1925-1935.
Thompson, K. H. & Orvig, C. 2006b. Vanadium in diabetes: 100 years from Phase 0 to Phase I. *J. Inorg. Biochem.,* 100**,** 1925-1935.
Treviño, S. & Diaz, A. 2020. Vanadium and insulin: Partners in metabolic regulation. *J. Inorg. Biochem.,* 208**,** 111094.
Uk Lee, U., Joo, H.-J., Park, K.-M., Mal, S. S., Kortz, U., Keita, B. & Nadjo, L. 2008. Facile Incorporation of Platinum(IV) into Polyoxometalate Frameworks: Preparation of [H2PtIVV9O28]5 and Characterization by 195Pt NMR Spectroscopy. *Angew. Chem. Int. Ed.,* 47**,** 793 - 796.
Wang, Q., Liu, T., Fu, Y., Wang, K. & Yang, X. 2010. Vanadium compounds discriminate hepatoma and normal hepatic cells by differential regulation of reactive oxygen species. *J Biol Inorg Chem,* 15**,** 1087-97.
Weinberg, Z. Y. & Puthenveedu, M. A. 2019. Regulation of G protein-coupled receptor signaling by plasma membrane organization and endocytosis. *Traffic* 20**,** 121–129.
Willsky, G., Chi, L., Godzala, M., Kostyniak, P., Smee, J., Trujillo, A., Alfano, J., Ding, W., Hu, Z. & Crans, D. 2011. Anti-diabetic effects of a series of vanadium dipicolinate complexes in rats with streptozotocin-induced diabetes. *Coord Chem Rev,* 255**,** 2258-2269.
Willsky, G., Halvorsen, K., Godzala, M., Chi, L., Most, M., Kaszynski, P., Crans, D., Goldfine, A. & Kostyniak, P. 2013. Coordination chemistry may explain pharmacokinetics and clinical response of vanadyl sulfate in type 2 diabetic patients. *Metallomics,* 5**,** 1491-1502.
Winter, P. W., Al-Qatati, A., Wolf-Ringwall, A. L., Schoeberl, S., Chatterjee, P. B., Barisas, B. G., Roess, D. A. & Crans, D. C. 2012. The anti-diabetic bis(maltolato)oxovanadium(iv) decreases lipid order while increasing insulin receptor localization in membrane microdomains. *Dalton Trans.,* 41**,** 6419-6430.
Wolf-Ringwall, A. L., Winter, P. W., Liu, J., Van Orden, A. K., Roess, D. A. & Barisas, B. G. 2011. Restricted lateral diffusion of luteinizing hormone receptors in membrane microdomains. *The J. Biol. Chem.,* 286**,** 29818-29827.
Wu, J., Hong, Y. & Xg, X. Y. 2016a. Bis(acetylacetonato)-oxidovanadium(IV) and sodium metavanadate inhibit cell proliferation via ROS-induced sustained MAPK/ERK activation but with elevated AKT activity in human pancreatic cancer AsPC-1 cells. *J Biol Inorg Chem***,** 1-11.
Wu, X., Peters, B., Rithner, C. & Crans, D. 2016b. Multinuclear NMR studies of aqueous Vanadium-HEDTA Complexes. *Polyhedron,* 114**,** 325–332.
Yamamoto, N., Schols, D., De Clercq, E., Debyser, Z., Pauwels, R., Balzarini, J., Nakashima, H., Baba, M., Hosoya, M. & Snoeck, R. 1992. Mechanism of anti-human

immunodeficiency virus action of polyoxometalates, a class of broad-spectrum antiviral agents. *Mol. Pharm.,* 42**,** 1109.
Yang, X. & Wang, K. 2016. Focusing on the Link between Diabetes, Alzheimer's Disease and Cancer for the Discovery of New Medicines. *Curr Top Med Chem,* 16**,** 675.
Yang, X., Wang, K., Lu, J. & Crans, D. 2003a. Membrane transport of vanadium compounds and the interaction with the erythrocyte membrane. *Coord Chem Rev,* 237**,** 103-111.
Yang, X.-G., Wang, K., Lu, J. & Crans, D. C. 2003b. Membrane transport of vanadium compounds and the interaction with the erythrocyte membrane. *Coord. Chem. Rev.,* 237**,** 103-111.
Yang, X.-G., Yang, X.-D., Yuan, L., Wang, K. & Crans, D. C. 2004. The Permeability and Cytotoxicity of Insulin-Mimetic Vanadium Compounds. *Pharm. Res.,* 21**,** 1026-1033.
Yoshikawa, Y., Sakurai, H., Crans, D., Micera, G. & Garribba, E. 2014. Structural and redox requirements for the action of anti-diabetic vanadium compounds. *Dalton Trans,* 43**,** 6965-6972.
Zizic, Z., Miladinovic, M., Stanic, M., Hadzibrahimovic, M., Zivic, M. & Zakrzekska, J. 2016. (51)V NMR investigation of cell-associated vanadate species in Phycomyces blakesleeanus mycelium. *Res Microbiol,* 167**,** 521-528.

Chapter 6 Small, truncated demethylmenaquinone (DMK) analogs as potential targets for the treatment of tuberculosis

6.1 Demethylmenaquinones (DMKs) – promising targets for tuberculosis treatment

Mycobacterium tuberculosis (*Mtb*) is an infectious disease and presents a significant healthcare challenge worldwide (Adewumi et al., 2020, Pujari et al., 2022). Specifically, mutation-mediated and acquired drug resistant tuberculosis (TB) causes 1.5 million human deaths annually (Adewumi et al., 2020). Many factors contribute to inefficiency of current TB treatments, including *Mtb*'s mutagenic ability, long duration of drug regimens and poor patient treatment compliance (Sukheja et al., 2017, Teh et al., 2007). Thus, there is an urgent need to develop new TB drugs with novel modes of action to avoid acquired multidrug resistance in bacterial pathogens and shorten drug regimens.

Finding novel drug targets against both dormant and growing *Mtb* remains one of the major goals of TB treatment. Recent efforts have focused on targeting the electron transport chain (ETC) on *Mtb* species (Pujari et al., 2022). Menaquinone (MK) is a major electron carrier in the bacterial electron transport chain (ETC) in the Gram-variable *Mtb* and many Gram-positive pathogens and, thus, a causative agent of TB (Koehn et al., 2019, Braasch-Turi et al., 2022a, Pujari et al., 2022). MKs belong to the naphthalene series of quinones and consist of the 1,4-napthoquinone headgroup and isoprenoid tails of varying lengths and degrees of unsaturation (Braasch-Turi et al., 2022a, da Costa et al., 2011, Kurosu and Begari, 2010). *Mtb* uses MK-9(II-H_2) as its primary electron carrier which is biosynthesized in bacteria (**Figure 6.1A-1B**) (Upadhyay et al., 2015, Upadhyay et al., 2018). MK-9(II-H_2) contains an isoprenyl side chain of nine isoprene units with the double bond of the one in the β-position hydrogenated (saturated, **Figure 6.1A**) (Upadhyay et al., 2015). In the ETC, MK-9(II-H_2) accepts electron from different electron donors and transfers

them to either oxidases or reductases (**Figure 6.1B**) (Upadhyay et al., 2015). Thus, the biosynthetic pathway of MK-9(II-H_2) has become of interest to develop potential targets for TB

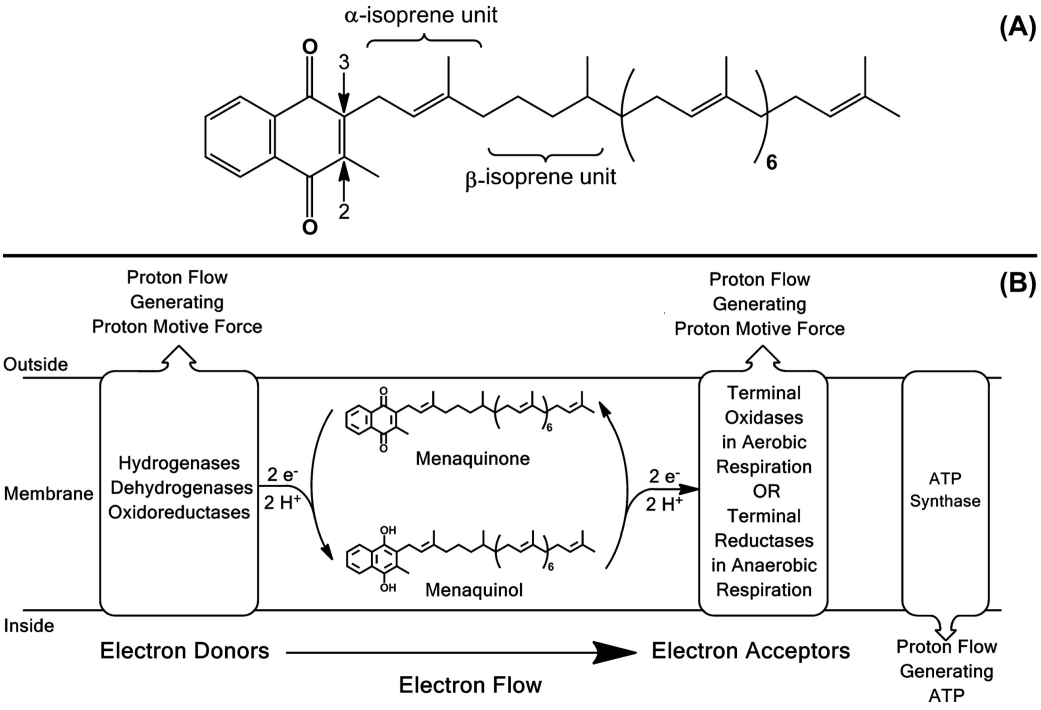

Figure 6.1. A) Structure of MK-9(II-H_2), a major electron carrier in *Mtb*. B) Schematic illustrating the role of MK-9(II-H_2) in bacterial respiration from (Upadhyay et al., 2015) under the ACS AuthorChoice open-access license.

treatment. MK-9 is a precursor to MK-9(II-H_2) and is biosynthesized from the corresponding DMK-9 analog in bacteria where the *menG* methyltransferase methylates the C2 position of the 1,4-napthoquinone ring (Puffal et al., 2018, Meganathan and Kwon, 2009). *MenG* is a membrane-associated enzyme which belongs to the SAM-dependent methyltransferase superfamily comprising of an α/β/α fold structure (Adewumi et al., 2020, Puffal et al., 2018). In the last step of biosynthesis, the double bond in the β-isoprene unit of the isoprenyl chain is reduced by the reductase *menJ* to form MK-9 (II-H_2) (Puffal et al., 2018, Upadhyay et al., 2015, Upadhyay et al., 2018). Depletion of *menG* is detrimental to *Mtb,* resulting in the reduced oxygen consumption and

ATP production. Thus, *menG* has become one of the major drug targets for the treatment of TB (Adewumi et al., 2020).

In addition to MK, some bacterial species utilize demethylmenaquinone (DMK) for energy metabolism (Wissenbach et al., 1990). DMK is an essential precursor of bacterial MK biosynthesis. DMK also belongs to the naphthalene series of quinones and consists of the 1,4-napthoquinone headgroup and isoprenoid tails of varying lengths, except it lacks the methyl group at the C2 position (Meganathan and Kwon, 2009). Several DMK derivatives have been isolated from bacteria and reported in the literature (Pujari et al., 2022, Dunphy and Brodie, 1971). For example, DMK-7, DMK-8 and DMK-9 have been isolated from *Streptococcus faecalis*, whereas *Haemophilus parainfluenzae* contains DMK-5, DMK-6 and DMK-7 (Dunphy and Brodie, 1971). While MK exclusively acts as an electron carrier in aerobic bacterial respiration, both MKs and DMKs participate in the anaerobic bacterial respiration where terminal electron acceptors with less positive redox potential than the O_2/H_2O couple are involved (Sharma et al., 2012, Holländer, 1976, Wissenbach et al., 1990). MK is the only naphthoquinone involved in the fumarate or dimethylsulfoxide respiration, whereas DMK is most abundant in the nitrate respiration (Barker et al., 2014, Unden, 1988). MK and DMK also participate in the trimethylamine N-oxide (TMAO) respiration (Barker et al., 2014, Unden, 1988) Some bacteria, such as *E. coli*, utilize ubiquinone (UQ), MK and DMK in their ETC (Aussel et al., 2014, Unden and Bongaerts, 1997, Braasch-Turi et al., 2022b). Specifically, *E. coli* utilizes UQ for aerobic respiration, and MK and DMK – for anaerobic respiration due to their lower midpoint potentials (E'° = − 74 mV and + 36 mV, respectively) compared to UQ (E'° = +100 mV) (Aussel et al., 2014, Unden and Bongaerts, 1997). The presence of both MKs and DMKs in the bacterial anaerobic respiration remains unexplained.

Despite the growing interest in MKs and DMKs as potential drug targets, their chemical properties are poorly understood. Recent studies have reported novel syntheses of MK analogs with different isoprene units and degrees of unsaturation using Friedel-Crafts alkylation methods, and investigated their 3D conformation which will presumably help understand their electron-

transport properties in the ETC (Koehn et al., 2018a, Koehn et al., 2018b, Koehn et al., 2019, Braasch-Turi and Crans, 2020, Daines et al., 2003, Suhara et al., 2010). The field still lacks high-yielding syntheses of MKs, as most of them result in the mixtures of *cis/trans* isomers which are difficult to separate using common purification methods. Recent two-dimensional NMR studies have also established that small, truncated MK analogs, MK-1 and MK-2, adopt folded

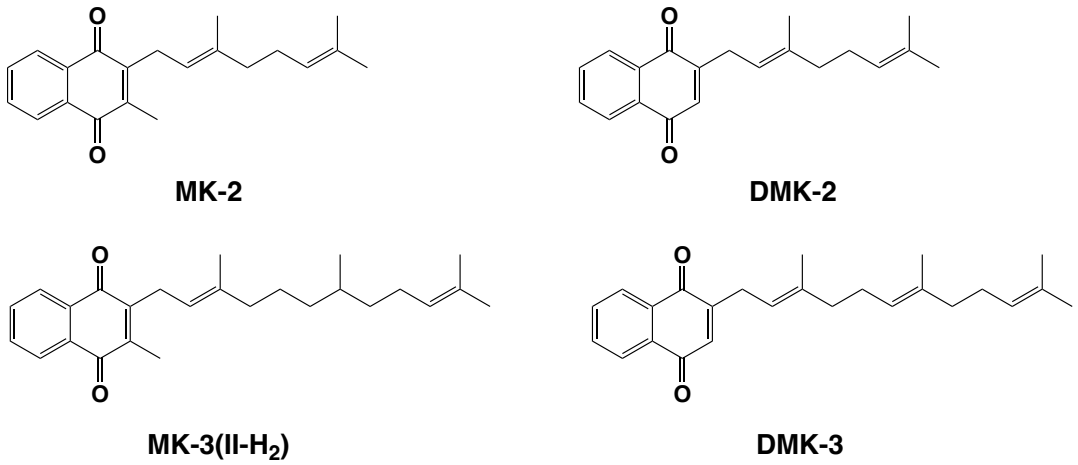

Figure 6.2. Structures of the reported small, truncated MK analogs, MK-2 and MK-3(II-H_2) and DMK analogs investigated in this work, DMK-2 and DMK-3.

conformations in both organic solvents and model membrane interfaces in which the isoprenyl tail folds over the 1,4-napthoquinone headgroup (**Figure 6.2**) (Koehn et al., 2018a, Koehn et al., 2018b). Another two-dimensional NMR study with MK-7 has established new methods to solve geometric structures of MK analogs with longer isoprenyl chains (Sitkowski et al., 2018). There are even fewer literature reports regarding the syntheses and chemical properties of DMKs, as most of them have. been extracted from bacteria and characterized using HPLC methods (Furomoto et al., 2007). Thus, developing novel syntheses of DMK analogs is of interest.

In this study, we have investigated the syntheses and fundamental properties of two small, truncated DMK analogs, DMK-2 and DMK-3 (**Figure 6.2**). We have confirmed the structure of the analogs using NMR methods. We have also investigated the redox properties of DMK-2 and DMK-3 using non-aqueous cyclic voltammetry to see how their structures affect their electron

transport ability. We have then tested DMK-2 and DMK-3 with *menG* to establish whether they are suitable substrates for methylation in bacteria.

6.2 Materials and Methods

6.2.1 General Materials

Sodium dithionite (85%), geraniol (98%) and *trans,trans*-farnesol (98%) were purchased from Oakwood Chemical and used as received. 1,4-napthoquinone (97%), boron trifluoride diethyl etherate and 1,4-dioxane (anhydrous, 99.8%) were purchased from Sigma Aldrich and used as received. Sodium sulfate (anhydrous) was purchased from Fischer Chemical and used as received. Silver nitrate, ferrocene and tetra-*n*-butylammonium perchlorate (TBAP) were purchased from Merck Millipore for electrochemistry experiments and used as received. TLC silica gel plates with F254 fluorescent indicator (20 x 20 cm, 210 - 270 μm layer thickness) and silica gel (high-purity grade, pore size 60 Å, 230-400 mesh particle size, 40-63 μm particle size) were purchased from Sigma Aldrich. Deuterated NMR solvents of $CDCl_3$ (chloroform-d, 99.8% atom % D) and dimethylsulfoxide (d_6-DMSO) (D 99.9%, + 0.05% V/V tetramethylsilane), were acquired from Cambridge Isotope. Distilled Deionized Water (DDI H_2O) was purified with a Barnstead E-pure system (18.2 MΩ-cm). All chemicals for the *menG* activity assay were acquired from Sigma Aldrich.

6.2.2 General Methods

All non-aqueous reactions were carried out under argon atmosphere in flame-dried glassware and were stirred on a magnetic stir plate using anhydrous solvent unless otherwise noted. Reactions were monitored by thin layer chromatography. All solvents were degassed with argon prior to carrying out syntheses and analytical experiments. ^{1}H and ^{13}C spectra were recorded on a 400 MHz Varian Model MR400 or a Bruker Model Avance Neo400 equipped with BBFO smart probe operating at 400 MHz or 101 MHz, respectively. Chemical shift values (δ) are reported in

ppm and referenced against the internal solvent peaks in ^{1}H NMR ($CDCl_3$, δ at 7.26 ppm) and in ^{13}C NMR ($CDCl_3$, δ at 77.16 ppm). All NMR spectra were acquired either at 25 or 26 °C. Integral values were determined using standard, uncalibrated NMR experiments and should be viewed accordingly. ^{1}H NMR spectra are reported as follows: chemical shift (multiplicity, coupling constant, integration). The following abbreviations are used to indicate multiplicities: s, singlet; d, doublet; t, triplet; q, quartet; m, multiplet; br, broad. NMR spectra were processed using MestReNova version 14.3.0. Details of NMR experiments are provided in representative experimental sections and captions of figures. The logP values were calculated using Chemicalize, an online platform for chemical calculations.

6.2.3 Synthesis of 1,4-napthoquinol

To a 500 mL round-bottom flask, diethyl ether (100 mL) was added, followed by the addition of 1,4-napthoquinone (4.59 g, 29.0 mmol, 1.00 equiv.). After dissolution of 1,4-napthoquinone, 100 mL of an 10% aq. solution of sodium hydrosulfite (9.99 g, 57.4 mmol, 1.00 equiv.) was added, and the reaction mixture immediately turned dark red. The reaction mixture was let to stir for 3 h at r.t. in air, and the solution turned clear yellow. The aqueous layer was separated and extracted with diethyl ether (3×100 mL). The combined organic extracts were washed with sat. $NaHCO_3$ (100 mL), followed by DDI H_2O (100 mL), and brine (100 mL). The combined organic extracts were dried with anhydrous Na_2SO_4 and then concentrated under reduced pressure at room temperature. The crude powder was triturated with pentane (50 mL), vacuum filtered, and washed with pentane (100 mL) to yield 3.03 g (66 %) as a pale purple solid. The formation of 1,4-naphthoquinol was confirmed by the presence of the singlets at 9.29 and 6.65 ppm in the ^{1}H NMR spectrum (400 MHz, d_6-DMSO, **Figure A5.1**).

6.2.4 Synthesis of *E*-2-(3,7-dimethylocta-2,6-dien-1-yl)naphthalene-1,4-dione or demethylmenaquinone-2 (DMK-2)

DMK-2 was synthesized using a modified procedure from the literature (Furomoto et al., 2007): To a 100 mL round-bottom Schlenk flask, ethyl acetate (16 mL) and 1,4-dioxane (16 mL) were added, and the flask was purged/evacuated with argon repeatedly. Then, crude naphthoquinol (1.82 g, 11.5 mmol, 1.77 equiv.) was added, followed by the addition of geraniol (1.92 g, 12.5 mmol, 1.93 equiv.) and the dropwise addition of fresh BF_3 etherate (0.920 g, 6.48 mmol, 0.80 mL, 1.00 equiv.). The reaction mixture was allowed to stir at 70−72 °C under reflux for 3 h under argon. The dark orange reaction mixture was quenched with ice H_2O (100 mL) and then extracted with diethyl ether (3×, 100 mL). The yellow organic extracts were washed with sat. $NaHCO_3$ (100 mL), washed with DDI H_2O (100 mL), washed with brine (100 mL), dried with anhydrous Na_2SO_4, and concentrated under reduced pressure at room temperature to yield 3.71 g of crude red oil. The crude oil was purified by flash column chromatography (1000 mL of 230−400 mesh SiO_2, 70 mm column, 10:1 pentane/ethyl acetate). The yellow oil obtained was dried under reduced pressure overnight, and further purified using preparative TLC (10:1 pentane/ethyl acetate) to yield 0.382 g (1.30 mmol, 20.1% yield) of DMK-2 as a yellow oil. ^1H NMR (400 MHz, $CDCl_3$) δ 8.08 (s, 1H), 7.69 (s, 1H), 7.26 (s, 1H), 5.04 (s, 2H), 3.38 (s, 1H), 3.36 (s, 1H), 2.04 (s, 5H), 1.99 (s, 2H), 1.78 (s, 3H), 1.62 (s, 4H), 1.56 (s, 3H).

6.2.5 Synthesis of 2-((2*E*,6*E*)-3,7,11-trimethyldodeca-2,6,10-trien-1-yl)naphthalene-1,4-dione (DMK-3)

To a 100 mL round-bottom Schlenk flask, ethyl acetate (16 mL) and 1,4-dioxane (16 mL) were added, and the flask was purged/evacuated with argon repeatedly. Then, crude naphthoquinol (1.82 g, 11.5 mmol, 1.77 equiv.) was added, followed by the addition of *trans, trans*-farnesol (2.78 g, 12.5 mmol, 1.93 equiv.) and the dropwise addition of fresh BF_3 etherate (0.920 g, 6.48 mmol, 0.80 mL, 1 equiv.). The reaction mixture was allowed to stir at 70−72 °C under reflux for 3 h under argon. The dark red reaction mixture was quenched with ice H_2O (100 mL) and then extracted with diethyl ether (3×, 100 mL). The yellow organic extracts were washed with sat. $NaHCO_3$ (100

mL), washed with DDI H_2O (100 mL), washed with brine (100 mL), dried with anhydrous Na_2SO_4, and concentrated under reduced pressure at room temperature to yield 3.71 g of crude red oil. The crude oil was purified by flash column chromatography (1000 mL of 230−400 mesh SiO_2, 70 mm column, 20:2 pentane/ethyl acetate). The yellow oil obtained was dried under reduced pressure overnight, and further purified using preparative TLC (10:1 pentane/ethyl acetate) to yield 0.469 g (1.30 mmol, 20.1% yield) of DMK-3 as a yellow oil. ^{1}H NMR (400 MHz, $CDCl_3$) δ 8.08 (dq, 2H), 7.72 (dq, *J* = 5.9, 3.3 Hz, 2H), 6.76 (s, 1H), 5.23 (m, 1H), 5.09 (tq, *J* = 8.4, 3.2 Hz, 2H), 3.30 (s, 1H), 3.28 (s, 1H), 2.17 (s, 7H), 2.11 (dd, *J* = 10.0, 6.1 Hz, 3H), 2.04 (s, 3H), 2.01 – 1.95 (m, 2H), 1.68 (s, 6H), 1.62 – 1.60 (m, 3H), 1.58 (s, 4H).

6.2.6 Cyclic Voltammetry

Electrodes: A glassy carbon working electrode (BASi MF2012, 3.0 mm diameter, area of 0.09 cm^2), a platinum wire auxiliary electrode (BASi MW1032), and a non-aqueous Ag^+/Ag reference electrode (BASi MW1085) were used. The Ag^+/Ag electrode was constructed by using the same solvent as the MK-*n* solution with 0.10 M TBAP and 0.010M $AgNO_3$ to eliminate any liquid junction potentials. All halfwave potentials are referenced to the external standard of ferrocene (Fc), where Fc^+/Fc $E_{1/2}$ = 0 V.

Sample preparation: The solutions of all complexes had a final concentration of 2.0 mM in 100 mM TBAP in dry acetonitrile solution. A 10.0 mM ferrocene solution (in 100 mM TBAP in dry acetonitrile solution) was used as an external reference. A 2.0 mM silver nitrite solution was used to fill a refillable Ag reference electrode. Acetonitrile (HPLC grade) was dried using 3 Å molecular sieves for at least 48 h prior to use. All samples were degassed using Ar for 10 minutes prior to cyclic voltammogram collection.

Instrumentation and Experimental Parameters: Cyclic voltammetry experiments were carried out using a WaveDriver 40 DC Bipotentiostat/Galvanostat and a Low Volume Three Electrode Cell Basic Kit (AF01CKT1006) purchased from Pine Research Instrumentation. AfterMath v 1.5.9807

data acquisition The software used during was with the iR Compensation option turned off, while eL-Chem Viewer and Microsoft Excel were used for post-acquisition processing. All cyclic voltammograms were externally referenced to ferrocene. Normal cyclic voltammograms were recorded in triplicate using the following parameters for each sample:

Ferrocene external standard: sweep rate of 100 mV/s, 2 segments, initial potential of 1.0 V, vertex potential of -1.5 V, final potential of 1.0 V.

DMK-2: sweep rate of 100 mV/s, 2 segments, initial potential of -0.25 V, vertex potential of -2.75 V, final potential of -0.25 V.

DMK-3: sweep rate of 100 mV/s, 2 segments, initial potential of -0.25 V, vertex potential of -2.50 V, final potential of -0.25 V.

6.2.7 Methylation Experiments with *menG*

Typical assay mixtures (100 μL) contained 100 mM Tris-HCl (pH 8.0), 1 mM DTT, 5 mM $MgCl_2$, 0.1% CHAPS (w/v), 3.4-3.5 µg of DMK-2 and DMK-3, and 40 μM [^{14}C] SAM. Reactions were initiated by the addition of 25−100 μg of partially purified *M. smegmatis* membrane protein, incubated at 37 °C for 1 h, and stopped by the addition of 0.1 M acetic acid in methanol (0.5 mL). The radiolabeled reaction products were extracted with hexane (2 × 3 mL), and the combined extracts were washed with 1 mL of water. The upper organic phase was collected, evaporated to dryness under N_2, and dissolved in $CHCl_3$. An aliquot was subjected to liquid scintillation counting [in 5 mL of Ultima Gold scintillation fluid (PerkinElmer) on a Beckman Coulter LS 6500], and the remaining portion along with authentic standards (DMK-8) (Pujari et al., 2022) was loaded on reversed-phase TLC plates (Whatman KC 18F Silica gel 60 Å), which were developed in acetone/water (97:3 v/v). The positions of authentic standards were visualized under ultraviolet (UV) light for 15 days, and radioisotope distribution was detected by phosphorimaging (Typhoon TRIO, Amersham Biosciences) and quantified using ImageQuant TL v2005 software (Amersham Biosciences).

6.3 Results and Discussion

6.3.1 Synthesis

Herein, we report novel syntheses of DMK-2 and DMK-3 using Friedel-Crafts alkylation methods with a boron trifluoride catalyst (**Figure 6.3B-3C**). DMK-2 has been synthesized using a

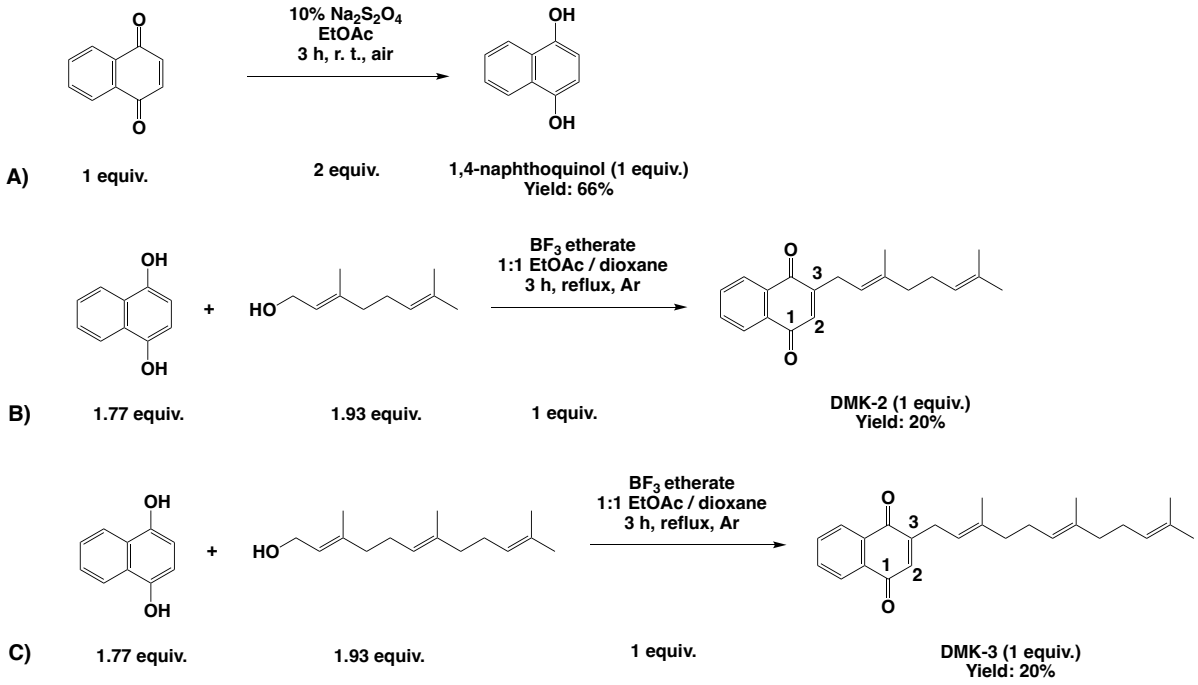

Figure 6.3. A) Synthetic route to prepare 1,4-naphthoquinol from 1,4-naphthoquinone and sodium dithionite. B) Synthetic route to prepare DMK-2 from 1,4-napthoquinol and geraniol using Lewis acid catalyst conditions. C) Synthetic route to prepare DMK-3 from 1,4-naphthoquinol and *trans,trans*-farnesol using Lewis acid catalyst conditions .

modified method from the literature (Furomoto et al., 2007) to yield 0.382 g of pure DMK-2. In the first study, DMK-2 has been isolated from hairy roots of *Sesamum indicum L.* using column chromatography (MeOH :CH_2Cl_2 1:1), purified using HPLC and characterized using ^{1}H NMR, ^{13}C

NMR, FTIR, UV-Vis and HR-EIMS data (Furomoto et al., 2007). The advantage of our method

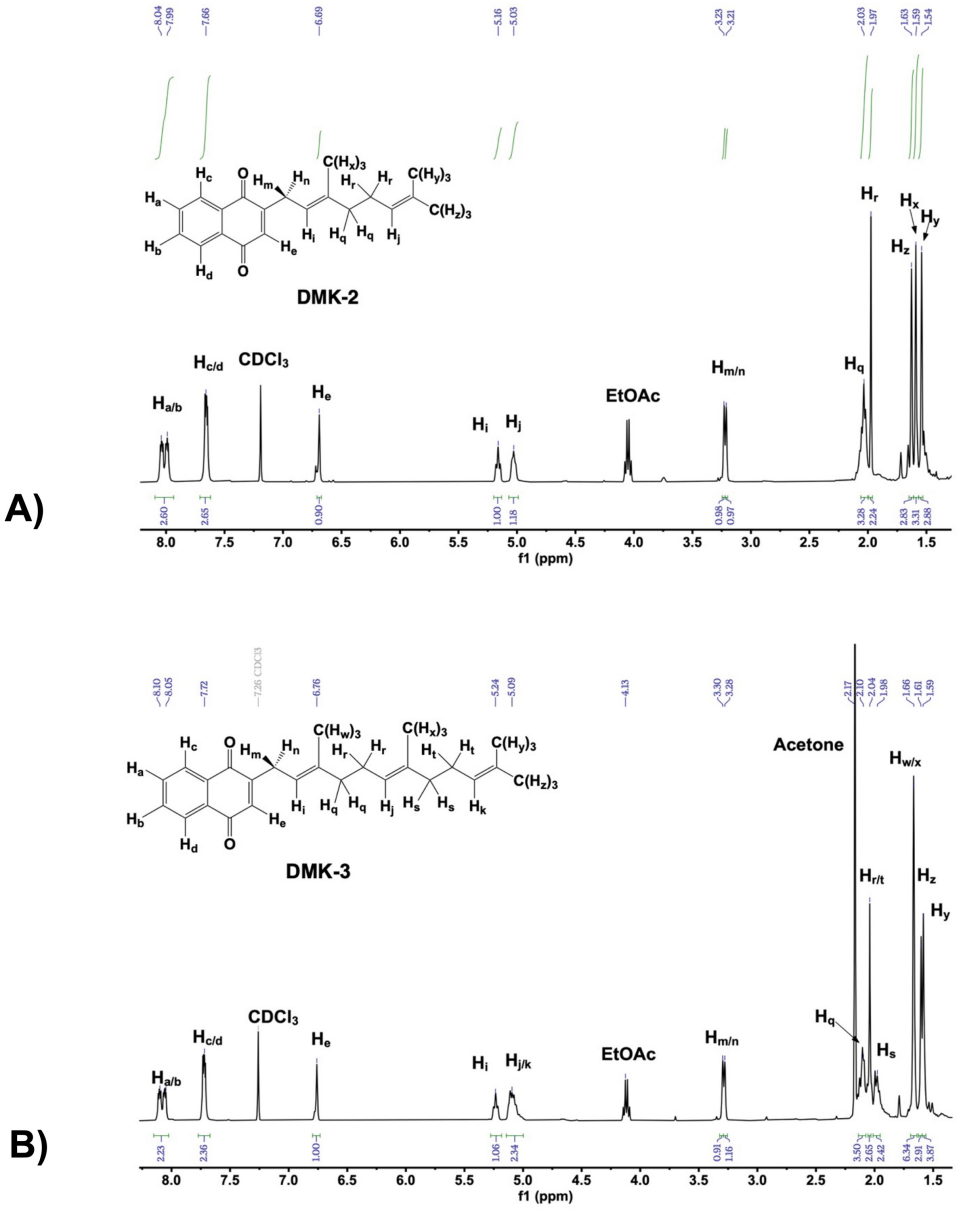

Figure 6.4. ^{1}H NMR (400 MHz, $CDCl_3$, 10 mM) spectra of A) DMK-2 and B) DMK-3. The peak assignments are provided within the figures.

compared to the literature method is improved yields due to increased reaction times and optimized purification protocols. The method has been developed based on the reported syntheses of the MK derivatives with different isoprene units and degrees of unsaturation where

1,4-menadiol was alkylated using Lewis acid catalyst conditions (Koehn et al., 2018a, Koehn et al., 2018b, Koehn et al., 2019, Suhara et al., 2010). In the first step of the synthesis, 1,4-napthoquine was reduced to 1,4-naphthoquinol using sodium dithionite (**Figure 6.3A**). In the second step, geraniol was coupled to 1,4-naphthoquinol using a boron trifluoride catalyst to yield DMK-2 in a 20% yield (**Figure 6.3B**). The isolation of DMK-2 was confirmed using ^{1}H NMR (**Figure 6.4A**), and the assignments of the peaks on the isoprenyl tail were confirmed using ^{1}H-^{13}C HSQC (**Figure A5.2**). A low yield could be explained by an extensive alkylation at the C-2 position, since both C-2 and C-3 positions are likely to form a secondary carbocation and get

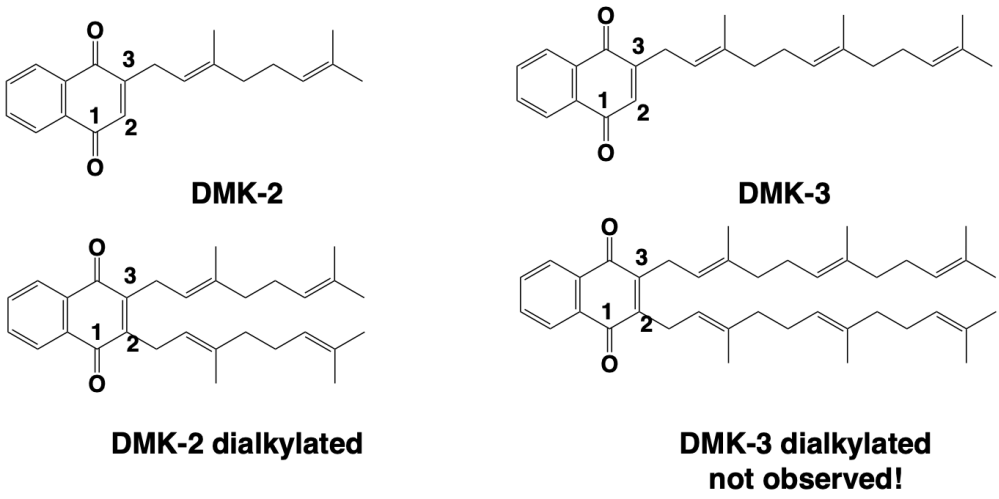

Figure 6.5. The DMK-2 and DMK-3 mono- and dialkylated products formed by using Friedel-Crafts alkylation methods with a boron trifluoride catalyst.

alkylated. According to the NMR analysis, the synthesis of DMK-2 has resulted in two products, a C-3 alkylated product and a C-2,3 di-alkylated product (**Figures 6.5A, A5.3**). The products have coeluted after purification by flash column chromatography and have been then successfully separated using preparative TLC using a 10:1 hexane : ethyl acetate solvent system. The formation of dialkylated products presents a major challenge in the DMK-2 synthesis and purification, similar to that of the MK-2 analog. In the MK-2 synthesis, the C-2 position on the naphthoquinone ring is more likely to get alkylated due to the presence of the methyl group which

stabilizes the tertiary carbocation intermediate. Thus, future work should explore other catalysts that would result in a selective alkylation at the C-3 position on the naphthoquinone ring.

The synthesis and purification of DMK-3 have not been reported previously (**Figure 6.3C**), and the method was based on the reported methods to synthesize partially and fully saturated MK-3 analogs using a boron trifluoride catalyst (Koehn et al., 2018a). The isolation of DMK-3 was confirmed using ^{1}H NMR (**Figure 6.4B**)., and the assignments of the peaks on the isoprenyl tail were confirmed using HSQC (**Figure A5.4**). The novel preparation of DMK-3 using *trans,trans*-farnesol has resulted in the formation of a C-3 alkylated product. Both C-2 and C-3 are likely to get alkylated due to the likelihood of the formation of a secondary carbocation at both C-2 and C-3 carbons (**Figure 6.5**). The formation of the dialkylated product, however, is unlikely, as the isoprenoid tail with three isoprene units is much more hindered than that with two isoprene units. The product was purified using preparative TLC (10:1 hexane : EtOAc) to get rid of the excess starting material. The synthesis of MK-3 has not been reported; however, previous studies report the difficulty of selective C-3 alkylation to yield other partially and fully saturated MK-3 derivatives, such as MK-3(II-H_2) and MK-3(I,II,III-H_6) (Koehn et al., 2018a). Future work should explore other catalysts that would allow to result in a selective alkylation at the C-3 position on the naphtoquinone ring, in addition to more robust purification methods of (*2E,6E*)-DMK-3.

6.3.2 Hydrophobicity of the DMK Analogs

The logP values have been calculated for the DMK analogs using Chemicalize calculator to see how their observed electrochemical properties depend on hydrophobicity. The calculated logP values have been compared to those of MK-1 and MK-2 (**Table 6.1**), small, truncated MK analogs that have been reported in the literature. The calculated logP values have shown

Table 6.1. The logP values of MK and DMK analogs, and their respective headgroups. The calculations were carried out using Chemicalize software.

Compound	Calculated logP Value
MK-1	2.72

Table 6.1. The logP values of MK and DMK analogs, and their respective headgroups. The calculations were carried out using Chemicalize software.

MK-2	4.25
DMK-2	3.90
DMK-3	5.42
Menadione	1.26
Naphthoquinone	0.91

that the removal of the methyl group from the naphthoquinone ring significantly decreases the logP, as seen with the logP values of MK-2 and DMK-2 (4.25 and 3.90, respectively). Increasing the length of the isoprenoid tail increases the logP, as evidenced by the 5.42 logP value of DMK-3. In the future, we would like to compare the logP values of all reported MK analogs to see which functionality has the greatest impact on logP.

Interestingly, the hydrophobicity of the DMK and MK analogs does not have much effect on the observed redox properties. Both DMK-2 and DMK-3, for example, have almost identical half-wave potential values, whereas MK-2 has greater half-wave potential values. The redox properties, in this case, are affected by the hydrophobicity of the headgroups where menadione and naphthoquinone have the logP values of 1.26 and 0.91, respectively.

6.3.3 Characterization of DMK-2 and DMK-3 by Cyclic Voltammetry

We have carried out the first electrochemical analyses of DMK-2 and DMK-3 to demonstrate how their structures affect their electron transport ability. Acetonitrile has been chosen due to its high dielectric constant and a wide potential window of 2.7 V. The cyclic voltammograms (CVs) of DMK-2 and DMK-3 in acetonitrile are shown in **Figure 6.6**. In both CVs, two distinct reversible peaks are shown. The peak on the right corresponds to the first one-electron reduction of the quinone to the semiquinone, $Q/Q^{\bullet -}$. The peak on the left corresponds to

the second one-electron reduction of the semiquinone to the dianion $Q^{\bullet-}/Q^{2-}$. The peak corresponding to the $Q^{\bullet-}/Q^{2-}$ reduction has a smaller peak current due to the repulsion of the semiquinone radical from the surface of the working electrode. The half-way potentials ($E_{1/2}$) have

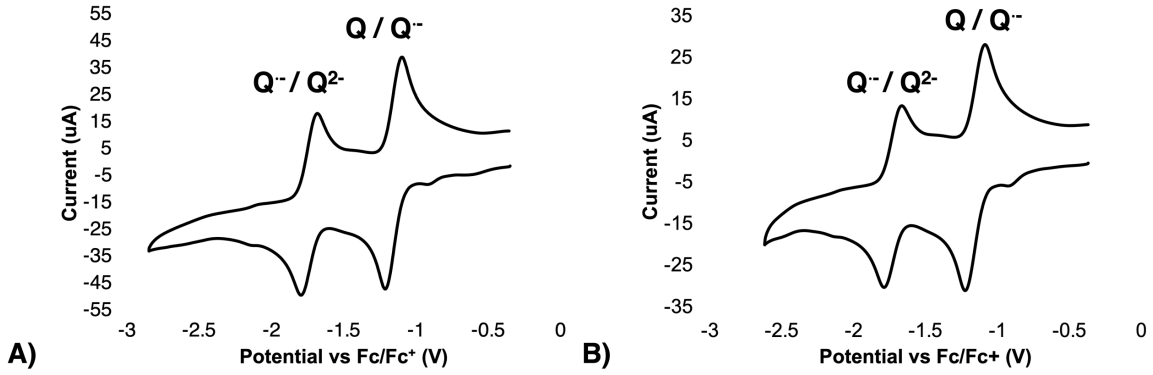

Figure 6.6. Representative CVs of A) 2.0 mM DMK-2 and B) 2.0 mM DMK-3 in CH_3CN collected using a 100 mV/s scan rate. The potentials are referenced to the Fc^+/Fc couple (2 mM) determined in CH_3CN. From left to right, redox processes are $Q^{\bullet-}/Q^{2-}$and $Q/Q^{\bullet-}$.

been calculated and tabulated for both DMK-2 and DMK-3, and compared to those of MK-2 (**Table 6.2**): The results have shown that both DMK-2 and DMK-3 have almost identical half-way potentials for both $Q/Q^{\bullet-}$ and $Q^{\bullet-}/Q^{2-}$, meaning that the redox properties are unaffected by the length of the isoprene tail. Additionally, similar half-wave potentials are observed because of the same degree of unsaturation of both analogs.

The half-way potentials of DMKs have been compared to those of MK-2. MK-2 has the same degree of unsaturation of its isoprene tail; however, it is more lipophilic due to the presence of the methyl group at the C2 position of the naphthoquinone ring. Overall, both classes exhibit the same trend where the peak current of the first $Q/Q^{\bullet-}$ reduction wave is greater than that of the second $Q^{\bullet-}/Q^{2-}$ reduction wave. MK-2, however, has more negative half-way potentials for both reductions, meaning that it is harder to reduce than the DMK analogs (Koehn et al., 2018a). This is likely due to the presence of the methyl group at the C2 position of the naphthoquinone ring, making MK-2 more lipophilic. In the future electrochemical analyses, we would like to establish

how the degree of unsaturation of the isoprenoid tail and the nature of the headgroup affect the redox properties of MK and DMK analogs.

Table 6.2. Cyclic voltammetry data of DMK-2, DMK-3 and MK-2 analogs. All CVs were collected in 2.0 mM solutions of dry acetonitrile.

Compound	$E_{1/2}$ of $Q/Q^{\bullet-}$ vs Fc/Fc^{+} (V)	$E_{1/2}$ of $Q^{\bullet-}/Q^{2-}$ vs Fc/Fc^{+} (V)	I_{PA}/I_{PC} Of $Q/Q^{\bullet-}$	I_{PA}/I_{PC} Of $Q^{\bullet-}/Q^{2-}$	D_0 x 10^{-6} (cm^2/s)	Reference
DMK-2	-1.155 ± 0.002	-1.740 ± 0.004	0.94	1.0	0.68	This work
DMK-3	-1.155 ± 0.004	-1.727 ± 0.009	1.1	1.0	0.24	This work
MK-2	-1.230 ± 0.006	-1.90(2) ± 0.031	0.90	0.90	3.7	(Koehn et al., 2018b)

6.3.4 Methylation Activity

The DMK-2 and DMK-3 analogs were tested in the *menG* assay to see if they are suitable substrates for methylation in bacteria. The assays were carried out using partially purified *Mycobacterium smegmatis* membranes as a *menG* source. The products of the assay were loaded on a reverse-phase TLC and compared to the DMK-8 standard acquired from external collaborators. The reverse-phase TLC was then exposed to UV light for 15 days to visualize methylation products. The data has shown that both DMK-2 and DMK-3 were methylated which was evident by the formation of two distinct spots, corresponding to MK-2 and MK-3, respectively (**Figure 6.7**). The formation of MK-3 in the *menG* assay was observed after 8 days of exposure to UV light, whereas the formation of DMK-2 was observed after 15 days after of exposure to UV light. The presence of other product bands is caused by methylation of other membrane lipids, since the *Mycobacterium smegmatis* membranes were partially purified.

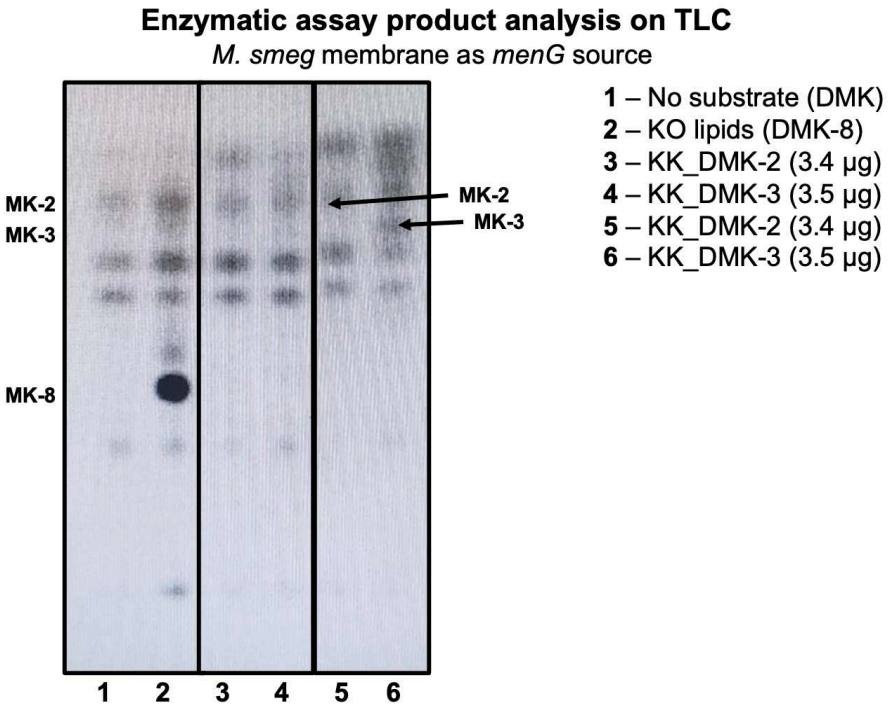

Figure 6.7. Reverse-phase TLC showing methylation products from the *menG* assay after 15 days of exposure to UV light. The methylation products of DMK-2 and DMK-3 were compared to those of the DMK-8 standard obtained from external collaborators. Different parts of the reverse-phase TLC plate were moved closer for clarity.

The data show that both DMK-2 and DMK-3 are methylated in the presence of dithiothreitol (DTT), a reductant used in the *menG* assay. After the addition of DTT, DMKs undergo a reduction reaction to form demethylmenaquinol-2 and demethylmenaquinol-3, respectively. Similar observations were reported in a recent study with DMK-8 where DMK-8 methylated to yield MK-8 in the presence of DTT (Pujari et al., 2022). According to previous reports, quinol is a substrate for methylation in ubiquinone biosynthesis where the C2 position is methylated via an electrophilic aromatic substitution (Houser and Olson, 1977, Sun et al., 2005). Thus, the presence of DTT in the assay is crucial to the formation of the quinol species and, ultimately, methylation of the DMK substrates by *menG*. The MK-2 product band, however, is rather faint and overlaps with the lipid methylation product band which cannot be identified. In future *menG* activity assays, the MK-2 product mixture should be spiked with a pure MK-2 standard to confirm the formation of MK-2. Overall, the assay results have shown that small, truncated DMK analogs are suitable substrates

for methylation in bacteria, although DMK-3 results in a higher methylation activity compared to DMK-2.

6.4 Conclusions

The study presented here describes the fundamental chemical properties of small, truncated DMK analogs, and their activity with *menG* methyltransferase enzyme. DMKs are biosynthetic precursors to MK and are, thus, essential components of the bacterial ETC. We synthesized DMK-2 and DMK-3 analogs using modified procedures from the literature and novel methods, and isolated pure *trans* isomers which was confirmed by 1D and 2D NMR methods. The cyclic voltammetry studies in acetonitrile demonstrated that the electron transport ability of the DMK analogs is unaffected by the length of the isoprenoid tail but rather the nature of the headgroup. The conclusion was reached by comparing the CV data for DMK-2 and DMK-3 to the reported CV data of MK-2. The MK-2 analog was harder to reduce due to the presence of the methyl group at the C2 position which confirmed our hypothesis. The results of the *menG* assay showed that both DMK-2 and DMK-3 got methylated in the presence of dithiothreitol, meaning that they are suitable substrates for methylation in bacteria, although DMK-3 exhibited a higher methylation activity. Overall, this first study enhanced the understanding the properties of small, truncated DMKs and their roles in bacterial ETC. Very few studies were carried out with DMKs and, hopefully, this fundamental knowledge will lead to more explorations of the properties of DMKs moving forward.

6.5 References

Adewumi, A. T., Soremekun, O. S., Ajadi, M. B. & Soliman, M. E. S. 2020. Thompson loop: opportunities for antitubercular drug design by targeting the weak spot in demethylmenaquinone methyltransferase protein. *RSC Advances,* 10**,** 23466-23483.

Aussel, L., Pierrel, F., Loiseau, L., Lombard, M., Fontecave, M. & Barras, F. 2014. Biosynthesis and physiology of coenzyme Q in bacteria. *Biochim. Biophys. Acta, Bioenerg.,* 1837**,** 1004-1011.

Barker, C. S., Meshcheryakova, I. V., Sasaki, T., Roy, M. C., Sinha, P. K., Yagi, T. & Samatey, F. A. 2014. Randomly selected suppressor mutations in genes for NADH:quinone oxidoreductase-1, which rescue motility of a Salmonella ubiquinone-biosynthesis mutant strain. *Microbiology,* 160**,** 1075-1086.

Braasch-Turi, M. & Crans, D. C. 2020. Synthesis of Naphthoquinone Derivatives: Menaquinones, Lipoquinones and Other Vitamin K Derivatives. *Molecules,* 25**,** 4477.

Braasch-Turi, M. M., Koehn, J. T. & Crans, D. C. 2022a. Chemistry of Lipoquinones: Properties, Synthesis, and Membrane Location of Ubiquinones, Plastoquinones, and Menaquinones. *Int. J. Mol. Sci.,* 23**,** 12856.

Braasch-Turi, M. M., Koehn, J. T., Kostenkova, K., Van Cleave, C., Ives, J. W., Murakami, H. A., Crick, D. C. & Crans, D. C. 2022b. Electron Transport Lipids Fold Within Membrane-Like Interfaces. *Front. Chem.,* 10.

Da Costa, M. S., Albuquerque, L., Nobre, M. F. & Wait, R. 2011. 9 - The Extraction and Identification of Respiratory Lipoquinones of Prokaryotes and Their Use in Taxonomy. *In:* RAINEY, F. & OREN, A. (eds.) *Methods Microbiol.*: Academic Press.

Daines, M. A., Payne, J. R., Humphries, E. M. & Abell, D. A. 2003. The Synthesis of Naturally Occurring Vitamin K and Vitamin K Analogues. *Curr. Org. Chem.,* 7**,** 1625-1634.

Dunphy, P. J. & Brodie, A. F. 1971. [233] The structure and function of quinones in respiratory metabolism. *Methods in Enzymology.* Academic Press.

Furomoto, T., Ohara, T., Kubo, T., Kawanami, Y. & Fujui, H. 2007. 2-Geranyl-1,4-naphthoquinone, a Possible Intermediate of Anthraquinones in a Sesamum indicum Hairy Root Culture. *Biosci., Biotechnol., Biochem.,* 71**,** 2600-2602.

Holländer, R. 1976. Correlation of the function of demethylmenaquinone in bacterial electron transport with its redox potential. *FEBS Lett.,* 72**,** 98-100.

Houser, R. M. & Olson, R. E. 1977. 5-demethylubiquinone-9-methyltransferase from rat liver mitochondria. Characterization, localization, and solubilization. *J. Biol. Chem.,* 252**,** 4017-4021.

Koehn, J. T., Beuning, C. N., Peters, B. J., Dellinger, S. K., Van Cleave, C., Crick, D. C. & Crans, D. C. 2019. Investigating Substrate Analogues for Mycobacterial MenJ: Truncated and Partially Saturated Menaquinones. *Biochemistry,* 58**,** 1596-1615.

Koehn, J. T., Crick, D. C. & Crans, D. C. 2018a. Synthesis and Characterization of Partially and Fully Saturated Menaquinone Derivatives. *ACS Omega,* 3**,** 14889-14901.

Koehn, J. T., Magallanes, E. S., Peters, B. J., Beuning, C. N., Haase, A. A., Zhu, M. J., Rithner, C. D., Crick, D. C. & Crans, D. C. 2018b. A Synthetic Isoprenoid Lipoquinone, Menaquinone-2, Adopts a Folded Conformation in Solution and at a Model Membrane Interface. *J. Org. Chem.,* 83**,** 275-288.

Kurosu, M. & Begari, E. 2010. Vitamin K2 in Electron Transport System: Are Enzymes Involved in Vitamin K2 Biosynthesis Promising Drug Targets? *Molecules,* 15**,** 1531-1553.

Meganathan, R. & Kwon, O. 2009. Biosynthesis of Menaquinone (Vitamin K₂) and Ubiquinone (Coenzyme Q). *EcoSal Plus,* 3.

Puffal, J., Mayfield, J. A., Moody, D. B. & Morita, Y. S. 2018. Demethylmenaquinone Methyl Transferase Is a Membrane Domain-Associated Protein Essential for Menaquinone Homeostasis in Mycobacterium smegmatis. *Frontiers in Microbiology,* 9.

Pujari, V., Rozman, K., Dhiman, R. K., Aldrich, C. C. & Crick, D. C. 2022. Mycobacterial MenG: Partial Purification, Characterization, and Inhibition. *ACS Infect. Dis.,* 8**,** 2430-2440.

Sharma, P., Teixeira De Mattos, M. J., Hellingwerf, K. J. & Bekker, M. 2012. On the function of the various quinone species in Escherichia coli. *The FEBS Journal,* 279**,** 3364-3373.

Sitkowski, J., Bocian, W. & Szterk, A. 2018. The application of multidimensional NMR analysis to cis/trans isomers study of menaquinone-7 (vitamine K2MK-7), identification of the (E,Z3,E2,ω)-menaquinone-7 isomer in dietary supplements. *J. Mol. Struct.,* 1171**,** 449-457.

Suhara, Y., Wada, A., Tachibana, Y., Watanabe, M., Nakamura, K., Nakagawa, K. & Okano, T. 2010. Structure–activity relationships in the conversion of vitamin K analogues into menaquinone-4. Substrates essential to the synthesis of menaquinone-4 in cultured human cell lines. *Bioorg. Med. Chem.,* 18**,** 3116-3124.

Sukheja, P., Kumar, P., Mittal, N., Li, S.-G., Singleton, E., Russo, R., Perryman, A. L., Shrestha, R., Awasthi, D., Husain, S., Soteropoulos, P., Brukh, R., Connell, N., Freundlich, J. S. & Alland, D. 2017. A Novel Small-Molecule Inhibitor of the Mycobacterium tuberculosis Demethylmenaquinone Methyltransferase MenG Is Bactericidal to Both Growing and Nutritionally Deprived Persister Cells. *mBio,* 8**,** e02022-16.

Sun, W., Xu, X., Pavlova, M., Edwards, A. M., Joachimiak, A., Savchenko, A. & Christendat, D. 2005. The crystal structure of a novel SAM-dependent methyltransferase PH1915 from Pyrococcus horikoshii. *Protein Sci.,* 14**,** 3121-3128.

Teh, J. S., Yano, T. & Rubin, H. 2007. Type II NADH:Menaquinone Oxidoreductase of Mycobacterium tuberculosis. *Infect. Disord.: Drug Targets,* 7**,** 169-181.

Unden, G. 1988. Differential roles for menaquinone and demethylmenaquinone in anaerobic electron transport of E. coli and their fnr-independent expression. *Arch. Microbiol.,* 150**,** 499-503.

Unden, G. & Bongaerts, J. 1997. Alternative respiratory pathways of Escherichia coli: energetics and transcriptional regulation in response to electron acceptors. *Biochim. Biophys. Acta, Bioenerg.,* 1320**,** 217-234.

Upadhyay, A., Fontes, F. L., Gonzalez-Juarrero, M., Mcneil, M. R., Crans, D. C., Jackson, M. & Crick, D. C. 2015. Partial Saturation of Menaquinone in Mycobacterium tuberculosis: Function and Essentiality of a Novel Reductase, MenJ. *ACS Cent. Sci.,* 1**,** 292-302.

Upadhyay, A., Kumar, S., Rooker, S. A., Koehn, J. T., Crans, D. C., Mcneil, M. R., Lott, J. S. & Crick, D. C. 2018. Mycobacterial MenJ: An Oxidoreductase Involved in Menaquinone Biosynthesis. *ACS Chem. Biol.,* 13**,** 2498-2507.

Wissenbach, U., Kröger, A. & Unden, G. 1990. The specific functions of menaquinone and demethylmenaquinone in anaerobic respiration with fumarate, dimethylsulfoxide, trimethylamine N-oxide and nitrate by Escherichia coli. *Arch. Microbiol.,* 154**,** 60-66.

Chapter 7 Summary, Concluding Remarks and Future Directions

7.1 Summary and Concluding Remarks

The research presented in this dissertation contributes to understanding of the fundamental properties of several classes of biologically relevant redox-active molecules, such as oxovanadium Schiff base complexes, dioxovanadium complexes, polyoxidovanadates and demethylmenaquinones, lipid-electron carriers in some types of bacteria.

Chapter one reviews the advances in V anticancer research over the last five years. The chapter provides an extensive review about different classes of vanadium compounds to treat different types of cancer, including V salts, coordination complexes and polyoxidovanadates. The review highlighted promising novel modes of delivery of V compounds, such as intratumoral injections and lipid nanoparticles, that are currently studied in the clinic to deliver highly cytotoxic vanadium species. The chapter also reviewed the advances in the diseases mechanistically similar to cancer, such as diabetes and cardiovascular diseases. The review emphasized the lack of the animal data about the efficacy and toxicity of different vanadium compounds which halts a more robust development of novel vanadium anticancer species.

Chapter two described the first report of vanadium(V) catecholate complexes with pyridine-containing Schiff bases. Vanadium(V) catecholates are reported promising agents to treat glioblastoma, an aggressive form of brain cancer. This study investigated whether the presence of the pyridine ring on the Schiff base improves cytotoxicity of vanadium(V) catecholates. One of the newly synthesized complexes; [VO(SALIEP)(DTB)], is a promising agent to treat glioblastoma (IC_{50} = 6 uM in T98g cells). The pyridine ring contributes to superior hydrolytic stability of the [VO(SALIEP)(DTB)] under the assay conditions, resulting in increased cytotoxicity of the complex in glioblastoma cells. The pyridine, however, increases the hydrophobicity of the complexes and, consequentially, decreases their uptake into T98g cells. The ^{51}V NMR and EPR spectroscopic

data showed that the VOSALIEP complexes with catechol and 4-*tert*-butylcatechol ligands readily reduce to V(IV) in solution which is attributes to changes in the core structure of the complexes. This very first EPR study with VOSALIEP complexes confirmed 1) the reduction of [VO(SALIEP)(CAT)] and [VO(Cl-SALIEP)(CAT)] complexes to V(IV) 2) the formation of two distinct V(IV) isomers in solution and 3) the formation of semiquinone radicals upon reduction of the V(V) species. The ^{1}H-^{1}H NOESY helped elucidate the 3-D structure of the major isomer of the most promising analog, [VO(SALIEP)(DTB)]. The UV-Vis data in media showed that the VOSALIEP complexes with catechol and 4-*tert*-butylcatechol ligands readily hydrolyze which confirms the necessity of the aliphatic substituents to stabilize the V(V) species. Overall, the study contributed to the understanding of the structure-activity relationships of vanadium(V) catecholates and demonstrated that the ligands with bulky aliphatic substituents are crucial for the stability of the V(IV/V) species.

Chapter three investigates the redox mechanism of the VOSALIEP and VOCl-SALIEP complexes with 4-*tert*-butylcatechol and di-*tert*-butylcatechol ligands by non-aqueous cyclic voltammetry. All four redox processes described here a diffusion-controlled, meaning that both V(IV) and V(V) species are stable and equilibrate in solution. The redox mechanism of the [VO(SALIEP)(DTB)] complex follows a reversible redox mechanism which indicates that the V(IV/V) are equally stable in solution. The complex exhibits two V(V) isomers which reduce to one V(IV) isomer at variable scan rates. The [VO(SALIEP)(4TB)], [VO(Cl-SALIEP)(4TB)] and [VO(Cl-SALIEP)(DTB)] follow a quasi-reversible redox mechanism. For the complexes with 4-*tert*-butylcatechol, V(V) species are more stable in solution and are present at a higher concentration. Both complexes form the second isomers over time which readily reoxidize back to the respective V(V) species. The [VO(Cl-SALIEP)(DTB)] also follows a quasi-reversible redox mechanism where the V(IV) species are more stable and are present at a higher concentration. The experiments with glutathione demonstrated that the catecholate undergo a redox complexation with glutathione which results in the higher concentration of the V(IV) species. This detailed cyclic voltammetry

study enhanced the understanding of the redox chemistry of the VOSALIEP complexes, although the complexity of the system will require the experiemtns under the assay conditions in the future.

Chapter four describes the first report of the oncolytic viral spread by vanadium(V) dipicolinates, dioxovanadium coordination complexes. The study investigated a parent analog, abbreviated $[VO_2(dipic)]^-$, and the analogs with Cl and OH groups in the para position, $[VO_2(Cl\text{-}dipic)]^-$ and $[VO_2(OH\text{-}dipic)]^-$. The *in vitro* assays were complemented by the ^1H and ^{51}V NMR speciation studies to understand the speciation of vanadium(V) dipicolinates under physiological conditions. The NMR data demonstrated the hydrolysis of the complexes under physiological conditions and generation of the vanadate, simple vanadium-oxo species. Thus, the vanadate primarily causes the spread of the oncolytic viruses. The ^1H and ^{51}V NMR data in reverse micelles showed that V(V) dipicolinates are located on the interface of the aqueous pool and hydrophobic region of model membranes which also contributes to their hydrolysis under physiological conditions. Future studies are needed to establish whether more hydrolytically stable vanadium species would further improve the oncolytic viral spread.

Chapter five describes the speciation experiments of Pt^{IV} and Mo^{VI} monosubstituted polyoxidovanadates abbreviated V_9X, large vanadium-oxo clusters, in mammalian media and explores their effects on signal transduction and luteinizing hormone receptor (LHR) signaling. The biological studies in CHO cells were complemented by ^{51}V NMR speciation studies under aqueous and assay conditions (DMEM, pH 7.4). The speciation data showed that both clusters hydrolyze in the mammalian media within one hour and predominantly form a vanadate-phosphate complex. The biological data showed that both V_9Mo and V_9Pt affect LHR expression and do not inhibit cell growth, since the clusters rapidly hydrolyze under the assay conditions. The clusters also significantly decrease the packing of membrane lipids for about 1 h. Overall, the V_9Pt and V_9Mo clusters have a much more significant effect on the LHR expression and lipid packing compared to the parent decavanadate cluster (V_{10}), a known species with reported anticancer,

antidiabetic and antituberculosis properties. Together, the first five chapters demonstrate 1) the diversity of applications of vanadium compounds for treatment of different types of cancer and 2) the efforts to develop vanadium-based anticancer therapeutics to treat different types of cancer based on the structure-activity relationships and detailed spectroscopic studies.

Chapter six describes the bioorganic work which investigated the fundamental properties of demethylmenaquinones (DMKs). DMKs are biosynthetic precursors to menaquinones, lipid electron carriers in many types of bacteria, including *Mycobacterium tuberculosis*. In this work, we described the syntheses of small DMK analogs, DMK-2 and DMK-3 using Friedel-Crafts alkylation methods. The low yields of the reactions could be explained by the lack of selectivity at the C-2 position. In addition, the synthesis of DMK-2 results in the formation of dialkylated products which was confirmed by ^{1}H NMR. The non-aqueous cyclic voltammetry characterization of the analogs demonstrated that the electron transport ability of DMKs is mainly affected by the nature of their headgroup rather than the length of the isoprene tail. The *menG* activity assay confirmed that both DMK-2 and DMK-3 are methylated by *menG* , a methyltransferase bacterial enzyme, to yield MK-2 and MK-3. Thus, DMKs are promising antitubercular targets; however, future experiments are needed to further understand the chemical properties and the observed activity in bacteria of non-native DMK analogs.

7.2 Future Directions

Chapter two describes the very first structure-activity study of vanadium(V) catecholate complexes. The study established which structural motifs increase hydrolytic stability and cytotoxicity of promising vanadium(V) catecholate complexes for glioblastoma treatment. The presence of the di-tert-butyl catecholate ligand is important to 1) stabilize the redox-active V(IV/V) species and 2) induce cytotoxicity by generating semiquinone radicals. Further spectroscopic studies would enhance the understanding of the redox properties of the VOSALIEP complexes. Specifically, EPR metal-ion stabilization experiments should be carried out with

[VO(SALIEP)(4TB)], [VO(Cl-SALIEP)(4TB)], [VO(Cl-SALIEP)(DTB)] in the presence of $Zn(OAc)_2$ to 1) investigate whether they form semiquinone radicals in solution and 2) investigate whether the presence of aliphatic substituents on the catecholate ligand prevents immediate oxidation to *V(IV) and semiquinone radical formation.* Further studies should also explore other structural modifications that could potentially improve hydrolytic stability and cytotoxicity of vanadium(V) catecholate complexes. Another future experiments would explore the syntheses of vanadium(V) catecholate complexes with other aliphatic substituents and/or catechol sources. Specifically, 5,6-dihydroxyindole ligands, biosynthetic precursors to melanin and serotonin, could be used as catechol sources. A hydrophilic nature of 5,6-dihydroxyindole (logP = 0.86) would require the addition of aliphatic substituents on the Schiff base to prevent hydrolysis under the assay conditions. Alternatively, aliphatic substituents could also be added onto a 5,6-dihydroxyindole ligand via Suzuki cross-coupling methods.

The work presented in chapter three could be complemented by future EPR experiments to understand the nature of V(IV) isomers that form in solution. Future Q-band EPR studies are needed to resolve the V(IV) isomers that form in solution, since they have similar spectral *parameters.* Similar Q-band EPR experiments could also be carried out with [VO(SALIEP)(4TB)], [VO(Cl-SALIEP)(4TB)], [VO(SALIEP)(DTB)], [VO(Cl-SALIEP)(DTB)] to 1) confirm whether the complexes reduce to multiple V(IV) isomers and 2) determine whether semiquinone radicals are formed upon reduction.

Chapter four presented the very first study of vanadium(V) coordination complexes with oncolytic viruses. Future efforts should focus on testing various classes of vanadium complexes to see whether more hydrolytically stable complexes better enhance the spread of oncolytic viruses. Once several promising complexes are determined, their chemical properties and stability should be studied at physiological conditions using a variety of spectroscopic methods, such as ^{1}H NMR, ^{51}V NMR, EPR and UV-Vis.

The study in chapter five investigated the effects of two monosubstituted polyoxidovanadates on the luteinizing hormone receptor (LHR). Previous work investigated the effects of the parent decavanadate and two mixed-valence polyoxidovanadates abbreviated V_{14} and V_{15}. Another study could be carried out with $[V^{IV}_{10}V^{V}_{8}O_{42}]^{5-}$, a mixed-valence polyoxidovanadates, to see a larger POV results in a greater effect on the LHR. All biological studies will be complemented by a ^{51}V and EPR speciation study of V_{18} under physiological conditions.

Chapter six presented the first study of the fundamental properties of demethylmenaquinone derivatives, potential targets to treat tuberculosis. Further experiments are needed to understand 1) the differences in the chemical properties between menaquinones and demethylmenaquinones and 2) how the chemical properties of demethylmenaquinone affect their electron transport ability. The ongoing efforts in the Crans lab focus on ^{1}H-^{1}H NOESY and ^{1}H-^{1}H ROESY NMR experiments with DMK-2 to determine the 3D conformation of DMK-2, in addition to the exploratory syntheses of other partially saturated and fully saturated DMK analogs. Ultimately, the 3D conformations of MK-2 and DMK-2 in different solvents should be compared to determine the effects of their 3D conformations on the observed redox properties. Future assay work should be carried out to further understand the activity of the DMK analogs. First, the *menG* activity assay should be optimized to see whether the observed methylation activity is concentration dependent. Second, the formation. of MK-2 methylation product could be confirmed by spiking the assay product mixture with a pure MK-2 standard. This is because the product band took 15 days to develop under the UV light and was hard to distinguish on the reverse phase TLC plate. Third, the NADH assay should be developed and optimized to test the electron transport ability of the DMK analogs. Since DMKs are very hydrophobic, using a detergent may be necessary to avoid solubility issues under the assay conditions.

Overall, the work in this dissertation builds a foundation for future research into developing better vanadium anticancer therapeutics and understanding the fundamental properties of demethylmenaquinones, promising antitubercular analogs.

Appendix I: Distribution of Work

Chapter 1

The introductory chapter summarizes the literature about the advances in vanadium anticancer research over the last five years. The chapter will be submitted to the book series *Metal Ions in Life Sciences* which links coordination chemistry and biochemistry with Kateryna Kostenkova as a primary author. Coauthors include Kameron Klugh and Debbie Crans. For this chapter, Kateryna Kostenkova did the literature search, wrote most of the manuscript, and made the figures. Kameron Klugh wrote parts of the manuscript and helped with manuscript editing. Debbie Crans wrote parts of the manuscript, provided valuable feedback and helped with manuscript editing.

Chapter 2

The material in chapter will be submitted to *Inorganic Chemistry* with Kateryna Kostenkova as a primary author. Coauthors include Dr. Aviva Levina, Drew Walters, Heide Murakami, Prof. Peter Lay and Debbie Crans. For this work, Kateryna Kostenkova carried out all synthetic work and spectroscopic characterization, wrote the manuscript, prepared the figures and supporting information. Dr. Aviva Levina carried out the biological experiments and wrote the Results section about the biological results. Drew Walters helped with the electrochemical characterization. Heide Murakami provided guidance on the 2D NMR section writeup. Profs. Peter Lay and Debbie Crans gave input and advice on the spectroscopic experiments and helped with editing of the manuscript.

Chapter 3

The cyclic voltammetry experiments in this chapter were carried out by Kateryna Kostenkova. Drew Walters helped with some of the electrochemical characterization. Kateryna Kostenkova wrote the chapter and interpreted the results. Dr. Aviva Levina, and Profs. Peter Lay and Debbie Crans gave input and advice on this project.

Chapter 4

The material in chapter was published in *Biometals* (Bergeron et. al, 2019) with Anabel Bergeron as a primary author. Kateryna Kostenkova carried out ^{1}H and ^{51}V NMR speciation and model membrane studies. Speciation modeling using HySS software was performed by Heide Murakami. Biological testing of the complexes was performed by Anabel Bergeron, Mohammad Selman, Rozanne from the Diallo group at the University of Ottawa. All coauthors helped with writing and editing of the manuscript.

Chapter 5

The material in chapter was published in *Frontiers of Chemical Biology* (Kostenkova et. al, 2023) with Kateryna Kostenkova as a primary author. Kateryna Kostenkova carried out the ^{51}V NMR speciation experiments and wrote the manuscript. Duaa Althumairy carried out biological testing with the luteinizing hormone receptor. Profs. Deborah Roess and Debbie Crans gave input on the projects and helped with writing and editing of the manuscript.

Chapter 6

The chapter described the initial efforts regarding studies of the fundamental properties of demethylmenaquinones. Kateryna Kostenkova carried out the syntheses and purification, NMR, and electrochemical characterization, calculated the logP values and wrote the chapter. Venugopal Pujari from the Prof. Crick lab helped with carrying out the *menG* activity assay. Profs. Debbie Crans and Dean Crick provided helpful feedback on the project and chapter writing.

References

Bergeron, A.; Kostenkova, K.; Selman, M. Murakami, H. A.; Owens, E.; Haribabu, N.; Arulanandam, R.; Diallo, J.-S.; Crans, D. C. Enhancement of oncolytic virotherapy by vanadium(V) dipicolinates. *Biometals*. **2019**, *32*, 545 – 561.

Kostenkova, K.; Althumairy, D.; Postal, K.; Arhouma, Z.; Rajan, A.; Kortz, U.; Barisas, B. G.; Roess, D.; Crans, D. C. Polyoxidovanadates $[Mo^{VI}V^{V}_{9}O_{28}]^{5-}$ and $[H_2Pt^{IV}V^{V}_{9}O_{28}]^{5-}$ interact with CHO cell plasma membrane lipids causing aggregation and activation of a G protein-coupled receptor. *Front. Chem*. *Biol*. **2023**, *2*:1126975. doi: 10.3389/fchbi.2023.1126975.

Appendix II: Supporting Information for Chapter 2

Table of Contents

Figure A2.27 Room temperature stacked EPR spectra (3,400 – 3,600 G) of [V^{IV}O(Cl-SALIEP)(Cat)] in 10.0 mM DMSO solutions with added $Zn(OAc)_2$ to trap the resulting semiquinone radicals.

VI Biological Data

Figure A2.28 Concentration-dependent viabilities of T98g (red lines) and HFF-1 (blue lines) cells after 72 h treatments with fresh (~1 min after dissolution) and aged (30 min at 310 K and 5% CO_2) solutions of the complexes.

I 1D NMR Characterization

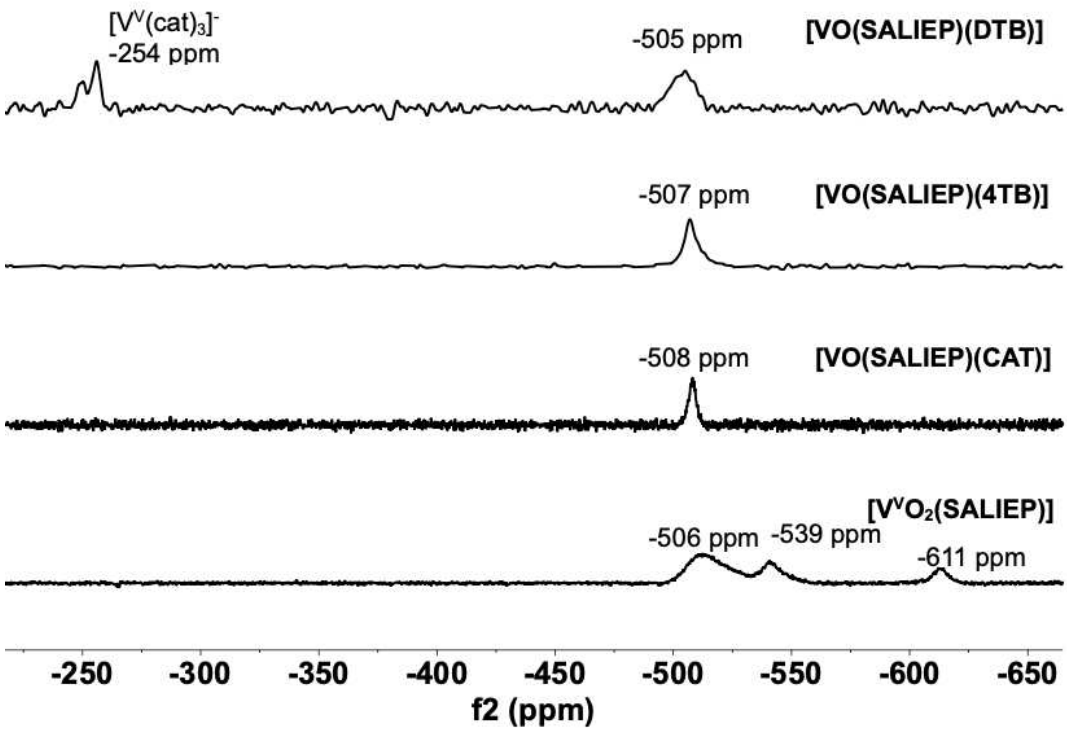

Figure A2.1 Stacked ^{51}V NMR plot of the [VO(SALIEP)X] series in d_6-DMSO.

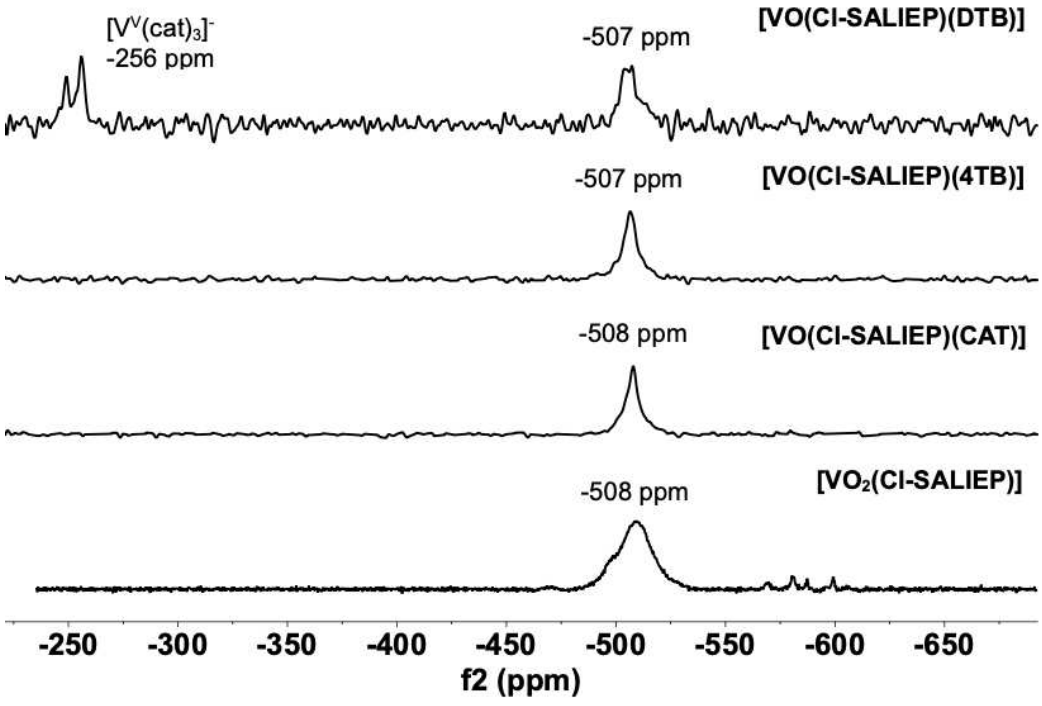

Figure A2.2. Stacked ^{51}V NMR plot of the [VO(Cl-SALIEP)X] series in d_6-DMSO.

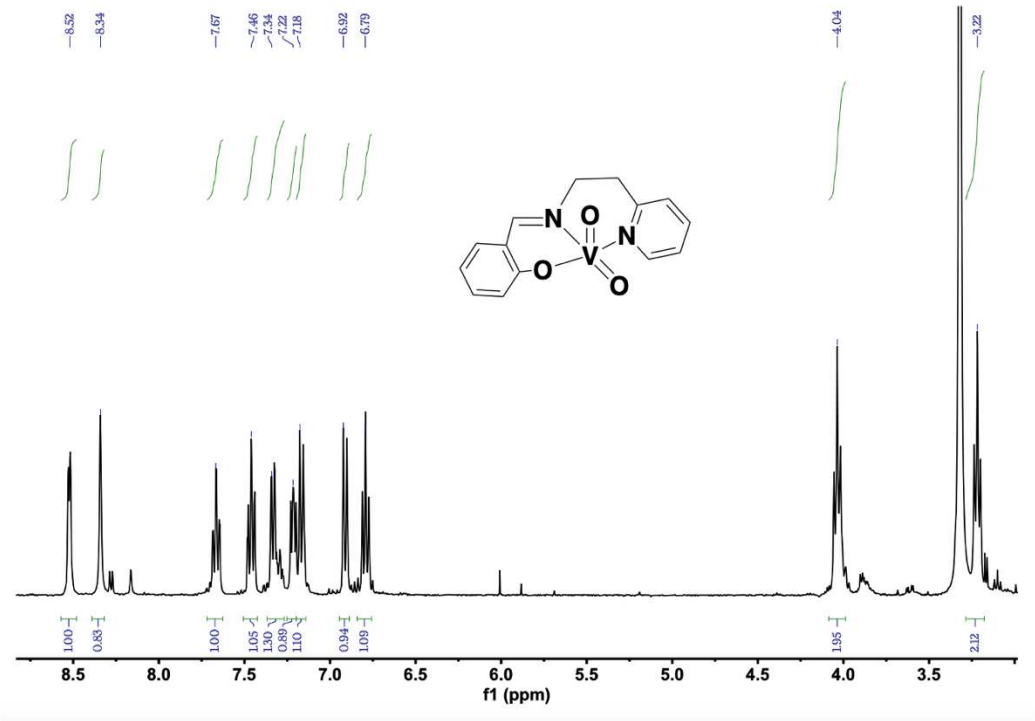

Figure A2.3 [1]H NMR of [VO_2(SALIEP)] in d_6-DMSO.

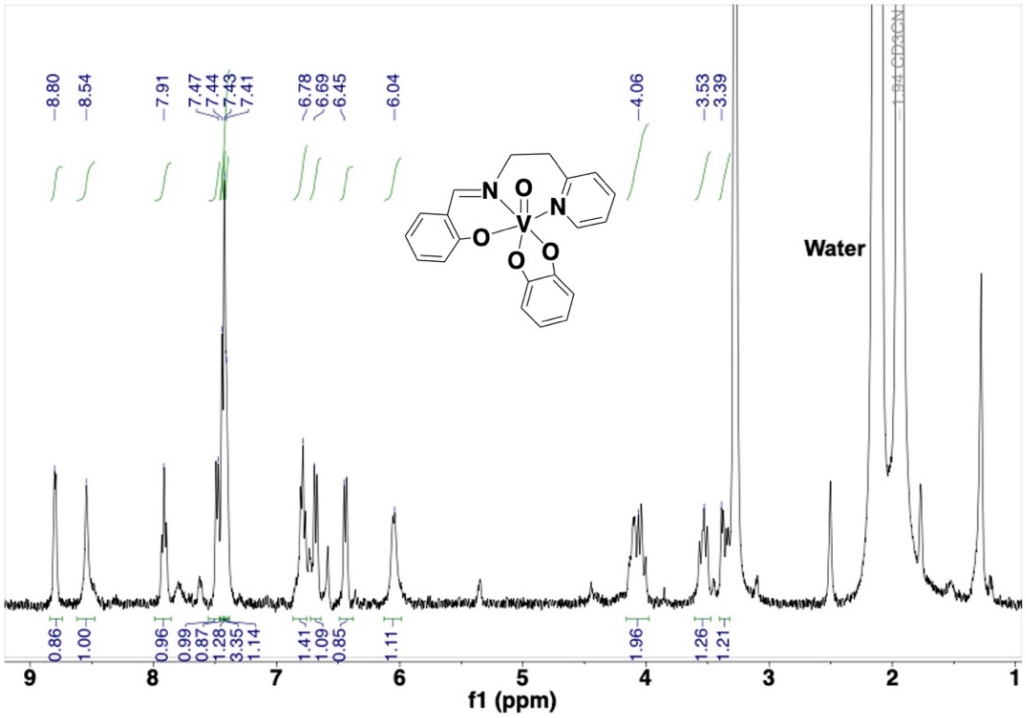

Figure A2.4 [1]H NMR of [VO(SALIEP)(Cat)] in d_3-MeCN.

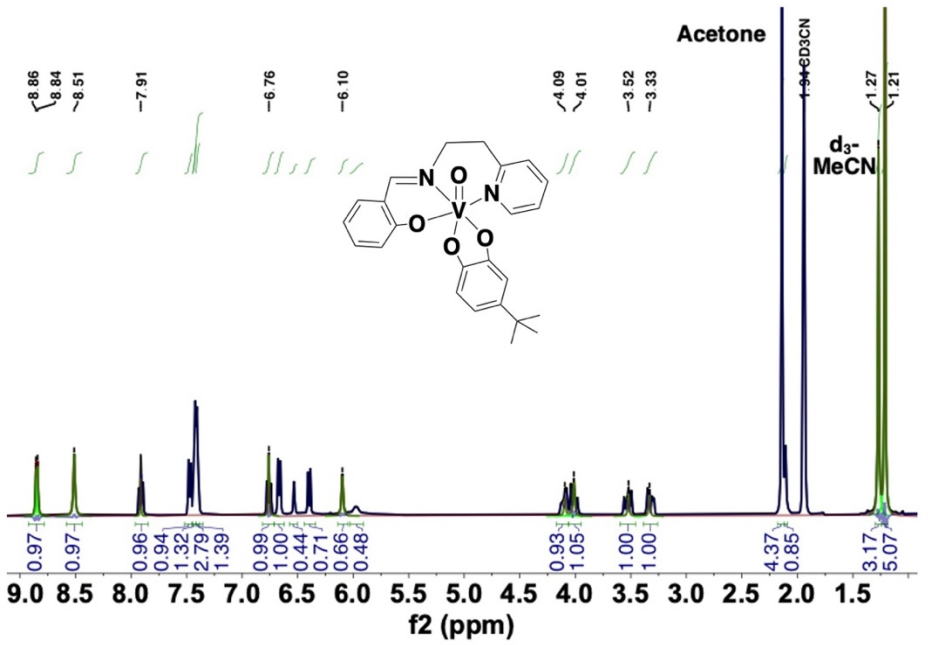

Figure A2.5 ^{1}H NMR of [VO(SALIEP)(4TB)] in *d*$_3$-MeCN.

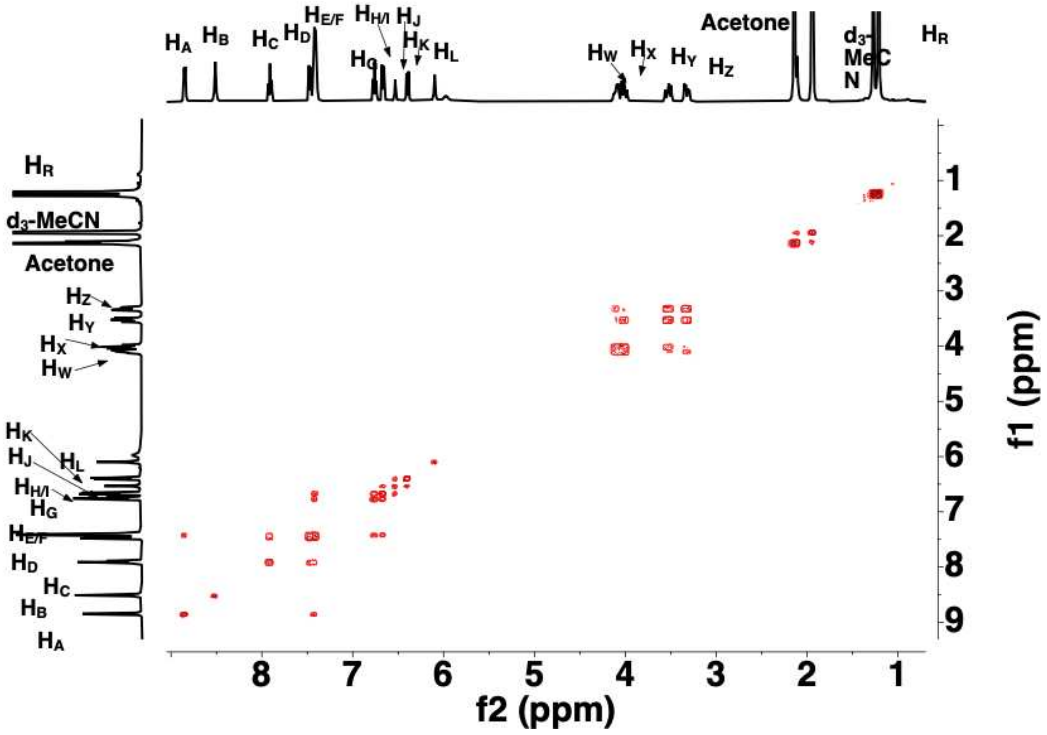

Figure A2.6 ^{1}H-^{1}H gCOSY NMR of [VO(SALIEP)(4TB)] in *d*$_3$-MeCN.

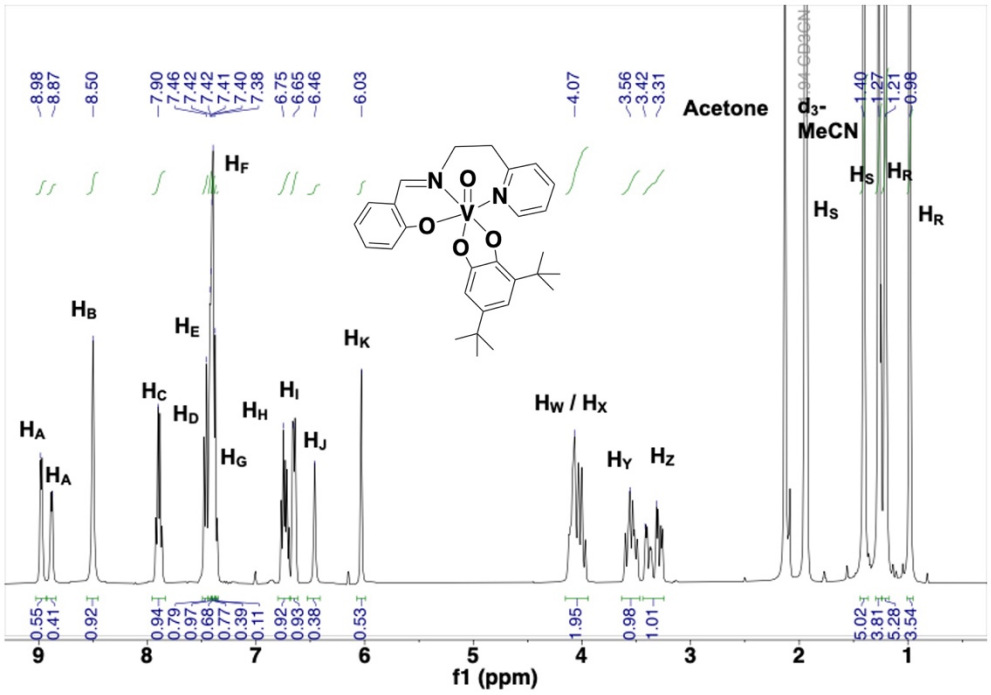

Figure A2.7 ^{1}H NMR of [VO(SALIEP)(DTB)] in d_3-MeCN.

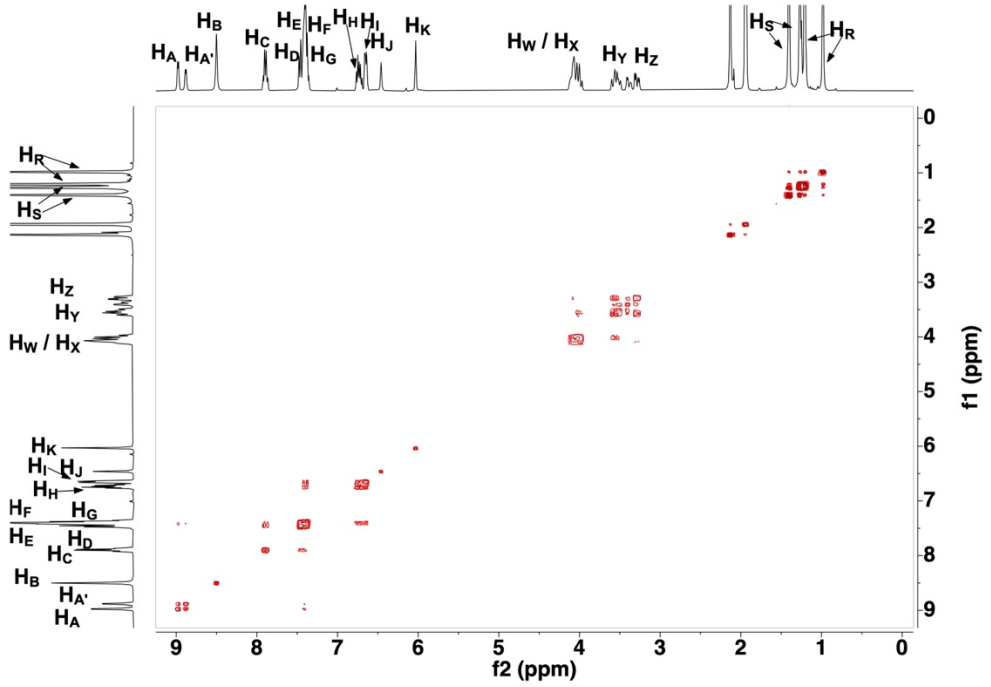

Figure A2.8 ^{1}H-^{1}H gCOSY NMR of [VO(SALIEP)(DTB)] in d_3-MeCN.

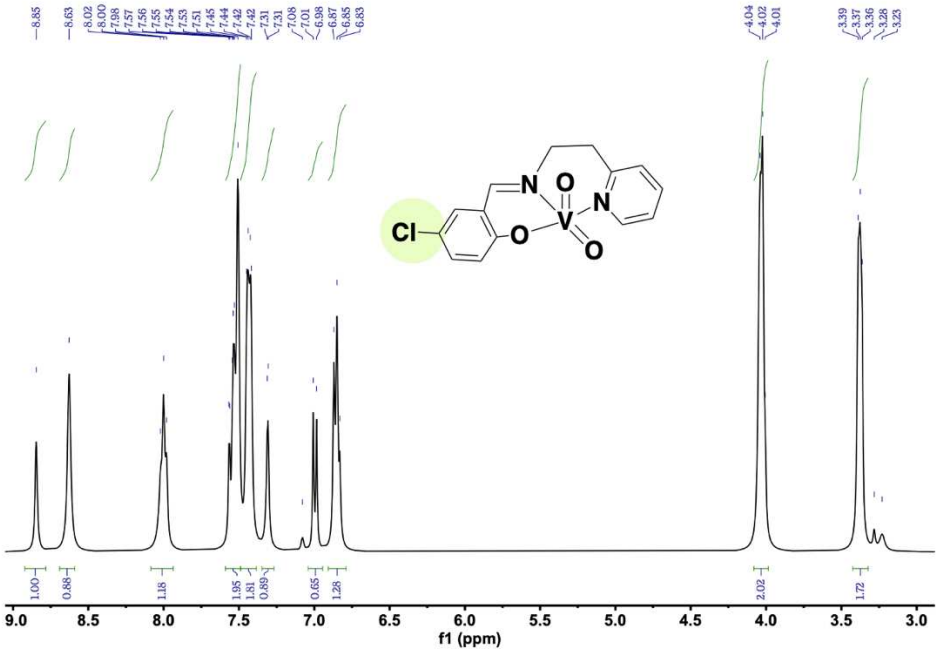

Figure A2.9 ^{1}H NMR of [VO_2(Cl-SALIEP)] in d_3-MeCN.

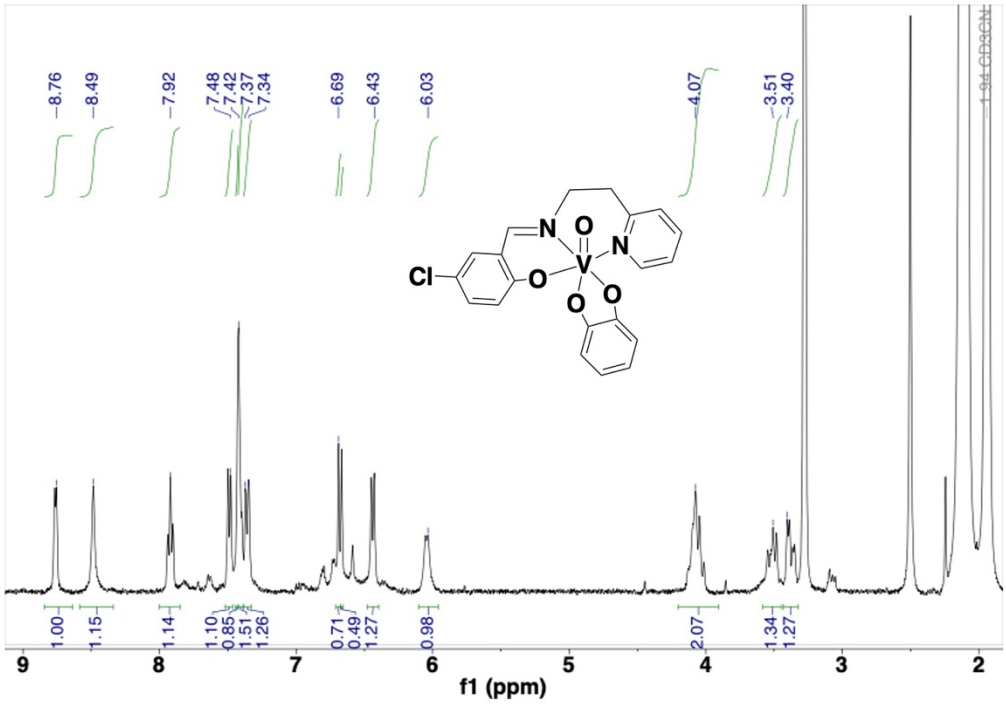

Figure A2.10 ^{1}H NMR of [VO(Cl-SALIEP)(Cat)] in d_3-MeCN.

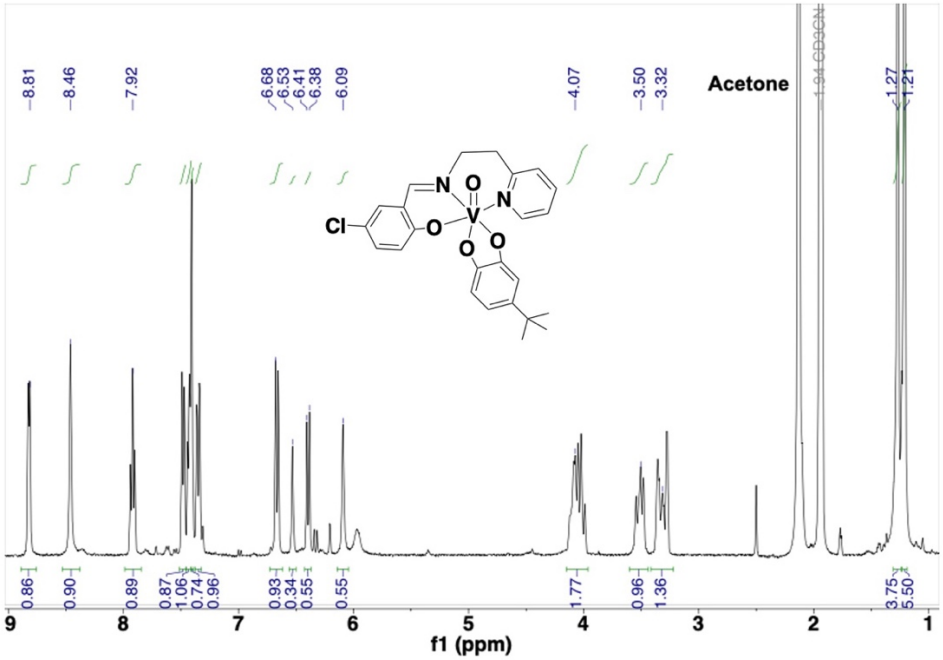

Figure A2.11 ^{1}H NMR of [VO(Cl-SALIEP)(4TB)] in d_3-MeCN.

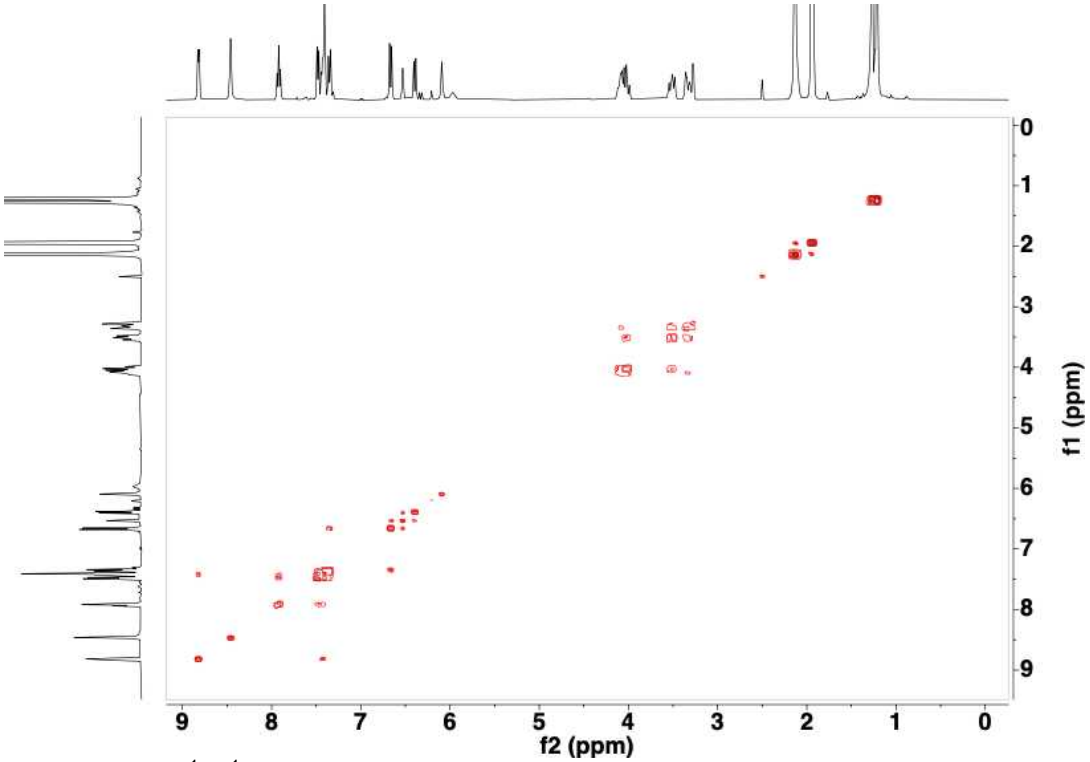

Figure A2.12 ^{1}H-^{1}H gCOSY NMR of [VO(Cl-SALIEP)(4TB)] in d_3-MeCN.

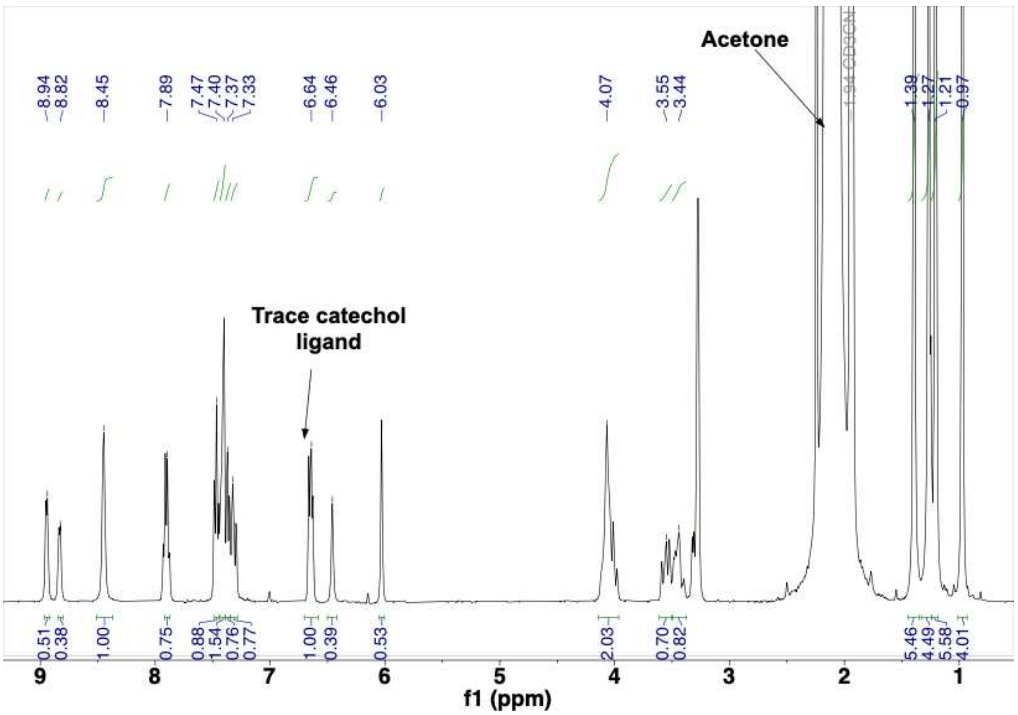

Figure A2.13 ^{1}H NMR of [VO(Cl-SALIEP)(DTB)] in d_3-MeCN.

II 2D NMR Characterization of [VO(SALIEP)(DTB)]

Table A2.1. Interproton distances of the [VO(SALIEP)(DTB) complex.
Note: the distances have been measured in PyMOL using energy-minimized 3D model.

Peaks	Interproton Distance, Å
H_R - H_A	2.0
H_R - H_E	3.2
H_R - H_C	5.4
H_R - H_D	6.2
H_R - H_I	6.1
H_R - H_G	8.4
H_R - H_H	9.7
H_R - H_F	9.0
H_R - H_B	7.9
H_R – $H_{W/Z}$	6.6
H_R – $H_{Y/Z}$	7.1
H_S - H_B	6.7
H_S - H_F	6.5
H_S - H_H	6.7
H_S - H_G	6.6
H_S - H_I	6.3
H_S - $H_{W/X}$	8.5
H_S – $H_{Y/Z}$	9.8
H_S - H_A	7.7
H_S - H_E	10.0
H_S - H_C	11.4
H_S - H_D	10.8

III UV-Vis Stability Studies

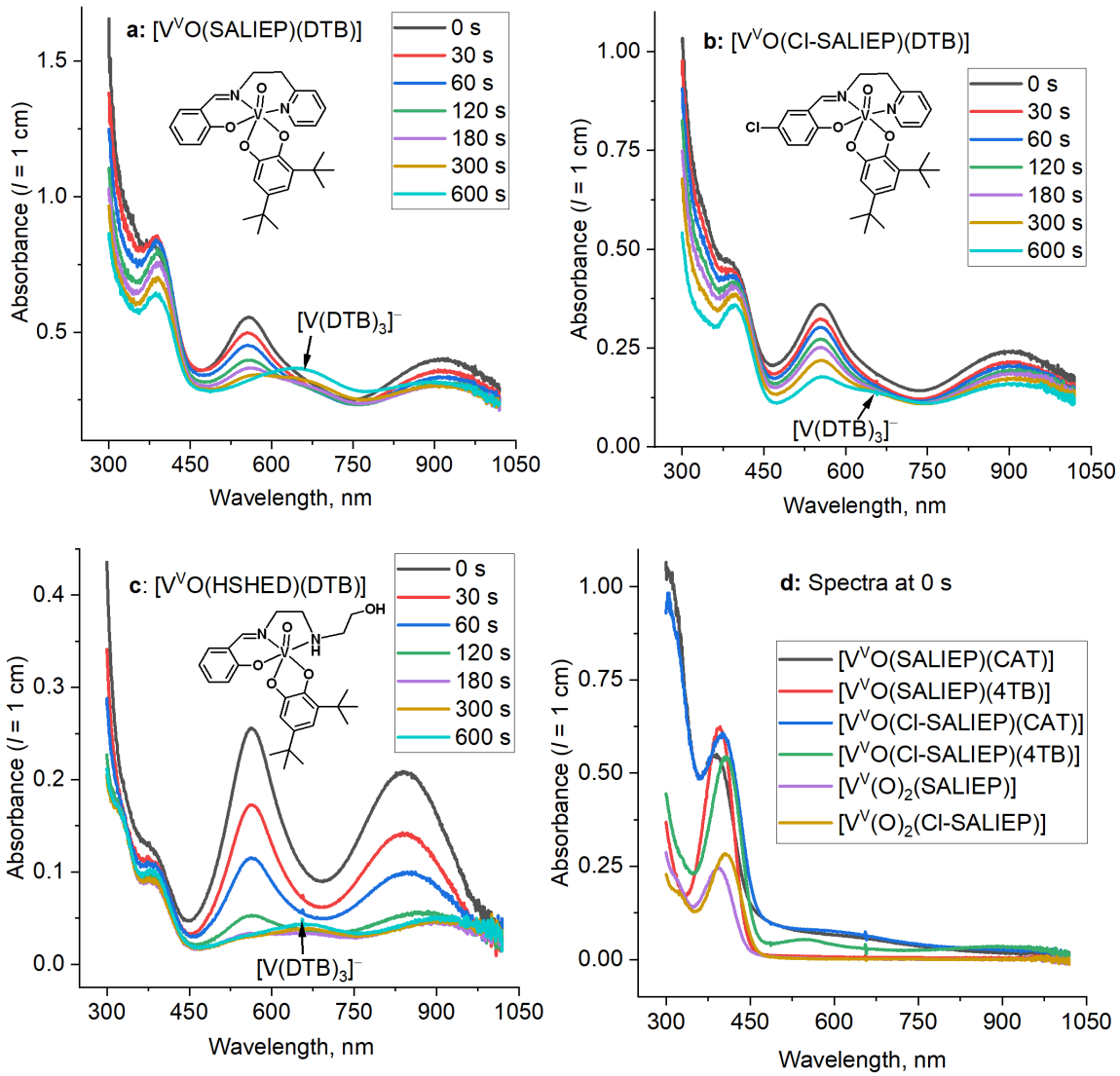

Figure A2.14. Comparison of time-dependent changes in UV-vis spectra of [V^{V}O(SALIEP)(DTB)] (**a**), [V^{V}O(Cl-SALIEP)(DTB)] (**b**) and [V^{V}O(HSHED)(DTB)] (**c**) in cell culture medium (DMEM without phenol red, supplemented with 2% vol. fetal calf serum and 10 mM HEPES, pH 7.4) at 310 K. Stock solutions of V(V) complexes (10 mM V in DMSO) were prepared immediately before the experiments and diluted 100-fold with the medium (final V concentrations, 100 mM). Figure (**d**) shows the UV-vis spectra of [V^{V}O(SALIEP)(Cat)], [V^{V}O(SALIEP)(4TB)], [V^{V}O(Cl-SALIEP)(Cat)] and [V^{V}O(Cl-SALIEP)(4TB)] (100 mM V) immediately after the addition to cell culture medium.

IV High-Resolution Mass Spectrometry

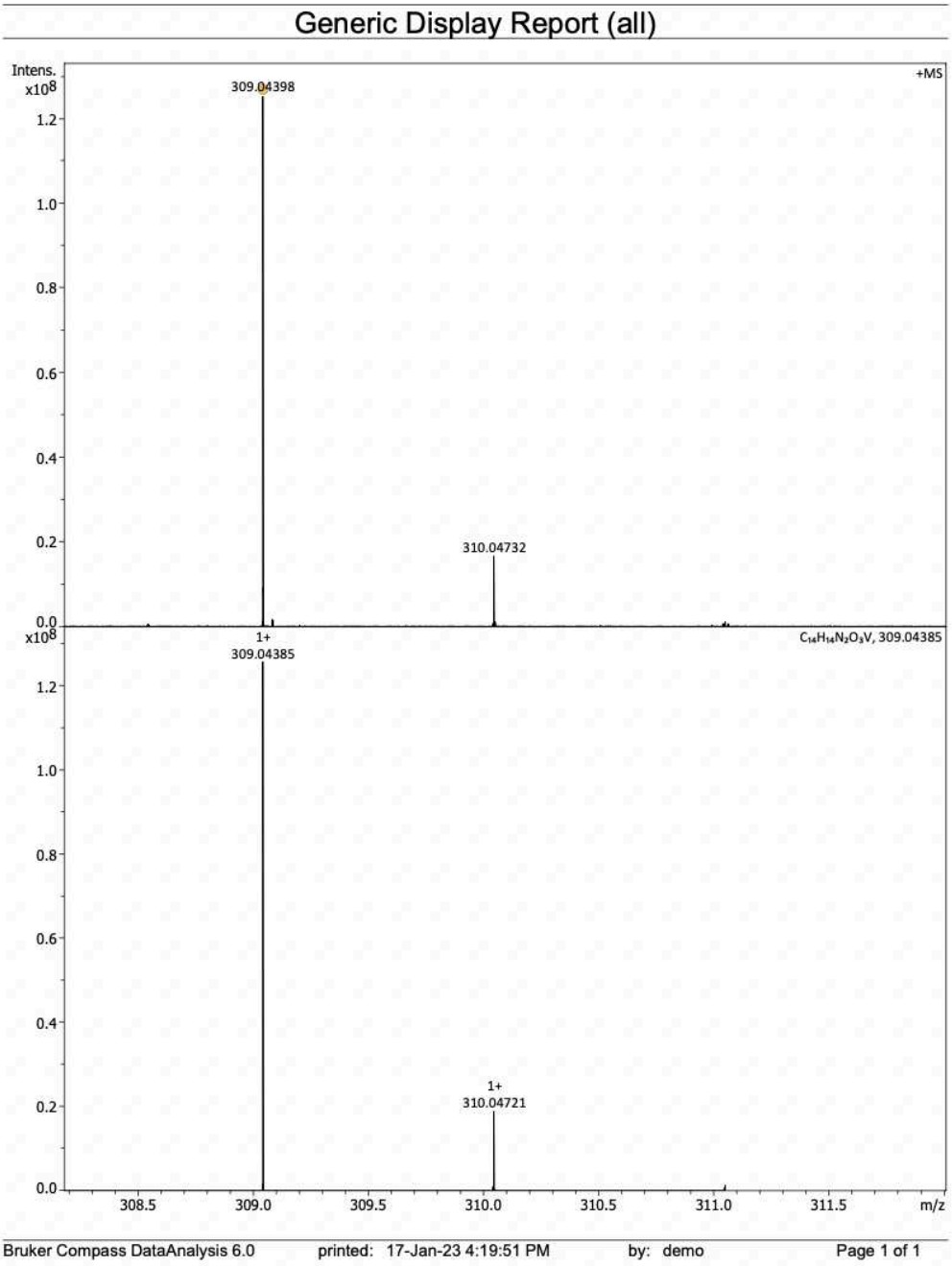

Figure A2.15. Experimental (top) and simulated (bottom) spectra of [VO_2(SALIEP)].

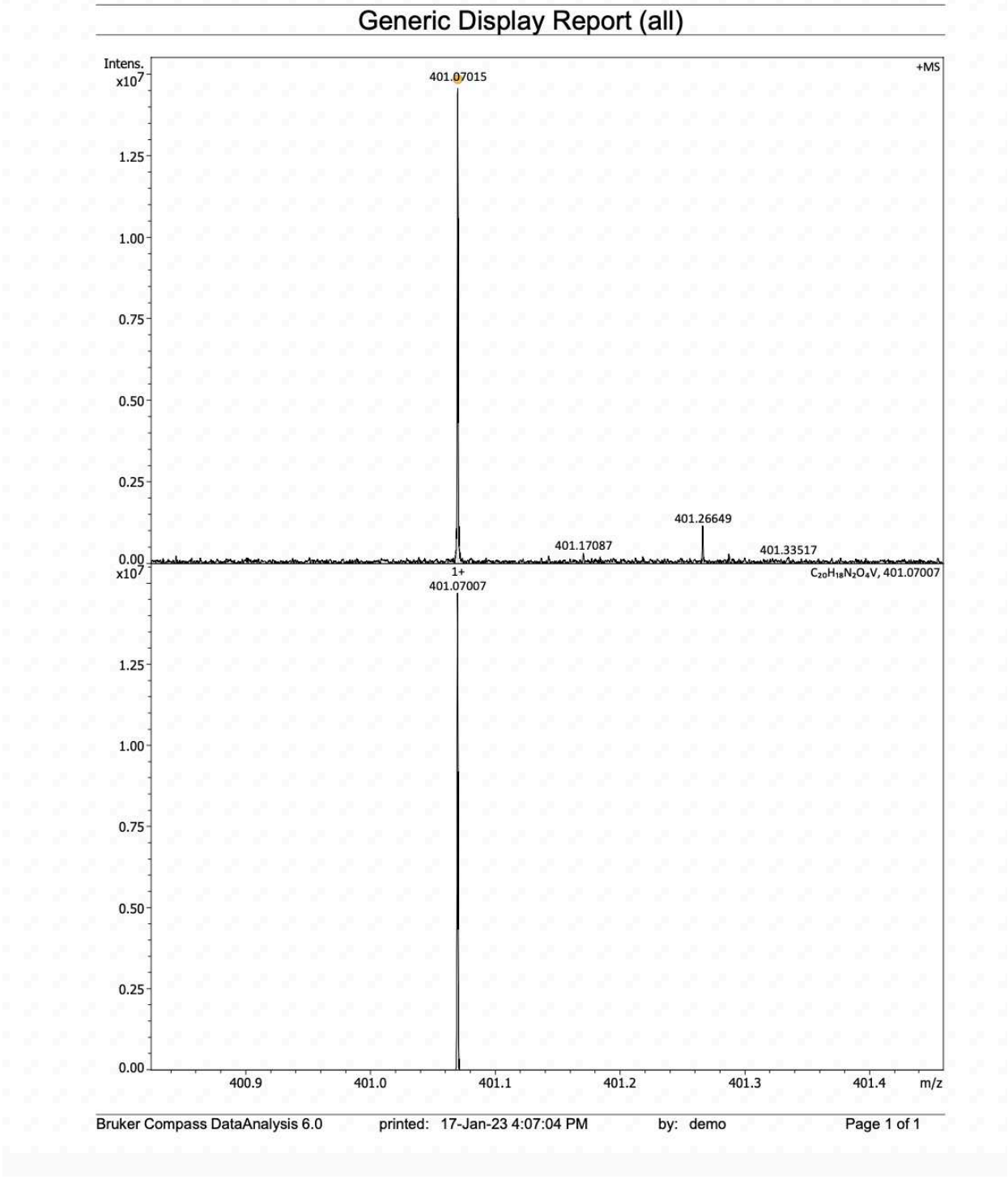

Figure A2.16. Experimental (top) and simulated (bottom) spectra of [VO(SALIEP)(Cat)].

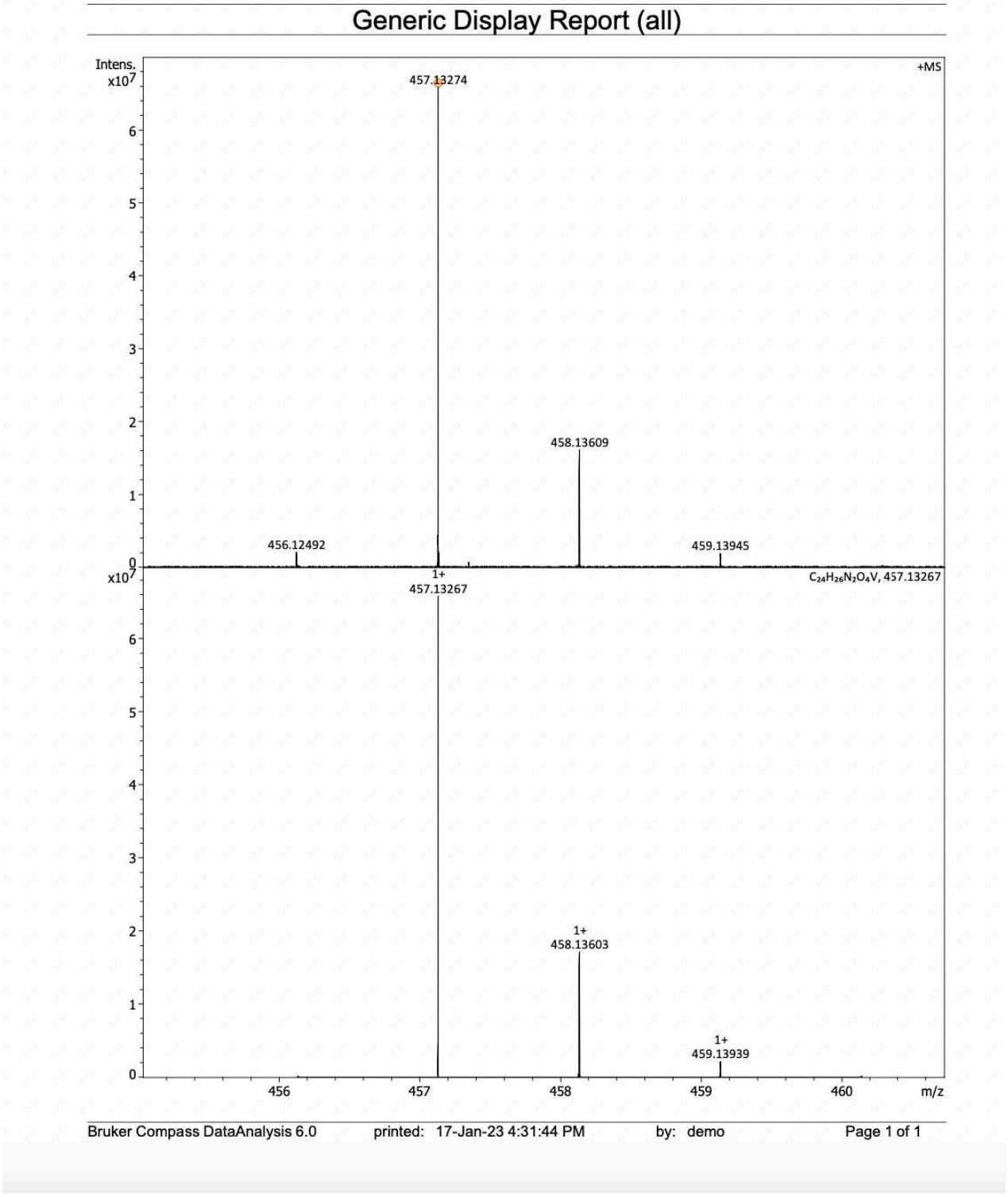

Figure A2.17. Experimental (top) and simulated (bottom) spectra of [VO(SALIEP)(4TB)].

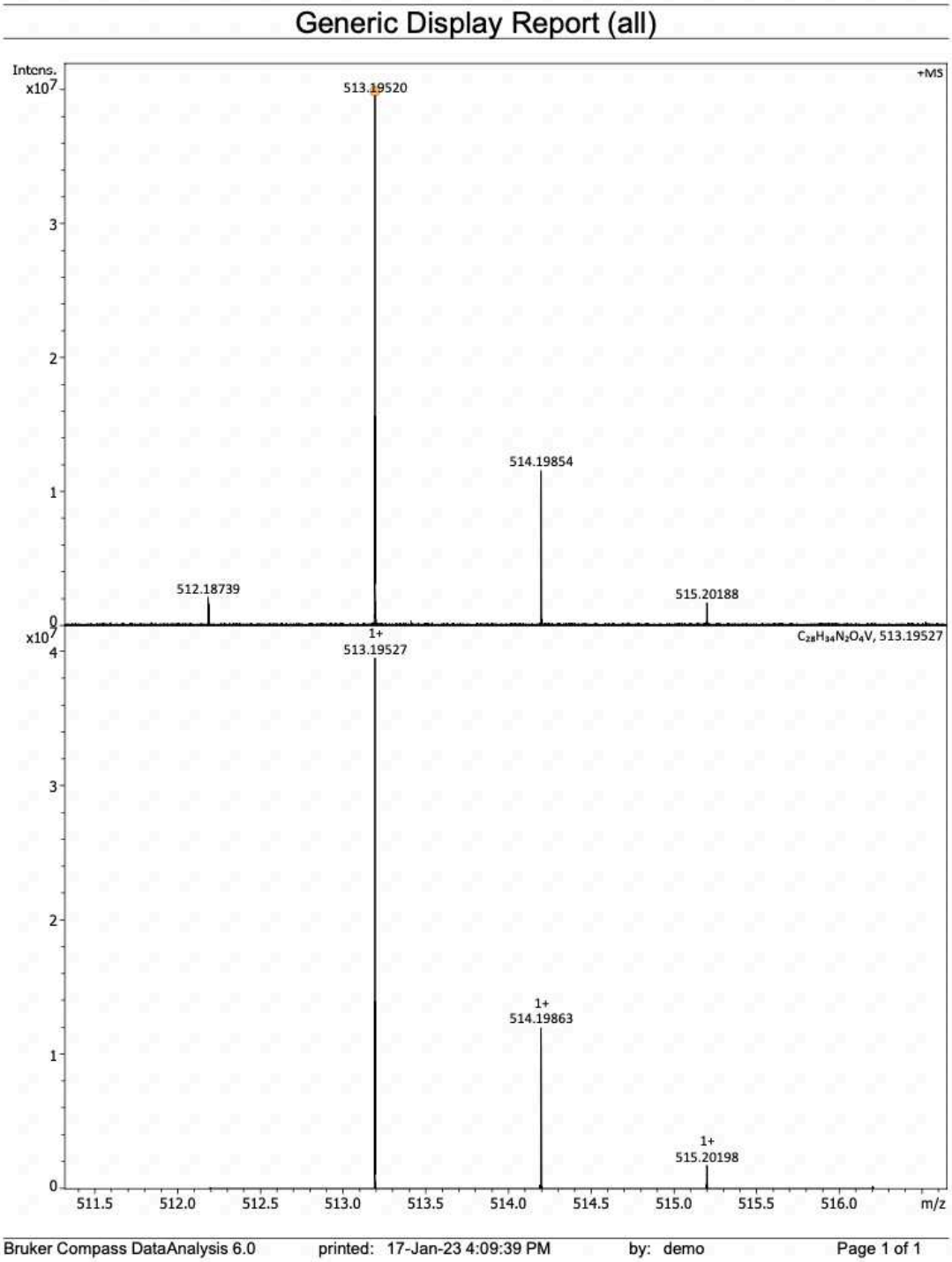

Figure A2.18. Experimental (top) and simulated (bottom) spectra of [VO(SALIEP)(DTB)].

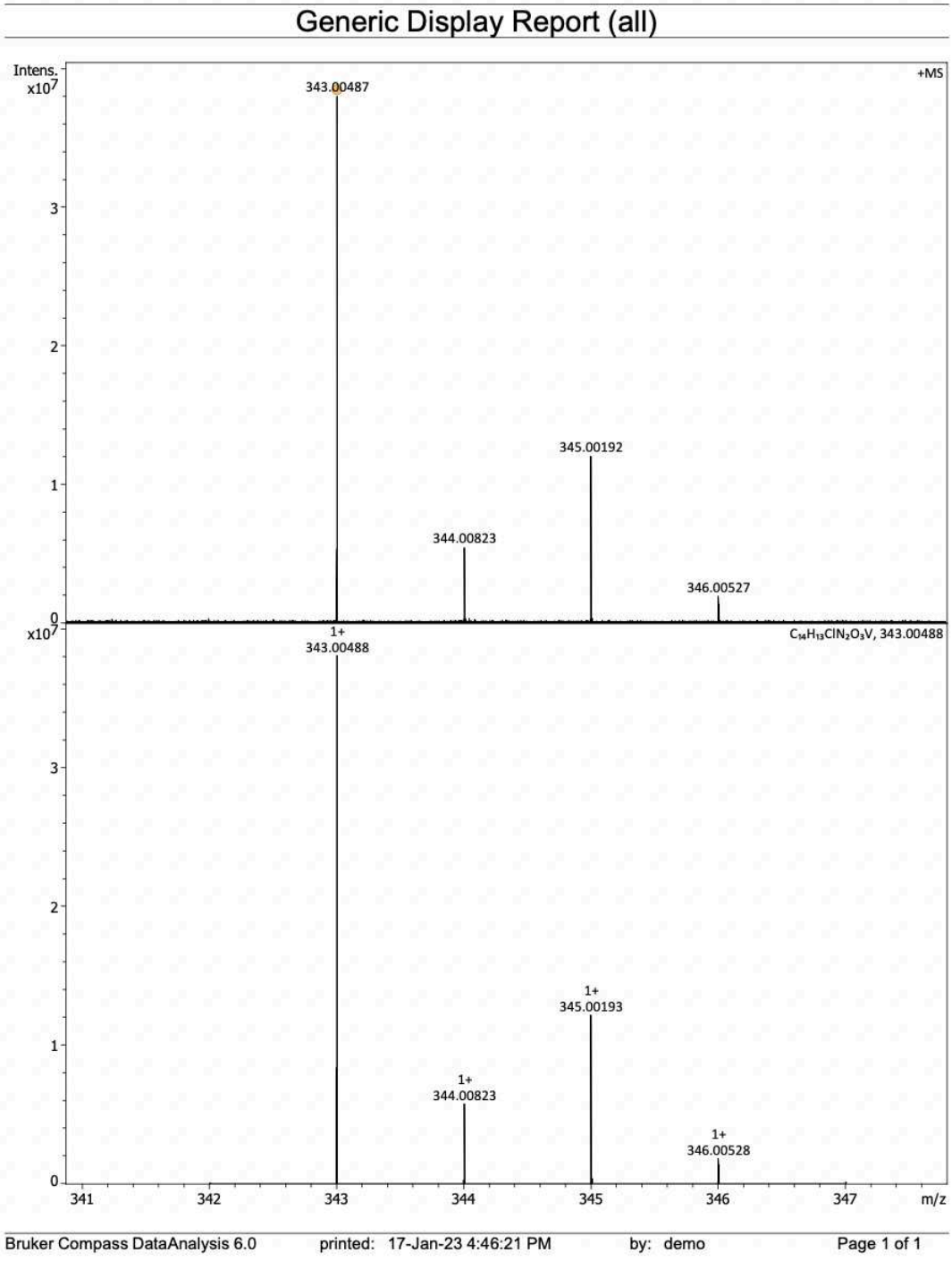

Figure A2.19. Experimental (top) and simulated (bottom) spectra of [VO_2(Cl-SALIEP)].

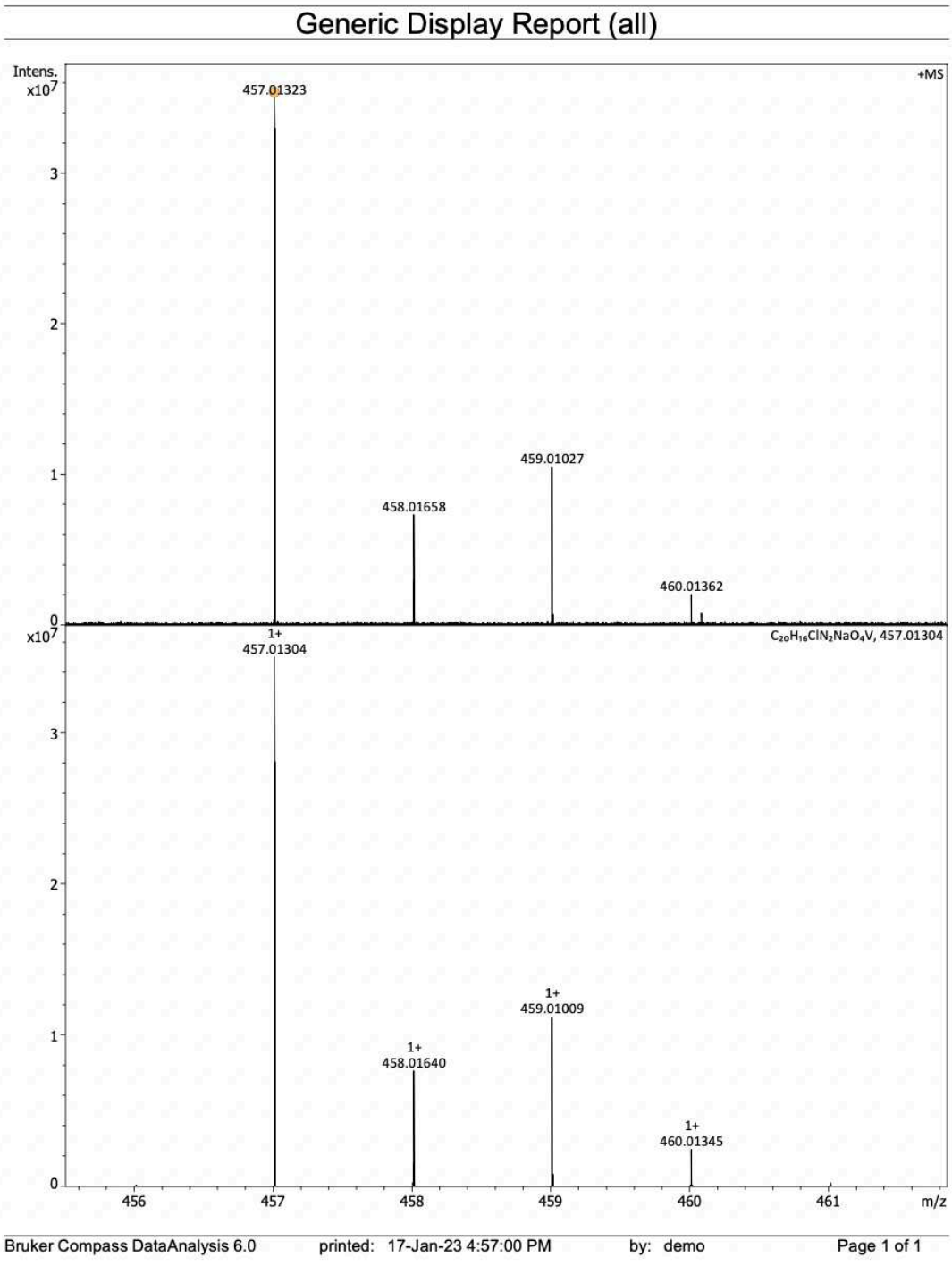

Figure A2.20. Experimental (top) and simulated (bottom) spectra of [VO(Cl-SALIEP)(Cat)].

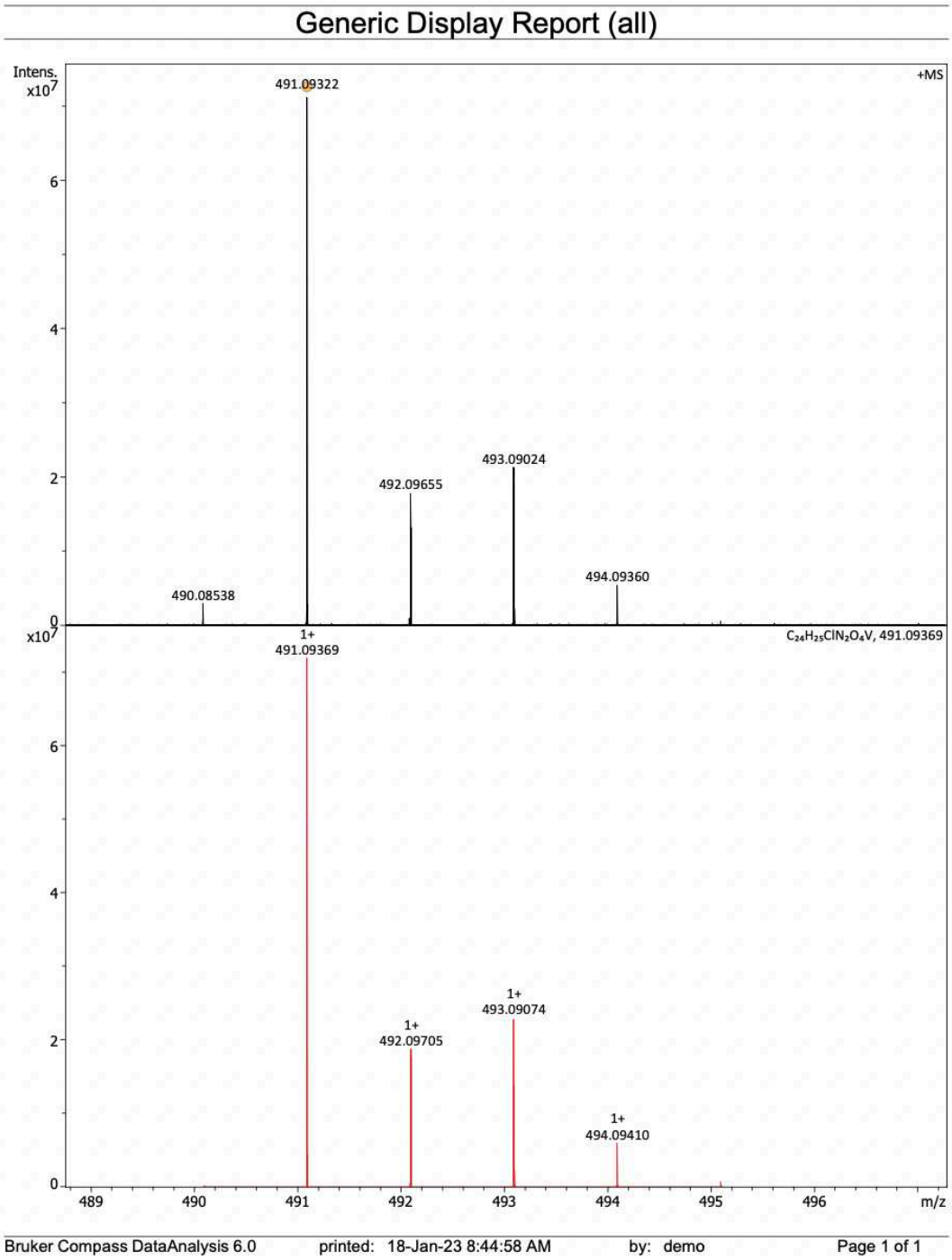

Figure A2.21. Experimental (top) and simulated (bottom) spectra of [VO(Cl-SALIEP)(4TB)].

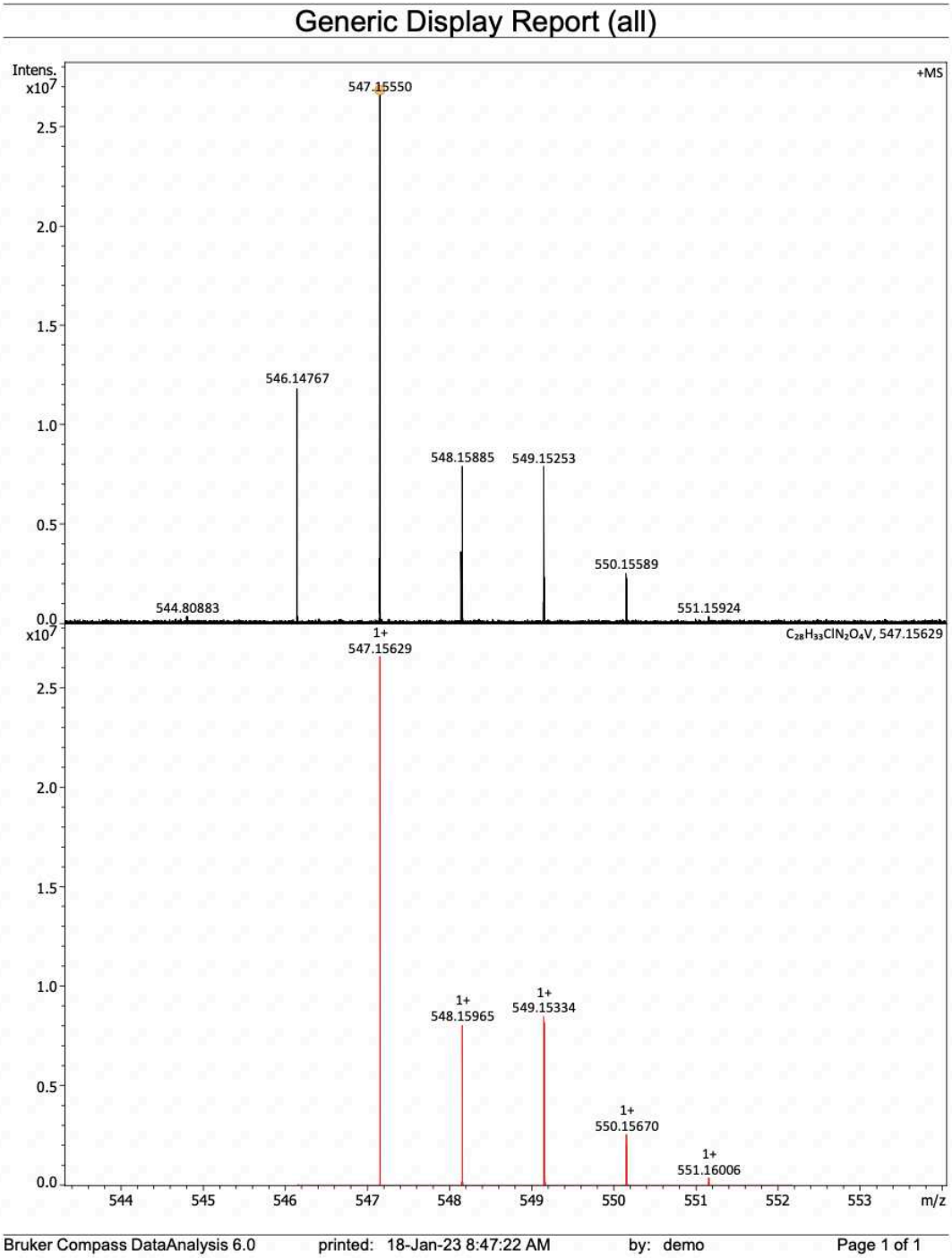

Figure A2.22. Experimental (top) and simulated (bottom) spectra of [VO(Cl-SALIEP)(DTB)].

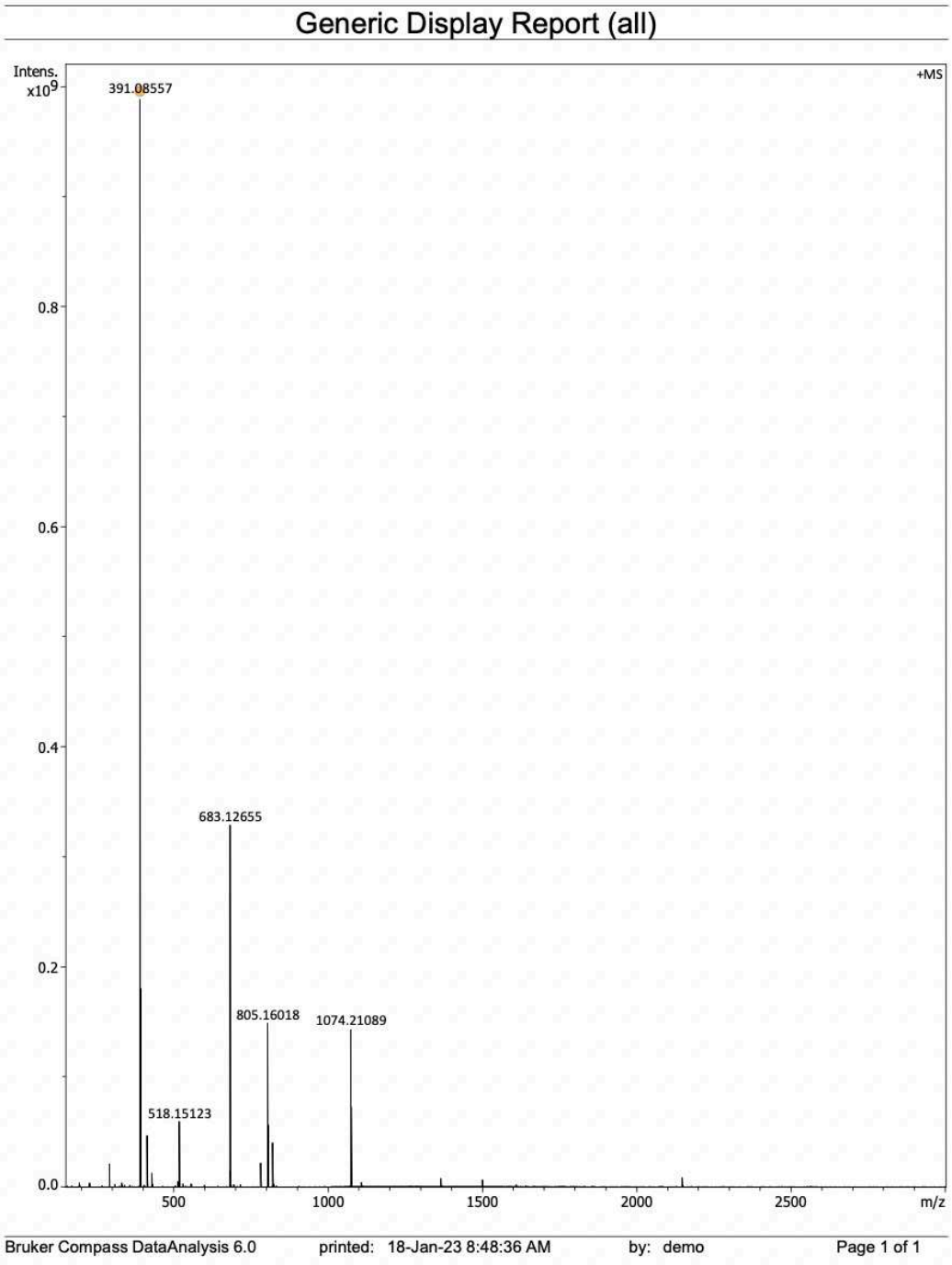

Figure A2.23. Experimental spectrum of [VO(SALIEP)(acac)].

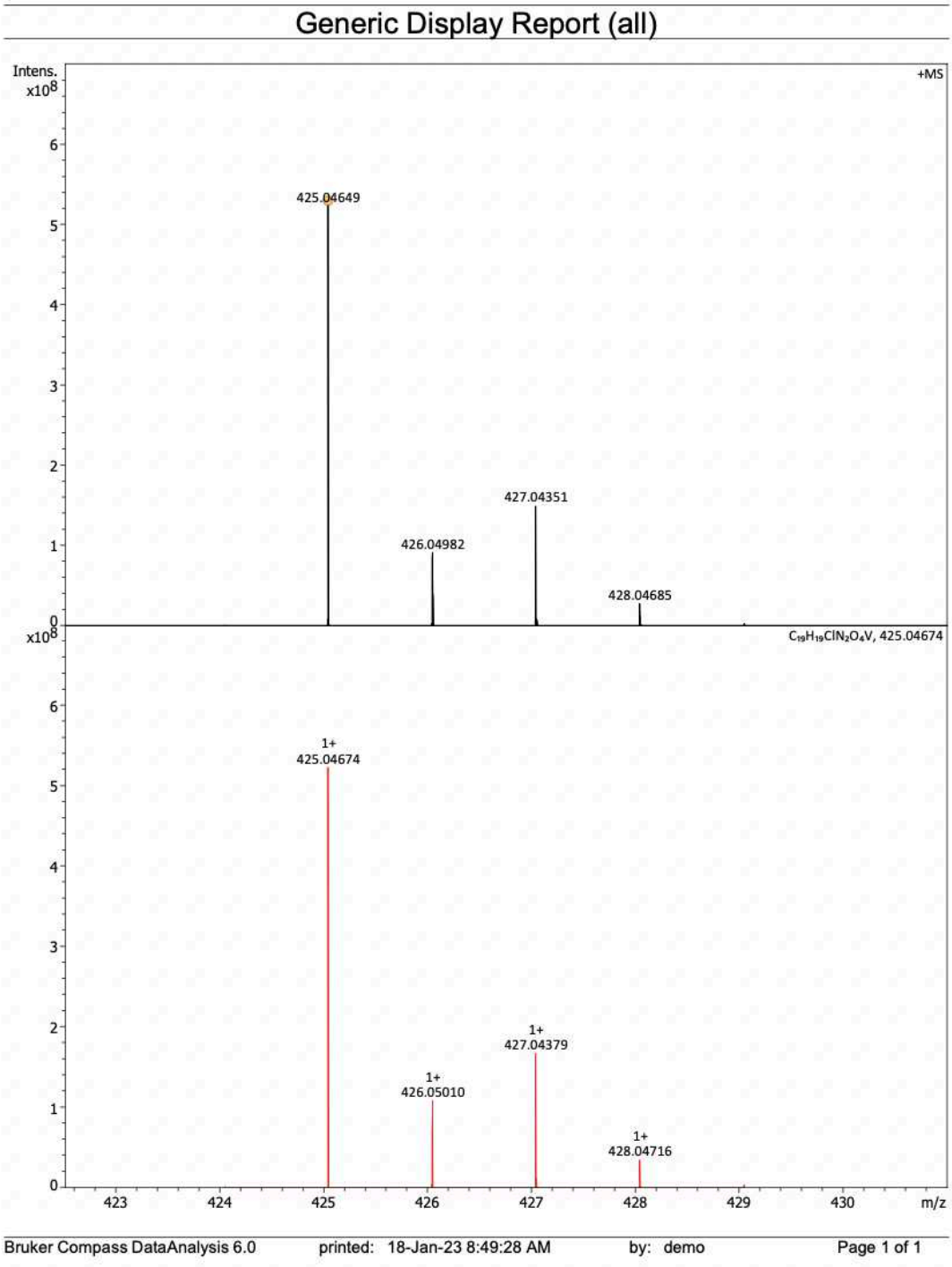

Figure A2.24. Experimental (top) and simulated (bottom) spectra of [VO(Cl-SALIEP)(acac)].

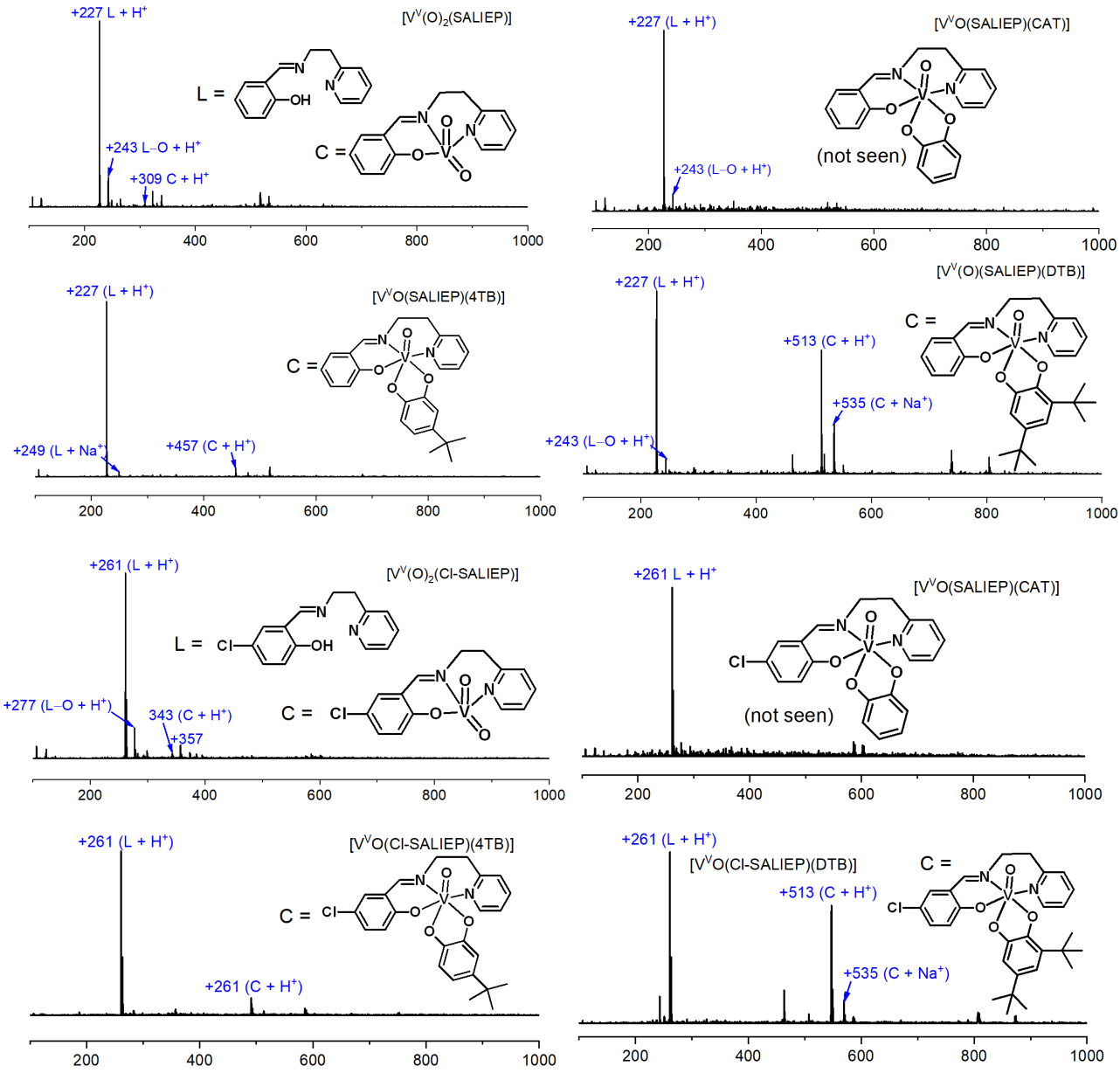

Figure A2.25. Typical low-resolution ESI-MS data for V(V) and V(IV) complexes. Spectra were collected immediately after dissolution of the solids in MeOH (~100 mM V).

V EPR

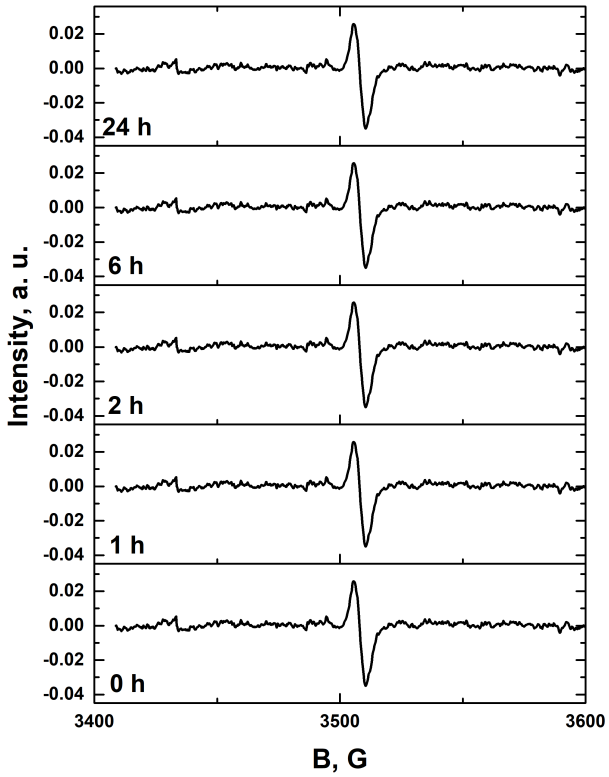

Figure A2.26. Room temperature stacked EPR spectra (3,400 – 3,600 G) of $[V^{IV}O(SALIEP)(Cat)]$ in 10.0 mM DMSO solutions with added $Zn(OAc)_2$ to trap the resulting semiquinone radicals.

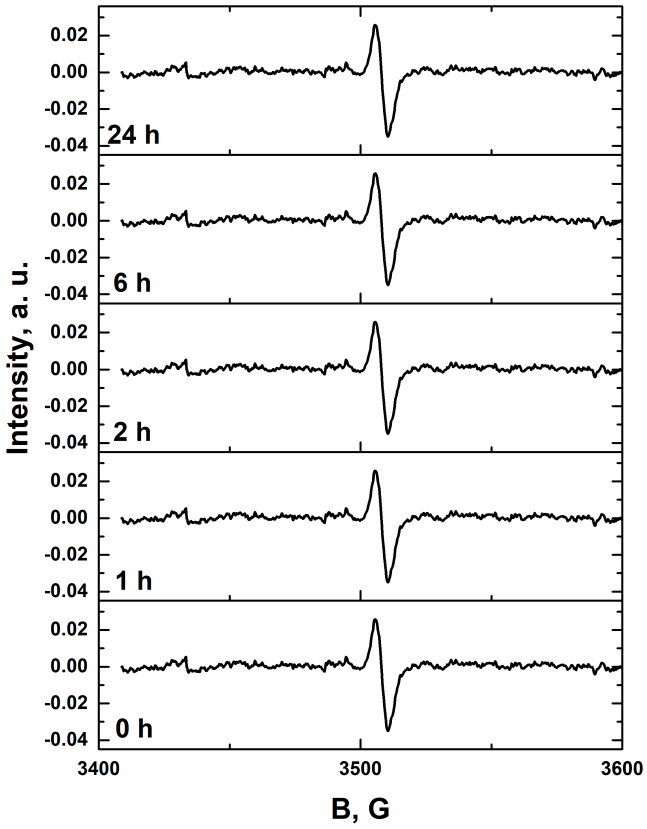

Figure A2.27. Room temperature stacked EPR spectra (3,400 – 3,600 G) of [$V^{IV}O$(Cl-SALIEP)(Cat)] in 10.0 mM DMSO solutions with added $Zn(OAc)_2$ to trap the resulting semiquinone radicals.

VI Biological Data

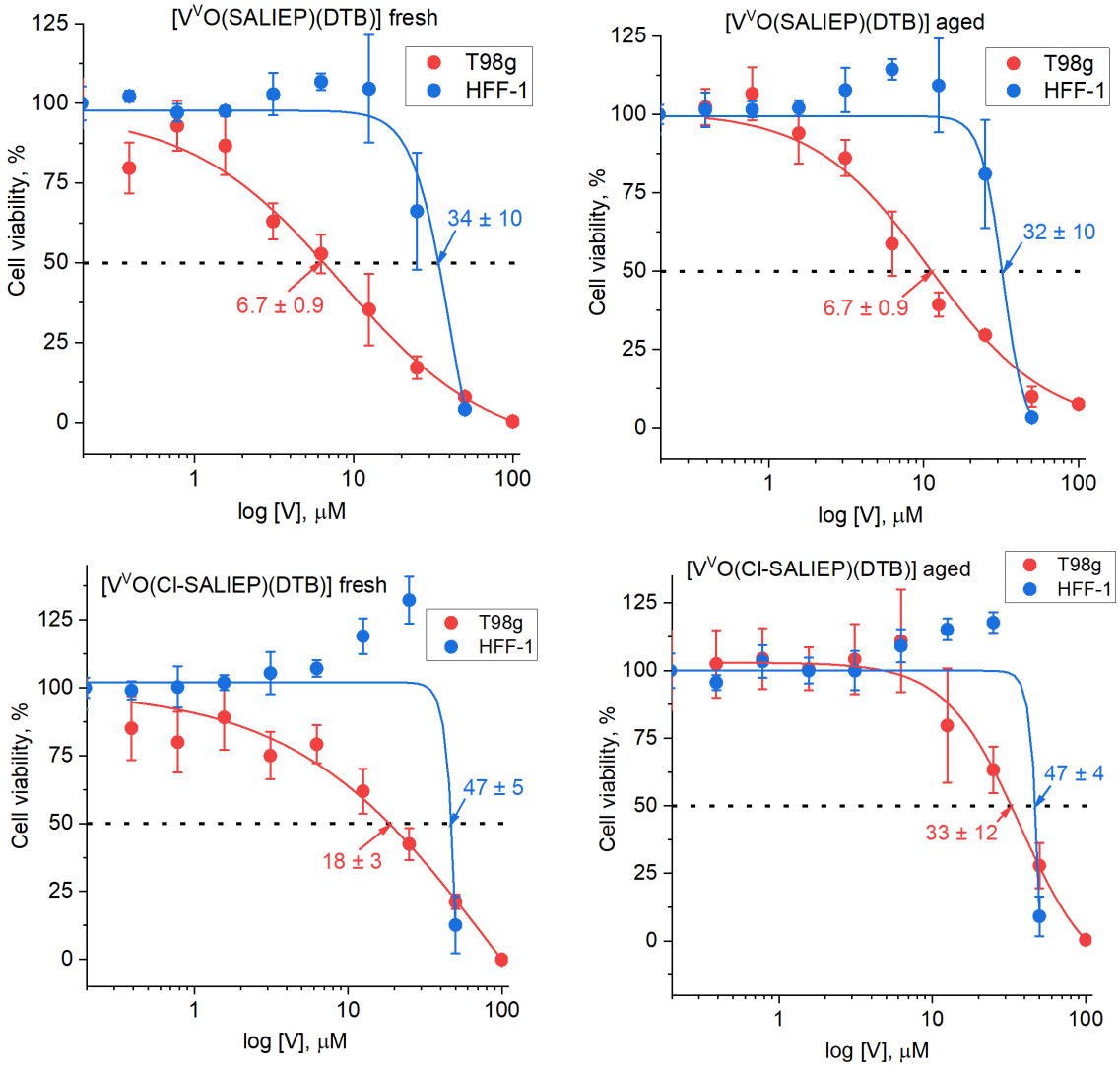

Figure A2.28. Concentration-dependent viabilities of T98g (red lines) and HFF-1 (blue lines) cells after 72 h treatments with fresh (~1 min after dissolution) and aged (30 min at 310 K and 5% CO_2) solutions of [$V^{V}O$(SALIEP)(DTB)], [$V^{V}O$(Cl-SALIEP)(DTB)], [$V^{V}O$(HSHED)(DTB)], and model solutions representing likely decomposition products (continued at the next page). Dots and error bars represent means and standard deviations of six replicate wells, and solid lines are sigmoidal fits of the experimental data. The only exception is the treatment of T98g cells with the mixture of Na_3VO_4 and $DTBH_2$, where a sigmoidal fit was not possible.

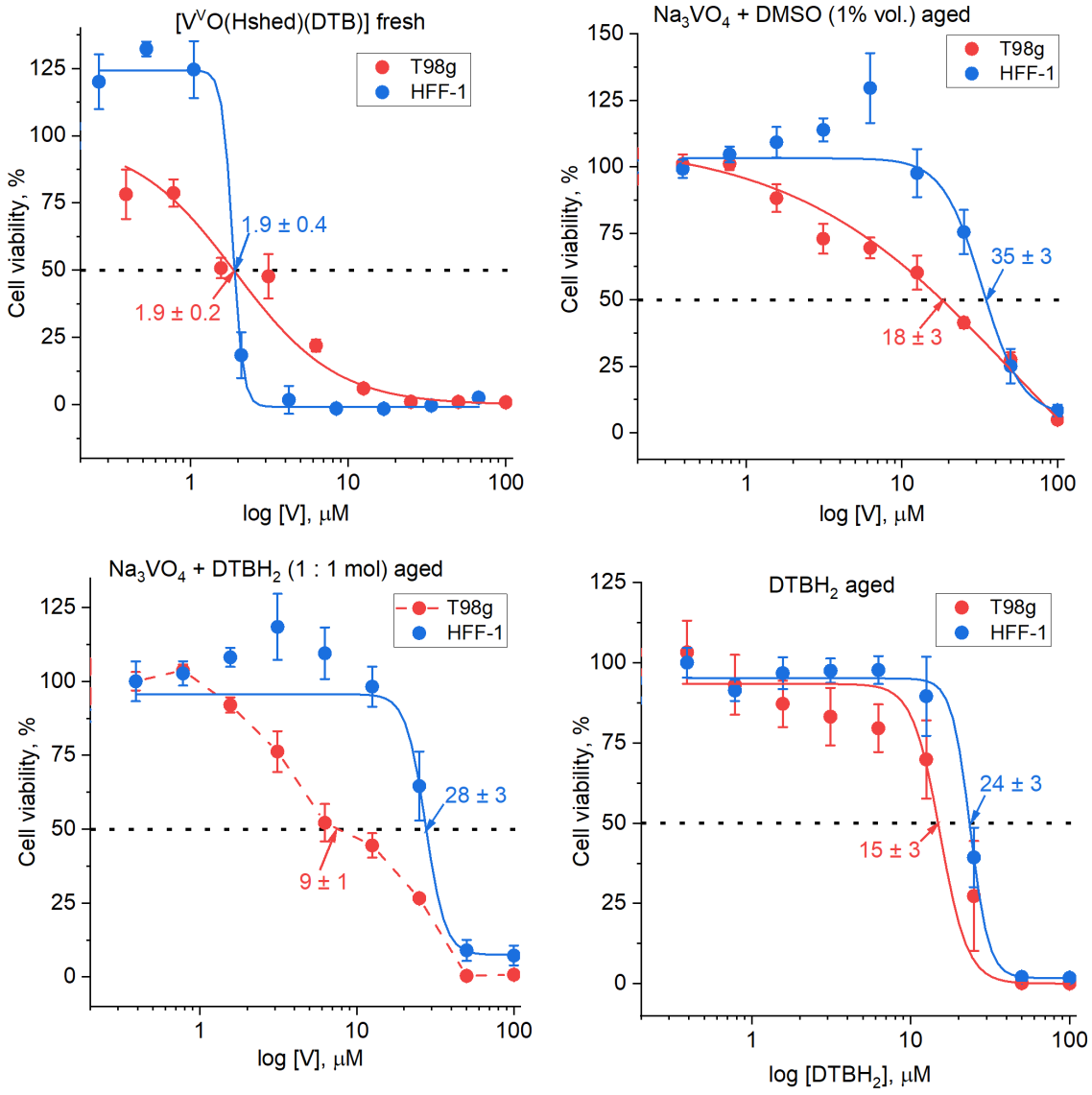

Figure A2.28 (end).

Appendix III: Supporting Information for Chapter 4

Section 1. Biological Data

The data shown in the manuscript was only the optimum concentration of effects – in this supplemental more information is provided.

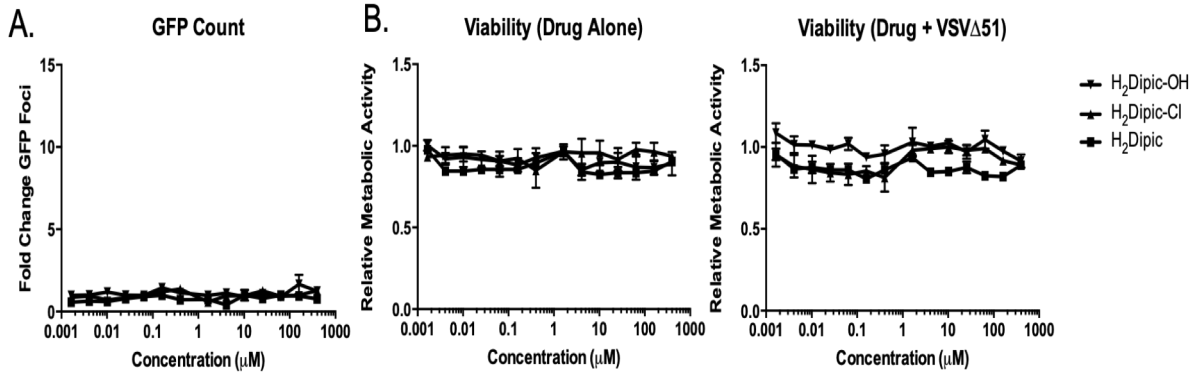

Supplemental Figure A3.1. Viability and GFP count of ligand controls. Human renal cell adenocarcinoma cells (786-0) were treated with free-ligand controls (0.002-400μM). 4 hours post treatment, cells were infected with VSVΔ51 expressing GFP at a multiplicity of infection (MOI) of 0.05. 24HPI, GFP images an indicator of viral replication, were captured and GFP foci quantified and normalized to untreated uninfected controls (A). 48hpi, the relative metabolic activity, an indicator of cell viability, was quantified (B) using the metabolic dye AlamarBlue® (530 excitation; 590 emission). Viability values are blank-controlled and normalized to uninfected untreated controls.

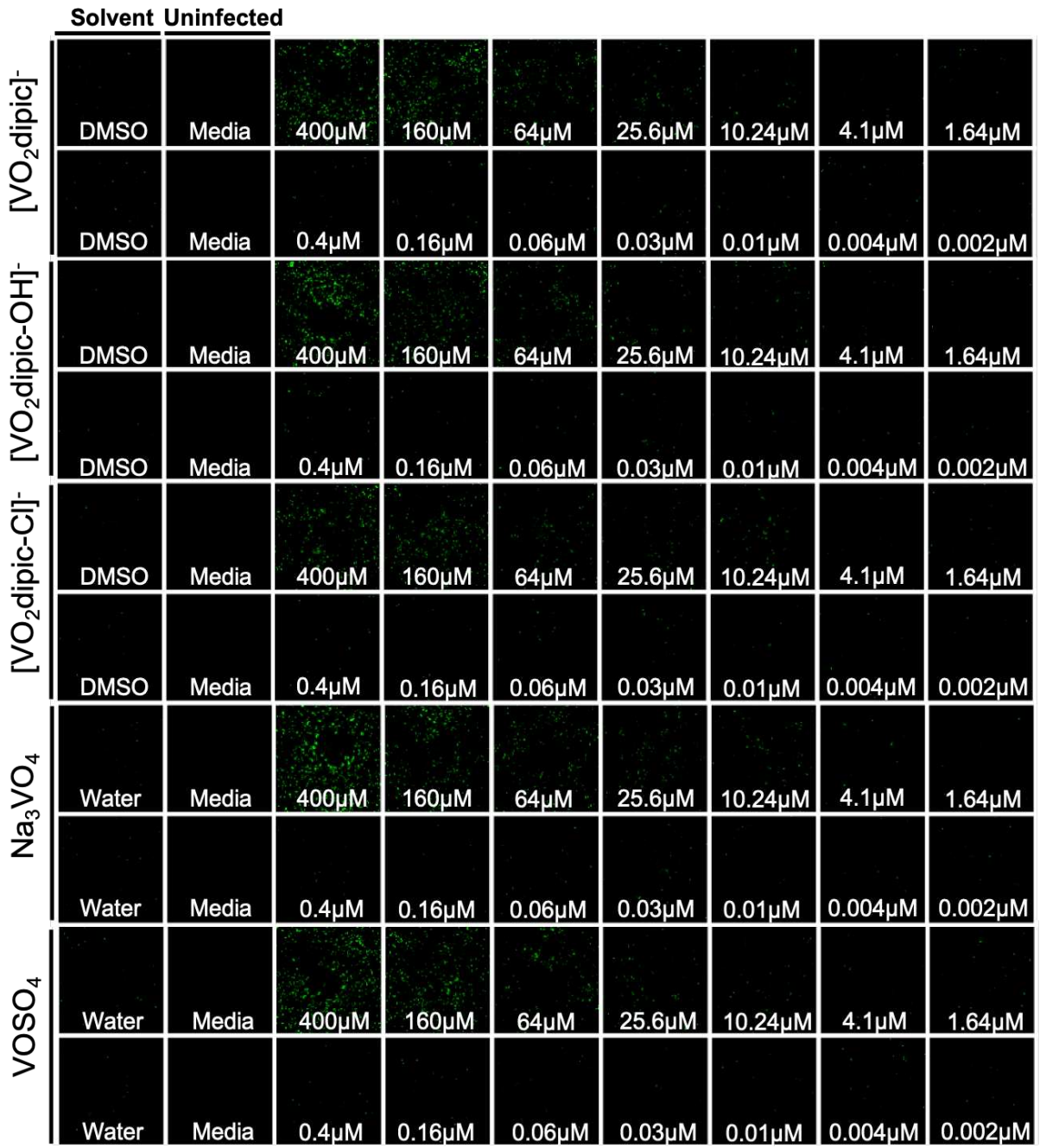

Supplemental Figure A3.2. GFP images of V-dipic compounds. 786-0 cells were pre-treated with compounds (0.002-400μM) or solvent alone (water or DMSO). 4 hours post treatment, cells were infected with VSVΔ51 expressing GFP at a multiplicity of infection (MOI) of 0.05. Untreated and uninfected cells (labelled 'Media') are shown as a negative control. As a reference, vanadate and vanadyl sulfate pre-treated cells are shown. 24HPI, GFP images were captured using fluorescence microscopy. The representative images of the full range of concentrations tested are presented. The n in the experiments is either 3 or 4.

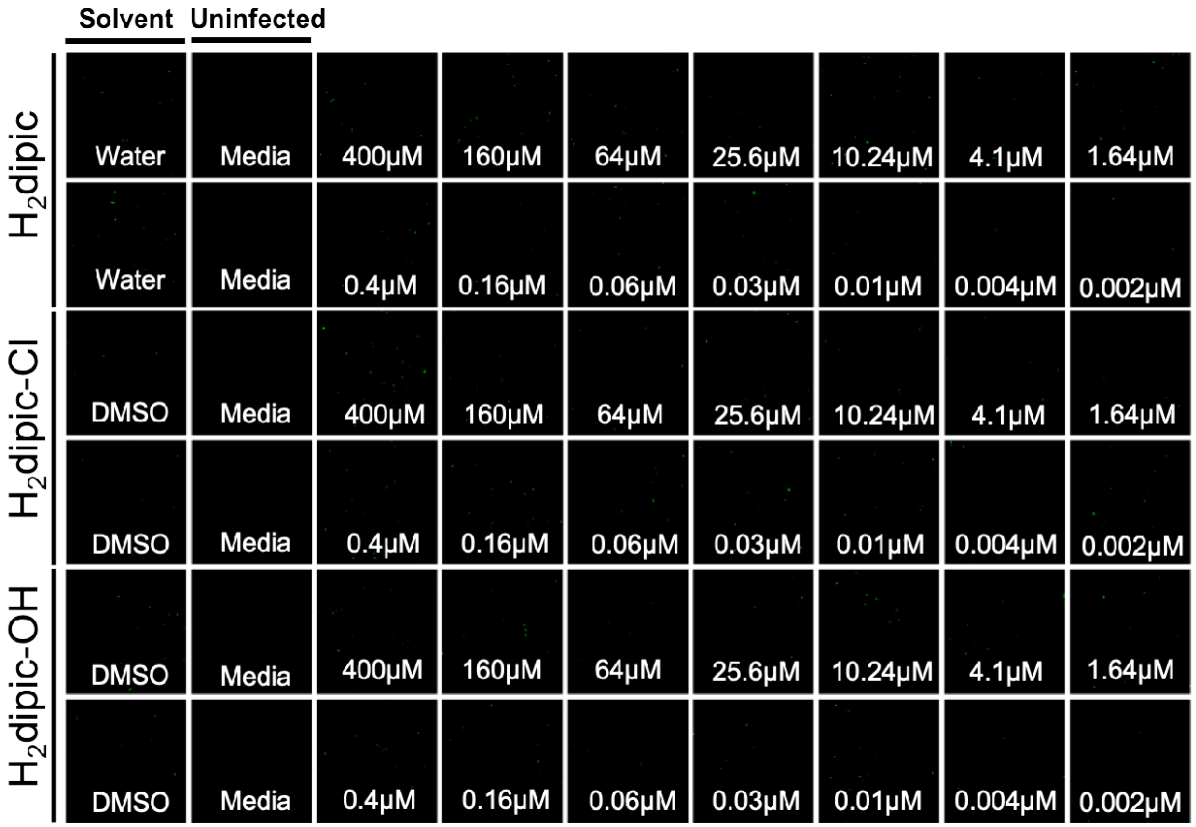

Supplemental Figure A3.3. GFP images of ligand controls. 786-0 cells were pre-treated with ligand controls or solvent alone (water or DMSO). 4 hours post treatment, cells were infected with VSVΔ51 expressing GFP at a multiplicity of infection (MOI) of 0.05. Untreated and uninfected cells (labelled 'Media') are shown as a negative control. 24HPI, GFP images were captured using by fluorescence microscopy. Representative images of the full range of concentrations tested are shown. The n in the experiments range from 2 to 4.

Section 2. Verification and Adjustment of Speciation Data for fit.

NMR spectra were recorded under conditions that speciation constants were determined previously (Crans et al 2000), and the experimental data was compared with these data. Once the previous work was verified, we used this data and recorded spectra at lower ionic strength for the fit in the cell culture media. This section thus describe how constants were obtained at the ionic strength consistent with that of the cell culture assays.

Supplemental Fig. A3.4. $[VO_2dipic]^-$ at pH = 6.60. The ^1H NMR spectra (a) and the ^{51}V NMR spectra (b) of aqueous solutions containing $[VO_2dipic]^-$ are shown

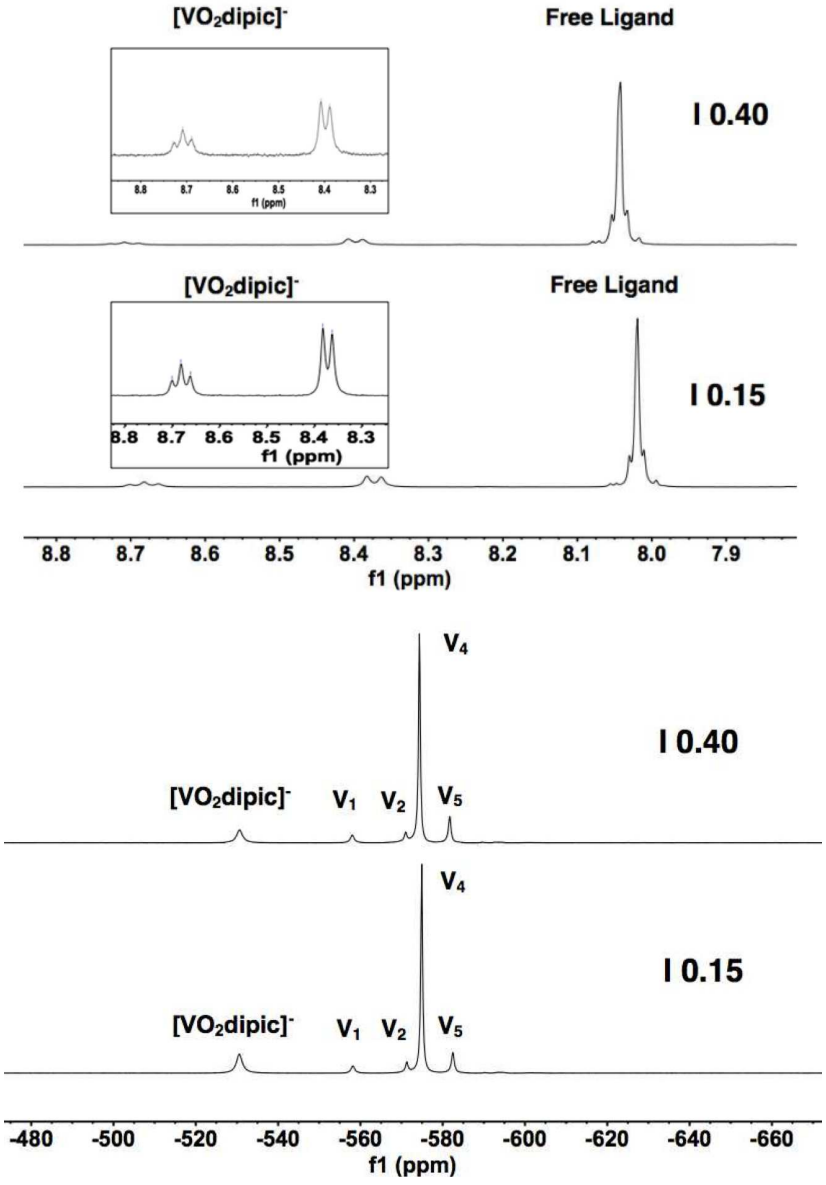

Using the data shown in for $[VO_2dipic]^-$ in **Fig. A3.4**, the concentrations of the species present at a given pH were calculated. The following concentrations were obtained by ^{51}V NMR spectroscopy: $[VO_2dipic^-]$. $[V_1]$ (=$[H_2VO_4^-]$), $[V_2]$, $[V_4]$ and $[V_5]$. The concentrations of $[VO_2dipic^-]$ and $[dipic^{2-}]$ were obtained by ^1H NMR spectroscopy. Those values were combined in the Supplemental **Table A3.1** below, and compared to the apparent formation constant calculated in the previous study which was 3.9×10^{-2} M^{-1} (Crans et al 2000). The measurements were done in triplicates, and the uncertainties for each concentration were calculated. The objective of the aforementioned calculations is to determine the apparent formation constant for the $[VO_2dipic]^-$ complex by using Equations (S1) and (S2). The calculation of the formation constants can be done by exclusively using the data obtained by by ^{51}V NMR where the $dipic^{2-}$ concentration is calculated by subtracting the concentration of the $[VO_2dipic^-]$ complex from the total concentration (in mM), or by ^1H NMR where the V_1 concentration from the ^{51}V studies is used in the calculation.

$$dipic^{2-}(or\ dipic - Cl^{2-}) + H_2VO_4^- \underset{+H^+}{\overset{-H^+}{\rightleftharpoons}} [VO_2dipic]^- \qquad \text{(S1)}$$

$$K_{eq} = \frac{[VO_2dipic]^-}{[dipic^{2-}][H_2VO_4^-]} \qquad \text{(S2)}$$

Supplemental Table A3.1. The concentrations, experimentally determined by ^{51}V and ^1H NMR, that were used to calculate the values for the apparent formation constant according to Eq (2).

			^{51}V NMR	^{51}V NMR	^{51}V NMR	^1H NMR	^1H NMR	^{51}V NMR	^1H NMR
[V-atom], mM	Ionic strength	pH	$[VO_2dipic]^-$	dipic	V_1	$[VO_2dipic]^-$	dipic	Formation Constant	Formation Constant
5.00	0.40	6.69	0.85 (± 0.07)	4.15 (± 0.07)	0.60 (± 0.04)	0.85(± 0.07)	4.15 (± 0.07)	**340**	**340**
5.00	0.40	6.60	0.75 (± 0.07)	4.25 (± 0.07)	0.60 (± 0.04)	0.75 (± 0.07)	4.25 (± 0.07)	**290**	**290**
5.00	0.40	6.55	0.80 (± 0.07)	4.20 (± 0.07)	0.60 (± 0.04)	0.80 (± 0.07)	4.10 (± 0.07)	**370**	**370**
5.00	0.40	6.60	0.90 (± 0.07)	4.10 (± 0.07)	0.65 (± 0.04)	0.90 (± 0.07)	4.20(± 0.07)	**290**	**290**
5.00	0.40	6.66	0.75 (± 0.07)	4.25 (± 0.07)	0.55 (± 0.04)	0.75(± 0.07)	4.25 (± 0.07)	**320**	**320**

	Average	**320 (± 30)**	**320 (± 30)**

Once the data at the 0.40 ionic strength was verified, similar measurements were done at the 0.15 ionic strength. Those measurements allowed the remaining data in Table S2 to be constructed. The difference in those two values was used to determine the β needed for the HySS calculations of the speciation. Once this difference was determined, the corresponding apparent constants for the $[VO_2dipic\text{-}Cl]^-$ and $[VO_2dipic\text{-}OH]^-$ were obtained.

Supplemental Table A3.2. The concentrations, experimentally determined by ^{51}V and ^{1}H NMR, that were used to calculate the values for the apparent formation constant according to Eq (S2).

			^{51}V NMR	^{51}V NMR	^{51}V NMR	^{1}H NMR	^{1}H NMR	^{51}V NMR	^{1}H NMR
[V-atom], mM	Ionic strength	pH	$[VO_2dipic]^-$	dipic	V_1	$[VO_2dipic]^-$	dipic	Formation Constant	Formation Constant
5.00	0.15	6.60	0.65 (± 0.10)	4.35 (± 0.10)	1.05 (± 0.18)	0.65 (± 0.10)	4.35 (± 0.10)	**124**	**149**
5.00	0.15	6.60	0.75 (± 0.10)	4.25 (± 0.10)	0.75 (± 0.18)	0.75 (± 0.10)	4.25 (± 0.10)	**240**	**240**
5.00	0.15	6.60	0.85 (± 0.10)	4.15 (± 0.10)	0.60 (± 0.18)	0.65 (± 0.10)	4.35 (± 0.10)	**230**	**130**
							Average	**156 (± 80)**	**207 (± 50)**
25.00	0.15	6.60	5.00 (± 0.50)	4.70 (± 0.50)	1.00 (± 0.00)	4.75 (± 0.50)	20.25 (± 0.50)	**200**	**240**
25.00	0.15	6.60	4.50(± 0.50)	21.25 (± 0.50)	1.00 (± 0.00)	4.25 (± 0.50)	20.75 (± 0.50)	**180**	**210**
25.00	0.15	6.60	4.00(± 0.50)	22.00 (± 0.50)	1.00 (± 0.00)	5.25 (± 0.50)	19.75 (± 0.50)	**160**	**270**
							Average	**128 (± 20)**	**237 (± 32)**

Supplemental Fig. A3.5 $[VO_2dipic]^-$ at pH = 6.00. The ^1H NMR spectra (a) and the ^{51}V NMR spectra (b) of aqueous solutions containing $[VO_2dipic]^-$ are shown.

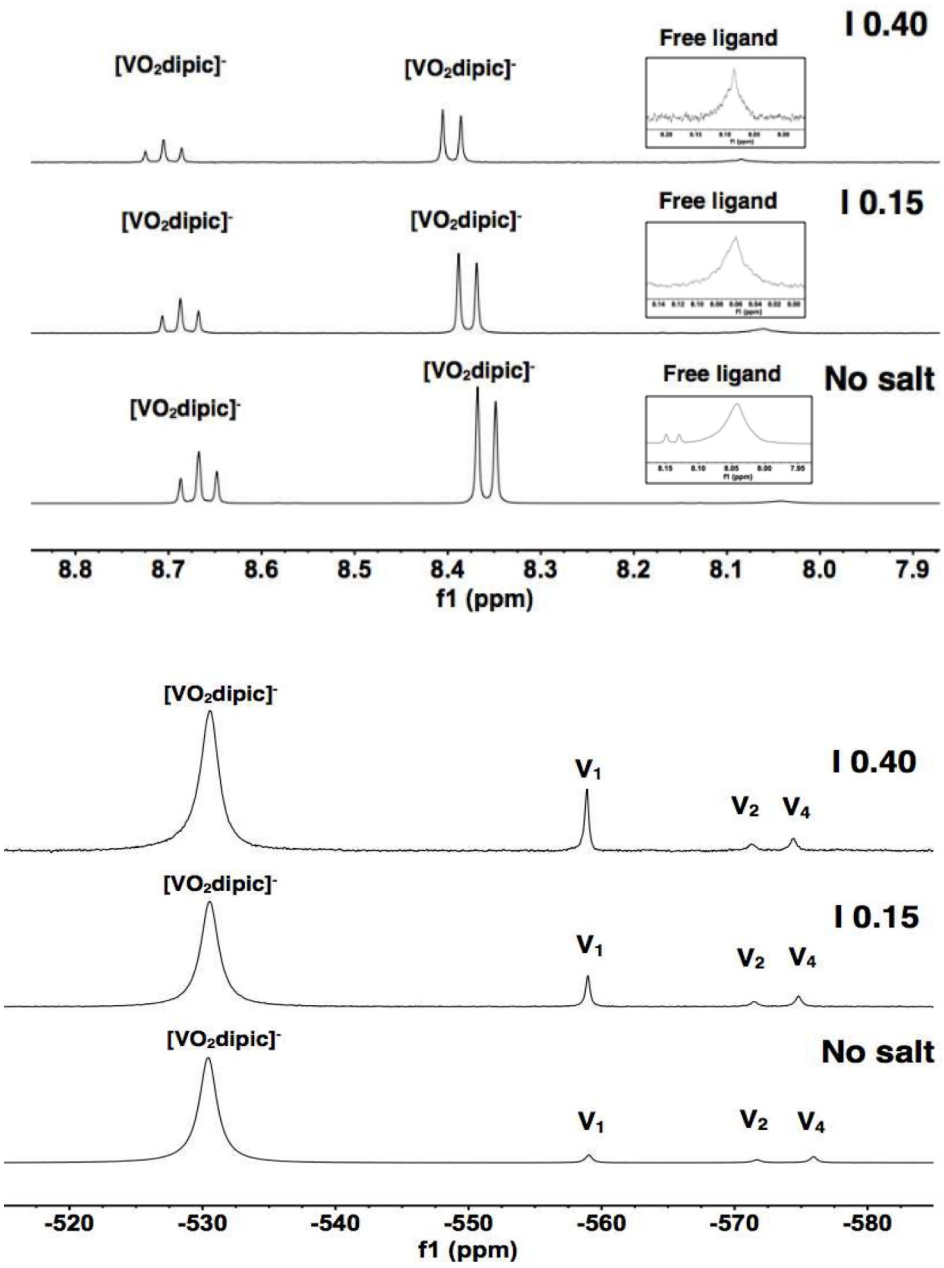

Supplemental Fig. A3.6. [VO_2dipic-Cl]$^-$ at pH = 6.00. The ^{1}H NMR spectra (a) and the ^{51}V NMR spectra (b) of aqueous solutions containing [VO_2dipic-Cl]$^-$ are shown.

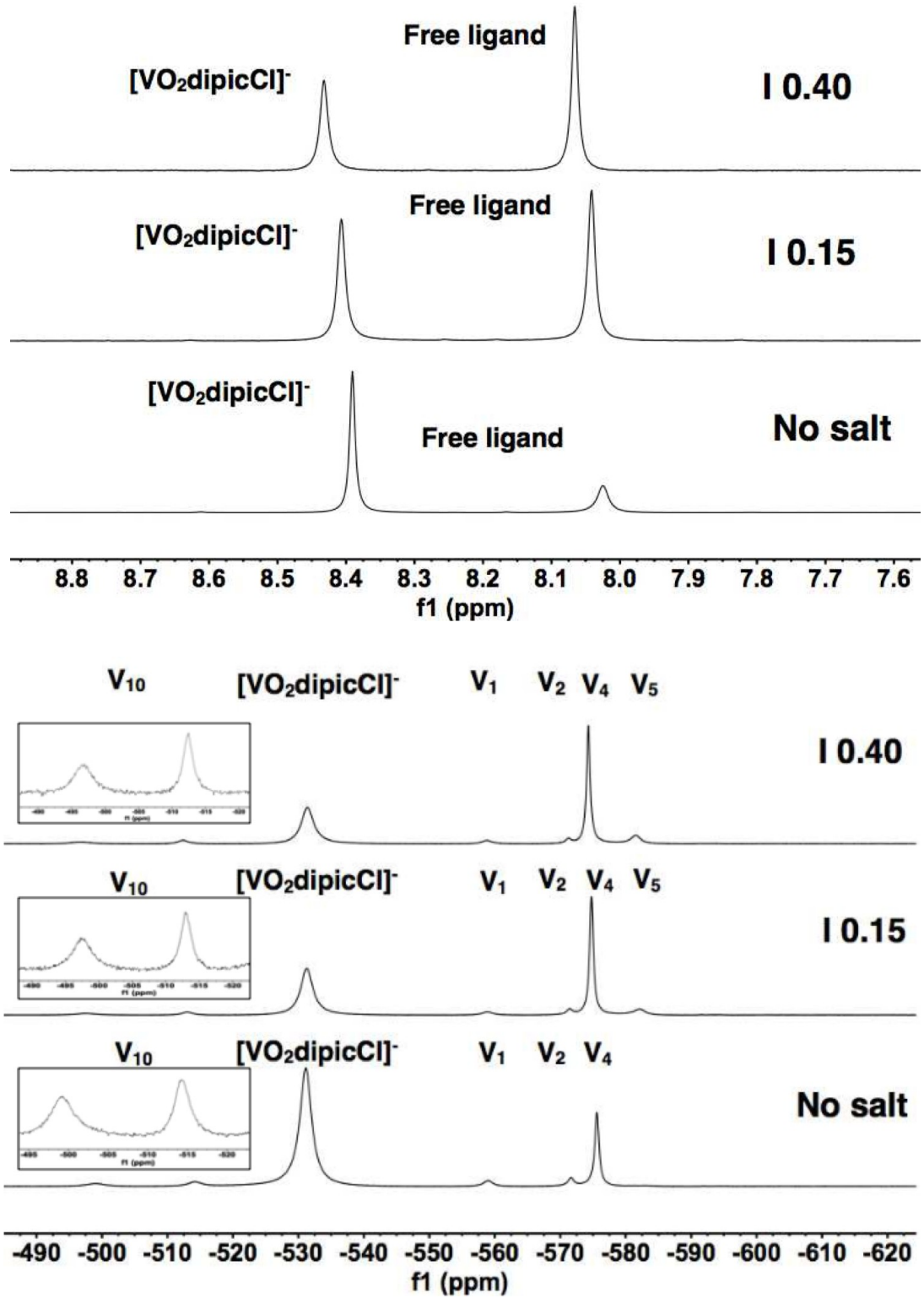

Supplemental Fig. A3.7. [VO_2dipic-Cl]$^-$ at pH = 5.50. The ^{1}H NMR spectra (a) and the ^{51}V NMR spectra (b) of aqueous solutions containing [VO_2dipic-Cl]$^-$ are shown

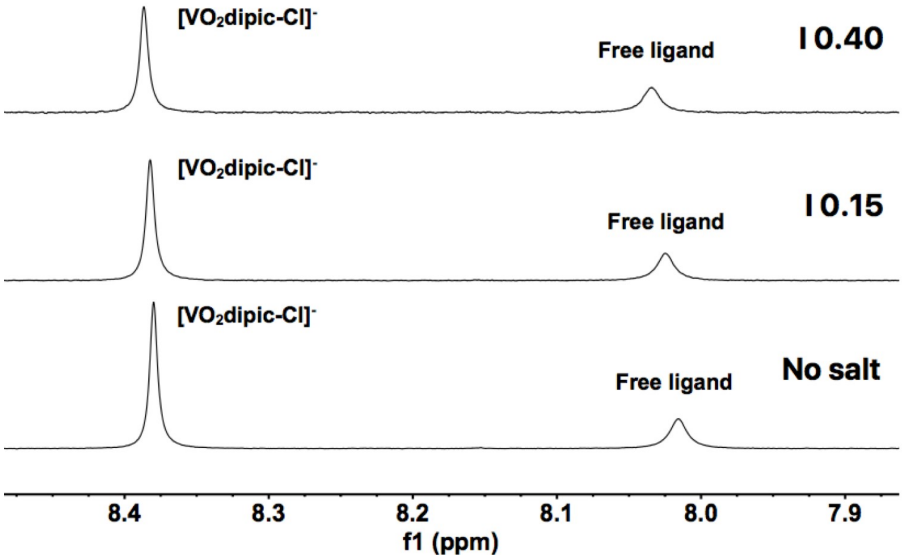

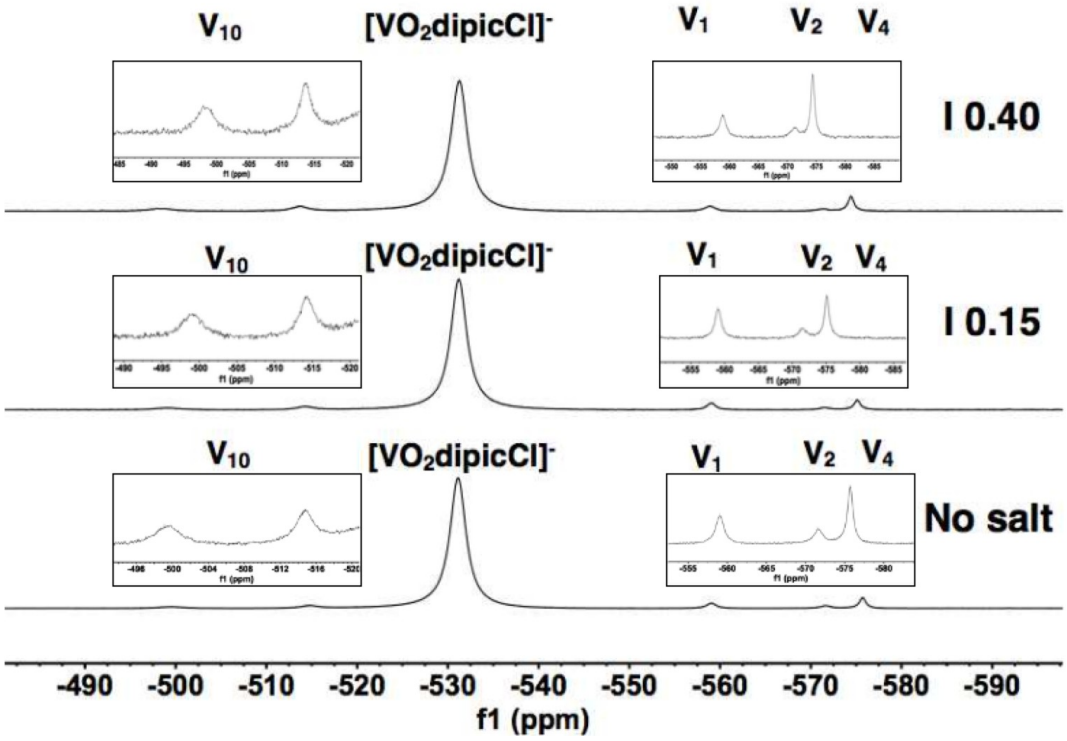

Section 3. Speciation Predictions of $[VO_2dipic]^-$, $[VO_2dipic\text{-}Cl]^-$, and $[VO_2dipic\text{-}OH]^-$

Determination of cell culture media ionic strength

The ionic strength, μ, of the media for cell assays was calculated using the equation for ionic strength (S3) assuming that the pH of the medium is 7.4.

$$\mu = {}^1/_2 \sum_1^n c_i z_i^2 \quad \text{(S3)}$$

The composition of the Dulbecco's Modified Eagle's Medium was found from Levina et al. 2017 and the components are listed in Supplemental Table S3. The composition of the AlbuMAX was from the product page found on ThermoFisher (https://www.thermofisher.com/order/catalog/product/11020021?CID=AFLBC-11020021) is listed in Supplemental Table S3. The composition of the fetal bovine serum used in the calculations was obtained from the average values given in Lindl et al. The charges of each medium component at pH 7.4 were determined and squared. These calculated charges were then multiplied by the corresponding concentration of each ion in the solution. All the ions were summed and then multiplied by one-half to get the ionic strength of 0.17 M. This result allows us to use the experimental values at I = 0.15 M to do the speciation calculations on the vanadium compounds added to the cells. NMR analysis of the compounds in the media showed a significant difference in the concentration of $[VO_2dipic]^-$ at different ionic strengths. This shows the importance of calculating the ionic strength of the media so we know how compounds will speciate once they've been added to the cells and what major compounds will remain to influence the results of the experiment.

Supplemental Table S3. Listing the components in the Dulbecco's Modified Eagle's Medium (Levina et al. 2017) and the components in the AlbuMAX (product page found on ThermoFisher https://www.thermofisher.com/order/catalog/product/11020021?CID=AFLBC-11020021)

Ion	From Compound	Molar Concentration	Contribution to Ionic Strength
Dulbecco's Modified Eagle's Medium (Levina et al. 2017)			
Na (+)	NaCl	1.1E-1	1.1E-1
	NaHCO3	4.4E-2	4.4E-2
	Na_2HPO_4	7.8E-4	1.6E-3
	Sodium Pyruvate	1.0E-3	1.0E-3
	Fetal Bovine Serum	1.4E-3	1.4E-3
	Na_2SeO_3	2.9E-8	5.8E-8
K (+)	KCl	5.4E-3	5.4E-3
	Fetal Bovine Serum	1.1E-4	1.1E-4
Ca (2+)	$CaCl_2$	1.8E-3	7.2E-3
	Fetal Bovine Serum	3.4E-5	1.3E-4
	Calcium d-panthothenate	8.4E-6	3.4E-5

Mg (2+)	$MgSO_4$	8.1E-4	3.2E-3
	Ascorbic Acid Phosphate	7.8E-6	9.4E-5
Se (2+)	Fetal Bovine Serum	3.3E-9	1.3E-8
Urate (+)	Fetal Bovine Serum	1.7E-6	1.7E-6
Creatinine (+)	Fetal Bovine Serum	2.7E-6	2.7E-6
Choline (+)	Choline Chloride	2.9E-5	2.9E-5
$C_{12}H_{18}N_4OS$ (2+)	Thiamine Hydrochloride	1.2E-5	1.2E-5
Cu (2+)	$CuSO_4$	5.0E-9	2.0E-8
Fe (3+)	$Fe(NO_3)_3$	2.5E-7	2.3E-6
Mn (2+)	$MnSO_4$	2.0E-10	8E-10
NH4 (+)	NH_4VO_3	2.5E-9	2.5E-9
Lysine (+)	Amino Acids	2.7E-9	2.7E-9
Histidine (+)	Amino Acids	6.7E-5	6.7E-5
Arginine (+)	Amino Acids	2.0E-5	2.0E-5
Cl (-)	NaCl	1.1E-1	1.1E-1
	KCl	5.4E-3	5.4E-3
	$CaCl_2$	1.8E-3	3.6E-3
	Fetal Bovine Serum	1.0E-3	1.0E-3
	Choline Chloride	2.9E-5	2.9E-5
	Thiamine Hydrochloride	1.2E-5	1.2E-5
HCO_3 (-)	$NaHCO_3$	4.4E-2	4.4E-2
SO_4 (2-)	$MgSO_4$	8.1E-4	3.2E-3
	$CuSO_4$	5.0E-9	2.2E-8
	$MnSO_4$	2.0E-10	8.0E-10
HPO_4 (2-)	Na_2HPO_4	7.8E-4	3.1E-3
$C_{12}H_{12}O_{18}P_2$ (3-)	Ascorbic Acid Phosphate	7.8E-6	1.4E-4
$C_3H_3O_3$ (-)	Sodium Pyruvate	1.0E-3	1.0E-3
PO_4 (3-)	Fetal Bovine Serum	1.0E-5	9.3E-5
$C_9H_{16}NO$ (-)	Calcium d-panthothenate	8.4E-6	1.7E-5
NO_3 (-)	$Fe(NO_3)_3$	2.5E-7	7.5E-7
SeO_3 (2-)	Na_2SeO_3	2.9E-8	1.2E-7
VO_3 (-)	NH_4VO_3	2.5E-9	2.5E-9
Aspartic Acid (-)	Amino Acids	2.0E-5	2.0E-5
Glutamic Acid (-)	Amino Acids	2.0E-5	2.0E-5
		Sum of Contributions	**0.35** (3.5E-1)
		Total Ionic Strength	**0.17** (1.7E-1)

In addition, a number of components, including Albu, were added to the minimal media.

Supplemental Table S4. Listing the components in the Dulbecco's Modified Eagle's Medium (Levina et al. 2017) and the components in the AlbuMAX (product page found on ThermoFisher https://www.thermofisher.com/order/catalog/product/11020021?CID=AFLBC-11020021) that were deamed a neutral and not contribution htr

Compound	**Molar Concentration**
Glucose	2.5E-2
Uncharged Amino Acids (Gln, Ile, Leu, Gly, Ser, Phe, Tyr, Cyt, Met, Ala, Asn, Trp)	3.7E-3
AlbuMax	4.0E-4
Folic Acid	4.1E-6
Glutathione	3.3E-6
Inositol	4.0E-5
Niacinamide	3.3E-5
Pyroxidine hydrochloride	2.0E-5
Riboflavin	1.1E-6
Holo-transferrin	9.4E-8
Insulin	1.7E-6
Penicillin G	1.8E-4
Streptomycin	1.7E-4
Fungizone	1.9E-7
Ethanolamine	3.1E-5
Phenol red	4.2E-5

As summarized in the Supplemental Table S4 the total contributions are not small but when all summed up the it comes out to 0.17. This result show that we should use the parameters reported for 0.15 ionic strength with estimating the content of intact V-complexes.

Parameters for Speciation Calculations at 0.15 ionic strength for $[VO_2dipic]^-$, $[VO_2dipic\text{-}Cl]^-$, and $[VO_2dipic\text{-}OH]^-$

The speciation profiles are generated using reported values, and those derived in this system. The specific parameters are listed below for an environment near an ionic strength of 0.15.

Supplemental Table S5. Formation constants of Vanadate species in a 0.15M NaCl system Table

1. Notations, Compositions, Formation Constants (log ß), and Acidity Constants (pKa) for the H^+-$H_2VO_4^-$, System [I = 0.15) NaCl M, 25 °C]

	Binary System ($H_2VO_4^-$-H^+)			
(p, q)	Formula	log β	pKa values	ref
1, 2	VO_2^+	7.00		Elvingson, K., et al. *Inorg. Chem.* **1996.** *35*, 3388-3393
1, -1	HVO_4^{2-}	-8.17		
1, 0	$H_2VO_4^-$	0.00	8.17	
2, -2	$H_2V_2O_7^{4-}$	-16.19		
2, -1	$HV_2O_7^{3-}$	-5.85	10.34	
2, 0	$H_2V_2O_7^{2-}$	2.65	8.50	
4, -2	$V_4O_{13}^{6-}$	-9.98		
4, -1	$HV_4O_{12}^{5-}$	-0.63	9.35	
4, 0	$V_4O_{12}^{4-}$	9.24		
5, 0	$V_5O_{15}^{5-}$	11.17		
10, 4	$V_{10}O_{28}^{6-}$	50.28		
10, 5	$HV_{10}O_{28}^{5-}$	56.90	6.62	
10, 6	$H_2V_{10}O_{28}^{4-}$	61.07	4.17	
10, 7	$H_3V_{10}O_{28}^{3-}$	62.93	1.86	

Supplemental Table S6. Formation constants of $[VO_2dipic]^-$ complex in a 0.15M NaCl system. Notations, Compositions, Formation Constants (log ß), and Acidity Constants (pKa) for the $H_2VO_4^-$-H^+-dipic System [I = 0.15 NaCl M, 25 °C]

Binary (H^+-dipic) and Ternary System ($H_2VO_4^-$-H^+-dipic)				
	Formula	log β	pKa	ref
0, 1, 1	Hdipic	4.56	4.56	Crans, D. C.; *Inorg. Chem.* **2000,** *39*, 4409-4416
0, 2, 1	H_2dipic H_3dipic	6.60	2.04	
0, 3, 1	H_2Vdipic	7.19	0.59	
1, 2, 1		15.41 *		
1, 3, 1	H_3Vdipic	15.92 *	0.51	

Supplemental Table S7. Formation constants of $[VO_2dipic\text{-}Cl]^-$ complex in a 0.15M NaCl system. Notations, Compositions, Formation Constants (log ß), and Acidity Constants (pKa) for the $H_2VO_4^-$-H^+-dipic-Cl [I = 0.15 NaCl M, 25 °C]

Ternary System ($H_2VO_4^-$-H^+-dipic-Cl)				
(p, q, r)	log β	Formula	pKa	ref
0, 1, 1	3.83	Hdipic-Cl		Smee, J. J., et al. *J. Inorg. Biochem.* **2009**, *103,* 575-584
0, 2, 1	6.10	H_2dipic-Cl	2.21	
0, 3, 1	6.60	H_3dipic-Cl	0.50	
1, 2, 1	15.31 *	H_2Vdipic-Cl		
1, 3, 1	15.82 *	H_3Vdipic-Cl	0.51	

Supplemental Table S8. Formation constants of $[VO_2dipic\text{-}OH]^-$ complex in a 0.15 M NaCl system. Notations, Compositions, Formation Constants (log ß), and Acidity Constants (pKa) for the $H_2VO_4^-$-H^+-dipic-OH [I = 0.15) NaCl M, 25 °C]

Ternary System ($H_2VO_4^-$-H^+-dipic-OH)				
(p, q, r)	log β	Formula	pKa	ref
0, 0, 1	0.00	$DipicO^{3-}$		Jakusch, T., et al.; *J. Inorg. Biochem.* **2003,** *95*, 1-13
0, 1, 1	10.75	Dipic-OH^{2-}	10.75	
0, 1, 2	13.93	Hdipic-OH^-	3.08	
0, 1, 3	15.20	H_2Vdipic-OH	1.40	
1, 1, 1	12.70	$[VO_2(dipicO)(OH)]^{3-}$		
1, 1, 2	20.56	$[VO_2(dipicO)]^{2-}$	7.90	
1, 1, 3	24.26	$[VO_2$(dipic-OH)]-	3.70	

In addition to the $[VO_2dipic]^-$ and $[VO_2dipic\text{-}Cl]^-$ profiles that are shown in the manuscript, we also show the corresponding profiles for the $[VO_2dipic\text{-}OH]^-$ here, since this compound was also tested. This complex because of the OH group has one more proton and thus one more protonation state. However, the speciation is similar to the other systems if the two speciation steps are combined.

Supplemental Fig. A3.8. The speciation profile for $[VO_2dipic\text{-}OH]^-$ is shown using total V- concentrations of 0.400 μM, 0.164 μM and 1.0 μM. The calculations were done using the vanadate oligomerization constants for 0.15 M NaCl.

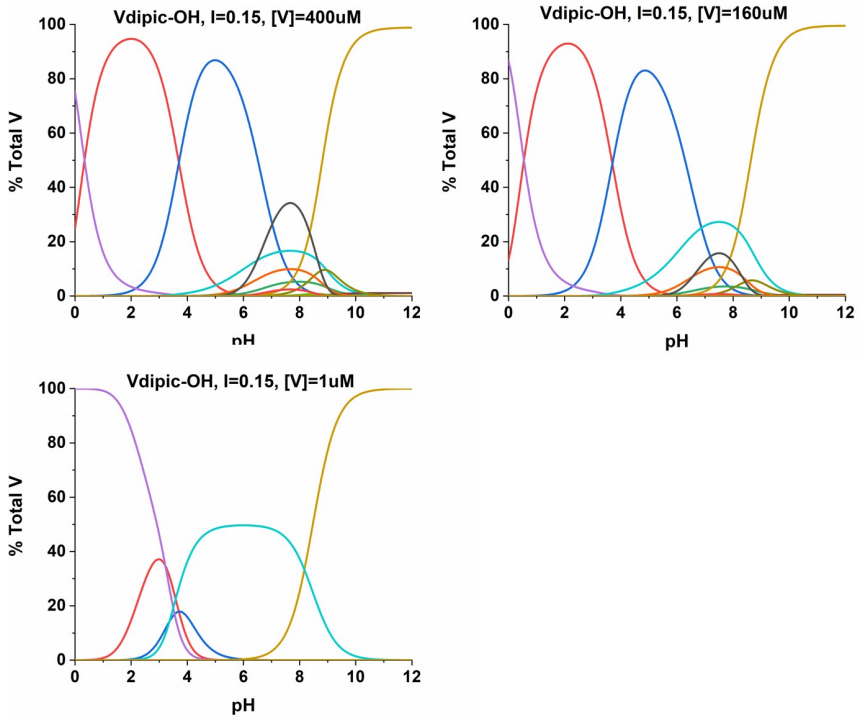

Appendix IV: Supporting Information for Chapter 5

Table of Contents

I Speciation Data for the V_9Pt and V_9Mo complexes

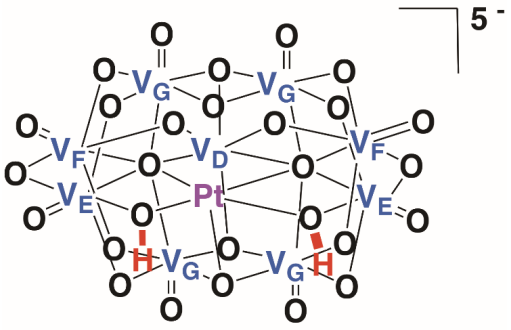

Fig. A4.1. A structure of the V_9Pt complex with the correct assignment of the peaks in the ^{51}V NMR.

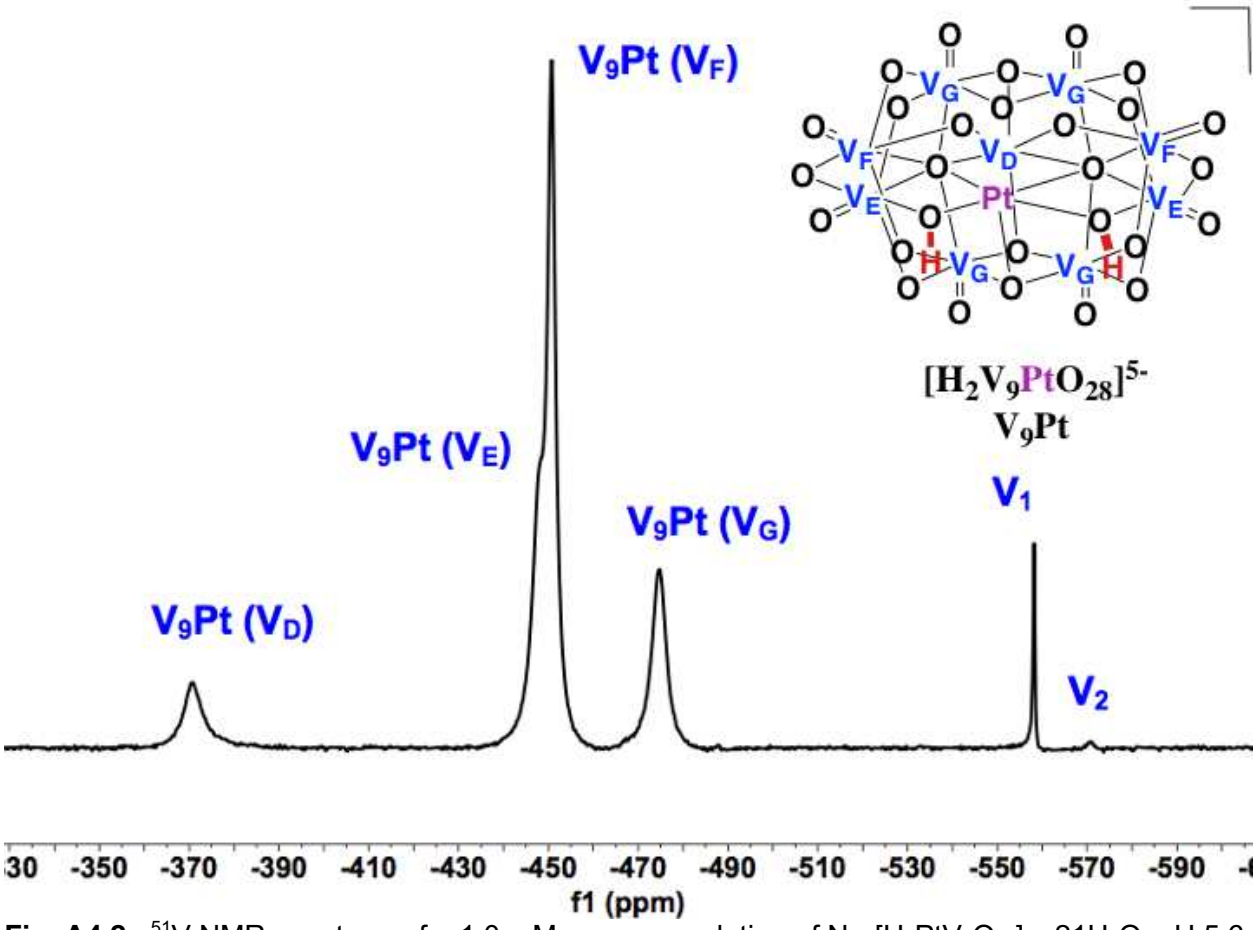

Fig. A4.2. ^{51}V NMR spectrum of a 1.0 mM aqueous solution of $Na_5[H_2PtV_9O_{28}]$ x $21H_2O$, pH 5.6, The insert presents the structure of the $[H_2PtV_9O_{28}]^{5-}$ (V_9Pt) anion present in solution with the assignments for the non-equivalents vanadium(V) atoms V_D - V_G. Signals at - 558 and -571 ppm were attributed to V_1 and V_2, respectively.

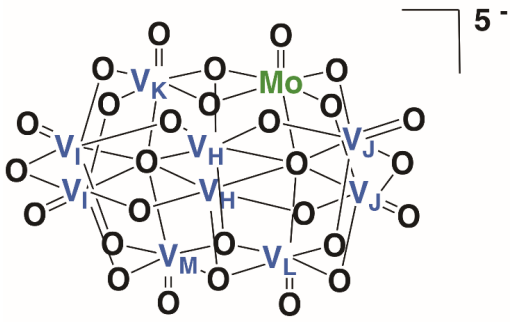

$[V_9MoO_{28}]^{5-}$

V_9Mo

Fig. A4.3. A structure of the V_9Mo complex with the correct assignment of the peaks in the ^{51}V NMR.

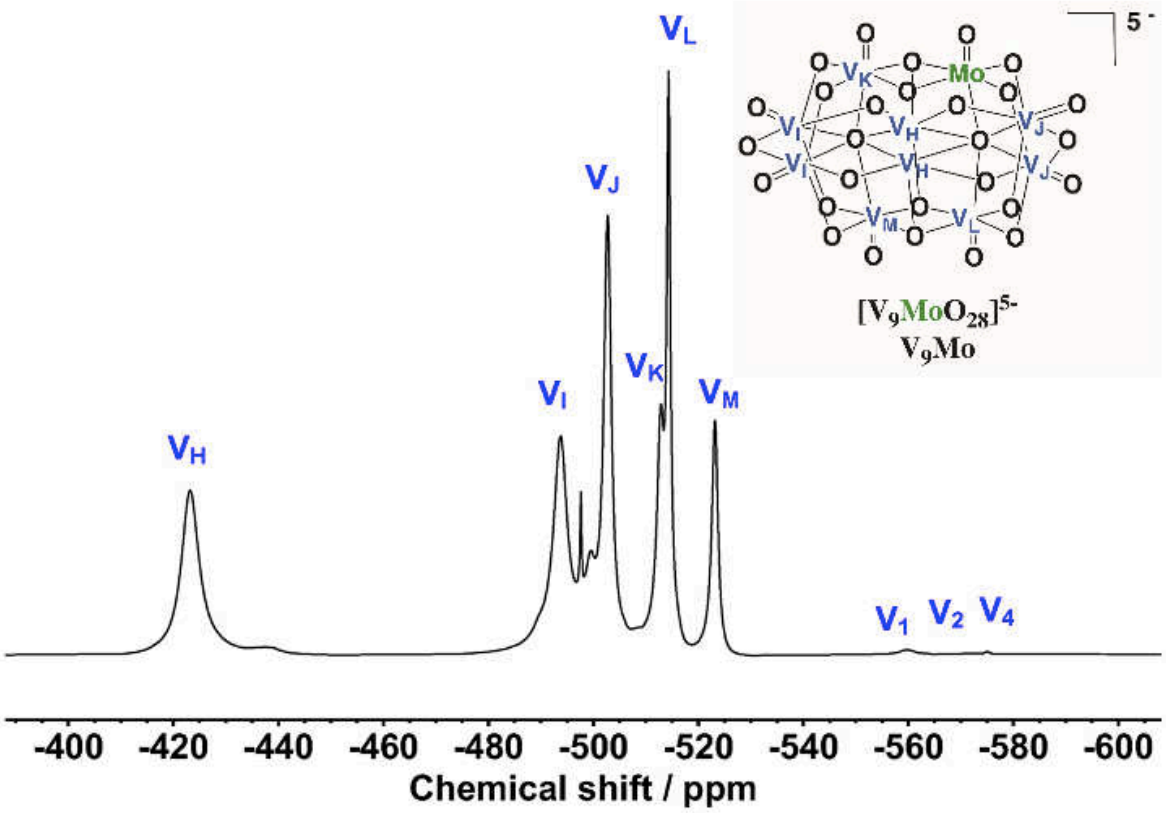

Fig. A4.4. ^{51}V NMR spectrum of a 100 mM V_9Mo aqueous solution at pH = 5.06, as described in the Materials and Methods section. The insert presents the structure of the $[V_9MoO_{28}]^{5-}$ (V_9Mo) anion and the assignments for the non-equivalents vanadium(V) atoms V_H - V_M. Signals at -558, 570 and -574 ppm were attributed to V_1, V_2 and V_4, respectively.

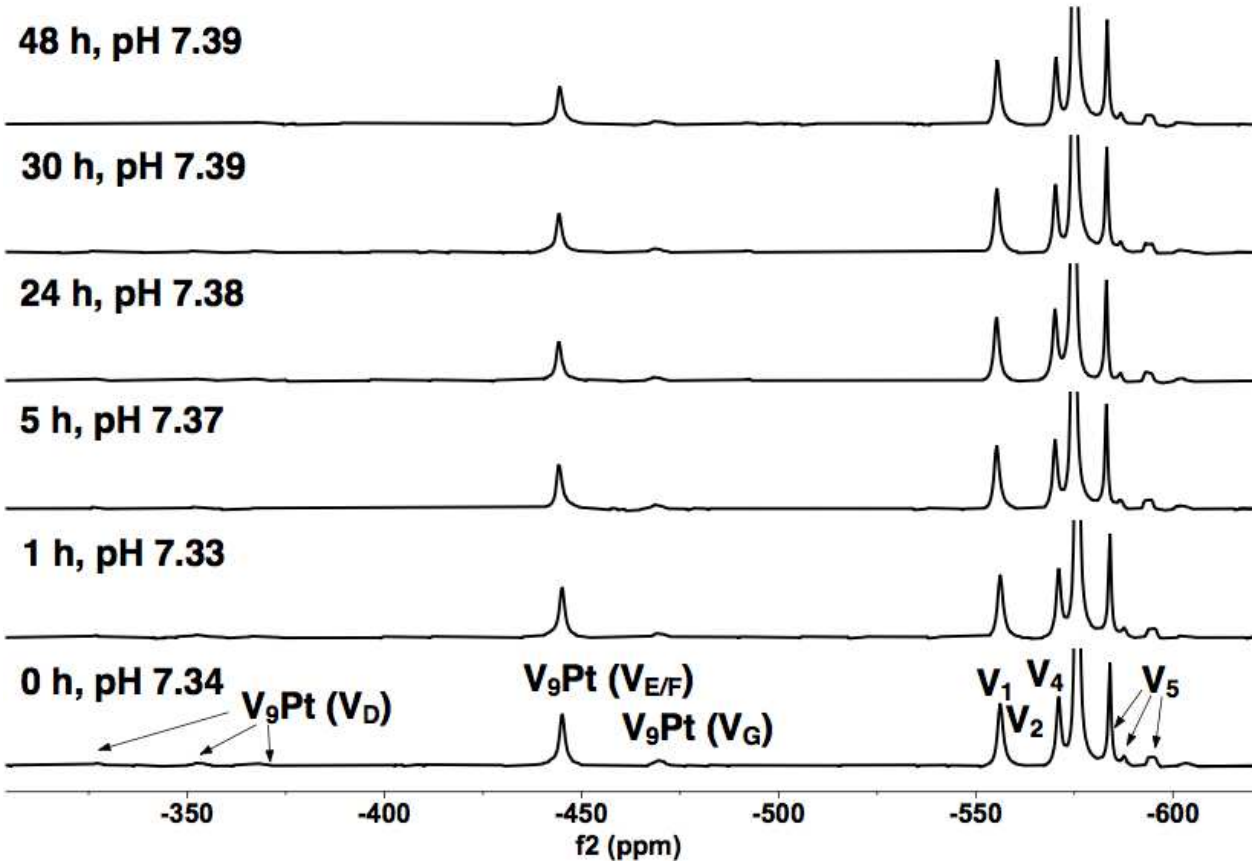

Fig. A4.5. ^{51}V NMR spectra showing the speciation data of the V_9Pt complex in aqueous (1.0 mM) solution with added 0.0054 M KCl and 0.11 M NaCl over 48 h.

Anions monitored	Signals observed by ^{51}V NMR spectroscopy					
Compound and time / conditions	V_9Pt (%)	V_9Pt minor isomers (%)	V_1 (%)	V_2 (%)	V_4 (%)	V_5 (%)
V_9Pt / 0 h Aq. Aq. with added Cl^- Media	33.8% 7.9% 0%	1.1% 0.3% 0%	3.2% 7.5% V_1 + PV 19.0%	5.4% 7.3% 10.0%	49.3% 68.0% 63.0%	7.0% 9.7% 7.0%
V_9Pt / 1 h Aq. Aq. with added Cl- Media	33.4% 7.4% 0%	0.7% 0.4% 0%	3.3% 7.5% V_1 + PV 19.0%	6.2% 7.4% 13.0%	50.1% 68.2% 62.0%	6.4% 10.1% 4.0%
V_9Pt / 5 h Aq. Aq. with added Cl- Media	33.5% 6.4% 0%	0.4% 0.2% 0%	3.1% 7.7% V_1 + PV 19.0%	5.1% 7.3% 11.0%	51.0% 68.3% 62.0%	7.0% 10.6% 6.0%
V_9Pt / 24 h Aq. Aq. with added Cl- Media	33.0% 6.5% 0%	1.0% 0.3% 0%	3.1% 7.6% V_1 + PV 20.0%	5.0% 8.5% 14.0%	51.2% 69.8% 63.0%	7.0% 8.2% 4.0%
V_9Pt / 30 h Aq. Aq. with added Cl- Media	33.8% 6.2% 0%	1.1% 0.2% 0%	3.2% 7.6% V_1 + PV 20.0%	5.4% 6.7% 12.0%	49.3% 69.7% 63.0%	7.0% 10.6% 5.0%
V_9Pt / 48 h Aq. Aq. with added Cl- Media	33.6% 6.1% 0%	0.3% 0.2% 0%	3.1% 7.5% V_1 + PV 20.0%	5.4% 6.7% 12.0%	51.0% 70.4% 61.0%	6.6% 10.3% 5.0%
* PV = V(V) phosphate complex						

Table A4.1. A summary of the speciation data of the V_9Pt complex collected at t = 0, 1, 5, 24, 30 and 48 h in a 1.0 mM aqueous control solution and 1.0 mM solutions in DMEM media.

Anions monitored	Signals observed by ^{51}V NMR spectroscopy

Compound and time / conditions	V_9Mo (%)	V_{10} (%)	V_1 (%)	V_2 (%)	V_4 (%)	V_5 (%)
V_9Mo / 0 h Aqueous Media	13.5% 16.5%	5.5% 7.5%	74.0% V_1+PV 66.0%	4.0% 1.0%	0% 0%	0% 0%
V_9Mo / 1 h Aqueous Media	13.5% 0%	2.5% 0%	70.0% V_1+PV 95.0%	2.0% 6.0%	0% 2.0%	0% 0%
V_9Mo / 5 h Aqueous Media	13.0% 0%	1.0% 0%	74.0% V_1+PV 94.0%	0% 5.0%	0% 2.0%	0% 0%
V_9Mo / 24 h Aqueous Media	16.0% 0%	5.0% 0%	74.0% V_1+PV 94.0%	0% 4.0%	0% 3%	0% 0%
V_9Mo / 30 h Aqueous Media	18.0% 0%	4.0% 0%	74.0% V_1+PV 94.0%	0% 4.0%	0% 3.0%	0% 0%
V_9Mo / 48 h Aqueous Media	12.5% 0%	0.5% 0%	77.0% V_1+PV 97.0%	0% 5.0%	0% 3.0%	0% 0%
* PV = V(V) phosphate complex						

Table A4.2. A summary of the speciation data of the V_9Mo complex collected at t = 0, 1, 5, 24, 30 and 48 h in a 1.0 mM aqueous control solution and 1.0 mM solutions in DMEM media.

II Biological Data

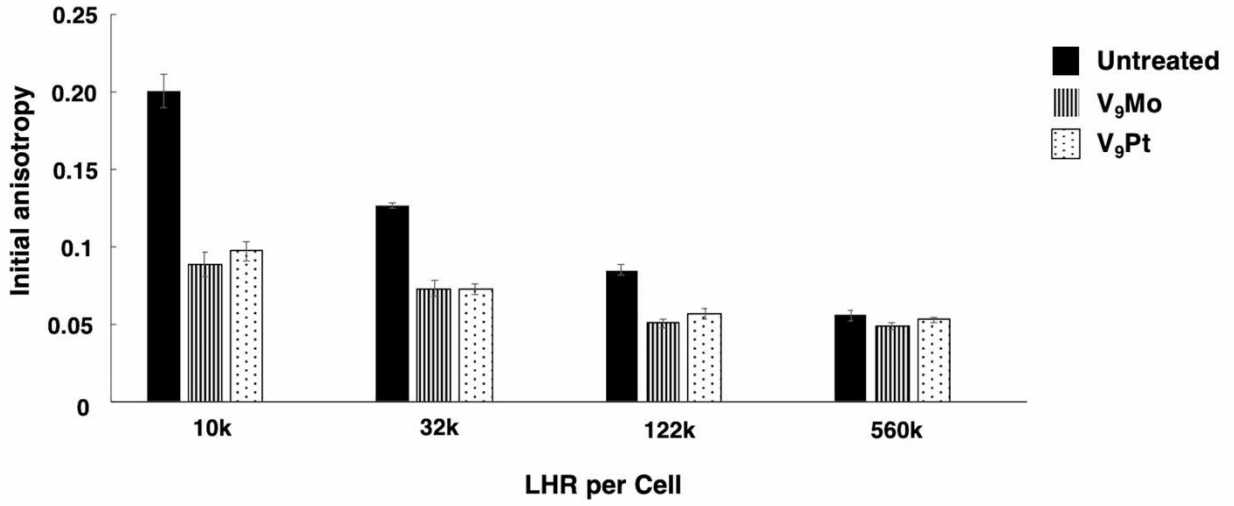

Figure A4.6. Values for the initial anisotropy measured for eYFP covalently linked to LHR using polarized homo-FRET methods. Smaller values for initial anisotropy are indicative of LHR aggregation. Pre-treatment of cells with V_9Mo or V_9Pt decreased values for initial anisotropy for receptors on cells expressing 10,000, 32,000, 122,000 and 560,000 LHR per cell. Both initial anisotropy values and values for V9X-treated cells did not differ significantly from those of untreated and V10-treated cells reported previously (Althumairy et al., 2020b).

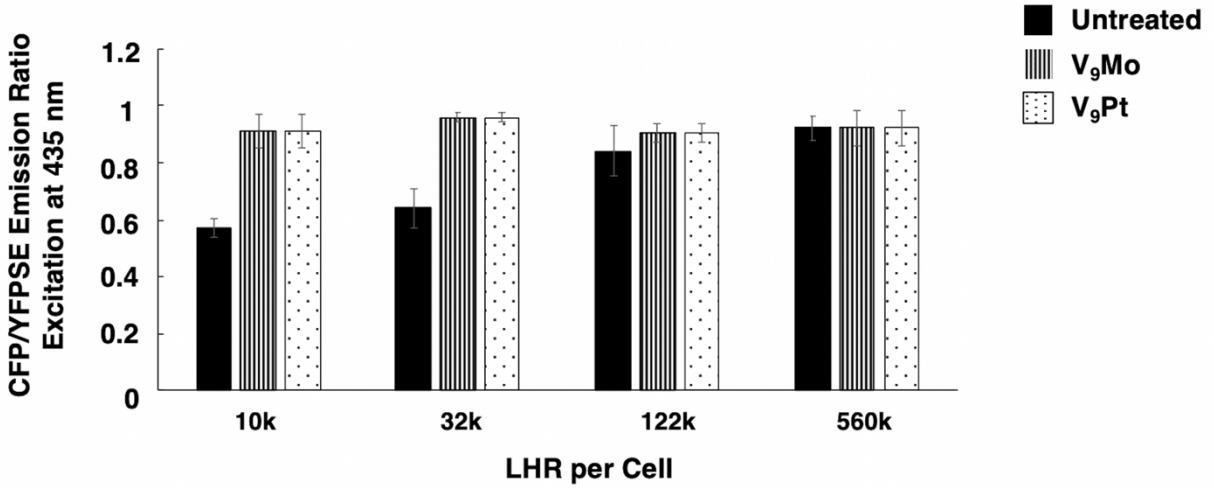

Figure A4.7. The effects of LHR numbers per cell on intracellular cAMP levels in untreated (control) cells or cells treated with V_9Mo and V_9Pt. ICUE3 was used as a cAMP reporter molecule. When there is an increase in intracellular cAMP, cAMP binds to ICUE3, reduces energy transfer between CFP and YFP (YFPSE) upon exposure of ICUE3 to 435 nm. light and increases the CFP/YFPSE ratio. In the absence of cAMP, there is increased energy transfer from CPF to YFP, an increase in sensitized emission by YFP, and a reduction in the CFP/YFPSE ratio. Data shown are the mean and S.E. of 25-43 individual measurements depending on the treatment.

Appendix V: Supporting Information for Chapter 6

Table of Contents

I NMR Characterization

I NMR Characterization

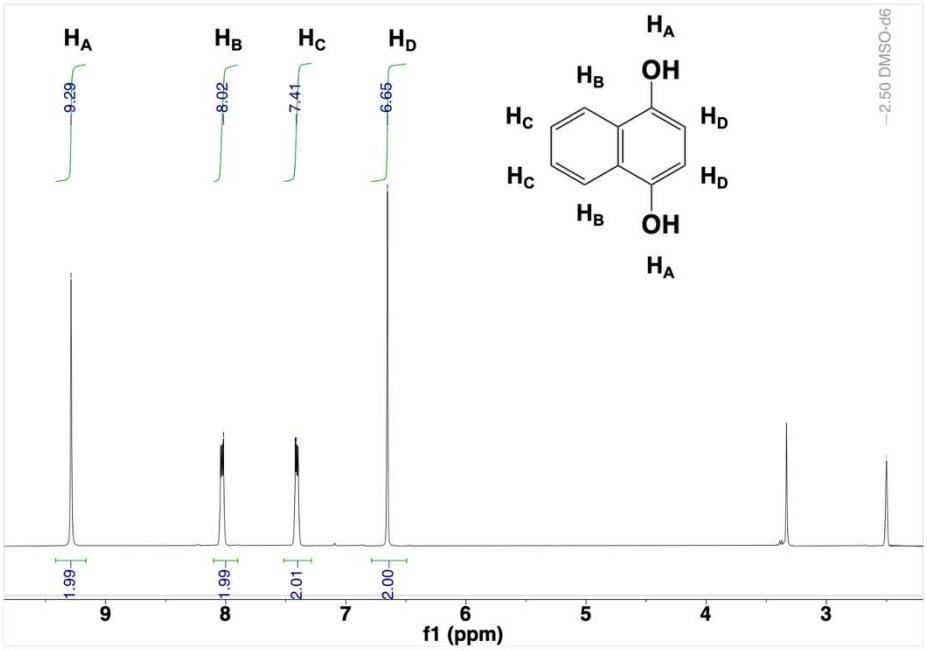

Figure A5.1. ^{1}H NMR of 1,4-naphthoquinol in d_6-DMSO.

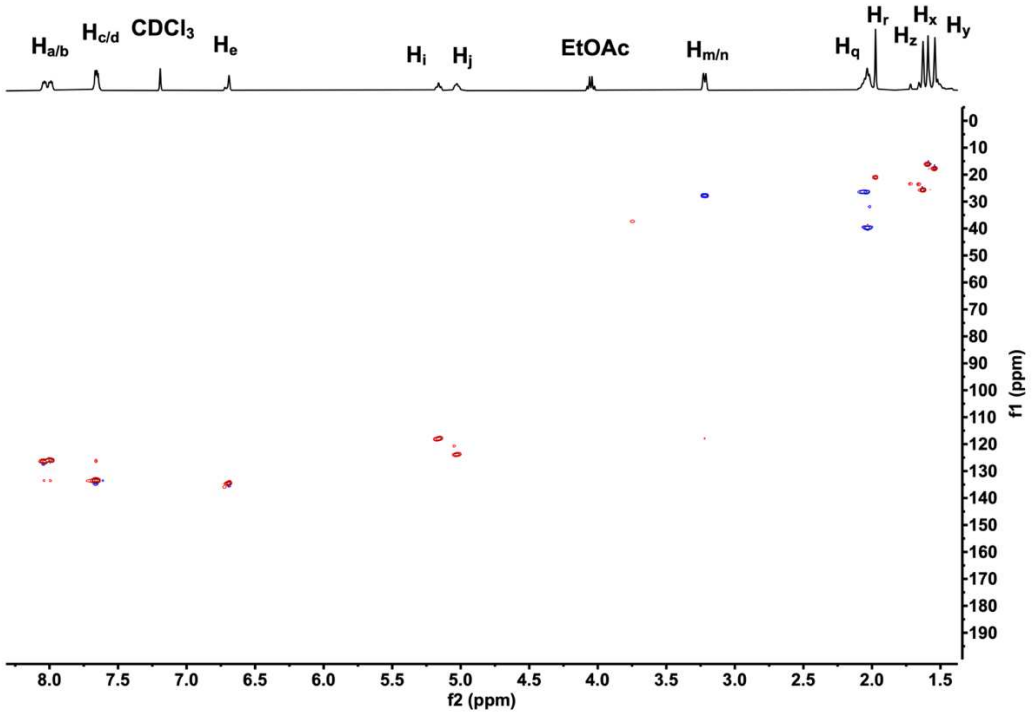

Figure A5.2. ^{1}H-^{13}C HSQC of DMK-2 in $CDCl_3$

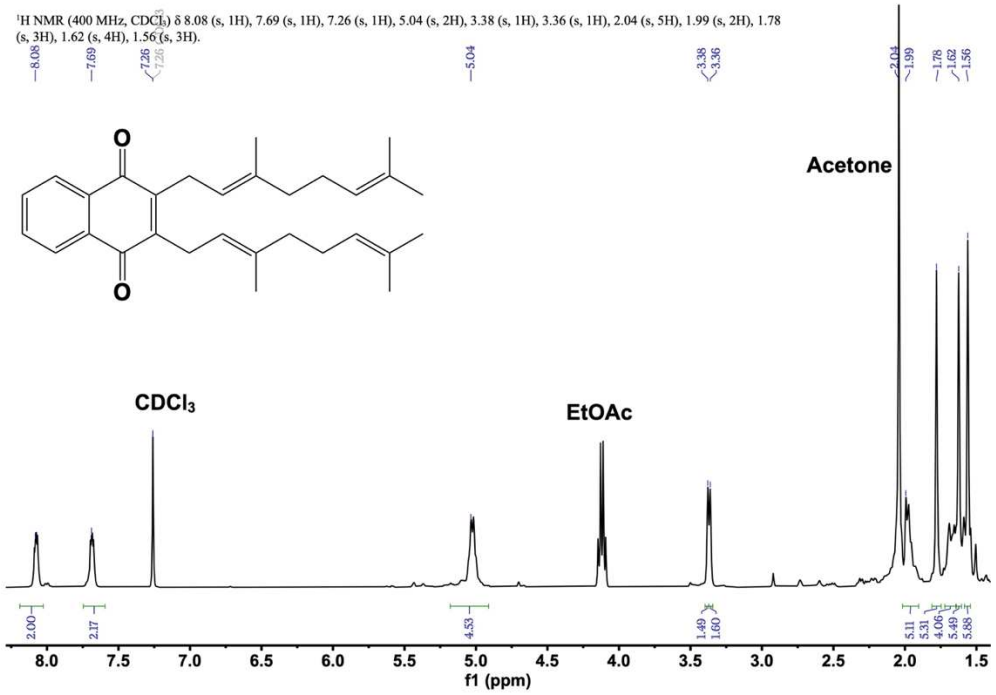

Figure A5.3. ^{1}H NMR of DMK-2 dialkylated product in $CDCl_3$.

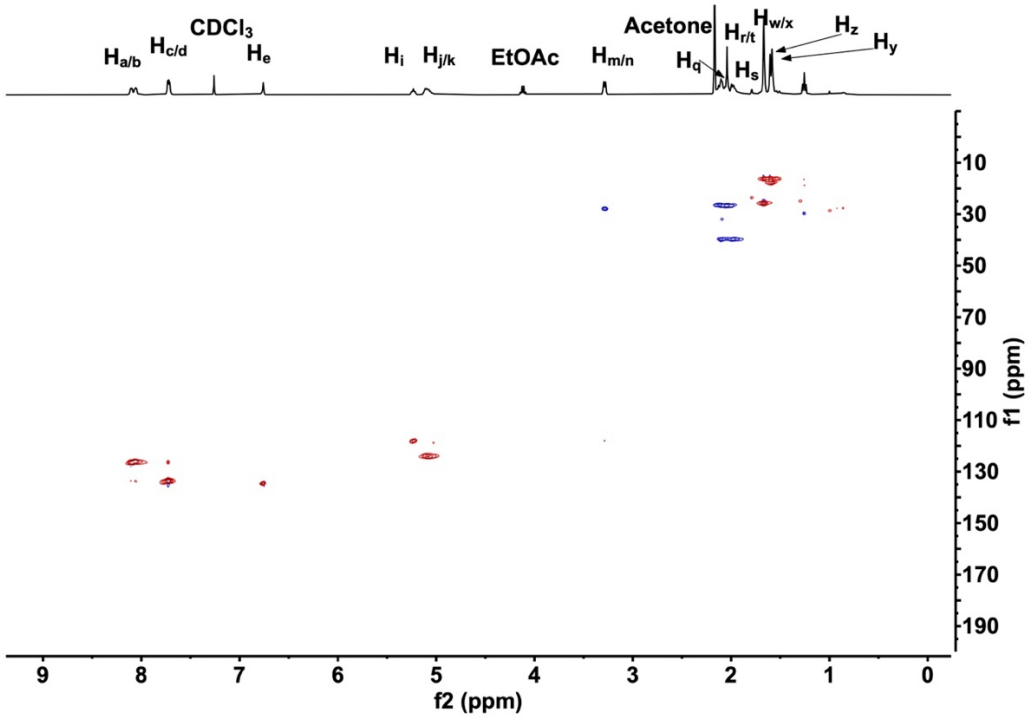

Figure A5.4. ^{1}H-^{13}C HSQC of DMK-3 in $CDCl_3$.

Appendix VI: Enhancement of oncolytic virotherapy by vanadium(V) dipicolinates

This is the manuscript that corresponds to Chapter 4 and is published in *Biometals* (Bergeron et. al, 2019).

References

Bergeron, A.; **Kostenkova, K.**; Selman, M. Murakami, H. A.; Owens, E.; Haribabu, N.; Arulanandam, R.; Diallo, J.-S.; Crans, D. C. Enhancement of oncolytic virotherapy by vanadium(V) dipicolinates. *Biometals*. **2019**, *32*, 545 – 561.

Biometals (2019) 32:545–561
https://doi.org/10.1007/s10534-019-00200-9

Enhancement of oncolytic virotherapy by vanadium(V) dipicolinates

Anabel Bergeron · Kateryna Kostenkova · Mohammed Selman · Heide A. Murakami · Elizabeth Owens · Naveen Haribabu · Rozanne Arulanandam · Jean-Simon Diallo · Debbie C. Crans

Received: 7 May 2019 / Accepted: 21 May 2019 / Published online: 17 June 2019

Abstract Oncolytic viruses rewire the immune system and can lead to long-lasting antitumor defenses against primary and metastatic tumors. However, results from clinical studies have shown heterogeneity in responses suggesting that multiplexed approaches may be necessary to consistently generate positive outcomes in patients. To this end, we explored the combination of oncolytic rhabdovirus VSVΔ51 with vanadium(V) dipicolinate derivatives, which have already been explored for their antidiabetic properties in animal models. The combination of vanadium-based dipicolinate compounds with VSVΔ51 significantly increased viral replication and cytotoxicity in the human renal cell carcinoma cell line 786-0. The effects of three vanadium(V)-dipicolinate coordination complexes ($[VO_2dipic]^-$, $[VO_2dipic\text{-}OH]^-$ and $[VO_2dipic\text{-}Cl]^-$ with –OH or –Cl in the para position) were compared to that of the simple salts using spectroscopy and speciation profiles. Like the vanadate salts and the vanadyl cation, all dioxovanadium(V) dipicolinate complexes tested were found to increase viral infection and cytotoxicity when used in combination with VSVΔ51. Viral sensitization is dependent on the vanadium since free dipicolinate ligands exerted no effect on viral infection and viability. The ability of these complexes to interact with interfaces and the stability of the complexes were evaluated under physiological conditions. Results indicate that these complexes undergo hydrolysis in cell culture media thereby generating vanadate. The vanadium dipicolinate derivatives in the context of immunovirotherapy shares similarities with previous studies exploring the antidiabetic properties of the compounds. The synergy between vanadium compounds and the oncolytic virus suggests that these compounds may be valuable in the development of novel and effective pharmaco-viral therapies.

Electronic supplementary material The online version of this article (https://doi.org/10.1007/s10534-019-00200-9) contains supplementary material, which is available to authorized users.

A. Bergeron · M. Selman · N. Haribabu · R. Arulanandam · J.-S. Diallo (✉)
Center for Innovative Cancer Research, Ottawa Hospital Research Institute, Ottawa, ON, Canada
e-mail: jsdiallo@ohri.ca

A. Bergeron · M. Selman · J.-S. Diallo
Department of Biochemistry, Microbiology and Immunology, Faculty of Medicine, University of Ottawa, Ottawa, ON, Canada

K. Kostenkova · H. A. Murakami · E. Owens · D. C. Crans (✉)
Department of Chemistry, Colorado State University, Fort Collins, CO, USA
e-mail: debbie.crans@colostate.edu

D. C. Crans
Cell and Molecular Biology Program, Colorado State University, Fort Collins, CO, USA

Keywords Oncolytic virus · Vanadium · Cancer · Dipicolinate derivatives · Vanadium(V) · Coordination complexes

Abbreviations

AOT	Sodium aerosol-OT (sodium salt of bis(2-ethylhexyl)sulfosuccinate)
BEOV	Bis(ethylmaltolato)oxovanadium(IV)
BMOV	Bis(maltolato)oxovanadium(IV)
DSS	3-Trimethylsilyl-1-propanesulfonic acid sodium salt
H_2dipic	Dipicolinic acid, 2,6-pyridinedicarboxylic acid
H_2dipic-OH	4-Hydroxydipicolinic acid
H_2dipic-Cl	4-Chlorodipicolinic acid
HPI	Hours post infection
GFP	Green fluorescent protein
MOI	Multiplicity of infection
OV	Oncolytic virus
T-VEC	Talimogene laherparepvec
$[VO_2dipic]^-$	Dioxovanadium(V) dipicolinate
$[VO_2dipic\text{-}OH]^-$	Dioxovanadium(V) 4-hydroxydipicolinate
$[VO_2dipic\text{-}Cl]^-$	Dioxovanadium(V) 4-chlorodipicolinate
VSV	Vesicular stomatitis virus

Introduction

For over a century, vanadium compounds have been studied for their various health benefits (Lyonnet et al. 1899; Kieler et al. 1965; Kopfmaier et al. 1981; Murthy et al. 1986; D'Cruz et al. 2002; Evangelou et al. 2002; Storr et al. 2006; Etcheverry et al. 2008; Thompson et al. 2009; Bishayee et al. 2010; Wang et al. 2010; Petanidis et al. 2013; Willsky et al. 2013; Yoshikawa et al. 2014; Kioseoglou et al. 2015; León et al. 2015; Pessoa et al. 2015a; Scior et al. 2016; Kowalski et al. 2017; Leon et al. 2017; Crans et al. 2018, 2019). For instance, several classes of vanadium compounds such as vanadium salts (Lyonnet et al. 1899; Kieler et al. 1965), organometallic vanadium compounds (Kopfmaier et al. 1981; Murthy et al. 1986) and coordination complexes (D'Cruz et al. 2002; Etcheverry et al. 2008; Wang et al. 2010; Petanidis et al. 2013; Yoshikawa et al. 2014; León et al. 2015; Kowalski et al. 2017; Sanna et al. 2017) are effective in the treatment of diabetes, cancer and other illnesses. Several vanadium compounds and salts have been subject to animal studies and progressed to human Phase 1 and 2 clinical trials (Goldfine et al. 2000; Storr et al. 2006; Willsky et al. 2013; Crans 2015). In the past decades, the major focus has been on anti-diabetic investigations until recently when the front runner drug bis(ethylmaltolato)oxovanadium(IV) BEOV (Fig. 1) went off patent in 2011 (Thompson and Orvig 2006; Thompson et al. 2009; Crans 2015). Phase 2 studies were completed with BEOV but funding for Phase 3 studies was not raised before the patent expired, thereby bringing clinical investigation to a halt. As a result, novel applications have been explored for vanadium compounds—their antineoplastic actions and potential as orphan drugs or food additives have been the focus of growing scientific efforts (Pessoa et al. 2015a; Leon et al. 2017; Crans et al. 2018). Structural studies have been conducted exploring the interactions with phosphatases and the molecular details in this process (Davies et al. 2004; McLauchlan et al. 2015; Wu et al. 2016a). In addition, studies have shown a correlation between the anti-cancer and anti-diabetic effects of some coordination complexes (Wu et al. 2016a; Yang and Wang 2016; Crans et al. 2018).

Oncolytic viruses (OVs) are nonpathogenic viruses with natural or engineered tropism for cancer cells. They stimulate an antitumor immune response through direct oncolysis, by disrupting tumor vasculature and by recruiting the immune system thereby converting an immunosuppressive tumor microenvironment into a pro-immune ecosystem (Achard et al. 2018). These immune responses mediated by both the innate and adaptive arms confer durable and systemic protection against malignancies and prevent recurrence. In recent years, the number of clinical trials

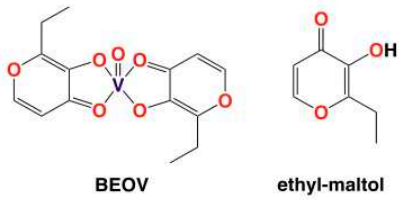

Fig. 1 The structures of bis(ethylmaltolato)oxovanadium(IV) (BEOV) and the free ethyl-maltol ligand, 2-ethyl-3-hydroxy-4H-pyran-4-one

involving OVs has significantly increased, and Talimogene laherparepvec (T-VEC), a modified herpes simplex virus type 1, was approved by the Food and Drug Administration for the treatment of advanced melanoma (Rehman et al. 2016). The therapeutic potential of OVs is widely recognized, but thus far, OV monotherapies have only been successful in a subset of patients in the clinic. Recently, efforts have been geared towards the development of multimodal therapeutic strategies to increase efficacy. Combinations involving chemotherapies, immune checkpoint inhibitors or small molecule modulators of cellular innate immunity with various OV platforms are being investigated (reviewed in (Phan et al. 2018).

Recently, vanadium compounds were tested and found to be highly effective in combination with oncolytic viruses (Selman et al. 2018). Multiple vanadium compounds improved the infection of cancer cell lines by oncolytic RNA viruses, and killing of both infected and surrounding uninfected cells in vitro (Selman et al. 2018). Most importantly, in murine models of glioma and carcinoma, the dual therapy improved survival and increased T cell infiltration in the tumor microenvironment (Selman et al. 2018). Our findings suggest that vanadium compounds influence the immune system, an observation which is supported by previous studies. For example, pervanadate was shown to increase interleukin-2 secretion and T cell activation in the human Jurkat T cell line (Secrist et al. 1993) and human peripheral blood mononuclear cells (O'Shea et al. 1992). Nevertheless, the mechanism by which these compounds exert immunostimulatory and viral sensitizing effects remains poorly understood.

Many effects of vanadium compounds including but not limited to their anti-diabetic properties have been documented in cells, animals and humans (Evangelou et al. 2002; Etcheverry et al. 2008; Bishayee et al. 2010; Willsky et al. 2013; Kioseoglou et al. 2015; Pessoa et al. 2015a; Leon et al. 2017; Crans et al. 2018, 2019) and some effects including their insulin mimetic effects are attributed to the inhibition of phosphatases (McLauchlan et al. 2015). Potent inhibition has been reported with protein tyrosine phosphatases; however, less inhibition is observed for protein serine/threonine phosphatases and other phosphorylases (McLauchlan et al. 2015; Pessoa et al. 2015b; Scior et al. 2016). X-ray structures of several vanadium-phosphatases have been described, and many vanadium-protein crystals contained a vanadate (McLauchlan et al. 2015). Thus, those molecular studies support the possibility that some vanadium compounds act through vanadate and that the complex is simply a vehicle delivering the vanadium to the phosphatase (McLauchlan et al. 2015). For example, in vivo studies have confirmed that bis(maltolato)oxovanadium(IV) (BMOV) loses the ligand upon cell absorption, and that cellular membranes may assist in dissociating the ligand from the metal ion (Thompson et al. 2003).

In this study, we have preselected one class of vanadium coordination complexes, dioxovanadium(V) dipicolinates (Fig. 2) as a first series of compounds for structure–activity relationship studies based on their chemical and antidiabetic properties (Crans et al. 2003b; Buglyo et al. 2005; Li et al. 2009; Willsky et al. 2011) and to further explore their predicted effects in enhancing RNA oncolytic viruses like VSVΔ51 (Selman et al. 2018). Specifically, we examine three vanadium(V) dipicolinate complexes: ($[VO_2dipic]^-$, $[VO_2dipic\text{-}OH]^-$ and $[VO_2dipic\text{-}Cl]^-$) where the dipicolinate was substituted with –OH or –Cl in the para position (Fig. 2). The substituent changes the properties of the compounds, their stability in aqueous solution and their ability to penetrate cells (Crans 2000; Yang et al. 2003; Willsky et al. 2011). The chemistry of the vanadium(V) dipicolinate complexes has been described, and the pH stability shows that the complexes are more stable at acidic pH values (Buglyo et al. 2005; Willsky et al. 2011; Crans 2015). The parent dioxovanadium(V) dipicolinate complex is known to lose its

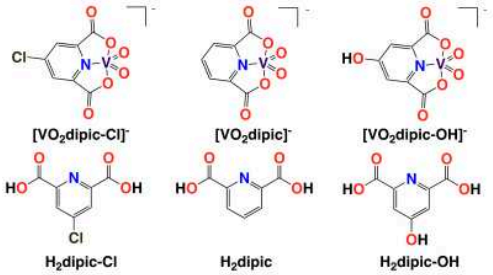

Fig. 2 The structures of V(V)-dipicolinate complexes (top row) and the corresponding free ligands shown in the protonated state (bottom row) investigated in this study. Compounds are identified by abbreviations and full names, provided in the abbreviations list

ligand at a neutral pH, although this complex readily penetrates interfaces and is thus presumed to enter cells (Crans et al. 2000, 2003b, 2006). When the complexes decompose, not only the free ligand but also the vanadate forms. As a result, the effects of the vanadium-dipicolinate compounds should be compared to the vanadate salt alone (Buglyo et al. 2005; Li et al. 2009; Willsky et al. 2011). Furthermore, since vanadium undergoes redox chemistry under physiological conditions, the effects should be compared to the effects of vanadyl cation as well (Buglyo et al. 2005; Li et al. 2009; Willsky et al. 2011). We present herein the biological responses of three vanadium(V) dipicolinate complexes upon oncolytic virus infection of cancer cells. These studies are further complemented with an analysis of the stability of the compounds under physiological conditions.

Materials and methods

General chemicals

$[VO_2dipic\text{-}X]^-$ derivatives were prepared from the corresponding ligands and vanadate as described previously for $NH_4[VO_2dipic]$ (Crans et al. 2000), $NH_4[VO_2dipic\text{-}OH]$ (Crans et al. 2003b) and $Na[VO_2dipic\text{-}Cl]$ (Li et al. 2009). The relevant chemicals were purchased from Sigma Aldrich and used without purification. Isooctane (2,2,4-trimethylpentane, 99.8%), activated charcoal (99.5%), deuterium oxide (99.9%), sodium hydroxide ($\geq$ 98%) and hydrochloric acid (37%) were purchased from Sigma Aldrich and used without further purification.

Sodium aerosol-OT (AOT) (sodium salt of bis(2-ethylhexyl)sulfosuccinate, $\geq$ 99.0%) was purchased from Sigma Aldrich and further purified, as has been reported previously, to remove acidic impurities (Crans et al. 2006). To do so, 50.0 g AOT was dissolved into 150 mL of methanol to which 15 g of activated charcoal was added. This suspension was stirred on a shaker for 2 weeks and then filtered to remove the activated charcoal. The filtrate was dried under rotary evaporation at 50 °C until the water content was below 0.2 molecules of water per AOT, as determined by ^1H NMR spectroscopy. The pH was adjusted throughout this study using solutions of NaOH or HCl mixed in D_2O to reach the final concentrations of 0.10 M. NaOH and HCl dissolved in D_2O are referred to as NaOD and DCl, respectively.

The human renal cell carcinoma cells (786-0) were acquired from the America Type Culture Collection. Dulbecco's modification of Eagle's medium (Corning, Manassas, Virginia) was supplemented with 10% (v/v) fetal bovine serum (CanSera, Etobicoke, Canada) and 1% (v/v) penicillin–streptomycin (Gibco Life Technologies, Waltham, Massachusetts) and 30 mM HEPES buffer.

Cell culture treatments and infection

The 786-0 cells were grown in supplemented Dulbecco's modification of Eagle's medium as specified above. Incubators were kept at 37 °C with 5% CO_2. The recombinant vesicular stomatitis virus (VSV, Indiana serotype) with a deletion in the M protein (methionine 51) and expressing GFP was grown and purified as previously described (Diallo et al. 2012).

For evaluation of compounds in our cell culture system, 786-0 cells were grown to confluency and treated with vanadium compounds or ligand controls (0.002–400 μM) using the Biotek Precision XS pipetting system. Four hours later, cells were infected with VSVΔ51 expressing green fluorescent protein (GFP) at a multiplicity of infection (MOI) of 0.05 or mock infected with media alone.

At 24 h post infection (HPI), GFP images were captured by fluorescence microscopy (ArrayScan, ThermoFisher Scientific) and GFP foci quantified. Cell viability was assessed using the metabolic dye AlamarBlue® by measuring fluorescence (530 nm excitation, 590 nm emission) at 48HPI using the BioTek Microplate Reader (BioTek Instruments Inc.) after a 2.5 h incubation.

Speciation calculations and analysis

Solution speciation are measured using potentiometry and spectroscopic methods resulting in quantification of species with defined stoichiometry (Kiss et al. 2008; Crans et al. 2013). Details in the speciation of $[VO_2dipic]^-$ has been reported, and information on other V-dipic derivatives have been described as well albeit in less detail. The complexes are defined by the notation (p, q, r). Equation (1) shows H^+, a metal ion (M), and a ligand (L) forming a complex with the stoichiometry defined by p, q, and r in an equilibrium

reaction, respectively. The resulting formation constant β (p, q, r) is shown in Eq. (2), where the concentrations of H^+, M, and L (which are the dipic derivatives investigated here) are multiplied by each other and divided by the concentration of the complex. Speciation chemistry is defined by a series of constants that represent the system (Kiss et al. 2008; Crans et al. 2013). Using these constants will allow for prediction of species distribution at defined parameters.

$$pH^+ + qM + rL \rightleftharpoons (H^+)_p(M)_q(L)_r \quad (1)$$

$$\beta(p,q,r) = \frac{(H^+)_p(M)_q(L)_r}{(H^+)^p + (M)^q + (L)^r} \quad (2)$$

Formation constants are reported in the literature values at a 0.40 ionic strength for $[VO_2dipic]^-$ and $[VO_2dipic\text{-}OH]^-$ (Crans et al. 2003a, b). However, a comparison of more derivatives was done at a lower ionic strength (Willsky et al. 2011). The vanadate oligomeric speciation constants are reported at several ionic strengths including 0.15 (Elvingson et al. 1996), 0.40 (Crans et al. 2000), 0.60 (Pettersson et al. 1983) and 3.00 (Pettersson et al. 1985). We carried out NMR studies quantitating $[VO_2dipic]^-$ both at a low ionic strength (no salts added), at 0.15 and at 0.40 in order to evaluate the effects of ionic strength on intact complexes. Since the concentrations of intact complexes are dependent on ionic strengths, we modelled the speciation profiles to accurately estimate the amounts of intact complexes during the biological treatment (see the Supplemental Material).

Generation of $[VO_2dipic]^-$ and $[VO_2dipic\text{-}Cl]^-$ speciation profiles

The formation constants are known for some ionic strengths, and speciation profiles can be calculated for these conditions using the known pH-dependent apparent equilibrium constants, see Eqs. (3) and (4) (Alberty 2000). NMR measurements were done to determine the amounts of the parent $[VO_2dipic]^-$ complex at 0.40 ionic strength to confirm the reported values (Crans et al. 2000). Then, NMR studies were performed at other ionic strengths to verify the known $[VO_2dipic]^-$. These studies confirmed the amounts of both $[VO_2dipic]^-$ and $[VO_2dipic\text{-}Cl]^-$ present to quantify the amounts of $[VO_2dipic]^-$ and $[VO_2dipic\text{-}Cl]^-$ under varying conditions. Using the formation constants, speciation profiles could be calculated using the HySS2009 program (Alderighi et al. 1999), and were used to predict the parent $[VO_2dipic]^-$ complex at the ionic strength 0.40 at which the formation constants have been reported for both vanadate oligomers and the $[VO_2dipic]^-$ complex (Crans et al. 2000). These calculations allow comparisons between calculated and experimentally measured $[VO_2dipic]^-$ to verify the approach.

$$dipic^{2-}\left(dipic - Cl^{2-}\right) + H_2VO_4^- \rightleftharpoons [VO_2dipic]^- + 2OH^- \quad (3)$$

$$K_{eq} = \frac{[VO_2\,dipic]^-}{[dipic^{2-}][H_2VO_4^-]} \quad (4)$$

$$\mu = {}^1/_2 \sum_1^n c_i z_i^2 \quad (5)$$

The speciation profiles should be calculated at the ionic strength of the cell culture media, and this ionic strength is calculated using Eq. (5). The details of the calculation are shown in the Supplemental Material, and the result was found to be 0.17. Accordingly, the speciation evaluations in this manuscript were continued using an ionic strength of 0.15. NMR measurements were done at ionic strength I = 0.15. This was followed by calculations carried out using the oxovanadate formation constants determined at ionic strength I = 0.15. We also investigated Na[VO_2-dipic-OH]. Studies of this system were carried out in detail (Crans et al. 2000) and are presented in the Supplemental Material. The medium that has an ionic strength of 0.20 or 0.15 was used.

Preparation of aqueous $[VO_2dipic]^-$ stock solution to verify formation constants

A solution of $[VO_2dipic]^-$ was prepared by dissolving 5.00 mM $[VO_2dipic]^-$ (6.20 mg, 0.0250 mmol) or 25.0 mM $[VO_2dipic]^-$ (31.0 mg, 0.125 mmol) in D_2O (5.00 mL) containing appropriate KCl to make up an ionic strength of 0.40. This 5.00 mM solution was then pipetted into appropriate aliquots, and the pD (pD = pH + 0.4) (Glasoe and Long 1960) of each was adjusted by a dropwise addition of NaOD or DCl (both 0.10 M). Solutions of $[VO_2dipic]^-$ were similarly prepared containing appropriate NaCl to make up an ionic strength of 0.15.

^{51}V and ^{1}H NMR measurements were done to determine the amounts of $[VO_2dipic]^-$ complex and $[VO_2dipic\text{-}Cl]^-$ complexes, the corresponding free ligands and V_1 concentrations in these samples to confirm that the calculations are in agreement with previous reports on these systems (see Table S1) (Crans et al. 2000). Then HySS calculations were done using the parameters obtained for 0.15 ionic strength, showing speciation profiles.

Preparation of aqueous $[VO_2dipic\text{-}Cl]^-$ stock solution for membrane model studies

A stock solution of $[VO_2dipic\text{-}Cl]^-$ was prepared by dissolving $[VO_2dipic\text{-}Cl]^-$ (7.06 mg, 0.0250 mmol) in D_2O (1.00 mL). This 25.0 mM solution was then pipetted into appropriate aliquots, and the pD (pD = pH + 0.4) of each was adjusted by a dropwise addition of NaOD or DCl (each 0.10 M).

Preparation of AOT-isooctane stock solution and reverse micelles

A 750 mM AOT-isooctane stock solution was prepared by dissolving the sodium salt of AOT (8.34 g, 18.8 mmol) in 25.0 mL isooctane; the solution was vortexed until clear (Stahla et al. 2008). The w_0 ($[D_2O]/[AOT]$) values of 8, 12 and 20 were prepared by adding calculated volumes of an aqueous $[VO_2dipic\text{-}Cl]^-$ and an AOT—isooctane stock solutions. For the varying pH studies, the pD (pD = pH + 0.4) of the w_0 12 samples was adjusted by a dropwise addition of NaOD and DCl (each 0.10 M) until the desired pH was reached.

^{1}H and ^{51}V NMR studies on reverse micelles

The ^{1}H and ^{51}V NMR experiments were recorded on a 400 MHz Bruker NMR spectrometer at 400 MHz and 105.2 MHz. The ^{1}H NMR parameters were as follows: 16 scans in the F1 domain, 1.0 s relaxation delay, 45° pulse angle, and 11 µs pulse. The ^{1}H NMR spectra were reported against an external reference, DSS at 0 ppm, and the reverse micelle samples were referenced using the septet at 1.67 ppm for AOT. The ^{51}V NMR parameters were as follows: 4096 scans in the F1 domain, 0.01 s relaxation delay, 45° pulse angle, and 16µs pulse. The ^{51}V NMR of reverse micelle samples were reported relatively to $VOCl_3$ at 0 ppm and spectra were referenced against an external reference of an aqueous $NaHVO_4$ solution at pH 12 (two signals at 535.7 ppm and 560.4 ppm) (Wu et al. 2016b; Zizic et al. 2016). The data was processed using MestreNova NMR processing software (Version 10.0.1).

Results

High-throughput screen

A screen was undertaken to test the ability of vanadium(V)-dipic compounds and free ligands to enhance VSVΔ51 infection in cancer cells (Fig. 3). The 786-0 cells were chosen as a model because they are inherently resistant to VSVΔ51 infection compared to other cancer cell lines. The parent complex, $[VO_2dipic]^-$ and its ligand 2,6-dicarboxylatopyridine, a second complex, $[VO_2dipic\text{-}Cl]^-$ and its free ligand 4-hydroxy-2,6-dicarboxylatopyridine, as well as the $[VO_2(dipic\text{-}Cl)]^-$ complex, which was recently investigated in detail as an insulin-enhancing agent (Li et al. 2009) and corresponding ligand 4-chloro-2,6-dicarboxylatopyridine ($H_2dipic\text{-}Cl$) were each synthesized and reconstituted in DMSO. Complexes, free ligands, as well as sodium vanadate (Na_3VO_4) and vanadyl sulfate ($VOSO_4$) control compounds were then serially diluted and transferred onto 786-0 cells at final concentrations of 0.002-400uM. After 4 h, cells were infected with recombinant VSVΔ51 encoding the GFP protein, as a measure of viral infection. Twenty-four hours later, when GFP transgene expression was maximal, fluorescence microscopy images were collected for each compound and GFP foci quantified (Fig. 4). The results for $[VO_2dipic\text{-}Cl]^-$, $H_2dipic\text{-}Cl$, $[VO_2dipic]^-$, $[VO_2dipic\text{-}OH]^-$, $H_2dipic\text{-}OH$, vanadyl sulfate ($VOSO_4$) and sodium vanadate (prepared from Na_3VO_4) are presented at the respective concentration for each compound yielding maximum GFP counts, and are compared to water, media or solvent (DMSO) controls (Fig. 4). Images of the full dose range are presented in the Supplemental Material. As shown in Figs. S3 and S4 and Fig. 4, all three dipic complexes show effects identical to that of vanadate and vanadyl sulfate in enhancing VSVΔ51-GFP infection of 786-0 cells while the three dipic ligands show no effects on viral infection.

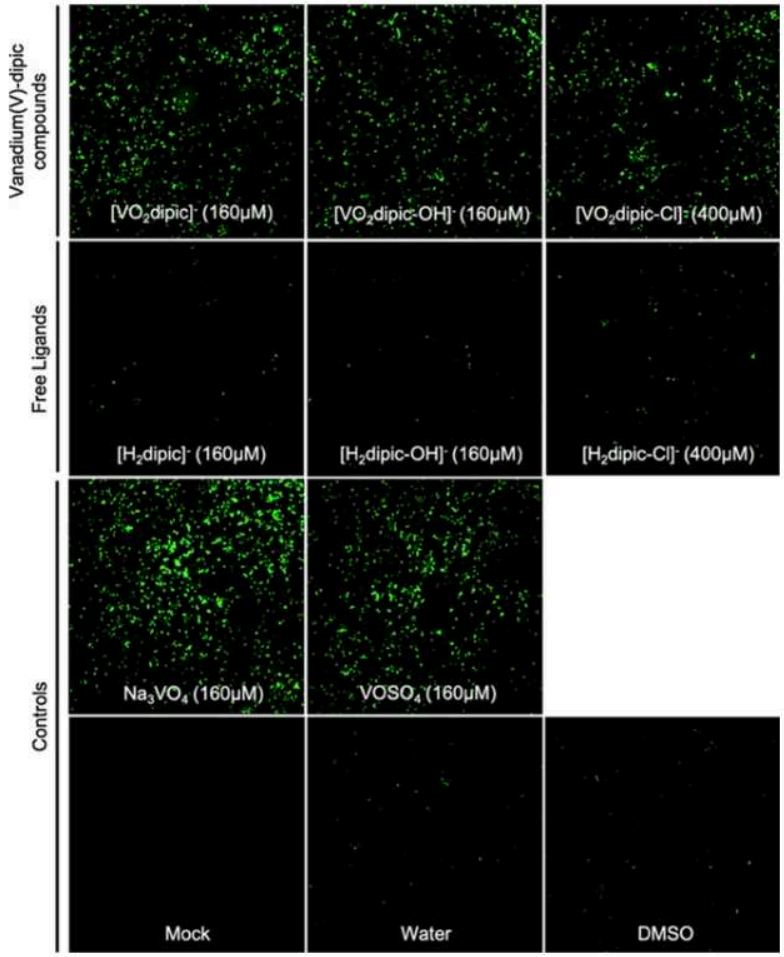

Fig. 3 Resistant human renal cell adenocarcinoma (786-0 cells) were pre-treated with dioxovanadium(V) dipicolinate complexes and ligand controls at indicated concentrations for 4 h. The cells were then infected with VSVΔ51 expressing GFP (MOI 0.05). Representative fluorescence images at peak GFP count are shown (n = 2–4, 24HPI). As a control, images of untreated uninfected ('Mock'), solvent-treated and ligand treated cells are presented

Since neither of the ligands tested were able to impact GFP counts in VSVΔ51 infected cells compared to vehicle controls, the observed enhancement in GFP expression and thus viral replication upon treatment with our complexes can therefore be attributed to the presence of the vanadium complex. Indeed, treatment with $[VO_2dipic]^-$ and $[VO_2dipic\text{-}OH]^-$ resulted in increased VSVΔ51 infection in 786-0 cells at concentrations ranging between 10-400 μM as shown by fluorescence images and GFP counts (Figs. 3, 4). Since the complexes are likely to decompose under the biological conditions used, vanadate and vanadyl cations will form and biological responses should be compared with the effects of these salts. From Figs. 3, 4 it is seen that both the vanadium(V) and vanadium(IV) salts are effective virus enhancers (as previously reported in Selman et al. 2018) and that the three V-dipicolinate complexes have similar effects as the vanadate and vanadyl cations.

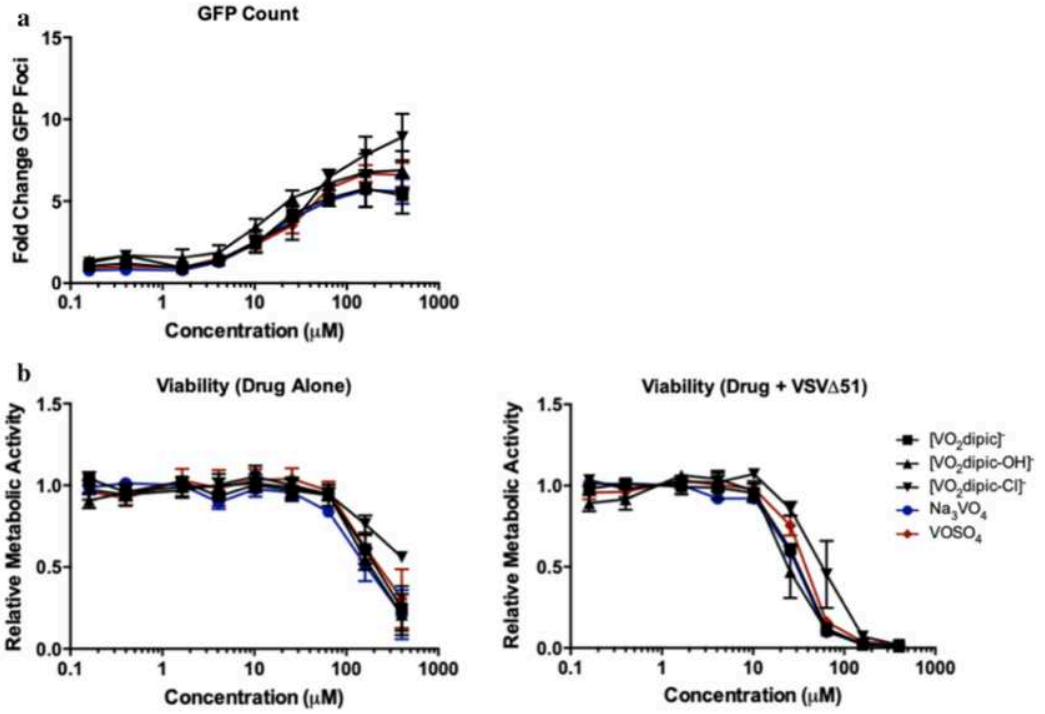

Fig. 4 Viability and GFP count. The 786-0 cells were treated with V-dipicolinate compounds or respective free-ligand controls (see Supplemental Material Fig. S2) for 4 h. As a reference, cells were treated with vanadate (Na_3VO_4) and vanadyl sulfate ($VOSO_4$) in parallel. After treatment, cells were infected with VSVΔ51 expressing GFP at a MOI of 0.05. GFP images were captured 24 h post infection (24 HPI) as an indicator of viral replication. GFP foci were quantified and normalized to untreated infected baseline values (**a**). In (**b**), at 48 HPI, the relative metabolic activity, an indicator of cell viability, was quantified using the metabolic dye AlamarBlue® (fluorescence 530 nm excitation; 590 nm emission). Values are blank-controlled and normalized to untreated uninfected controls. The drug concentration at which half the cell population is killed (lethal dose; LD_{50}) is calculated for each compound (n = 2–4), error bars represent SEM

Cell viability

The effects of vanadium(V) complexes, ligands and vanadate on cell viability were measured 48 h after addition of VSVΔ51 or mock infection using the metabolic dye AlamarBlue® (Rampersad 2012). When cells were treated with vanadium compounds alone (Fig. 4b and Table 1), some reduction in viability was observed at concentrations exceeding about 100 μM, with the chloro-dipicolinate being the least cytotoxic complex. The combination of vanadium compounds and VSVΔ51 results in a synergistic decline in cancer cell viability. As expected, the vanadium compound concentration which results in maximal GFP foci counts (Fig. 4a and Fig. S2) also corresponds to the concentration at which the viability of the 786-0 cells treated with the combination therapy drops sharply (Fig. 4b and Fig. S2). Notably, the LD_{50} of the V-dipicolinate complexes drops approximately tenfold in the presence of VSVΔ51 (Table 1). The chloro-dipicolinate shows the highest LD_{50} in the combination treatment and correlates well with the toxicity of the compounds alone. No effects on cell viability are observed with free ligands as shown in Fig. S2 suggesting that the synergistic increase in cytotoxicity upon infection is dependent on the presence of the vanadium.

Table 1 The LD_{50} values for $[VO_2dipic\text{-}Cl]^-$, $[VO_2dipic]^-$, $[VO_2dipic\text{-}OH]^-$, and sodium vanadate ($H_2VO_4^-$)

Compound	LD_{50} values of drug alone (μM)	LD_{50} values of drug + VSVΔ51 (μM)
$[VO_2dipic]^-$	250	31
$[VO_2dipic\text{-}OH]^-$	220	28
$[VO_2dipic\text{-}Cl]^-$	560	62
Na_3VO_4	180	29
$VOSO_4$	290	39

See Supplemental Material for corresponding the LD50 values for deprotonated ligands of H_2dipic, H_2dipic-Cl and H_2dipic-OH observed at neutral pH (n = 2–4)

These results show convincingly that the V-dipicolinate complexes have similar viral sensitizing and cytotoxic effects as the V-salts. However, the oncolytic activity of the combination of V-compound and VSVΔ51 was dramatically more profound than the compound or virus alone. Building on these findings, we next sought to investigate the forms of the vanadium compounds under conditions representative of the cell culture media.

Verification of the known speciation constant at pH 6.60

First, the ^{51}V and ^{1}H NMR spectra were recorded at pH 6.00 at ionic strengths of 0.40, 0.15 and without any addition of salt. As shown in Fig. 5, there are large differences in how much complex is formed at these different ionic strengths, as is evidenced by the ratio of the complex and free ligand peaks. These differences show that it is critical to select proper ionic strength to predict speciation for conditions in which compounds interact with the host. The calculation of ionic strength of the media was done using Eq. (5). As detailed in the Supplemental Material, more than 40 components in the media were evaluated with regard to the charge and their respective contribution to the ionic strength. Assuming that the contributions of serum albumin and other minor components were negligible, the total ionic strength was found to be 0.17. This ionic strength is similar to the speciation studies reported generated in aqueous solutions with NaCl up to an ionic strength of 0.15 (Elvingson et al. 1996). The constants were determined in these studies for vanadate oligomers and were chosen to be used for prediction of speciation in media described in this work. The ionic strength of the growth medium was calculated using Eq. (5). The known pH-dependent apparent equilibrium constants were calculated by using the concentrations obtained by ^{1}H and and ^{51}V NMR spectroscopies, see Eqs. (4) and (5). Then, NMR studies were performed to verify

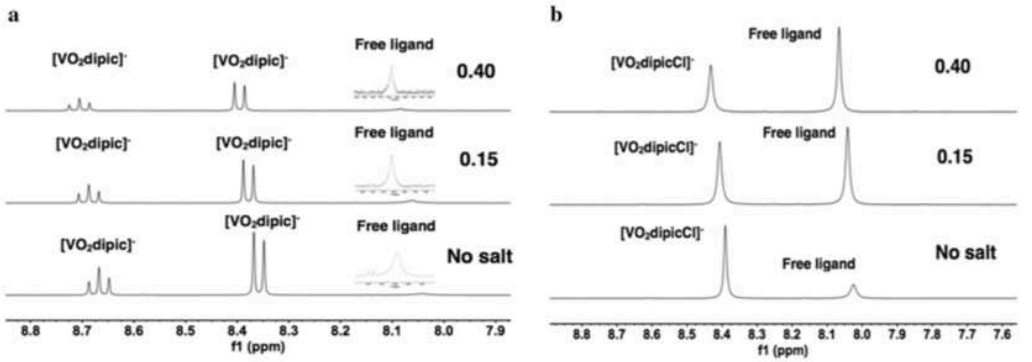

Fig. 5 The ^{1}H NMR spectra recorded in solutions of $[VO_2dipic]^-$ at pH 6.00 (**a**) and $[VO_2dipicCl]^-$ at pH 6.00 (**b**) at no added salt (bottom), 0.15 M KCl and at 0.40 M KCl

the known fits with $[VO_2dipic]^-$ in order to then carry out studies with both $[VO_2dipic]^-$ and $[VO_2dipic\text{-}Cl]^-$ compounds to quantify the amounts of $[VO_2dipic]^-$ and $[VO_2dipic\text{-}Cl]^-$ at the ionic strength of the cell culture media.

Spectra of the $[VO_2dipic]^-$ complex and the free ligand are reported at 0.40 ionic strength were repeated at pH 6.60 to verify that ^{51}V and ^{1}H NMR spectroscopies accurately describe the stability of the $[VO_2dipic]^-$ complex. These NMR spectra were done at several pH values, but specifically compared to the pH 6.60 data with the apparent formation constant reported previously (Crans et al. 2000). Using the data at pH 6.60, the apparent formation constant for $[VO_2dipic]^-$ was found to be 3.9×10^{-2} M^{-1}, and thus verifying this approach to obtain parameters needed to do the speciation profile calculations (Figs. S4 and Table S1).

Speciation constants developed to estimate intact vanadium(v) dipicolinate complex in cell culture media

Spectra of the $[VO_2dipic]^-$ complex, the free dipic ligand and the corresponding $[VO_2dipic\text{-}Cl]^-$ complex and its free ligand at 0.15 ionic strength were recorded using ^{1}H and ^{51}V NMR spectroscopies. These NMR spectra are shown in the Supplemental Material (Figs. S4–S7). Using the measured pKa value for H_2dipic and $H_2dipic\text{-}Cl$ and the apparent formation constants for $[VO_2(dipic)]^-$ and $[VO_2dipic\text{-}Cl]^-$ allowed for the calculation of speciation profiles for both complexes. The speciation of these systems is shown in Fig. S8 from pH 5 though 9 at the concentration that the NMR spectra were recorded at. However, for the studies described here, the speciation profiles were calculated for 0.16 mM which is near or at the concentration where the greatest amount of virus enhancement was observed for $[VO_2(dipic)]^-$ and $[VO_2dipic\text{-}OH]^-$.

According to the speciation profiles for the low end of the dose response range (0.002 μM), there is a little of the intact $[VO_2dipic]^-$, $[VO_2dipic\text{-}OH]^-$ and $VO_2dipic\text{-}Cl]^-$ complexes, whereas at the high end of the dose response range (0.4 mM) observable amounts of complexes are present. The speciation profiles of the $[VO_2dipic]^-$ and $[VO_2dipic\text{-}Cl]^-$ complexes illustrated in Fig. 6 are shown at the limiting concentrations which results in maximal GFP foci counts (Fig. 4a and Fig. 2S) which is also the concentration where the viability of the 786-0 cells treated with the combination therapy drops sharply (Fig. 4b and Fig. 2S). The concentration at the peak GFP count was observed at 160 μM for both $[VO_2dipic]^-$ and $[VO_2dipic\text{-}OH]^-$ complexes and at 400 μM for the $[VO_2dipic\text{-}Cl]^-$ complex. Viability and GFP data for the $[VO_2dipic]^-$, $[VO_2dipic\text{-}OH]^-$ and $[VO_2dipic\text{-}Cl]^-$ complexes are indistinguishable from the effects observed with vanadate at 160 μM. The LD_{50} of the $[VO_2dipic\text{-}Cl]^-$ complex when combined with VSVΔ51 is twice that of the $[VO_2dipic]^-$ compound combined with virus (Fig. 4). These observations show that the $[VO_2dipic]^-$ and the $[VO_2dipic\text{-}OH]^-$ complexes may be slightly more effective although it is not statistically significant. This interpretation is supported since the speciation shows similar amount of complex present in solutions when the virus enhancement takes place. This would suggest that regardless whether some of these coordination complexes are intact or hydrolyzed in the incubation media, similar responses may facilitate the uptake of the compounds by cancer cells so the interactions of the $[VO_2dipic\text{-}Cl]^-$ complex was explored by studies in the microemulsion cellular system for comparison with similar studies done with $[VO_2dipic]^-$.

Interactions of $[VO_2dipic\text{-}Cl]^-$ complex with model membrane interfaces

The interaction of the $[VO_2dipic\text{-}Cl]^-$ complex with model membrane interfaces was investigated using a microemulsion system, specifically in 750 mM AOT/isooctane reverse micelles. Microemulsions are useful in the investigation of molecular placement of molecules at the interface, and the aforementioned system has been well-studied and characterized in detail (Baruah et al. 2006; Correa et al. 2012). Studies were done at different pH values of the aqueous solution containing $[VO_2dipic\text{-}Cl]^-$ complex prior to addition to the AOT/isooctane suspension, but no changes were observed in the chemical shifts for the complex indicative of no changes in the protonation state near the physiological pH range (Figs. S6, S7). Studies were then done at pH 5.50 and 6.00 (see the Supplemental Material (Figs. S6, S7)) demonstrating that these complexes tend to be more stable in acidic media. The $[VO_2dipic\text{-}Cl]^-$ complex was found to be less stable than either $[VO_2dipic\text{-}OH]^-$ or

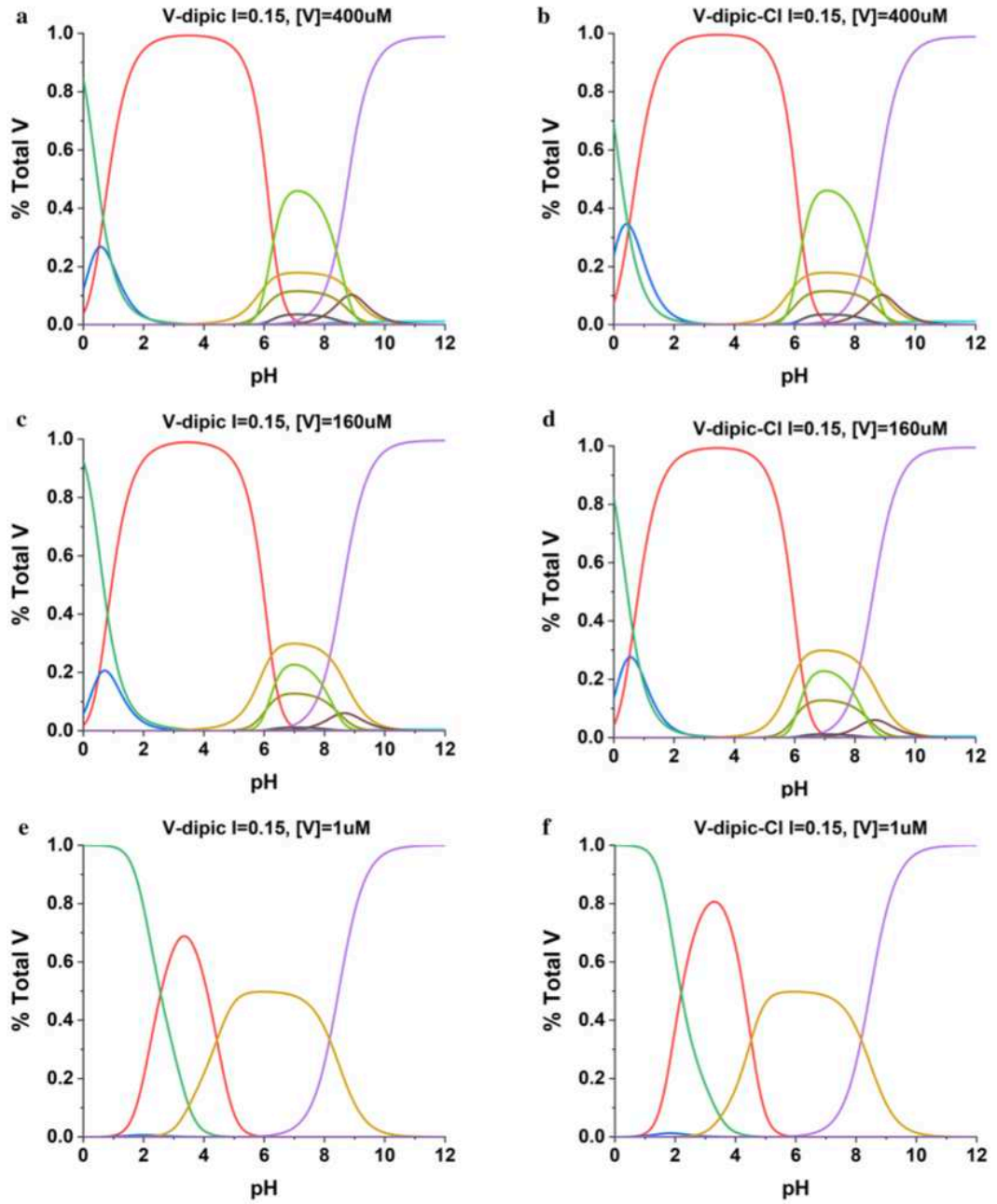

Fig. 6 The speciation profiles for $[VO_2dipic]^-$ (**a**, **c**, **e**) and $[VO_2dipic\text{-}Cl]^-$ (**b**, **d**, **f**) are shown using total V-concentrations of 400 μM mM (**a**, **b**), 160 μM (**c**, **d**) and 1.0 **μ**M (**e**, **f**). The calculations were done using the vanadate oligomerization constants for 0.15 M NaCl (Elvingson et al. 1996). Key for the curves: red $[VO_2dipic]^-$ or $[VO_2dipic\text{-}Cl]^-$; blue $H[VO_2dipic]$ or $H[VO_2dipic\text{-}Cl]$; purple V_1 (HVO_4^{2-}); green VO^{2+}; beige V_1 ($H_2VO_4^-$); light green V_4 ($V_4O_{12}^{4-}$); olive V_2 ($H_2V_2O_7^{2-}$)

$[VO_2dipic]^-$ complexes which is consistent with previous report (Li et al. 2009; Smee et al. 2009; Willsky et al. 2011), and may explain the observed inferior potency and cytotoxicity of the chlorodipicolinate complex (Fig. 4).

To examine the possibility that the complexes reside in the water pool or near the interface, the size of the reverse micelles was changed, and the system was observed using both ^1H and ^{51}V NMR spectroscopies, Fig. 7. It has previously been documented that complexes penetrating the interface show no differences in ^{51}V NMR chemical shifts upon placement into the reverse micelle (Crans et al. 2006; Sostarecz et al. 2014). If the compound associates with the interface as well as the water pool, then there is an observed change in the ^1H NMR chemical shifts defined by the particular location of the compound as the size of the reverse micelle changes; this is caused by the decrease of the size of the water pool and the change of the interface-water layer (Crans et al. 2011; Sostarecz et al. 2014). A solution of $[VO_2dipic\text{-}Cl]^-$ was added to reverse micelles ranging from sizes 8 to 20. As shown in Fig. 6, there are two signals observed above 8 ppm; the signal near 8.1 ppm is due to the free ligand and the signal at 8.3 ppm is due to the $[VO_2dipic\text{-}Cl]^-$ complex. The observed downfield shift of the ^1H NMR peaks as the reverse micelle increased in size is consistent with the complex penetrating the interface albeit perhaps not as deeply as the parent complex (Crans et al. 2006; Sostarecz et al. 2014).

In contrast, the ^1H peaks corresponding to the free ligand were found to shift upfield. This shift is generally associated with interactions of the solute with the interface near the water pool which are different than that of the corresponding complex (Crans et al. 2011). The visual representation of the suggested average locations of the $[VO_2dipic\text{-}Cl]^-$ complex and the free chlorodipic ligand is shown in Fig. 8. The location suggested previously for the $[VO_2dipic]^-$ complex is high up in the tails which is not quite accurate for the $[VO_2dipic\text{-}Cl]^-$ complex (Crans et al. 2006; Sostarecz et al. 2014). The dipic ligand is more mobile and moves up and down ranging from the deep tails to the headgroup; however, the chemical shift varies from 8.1 ppm for w_0 6 to 7.9 ppm for w_0 12 which is similar to the changes in chemical shift of the chlorodipic-ligand, shown in the schematic representation in Fig. 7.

Discussion

In this paper we investigate the capacity of one class of vanadium coordination complexes, dioxovanadium(V) dipicolinates, to enhance oncolytic virus infection. These complexes have been selected as the first series of compounds to evaluate because of their five-coordinate geometry (Willsky et al. 2011; Crans et al. 1996), and because their chemical (Crans 2000; Crans et al. 2003b; Li et al. 2009; Smee et al. 2009) and their antidiabetic properties have been characterized extensively (Crans et al. 2003b; Willsky et al. 2011), thus making it possible to investigate the pharmacochemical properties of vanadium complexes

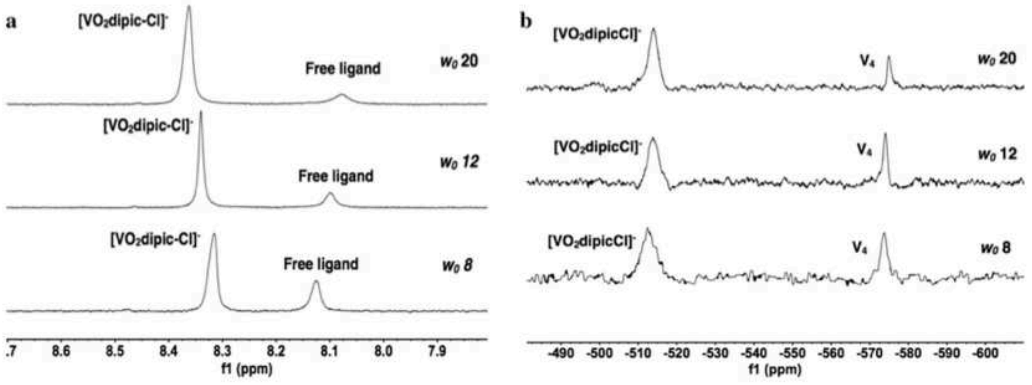

Fig. 7 ^1H (**a**) and ^{51}V (**b**) NMR spectra of 750 mM AOT/isooctane suspensions containing $[VO_2dipic\text{-}Cl]^-$ complex (concentrations ranging from 2.25 to 5.25 mM) in sizes w_0 8–20

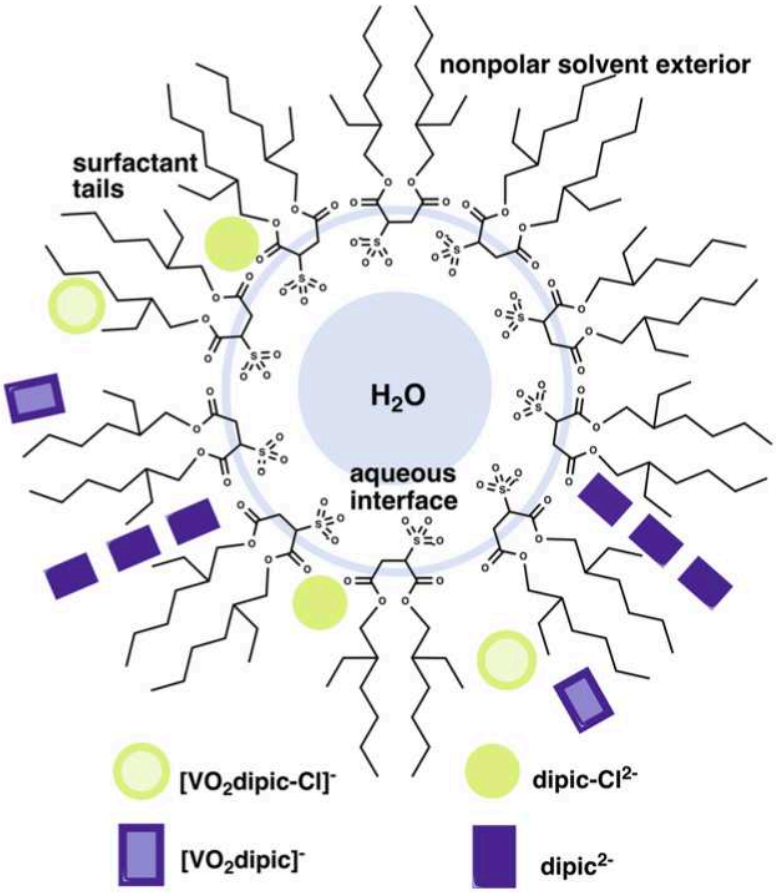

Fig. 8 Schematic representation of the average locations of the $[VO_2dipic\text{-}Cl]^-$ complex and the free chlorodipic ligand in a reverse micelle compared to the $[VO_2dipic]^-$ complex and the free dipic ligand

in enhancing OV activity. The studies described in this work are conducted using speciation analysis with the intent to examine the nature of the active form. The complexes selected have a well-known chemistry, and some biological responses of these vanadium coordination complexes have been reported (Crans et al. 2003b; Li et al. 2009; Smee et al. 2009; Willsky et al. 2011). Because several classes of vanadium compounds have been reported to have both anti-cancer and anti-diabetic effects, it is of interest to learn the similarity of how the enhancement of oncolytic viruses compares with the anti-diabetic and anti-cancer effects with different classes of vanadium compounds, such as the vanadium(V) dipicolinates tested in this study.

The hydrolytic chemistry of V-dipicolinate compounds has been studied extensively (Crans 2000; Crans et al. 2003b; Li et al. 2009; Smee et al. 2009), and thus facilitates the analysis of the observed oncolytic effects of these vanadium compounds. All the vanadium(V) dipicolinate compounds were found to be more stable at the acidic pH values, with the parent $[VO_2dipic]^-$ complex showing the highest stability (Crans 2000; Crans et al. 2003b; Li et al. 2009; Smee et al. 2009; Willsky et al. 2011). However, the difference in stability was modest, and unlikely to impact biological activity. It is therefore important that the effects of these complexes should be compared to those of the simple salts, the vanadate anion and the vanadyl cation. In this work we modeled the expected speciation under the condition of the virus

infection for both the $[VO_2dipic\text{-}Cl]^-$ and the parent $[VO_2dipic]^-$ complex. Much work has been done on the speciation and binding of the complexes to transferrin and serum albumin (Sanna et al. 2009a, b, 2012), however, since these studies were exclusively done in cell culture, such considerations are not appropriate for the studies reported here. We find that the anticipated concentrations of the intact complexes are within a factor of two, and that this is consistent with the observed differences in the LD_{50} values.

No statistically distinguishable differences could be observed in the normalization of blood glucose levels between all the different vanadium(V)-dipicolinates tested (the parent, –OH, –Cl, $–NH_2$, $–NO_2$ substituted vanadium(V) dipicolinates) (Willsky et al. 2011). Trends of improved activity were, however, reported for the parent $[VO_2dipic]^-$ complex (Crans et al. 2003b; Li et al. 2009; Willsky et al. 2011). These results are consistent with the interpretation that the action of the vanadium compounds is a result of the vanadate after it dissociates from the coordination complex. It was, therefore, of interest to investigate if compound degradation was observed during viral sensitization. The fact that all three vanadium(V)-dipicolinate complexes show similar enhancement of virus infection compared to vanadate and vanadyl cation confirms that for these three complexes and the two salts, the effects are likely to be caused by the vanadium.

The possibility that the dipicolinate ligands may mainly serve to assist with absorption of the compounds was examined both in a simple membrane model study with $[VO_2dipic\text{-}Cl]^-$ and microemulsions, thereby testing how the complex responds as it approaches interfaces. The studies showed that the $[VO_2dipic\text{-}Cl]^-$ complex, as well as that of $[VO_2dipic]^-$, associates with the interface. However, whereas the parent complex can penetrate the interface (Crans et al. 2006), the $[VO_2dipic\text{-}Cl]^-$ is likely to associate more with the interface, and is not able to overcome the hydrolysis as much as the parent complex. The biological studies show no statistical significant difference between the complexes (Crans et al. 2003b; Li et al. 2009; Willsky et al. 2011), thereby suggesting that the ligands are not different to the point of exerting a robust biological effect.

Oncolytic virotherapy has led to durable responses in only a small portion of patients when used as single agents. To improve therapeutic outcomes, several pharmaco-viral strategies are currently being explored. For example, the JAK inhibitor ruxolitinib, dimethyl fumarate, histone deacetylase inhibitor, mTOR inhibitors and other novel synthetic compounds have all been tested preclinically in combination with oncolytic rhabdoviruses like VSVΔ51 (reviewed in Phan et al. 2018). Adding to this list, our group has shown that vanadate improves oncolytic VSVΔ51 spread, bystander killing, and the combination therapy can lead to robust anti-tumor immunity in murine models (Selman et al. 2018). Herein, we further demonstrate that vanadium(V)-dipicolinate complexes enhance OVs in a fashion consistent with the hydrolysis of the complexes into active vanadate as reported in anti-diabetic studies. The results of the current study suggest that improving vanadium compound stability and their ability to traverse lipid membranes could lead to improvements in potency. This is an important pursuit when contemplating vanadium compounds as adjuvants specifically catered to oncolytic viruses, much like aluminum oxides (Li et al. 2008) have and continue to be used as adjuvants for vaccines for infectious disease. Further studies will be required to better understand the implication of the observed lipid association of dipicolinate compounds in terms of the previously reported mechanism of action in the context of OV therapy, which involves a shift in the phosphorylation pattern of STAT1 and STAT2 (Selman et al. 2018), as well as the role of cellular phosphatases.

Acknowledgements AB holds a QEII Ontario Graduate Scholarship and a Hans K. Uhtoff scholarship. MS was awarded a Canadian Institutes of Health Research (CIHR) doctoral scholarship. JSD thanks Terry Fox Research Institute Program Project grant for funding. JSD also holds a New Investigator award from CIHR in Infection and Immunity. DCC received funding from the Arthur Cope foundation administered by the American Chemical Society. The authors thank all funding agencies for their generous support of scholarships and grants.

References

Achard C, Surendran A, Wedge M, Ungerechts G, Bell J, Ilkow C (2018) Lighting a Fire in the tumor microenvironment using oncolytic immunotherapy. EBioMedicine 31:17–24

Alderighi L, Gans P, Ienco A, Peters D, Sabatini A, Vacca A (1999) Hyperquad simulation and speciation (HySS): a utility program for the investigation of equilibria involving

soluble and partially soluble species. Coord Chem Rev 184:311–318

Baruah B, Roden J, Sedgwick M, Correa N, Crans D, Levinger N (2006) When is water not water? Exploring water confined in large reverse micelles using a highly charged inorganic molecular probe. J Am Chem Soc 128:12758–12765

Bishayee A, Waghray A, Patel M, Chatterjee M (2010) Vanadium in the detection, prevention and treatment of cancer: the in vivo evidence. Cancer Lett 294:1–12

Buglyo P, Crans D, Nagy E, Lindo R, Yang L, Smee J, Jin W, Chi L, Godzala M, Willsky G (2005) Aqueous chemistry of the vanadium(III) (V-III) and the V-III-dipicolinate systems and a comparison of the effect of three oxidation states of vanadium compounds on diabetic hyperglycemia in rats. Inorg Chem 44:5416–5427

Correa N, Suilber J, Riter R, Levinger N (2012) Nonaqueous polar solvents in reverse micelle systems. Chem Rev 112:4569–4602

Crans D (2000) Chemistry and insulin-like properties of vanadium(IV) and vanadium(V) compounds. J Inorg Biochem 80:123–131

Crans D (2015) Antidiabetic, chemical, and physical properties of organic vanadates as presumed transition-state inhibitors for phosphatases. J Org Chem 80:11899–11915

Crans D, Keramidas A, Drouza C (1996) Organic vanadium compounds—transition state analogy with organic phosphorus compounds. Phosphorus, Sulfur Silicon Relat Elem 109–110:245–248

Crans D, Yang L, Jakusch T, Kiss T (2000) Aqueous chemistry of ammonium (dipicolinato)oxovanadate(V): the first organic vanadium(V) insulin-mimetic compound. Inorg Chem 39:4409–4416

Crans D, Mahroof-Tahir M, Johnson M, Wilkins P, Yang L, Robbins K, Johnson A, Alfano J, Godzala M, Austin L, Willsky G (2003a) Vanadium(IV) and vanadium(V) complexes of dipicolinic acid and derivatives. Synthesis, X-ray structure, solution state properties and effects in rats with STZ-induced diabetes. Inorg Chim Acta 356:365–378

Crans D, Yang L, Alfano J, Chi L, Jin W, Mahroof-Tahir M, Robbins K, Toloue M, Chan L, Plante A, Grayson R, Willsky G (2003b) (4-Hydroxypyridine-2,6-dicarboxylato)oxovanadate(V)-a new insulin-like compound: chemistry, effects on myoblast and yeast cell growth and effects on hyperglycemia in rats with STZ-induced diabetes. Coord Chem Rev 237:13–22

Crans D, Rithner C, Baruah B, Gourley B, Levinger N (2006) Molecular probe location in reverse micelles determined by NMR dipolar interactions. J Am Chem Soc 128:4437–4445

Crans D, Trujillo A, Pharazyn P, Cohen M (2011) How environment affects drug activity: localization, compartmentalization and reactions of a vanadium insulin-enhancing compound, dipicolinatooxovanadium(V). Coord Chem Rev 255:2178–2192

Crans D, Woll K, Prusinskas K, Johnson M, Norkus E (2013) Metal Speciation in Health and Medicine Represented by Iron and Vanadium. Inorg Chem 52:12262–12275

Crans D, Yang L, Haase A, Yang X (2018) Health benefits of vanadium and its potential as an anticancer agent. Met Ions Life Sci 18:251

Crans D, Barkley N, Montezinho L, and Castro M (2019). Vanadium Compounds as enzyme inhibitors with a focus on anticancer effects. In: Angela Casini AVASMM (ed) Metal-based Anticancer Agents. pp 169–195

D'cruz O, Uckun F (2002) Metvan: a novel oxovanadium(IV) complex with broad spectrum anticancer activity. Expert Opin Invest. Drugs 11:1829–1836

Davies D, Hol W (2004) The power of vanadate in crystallographic investigations of phosphoryl transfer enzymes. FEBS Lett 577:315–321

Diallo J, Vähä-Koskela M, Boeuf FL, Bell J (2012) Propagation, purification, and in vivo testing of oncolytic vesicular stomatitis virus strains. Oncol Viruses 797:127–140

Elvingson K, Gonzalez Baro A, Pettersson L (1996) Speciation in vanadium bioinorganic systems. 2. An NMR, ESR, and potentiometric study of the aqueous H + -vanadate-maltol system. Inorg Chem 35:3388–3393

Etcheverry S, Ferrer E, Naso L, Rivadeneira J, Salinas V, Williams P (2008) Antioxidant effects of the VO(IV) hesperidin complex and its role in cancer chemoprevention. J Biol Inorg Chem 13:435–447

Evangelou A, Kolettas E, Tenopoulou M, Galaris D, Gonos E, Manos G (2002) Vanadium inhibits HaCaT cell proliferation but does not cause apoptosis. Met Ions Biol Med 7:154–158

Glasoe P, Long FA (1960) Use of glass electrodes to measure acidities in deuterium oxide. J Phys Chem 64:188–190

Goldfine A, Patti M, Zuberi L, Goldstein B, Leblanc R, Landaker E, Jiang Z, Willsky G, Kahn C (2000) Metabolic effects of vanadyl sulfate in humans with non—insulin-dependent diabetes mellitus: in vivo and in vitro studies. Metabolism 49:400–410

Kieler J, Gromek A, Nissen N (1965) Studies on the antineoplastic effect of vanadium salts. Acta Chir Scand Suppl 343:154–164

Kioseoglou E, Petanidis S, Gabriel C, Salifoglou A (2015) The chemistry and biology of vanadium compounds in cancer therapeutics. Coord Chem Rev 301–302:87–105

Kiss T, Jakusch T, Hollender D, Dornyei A, Enyedy E, Pessoa J, Sakurai H, Sanz-Medel A (2008) Biospeciation of antidiabetic VO(IV) complexes. Coord Chem Rev 252:1153–1162

Kopfmaier P, Wagner W, Hesse B, Köpf H (1981) Tumor inhibition by metallocenes: activity against leukemias and detection of the systemic effect. Europ J Cancer 17:665–669

Kowalski S, Hac S, Wyrzykowski D, Zauszkiewicz-Pawlak A, Inkielewicz-Stepniak I (2017) Selective cytotoxicity of vanadium complexes on human pancreatic ductal adenocarcinoma cell line by inducing necroptosis, apoptosis and mitotic catastrophe process. Oncotarget 8:60324–60341

Leon I, Diez P, Baran E, Etcheverry S, Fuentes M (2017) Decoding the anticancer activity of VO-clioquinol compound: the mechanism of action and cell death pathways in human osteosarcoma cells. Metallomics 9:891–901

León I, Cadavid-Vargas J, Tiscornia I, Porro V, Castelli S, Katkar P, Desideri A, Bollati-Fogolin M, Etcheverry S (2015) Oxidovanadium (IV) complexes with chrysin and silibinin: anticancer activity and mechanisms of action in a human colon adenocarcinoma model. J Biol Inorg Chem 20:1175–1191

Li H, Willingham S, Ting J, Re F (2008) Cutting edge: inflammasome activation by alum and alum's adjuvant effet are mediated by NLRP3. J Immunol 181:17–21

Li M, Ding W, Smee J, Baruah B, Willsky G, Crans D (2009) Anti-diabetic effects of vanadium(III, IV, V)-chlorodipicolinate complexes in streptozotocin-induced diabetic rats. Biometals 22:895–905

Lyonnet B, Martz S, Martin E (1899) L'emploi therapeutique des derives du vanadium. La Presse Méd 1:191–192

Mclauchlan C, Peters B, Willsky G, Crans D (2015) Vanadium-phosphatase complexes: phosphatase inhibitors favor the trignonal bipyramidal transition state geometries. Coord Chem Rev 301–302:163–199

Murthy M, Toney J, Rao L, Kuo L, Marks T (1986) Pharmacologic studies on the new antitumor agent vanadocene dichloride (VDC). Proc Am Assoc Cancer Res 27:279–279

O'Shea JJ, McVicar DW, Bailey TL, Burns C, Smyth MJ (1992) Activation of human peripheral blood T lymphocytes by pharmacological induction of protein-tyrosine phosphorylation. Proc Natl Acad Sci USA 89(21):10306–10310

Pessoa J, Etcheverry S, and Gambino D (2015a). Vanadium compounds in medicine. In: Conte V and Giulia L (eds) The Ninth International Symposium on the chemistry and biological chemistry of vanadium. Padova, Italy

Pessoa J, Etcheverry S, Gambino D (2015b) Vanadium compounds in medicine. Coord Chem Rev 301:24–48

Petanidis S, Kioseoglou E, Hadzopoulou-Cladaras M, Salifoglou A (2013) Novel ternary vanadium-betaine-peroxido species suppresses H-ras and matrix metalloproteinase-2 expression by increasing reactive oxygen species-mediated apoptosis in cancer cells. Cancer Lett 335:387–396

Pettersson L, Hedman B, Andersson I, Ingri N (1983) Multicomponent polyanions. 34. P potentiometric and 51 V NMR study of equilibria in the H + -HVO42- system in the 0.6 M Na(Cl) medium covering the range 1£-1 g[H +]£10. Chem Scrip 22:254–264

Pettersson L, Andersson I, Hedman B (1985) Multicomponent polyanions. 37. A potentiometric and 51 V-NMR study of equilibria in the H + -HVO42- system in 3.0 M-Na(ClO4) medium covering the range 1£-1 g[H +]£10. Chem Scr 25:309–317

Phan M, Watson M, Alain T, Diallo J (2018) Oncolytic viruses on drugs: achieving higher therapeutic efficacy. ACS Infect Dis 4:1448–1467

Rampersad S (2012) Multiple applications of alamar blue as an indicator of metabolic function and cellular health in cell viability bioassays. Sensors 12:12347–12360

Rehman H, Silk A, Kane M, Kaufman H (2016) Into the clinic: Talimogene laherparepvec (T-VEC), a first-in-class intratumoral oncolytic viral therapy. J Immunother Cancer 4:53

Sanna D, Garribba E, Micera G (2009a) Interaction of VO2 + ion with human serum transferrin and albumin. J Inorg Biochem 103:648–655

Sanna D, Micera G, Garribba E (2009b) On the transport of vanadium in blood serum. Inorg Chem 48:5747–5757

Sanna D, Buglyo P, Micera G, Garribba E (2012) Biotransformation of BMOV in the presence of blood serum proteins. Metabolomics 4:33–36

Sanna D, Ugone V, Micera G, Buglyo P, Biro L, Garribba E (2017) Speciation in human blood of Metvan, a vanadium based potential anti-tumor drug. Dalton Trans 46:8950–8967

Scior T, Guevara-Garcia J, Do Q, Bernard P, Laufer S (2016) Why antidiabetic vanadium complexes are not in the pipeline of "big pharma" drug research? A critical review. Curr Med Chem 23:2874–2891

Secrist JP, Burns LA, Karnitz L, Koretzky GA, Abraham RT (1993) Stimulatory effects of the protein tyrosine phosphatase inhibitor, pervanadate, on T-cell activation events. J Biol Chem 268(8):5886–5893

Selman M, Rousso C, Bergeron A, Son H, Krishnan R, El-Sayes N, Varette O, Chen A, Le Boeuf F, Tzelepis F, Bell J, Crans D, Diallo J (2018) Multi-modal potentiation of oncolytic virotherapy by vanadium compounds. Mol Ther 26:56–69

Smee J, Epps J, Ooms K, Bolte S, Polenova T, Baruah B, Yang L, Ding W, Li M, Willsky G, La Cour A, Anderson O, Crans D (2009) Chloro-substituted dipicolinate vanadium complexes: synthesis, solution, solid-state, and insulin-enhancing properties. J Inorg Biochem 103:575–584

Sostarecz A, Gaidamauskas E, Distin S, Bonetti S, Levinger N, Crans D (2014) Correlation of insulin-enhancing properties of vanadium-dipicolinate complexes in model membrane systems: phospholipid Langmuir monolayers and AOT reverse micelles. Chem Eur J 20:5149–5159

Stahla M, Baruah B, James D, Johnson M, Levinger N, Crans D (2008) 1H NMR studies of aerosol-OT reverse micelles with alkali and magnesium counterions: preparation and analysis of MAOTs. Langmuir 24:6027–6035

Storr T, Thompson K, Orvig C (2006) Design of targeting ligands in medicinal inorganic chemistry. Chem Soc Rev 36:534–544

Thompson K, Orvig C (2006) Vanadium in diabetes: 100 years from phase 0 to phase I. J Inorg Biochem 100:1925–1935

Thompson K, Liboiron B, Sun Y, Bellman K, Setyawati I, Patrick B, Karunaratne V, Rawji G, Wheeler J, Sutton K, Bhanot S, Cassidy C, Mcneill J, Yuen V, Orvig C (2003) Preparation and characterization of vanadyl complexes with bidentate maltol-type ligands; in vivo comparisons of anti-diabetic therapeutic potential. J Biol Inorg Chem 8:66–74

Thompson K, Lichter J, Lebel C, Scaife M, Mcneill J, Orvig C (2009) Vanadium treatment of type 2 diabetes: a view to the future. J Inorg Biochem 103:554–558

Wang Q, Liu T, Fu Y, Wang K, Yang X (2010) Vanadium compounds discriminate hepatoma and normal hepatic cells by differential regulation of reactive oxygen species. J Biol Inorg Chem 15:1087–1097

Willsky G, Chi L, Godzala M, Kostyniak P, Smee J, Trujillo A, Alfano J, Ding W, Hu Z, Crans D (2011) Anti-diabetic effects of a series of vanadium dipicolinate complexes in rats with streptozotocin-induced diabetes. Coord Chem Rev 255:2258–2269

Willsky G, Halvorsen K, Godzala M, Chi L, Most M, Kaszynski P, Crans D, Goldfine A, Kostyniak P (2013) Coordination chemistry may explain pharmacokinetics and clinical response of vanadyl sulfate in type 2 diabetic patients. Metallomics 5:1491–1502

Wu J, Hong Y, Xg XY (2016a) Bis(acetylacetonato)-oxidovanadium(IV) and sodium metavanadate inhibit cell proliferation via ROS-induced sustained MAPK/ERK

activation but with elevated AKT activity in human pancreatic cancer AsPC-1 cells. J Biol Inorg Chem 21:1–11
Wu X, Peters B, Rithner C, Crans D (2016b) Multinuclear NMR studies of aqueous vanadium-HEDTA complexes. Polyhedron 114:325–332
Yang X, Wang K (2016) Focusing on the link between diabetes, Alzheimer's disease and cancer for the discovery of new medicines. Curr Top Med Chem 16:675
Yang X, Wang K, Lu J, Crans D (2003) Membrane transport of vanadium compounds and the interaction with the erythrocyte membrane. Coord Chem Rev 237:103–111
Yoshikawa Y, Sakurai H, Crans D, Micera G, Garribba E (2014) Structural and redox requirements for the action of anti-diabetic vanadium compounds. Dalton Trans 43:6965–6972
Zizic Z, Miladinovic M, Stanic M, Hadzibrahimovic M, Zivic M, Zakrzekska J (2016) (51)V NMR investigation of cell-associated vanadate species in Phycomyces blakesleeanus mycelium. Res Microbiol 167:521–528

Appendix VII: Polyoxidovanadates $[Mo^{VI}V^{V}_{9}O_{28}]^{5-}$ and $[H_2Pt^{IV}V^{V}_{9}O_{28}]^{5-}$ interact with CHO cell plasma membrane lipids causing aggregation and activation of a G protein-coupled receptor

This is the manuscript that corresponds to Chapter 5 and is published in *Frontiers in Chemical Biology* (Kostenkova et. al, 2023).

References

Kostenkova, K.; Althumairy, D.; Postal, K.; Arhouma, Z.; Rajan, A.; Kortz, U.; Barisas, B. G.; Roess, D.; Crans, D. C. Polyoxidovanadates $[Mo^{VI}V^{V}_{9}O_{28}]^{5-}$ and $[H_2Pt^{IV}V^{V}_{9}O_{28}]^{5-}$ interact with CHO cell plasma membrane lipids causing aggregation and activation of a G protein-coupled receptor. *Front. Chem*. *Biol*. **2023**, *2*:1126975. doi: 10.3389/fchbi.2023.1126975.

frontiers | Frontiers in Chemical Biology

TYPE Original Research
PUBLISHED 07 April 2023
DOI 10.3389/fchbi.2023.1126975

OPEN ACCESS

EDITED BY
Mi Hee Lim,
Korea Advanced Institute of Science and Technology (KAIST), Republic of Korea

REVIEWED BY
Enrique González-Vergara,
Instituto de Ciencias de la Benemérita Universidad Autónoma de Puebla, Mexico
Boris-Marko Kukovec,
University of Split, Croatia

*CORRESPONDENCE
Deborah A. Roess,
deborah.roess@colostate.edu
Debbie C. Crans,
debbie.crans@colostate.edu

†These authors have contributed equally to this work

SPECIALTY SECTION
This article was submitted to Molecular Sciences, a section of the journal Frontiers in Chemical Biology

RECEIVED 21 December 2022
ACCEPTED 03 February 2023
PUBLISHED 07 April 2023

CITATION
Kostenkova K, Althumairy D, Rajan A, Kortz U, Barisas BG, Roess DA and Crans DC (2023), Polyoxidovanadates $[Mo^{VI}V^{V}_{9}O_{28}]^{5-}$ and $[H_2Pt^{IV}V^{V}_{9}O_{28}]^{5-}$ interact with CHO cell plasma membrane lipids causing aggregation and activation of a G protein-coupled receptor. *Front. Chem. Biol* 2:1126975. doi: 10.3389/fchbi.2023.1126975

Polyoxidovanadates $[Mo^{VI}V^{V}_{9}O_{28}]^{5-}$ and $[H_2Pt^{IV}V^{V}_{9}O_{28}]^{5-}$ interact with CHO cell plasma membrane lipids causing aggregation and activation of a G protein-coupled receptor

Kateryna Kostenkova[1†], Duaa Althumairy[2†], Ananthu Rajan[3], Ulrich Kortz[3], B. George Barisas[1,4], Deborah A. Roess[4,5]* and Debbie C. Crans[1,4]*

[1]Department of Chemistry, Colorado State University, Fort Collins, CO, United States, [2]Department of Biological Sciences, King Faisal University, Al-Ahsa, Saudi Arabia, [3]Department of Life Sciences and Chemistry, Jacobs University, Bremen, Germany, [4]Cell and Molecular Biology Program, Colorado State University, Fort Collins, CO, United States, [5]Department of Biomedical Sciences, Colorado State University Fort Collins, Fort Collins, CO, United States

Mono substituted heteropolyoxidovanadates, when compared to effects of a corresponding isopolyoxidovanadate (POV), were found to be more effective initiators of signal transduction by a G protein-coupled receptor (GPCR), specifically the luteinizing hormone receptor (LHR). Here we report that LHRs signal productively when CHO cells expressing the receptor are treated with two heteropolyoxidovanadates Pt^{IV} in monoplatino(IV)nonavanadate(V) ($[H_2Pt^{VI}V^{V}_{9}O_{28}]^{5-}$, V_9Pt), and Mo^{IV} in monomolybdo(VI)nonavanadate(V) ($Mo[^{VI}V^{V}_{9}O_{28}]^{5-}$, V_9Mo). Both substituted decavanadate derivatives were more effective than decavanadate which is more charged, has greater stability and forms the $[V_{10}O_{28}]^{6-}$ anion (V_{10}) in cell culture medium at pH 7.4. For viable CHO cells expressing 10 k or 32 k LHR/cell and treated with 11 μM V_9Pt and 13 μM V_9Mo, mono substituted heteropolyoxidovanadates significantly decreased the packing of plasma membrane lipids for about 1 h. This brief change in membrane structure was accompanied by increased aggregation of LHR and cell signaling as indicated by increased intracellular levels of cAMP. More pronounced changes in lipid packing and LHR signaling were associated with short acting heteropolyoxidovanadates than with the more stable V_{10}. When LHR was overexpressed, V_9Pt and V_9Mo had little or no effect on membrane lipid packing or receptor aggregation and the LHR was constitutively activated as indicated by elevated intracellular cAMP levels. Speciation of V_9Pt and V_9Mo in H_2O and cell medium was monitored using ^{51}V NMR spectroscopy and confirmed that V_9Pt and V_9Mo had greater effects on CHO cells despite decomposing more rapidly in the cell growth medium. Thus, under conditions that promote CHO cell growth, V_9Pt and V_9Mo, despite their smaller molecular charge and their reduced stability, favor LHR signaling over that induced by V_{10}. Importantly, under the same experimental conditions, CHO cells treated with V_9Pt and V_9Mo do not exhibit as strong toxic effects observed for cells treated with the longer lived V_{10}. In summary, unlike the longer lived V_{10} which is more growth inhibitory to cells, monosubstituted heteropolyoxidovanadates are more effective in transiently initiating signaling by a G protein-coupled receptor but, because of rapid hydrolysis, inhibit cell growth less.

KEYWORDS

vanadium, decavanadate, signal transduction, polyoxovanadates, luteinizing hormone receptor, GPCR, speciation chemistry, monosubstituted decavanadates

1 Introduction

Polyoxidovanadates (POVs) are oxo-clusters containing octahedral vanadium metal ions vanadium oxo-cluster building blocks. These clusters are classified as homo- or heteropolyoxovanadates now also known as heteropolyoxidovanadates depending on whether their metal ion content is solely vanadium or vanadium with other metal ions. Isopolyoxidovanadates have specific nuclearities such as one, two, four, five, ten, 12 and 18 (Pope, 1983; Pope and Müller, 1991; Crans, 1994; Hill, 1998; Crans et al., 2004; Hayashi, 2011; Bijelic et al., 2019; Treviño and Diaz, 2020; Pessoa et al., 2021) and properties such as stability and redox potential that vary depending on their structures. Replacement of one of the metal ion with another metal provides a number of novel heteropolyoxidovanadates molecules with a wide range of properties. Recently studies of POVs (Mutlu et al., 2017; Samart et al., 2018; Sánchez-Lara et al., 2018; Treviño and Diaz, 2020; Treviño and González-Vergara, 2019; Aureliano et al., 2021; Aureliano et al., 2022) have shown that the anions were highly active and had biological properties that differed from the parent homopolyoxidometalate. Although some information is available on the interactions of isopolyoxidometalates with enzymes with distinct selectivity, there is little information comparing the biological effects of the POVs with heteropolyoxidovanadates and no consistent patterns identified for their effects (Crans, 1994). As examples, the isopolyoxidovanadates have more potent effects on glycerol-3-phosphate dehydrogenase and 6-phosphogluconate dehydrogenase activity (Crans, 1994), isopolyoxidomolybdates are more potent in their effects on glucose-6-phosphate dehydrogenase (Crans, 1993) and the heteropolyoxidovanadates are most potent in affecting recombinant and native reverse transcriptase activity (Yamamoto et al., 1992).

In this manuscript, we compare the effects of two monosubstituted isopolymetalates, two (POVs), monomolybdo(VI)nonavanadate(V) ($[^{VI}V^{V}_{9}O_{28}]^{5-}$, abbreviated V_9Mo) and monoplatino(IV)nonavanadate(V) ($[H_2Pt^{VI}V^{V}_{9}O_{28}]^{5-}$, abbreviated V_9Pt), with those of decavanadate ($[V_{10}O_{28}]^{6-}$, abbreviated V_{10}) on activation of luteinizing hormone receptors (LHR) expressed in Chinese hamster ovary (CHO) cells, a eukaryotic cell line. Comparing polyoxidometalates V_9Pt and V_9Mo effects on a eukaryotic cell membrane with V_{10} is important because it begins to address structural features of these molecules necessary for their selective interaction with cell membranes is an isopolyoxidometalate that consists of ten octahedral vanadium (V) atoms, eight of which are bound to one terminal oxo ligand and five of those sharing oxygens in their octahedra (Figure 1) (Crans et al., 1994; Crans and Willsky, 1997; Aureliano and Crans, 2009). The last two vanadium atoms are internal and have six bridging oxygens in their octahedra. The V_{10} structure is a compact ion and has the dimensions of 5.8 A° × 7.8 A° × 8.4 A° (Crans et al., 1994). Although the two POVs used in these studies are structurally similar to V_{10}, the replacement of one vanadium atom with either Pt^{IV} and Mo^{VI} results in a molecule with a different charge distribution and lower symmetry compared to the all-V-containing V_{10} (Figure 1). In the V_9Pt cluster, one of the two internal vanadium atoms is replaced by a platinum(IV) atom (Figure 1) and the charge on the V_9Pt ion is minus five due to the exchange of one central addenda site by a Pt^{IV} ion. The dimensions of V_9Pt (5.5 A° × 7.7 A° × 8.5 A°) are similar to those of the V_{10}, calculated from XRD data (Crans et al., 1994; Uk Lee et al., 2008). The crystal structure shows the complex with a C_{2v} point group symmetry, with two protons found on the polyanion located on oxygens bridging Pt and V (Uk Lee et al., 2008). These protons are key for the formation of a dimer, $[H_4(Pt^{IV}V_9O_{28})_2]^{10-}$, through four O-H···O hydrogen bonds. Although hydrogen bonds between two V_9Pt ions persist at ambient temperature after dissolving the polyanion salt in water, heating results in discrete V_9Pt ions (Uk Lee et al., 2008; Dugar et al., 2016). In the V_9Mo cluster, one of the surface vanadium atoms on the cluster is replaced by molybdenum (Sánchez-Lombardo et al., 2016). Single-crystal X-ray analysis of the polyoxidometalate $[(CH_3)_4N]_4$ $[H_2MoV_9O_{28}]$ $Cl{\cdot}6H_2O$] has indicated that the molybdenum atom can occupy four different "capping" metal atom positions (Strukan et al., 1997). Although this structure is not deposited in the Cambridge Crystal Structure Database, we assume that the POM dimensions are very similar, because the Mo–O and V–O bond lengths are close in lenth. Despite the different molecular composition, the spectroscopic properties of V_9Pt, V_9Mo and V_{10} vary as do their solubility and stability in the cell growth medium used in these studies.

Vanadium coordination complexes have been the focus of recent work in cell systems (Scalese et al., 2019; Treviño and Diaz, 2020; Pessoa et al., 2021; Loizou et al., 2021, He et al., 2020; Biswas et al., 2022; Ferretti and León, 2022; Ribeiro et al., 2022; Semiz, 2022; Althumairy et al., 2020a; Sahu et al., 2022). Our group has shown that bismaltolatodioxovanadium(IV) (BMOV) and polyoxidovanadates are able to initiate signaling by the luteinizing hormone receptor (LHR), a G-protein coupled receptor (GPCR) (Roess et al., 2008; Crans et al., 2011; Winter et al., 2012; Al-Quatati et al., 2013; Althumairy et al., 2020b; Althumairy et al., 2020c; Althumairy et al., 2020d; Samart et al., 2020). The hydrophobic coordination complexes appear to initiate LHR signaling through interactions of the coordination complex with the external surface of the cell membrane and potential penetration of the complex into the lipid bilayer (Althumairy

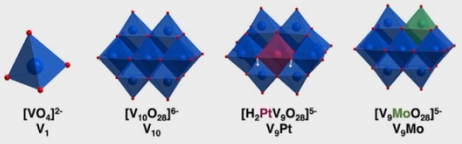

FIGURE 1
Polyhedral representations of $[VO_4]^{2-}$ (V_1) $[V_{10}O_{28}]^{6-}$ (V_{10}) $[H_2PtV_9O_{28}]^{5-}$ (V_9Pt) and $[Mo^{VI}V_9O_{28}]^{5-}$ (V_9Mo) showing molecular differences in these compounds at pH 7.4. The Pt is shown in maroon and the Mo is shown in green in the molecular structures.

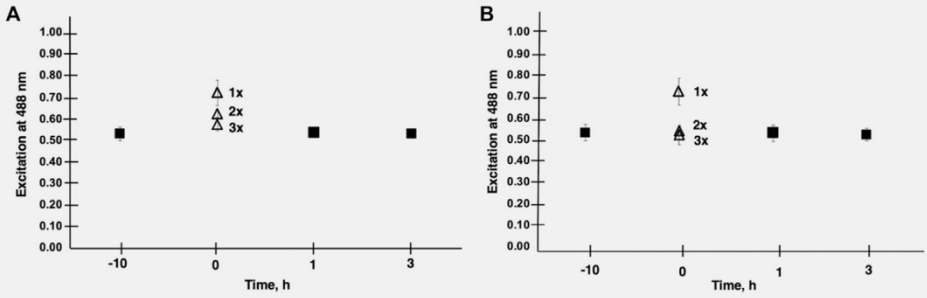

FIGURE 2
Membrane lipid order is shown in CHO cells treated with V_9Mo Panel **(A)** and V_9Pt Panel **(B)**. Results were obtained from the emission ratio of Di-4-ANEPPDHQ at 640/545 nm with excitation at 488 nm. A decrease in lipid order was indicated by increased emission at 640 nm relative to emission at 545 nm. The effects of washing cells with PBS a second (2 x) and third (3 x) time on lipid order was assessed at time 0 for both V_9Mo and V_9Pt. A second wash (2 x) increased lipid order and three washes (3 x) increased lipid order to values seen in untreated cells.

TABLE 1 Calculated values for the IC_{50} in Chinese Hamster Ovary (CHO) cells treated with V_9Pt and V_9Mo.

V-compound	IC_{50} per V-compound (μM)	IC_{50} per V-atom (μM)	Selected concentration for each V-compound (μM)
V_9Pt	12.9 ± 0.5	116 ± 5	10.0
V_9Mo	10.8 ± 0.6	97 ± 6	8.0

et al., 2020a; Samart et al., 2020, Winter et al., 2012; Crans et al., 2022). V_{10} is one of the POVs that has been found to be particularly potent in activation of LHR (Althumairy et al., 2020c) and the Type I Fc receptor (FcRI) (Al-Quatati et al., 2013). V_{10}, part of a class of polyoxometalates (polyoxidometalate) which are anionic metal-oxo clusters, has potential applications in the field of medicine (Pope and Müller, 1994; Rhule et al., 1998; Hasenknopf, 2005; Bijelic et al., 2018; Bijelic et al., 2019). Decametalates have anticancer and antidiabetic effects in eukaryotic cell lines and tissues and inhibit the growth of prokaryotic *Mycobacterium tuberculosis* mc2 6,230 (*M. tb*) and *Mycobacterium smegmatis* mc2 155 (*M. smeg* is now reclassified as a *Mycolicibacterium*) (Aureliano et al., 2021; Aureliano et al., 2022). Interestingly, in bacterial cell lines, inhibitory growth effects of V_{10} were greater than the effects of the known potent phosphatase inhibitor monovanadate (V_1) (Figure 1) (Samart et al., 2018; Kostenkova et al., 2021). The wide range of biological effects of decametalates in prokaryotic and eukaryotic cells motivates further work with these compounds given their potential pharmacologic value.

One mechanism of action used by several reported V-compounds is initiated through interactions of vanadium compounds with eukaryotic cell membranes either through intercalation or interactions at the membrane interface to alter the packing of plasma membrane lipids. Changes in lipid packing, in turn, drive the reorganization of the LHR in the membrane with receptors becoming concentrated in plasma membrane microdomains which function as signaling platforms for the receptor (Samart et al., 2018; Samart et al., 2020). Upon LHR aggregation, necessary for signal transduction by functional LHR, the receptor initiates intracellular signaling, producing elevated intracellular levels of cAMP (Smith et al., 2006; Wolf-Ringwall et al., 2011). In the case of V_{10}, the mechanism of action is not likely to involve penetration or direct interaction of V_{10} at the membrane interface because the highly charged V_{10} polyanion remains outside the membrane. Of interest here are the biological effects of similar decametalates and, importantly, whether the lower charged V_9Mo and V_9Pt are capable of initiating albeit indirectly, LHR activation despite reduced stability compared to V_{10} in the eukaryotic cell medium.

2 Materials and methods

2.1 General materials

CHO-K1 cells were a kind gift from Dr. Takamitsu Kato at Colorado State University. Dulbecco's Modified Eagle medium (DMEM) with added geneticin was purchased from Corning Cellgro. Cell medium also contained penicillin/streptomycin and L-glutamine purchased from Gemini Bio-Products (West Sacramento, CA) and fetal bovine serum (FBS) purchased from Atlas Biologicals (Fort Collins, CO). The 100X MEM non-essential amino acid solution, sodium metavanadate ($NaVO_3$) and bovine albumin were from Sigma-Aldrich (St. Louis, MO). Trypsin-EDTA (0.25%) was supplied by Fisher Scientific Co. (Pittsburgh, PA), Optimal-MEM was obtained from Life Technologies (Carlsbad, CA). Glass-bottom cell culture dishes (CA35 mm diameter) used for optical measurements were obtained from *In Vitro* Scientific (Sunnyvale, CA).

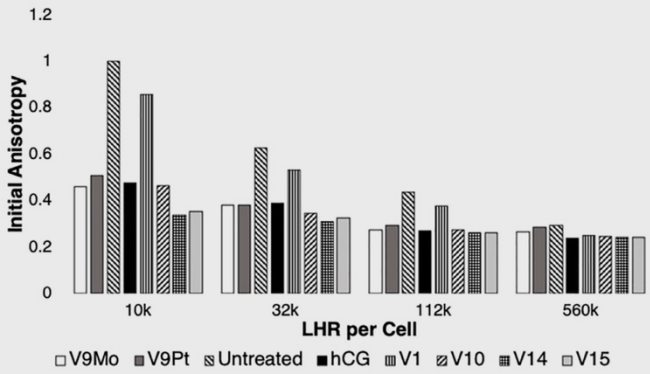

FIGURE 3
Data for treatment of the initial anisotropy measured for eYFP covalently linked to LHR using polarized homo-FRET methods was obtained by replotting data obtained in this work shown in Supplementary Figure S6 and combined with previous reported results (Althumairy et al., 2020c). The data is normalized relative to controls which were set to 1.0. Values for initial anisotropy less than 1.0 are indicative of LHR aggregation after treatment with V_9Pt and V_9Mo (this work) or with hCG, V_1, V_{10}, V_{14} or V_{15} as determined previously (Althumairy et al., 2020c). Pre-treatment of cells with hCG, V_1, V_9Pt, V_9Mo, V_{10}, V_{14} or V_{15} decreased values for initial anisotropy for LHR on cells expressing 10,000 or 32,000 LHR per cell plasma membranes. V_9Mo and V_9Pt had similar effect on LHR aggregation as did hCG and V_{10}. When cells expressed non-physiologically high numbers of LHR per cell (122,000 LHR/cell), receptors were already extensively aggregated. The conditions hCG, V_9Pt, V_9Mo, V_{10}, V_{14}, and V_{15} increased receptor aggregation while V_1 had no statistically significant effect on receptor clustering. There were no statistically significant effects of any treatment when CHO cells expressed 560,000 LHR per cell.

$NaVO_3$ and sodium molybdate (Na_2MoO_4) were purchased from Sigma Aldrich and used without purification. Monoplatinononavanadate ($[H_2PtV_9O_{28}]^{5-}$, abbreviated V_9Pt) the sodium salt was prepared as reported previously (Na_5 $[H_2PtV_9O_{28}]\cdot 21H_2O$) (Uk Lee et al., 2008; Kostenkova et al., 2021). The peaks observed in ^{51}V NMR confirm the synthesis of the compound and are identical to those reported in the literature (Supplementary Figures S1-S2) (Uk Lee et al., 2008; Kostenkova et al., 2021). Monomolybdononavanadate ($[MoV_9O_{28}]^{5-}$) abbreviated V_9Mo) solution was freshly prepared following the reported procedure for the sodium salt (Na_5 $[MoV_9O_{28}]\cdot 10H_2O$) (Sánchez-Lombardo et al., 2016; Kostenkova et al., 2021). The peaks observed in ^{51}V NMR confirm the synthesis of the compound and were identical to those reported in the literature (Supplementary Figures S3-S4) (Sánchez-Lombardo et al., 2016; Kostenkova et al., 2021). The pH in NMR speciation experiments was adjusted by using either 0.1 M HCl or 0.1 M NaOH prepared in doubly deionized water (DDI) water.

2.2 Methods

2.2.1 NMR spectra

All NMR spectra were recorded using a Bruker NMR spectrometer at 105.2 MHz for ^{51}V, and a Varian NMR spectrometer at 131.5 MHz for ^{51}V at ambient temperature. Varian 500 MHz NMR spectrometer was manually calibrated by using a 5 mm broadband probe. The ^{51}V NMR spectra were recorded in DDI water (controls) and DMEM medium to determine speciation of V_9Mo and V_9Pt at several time-points (0, 1, 5, 24, 30 and 48 h) during the experiment. The ^{51}V NMR spectra were recorded using the following parameters: 4,096 scans in the f1 domain, 0.01 s relaxation delay, O1p = −500 ppm, SW = 900 ppm, and a 16 μs pulse in a 45° pulse angle without lock and shimming turned on. The ^{51}V NMR spectra were reported relative to neat $VOCl_3$ at 0 ppm but experimentally referenced against an $NaVO_4$ solution at pH 12 (two signals one for V_1 at −535.7 ppm and the other for V_2 at −560.4 ppm) as an external reference) (Samart et al., 2018; Althumairy et al., 2020c). The MestreNova NMR processing software (version 14.0.1) was used for data processing.

2.2.2 Preparation of the stock solutions for speciation studies

The stock solution of V_9Pt (2.0 mM) was prepared by dissolving solid (0.0140 g, 0.0100 mmol) Na_5 $[H_2PtV_9O_{28}]\cdot 21H_2O$ in 5.00 ml DDI water. The stock solution of V_9Mo (2.0 mM) was prepared by using the desired volumes of DDI water and a 100 mM V_9Mo stock solution; the pH was adjusted to 5.0 by a dropwise addition of 0.1 M NaOH and 0.1 M HCl. The 1.0 mM control solutions of V_9Mo and V_9Pt were prepared by mixing 1,000 μL of the appropriate 2.0 mM stock solution with 1,000 μL of DDI H_2O. The 1.0 mM solutions of V_9Mo and V_9Pt in serum-free media prepared using the same method from 500 ml of DMEM, 5.0 ml of each penicillin/streptomycin, 100x non-essential amino acid solution, and L-glutamine solution. The pH of all solutions was measured at each indicated time-points (0, 1, 5, 24, 30 and 48 h) to determine possible changes in vanadium speciation during the 48h period of the experiment.

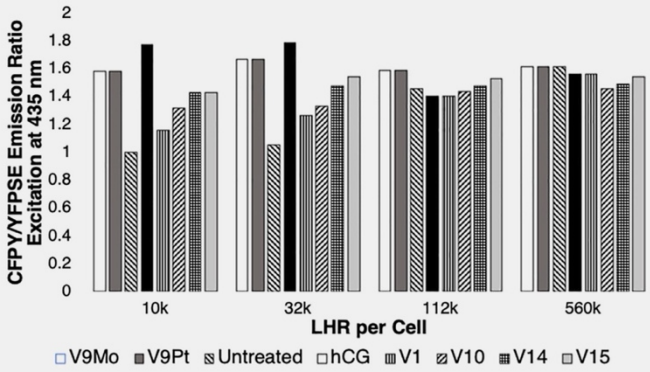

FIGURE 4
The effects of LHR numbers per cell on intracellular cAMP levels in the absence (untreated) or in the presence of cells treated with hCG, V_1, V_9Pt, V_9Mo, V_{10}, V_{10}, V_{14} or V_{15}. Data obtained in this work or reported previously (Althumairy et al., 2020c) is normalized with respect to the control value (1.0). An increase in intracellular cAMP is indicated by reduced energy transfer between CFP and YFP (YFPSE) upon exposure of ICUE3 to 435 nM light and an increase in the CFP/YFPSE ratio. Data shown from either this work or from a previous study (Althumairy et al., 2020c) are the mean of 25–43 individual measurements.

2.2.3 Preparation of the 1.0 mM V_9Pt solution with 0.11 M NaCl and 0.0054 M KCl for speciation studies

The 1.0 mM stock solution of V_9Pt with 0.11 M NaCl and 0.0054 M KCl was prepared by dissolving solid Na_2 $[H_2PtV_9O_{28}]\cdot 21H_2O$ (0.0070 g, 5.0 mmol), NaCl (0.032 g, 0.55 mmol) and KCl (0.0020 g, 0.027 mmol) in 90% H_2O/10% D_2O (4.5 ml DDI H_2O/0.5 ml D_2O). The pH of the solution was adjusted to 7 (pH = 7.4) with 0.05 M NaOH. The pH of the sample was measured at several time-points (0, 1, 5, 24, 30 and 48 h) to determine the changes in vanadium speciation over 48 h.

2.2.4 Effects of V_9Pt and V_9Mo on CHO cell viability

Cell growth was assessed using a resazurin-based fluorometric assay and serial diluted stock solutions of V_9Pt and V_9Mo into DMEM cell media as previously described (Althumairy et al., 2020c). Approximately 20,000 cells/well were seeded in 96-well plates in 100 µL free serum media. Cells were allowed to attach to plate surfaces for 3 h and then treated with solutions of 1.0, 5.0, 10, 50 or 100 µM of V_9Pt or V_9Mo together with 10% resazurin for 3 h to obtain a baseline value for cell viability (t = 0). A separate population of cells in 96 well plates were similarly treated for 12 h before the addition of 10% resazurin followed by an additional 3 h incubation (t = 15 h). Fluorescence measurements at t = 0 and t= 15 h were made using an excitation wavelength of 530 nm and measurement of fluorescence emission at 590 nm. The compound concentration where cell viability was 50% of the cell number at t = 0 was designated as the IC_{50} and was estimated by curve fitting to log values for both V_9Pt and V_9Mo (data not shown) to be 12.9 µM for V_9Pt and 10.8 µM for V_9Mo. The concentrations of V_9Pt and V_9Mo used in subsequent cell experiments, 10 µM and 8 µM, respectively, were less than the IC_{50} values for each compound and were concentrations that were efficacious without causing high levels of cell death during the cell treatment.

2.2.5 V_9Pt and V_9Mo effects on CHO cell membrane lipid order

An environmentally sensitive styryl dye, di-4-ANEPPDHQ, was used to evaluate effects of V_9Pt and V_9Mo on membrane lipid order. This approach has been described in detail previously (Althumairy et al., 2020c). Briefly, CHO cells (0.5 ml) grown to at least 80% confluence in 50 ml cell culture flasks and treated with 1.0 ml trypsin-EDTA (0.25%) for 3 min were placed in a 35 mm glass-bottom Petri dish. After 12 h, cells were washed twice with phosphate-buffered saline (PBS) at pH 7.3 and then incubated in cell medium alone or in medium containing 10 µM V_9Pt or 8 µM V_9Mo. At time 0, a Petri dish containing CHO cells was labeled for 15 min with 200 µL of a stock solution containing 1.5 µM di-4-ANEPPDHQ before washing cells once, covering the cell layer with PBS and imaging cells (Althumairy et al., 2020b). Remaining Petri dishes were treated with 11 mM V_9Pt or 13 mM V_9Mo in media for 10 h, washed with PBS, covered in medium free serum and imaged at times 0, 1, and 3 h after labeling with di-4-ANEPPDHQ. The Zeiss Axiovert 200 M inverted microscope used for imaging was equipped with a 63 ×1.2 NA water objective and an Andor Du897 E EMCCD camera. Cell samples were illuminated using an arc lamp with a 480/30x or 495/20x excitation filter. Fluorescence emission was collected in channel one using a 535/40 nm filter and in channel two using a 620/40 nm filter and MetaFluor software. ImageJ software was used for background correction calculation of the fluorescence intensity ratio at 620nm/535 nm. Repeated cell washing was used in some experiments to evaluate the interactions of V_9Pt or V_9Mo with membrane lipids. As shown

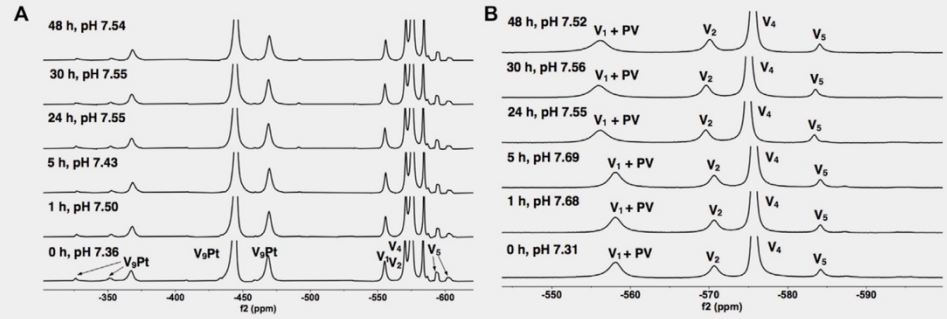

FIGURE 5
^{51}V NMR spectra of V_9Pt in **(A)** the 1.0 mM aqueous control solution and **(B)** the 1.0 mM solution in DMEM as a function of time. The signals (in ppm) are assigned to V_9Pt as follows: −379 (V_D), −445 ($V_{E/F}$) and −470 (V_C), a combined V_1 + PV signal (−573), V_2 (−571), V_4 (−575) and V_5 (-584 -592 and -602). The V_9Pt signals are identical to those reported in the literature (Kostenkova et al., 2021).

in Figure 2, cells at t=0 were washed two additional times designated 2x and 3x, prior to assessment of membrane lipid.

2.2.6 LHR aggregation determined by Polarized homo-fluorescence resonance energy transfer

The extent of LHR aggregation was determined using polarized homo-transfer fluorescence resonance energy transfer methods (referred to as homo-FRET) and performed as previously described (Althumairy et al., 2020c). Cells grown as described above were plated in 35 mm glass-bottom Petri dishes and allowed to attach to the glass surface for 12 h. Cells were then washed with PBS at pH 7.3 and treated for 10 h with solutions containing either 10 μ M V_9Pt or 8 μ M V_9Mo. After washing once to remove V_9Pt or V_9Mo, cells were covered with serum-free medium and imaged using homo-FRET protocols immediately at t = 0 or after further incubation for 1 h or 3 h, respectively (Althumairy et al., 2020c). At least five cells were examined from each Petri dish and a minimum of 30 cells were examined for each measured condition. Results are expressed as the mean ± SEM of individual measurements. Statistical evaluation of mean differences in untreated and treated groups were analyzed using a one-way ANOVA followed by the Tukey multiple comparison test and Student's t-test using R version 3.3.1. p values <0.05 were considered statistically significant.

2.2.7 Intracellular cAMP levels in V_9Pt- and V_9Mo-treated cells

Fluorescence assays of intracellular cyclic adenosine monophosphate (cAMP) were performed using a cAMP reporter ICUE3 expressed in CHO cells from an ICUE3 plasmid provided by Dr. Jin Zhang (DiPilato and Zhang, 2009) and methods in our laboratory that have been previously described in detail (Althumairy et al., 2020c). After transfection of CHO cells with the ICUE3 plasmid, images were acquired from cells in PBS to establish baseline levels of intracellular cAMP. The cell medium was then exchanged with solutions containing 10 μ M V_9Pt or 8 μ M V_9Mo. Cells were incubated for 15 min and reimaged. To evaluate eYFP emission and eYFP sensitized emission (YFPSE) due to energy transfer from CFP, images were acquired used a 63 × 1.2 NA water objective in a Zeiss Axiovert 200 M inverted microscope with an Andor Du897 E EMCCD camera, arc lamp excitation with a 436DF20 excitation filter and two emission filters, 480DF40 for CFP and 535DF30. After background subtraction from the fluorescence images, data were analyzed using ImageJ software to calculate the emission intensity ratio of CFP/YFPSE. For each Petri dish, two to five cells were observed, and data were collected from a minimum of 15 cells for each treatment condition.

3 Results

3.1 Effects of V_9Mo and V_9Pt on lipid order in CHO cell plasma membranes

In initial experiments, we evaluated whether the water-soluble transition metal monosubstituted POVs, V_9Pt or V_9Mo, both less charged than V_{10}, had similar effects to those of V_{10} on membrane lipid order. We have previously shown that V_{10} decreases membrane lipid order in CHO cells for over 6 h (Althumairy et al., 2020c). Most previously investigated V-compounds are more hydrophobic coordination complexes and hence penetrate the membrane when exerting their function (Winter et al., 2012; Althumairy et al., 2020b), However, we found that in addiiton to V_{10}, V_{14} ($(K(NH_4)_4\ [H_6V_{14}O_{38}(PO_4)]11H_2O)$) and V_{15} ($[(CH_3)_4N]_6[V_{15}O_{36}(Cl)]$) had effects on membrane lipid order (Althumairy et al., 2020c). Initially we evaluated IC_{50} values for V_9Pt or V_9Mo and, based on the IC_{50}, selected a lower concentration for each compound for use in subsequent experiments (Table 1). Lipid order in treated cells was decreased compared to untreated cells as indicated by an increase in the ratio of emission of di-4-ANEPPDHQ at 640/545 nm. After one washing of cells to remove excess V_9Pt or V_9Mo, lipid packing was evaluated at one or 3 h. At 1 h, lipid packing had returned to baseline values which

TABLE 2 Speciation data of the V_9Pt and V_9Mo clusters collected at t = 0, 24, and 48 h in 1.0 mM aqueous solutions (V_9Pt and V_9Mo), aqueous solution with added chloride anions and 1.0 mM solutions in DMEM media. No adjustments have been done to account for the polyoxidovanadates' hydrolysis.

Anions monitored	Signals observed by ^{51}V NMR spectroscopy								
Compound and time/ conditions	V_9Pt (%)	V_9Pt minor isomers (%)	V_9Mo (%)	V_{10} (%)	V_1 (%)	V_2 (%)	V_4 (%)	V_5 (%)	References
V_9Pt/0 h Aqueous Aq. With added Cl^- Media	33.8% 7.9% 0%	1.1% 0.3% 0%	- - -	- - -	3.2% 7.5% V_1+PV 19.0%	5.4% 7.3% 10%	49.3% 68.0% 63.0%	7.0% 9.7% 7.0%	
V_9Pt/24 h Aqueous Aq. with added Cl^- Media	33.0% 6.5% 0%	1.0% 0.3% 0%	- - -	- - -	3.1% 7.6% V_1+PV 20.0%	5.0% 8.5% 14.0%	51.2% 69.8% 63.0%	7.0% 8.2% 4.0%	
V_9Pt/48 h Aqueous Aq. with added Cl^- Media	33.6% 6.1% 0%	0.3% 0.2% 0%	- - -	- - -	3.1% 7.5% V_1+PV 20.0%	5.4 6.7% 12.0	51.0% 70.4% 61.0%	5.1% 10.3% 5.0%	
V_9Mo/0 h Aqueous Media	- -	- -	17.5% 16.5%	9.5% 7.5%	74.0% V_1+PV 66.0%	4.0% 1.0%	0% 0%	0% 0%	
V_9Mo/24 h Aqueous Media	- -	- -	21.5% 0%	10.5% 0%	74.0% V_1+PV 94.0%	0% 4.0%	0% 3.0%	0% 0%	
V_9Mo/48 h Aqueous Media	- -	- -	18.0% 0%	6.0% 0%	77.0% V_1+PV 97.0%	0% 5.0%	0% 3.0%	0% 0%	
V_{10}/0 h Aqueous Media	- -	- -	- -	56.9 89.3	14.6 V_1+PV 7.54	10.7 2.11	17.6 1.05	0.21 -	Althumairy et al. (2020a)
V_{10}/24 h Aqueous Media	- -	- -	- -	47.3 5.00	13.7 V_1+PV 20.6	10.5 12.6	28.4 56.7	- 5.37	Althumairy et al. (2020b)

* PV = V(V) phosphate species.

** Considering the lack of stability of some polyoxidovanadates, the values given in Table 2 have been reported without adjusting for hydrolysis under assay conditions.

suggests that V_9Mo and V_9Pt effects on membrane lipid order were short lived. These results contrasted sharply with similar experiments with V_{10} where a single washing of V_{10} treated cells did not markedly affect membrane lipid order for at least 6 h (Althumairy et al., 2020c).

Because effects on membrane lipid order for V_9Pt and V_9Mo were short-lived, we evaluated the extent of V_9Pt and V_9Mo association with the membrane further by washing cells two additional times at time 0 as shown in Figure 2. Washing cells three times increased lipid packing to baseline values for both V_9Pt- and V_9Mo-treated cells indicating that these POVs exerted effects on membrane lipids while being only weakly associated with the cell membrane.

3.2 Aggregation of LHR

Effects of V_9Pt and V_9Mo treatment on LHR aggregation were examined using CHO cell lines stably expressing different levels of LHR receptors in the plasma membranes: 10,000 LHR, 32,000 LHR, 122,000 LHR or 560,0000 LHR, respectively (Figure 3 and Supplementary Figure S6). When cells expressed 10,000 or 32,000 LHR per cell, preincubation of cells with 10 μM V_9Pt or 8 μM V_9Mo produced significant aggregation of LHR and decreased lipid order in CHO cell membranes. As we have seen previously (Althumairy et al., 2020d), cells expressing higher, non-physiological numbers of LHR per cell have LHRs that are extensively aggregated. For cells with 122,000 LHR per cell, V_9Mo and V_9Pt caused modest but significant effects on receptor aggregation. For cells expressing 560,000 LHR per cell, there was no further aggregation of LHR when cells were treated with either V_9Pt or V_9Mo suggesting that the constitutive LHR aggregation due to receptor overexpression on untreated cells was not affected by changes in lipid order as has been previously observed.

In Figure 3 the data from Supplementary Figure S6 on the effects of V_9Pt and V_9Mo treatment on LHR aggregation was replotted with previously reported data for cells expressing 10,000, 32,000, 122,000 or 560,000 LHR per cell and treated with V_1, V_{10}, V_{14} ($(K(NH_4)_4\ [H_6V_{14}O_{38}(PO_4)]11H_2O)$) and V_{15} ($([[(CH_3)_4N]_6\ [V_{15}O_{36}(Cl)]]$) (Althumairy et al., 2020c). The control values (untreated cells) were very similar and Figure 7 shows that the initial anisotropies with V_9Pt or V_9Mo treatment were similar to those previously reported for V_{10}-treated cells. Interestingly, V_9Pt, V_9Mo and V_{10} are less effective when CHO cells express lower LHR receptor numbers per cell compared to the larger multivalent oxidometalates V_{14} and V_{15}. For CHO cells with higher LHR receptor numbers, the effects of these compounds are similar. This may be due simply to pre-existing and extensive clustering of LHR when receptor numbers are high; membrane aggregation as evaluated here or, for example, binding of human chorionic gonadotropin (hCG) to the receptor (Althumairy et al., 2020c) which has no notable effects on cells where receptors were already highly aggregated.

3.3 Effects of V_9Mo and V_9Pt on cAMP levels in CHO cells

A low intracellular level of cAMP is indicated by a low CFP/YFPSE emission ratio. As shown in Figure 4, when examining cells expressing 10,000 LHR per cell, the increase in intracellular cAMP was most apparent with V_9Mo or V_9Pt treatment. Untreated

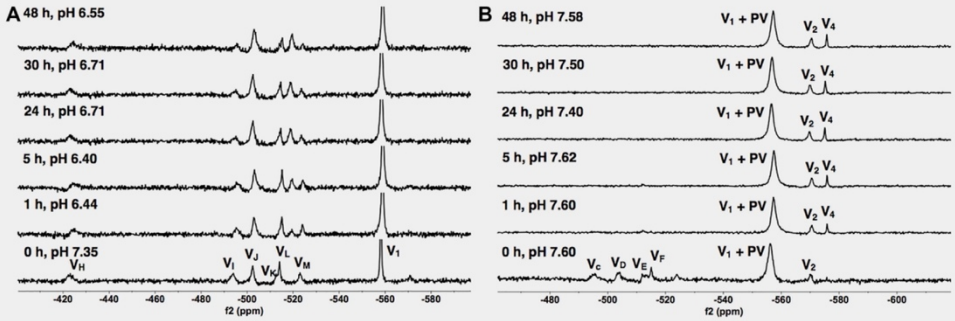

FIGURE 6
^{51}V NMR spectra of V_9Mo in **(A)** the 1.0 mM aqueous control solution and **(B)** the 1.0 mM solution in DMEM as a function of time. The signals (in ppm) are assigned (V_{1-4}, V_I, V_J, V_K, V_L and V_M = -423, -494, -503, -513, -515 and −523), the combined V1 + PV (−563) and V2 (−570). The V9Mo peaks are identical to those reported in the literature (Kostenkova et al., 2021).

receptors exhibit low basal levels of intracellular cAMP as indicated by the low ratio of CFP/YFPSE. However, as the number of LHR receptors increased the ratio of CFP/YFPSE increased showing that the levels of intracellular cAMP in untreated cells increases with increasing numbers of LHR per cell. Treating cells with either V_9Mo or V_9Pt significantly increased intracellular cAMP levels in CHO cells expressing 10,000 and 32,000 LHR expressed per cell. When cells overexpressed LHR, as shown in the experiments with either 122,000 or 560,000 LHR per cell, the addition of V_9Mo and V_9Pt had little or no effect on intracellular cAMP levels which were already high. These overexpressed receptors are pre-clustered, presumably due to high expression levels in the cell membrane, and, as a result, constitutively active as indicated by high levels of intracellular cAMP in untreated cells.

As shown in Figure 3, exposing CHO cells to either V_9Mo or V_9Pt caused anisotropy values to decrease, indicating LHR aggregation. There is a relationship between receptor clustering and intracellular levels of cAMP expressed by the CFP/YFPSE emission ratio shown in Figure 4**.** The increasing basal levels of intracellular cAMP in untreated cells with increasing numbers of LHR per cell were associated with decreasing initial anisotropies and plotted as 1.0. The data for V_9Mo or V_9Pt was plotted as the percentage of the control. Combining the data determined in this work and shown in Supplementary Figure S7 and plotted in Figure 4 with the data for hCG, V_1, V_{10}, V_{14} and V_{15}-treated CHO cells reported previously (Althumairy et al., 2020c) shows a similar pattern for hCG, V_1, V_9Pt and V_9Mo, V_{10}, V_{14} and V_{15}-treated cells expressing 10,000, 32, 000, 122,000, or 560,000 LHR per cell. In summary, receptors that were extensively clustered in response to the POVs described in this work or clustered as a result of LHR overexpression, were actively signaling as indicated by high cAMP levels. When considering cells expressing 10,000 LHR per cell, receptors needed to be activated by treatment of one of the V-anions. Figure 4 shows that V_9Pt and V_9Mo treatment produces a higher level of signaling than either hCG, a naturally occurring ligand for LHR, or any of the other V-containing compounds. Considering that V_9Pt and V_9Mo hydrolyze quickly, this suggests that signaling happens very quickly after POVs are added to the assay solution. Moreover, the higher toxicity observed with V_{10} and higher multivalent POVs was not seen with V_9Pt and V_9Mo. In summary, V_9Pt and V_9Mo were both more effective in affecting membrane lipid organization and LHR-mediated cell signaling than the more stable, higher charged V_{10} and multivalent POV. These studies document that monosubstituted isopolymetalates are more efficacious as signaling agents while causing less toxicity than corresponding unsubstituted isopolymetalates.

3.4 Speciation and stability of V_9Pt and V_9Mo in H_2O and DMEM

Transition metal ion monosubstitution breaks the symmetry of V_{10}, resulting in different chemical shifts and relative signal intensities in ^{51}V NMR spectra, such as 2:4:4 in V_{10} to 1:6:2 in V_9Pt. Monosubstitution with Pt^{IV} in V_{10} results in four different types of vanadium atoms, for which two of the ^{51}V signals overlap, generating a total of three signals for the ^{51}V NMR spectrum of V_9Pt (V_D at -371.0, $V_{E/F}$ at -450.9, and V_G at -475.0 ppm) Figure 5. To assess V_9Pt speciation over the time course of cell studies, time-dependent ^{51}V NMR speciation studies of both V_9Pt and V_9Mo clusters were carried out in aqueous solutions and DMEM media at pH ≈ 7.4 over 48 h.

The ^{51}V NMR spectra in Figures 5A, B show that although the speciation of the V_9Pt in the aqueous solution with pH of 1.0 mM of V_9Pt maintained near pH 7.4 showed limited hydrolysis of PtV_9, the addition of PtV_9 to DMEM show extensive and immediate hydrolysis (Figure 5; Table 2). Overall, the ^{51}V NMR data indicates that the vanadate (V_1), forms rather quickly after dissolution of V_9Pt cluster in the media and that V_1 is the main component found in the media by the time sample is analyzed by ^{51}V NMR spectroscopy. The lack of stability in the DMEM media could be attributed to either higher pH (pH 7.4 rather than pH 6.6 in the Middelbrook 7H9 broth media used for cultivation of

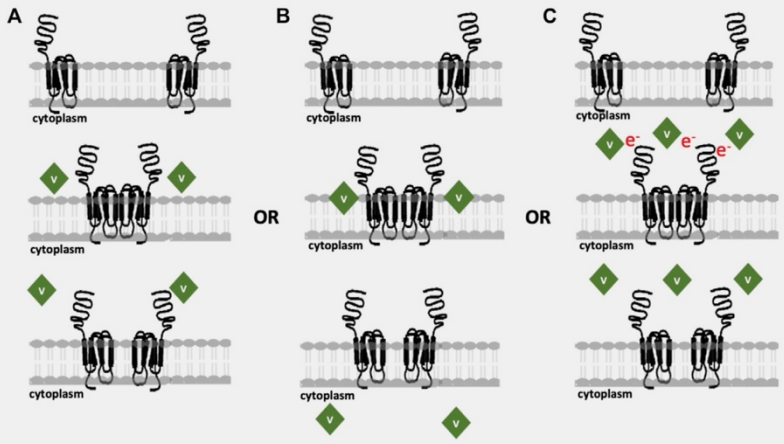

FIGURE 7
Updated proposed models for the modes of action of various vanadium compounds on cell membranes where cells express 10,000 LHR in plasma membrane per cell, at a comparatively low receptor density. **(A)** V-Compounds interact with CHO cell membranes and are not internalized; **(B)** V-compounds impact the lipid bilayer followed by POV hydrolysis and internalization of the resulting species; or **(C)** POVs exert the effects through an electron transfer process and no internalization is necessary for response. The image is adopted from (Althumairy et al., 2020c) with updates.

4 Discussion

To attribute the effects of the two POVs and compare their effects to those of V_{10} and V_1 and the two multivalent POVs, we examined the stability and speciation of V_9Pt and V_9Mo both in aqueous stock solution and DMEM media. We monitored the speciation using ^{51}V NMR spectroscopy and the species forming under the condition of the biological studies are summarized in Table 2. The replacement of one V-atoms in the V_{10} molecule cause a difference in overall charge from -6 for V_{10} to -5 for V_9Pt and V_9Mo whereas the structure of the decametalate remains very similar. Previous work has shown that V_9Pt is stable in the acidic bacterial media (Kostenkova et al., 2021) and that V_{10} partially hydrolyzes in DMEM over 10 h so we were surprised to see that V_9Pt hydrolyzed almost immediately in these studies. Similarly, the V_9Mo was found to hydrolyze within 1 h at the neutral pH values and medium used in this work which is faster than reported previously (Kostenkova et al., 2021). There are differences in the mediums use for bacterial 7H9 cells and eukaryotic CHO cells with higher Cl^- concentrations in 7H9 medium. To determine whether the reduced stability of V_9Pt in CHO cell growth medium could be attributed to Cl^- concentrations, we carried out time-dependent speciation experiments in an aqueous solution with added chloride anions (Supplementary Figure S5, Supplementary Table S1 and Supplementary Figure S1). The concentration of the added chloride salts produced a solution that was equivalent to that found in DMEM (0.0054 M KCl and 0.11 M NaCl). Since our results have shown that the stability and speciation of V_9Pt is identical in aqueous solutions with and without added chloride anions, we conclude that the lower stability of V_9Pt in this medium is caused by other factors which may include the various additives used with mediums prepared for 7H9 and CHO cells as well as differences in the medium pH. For CHO cells studies, DMEM is supplemented with penicillin, streptomycin, L-glutamine, and protein-rich fetal bovine serum as well as geneticin to maintain stable expression of LHR in CHO cells. Any one of these additives or some combination of these additives may account for observed differences in V_9Pt stability when compared to studies of this molecule in bacterial cells. In addition, the possibility that any such species or a hydrolysis product of the V_9Pt or V_9Mo is an active species is very unlikely, since such species are not observed by ^{51}V NMR spectroscopy and therefore would be present at very low concentrations and hence very potent if such species was effective in initiating LHR signaling.

Some polyoxidometalates remain intact while others hydrolyze under the conditions of the biological studies, thus, carrying out speciation experiments under biological conditions is crucial to understanding their biological activities (Kiss et al., 2000; Bougie and Bisaillon, 2006; Postal et al., 2016; Levina et al., 2017; Levina and Lay, 2017; Nunes et al., 2021; Pessoa and Correia, 2021). Interestingly, growth inhibition of CHO cells by V_9Pt and V_9Mo is weaker than the growth inhibition observed for V_{10}-treated cells. A previous study of mixed valence POVs with LHR also investigated their stability and speciation at pH 7.4 using ^{51}V NMR and EPR spectroscopies. (Althumairy et al., 2020c). V_{15} is particularly interesting in that it contains 7 V (V) and 8 V (IV) and that part of its decomposition involves oxidation to the V_{15}—that is an all V (V) anion (Nunes et al., 2012; Postal et al., 2016). The results have therefore shown that V_{15} remains intact in DMEM at 0 and 24 h with the trace level of the reduced V (IV) species present until 24 h at ambient temperature EPR spectra (Althumairy et al., 2020c). V_{14}, in contrast, partially hydrolyzes starting at 0 h and is completely hydrolyzed at

24 h, as evidenced in the ambient temperature EPR spectra in DMEM (Althumairy et al., 2020c). The growth inhibition of V_9Pt and V_9Mo is also weaker than the growth inhibition observed for V_{14} and V_{15}. This is most readily understood if one considers that V_{10} and V_{15} are more stable than V_9Pt and V_9Mo. In the case of V_{14}, the situation is less obvious because this species easily decomposes. However, because both V_9Pt and V_9Mo are significantly more potent growth inhibitors than V_1, decomposition of these compounds to V_1 does not explain their observed effects on cell growth.

In this work, we investigated the effects on lipid order in CHO cells treated with V_9Mo and V_9Pt after repeated (three times) washings at t = 0. The lipid order was monitored measuring the emission at 640 nm relative to emission at 545 nm followed by excitation of the fluorophore with 488 nm light; decreased ratios is indicative of a decrease in lipid order. A decrease in the emission ratio after the first, the second (2 x) and the third (3 x) wash indicated increased lipid order compared to untreated cells (Figure 2). Because the extent of lipid packing returned to baseline values with repeated cell washing, it appears that these compounds have not penetrated the cells. Various experiments with either one cell wash or repeated cell washings were done previously for V_1, $VOSO_4$, BMOV and selected POVs-treated cells. With BMOV and $VOSO_4$ we showed that removing the V-compound with a single wash from cells with a low number of LHR per cell (10,000 LHR/cell) a greater increase in lipid packing was observed for the $VOSO_4$-treated cells compared to BMOV-treated cells (Althumairy et al., 2020a). After 24 h the lipid packing returned to levels near those of untreated cells suggesting that treatment with BMOV and $VOSO_4$ does not cause significant compound internalization.

Although studies using multiple cell washes have only recently been carried out, it is possible to compare the effects of single cell washes in cells treated with oxidovanadate and POVs with variable stabilities. V_1, V_{10} and V_{15} effects on lipid packing (Althumairy et al., 2020c) can be compared with those seen for V_9Mo-treated and V_9Pt-treated cells where cell treatment is followed by washing cells once. Under these conditions, V_1, V_{10} and V_{15} did not wash off cells as readily as did V_9Mo and V_9Pt which suggests that V_1, V_{10} and V_{15} are associated more closely with the membrane interface or, alternatively, that they are being at least partially internalized. Nonetheless, V_9Mo and V_9Pt can more effectively initiate LHR signaling; the observed increase in intracellular cAMP suggests that the signaling response must be very rapid despite hydrolyzing of V_9Mo and V_9Pt and that this rapid response is at least partially distinct from the more slowing developing effects on cell growth inhibition. It is likely that termination of LHR signaling in these experiments is due to the reestablishment of reduced membrane lipid packing, disaggregation of LHR and movement of LHR out of raft domains. Previous studies of LHR activated by the receptor ligand human chorionic gonadotropin (hCG), show that LHR become aggregated in membrane rafts and actively signal upon binding of hCG (Lei et al., 2007). Chemical disruption of the raft signaling platforms through cholesterol extraction from the plasma membrane is sufficient to eliminate signaling initiated by binding of hCG to LHR and LHR aggregation (Smith et al., 2006; Wolf-Ringwall et al., 2011). These studies led to the development of several mechanisms that are shown schematically in Figure 7 but do not rule out the possibility that vanadium compounds used in these experiments are interacting with the receptor.

Figure 7 shows various mechanisms previous proposed for the reported vanadium compounds interactions with cells that initiate signaling by LHR or other GCPRs. Because the POVs forms multiple species in media, it is likely that more than one type of interaction is taking place. Some species may interact with cells as shown in Figure 7A, while others use alternative mechanisms as summarized in Figure 7B or Figure 7C. For example, $VOSO_4$ and BMOV are likely to follow the mechanism illustrated in Figure 7B. However, washing experiments where one wash returns lipid organization to levels seen in untreated cells suggest that internalization is minimal (see (Althumairy et al., 2020a; Althumairy et al., 2020b), Figure 7A) demonstrates the interactions occurring for compounds like V_{14} and V_{15} and potentially V_9Mo and V_9Pt that interact with extracellular structures but due to their high hydrophilicity are unlikely to insert in lipid bilayers. Whether these compounds can perturb membrane structures or, as an example, alter LHR interactions with cholesterol (reviewed by (Sarkar and Chattopadhyay, 2020)), alter trafficking of this GPCR in the membrane as has been proposed for other Type A GPCRs (Weinberg and Puthenveedu, 2019) or indirectly increase homo-oligomerization of LHRs to activate signal transduction (Milligan et al., 2019) is not known. However, for hydrophilic compounds, interaction with the protein is likely to be responsible for some of the cellular changes in lipid packing that are observed.

Lipid bilayer interactions with lipophilic species and internalization of these V-compounds is an attractive alternative mechanism for lipophilic compounds that can penetrate the membrane. Many compounds and drugs must transit the plasma membrane, enter the cell cytoplasm before targeting intracellular structures (Chen et al., 2022). Transport of many compounds across a membrane depends on suitable membrane transporters that could facilitate the transport of specific compounds (Jafurulla et al., 2011). For example, the addition of DIDS stopped the internalization of V-compounds such as $VO(acac)_2$, BMOV and vanadate across erythrocyte membrane (Yang et al., 2003; Yang et al., 2004) but had no effect on transport of these same compounds in Caco-2 cells (Yang et al., 2004). These results demonstrate that a suitable transporter exists in erythrocytes but not in Caco-2 cells. Lipoidal diffusion is an alternative mechanism for drug movement across membrane barriers as described in detail in (Smith et al., 2014; McLauchlan et al., 2015). The mechanism shown in Figure 7C describe compounds that can weakly associate with the membrane-protein complex and initiate signaling though possible electron transfer. These compounds would be able to exert their mode of action without requiring internalization of the derivatives. Considering these mechanisms, it is important to determine the association of the compound with the membrane as well as whether internalization is taking place. V_1, $V_{10,}$ V_{14} and $V_{15,}$ as reported previously (Althumairy et al., 2020c), are associated with the cell membrane where they modulate membrane lipid packing and are not readily removed with 1 cell washing. This suggests some degree of internalization of these compounds at the membrane interface. In contrast, V_9Mo and V_9Pt are lost quickly from the cell membrane, a process that can be accelerated by washing cells repeatedly. These two compounds are examples of compounds that are not internalized and may act through mechanisms shown in Figures 7A, C.

5 Conclusion

These studies demonstrate that the interactions of two monosubstituted decavanadates, monoplatino(IV)nonavanadate(V) ($[H_2Pt^{VI}V^{V}_{9}O_{28}]^{5-}$, abbreviated V_9Pt, and monomolybdo(VI) nonavanadate(V) ($[Mo^{VI}V^{V}_{9}O_{28}]^{5-}$, abbreviated V_9Mo, with the eukaryotic cell plasma membrane directly decrease the packing of membrane lipids. The two monosubstituted decavanadates indirectly drive aggregation of LHR, a G protein-coupled receptor, in CHO cells when the receptor is not over-expressed in CHO cell membranes. These monosubstituted decavanadates are very effective in initiating LHR signaling, despite their hydrolytic instability and short life span under our assay conditions. This rapid signaling stands in contrast to the slower inhibitory effects on cell growth. The monosubstituted decavanadates therefore demonstrate selective signaling and lower toxicity manifested in terms of growth inhibition and since they hydrolyze fast and show less growth effects when compared to corresponding unsubstituted isopolyvanadates such as the decavanadate anion. In summary, $V_{10}O_{28}^{6-}$ is less efficient at initiating cell signaling while causing greater growth inhibition and hence cell toxicity. These studies have uncovered differences in cellular effects induced by decavanadate and monosubstituted derivatives V_9Pt and V_9Mo that may be of pharmacologic importance. Monosubstituted derivatives initiated a more rapid and greater signaling response that did V_{10}, possibly because of their structure and lower charge. Of benefit to cells, toxic effects of the monosubstituted derivatives are lessened because of their reduced stability compared to V_{10}.

Data availability statement

The original contributions presented in the study are included in the article/Supplementary Material, further inquiries can be directed to the corresponding authors.

Author contributions

Project conception DC and DR; Project management DR and DC; Experimental design DR, DA, DC, KK, and BB; Experiments DA, KK, and AR; Verification DR, DC, DA, KK, and UK; Manuscript preparation DR, DC, and KK; Editing DR, DC, KK, UK, BB, DA, and AR; Grant funding DC and DR. All authors helped edit and have approved the submitted manuscript.

Funding

DC and DR thank Colorado State University and a private donor for support. UK thanks the German Research Foundation (DFG) and Jacobs University for research support.

Acknowledgments

The authors wish to thank the Colorado State University Analytical Resources Core Facility, RRID: SCR_021758 for instrument access, and Michele Mailhot for experimental consultation with the NMR spectroscopy.

Conflict of interest

The authors declare that the research was conducted in the absence of any commercial or financial relationships that could be construed as a potential conflict of interest.

Publisher's note

Supplementary material

The Supplementary Material for this article can be found online at: https://www.frontiersin.org/articles/10.3389/fchbi.2023.1126975/full#supplementary-material

References

Al-Qatati, A., Fontes, F. L., Barisas, B. G., Zhang, D., Roess, D. A., and Crans, D. C. (2013). Raft localization of Type I Fcε receptor and degranulation of RBL-2H3 cells exposed to decavanadate, a structural model for V2O5. *Dalton Trans.* 42, 11912–11920. doi:10.1039/c3dt50398d

Althumairy, D., Murakami, H. A., Colclough, R., Barisas, B. G., Roess, D. A., and Crans, D. C. (2020a). *Vanadium catalysis*. London, United Kingdom: Publishers Royal Society of Chemistry. Chapter 21. Vanadium Compounds as Indirect Activators of a G Protein-coupled Receptor.

Althumairy, D., Murakami, H. A., Zhang, D., Barisas, B. G., Roess, D. A., and Crans, D. C. (2020b). Effects of vanadium(IV) compounds on plasma membrane lipids lead to G protein-coupled receptor signal transduction. *J. Inorg. Biochem.* 203, 110873. doi:10.1016/j.jinorgbio.2019.110873

Althumairy, D., Postal, K., Barisas, B. G., Nunes, G. G., Roess, D. A., and Crans, D. C. (2020c). Polyoxometalates function as indirect activators of a G protein-coupled receptor. *Metallomics* 12, 1044–1061. doi:10.1039/d0mt00044b

Althumairy, D., Roess, D. A., and Barisas, B. G. (2020d). Effects of luteinizing hormone receptor expression level on receptor aggregation and function. *Biophysical J.* 118, 95a. doi:10.1016/j.bpj.2019.11.680

Aureliano, M., and Ohlin, C. A. (2014). Decavanadate *in vitro* and *in vivo* effects: Facts and opinions. *J. Inorg. Biochem.* 137, 123–130. doi:10.1016/j.jinorgbio.2014.05.002

Aureliano, M., and Crans, D. C. (2009). Decavanadate (V10O286-) and oxovanadates: Oxometalates with many biological activities. *J. Inorg. Biochem.* 103, 536–546. doi:10.1016/j.jinorgbio.2008.11.010

Aureliano, M., Gumerova, N. I., Sciortino, G., Garribba, E., Mclauchlan, C. C., Rompel, A., et al. (2022). Polyoxidovanadates' interactions with proteins: An overview. *Coord. Chem. Rev.* 454, 214344. doi:10.1016/j.ccr.2021.214344

Aureliano, M., Gumerova, N. I., Sciortino, G., Garribba, E., Rompel, A., and Crans, D. C. (2021). Polyoxovanadates with emerging biomedical activities. *Coord. Chem. Rev.* 447, 214143. doi:10.1016/j.ccr.2021.214143

Bijelic, A., Aureliano, M., and Rompel, A. (2019). Polyoxometalates as potential next-generation metallodrugs in the combat against cancer. *Angew. Chem. Int. Ed.* 58, 2980–2999. doi:10.1002/anie.201803868

Bijelic, A., Aureliano, M., and Rompel, A. (2018). The antibacterial activity of polyoxometalates: Structures, antibiotic effects and future perspectives. *Chem. Commun.* 54, 1153–1169. doi:10.1039/c7cc07549a

Biswas, B. K., Biswas, N., Saha, S., Rahaman, A., Mandal, D. P., Bhattacharjee, S., et al. (2022). Interaction with bioligands and *in vitro* cytotoxicity of a new dinuclear dioxido vanadium(V) complex. *J. Inorg. Biochem.* 237, 111980. doi:10.1016/j.jinorgbio.2022.111980

Bougie, I., and Bisaillon, M. (2006). Inhibition of a metal-dependent viral RNA triphosphatase by decavanadate. *Biochem. J.* 398, 557–567. doi:10.1042/bj20060198

Crans, D. C., Smee, J. J., Gaidamauskas, E., and Yang, L. (2004). The chemistry and biochemistry of vanadium and the biological activities exerted by vanadium compounds. *Chem. Rev.* 104, 849–902. doi:10.1021/cr020607t

Crans, D. C., Brown, M., and Roess, D. A. (2022). Vanadium compounds promote biocatalysis in cells through actions on cell membranes. *Catal. Today* 388-389, 216–223. doi:10.1016/j.cattod.2020.07.027

Crans, D. C. (1994). Enzyme interactions with labile oxovanadates and other polyoxometalates. *Comments Inorg. Chem.* 16, 35–76. doi:10.1080/02603599408035851

Crans, D. C., Henry, L., Cardiff, G., and Posner, B. I. (2019). Developing vanadium as an antidiabetic or anticancer drug: A clinical and historical perspective. *Mater. Ions Life Sci.* 19. doi:10.1515/9783110527872-008

Crans, D. C. (1993). Interactions of oxovanadates and selected oxomolybdates with proteins. *Mol. Eng.* 3, 277–284. doi:10.1007/bf00999638

Crans, D. C., Mahroof-Tahir, M., Anderson, O. P., and Miller, M. M. (1994). X-Ray structure of (NH4)6(gly-gly)2V10O28.cntdot.4H2O: Model studies for polyoxometalate-protein interactions. *Inorg. Chem.* 33, 5586–5590. doi:10.1021/ic00102a036

Crans, D. C., Schoeberl, S., Gaidamauskas, E., Baruah, B., and Roess, D. A. (2011). Antidiabetic vanadium compound and membrane interfaces: Interface-facilitated metal complex hydrolysis. *J. Biol. Inorg. Chem. S.* 16, 961–972. doi:10.1007/s00775-011-0796-5

Crans, D. C., and Willsky, G. R. (1997). *Oxovanadate and oxomolybdate cluster interactions with enzymes and whole cells the Proceedings from the 25th Steenbock Symposium*. Madison, WI, United States: University of Wisconsin-Madison.

Dipilato, L. M., and Zhang, J. (2009). The role of membrane microdomains in shaping β2-adrenergic receptor-mediated cAMP dynamics. *Mol. Biosyst.* 5, 832–837. doi:10.1039/b823243a

Dugar, S., Izarova, N. V., Mal, S. S., Fu, R., Joo, H.-C., Lee, U., et al. (2016). Characterization of PtIV-containing polyoxometalates by high-resolution solid-state 195Pt and 51V NMR spectroscopy. *New J. Chem.* 40, 923–927. doi:10.1039/c5nj01242b

Favre, D., Harmon, J. F., Zhang, A., Miller, M. S., and Kaltashov, I. A. (2022). Decavanadate interactions with the elements of the SARS-CoV-2 spike protein highlight the potential role of electrostatics in disrupting the infectivity. *cycle, J. Inorg. Biochem.* 234, 111899. doi:10.1016/j.jinorgbio.2022.11189

Feng, B., Dong, Y., Shang, B., Zhang, B., Crans, D. C., and Yang, X. (2022). Convergent protein phosphatase inhibitor design for PTP1B and TCPTP: Exchangeable vanadium coordination complexes on graphene quantum dots. *Adv. Funct. Mater.* 32, 2108645. doi:10.1002/adfm.202108645

Ferretti, V. A., and León, I. E. (2022). An overview of vanadium and cell signaling in potential cancer treatments. *Inorganics* 10, 47. doi:10.3390/inorganics10040047

Hasenknopf, B. (2005). Polyoxometalates: Introduction to a class of inorganic compounds and their biomedical applications. *Front. Biosci.* 10, 275–287. doi:10.2741/1527

Hayashi, Y. (2011). Hetero and lacunary polyoxovanadate chemistry: Synthesis, reactivity and structural aspects. *Coord. Chem. Rev.* 255, 2270–2280. doi:10.1016/j.ccr.2011.02.013

He, Z., Han, S., Zhu, H., Hu, X., Li, X., Hou, C., et al. (2020). The protective effect of vanadium on cognitive impairment and the neuropathology of alzheimer's disease in APPSwe/PS1dE9 mice. *Front. Mol. Neurosci.* 13, 21. doi:10.3389/fnmol.2020.00021

Hill, C. L. (1998). Introduction: Polyoxometalates - multicomponent molecular vehicles to probe fundamental issues and practical problems. *Chem. Rev.* 98, 1–2. doi:10.1021/cr960395y

Jafurulla, M., Tiwari, S., and Chattopadhyay, A. (2011). Identification of cholesterol recognition amino acid consensus (CRAC) motif in G-protein coupled receptors. *Biochem. Biophysical Res. Commun.* 404, 569–573. doi:10.1016/j.bbrc.2010.12.031

Kiss, T., Kiss, E., Garribba, E., and Sakurai, H. (2000). Speciation of insulin-mimetic VO(IV)-containing drugs in blood serum. *J. Inorg. Biochem.* 80, 65–73. doi:10.1016/s0162-0134(00)00041-6

Kostenkova, K., Arhouma, Z., Postal, K., Rajan, A., Kortz, U., Nunes, G. G., et al. (2021). PtIV- or MoVI-substituted decavanadates inhibit the growth of Mycobacterium smegmatis. *J. Inorg. Biochem.* 217, 1–10. doi:10.1016/j.jinorgbio.2021.111356

Lee, U., Joo, H. C., Park, K.-M., Mal, S. S., Kortz, U., Keita, B., et al. (2008). Facile incorporation of platinum(IV) into polyoxometalate frameworks: Preparation of [H2PtIVV9O28]5 and characterization by 195Pt NMR spectroscopy. *Angew. Chem. Int. Ed.* 47, 793–796. doi:10.1002/anie.200703082

Lei, Y., Hagen, G. M., Smith, S. M., Liu, J., Barisas, G., and Roess, D. A. (2007). Constitutively-active human LH receptors are self-associated and located in rafts. *Mol. Cell. Endocrinol.* 260-262, 65–72. doi:10.1016/j.mce.2005.11.046

Levina, A., Crans, D. C., and Lay, P. A. (2017). Speciation of metal drugs, supplements and toxins in media and bodily fluids controls *in vitro* activities. *Coord. Chem. Rev.* 352, 473–498. doi:10.1016/j.ccr.2017.01.002

Levina, A., and Lay, P. A. (2017). Stabilities and biological activities of vanadium drugs: What is the nature of the active species? *Chem. Asian J.* 12, 1692–1699. doi:10.1002/asia.201700463

Loizou, M., Hadjiadamou, I., Drouza, C., Keramidas, A. D., Simos, Y. V., and Peschos, D. (2021). Vanadium(V) complexes with siderophore vitamin E-hydroxylamino-triazine ligands. *Inorganics* 9, 73. doi:10.3390/inorganics9100073

Mclauchlan, C. C., Peters, B. J., Willsky, G. R., and Crans, D. C. (2015). Vanadium-phosphatase complexes: Phosphatase inhibitors favor the trigonal bipyramidal transition state geometries. *Coord. Chem. Rev.* 301-302, 163–199. doi:10.1016/j.ccr.2014.12.012

Milligan, G., Ward, R. J., and Marsango, S. (2019). GPCR homo-oligomerization. *Curr. Opin. Cell. Biol.* 57, 40–47. doi:10.1016/j.ceb.2018.10.007

Mutlu, E., Cristy, T., Graves, S. W., Hooth, M. J., and Waidyanatha, S. (2017). Characterization of aqueous formulations of tetra- and pentavalent forms of vanadium in support of test article selection in toxicology studies. *Environ. Sci. Pollut. Res.* 24, 405–416. doi:10.1007/s11356-016-7803-x

Nunes, G. G., Bonatto, A. C., De Albuquerque, C. G., Barison, A., Ribeiro, R. R., Back, D. F., et al. (2012). Synthesis, characterization and chemoprotective activity of polyoxovanadates against DNA alkylation. *J. Inorg. Biochem.* 108, 36–46. doi:10.1016/j.jinorgbio.2011.11.019

Nunes, P., Correia, I., Cavaco, I., Marques, F., Pinheiro, T., Avecilla, F., et al. (2021). Therapeutic potential of vanadium complexes with 1,10-phenanthroline ligands, quo vadis? Fate of complexes in cell media and cancer cells. *J. Inorg. Biochem.* 217, 111350. doi:10.1016/j.jinorgbio.2020.111350

Chen, R.C., Kang, R., and Tang, D. (2022). The mechanism of HMGB1 secretion and release). *Exp. Mol. Sci.* 54, 91–102. doi:10.1038/s12276-022-00736-w

Pessoa, J. C., and Correia, I. (2021). Misinterpretations in evaluating interactions of vanadium complexes with proteins and other biological targets. *Inorganics* 9, 17. doi:10.3390/inorganics9020017

Pessoa, J. C., Santos, M. F. A., Correia, I., Sanna, D., Sciortino, G., and Garribba, E. (2021). Binding of vanadium ions and complexes to proteins and enzymes in aqueous solution. *Coord. Chem. Rev.* 449, 214192. doi:10.1016/j.ccr.2021.214192

Pope, M. T. (1983). *Heteropoly and isopoly oxometalates*. Berlin: Springer-Verlag.

Pope, M. T., and Müller, A. (1991). Polyoxometalate chemistry: An old field with new dimensions in several disciplines. *Angewandte Chemie Int. Ed. Engl.* 30, 34–48. doi:10.1002/anie.199100341

Pope, M. T., and Müller, A. (1994). *Polyoxometalates: From platonic solids to anti-retroviral activity*. Dordrecht: Springer.

Postal, K., Maluf, D. F., Valdameri, G., R¨Udiger, A. L., Hughes, D. L., De S´A, E. L., et al. (2016). Chemoprotective activity of mixed valence polyoxovanadates against diethylsulphate in *E. coli* cultures: Insights from solution speciation studies. *RSC Adv.* 6, 114955–114968. doi:10.1039/c6ra15826a

Rhule, J. T., Hill, C. L., Judd, D. A., and Schinazi, R. F. (1998). Polyoxometalates in medicine. *Chem. Rev.* 98, 327–358. doi:10.1021/cr960396q

Ribeiro, N., Bulut, I., Pósa, V., Sergi, B., Sciortino, G., Pessoa, J. C., et al. (2022). Solution chemical properties and anticancer potential of 8-hydroxyquinoline hydrazones and their oxidovanadium(IV) complexes. *J. Inorg. Biochem.* 235, 111932. doi:10.1016/j.jinorgbio.2022.111932

Roess, D. A., Smith, S. M. L., Winter, P., Zhou, J., Dou, P., Baruah, B., et al. (2008). Effects of vanadium-containing compounds on membrane lipids and on microdomains used in receptor-mediated signaling. *Chem. Biodiversity* 5 (8), 1558–1570. doi:10.1002/cbdv.200890144

Sahu, G., Patra, S. A., Mohanty, M., Lima, S., Pattanayak, P. D., Kaminsky, W., et al. (2022). Dithiocarbazate based oxidomethoxidovanadium(V) and mixed-ligand oxidovanadium(IV) complexes: Study of solution behavior, DNA binding, and anticancer activity. *J. Inorg. Biochem.* 223, 111844. doi:10.1016/j.jinorgbio.2022.111844

Samart, N., Althumairy, D., Zhang, D., Roess, D. A., and Crans, D. C. (2020). Initiation of a novel mode of membrane signaling: Vanadium facilitated signal transduction. *Coord. Chem. Rev.* 416, 213286. doi:10.1016/j.ccr.2020.213286

Samart, N., Arhouma, Z., Kumar, S., Murakami, H. A., Crick, D. C., and Crans, D. C. (2018). Decavanadate inhibits mycobacterial growth more potently than other oxovanadates. *Front. Chem.* 6, 519. doi:10.3389/fchem.2018.00519

Sánchez-Lara, E., Treviño, S., Sánchez-Gaytán, B. L., Sánchez-Mora, E., Eugenia Castro, M., Meléndez-Bustamante, F. J., et al. (2018). Decavanadate salts of cytosine and metformin: A combined experimental-theoretical study of potential metallodrugs against diabetes and cancer. *Front. Chem.* 6, 402. doi:10.3389/fchem.2018.00402

Sánchez-Lombardo, I., Baruah, B., Alvarez, S., Werst, K. R., Segaline, N. A., Levinger, N. E., et al. (2016). Size and shape trump charge in interactions of oxovanadates with self-assembled interfaces: Application of continuous shape measure analysis to the decavanadate anion. *New J. Chem.* 40, 962–975. doi:10.1039/c5nj01788b

Sarkar, P., and Chattopadhyay, A. (2020). Cholesterol interaction motifs in G protein-coupled receptors: Slippery hot spots? *Syst. Biol. Med.* 12 (4), e1481. doi:10.1002/wsbm.1481

Scalese, G., Machado, I., Correia, I., Pessoa, J. C., Bilbao, L., Pérez-Diaz, L., et al. (2019). Exploring oxidovanadium(iv) homoleptic complexes with 8-hydroxyquinoline derivatives as prospective antitrypanosomal agents. *New J. Chem.* 43, 17756–17773. doi:10.1039/c9nj02589h

Semiz, S. (2022). Vanadium as potential therapeutic agent for COVID-19: A focus on its antiviral, antiinflamatory, and antihyperglycemic effects. *J. Trace Elem. Med. Biol.* 69, 126887. doi:10.1016/j.jtemb.2021.126887

Smith, D., Artursson, P., Avdeef, A., Di, L., Ecker, G. F., Faller, B., et al. (2014). Passive lipoidal diffusion and carrier-mediated cell uptake are both important mechanisms of membrane permeation in drug disposition. *Mol. Pharm.* 11, 1727–1738. doi:10.1021/mp400713v

Smith, S. M. L., Lei, Y., Liu, J., Cahill, M. E., Hagen, G. M., Barisas, B. G., et al. (2006). Luteinizing hormone receptors translocate to plasma membrane microdomains after binding of human chorionic gonadotropin. *Endocrinology* 147, 1789–1795. doi:10.1210/en.2005-1046

Strukan, N., Cindric, M., and Kamenar, B. (1997). Synthesis and structure of [(CH3)4N]4[H2MoV9O28]Cl·6H2O. *Polyhedron* 16, 629–634. doi:10.1016/0277-5387(96)00316-6

Treviño, S., and Diaz, A. (2020). Vanadium and insulin: Partners in metabolic regulation. *J. Inorg. Biochem.* 208, 111094. doi:10.1016/j.jinorgbio.2020.111094

Weinberg, Z. Y., and Puthenveedu, M. A. (2019). Regulation of G protein-coupled receptor signaling by plasma membrane organization and endocytosis. *Traffic* 20, 121–129. doi:10.1111/tra.12628

Winter, P. W., Al-Qatati, A., Wolf-Ringwall, A. L., Schoeberl, S., Chatterjee, P. B., Barisas, B. G., et al. (2012). The anti-diabetic bis(maltolato)oxovanadium(iv) decreases lipid order while increasing insulin receptor localization in membrane microdomains. *Dalton Trans.* 41, 6419–6430. doi:10.1039/c2dt30521f

Wolf-Ringwall, A. L., Winter, P. W., Liu, J., Van Orden, A. K., Roess, D. A., and Barisas, B. G. (2011). Restricted lateral diffusion of luteinizing hormone receptors in membrane microdomains. *J. Biol. Chem.* 286, 29818–29827. doi:10.1074/jbc.m111.250969

Yamamoto, N., Schols, D., De Clercq, E., Debyser, Z., Pauwels, R., Balzarini, J., et al. (1992). Mechanism of anti-human immunodeficiency virus action of polyoxometalates, a class of broad-spectrum antiviral agents. *Mol. Pharmacol.* 42, 1109–1117.

Yang, X.-G., Wang, K., Lu, J., and Crans, D. C. (2003). Membrane transport of vanadium compounds and the interaction with the erythrocyte membrane. *Coord. Chem. Rev.* 237, 103–111. doi:10.1016/s0010-8545(02)00247-3

Yang, X.-G., Yang, X.-D., Yuan, L., Wang, K., and Crans, D. C. (2004). The permeability and cytotoxicity of insulin-mimetic vanadium compounds. *Pharm. Res.* 21, 1026–1033. doi:10.1023/b:pham.0000029293.89113.d5

Appendix VIII: Open questions on the biological roles of first-row transition metals

This comment concerns the biological roles of first-row transition metals is published in *Communications Chemistry* (Crans, Kostenkova 2020).

References

Crans, D. C.; Kostenkova, K. Open questions on the biological roles of first-row transition metals. *Comms. Chem*. **2020**, *3*, 104.

COMMUNICATIONS CHEMISTRY

COMMENT

https://doi.org/10.1038/s42004-020-00341-w OPEN

Open questions on the biological roles of first-row transition metals

Debbie C. Crans [1,2]✉ & Kateryna Kostenkova [1]

First-row transition metals play several roles in biological processes and in medicine, but can be toxic in high concentrations. Here the authors comment on the sensitive biochemistry and speciation chemistry of the first-row transition metals, and outline some of the remaining questions that have yet to be answered.

Five of the ten first-row transition metals are essential to human health, including manganese, iron, cobalt, copper, and zinc[1,2]. Three more first-row transition elements have shown some beneficial biological effects including chromium, vanadium, and nickel. Typically, these metals are consumed in a varied diet or as nutritional additives where, in the human body, they serve both structural and functional roles including the maintenance of cellular functions involved in a wide range of biological activities. However, normal function requires that the levels of the metal ions are maintained within an acceptable range; lower concentrations may result in a nutritional deficiency and higher concentrations may result in toxicity (Fig. 1)[3]. In addition, the physical properties of first-row elements, particularly titanium and nickel, are important for preparation of new materials and alloys, resulting in technological advantages that improve the quality of life. Nine of the ten first-row transition metals have densities larger than 5.0 g/cm^3 which, by some definitions, classifies them as 'heavy metals'. Although this definition may be commonly used by some, it is not embraced by chemists primarily because this definition depends on the density of the metal rather than its chemical properties. Furthermore, the negative connotation associated with the term 'heavy metal' and the toxicity of metals such as cadmium and mercury stands in opposition to the fact that five of the first-row transition elements are essential to life. A more concise definition of the vague term 'heavy metal' can be based on chemical properties and would include the block of metals in Groups 3 to 16 that are in periods 4 and greater[4]. This definition of 'heavy metals' does not involve first-row elements but only second and third-row transition metals. However, even this definition is debated[4]. It is however clear that none of the five essential first-row transition metals are toxic 'heavy metals'.

The chemistry of all first-row transition metals is very sensitive to their environment[6]. In the presence of water, each metal ion forms hydrated ions which undergo pH and concentration-dependent chemistry that is dictated by the presence of metabolites, proteins, and other biological components (Fig. 1a). It is important to recognize that redox active metal ions do not exist

[1] Department of Chemistry, 1301 Center Ave., Colorado State University, Fort Collins, CO 80523, USA. [2] Cell and Molecular Biology Program, 1301 Center Ave., Colorado State University, Fort Collins, CO 80523, USA. ✉email: debbie.crans@colostate.edu

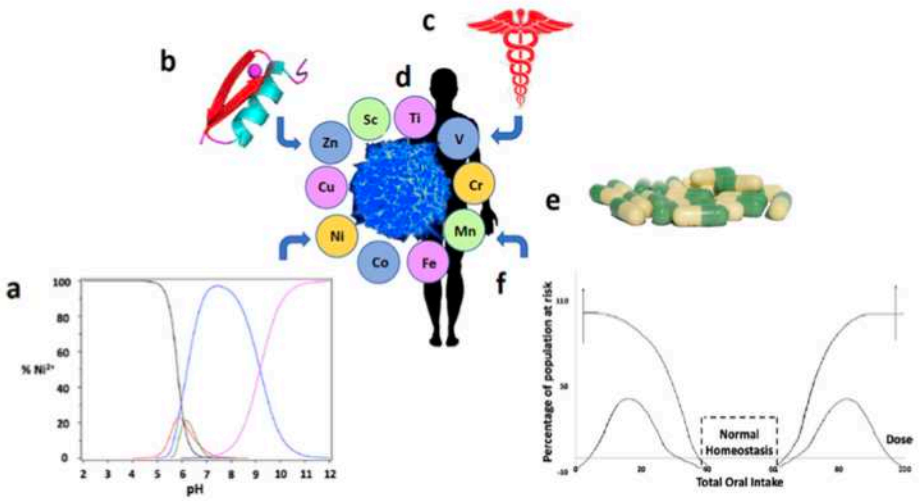

Fig. 1 Schematic representing the chemistry and metabolism of the first-row transition metal ions. The speciation diagram reports on the forms of Ni^{2+} at a changing pH[5] (**a**), Zn^{2+} ion bound to the zinc finger motif (**b**), the ten first-row transition metal ions in cells and human beings (**c**) are responsible for the health of the human (**d**), but may need to be supplemented (**e**) in order to achieve oral homeostasis (**f**). **a** Adapted with permission from ref. [5] **b** and **e** were prepared by the authors. **c**, **d** and **f** were reproduced with modifications: Caduceus, Eliot Lash from Wikimedia Commons; Healthy human T-cell, NIAID from http://www.nih.gov; Essential Metal Uptake diagram, Van Cleave et al. from MDPI (ref. [2])/under the Creative Commons Attribution-Share Alike 3.0 Unported license (https://creativecommons.org/licenses/by-sa/3.0/deed.en).

as free ions in cells[7]. As a result, these metals undergo speciation chemistry governed by the metal ion's oxidation state, the local pH, the ionic strength, and the stability of metal complexes with biological molecules[6,8]. Depending on the specific conditions, several of the metal ions form multinuclear species in aqueous solution, and as such many activities and functions will not be linear but very sensitive to concentrations and association with biomolecules. Appreciation of classical speciation chemistry increases when it becomes obvious that the identification of components in the system demystifies poorly understood processes in biology[9].

Typically, the first-row transition metal ions are bound to proteins in the cellular system[10]. More than 30% of the proteins in the genome bind metal ions, and some of these bind the metal ions with such a high affinity that the metal ion is difficult to separate from the protein. Protein complexation to a metal ion prevents the redox formation of undesired reactive oxygen species (ROS) by the metal ion. This, however, requires that the bound metal ions are utilized by transfer of the metal ion to a target protein. Processes involving metal transfer reactions can be difficult to study because the reacting metal peptide complex is very likely to have very similar spectroscopic signatures to the product metal peptide complex[11]. Importantly, changes in affinities of the metal ions in different oxidation states are important in facilitating cell uptake and transfer reactions. Manganese, iron, cobalt, and copper are the four essential elements that exhibit rich redox chemistry under physiological conditions. These metal ions are associated with multiple enzymes, and are involved in many cellular redox processes[9,12–14].

Iron is essential for human life as hemoglobin and as an intricate part of respiration enzymes, particularly those containing hemes[12–14]. The chemistry of both Fe(II) and Fe(III) is important for binding and function of many other redox proteins, including non-heme proteins. Ligand coordination to iron is important to allow the redox cycling without the involvement of Fenton chemistry and generation of uncontrolled ROS at the cellular level[11]. Similarly, copper is involved in function of many redox enzymes as well. Cu(I), Cu(II), and Cu(III) are bound to many proteins and cellular components with high affinity[7,9]. Although manganese and cobalt have less prominent roles than iron and copper, they too are involved in specific processes essential for life. For example, manganese is a cofactor for the enzyme superoxide dismutase responsible for scavenging ROS. Cobalt is bound to a heme in vitamin B_{12} which is the only vitamin to contain a metal ion. Studies of these systems continue to be important. An increased consideration of the metal coordination chemistry will benefit the insights into these systems and uncover new details about their modes of action. Studies with zinc, which is the fifth essential element and the only non-redox active cation, are also important because zinc has either a structural or functional role in more than 300 different proteins[13,14]. One role of zinc is in maintaining the folding of the DNA-binding domains of eukaryotic transcription factors including zinc finger transcription factors. Recent investigations have demonstrated numerous previously unknown activities including hormone-like activities which highlights the notion that even non-redox active ions can have crucial roles in biological systems. The large number of clinical trials involving zinc shown in Table 1 demonstrates the interest in this metal. Importantly, future investigations of these metals in biological systems should be done in the context of metal coordination chemistry within and outside the range of normal homeostasis.

Three additional elements have some reported beneficial effects include chromium, vanadium, and nickel. Chromium, considered to be an essential metal for some time, is probably the most controversial element in the periodic table[1,8]. Careful speciation studies have shown that Cr(III) is not as inert as previously believed and can convert to Cr(V) and Cr(VI) ions which are highly toxic[8]. Like chromium, both beneficial and toxic effects have been reported for vanadium and nickel. For many years,

Table 1 Clinical trials involving compounds containing first-row transition metals registered with the National Institutes of Health (NIH).

Transition metal	Total clinical trials	Active[a] clinical trials	Conditions/disease	Interventions/procedure
Scandium	4	2	Melanoma/gingival recession	Isolated hepatic perfusion (IHP)/Laser procedures
Titanium	540	134	A wide range of Ti-based implants	Surgical insertion
Vanadium	12	2	Preeclampsia/prediabetes/cancer	Oral administration
Chromium	256	62	Type 2 diabetes, coronary artery disease, obesity, HIV, polycystic ovary	Oral administration
Manganese	73	17	Vitamin and micronutrient deficiency	Oral administration
Iron	3234	776	anemia, iron deficiency, obesity, type 2 diabetes	Oral administration
Cobalt	299	67	B-cell lymphoma, coronary artery disease, osteoarthritis, melanoma, coronary artery stenosis	Oral administration
Nickel	118	28	Malocclusion, knee osteoarthritis, malignant glioma, impacted tooth, sickle cell disease	Orthodontic arch wire, EXD-959 Bracket System, Surgery, Oral administration
Copper	393	83	Menkes disease, contraception, cancer, amyotrophic lateral sclerosis, HIV, vitamin and mineral deficiency, Wilson disease, vitamin D deficiency	Oral administration, surgery
Zinc	1797	182	HIV, sepsis, hemophilia B, dental pulp necrosis, Mucopolysaccharidosis II, vitamin A and D deficiency, fluoride poisoning, zinc deficiency, cancer, type II diabetes, type 1 diabetes	Oral administration

Taken from https://www.clinicaltrials.gov
[a]"Active" includes funded trials that are either recruiting or completing data analysis.

vanadium compounds were developed as insulin enhancing agents. Current studies focus on using vanadium-based compounds as anticancer agents which include flavonoid vanadium complexes[2] and coordination complexes for immunotherapy applications[15]. Nickel appears to be an important part of the microflora in the human gut where it is a cofactor for the enzyme urease[2]. On the other hand, Ni-containing alloys often used in jewelry are known to cause an allergenic response in about 30% of women. This application is countered by to the use of Ni-containing alloy implants added to mend broken bones and represents an example of beneficial and toxic effects of this metal[2].

Titanium is a first-row transition metal ion that has no known biological function despite being readily transported in the human blood where it readily binds to proteins such as human serum albumin. Titanium metal is a common component of alloys ranging from dental implants to orthopedic prosthetics and many clinical trials have been completed and others are underway. However, even for this supposedly non-toxic element, there are some reports that the metal alloys are not completely stable; some cationic forms of titanium leach from the metal surfaces[13]. The biological and potentially toxic response of each system should be carefully considered, particularly since such a large number of clinical trials are ongoing with this element (Table 1). Scandium is non-essential to human health and has no known biological function in the biosphere. Its low abundance has precluded many studies until recently. Potential applications of scandium are currently being investigated in two clinical trials (Table 1).

Essential nutrients for human health include the 13 known vitamins A, C, D, E, K, and the eight B vitamins (thiamine (B1), riboflavin (B2), niacin (B3), pantothenic acid (B5), pyroxidine (B6), biotin (B7), folate (B9), and cobalamin (B12). Unlike minerals, vitamins in biological systems can be metabolized to carbon dioxide and water while metal ions must be removed by excretion. The bioprocessing of these metal ions and their recycling remain a complex matter, which require an evaluation of their speciation chemistry. Unfortunately, studies integrating metal speciation with pharmacokinetic and pharmacodynamic properties of metal ions are also quite costly[13,14]. Nonetheless, metabolism provides additional avenues for formation of active biological substances. That is, if the ligand bound to a metal is changed during bioprocessing, a new complex with a different coordination and speciation chemistry is formed which may also have beneficial biological activity and significantly prolong the effects of the originally administered therapeutic[9].

Finally, we wish to point out the utility of these elements as therapeutic and diagnostic agents. To document their use, we have tabulated the number of completed and active clinical trials that have been carried out with these ten elements (Table 1). Since five of the first-row transition metals are essential elements, many of their applications are related to bringing the concentration of these elements into the normal concentration range so it is neither too low or too high, thus causing disease. Accordingly, a large number of clinical trials are associated with iron, zinc, copper, cobalt, and manganese. Many applications of titanium and nickel relate to their physical properties and concern their use as alloys in implants. Development of therapeutic and diagnostic agents continues because of the increasing need to monitor and cure diseases[16]. However, technical advances change the requirements for the agents, as illustrated by the recent report where the compound's reactivity was considered an advantage because injections were made directly into the tumor, and the reactivity of the compound affects cancerous tissue[17]. Multiple uses of the first-row transition metal ions in medicine are already in place in the clinic and other promising uses are being developed with the potential of improving human health.

Received: 15 May 2020; Accepted: 2 June 2020;
Published online: 07 August 2020

References

1. Sigel, H. & Sigel, A. The bio-relevant metals of the periodic table of the elements. *Z. Naturforsch.* **74**, 461–471 (2019).
2. Van Cleave, C. & Crans, D. C. The first row transition metals in the periodic table of medicine. *Inorganics* **7**, 111 (2019).
3. Chambers, A. et al. An exposure-response curve for copper excess and deficiency. *J. Tox. Environ. Health, Part B* **13**, 546–578 (2010).
4. Hawkins, S. What is a "Heavy Metal"? *J. Chem. Ed.* **74**, 1374 (1997).
5. Baes, C. F. & Mesmer, R. S. *The Hydrolysis of Cations*. (John Wiley & Sons, New York, 1976).
6. Marcio, L. et al. The peculiar behavior of Picha in the formation of metallacrown complexes with Cu(II), Ni(II) and Zn(II), in aqueous solution. *Dalton Trans.* **44**, 3237–3250 (2015).
7. Rae, T. D., Schmidt, P. J., Pufahl, R. A., Culotta, V. C. & O'Halloran, T. V. Undetectable intracellular free copper: the requirement of a copper chaperone for superoxide dismutase. *Science* **284**, 805–808 (1999).
8. Kiss, Y., Enyeda, E. A. & Jakusch, T. Development of the application of speciation in chemistry. *Coor. Chem. Rev.* **352**, 401–423 (2017).
9. Levina, A., Crans, D. C. & Lay, P. A. Speciation of metal drugs, supplements and toxins in media and bodily fluids controls *in vitro* activities *Coor. Chem. Rev.* **352**, 473–498 (2017).
10. Mounicou, S., Szpunar, J. & Lobinski, R. Metallomics: the concept and methodology. *Chem. Soc. Rev.* **38**, 1119–1138 (2009).
11. Beuning, C., Mestre-Voegtlé, B., Faller, P., Hureau, C. & Crans, D. C. Measurement of inter-peptidic Cu(II) exchange rate constants by static fluorescence quenching of tryptophan. *Inorg. Chem.* **57**, 4791–4794 (2018).
12. Valko, M., Morris, H. & Cronin, M. T. D. Metals, toxicity and oxidative stress. *Curr. Med. Chem.* **12**, 1161–1208 (2005).
13. Casini, A., Vessieres, A. & Meier-Menches, S. M. (Eds.) *Metal-based Anticancer Agents* (The Royal Sociey of Chemistry, 2019).
14. Sigel, A., Sigel, H., Freisinger, E. & Sigel, R. K. O. Metallo-drugs: development and action of anticancer agents. *Met. Ions Life Sci.* **18**, (2018).
15. Selman, M. et al. Multi-modal potentiation of oncolytic virotherapy by vanadium compounds. *Mol. Ther.* **26**, 56–69 (2018).
16. Barry, N. P. E. & Sadler, P. J. Exploration of the medical periodic table: toward new targets. *Chem. Commun.* **49**, 5106–5131 (2013).
17. Levina, A. et al. A short-lived but highly cytotoxic vanadium(V) complex as a promising drug candidate for brain cancer treatment by intratumoral injections. *Angew. Chem.* in press https://doi.org/10.1002/anie.202005458 (2020).

Acknowledgements

D.C.C. and K.K. thank Drs. Christopher Roberts and Deborah A. Roess and Miss Kaitlin Doucette for reading and commenting on this manuscript. We thank Cameron Van Cleave for assistance with preparation of Fig. 1.

Author contributions

D.C.C. initiated and supervised the project. K.K. carried out literature searches and together D.C.C. and K.K. fine-tuned ideas and finished writing the paper. K.K. also prepared the figure and the table.

Competing interests

The authors declare no competing interests.

Additional information

Correspondence and requests for materials should be addressed to D.C.C.

Reprints and permission information is available at http://www.nature.com/reprints

Publisher's note Springer Nature remains neutral with regard to jurisdictional claims in published maps and institutional affiliations.

Appendix IX: Pt^{IV}- or Mo^{VI}-substituted decavanadates inhibit the growth of *Mycobacterium smegmatis*

This manuscript concerns the ^{51}V NMR speciation studies and bacterial growth inhibition experiments of two Pt^{IV}- or Mo^{VI}-substituted decavanadates and is published in *Journal of Inorganic Biochemistry* (Kostenkova et. al, 2021).

References

Kostenkova, K.; Arhouma, Z.; Postal, K.; Rajan, A.; Kortz, U.; Nunes, G. G.; Crick, D. C.; Crans, D. C. Pt^{IV}- or Mo^{VI}-substituted decavanadates inhibit the growth of *Mycobacterium smegmatis. J. Inorg. Biochem*. **2021**, 217, 1 - 10 (article 111356).

Journal of Inorganic Biochemistry 217 (2021) 111356

Contents lists available at ScienceDirect

Journal of Inorganic Biochemistry

journal homepage: www.elsevier.com/locate/jinorgbio

Pt^{IV}- or Mo^{VI}-substituted decavanadates inhibit the growth of *Mycobacterium smegmatis*

Kateryna Kostenkova [a,1], Zeyad Arhouma [a,b,1], Kahoana Postal [a,c], Ananthu Rajan [d], Ulrich Kortz [d], Giovana G. Nunes [c], Dean C. Crick [b,e], Debbie C. Crans [a,b,*]

[a] Department of Chemistry, Colorado State University, Fort Collins, CO 80523, United States
[b] Cell and Molecular Biology Program, Colorado State University, Fort Collins, CO 80523, United States
[c] Department of Chemistry, Universidade Federal do Paraná, Curitiba, Paraná, Brazil
[d] Department of Life Sciences and Chemistry, Jacobs University, 28759 Bremen, Germany
[e] Microbiology, Immunology, and Pathology Department, Colorado State University, Fort Collins, CO 80523, United States

ARTICLE INFO

Keywords:
Vanadium
polyoxovanadates
heteropolyoxovanadates
speciation chemistry
Mycobacterium smegmatis
spectroscopic characterization

ABSTRACT

Inhibitory effects of two monosubstituted decavanadates by Pt^{IV} in monoplatino(*IV*)nonavanadate(V) ($[H_2Pt^{IV}V_9O_{28}]^{5-}$, V_9Pt), and by Mo^{IV} in monomolybdo(*VI*)nonavanadate(V) ($[Mo^{VI}V_9O_{28}]^{5-}$,V_9Mo) were investigated against the growth of *Mycobacterium smegmatis* with the EC_{50} values of 0.0048 mM and 0.015 mM, respectively. These compare to the reported inhibitory value for decavanadate ($[V_{10}O_{28}]^{6-}$/$[HV_{10}O_{28}]^{5-}$, V_{10}) on *Mycobacterium smegmatis* (EC_{50} = 0.0037 mM). Time-dependent ^{51}V NMR spectroscopic studies were carried out for all three polyanions in aqueous solution, biological medium (7H9), heated and non-heated supernatant to evaluate their stability in their respective media, monitor their hydrolysis to form various oxovanadates over time and calculate the EC_{50} values. These studies allow us to calculate adjusted and maximum EC_{50} for the polyoxovanadate (POV) present in solution at the beginning of the study when there is most intact anion in the media and thus the EC_{50} values represent the initial effects of the POVs. The results have shown that V_{10} is 1.3 times more potent than V_9Pt and 4 times more potent than V_9Mo, indicating that the inhibitory effects of monosubstituted polyanions are related to the V_{10} structure. We attributed the minor differences in the growth inhibitory effects to the differences in charges (5- *vs* 6-) of V_9Pt and V_9Mo compared to V_{10} and/or the differences in the chemical composition. We concluded that the potency of the growth inhibition by V_{10} is mainly due to the chemical properties of the vanadium and the decametalate's unique structure even though the presence of the *Mycobacterium smegmatis* facilitate hydrolysis of the anions.

Synopsis: Two decavanadate derivatives, monoplatino(*IV*)nonavanadate(V) ($[H_2Pt^{IV}V_9O_{28}]^{5-}$), monomolybdo (*VI*)nonavanadate(V) ($[Mo^{VI}V_9O_{28}]^{5-}$) and decavanadate are more potent growth inhibitors of *Mycobacterium smegmatis* than monomeric vanadate. The spectroscopic characterization carried out in the growth medium led to the conclusion that both the decavanadate structure and its properties are important for its growth effects.

1. Introduction

The applications of polyoxometalates (POMs) have increased in the medical field because of the continuing reports of POMs, including polyoxovanadates (POVs), with promising biological effects, despite the challenges with low biocompatibility and compound accessibility [1–6]. The presence of vanadium in different clusters leads to an increased antiproliferative activity compared to that of polyoxomolybdates and polyoxotungstates [7–10]. POVs with antidiabetic, antibacterial and anticancer agents have been reported and their activity has been attributed to their effects on different enzymes. The enzyme and proteins include actin [11], kinases [12], and ATPases [13], as well as hormone-

Abbreviations: POM, polyoxometalate; POV, polyoxovanadate; STZ, streptozotocin; 7H9, the liquid growth medium used for *Mycobacteria* cultures; V_1, vanadate monomer, VO_4^{3-}; V_2, vanadate dimer, $H_2V_2O_7^{2-}$; V_4, vanadate tetramer, $V_4O_{12}^{4-}$; $Vcit^-$, vanadium(V) citrate complex; V_2cit^{2-}, vanadium(V) citrate complex (dimer); PV, vanadophosphate complex, $HVPO_7^{3-}$; OD, optical density.

* Corresponding author at: Department of Chemistry, Colorado State University, Fort Collins, CO 80523, United States.
E-mail address: debbie.crans@colostate.edu (D.C. Crans).

[1] These authors contributed equally to this work.

https://doi.org/10.1016/j.jinorgbio.2021.111356
Received 12 October 2020; Received in revised form 7 January 2021; Accepted 12 January 2021
Available online 19 January 2021
0162-0134/

like responses associated with the activation of a high-affinity receptor of the Fc region of the immunoglobin E (IgE), an antibody also known as FcεRI, is important in signal transduction [14] and the indirect activation of a G protein-coupled receptor [15]. In the recent study, novel Lindquist-type hexavanadate hybrids covalently linked to a β-alanine ethyl ester and L-alanine were designed and synthesized as a first step for site-specific delivery of a POM [16]. Two polyanions were derived from the carboxyl-derivative of Lindqvist-type hexavanadate parent, $[Bu_4N]_2[V_6O_{13}\text{-}\{(OCH_2)_3CCH_2OOCCH_2CH_2\text{-}COOH\}_2]$ [16]. These novel polyanions were found to be effective against carcinoma cell lines, and their activities were higher than that of the commercial drug 5-fluorouracil (5-FU) [16]. Similarly, a POV nanocage consisting of $\{V_5O_9Cl\}$ molecular building blocks and the organic triazine-benzoic acid linker was found to have antitumor properties [17]. These results show the biomedical potential of such compounds and suggest that the desirable effects of POVs are of interest. Therefore, the fundamental knowledge about the properties of vanadium-containing-oxo-clusters, particularly their effects on biological responses, is essential.

Decavanadate ($[V_{10}O_{28}]^{6-}$, abbreviated V_{10}) is an isopolyoxometalate that has been found to exhibit a range of biological activities including the interactions with Na^+, K^+, and Ca^{2+}- ATPases [18], inhibition of protein phosphatases, as well as crystallization with various enzymes including a protein tyrosine phosphatase (PTP), DNA polymerases and nucleases [19–24]. In addition to its ability to normalize elevated blood glucose levels in streptozotocin (STZ)-induced diabetic rats, decavanadate exhibits its effects in various biological systems including signal transduction activation of FcεRI [15,25]. The effects of decametalates on bacteria remain less explored than their anticancer and antidiabetic effects [26]. Recently, decavanadate was found to inhibit the growth of *Mycobacterium tuberculosis* mc^2 6230 (*M. tb*) and *Mycobacterium smegmatis* mc^2 155 (*M. smeg*), and was also found to be much more potent than the monovanadate (V_1), a known phosphatase inhibitor (Fig. 1) [27]. In the following work, we examine the effects of two known substituted polyoxovanadates, monomolybdononavanadate ($[V_9MoO_{28}]^{5-}$, abbreviated V_9Mo) and monoplatino(IV)-nonavanadate ($[H_2PtV_9O_{28}]^{5-}$, abbreviated V_9Pt), on the growth of *M. smeg*. These POVs have structures very similar to the V_{10}; however, replacing individual vanadium atoms by Pt^{IV} and Mo^{VI} results in a different chemical composition, such as a slightly lower symmetry and, most importantly, a lower charge by one unit, compared to the parent V_{10} (Fig. 1) [22,28,29].

V_{10} is a compact polyanion that consists of ten octahedrally coordinated vanadium(V) atoms, eight of which contain one terminal oxo ligand and five shared oxygens in their octahedra, and two of which are located in the interior with six bridging oxygens in their octahedra (Fig. 1) [22,30,31]. Its structure has the dimensions of 5.8 Å × 7.8 Å × 8.4 Å with an overall net charge of minus 6 at pH 7.4 [30]. In the V_9Pt cluster, one of the two internal vanadium atoms is replaced by a platinum(IV) atom (Fig. 1). Unlike V_{10}, the V_9Pt ion has a minus 5 charge due to the replacement of one central addenda site by a Pt^{IV} ion. The dimensions of V_9Pt are similar to those of the decavanadate (5.5 Å × 7.7 Å × 8.5 Å), calculated from the XRD data [29]). The crystal structure of the protonated salt shows that the complex has a C_{2v} point group symmetry, and the two protons on the polyanion are located on oxygens bridging Pt and V. These protons are important for the formation of a dimer assembly, $[H_4(Pt^{IV}V_9O_{28})_2]^{10-}$, through four interanion O-H···O hydrogen bonds [29]. These hydrogen bonds between two V_9Pt ions persist even after dissolving the polyanion salt in water, as shown by broad ^{51}V NMR lines, but upon heating they are broken, resulting in discrete V_9Pt ions. In the V_9Mo cluster, one of the external vanadium atoms is replaced by molybdenum [28]. Single-crystal X-ray analysis of the analogous $[(CH_3)_4N]_4[H_2MoV_9O_{28}]Cl{\cdot}6H_2O$] polyanion has shown a random distribution of molybdenum and vanadium atoms over four "capping" metal atom positions [32]. Since the structure is not available

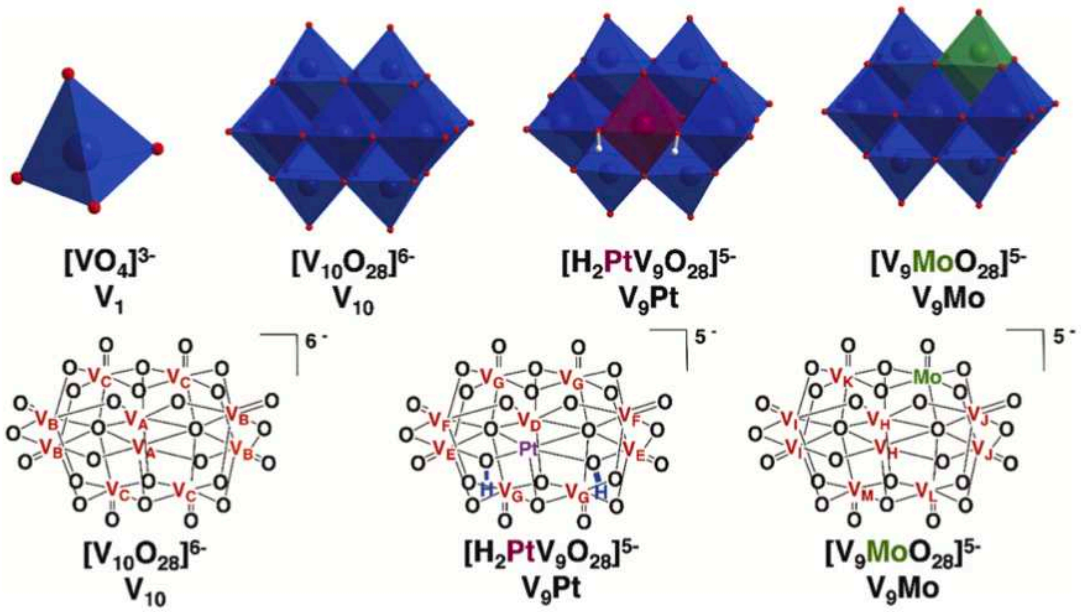

Fig. 1. Structures and polyhedral representations of $[VO_4]^{2-}$ (V_1), $[V_{10}O_{28}]^{6-}$ (V_{10}), $[H_2PtV_9O_{28}]^{5-}$ (V_9Pt) and $[Mo^{VI}V_9O_{28}]^{5-}$ (V_9Mo) illustrating the differences between the simple vanadate ion and the polyanions investigated in this work at pH 7.4. For illustrative purposes, Pt is depicted in maroon and Mo is depicted in green. The V atoms in the structures and in the ^{51}V NMR spectra below are labeled as V_A - V_C in V_{10}, V_D – V_G in V_9Pt and V_H - V_M in V_9Mo. (For interpretation of the references to color in this figure legend, the reader is referred to the web version of this article.)

in the Cambridge Crystal Structure Database, we assumed that the dimensions of the POM are very similar because of the similarity in the Mo—O and V—O bond lengths. Due to their different composition, the spectroscopic properties of the structurally related V_9Pt, V_9Mo and V_{10} are different, as well as their solubilities and stabilities in biological medium.

The biological effects of V_{10} have been explored in many types of microorganisms, including *M. tb* and *M. smeg*, in previous studies which are summarized in Table 1. However, these studies focus on the effects of V_{10} and not the substituted V_{10}'s. Such studies investigate the inherent effects of the decavanadate structure, since substituted V_{10}'s are structurally similar to the parent V_{10} but have slightly different properties. The inhibition of V_{10} in *Mycobacteria* was significantly more potent than other oxovanadates and hence further investigations of the nature of this inhibition were made were in this bacterium. *M. tb* and *M. smeg* have a very thick, waxy membrane, compared to that of *E. coli,* which is known to be very hydrophobic and impenetrable by many compounds. This makes the development of anti-tuberculosis drugs very challenging [33–36]. Two phosphatases have been identified in the genome of the *M. tb,* and both are believed to be secreted and, thus, found outside the cell [37–39]. Previous studies have shown that the *M. tb and M. smeg* extrude a component which attributes to the rapid hydrolysis of the decavanadate in the growth medium [27]. We suggest that this component effectively reduces the stability of V_{10} after its interaction with growth medium, nevertheless, the biological activity of the decavanadate is stronger than that of the monovanadate (V_1) [27]. Accompanying speciation studies in the cell culture media allow us to calculate adjusted EC_{50} values for the POVs present in solution at the beginning of the study. The adjusted EC_{50} values represent the minimum effect these compounds exert and this is important in the event of the compounds' decomposition under given conditions.

We hypothesize that the replacement of one vanadium by another metal, such as Mo and Pt, impacts properties of the V_9X polyanions and causing different biological responses than observed with V_{10}. To test our hypothesis, we examined the effects of these monosubstituted isostructural V_{10}s in *M. smeg* and their stability in media in order to demonstrate that the effects are not simply caused by the polyanion's stability. Hence our studies were accompanied by the detailed spectroscopic investigation of the species formed in the growth medium and a calculation of the EC_{50} value of the growth inhibitor of *M. smeg* based on the observation of the species at the beginning of the experiment in the growth medium determining a maximum EC_{50} for all the decametalates.

2. Materials and methods

2.1. General materials

Sodium metavanadate ($NaVO_3$) and sodium molybdate (Na_2MoO_4) were purchased from Sigma Aldrich and used as received. Monoplatinononavanadate ($[H_2PtV_9O_{28}]^{5-}$, abbreviated V_9Pt) was synthesized following the reported procedure for preparation of the sodium salt ($Na_5[H_2PtV_9O_{28}]\cdot 21H_2O$) [29]. The pH throughout this study was adjusted by using solutions of HCl and NaOH mixed in doubly deionized water (DDI) water, resulting in final concentrations of 6 M HCl, 0.1 M HCl and 0.1 M NaOH, respectively. All materials and solutions used in the cell culture were purchased and used as received. The Difco™ Middlebrook 7H9 Broth medium (BD Biosciences, final pH = 6.6 ± 0.2 (Ref no. 271310)) was autoclaved before use. Oleic acid (Sigma Aldrich), albumin (VWR), dextrose (Sigma Aldrich), and Tyloxapol (Chem-Impex Int'l Inc) were used as received for the biological assays. The bacterial stock was grown and incubated by shaking in 50 mL polypropylene conical tubes (30 × 115 mm) for 24 h at 37 °C before the addition to a 96 well microplate.

Table 1
Previous studies of various decavanadates (V_{10}) in other microorganisms.

Solid decavanadates tested	Microorganism[a,b]	Year	Ref
$(tert\text{-}BuNH_3)_6[V_{10}O_{28}]$	Bacteria – *Streptococcus pneumoniae*[b]	1997	N. Fukuda and T. Yamase, Biol. Pharm. Bull. 20 (8) (1997) 927–930
$(C_6H_{14}N_5O)_4[H_2V_{10}O_{28}]\cdot 9H_2O$ $(C_6H_{14}N_5O)_6[V_{10}O_{28}]\cdot 4H_2O$ *$C_6H_{14}N_6O$ = Moroxydine or ABOB[c,d]	Bacteria – *Staphylococcus aureus*,[b] *Staphylococcus epidermis*,[b] MRSA (methicillin-resistant *Staphylococcus aureus*),[b] MRSE (Methicillin-resistant *Staphylococcus epidermis*)[b]	2004	S.X.Liu, et al. Chemical Journal of Chinese Universities -Chinese Edition- 25(6) (2004) 997–1001
chitosan–$Ca_3V_{10}O_{28}$	Bacteria –*Eschercihia coli*,[a] *Staphylococcus aureus*[b]	2005	S. Chen, et al. Carbohydrate Polymers 64 (2006) 92–97
$V_{10}O_{28}^{6-}$ [e]	Virus – *Chlorella* virus	2006	I.Bougie and M. Bisaillon, Biochem. J. 398 (2006) 557–567
$(NH_4)_6[V_{10}O_{28}]\cdot 6H_2O$	Protozoa – *Leishmania tarentolae*	2012	T. L. Turner, et al. Journal of Inorganic Biochemistry 108 (2012) 96–104
$[H_2V_{10}O_{28}][4\text{-picH}]_4\cdot 2H_2O$ *4-pic = 4-picoline	Bacteria – *Pseudomonas aeruginosa*, *Bacillus cirroflagellosus*, Fungi – *Aspergillus niger*, *Penicillium notatum*	2014	Shahid, M., et al. J Clust Sci 25 (2014) 1435–1447
$[4\text{-}(CH_3O)C_6H_4CH_2NH_3]_6$ $V_{10}O_{28}\cdot 2H_2O$	Bacteria – *Enterococcus feacium*	2015	S. Toumi, et al. J Clust Sci 26 (2015) 1821–1831
$V_{10}O_{28}^{6-}$ [e]	Protozoa – *Leishmania tarentolae*	2018	B. M. Dorsey, et al. Front. Chem. 6 (2018) 109
$Zn_3(FLC)_6V_{10}O_{28}\cdot 10H_2O$ *FLC = fluconazole	Fungi – *Candida albicans*, 1 *Candida glabrata*, *Candida krusei*, *Candida parapsilosis*, *Cryptococcus tropicalis*	2018	S. Guo, et al. Molecules 23 (2018) 1122
$Na_6V_{10}O_{28}$	Mycobacteria – *Mycobacterium smegmatis*, *Mycobacterium tuberculosis*	2018	N. Samart, et al. Front. Chem. 6 (2018) 519
(3-Hpca)4$[H_2V_{10}O_{28}]\cdot 2H_2O\cdot 2$(3-pca) *3-pca = 3-pyridinecarboxamide $(4\text{-Hpca})_4[H_2V_{10}O_{28}]\cdot 2$(4-pca) *4-pca = 4-pyridinecarboxamide	Protozoa – *Giardia intestinalis* Bacteria – *Escherichia coli*[a]	2018	J. M. Missina, et al. Inorg. Chem. 57, 19 (2018) 11930–11,941
$(NH_4)_4(HMTA—H)_2V_{10}O_{28}\cdot 4H_2O$ *HMTA = hexamethylenetetramine	Bacteria – *Escherichia coli*,[a] *Salmonella typhimurium*,[a] *Enterococcus feacium*,[b]	2019	D. Jammazi, et al. Polyhedron 168 (2019) 146–154

(*continued on next page*)

Table 1 (*continued*)

Solid decavanadates tested	Microorganism[a,b]	Year	Ref
	Streptocoque B (*Streptococcus agalactiae*)[b] Fungi – *Candida albicans*		
$(NH_4)_6V_{10}O_{28}$	Bacteria – *Escherichia coli*[c]	2019	D. Marques-da-Silva, et al. New J. Chem. 43 (2019) 17577–17,587

[a] Gram negative bacteria.
[b] Gram positive bacteria.
[c] $C_6H_{14}N_6O$ = Moroxydine.
[d] $C_5H_{14}N_6O$ = ABOB.
[e] no cation was indicated in the study.

2.2. General methods

All NMR spectra were recorded at an ambient temperature using a Bruker NMR spectrometer at 105.2 MHz for ^{51}V and 400.13 MHz for ^{1}H. The ^{51}V NMR spectra were recorded in DDI water, 7H9 medium, supernatant and heated supernatant at several time-points (0, 1, 5 and 24 h) to determine changes in speciation of V_9Mo and V_9Pt during a 24 h interval. The parameters used for the ^{51}V NMR studies were as follows: 4096 scans in the f1 domain, O1P = −500 ppm, SW = 990 ppm, 0.01 s relaxation delay, 45° pulse angle, 16 μs pulse; the locking was off and the shimming was skipped. The ^{51}V NMR spectra were reported relatively to a neat $VOCl_3$ solution at 0 ppm and referenced against an external reference of an aqueous $NaVO_4$ solution at pH 12 (two signals at −535.7 ppm and − 560.4 ppm) [15]. The data was processed using MestreNova NMR processing software (version 14.0.1).

2.3. Preparation of the monomolybdononavanadate solution

Monomolybdononavanadate ($[V_9MoO_{28}]^{5-}$, abbreviated V_9Mo) solution was freshly prepared by using a modified procedure from the literature [28]: sodium metavanadate (0.5501 g, 4.500 mmol) and sodium molybdate (0.1216 g, 0.5000 mmol) were dissolved in 15.0 mL of DDI water, resulting in a 5:1 vanadium to molybdenum molar ratio. The solution was boiled at 95 °C for 7 min to ensure the dissolution of sodium metavanadate. The solution pH was adjusted from 6.00 to 5.00 by a dropwise addition of 6 M HCl, resulting in a clear bright orange solution, and the final volume was adjusted to 25.0 mL with DDI water. The final stock solution (100.0 mM total vanadium) was characterized by ^{51}V NMR to determine the relative concentrations of V_9 and V_{10}.

2.4. Preparation of the stock solutions for speciation studies

A 2.0 mM stock solution of V_9Pt was prepared by dissolving solid $Na_5[H_2PtV_9O_{28}]\cdot 21H_2O$ (0.0140 g, 0.0100 mmol) in 5.0 mL DDI water. A 2.0 mM stock solution of V_9Mo was prepared by using appropriate volumes of a 100 mM V_9Mo stock solution and DDI water; the pH was adjusted to 5.00 by a dropwise addition of 0.1 M HCl and 0.1 M NaOH if necessary. 1.0 mM control solutions of V_9Mo and V_9Pt were prepared by mixing 1000 μL of a 2.0 mM stock solution with 1000 μL of DDI H_2O. 1.0 mM solutions of V_9Mo and V_9Pt in 7H9 medium, supernatant and heated supernatant were prepared using the same method. The pH of all solutions was measured at several time-points (0, 1, 5 and 24 h) to determine changes in speciation during a 24 h interval.

2.5. Cell culture studies

Mycobacterium smegmatis mc^2 155 (*M. smeg*) was grown in the Middlebrook 7H9 medium (Ref no. 271310; Difco) supplemented with 10% OAD (oleic acid, albumin, dextrose), 0.2% (*v*/v) glycerol, and 10% Tyloxapol. Bacteria were incubated by shaking at 37 °C and left to grow overnight to mid-logarithmic growth phase to an optical density of 0.6–0.7 at 600 nm (OD_{600}).

2.6. Preparation of stock solutions of the vanadium compounds and inhibitory cell culture studies

The 4.0 mM solutions were prepared in DDI H_2O. The stock solutions of the vanadates were added to the Middlebrook 7H9 medium in 96 microplate wells and diluted to the final concentration of 1.0 mM. The final concentrations in a 96 well microplate were run in 10 serial 2-fold dilutions and ranged from 1.0 to 0.002 mM. The growth inhibitory effects of the vanadium complexes were determined by measuring the lowest concentration of complexes that inhibited the bacterial growth by 50% (EC_{50}) by using a Bio-Rad Benchmark Reader to check the cell viability at OD_{600} in 96 microplate wells. The data was collected in triplicate, and shown with error bars that represent standard deviations. Experiments were repeated and similar patterns were confirmed, and, in the case of V_{10}, the results are similar to those reported in the literature.

2.7. Spectroscopic speciation studies

The 2.0 mM aqueous stock solutions of vanadium compounds, V_9Pt and V_9Mo, were diluted to the final concentration of 1.0 mM in 2 mL aliquots to measure the speciation and hence the stability of the substituted decavanadates in water, in 7H9 medium (pH 6.58), non-heated 7H9 medium supernatant, and heated 7H9 medium supernatant at different time points (0, 1, 5 and 24 h) using ^{51}V NMR analysis. The pH of a V_9Mo aqueous solution was adjusted to 5.06 by the dropwise addition of 0.1 M HCl and 0.1 M NaOH. The ^{51}V NMR signals were integrated, and the amounts of species were measured in 1.0 mM solutions which was in the middle range of the concentrations studied in the culture growth. The results of all spectroscopic studies were compared to those of the control samples. The calculations determining the amounts of both the V_9Pt and V_9Mo complexes are provided below and summarized in the corresponding table in the Results section. The NMR data is shown and summarized in the Results and Supplemental Material sections.

The studies in the media in which the *M. smeg* had grown are referred to as the studies in media supernatant and were done prior to and after heating of the supernatant. The supernatant fraction came from the culture in which *M. smeg* was grown after shaking for 24 h at 37 °C. The culture was centrifuged at 2000 ×*g* for 20 min in a Beckman centrifuge model GS-6R. The cell pellet was removed, and the supernatant was collected and filtered to remove any remaining cells. The filtered supernatant was then divided into two fractions, the first fraction (non-heated supernatant) was added to the polyoxometalates. The second fraction was heated for 35–45 min at 80 °C (heated supernatant) to decompose most proteins that may have been secreted during the bacteria growth. The heated supernatant was centrifuged and filtered to remove any residual proteins prior to addition of the POVs.

2.8. Calculation of the V_9Pt concentration

The ^{51}V NMR analysis in aqueous solution shows three signals for V_9Pt at δ (ppm) -371.0 (V_D), −450.9 ($V_{E/F}$) and − 475.0 (V_G), and some formation of the hydrolysis products was observed in the form of V_1 (−558.5 ppm) and V_4 (−571.1 ppm). The percentage of the intact V_9Pt was calculated from the integration of the signals in the 1.0 mM spectrum collected at $t = 0$, determining the contribution of V_1 (3.9%) and V_4 (0.2%) (Table S1, Figs. S1-S2).

$$\%\mathbf{V_9Pt} = \left(V_D + V_{E/F} + V_G\right) x\ 100\% = (0.102 + 0.676 + 0.191)\ x\ 100\% = \mathbf{96.9}\%$$

2.9. Calculation of the V_9Mo concentration

The V_9Mo aqueous solution contains both V_9Mo and V_{10} complexes, and their concentrations are calculated below. The calculation also had to be adjusted for the presence of V_1 (27.8%), as it tends to form in solutions of lower concentrations. The peak assignment of the V_9Mo complex is provided in Fig. S7.

$$\%\mathbf{V_{10}} = [(1/2\,x\,(V_H + V_1 + V_I))\,x\,0.722]\,x\,100\%$$
$$= [(1/2\,x\,(0.160 + 0.141 + 0.235))\,x\,0.722]\,x\,100\% = \mathbf{19.3}\%$$

$$\%\mathbf{V_9Mo} = 100\% - \%V_{10} - \%V_1 = 100\% - 19.3\% - 27.8\% = \mathbf{52.9}\%$$

2.10. Calculation of the V_{10} concentration

The V_{10} aqueous solution also formed some hydrolysis projects when added to the media. The peak assignment of the V_{10} complex is −422, −499 and − 519 ppm as shown in Fig. S11.

3. Results

3.1. Biological studies: Growth inhibition of M. smeg mc^2 155 by substituted decavanadates

The inhibition of the *M. smeg* growth by the two substituted decavanadates, V_9Mo and V_9Pt, was evaluated in the 7H9 culture medium by measuring the EC_{50} values. The growth curves of *M. smeg* treated with different oxometalate concentrations (expressed in terms of the optical density at 600 nm, OD_{600}) are shown in the Supplemental Material (Figs. S14-S16), and a histogram in Fig. 2 compares the effects of V_9Mo and V_9Pt with V_{10}. The growth effect of V_{10} was measured previously [27], and was remeasured using the same dilution factors as the ones for V_9Mo and V_9Pt. The growth data in Fig. 2 was normalized to the growth OD at zero concentration of oxometalate. The order of the efficacy is monovanadate (V_1) – lowest effect (data not shown), followed by V_9Mo, V_9Pt and V_{10}. V_{10} and V_9Pt show comparable inhibitory effects and are 4-fold more potent than V_9Mo, while, V_9Mo is 12-fold more potent than V_1. The EC_{50} values calculated for two heteropolyoxometalates are shown in Table 2 and compared to those of the V_{10} and V_1 reported previously [27]. In Table 2, we also list the adjusted EC_{50} values for two

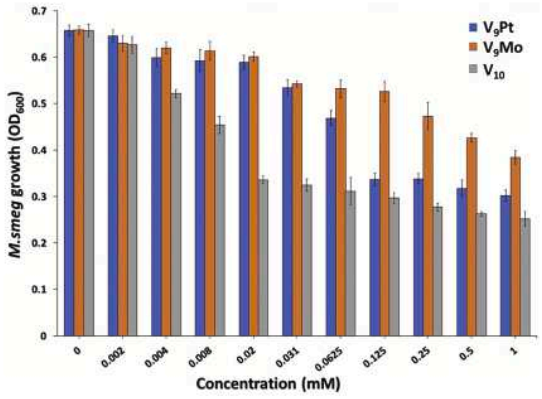

Fig. 2. Histogram showing the growth of *M. smeg* treated with V_9Pt (blue), V_9Pt (orange), and V_{10} (grey) respectively, with concentrations varying from 0.002 to 1.00 mM. Error bars shown are standard deviations determined in one growth study with triplicate readings. (For interpretation of the references to color in this figure legend, the reader is referred to the web version of this article.)

Table 2
The growth inhibitory concentration of **V_9Pt, V_9Mo, V_{10} and V_1** on *M. smeg* growth indicated as EC50 values.

	EC_{50} (mM)	St. Error	EC_{50} per V-atom/ mM	St. Error	Ref
V_9Pt[a]	0.0061	±0.0010	0.055	±0.009	This work
V_9Pt[b, adj]	0.0048	±0.0008	0.043	±0.007	This work
V_9Mo[a]	0.048	±0.026	0.43	±0.23	This work
V_9Mo[b, adj]	0.015	±0.008	0.14	±0.07	This work
V_{10}	0.0037	±0.0004	0.037	±0.004	Samart *et. al* 2018 [27]
V_{10}[b, adj]	0.0036	±0.0004	0.036	±0.004	Samart *et. al* 2018 [27] and this work
V_1	0.19	±0.07	0.19	±0.07	Samart *et. al* 2018 [27]

[a] The concentrations of V_{10}, V_9Pt and V_9Mo added to the solutions are given.
[b] The concentrations of these compounds change in the cell culture medium as described below, and the EC_{50} values were then recalculated based on ^{51}V NMR studies done at 1 mM samples at $t = 0$.
[adj] adjusted

oxometalates, considering detailed speciation described in the section below.

3.2. Speciation chemistry of substituted decavanadates: V_9Pt

The speciation chemistry of V_9Pt was examined by carrying out ^{51}V NMR studies in an aqueous solution, 7H9 medium (pH 6.58), supernatant, and heated supernatant over a 24 h period. The ^{51}V NMR spectra were compared to that of a 1.0 mM V_9Pt aqueous solution (**Figs. S3-S5**) under the same conditions. The ^{51}V NMR spectra in the 7H9 medium are presented in the manuscript, and the remaining spectra are included in the Supplemental Material. The Pt atom breaks the symmetry of the polyoxoanion, resulting in four different types of vanadium atoms, two of which overlap, generating a total of three signals for the V_9Pt (V_D, −371.0, $V_{E/F}$ −450.9, and V_G − 475.0 ppm). In comparison to the V_{10} spectra, the signals are slightly shifted and differ in the relative intensities from 2:4:4 in V_{10} to 1:6:2 in V_9Pt (refer to **Figs. S1-S2**) [29]. All spectra contain small amounts of V_1 and V_4 indicated by their weak signals. No significant changes were observed in the intensity of the signals of V_1 and V_4 over the course of the experiments.

The results of the spectroscopic studies of a 2.0 mM V_9Pt stock solution diluted to a final concentration of 1.0 mM in the 7H9 medium are shown in Fig. 3. Fig. 3 demonstrates that the V_9Pt polyanion remains intact with only small amounts (<5%) of vanadium oligomers and complexes forming in solution after 24 h. The spectrum collected at 0 h showed three signals of the V_9Pt, V_1 with a contribution of the vanadium-phosphate species ($HVPO_7^{3-}$, $V_1 + PV$), V_2, V_4 and vanadium citrate complexes (V_2cit^{2-}), a biogenic metal chelator present in the medium [40,41]. The percentage of each species measured at various time points remains almost unaltered even after 24 h (see Table 3). In the supernatant samples, in addition to the signals presented in the 7H9 medium, a new weak signal assigned to the $Vcit^-$ anion was observed. The amount of V_9Pt decreased from 96% in aqueous solution to 79% in the culture medium and approximately 74% in the supernatant. Similar chemistry was observed when the supernatant was heated (Fig. **S5** and Table **S1**).

As shown in Fig. 3, 21.1% of V_9Pt is hydrolyzed in the medium, making it necessary to adjust the EC_{50} value. Therefore, the adjusted EC_{50} value can be calculated as 78.9% of the value listed in Table 2. The actual EC_{50} value in Table 2 is listed as the "adjusted EC_{50} value in the medium", and the calculation is provided below.

$$\%\mathbf{V_9Pt} = (V_D + V_{E/F} + V_G)\,x\,100\% = (0.704 + 0.194 + 0.103)\,x\,100\%$$
$$= \mathbf{78.9}\%$$

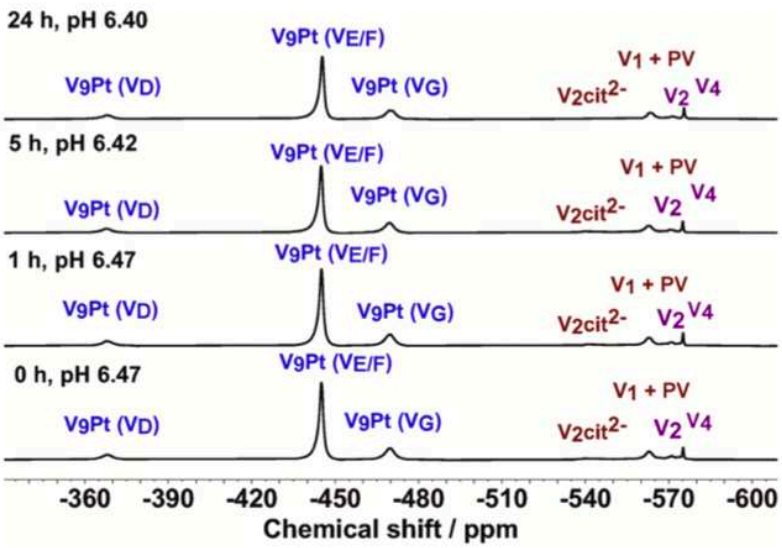

Fig. 3. ^{51}V NMR spectra of V_9Pt in the 7H9 medium as a function of time. The signals are assigned to the polyoxoanion V_9Pt as follows: (−379 (V_D), −445 ($V_{E/F}$) and − 470 (V_G)), the combined V_1 + PV signal (−573) [42], V_2 (−571) [43], V_4 (−575) [43], and V_2cit^{2-} (−541, −547) [40], where cit = citrate. The spectra recorded for a 1.0 mM aqueous solution of V_9Pt was recorded as a control and shown in **Fig. S2**. The V_9Pt peaks are identical to those reported in the literature [29].

Table 3
A summary of the species observed in the V_9Pt and V_9Mo in 1.0 mM solutions in 7H9 growth medium at $t = 0$ h.

^{51}V NMR Peak	Species	Integration/ fraction of total V(V)	Concentration in V-atoms, mM	Concentration in V_9X Molecules, mM
V_9Pt in the 7H9 medium				
V_G	V_9Pt	0.100	0.100	0.789
V_D	V_9Pt	0.710	0.710	
V_E	V_9Pt	0.194	0.194	
V_2cit^{2-}	V_2cit^{2-}	0.055	0.055	0.043
V_1 + PV	V_1 + PV	0.126	0.126	0.099
V_2	V_2	0.043	0.043	0.033
V_4	V_4	0.044	0.044	0.034
V_9Mo in the 7H9 medium				
V_H	V_9Mo + V_{10}	0.133	0.133	0.015
V_I	V_9Mo + V_{10}	0.115	0.115	0.013
V_J	V_9Mo + V_{10}	0.089	0.089	0.010
V_K	V_9Mo	0.060	0.060	0.007
V_L	V_9Mo	0.073	0.073	0.008
V_M	V_9Mo	0.018	0.018	0.002
V_1 + PV	V_1 + PV	0.491	0.491	0.055
V_2	V_2	0.037	0.037	0.004
V_4	V_4	0	0	0
V_2cit^{2-}	V_2cit^{2-}	0.044	0.044	0.005

$$\mathbf{EC_{50}}\ (\mathbf{V_9Pt}adj) = 0.0061\ \text{mM}\ x\ 0.789$$
$$= \mathbf{0.0048\ mM}\ (\mathbf{0.048\ mM\ per\ V\ atom})$$

3.3. Speciation chemistry of substituted decavanadates: V_9Mo

The speciation chemistry of the V_9Mo complex was studied by carrying out spectroscopic studies in an aqueous solution, 7H9 medium (pH 6.58), supernatant and heated supernatant over 24 h where the aqueous solutions of V_9Mo were used as controls. The spectra related to the aqueous speciation data are shown in Figs. **S6, S7, and 4.** In the aqueous solution, the peaks assigned V_H – V_M correspond to the V_9Mo peaks which are identical to the peaks of the 100.0 mM V_9Mo stock solution (**Figs. S6 and S7**). The peaks labeled V_H – V_J contain 65.2% (or 0.652 mM) of a V_9Mo oligomer and 34.8% (or 0.348 mM) of V_{10} (**Fig. S7**). The intensity of V_H-V_K and V_M signals stayed consistent throughout the experiment with the exception of V_L. The concentration of V_L increased over time and was almost equal to the concentration of V_M after 24 h (0.07 mM and 0.08 mM, respectively). The isomeric shifts in Fig. 4a and b (δ (ppm) = −423, −438*, −494, −503, −513, −515, −523 ppm) are identical to those reported previously as the fully deprotonated form of V_9Mo, $[MoV_9O_{28}]^{5-}$ (pKa 2.77). We attribute these spectral differences to changes in isomer content of V_9Mo which is consistent with the literature [44]. Since the growth studies are carried out at pH 6–6.5, the stability study with V_9Mo is also done in this pH range (pH 6.2–6.3). The pH of the V_9Mo stock solution was adjusted to 6.3, and the stability study was carried out and data is shown in Fig. 4b. These spectra show that increasing the pH from 5 to 6 results in the formation of only 18% of V_1 which is maintained over 24 h. Considering the higher stability of V_9Mo at slightly lower pH values, a decreasing amount of V_1 is, therefore, attributed to the increasing amount of V_{10} [44].

The results of the speciation studies of V_9Mo in 7H9 medium (pH 6.58), supernatant and heated supernatant are shown in Fig. 4 and **S8-S10** where all results are compared to a 1.0 mM aqueous V_9Mo solution at pH = 5.06 (Fig. 4a). From a 100.0 mM stock solution the sample was prepared by dilution of stock to a final concentration of 1.0 mM. The ^{51}V NMR experiments for the aqueous control were performed without any adjustment of the pH. The pH measured in the freshly prepared solution was 5.06 which remained the same throughout the experiment. Fig. 4b demonstrates that the V_9Mo polyanion remained intact over 24 h. However, vanadate monomer formed in the solution, and its concentration remained around 0.278 mM, or 27.8% for the duration of the study. Speciation of V_9Mo was evaluated in the 7H9 medium (pH 6.58) over 24 h and is shown in Fig. 4b. The pH has decreased upon the

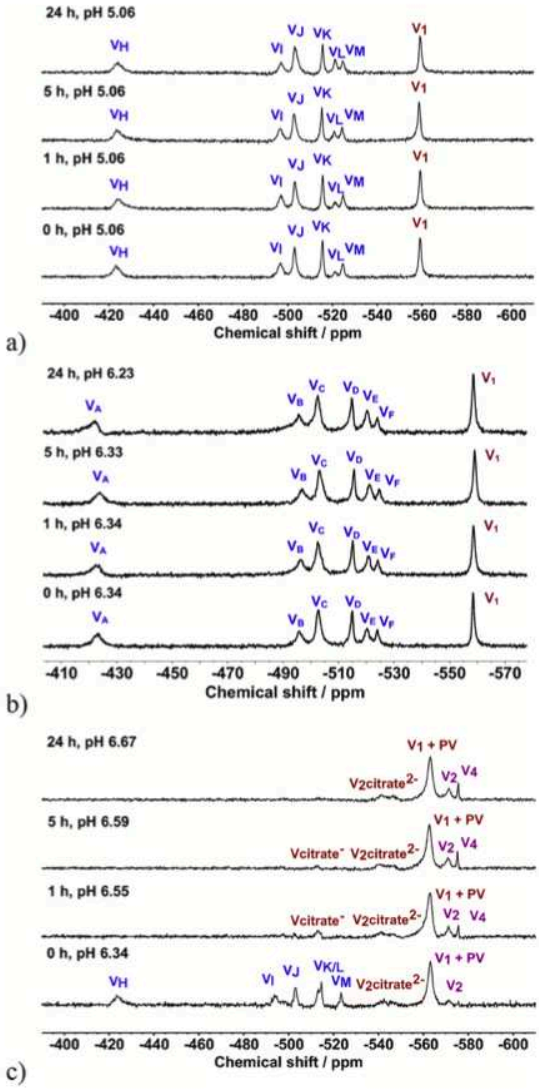

Fig. 4. Speciation studies of V_9Mo carried out by ^{51}V NMR in a function of time in a) 1.0 mM aqueous stock solution at pH 5.06, b) 1.0 mM aqueous solution at pH 6.2–6.3, and c) the 1.0 mM 7H9 growth medium. The identified vanadium (V) species δ (ppm) in 7H9 medium (near neutral pH) were for V_9Mo (V_H, V_I, V_J, V_K, V_L and V_M = −423 ppm, −494 ppm, −503 ppm, −513 ppm, −515 ppm and − 523 ppm), the combined V_1 + PV (−563) [42], V_2 (−570) [43], V_4 (−575) [43], $Vcit^-$ (−514) and V_2cit^{2-} (−543) [40] and at b) 1.0 mM aqueous solution of V_9Mo (at pH near 5). The V_9Mo peaks are identical to those reported in the literature [44].

addition of V_9Mo, resulting in the pH of 6.34 at t = 0 h. Fig. 4b demonstrates that part of V_9Mo hydrolyzes into the vanadium oligomers, V_1 + PV, V_2 and V_4 within 1 h which is evident by the disappearance of peaks V_H-V_J and V_M. This speciation profile is consistent with the literature, as V_9Mo is less stable at pH >6 [44]. The concentrations of V_1 + PV (where PV corresponds to the vanadium phosphate complex formed in solution), V_2 and V_4 increase after 24 h of incubation. After 1 h, vanadium(V) citrate complexes started to form at −544 ppm, corresponding to the V_2cit^{2-} complex, and at −517 ppm, corresponding to the $Vcit^-$ complex [40,41]. A broad peak at −544 ppm may represent the presence of several vanadium(V) citrate isomers, the concentrations of which increase after 24 h. The observed decrease in the stability of V_9Mo could be explained by the increasing pH and/or its interactions with the components in the 7H9 medium, indicated by the formation of the citrate and PV complexes.

The V_9Mo complex immediately falls apart in the non-heated supernatant (**Fig. S9**), resulting in the formation of several vanadium oligomers (V_1 + PV and V_2) and vanadium(V) citrate complexes: V_2cit^{2-} (a broad peak at −544 ppm) and $Vcit^-$ (−517 ppm). The concentration of V_1 + PV decreases from 0.96 mM to 0.77 mM and the concentrations of V_2 and vanadium(V) citrates increase as a function of time after 24 h. A lack of the stability of V_9Mo in the supernatant can be also explained by an increasing pH and its interactions with the supernatant leading to the formation of vanadium(V) citrate complexes. However, V_9Mo appears to be more stable in the heated supernatant (**Fig. S10**) because the complex does not form vanadium oligomers as quickly at 0 h, and significant amounts of V_9Mo are present after 1 h. At t = 0 h, V_1 + PV, V_2, and the citrate complexes start forming, and the tetramer (V_4) forms after 1 h. The trace amounts of the V_9Mo complex are present in the heated supernatant for 5 h, evident by the presence of the overlapping V_K and V_L peaks in the spectra, and the complex eventually falls apart after 24 h.

The ^{51}V NMR data was used to calculate the amounts of different vanadium species present at given experimental conditions. Using the integration values from the spectra, the fractions of all vanadium species were found and then used to calculate the amounts of all vanadium species at different time points (t = 0, 1, 5 and 24 h). A sample calculation is provided in the experimental section for a 1.0 mM V_9Mo control solution at 0 h. The results of these calculations are summarized in Table 2 which represents the changes in concentrations of different species over the course of 24 h.

As shown in Fig. 4c, 68.0% of V_9Mo is hydrolyzed in the medium, making it necessary to adjust its EC_{50} value. Therefore, the adjusted EC_{50} value can be calculated as 32.0% of the value listed in Table 2. The actual EC_{50} value in Table 2 is listed as the "adjusted EC_{50} value in the medium", and the calculation is provided below.

$$\%\mathbf{V_9Mo} = [(½*(V_H + V_I + V_J)) + V_K + V_L + V_M]*100\%$$
$$= [(½*(0.133 + 0.115 + 0.089)) + 0.060 + 0.073 + 0.018]*100\%$$
$$= \mathbf{32.0\%}$$

$$\mathbf{EC_{50}}\ (\mathbf{V_9Mo}, adj) = 0.048\ \text{mM}*0.320$$
$$= \mathbf{0.0154\ mM\ (0.0154\ mM\ per\ V-atom)}$$

The adjusted EC_{50} values of V_9Mo and V_9Pt clusters were also added to Table 2 to account for the presence of other vanadium oligomers in aqueous solutions. The EC_{50} value of V_9Pt (0.055 mM) is lower than the EC_{50} value of V_9Mo (0.43 mM) by a factor of 8 in terms of concentration, confirming that V_9Pt has shown more potent inhibitory effects on the bacterial growth (Fig. 2). The data in Table 2 shows that V_{10} is a more potent bacterial growth inhibitor than V_9Mo and V_9Pt V_9Mo with the EC_{50} value of 0.0069 mM. A previous study has shown that the inhibitory activity (the EC_{50} values) of V_{10} and V_1 were 0.0037 mM (0.037 mM in terms of V atoms) and 0.19 mM, respectively [27]. The biological data was supported by the ^{51}V NMR speciation data under the conditions needed for cell growth, providing more insights about the inhibitory activity of the clusters and their speciation chemistry.

3.4. Speciation chemistry of decavanadates: V_{10}

The speciation chemistry of the V_{10} complex was reported previously but some of these experiments are reported here for comparison at 1.0

mM. Spectroscopic studies in an aqueous solution, 7H9 medium, supernatant and heated supernatant over 24 h were reported previously [27]. Here we show the studies in the 7H9 media at 1.0 mM and in aqueous solution at pH 6–6.5 which was used as a control (**Fig. S11**). The spectra in 7H9 media are shown in Figs. **S12 and S13**. We note that the hydrolysis of the V_{10} increases dramatically when *M. smeg.* is added to the growth media as reported previously, **Fig. S13**.

4. Discussion

The biological effects of large POMs are well-known, and in this work we are investigating the subtle differences in properties caused by the transition metal ion substitution in the structure of a large anion. We recently reported dramatic differences between V_{10} and V_1 on the growth inhibition of *M. smeg.*, as V_{10} is 50-fold more potent than V_1 [27]. Exploring the inhibitory effects of monosubstituted decavanadates would allow to determine the properties of V_{10} that lead to those effects. Both V_9Pt and V_9Mo are structurally similar to V_{10}; in one cluster, the interior vanadium is replaced by the Pt ion, and in another cluster the surface vanadium is replaced by the Mo ion. Both POVs have a minus 5 charge which is different from the minus 6 charge of V_{10}. In this work, we investigate the growth inhibitory effects of the two substituted decavanadates, V_9Pt and V_9Mo, on *M. smeg* mc^2 *155*. Our results have demonstrated that V_{10} and V_9Pt show comparable inhibitory effects and are 4 times more potent than V_9Mo, while, V_9Mo is 12 times more potent than V_1. The weaker inhibitory effects by V_9Mo compared to the V_9Pt can be explained by its lack of stability in the growth medium although the V_{10} which also hydrolyzes in cell culture media is slightly more potent than V_9Pt. The similarities in the size and structure of all POVs are responsible for the observed growth inhibition that is greater than that of the vanadate monomer and other simple oxovanadates. One major differences between the V_{10} and the V_9Pt and V_9Mo is the difference in overall charge. In the following section we analyze their speciation chemistries in order to assure that we attribute the growth effects to the particular properties of monosubstituted V_{10}'s.

The inhibitory activity of V_9Pt and V_9Mo was evaluated by calculating the EC_{50} values. The EC_{50} values were initially calculated in terms of the concentration of molecules and V atoms added to the growth media, and then compared to the corresponding values of V_{10} and V_1 (Table 2). These EC_{50} calculations rely on the assumption that only one species is present in the V_9Mo and V_9Pt samples and no decomposition takes place. Since these clusters are unstable in the growth medium, speciation analysis must be carried out to properly attribute the observed growth effects of the POVs. Since V_9Pt and V_9Mo have different stabilities with the former being very stable, and the latter hydrolyzing pretty rapidly after addition to the media, the data at 0 h was used to adjust the EC_{50} calculations for consistency. That is these values represent the maximum EC_{50} in this system and the initial growth response when the compounds are added to the growth medium. Particularly in the case of the V_9Mo the compound is decomposing over time. As described in the manuscript, such analysis required time-dependent studies in the presence and absence of cells which led us to calculate the EC_{50} values reflecting the amounts of POVs present during the growth studies. This study compared stabilities of the POVs at 25 °C and since the growth studies were done at 37 °C, the decomposition is likely to have been even faster. Previous studies in aqueous solution show that decomposition of V_{10} follows first-order kinetics in a temperature-dependent manner with the rate of V_{10} hydrolysis being 6 times faster as the temperature is raised [45]. Another study with coordination complexes has shown that changes in vanadium oligomerization take place as the temperature changes [46]. It follows that the changes in coordination complexes as the temperature change are less than that observed in V_{10}. The adjusted values shown in Table 1 take into account the changes in V_{10} concentration upon addition to media, and these values represent the initial effects of the POVs.

The spectroscopic studies of the V_9Pt and V_9Mo complexes were carried out under four different conditions (aqueous solution, 7H9 medium, heated and non-heated supernatant) to illustrate both chemical and biological transformations that affect the stabilities of V_{10} and its monosubstituted derivatives. The 7H9 growth medium has nucleophilic components that hydrolyze polyoxovanadates over time, making the clusters decompose faster than under any other conditions. The speciation studies were also carried out in heated and non-heated supernatant. This was done because we found for V_{10}, that the *M. smeg* extruded a material that hydrolyzed V_{10}, therefore speciation studies needed to be carried out under conditions in the presence and absence of extruded components. The speciation data of both V_9Pt and V_9Mo complexes confirms that there is a difference in the species observed under different conditions which were measured and confirmed by ^{51}V NMR (Figs. 3, 4, **S5-S10**). The ^{51}V NMR data in the 7H9 medium is presented in the manuscript, since it was used to calculated the EC_{50} values, and the remaining data is presented in the Supplemental Material.

The ^{51}V NMR data has shown that the stabilities of both V_9Mo and V_9Pt are time-dependent. The V_9Pt cluster remains intact for extended periods of time with <10% of the complex falling apart within 24 h. Specifically, the 1.0 mM V_9Pt control remained intact with the small quantities of V_1 and V_4 present in the solution. The 1.0 mM V_9Mo control at pH 5.06 remained intact, with a gradual increase in the concentration one of the peaks over time (V_E) the signal intensity of which is proportional to the isomer content. (Table 2, **Fig. S8**). The results in the 7H9 medium for V_9Mo show immediate formation of oligomers (V_1 + PV and V_2), and $VCit^-$ complexes after the sample preparation. V_9Mo falls apart within one hour, resulting in the increasing concentrations of vanadium oligomers and the $VCit^-$ complex (Fig. 4) [40]. The concentrations of all species increase over 24 h, except that $Vcit^-$ eventually converts into the V_2cit^{2-} complex between 5 and 24 h. Contrary to these results, the V_9Pt complex stays intact in 7H9 medium with the increasing amounts of V_1 + PV,V_2, and V_2cit^{2-} complexes also form over time (Fig. 3).

The V_9Mo falls apart in the non-heated supernatant at 0 h, resulting in the immediate formation of large quantities of V_1 + PV (95.9% of the total vanadium) and a small amount of V_2 (**Fig. S9**). The amounts of the citrate complexes, $Vcit^-$ and V_2cit^{2-}, increase over 24 h. The concentrations of all species, except for the V_1 + PV, increase as a function of time and an increasing pH. The V_9Pt complex stays mostly intact in the supernatant, with the formation of V_1 + PV, V_2, V_4, $Vcit^-$, and V_2cit^{2-} also being observed (**Fig. S4**). The V_9Mo complex is considerably more stable in the heated supernatant which is evident by the presence of the V_D and V_F peaks at 1 h and the V_D peak at 5 h (**Fig. S10**). The complex eventually falls apart after 24 h, resulting in an increased isomer content. The V_9Pt exhibits a similar trend as seen under other conditions (**Fig. S5**). The analysis shows that a 1.0 mM V_9Mo solution in the 7H9 medium at 0 h has only 32.0% of V_9Mo per sample in contrast to a 1.0 mM V_9Pt solution that has 78.9% of V_9Pt. The higher stability of the V9Pt cluster results in the adjusted EC_{50} value to be similar to the EC_{50} based on the amount of cluster added to the solution. The lack of stability of the V_9Mo cluster results in a significant difference between the adjusted and original EC_{50} values (Fig. 2, Table 2). The EC_{50} values of V_{10} from the previous study were compared to those of V_9Pt and V_9Mo, indicating its most potent inhibitory effects. This pattern holds once the values are adjusted for the hydrolysis upon addition to the 7H9 media.

The changes in speciation chemistry were also confirmed by color observations over 24 h. The color changes of V_9Mo and V_9Pt were monitored in the aqueous solution, 7H9 medium, supernatant, and heated supernatant at different time points to confirm NMR data and the stability of the compounds. The colorimetric data is shown in the Supplemental Material (**Fig. S17**). The colors of the V_9Mo and V_9Pt solutions are pale yellow and orange, respectively, in all samples at 0 h. The V_9Mo samples have shown slight color changes in 7H9 medium, supernatant, and heated supernatant as the time increased which is consistent with the NMR data, indicating the decomposition of V_9Mo. The V_9Pt samples do not change color over 24 h, confirming the stability of V_9Pt which is consistent with the NMR data.

The biological activity of POVs and their derivatives have been reported in different systems, such as tuberculosis, cancer and diabetic cells, and animals [1,2,47,48]. Many studies have been investigating the activity of decavanadate and other polyoxometalates as antidiabetic and anticancer agents [3,5,49]. Incorporation of different transition metal ions can drastically change the biological activity of POMs which was documented in the nickel(II)-containing POV, $K_7[NiV_{13}O_{38}]$, showing antiproliferative activity against human tumor (KB) cells [7]. A recent study has shown that decavanadate is a growth inhibitor of two mycobacterial species, and their activity was significantly higher than that of a known phosphatase inhibitor V_1 [27]. The ability of a series of platinum(II) coordination complexes to act as anti-tuberculosis agents was also reported [50,51]. However, no studies were published using molybdenum compounds for anti-tuberculosis applications. This work demonstrated that the growth inhibitory effects of V_9Pt and V_9Mo, on *M. smeg mc2 155*, despite the similar structural arrangement to V_{10}, are significantly different. Although the higher stability of V_9Pt over V_9Mo may explain the greater effect of V_9Pt, the fact that V_{10} is less stable and more effective than V_9Pt, stability cannot be the only factor important for growth inhibitions.

In summary, the results have shown that the all vanadium-containing oxometalate is more potent than the corresponding Pt-substituted POV even though V_{10} hydrolyzes slowly in the media and more rapidly in the media upon addition of *M. smeg*. Similarly, a vanadium coordination complex has been recently been reported to be more potent than cisplatin in brain tumor cells [52]. The results presented here may suggest that different charges and other types of solution chemistry, including redox, are important factors contributing to the fine-tuning of the observed growth inhibition. Future studies must be carried out to deduce the mechanism of action of these POVs, and that other POVs must be evaluated under similar conditions to answer the questions raised by this study.

5. Conclusion

The following study investigated the inhibitory effects of two V_{10} derivatives, V_9Pt and V_9Mo, on the growth of *M. smeg*. Our results have shown that V_{10} is the most potent inhibitor, yet the V_9Pt cluster appears to be most stable under the growth conditions which was confirmed by the spectroscopic studies. The V_9Mo complex is the least potent inhibitor out of the three polyoxovanadates which may be in part be due to its lack of stability under the growth conditions. Although V_{10} was found to be relatively stable in media, the additions of the *M. smeg*. f facilitated hydrolysis of the anion. The speciation analysis included ^{51}V NMR studies confirming at least partial hydrolyses of the anions in 7H9 medium, non-heated and heated supernatant and formation of some vanadium-oxo oligomers, vanadium citrate and vanadophosphate polyanions. Our study demonstrated that the substitution of one V^V ion in V_{10} by a Pt^{IV} or a Mo^{VI} ion results in isostructural derivatives which also inhibit the growth of *M. smeg*., with the platinum(IV)-derivative PtV_9 exhibiting a slightly lower activity, but a higher solution stability than the parent V_{10} and the V_9Mo anions.

Author Contributions

Conceptualization – Crans; Data curation - KK, ZA, KP; Formal analysis – KK, ZA, Crans; Funding acquisition – Crans, GGN, UK; Investigation – KK, ZA, KP, AR; Methodology – KK, ZA, KP, AR; Project administration – Crans; Resources – Crans, Crick, GGN, UK; Software – KK, ZA, KP; Supervision – Crans; Validation – Crans, Crick, GGN, UK; Visualization- KK, ZA, KP; Writing - original draft – KK, Crans; Writing - review & editing - KK, Crans.

Declaration of Competing Interest

The authors declare that they have no known competing financial interests or personal relationships that could have appeared to influence the work reported in this paper.

Acknowledgements

DC Crans thanks Colorado State University and the Arthur Cope Scholar Foundations administered by the American Chemical Society for partial support. ZA thanks the Libyan Ministry of Education (University of Benghazi) for the fellowship to study at Colorado State University. KP and GGN thank the Coordenação de Aperfeiçoamento de Pessoal de Nível (CAPES) and CAPES/PrInt program for the scholarship supporting KP's visit to Colorado State University. UK thanks the German Research Foundation (DFG) and Jacobs University for research support. The authors thank Dr. Christopher D. Rithner for assistance in obtaining spectroscopic measurements at the Molecular Materials and Analysis (MMA) Center.

Appendix A. Supplementary data

Supplementary data to this article can be found online at https://doi.org/10.1016/j.jinorgbio.2021.111356.

References

[1] A. Bijelic, M. Aureliano, A. Rompel, Chem. Commun. 54 (2018) 1153–1169.
[2] A. Bijelic, M. Aureliano, A. Rompel, Angew. Chem. Int. Ed. 58 (2019) 2980–2999.
[3] J.C. Pessoa, S. Etcheverry, D. Gambino, Coord. Chem. Rev. 301-302 (2015) 24–48.
[4] D.C. Crans, I. Sánchez-Lombardo, C.C. McLauchlan, Front. Chem. 7 (2019) 1–16.
[5] J.T. Rhule, C.L. Hill, D.A. Judd, Chem. Rev. 98 (1998) 327–357.
[6] M.B. Colovic, M. Lackovic, J. Lalatovic, A.S. Mougharbel, U. Kortz, D.Z. Kristic, Curr. Med. Chem. 27 (2020) 362–379.
[7] Y. Liu, S. Tian, S. Liu, E. Wang, Transit. Met. Chem. 30 (2005) 113–117.
[8] A. Levina, P.A. Lay, Chem. Asian J. 12 (2017) 1692–1699.
[9] M. Pisano, C. Arru, M. Serra, G. Galleri, D. Sanna, E. Garribba, G. Palmieri, C. Rozzo, Metallomics 11 (2019) 1687–1699.
[10] A. Bijelic, C. Molitor, S.G. Mauracher, R. Al-Oweini, U. Kortz, A. Rompel, Chem. Bio. Chem. 16 (2015) 233–241.
[11] S. Ramos, J.J.G. Moura, M. Aureliano, J. Inorg. Biochem. 104 (2010) 1234–1239.
[12] S. Pluskey, M. Mahroof-Tahir, D.C. Crans, D.S. Lawrence, Biochem. J. 321 (1997) 333–339.
[13] G. Fraqueza, C.A. Ohlin, W.H. Casey, M. Aureliano, J. Inorg. Biochem. 107 (2012) 82–89.
[14] A. Al-Quatati, F.L. Fontes, G.B. Barisas, D. Zhang, D.A. Roess, D.C. Crans, Dalton Trans. 42 (2013) 11912–11920.
[15] D. Althumairy, K. Postal, B.G. Barisas, G.G. Nunes, D.A. Roess, D.C. Crans, Metallomics 12 (2020) 1044–1061.
[16] X. Hu, H. Wang, B. Huang, N. Li, K. Hu, B. Wu, Z. Xiao, Y. Wei, P. Wu, J. Inorg. Biochem. 193 (2019) 130–132.
[17] Y. Zheng, H. Gan, Y. Zhao, W. Li, Y. Wu, X. Yan, Y. Wang, J. Li, J. Li, X. Wang, Chem. Eur. J. 25 (2019) 15326–15332.
[18] L.C. Cantley, L. Josephson, R. Warner, M. Yanagisawa, C. Lechene, G. Guidotti, J. Biol. Chem. 251 (1977) 7421–7423.
[19] M.T. Pope, A. Müller, Angew. Chem. Int. Ed. 30 (1991) 34–48.
[20] C.C. McLauchlan, B.J. Peters, G.R. Willsky, D.C. Crans, Coord. Chem. Rev. 301 (2015) 163–199.
[21] N.K. Tonks, Nat. Rev. 7 (2006) 833–846.
[22] M. Aureliano, D.C. Crans, J. Inorg. Biochem. 103 (2009) 536–546.
[23] S.G. Sarafianos, U. Kortz, M.T. Pope, M.J. Modak, Biochem. J. 319 (1996) 619–626.
[24] S.-Y. Lee, A. Fiene, W. Li, T. Hanck, K.A. Brylev, V.E. Fedorov, J. Lecka, A. Haider, H.-J. Pietzsch, H. Zimmermann, J. Sevigny, U. Kortz, H. Stephan, C.E. Müller, Biochem. Pharmacol. 93 (2015) 171–181.
[25] D. Althumairy, X. Zhang, N. Baez, G. Barisas, D.A. Roess, G.R. Bousfield, D. C. Crans, Diseases 8 (2020) 1–24.
[26] Fukuda, T. Yamase, Biol. and Pharm. Bulletin. 20, 1997, 927 - 930.
[27] N. Samart, Z. Arhouma, S. Kumar, H.A. Murakami, D.C. Crick, D.C. Crans, Front. Chem. 6 (2018) 519.
[28] I. Irma Sanchez-Lombardo, B. Baruah, S. Alvarez, K.R. Werst, N.A. Segaline, N. E. Levinger, D.C. Crans, New J. Chem. 40 (2016) 962.
[29] U. Lee, H.-J. Joo, K.-M. Park, S.S. Mal, U. Kortz, B. Keita, L. Nadjo, Angew. Chem. Int. Ed. 47 (2008) 793–796.
[30] D.C. Crans, M. Mahroof-Tahir, O.P. Anderson, M.M. Miller, Inorg. Chem. 33 (1994) 5586–5590.
[31] D.C. Crans, B.J. Peters, X. Wua, C.C. McLauchlan, Coord. Chem. Rev. 344 (2017) 115–130.
[32] N. Strukan, M. Cindrid, B. Kamenar, Polyhedron 16 (1997) 629–634.
[33] L.F.G. Lopes, E.M. Carvalho, E.H.S. Sousa, Dalton Trans 49 (2020) 15988–16003.
[34] H. Chan, C.S. Pearson, C.M. Green, Z. Li, J. Zhang, G. Belfort, A. Shekhtman, H. Li, M. Belfort, J. Biol. Chem. 291 (2016) 22661–22670.

[35] A.M. Plutín, A. Alvarez, R. Mocelo, R. Ramos, E.E. Castellano, M.M. da Silva, L. Colina-Vegas, F.R. Pavan, A.A. Batista, Inorg. Chem. Commun. 63 (2016) 74–80.
[36] M. Williams, V. Mizrahi, B.D. Kana, Crit. Rev. Microbiol. 40 (2014) 18–29.
[37] C. Grundner, H.L. Ng, T. Alber, Structure 13 (2005) 1625–1634.
[38] B. Zhou, Y. He, X. Zhang, J. Xu, Y. Luo, Y. Wang, S.G. Franzblau, Z. Yang, R. J. Chan, Y. Liu, J. Zheng, Z.-Y. Zhang, PNAS 107 (2010) 4573–4578.
[39] N.K. Dutta, R. He, M.L. Pinn, Y. He, F. Burrows, Z.-Y. Zhang, P.C. Karakousis, ACS Infect. Dis. 2 (2016) 231–239.
[40] A. Gorzsás, K. Getty, I. Andersson, L. Pettersson, Dalton Trans. (2004) 2873–2882.
[41] M. Kaliva, E. Kyriakakis, A. Salifoglou, Inorg. Chem. 41 (2002) 7015–7023.
[42] I. Andersson, A. Gorzsas, C. Kerezsi, I. Toth, L. Pettersson, Dalton Trans. (2005) 3658–3666.
[43] D.C. Crans, B. Baruah, N.E. Levinger, Biomed. Pharmacother. 60 (2006) 174–181.
[44] O.W. Howarth, J. Chem. Soc. Dalton Trans. (1989) 1915–1923.
[45] S. Ramos, R.O. Duarte, J.J.G. Moura, M. Aureliano, Dalton Trans. (2009) 7985–7994.
[46] D.C. Crans, H. Holst, A.D. Keramidas, D. Rehder, Inorg. Chem. 34 (1995) 2524–2534.
[47] E. Sánchez-Lara, S. Treviño, B.L. Sánchez-Gaytán, E. Sánchez-Mora, M.E. Castro, F. J. Meléndez-Bustamante, M.A. Méndez-Rojas, E. González-Vergara, Front. Chem 6 (2018).
[48] K. Postal, D.F. Maluf, G. Valdameri, A.L. Rudiger, D.L. Hughes, E.L. de Sa, R. R. Ribeiro, E.M. de Souza, J.F. Soaresa, G.G. Nunes, RSC Adv. 6 (2016) 114955–114968.
[49] M. Aureliano, World J. Biol. Chem. 2 (2011) 215–225.
[50] A.M. Plutína, A. Alvareza, R. Moceloa, R. Ramosa, E.E. Castellano, M.M. da Silvac, L. Colina-Vegas, F.R. Pavand, A.A. Batistac, Inorg. Chem. Commun. 63 (2016) 74–80.
[51] G.G.S. Leite, L.C. Baeza, A.A. Batista, M.I.F. Barbosa, F.R. Pavan, C.Q.F. Leite, J. L. Silva, R.D.C. Hirata, M.H. Hirata, R.F. Cardoso, Bioinfo Publ. 5 (2013) 357–362.
[52] A. Levina, A.P. Vieira, A. Wijetunga, R. Kaur, J.T. Koehn, D.C. Crans, P.A. Lay, Angew. Chem. Int. Ed. 59 (2020) 15834–15838.

Appendix X: Highlighting the roles of metals and speciation in chemical biology

This manuscript concerns biological roles and speciation of first-row transition metals in chemical biology and gives a brief overview of transition-metal catalyzed reactions in chemical biology. The manuscript is published in *Current Opinion in Chemical Biology* (Kostenkova et. al, 2022).

References

Kostenkova, K.; Scalese, G.; Gambino, D.; Crans, D. C. Highlighting the roles of metals and speciation in chemical biology. *Curr. Op. Chem. Bio*. **2022,** *69, 1-11* (article 102155).

Available online at www.sciencedirect.com

ScienceDirect

Current Opinion in Chemical Biology

Highlighting the roles of transition metals and speciation in chemical biology

Kateryna Kostenkova[1], Gonzalo Scalese[1,2], Dinorah Gambino[2] and Debbie C. Crans[1,3]

Abstract

Transition metal ions play key structural and functional roles, affecting structures of biomolecules and enzyme function. The importance of transition metal ions in chemical biology is, thus, undisputed. However, the aqueous chemistry of metal ions is complicated because they form species in several protonation and redox states. In the presence of metabolites, metal ions can also form coordination complexes. The existence of several species is relevant because enzymes and membrane receptors can distinguish between species even when they are rapidly equilibrating. Thus, metal ions, enzyme cofactors, and therapeutic agents are sensitive to the metal ion speciation chemistry because it affects their interaction with enzymes and other biomolecules. Speciation is also crucial for metal-containing bioorthogonal reactions, since water and metabolites stabilize active catalysts, affect chemoselectivity and reaction yields.

Addresses

[1] Department of Chemistry, Colorado State University, Fort Collins, CO, 80523, USA

[2] Área Química Inorgánica, Facultad de Química, Universidad de la República, Montevideo, 11800, Uruguay

[3] Cell and Molecular Biology, Colorado State University, Fort Collins, CO, 80523, USA

Corresponding authors: Crans, Debbie C. (Debbie.crans@colostate.edu); Gambino, Dinorah (dgambino@fq.edu.uy)

Current Opinion in Chemical Biology 2022, **69**:102155

This review comes from a themed issue on **Bioinorganic Chemistry (2022)**

Edited by **Emily Que**

For complete overview of the section, please refer to the article collection Bioinorganic Chemistry (2022)

Available online 25 May 2022

https://doi.org/10.1016/j.cbpa.2022.102155

Keywords

Essential metals, Metal speciation, Cofactors, Reactivity, Transition metals, Enzyme recognition.

Abbreviations

Aβ, Amyloidβ; Au, gold; Bi, bismuth; Co, cobalt; Cu, copper; Fe, iron; GHW, tripeptide containing glycyl-histidyl-tryptophan; Mn, manganese; Ni, nickel; OAc, acetate; Pd, palladium; Pt^{IV}-V9, platinum monosubstituted decavanadate; Mo^{VI}-V9, molybdenum monosubstituted decavanadate; Sc, scandium; Sb, antimony; Ti, titanium; V, vanadium; V_1, vanadate monomer; V_2, vanadate dimer; V_4, vanadate tetramer; V_5, vanadate pentamer; V_{10}, decavanadate ($H_nV_{10}O_{28}^{(6-n)-}$); Zn, zinc.

Introduction

Many biological processes involve action of several classes of biomolecules including proteins, nucleic acids, lipids, carbohydrates, metabolites, and importantly, metal ions. This article highlights the importance and functions of transition metal ions in chemical biology [1–5]. Some metal ions are important to complement negatively charged proteins and metabolites and hence serve to maintain biomolecules in the form engaging in cellular processes [6]. Such metal ions are spectator counter ions whereas transition metal ions generally have a structural and/or catalytic function when associated with biomolecules [3,6–8]. In Figure 1A the 10 first-row transition metals are shown in blue [4,5]. Five of these metals are essential elements for human health and, thus, need to be consumed daily. Four of the metal ions, manganese (Mn), iron (Fe), cobalt (Co), and copper (Cu) are redox active. Particularly, the first-row essential transition metal ions, Mn, Fe and Cu are cofactors which bind to the enzymes and facilitate catalysis in metal ion-containing enzymes. These enzymes are referred to as metalloenzymes, and represent more than one-third of all enzymes [3,8]. Cobalt (Co) is also an essential element, and it does so by being a part of the vitamin B_{12} (Figure 1B). Co is the only transition metal ion that is part of a vitamin [4,5]. Vitamin B_{12} is a cofactor for enzymes in energy, DNA, lipid and amino acid metabolism. The fifth essential transition metal is zinc (Zn) which is the only redox inactive first-row essential transition metal ion [3–5]. Zn exerts its function by serving a structural role in metalloenzymes that catalyze hydrolytic and other non-redox reactions.

Three first-row non-essential transition metals that have been reported to have biological effects are vanadium (V), chromium (Cr), and nickel (Ni) [4,5]. Nature has developed extensive networks for the cellular uptake and transfer of transition metal ions to deliver them to the respective metal ion-containing proteins or other biological systems [7]. V and Cr act by binding to proteins such as phosphatases or by affecting the cellular redox state [9,10]. Ni^{2+} is a cofactor for urease and Ni-

Figure 1

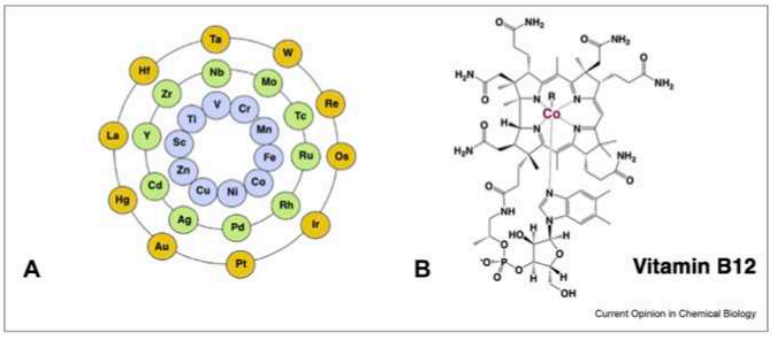

A) The transition metal ions are shown; in blue the 10 first row transition metals; in green the 10 second row transition metals; in yellow the 10 third row transition metals; **B**) Vitamin B_{12} (Co-containing vitamin and enzyme cofactor).

binding hydrogenases, dehydrogenases, and Ni-superoxide dismutase [11]. Titanium (Ti) and scandium (Sc) have limited effects in biological systems, Ti because the metal and its complexes are generally inert (although organometallic Ti complexes have been investigated as anticancer agents) and Sc because it is very rare and infrequently investigated [4,5]. Second- and third-row transition metals are less common in chemical biology except for in bioorthogonal reactions and in medicinal applications and are shown in Figure 1A as green (second row) and yellow (third row) elements. Each transition metal ion forms different species depending on the oxidation state of the metal ion and the concentration, pH and ionic strength in its local environment [9,12–21]. In addition, metabolites, particularly those that are effective metal ligands, contribute by forming coordination complexes, and thus increase the numbers of species that can form.

Speciation of transition metal ions

Transition metal ions in aqueous solution undergo hydrolysis reactions and form several species. In the following speciation, chemistry will be described for one early and one late transition metal, vanadium and iron. Speciation of vanadium (V) has been described previously in detail and will only briefly be summarized here [12–15,17,18,20–25].

Speciation of an early transition metal: Vanadium (V)

The colorless oxidovanadates near neutral pH rapidly exchange and form species with nuclearity of one (V_1), two (V_2), four (V_4), and five (V_5) vanadium atoms at mM concentrations and neutral and basic pH values [12–15,17,18,20–22]. Each of these species can exist in several protonation states, but only one protonation state, the deprotonated forms, are shown in Figure 2A. Decavanadate (V_{10}) is an orange or yellow compact cluster depending on the concentration and counter-ions; orange V_{10} formed from a solution of sodium V_{10} by the addition of a drop of acid (middle tube) is shown in Figure 2B and its structure is shown in Figure 2A. The speciation diagram with % species (in terms of V atoms) as a function of pH is shown in Figure 2C [23]. Three major V_{10} species with different protonation states are shown between pH 3 and 6.5. At pH 7 V_1. V_2, V_4, and V_5 are found in solutions added 50 mM of $NaVO_3$ [23]. These colorless species rapidly equilibrate at a neutral pH in contrast to the deprotonated V_{10}, which is kinetically stable and thermodynamically unstable at neutral and basic pH values. The wealth of species with different charges forming in solution makes the vanadium (V) species an ideal system to test the possibility whether the biological systems can distinguish different species in solution.

Speciation of a late transition metal: Iron (Fe)

The aqueous Fe^{2+}/Fe^{3+} speciation chemistry involves the formation of several species. Fe^{2+} exists as $Fe(H_2O)_6^{2+}$ at low pH and low concentration and the hydrated ions are shown in Figure 2D as $Fe(OH)^+$, $Fe(OH)_2$, $Fe(OH)_3^-$, and $Fe(OH)_4^{2-}$ [12,25]. Similarly, Fe^{3+} exists as a $Fe(H_2O)_6^{3+}$ cation (Figure 2E) [12]. The hydrated Fe(III) ions are acidic and lose protons at physiological pH and are shown in Figures 2E–2F as $Fe(OH)^{2+}$, $Fe(OH)_2^+$, $Fe(OH)_3$, and $Fe(OH)_4^-$ and similarly in Figure 2F including ions of higher nuclearity [12,25]. The fact that $Fe(H_2O)_6^{2+}$ is deprotonated above neutral pH whereas $Fe(H_2O)_6^{3+}$ is deprotonated at significantly lower pH reflects the differences in the hard-soft Lewis character and underlines the importance of properly assigning the metal ions associated with biomolecules. The speciation chemistry is controlled when the Fe ion is bound to a protein or a metabolite as the metal ion travels through bodily fluids

and enters cells until it reaches its biological target. Proteins that shuttle metal ions to their targets are called chaperones, and overcome the complex aqueous chemistry of transition metal ions [26]. However, delivery of the metal ion requires its dissociation from the transport protein before it can bind to another metalloprotein [26,27]. Importantly nature's strategy to using chaperones avoids most of the complex aqueous chemistry of the essential transition metal ions, Fe, Mn, and Cu [15,16,26].

Solutions prepared in laboratory settings are generally more concentrated (see the study by Crans et al. [12]), and to illustrate this point speciation is shown for two concentrations of Fe^{3+} at 0.001 and 0.010 mM in Figures 2E and 2F. At higher concentrations, species in solution aggregate and multinuclear species can become detectable. As shown for Fe^{3+}, dinuclear and trinuclear species are observed at 10-fold higher concentration at low pH (Figure 2F). In the following section, we will describe selected biological activities that vary with the species present in solution.

Biological effects of metal ions and complexes in chemical biology

The importance of speciation chemistry [9,12–15,17–25] to the field of chemical biology is reflected in the biological effects and activities of various metal species [12,16,24]. The ability of biomolecules to carry out natural and unnatural transformations is dependent on structure, function and location in cells or organisms. Many biomolecules are modified to increase solubility and important for their function; then they are neutralized by spectator ions. In cases, when the counter ions are transition metal ion, the biomolecules are metalloenzymes and the transition metal ions are cofactors. Even though speciation of the different metal ions varies, most of the metal ions have more than one form under standard physiological conditions at pH 7 [25].

Biological effects of metal ions and their speciation

The Crans group has been investigating active vanadium (V) species in various biological systems by carrying out speciation studies under physiological conditions, and has demonstrated that enzymes distinguish between different oxidovanadates in solutions of rapidly equilibrating vanadium (V) species [9,28]. For example, 6-phosphogluconate dehydrogenase is inhibited by a tetranuclear oxidovanadate species over other oxidovanadates of different nuclearities [29,30]. Similarly, glucose-6-phosphate dehydrogenase and aldolase select both dinuclear and tetranuclear oxidovanadates in the presence of the other equilibrating oxidovanadates of different nuclearities [30]. Decavanadate ($V_{10}O_{28}^{6-}$ abbreviated V_{10}), the most well-known and stable polyoxidovanadate is found to be an inhibitor for antioxidant enzymes [31] and ribonuclease [32] under conditions where the rapidly equilibrating oxidovanadates form.

V_{10} has been found to be a more potent inhibitor of *Mycobacteria tuberculosis* and *Mycobacteria smegmatis* growth than a simple monomeric vanadate by a factor of 100 [28]. Furthermore, the hydrolysis of V_{10} to vanadium oligomers in the growth media of *M. smegmatis* is accelerated because the bacterium extrudes a non-protein component that catalyzes the hydrolysis of V_{10}. The impact of the V_{10} core structure on the growth inhibition was explored by measuring the growth inhibition of Mo^{VI} or Pt^{IV}-monosubstituted decavanadates, MoV_9 and PtV_9 shown in Figure 3A [33]. The Pt^{IV}-monosubstituted decavanadate, PtV_9, is more stable than the V_{10} parent but less effective growth inhibitor compared to the parent [33]. The Mo^{VI}-monosubstituted decavanadate, MoV_9, is the least stable cluster compared to V_{10} and PtV_9 [33]. Even though the core structures of the polyanions are similar, their charges and stabilities are different and that was recognized by the *Mycobacterium smegmatis* cells. Similarly, growth inhibition has been reported for *Escherichia coli* [34], *Giardia Intestinalis* and VERO cells by V_{10} [35]. The luteinizing hormone receptor, a G protein-coupled receptor, can initiate signaling in the presence of polyoxidovanadates (POV) in CHO cells [36]. The active POVs investigated include V_{10} and two mixed-valence heteropolyoxidovanadates containing 14 and 15 V atoms and presumable is a result of the POV interactions with the membrane lipids and/or the cell membrane–lipid interface. These results show that speciation chemistry of oxidovanadates can impact biological responses in isolated enzymes, mammalian and bacterial cellular systems.

Metal–peptide complexes in chemical biology and their speciation

Metal ions form complexes with amino acids, peptides, and proteins. Much research has been done with di- and trivalent transition metal ions and amino acids, peptides, and proteins exploring the stability, structure and isomers forming in such solutions [24,37]. Most transition metal ions form multiple complexes with different stoichiometries and different protonation states. For example, four species were found for Cu^{2+} in the pH range 2–11 in the presence of two tripeptides, sarcosyl-L-leucyl-phenylalanine (Sar-Leu-Phe) and glycyl-L-leucyl-phenylalanine (Gly-Leu-Phe) [38]. These species were ML, MLH^{-1}, ML_2H^{-1} and MLH^{-2}, where M is Cu^{2+} and L represent the two tripeptides. Since amino acids and peptides are common metabolites, they are present in cellular systems and in biological media.

Delivery of a metal ion from one metal complex to another protein or peptide is very sensitive to the stabilities of the metal–peptide complexes [27,39]. These

Figure 2

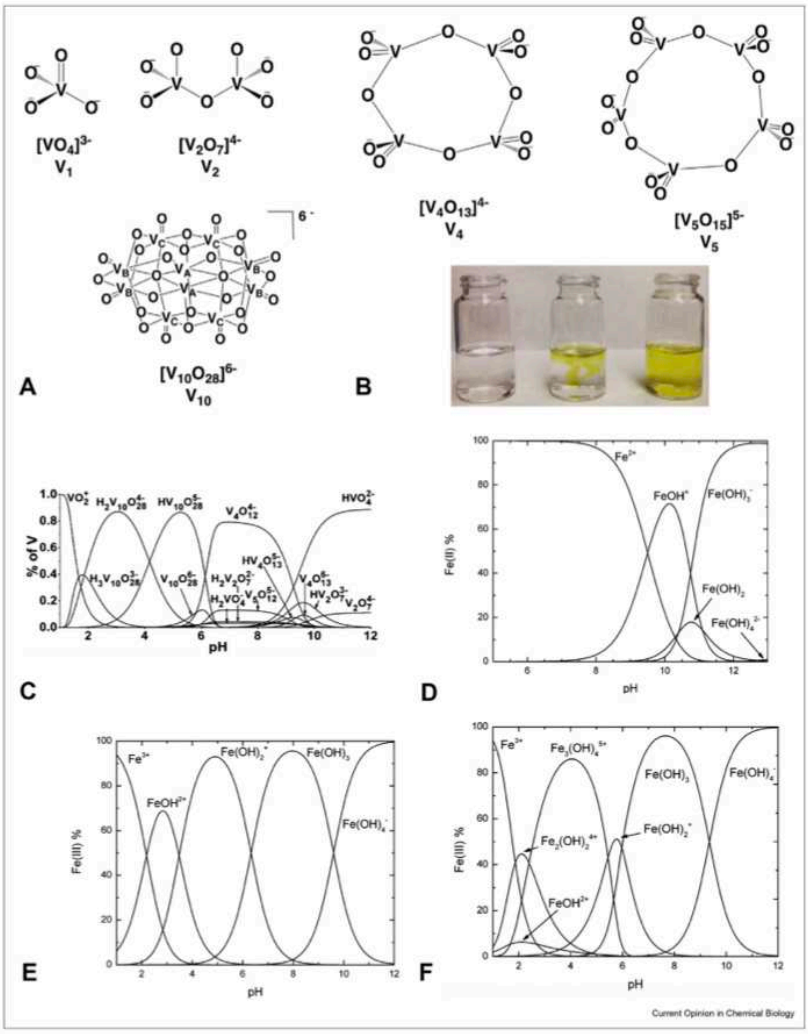

A) The deprotonated structures of colorless vanadium (V) species with one (V_1), two (V_2), four (V_4), and five (V_5) vanadium atoms and the orange decavanadate (V_{10}); **B**) an image of colorless vanadium (V) species (left) and orange vanadium (V) species (right) at acidic pH as well as a drop of acid into the solution of colorless vanadium (V) (middle); **C**) speciation diagram with % species (in terms of V-atoms) as a function of pH [23]; **D**) Speciation diagram of 0.001 mM Fe^{2+} showing the distribution of species that forms at different pH values (Crans et al., 2013) [12] **E**) Speciation diagram of 0.001 mM Fe^{3+} showing the distribution of species that forms at different pH values (Crans et al., 2013) [12]; **F**) Speciation diagram of 0.010 mM Fe^{3+} showing the distribution of species that forms at different pH values (Crans et al., 2013) [12]. The speciation profiles shown in **E**) and **F**) are shown at low concentrations which is near physiological. **D**) and **E**): adapted with permission from *Inorg. Chem.* **2013**, *52*, 21, 12262−12275 [12] Copyright © 2013 American Chemical Society.

Figure 3

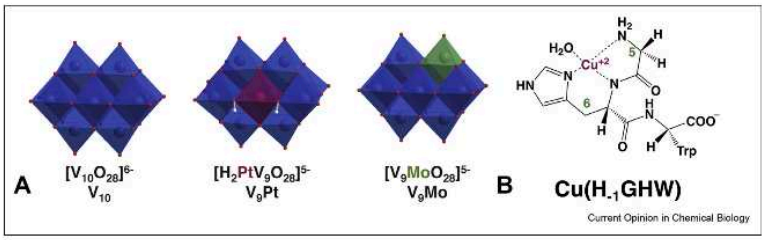

A) The structures of V_{10}, Pt^{IV}–V_9 and Mo^{VI}–V_9 [33]. Adapted with permission Elsevier. **B**) The tripeptide product that forms after abstracting the Cu^{2+} ion from the Cu- *Aβ* complex [27]. Adapted with permission from the American Chemical Society.

are equilibrium reactions, and both kinetics and thermodynamics must be favorable for the reactions to take place. In the specific case of a Cu^{2+}-tripeptide complex (Cu(H$_{-1}$GHW)) shown in Figure 3B, which is formed by removing the Cu^{2+} ion complexed to the peptide associated with Alzheimer's disease, Amyloid β (Aβ) and forming a complex with the tripeptide glycine–histidine–tryptophan (GHW) [27]. This reaction can be summarized by three steps shown in (1)–(3). In (1) Cu^{2+} anchors a site from Cu(Aβ) by the incoming peptide GHW. The pK_a values of the various anchors support the monodentate coordination of Cu^{2+} to small peptides through a imidazole ring (noted N_{Im}) in a His residue. In step (2) the incoming peptide is chelated via the His residues and the N-terminal amine in GHW following a pathway proposed previously [27]. In step (3) the peptide amide is deprotonated resulting in the complex with three 3 N's from the GHW peptide coordinated to the Cu^{2+} and one water molecule (see structure in Figure 3B). The coordination of the deprotonated amide N completes the Cu^{2+} exchange to form the final species, Cu(H$_{-1}$GHW), and releases the Aβ peptide (Figure 2B) [27].

$$(1)\ \mathrm{Cu}(A\beta) + \mathrm{GHW} \rightarrow Cu(A\beta)(\mathrm{N_{im}})\mathrm{GHW}$$

$$(2)\ \mathrm{Cu}\ (A\beta)(\mathrm{N_{im}})\mathrm{GHW} \rightarrow \mathrm{Cu}(A\beta)(\mathrm{NH_2-N_{im}})\mathrm{GHW}$$

$$(3)\ \mathrm{Cu}\ (A\beta)(\mathrm{NH_2-N_{im}})\mathrm{GHW} \rightarrow A\beta + \mathrm{Cu(H_{-1}GHW)}$$

Orthogonal reactions in chemical biology and their speciation

"Bioorthogonal chemistry" is a term coined by Carolyn R. Bertozzi in 2003 describing reactions that can take place inside living systems without interfering with innate biological processes [46]. The criteria for bioorthogonal reactions are that they are chemoselective, stable, fast, high-yielding, and compatible with the biological system. Click reactions are a subclass of bioorthogonal reactions and encompass a broad scope of additional reactions to those shown in Table 1 [43]. To work in cells all these systems must possess cell penetrating capabilities [47]. Many reactions have been developed that fulfill the requirements of bioorthogonality but only the reactions using transition metals as catalysts are summarized in Table 1. Both the second-row (shown in Figure 1A [12] in green) and the third-row (shown in yellow in Figure 1A) transition metals stand out in Table 1; these metals are important because of their catalytic activities resulting in some of the most successful bioorthogonal reactions.

Table 1 highlights 6 key transformations available for protein modification under cellular conditions using transition-metal catalysts. These reactions are inspired by successful organic reactions such as the Suzuki cross-couplings and Sonogashira cross-coupling reactions, S_NAr reactions, decaging (cleavage) reactions, olefin cross-metathesis and [3 + 2] dipolar cycloadditions. These reactions have been developed to proceed at a neutral pH and at 37°C. From Table 1, it is clear that Pd catalysts are most common in orthogonal transformations (shown in 3 types of transformations), followed by Ru catalysts (shown in 2 types of transformations) which confirms that the second-row transition metals are effective as catalysts for bioorthogonal reactions. Cleavage reactions often referred to as decaging reactions is the most diverse group of transformations catalyzed by a several first- and second-row transition metals. These reactions are categorized into subgroups of reactions depending on the trigger that initiate the cleavage reaction. For example, these triggers can be photo-, metal or small molecule induced. In addition, [3+2] dipolar cycloaddition reactions are catalyzed by a first row and essential transition metal Cu^I [41,43,45].

Speciation of transition metal catalysts is important, particularly because solvents such as water coordinate to the catalytic species. In the case of the Pd-catalyzed reactions, the speciation equilibria stabilize catalytic

Table 1

Common transition-metal catalyzed bioorthogonal transformations.

Reaction	Transition metal	Reported transformations	Reacting biomolecule/ functionality	Representative reaction product	Refs
Suzuki cross-coupling	**Pd**	a) Phosphine-free Suzuki b) Self-liganded Suzuki c) Homogeneous catalysis	a) Protein/cysteine or lysine residues b) Protein/cysteine or lysine residues c) Amino acid and peptide/ cysteine or lysine residues		[40–42]
Sonoga-shira	**Pd** (homo-geneous and hetero-geneous catalysts)	Cu-free Sonogashira (with alkyne-tag)	Protein/cysteine residues/ terminal alkynes and aryl iodides		[41]
S_NAr reactions	**Pd**	Arylation of Cys	Protein/cysteine residues		[41]
Chemical cleavage (often referred to as decaging) reactions	Prodrug activation **a) Pd** **b) Cu** **c) Ru, Ni** **d) Ni**	a) Lysine modification b) N_3–alkyne cycloaddition c) Triazoles (Ru, Ni) d) Allylcarbamate-protected amines	Protein a) lysine residues b) alkynes and azides c) alkynes and azides d) lysine residues		[41,43]

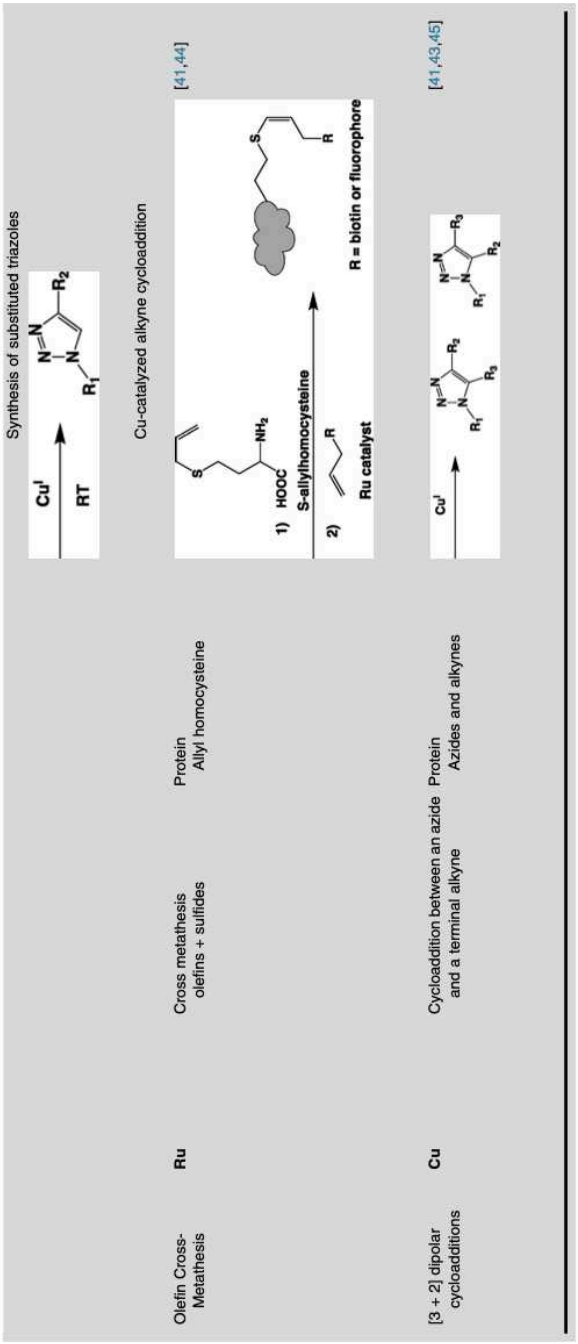
Synthesis of substituted triazoles
Cu-catalyzed alkyne cycloaddition
Olefin Cross-Metathesis
Ru
Cross metathesis olefins + sulfides
Protein Allyl homocysteine
[41,44]
1) HOOC
S-allylhomocysteine
2)
Ru catalyst
R = biotin or fluorophore
[3 + 2] dipolar cycloadditions
Cu
Cycloaddition between an azide and a terminal alkyne
Protein Azides and alkynes
[41,43,45]

species and intermediates [42,48]. Using a combination of spectroscopic, microscopic and kinetic measurements, speciation of the Pd species has been described during catalysis where Pd(II) is reduced to Pd(0) [42]. Reports have also observed the formation of monomeric, dimeric and trimeric forms of $Pd(OAc)_2$ in various solvents, which is attributed to the flexible coordination number of the catalyst as well as the impact of other reagents [42,49,50]. Importantly, the presence of water controls the amount of the active Pd(0) species released into reaction mixture. This chemistry is consistent with the fact that speciation chemistry is important for the success of bioorthogonal reactions.

Biological effects of metallodrugs and diagnostic agents and speciation

Almost all elements have some biological activity and/or medicinal application, as illustrated in the Periodic Table of Medicine [1–5]. Potential use of metal complexes in medicine is an area of bioinorganic chemistry that has gained much interest since the discovery of the potent antiproliferative activity of cisplatin in 1965 by Barnett Rosenberg [51–60]. There is a wide range of biological properties of transition metal ions containing metallodrugs and diagnostic agents [51–62] and here we mention only a few select systems in addition to the platinum based anticancer agents. Many metal-based compounds have been developed to treat cancer and some of those that have been clinically approved contain metal ions in addition to Pt such as Au, Pd, Fe, Bi, and one metalloid Sb [53]. Many more metal complexes have been or are currently in clinical trials [53]. Other approaches include development of new cell specific targets departing from the classical DNA target [53,61], various classes of organometallic compounds [57,58,61] as well as compounds targeting the anticancer immune response [56].

In addition to cancer, neurodegenerative diseases pose a serious threat to the aging world population but, unfortunately, their principal origins remain elusive [60]. Pathological features that are shared across multiple neurodegenerative disorders include inability to maintain metal ion homeostasis, proteopathy, oxidative stress, and neurotransmitter deficiencies. The three most abundant ions in the human body are Fe, Zn, and Cu and their concentrations are tightly regulated. The development of multifunctional compounds capable of simultaneously interacting with several pathological problems often involve molecules that can chelate these three metal ions as well as affect other functions [60].

Metal-containing antiparasitic agents have been developed for treatment neglected tropical diseases (NTDs), particularly of American trypanosomiasis, also referred to as Chagas' disease [52,62]. Potential chemotherapeutics such as Pt-. Pd- and V-containing compounds have been reported for treatment of the protozoan parasite *Trypanosoma cruzi* that cause Chagas' disease. Using omic-approaches parasite-specific targets have been unveiled including redox metabolism, the isoprenoid pathway, and the acidocalcisome metabolism, that are essential for parasite infection and survival within the mammalian host [62].

In addition to therapy, metal complexes are used for radiodiagnostics [54,55]. Metal complexes are important as therapeutic radiophamaceuticals (theranostic agents) and in this area main group and rare-earth metals are used in addition to transition metals ions [54]. Applications in imaging have been reported for a number agents spread over the entire periodic table [55]. For both these areas the metal complex stability is critically important to the function of the agents and hence much time has been and continue to be spent on development of ligands for the metal ions to create stable and better imaging agents.

Conclusion

In this article, we have described metal ions and metal compounds as important components of biological systems as spectator counter ions, enzyme cofactors, bioorthogonal agents, and potential therapeutics. Not only are the five essential transition metals important for human life, but many other transition metals exert bioactivities relevant to chemical biology and medicine.

The ability of biological entities to carry out natural and unnatural transformations is strongly dependent on structure, function, and cellular location of the biomolecule. Many biomolecules are charged to increase solubility necessary for their function and cellular location. Spectator counter ions which can be metal ions are therefore important to achieve neutrality. In cases when the counter ion is a transition metal ion, it is often important for function and structure of the biomolecule and when the biomolecules are metalloenzymes the transition metal ions are cofactors.

Speciation chemistry is particularly relevant in chemical biology because enzymes and other biological systems can distinguish between different metal ion species. For example, we have shown some glycolytic and pentose phosphate shunt enzymes can distinguish rapidly exchanging oxidovanadate. Similarly, V_{10} inhibits the growth of *M. smegmatis* much more effectively than the simple monomeric vanadate or the rapidly exchanging oxidovanadates. Speciation is important for transition-metal-catalyzed bioorthogonal reactions. For example, Pd-mediated catalysis is sensitive to speciation because water and metabolites coordinate to the active Pd

catalytic species and is stabilizing intermediates and species present in solution. Hence, speciation impact product selectivity and yields. Several metal complexes are used in the clinic to treat cancer and other diseases and other complexes are being explored as potential agents.

Author contributions

DCC Conceptualization; KK, GS, DCC, DG investigation; KK GS, Software; DCC, DG Project administration; DCC Supervision; DCC, DG visualization; DCC, KK Writing - original draft; DCC, KK, DG, GS Writing – review & editing.

Declaration of competing interest

The authors declare that they have no known competing financial interests or personal relationships that could have appeared to influence the work reported in this article.

Acknowledgments

GS acknowledges the support of the Agencia Nacional de Investigación e Innovación (ANII, Uruguay) through the grant MOV_CA_2020_1_162704 and of Comisión Académica de Posgrado UdelaR through the grant 9404. GS and DG acknowledge the support of PEDECIBA Uruguay. DCC thanks Colorado State University for funding.

References

Papers of particular interest, published within the period of review, have been highlighted as:

* of special interest
** of outstanding interest

1. Chadwick GL, Jimenez Otero F, Gralnick JA, Bond DR, Orphan VJ: **NanoSIMS imaging reveals metabolic stratification within current-producing biofilms**. *Proc Natl Acad Sci Unit States Am* 2019, **116**:20716–20724.

2. Garza-Lombo C, Posadas Y, Quintanar L, Gonsebatt ME, Franco R: **Neurotoxicity linked to dysfunctional metal ion homeostasis and xenobiotic metal exposure: redox signaling and oxidative stress**. *Antioxidants Redox Signal* 2018, **28**: 1669–1703.

3. Maret W: **Metallomics: the science of biometals and biometalloids**. In *Metallomics: the science of biometals*. Edited by Arruda MAZ, Springer International Publishing; 2018:1–20.

4. * Crans DC, Kostenkova K: **Open questions on the biological roles of first-row transition metals**. *Comm Chem* 2020, **104**:1–4.
This paper highlights the importance of first-row transition metal ions in biology and medicine. The paper also summarizes previous and ongoing clinical studies with first-row transition metals.

5. ** Van Cleave C, Crans DC: **The first row transition metals in the periodic table of medicine**. *INORGA* 2019, **7**:1–28.
The review describes the roles and medical applications of first-row transition metals. The article features the Periodic Table of Medicines which could be useful for teaching general and inorganic chemistry, and chemical biology.

6. Grauffel C, Dudev T, Lim C: **Metal affinity/selectivity of monophosphate-containing signaling/lipid molecules**. *J Chem Theor Comput* 2021, **17**:2444–2456.

7. Eom H, Song WJ: **Emergence of metal selectivity and promiscuity in metalloenzymes**. *J Biol Inorg Chem* 2019, **24**: 517–531.

8. Can M, Armstrong FA, Ragsdale SW: **Structure, function, and mechanism of the nickel metalloenzymes, CO dehydrogenase, and acetyl-CoA synthase**. *Chem Rev* 2014, **114**:4149–4174.

9. Crans DC: **Antidiabetic, chemical and physical properties of organic vanadates as presumed transition state inhibitors for phosphatases**. *J Org Chem* 2015, **80**:11899–11915.

10. Balali-Mood M, Naseri K, Tahergorabi Z, Khazdair MR, Sadeghi M: **Toxic mechanisms of five heavy metals: mercury, lead, chromium, cadmium, and arsenic**. *Front Pharmacol* 2021: 12.

11. Maier RJ, Benoit SL: **Role of nickel in microbial pathogenesis**. *INORGA* 2019, **7**:80.

12. Crans DC, Woll KA, Prusinskas K, Johnson MD, Norkus E: **Metal speciation in health and medicine represented by iron and vanadium**. *Inorg Chem* 2013, **52**:12264–12275.

13. Jakusch T, Costa Pessoa J, Kiss T: **The speciation of vanadium in human serum**. *Coord Chem Rev* 2011, **255**:2218–2226.

14. Pessoa JC, Correia I: **Misinterpretations in evaluating interactions of vanadium complexes with proteins and other biological targets**. *INORGA* 2021, **9**.

15. Rehder D: **The (biological) speciation of vanadate(V) as revealed by 51V NMR: a tribute on Lage Pettersson and his work**. *J Inorg Biochem* 2015, **147**:25–31.

16. ** Ajsuvakova OP, Tinkov AA, Willkommen D, Skalnaya AA, Danilov AB, Pilipovich AA, Aschner M, Skalny AV, Michalke B, Skalnaya MG: **Assessment of copper, iron, zinc and manganese status and speciation in patients with Parkinson's disease: a pilot study**. *J Trace Elem Med Biol* 2020, **59**: 126423.
The clinical study demonstrated the importance of metal speciation in patients with Parkinson's disease. Although total blood Cu levels did not change, a significant decrease in Cu/seruloplasmin-Cu and an increase in low molecular weight amino acid bound copper were observed. Furthermore, the levels of Mn-albumin complexes in patients with Parkinson's disease are 4-fold higher compared to the control group.

17. Gorzsas A, Andersson I, Pettersson L: **Speciation in aqueous vanadate-ligand and peroxovanadate-ligand systems**. *J Inorg Biochem* 2009, **103**:517–526.

18. Kiss T, Enyedy ÉA, Jakusch T: **Development of the application of speciation in chemistry**. *Coord Chem Rev* 2017, **352**: 401–423.

19. * Templeton DM, Ariese F, Cornelis R, Danielsson L-G, Muntau H, van Leeuwen HP, Lobinski R: **Guidelines for terms related to chemical speciation and fractionation of elements. Definitions, structural aspects, and methodological approaches (IUPAC Recommendations 2000)**. *Pure Appl Chem* 2000, **72**: 1453–1470.
Seminal paper describing the definitions related to speciation concepts.

20. Kiss T, Enyedy ÉA, Jakusch T, Dömötör O: **Speciation of metal complexes of medicinal interest: relationship between solution equilibria and pharmaceutical properties**. *Curr Med Chem* 2019, **26**:5080–5606.

21. Nunes P, Correia I, Marques F, Matos AP, dos Santos MMC, Azevedo CG, Capelo J-L, Santos HM, Gama S, Pinheiro T, Cavaco I, Pessoa JC: **Copper complexes with 1,10-phenanthroline derivatives: underlying factors affecting their cytotoxicity**. *Inorg Chem* 2020, **59**:9116–9134.

22. * Doucette KA, Hassell KN, Crans DC: **Selective speciation improves efficacy and lowers toxicity of platinum anticancer and vanadium antidiabetic drugs**. *J Inorg Biochem* 2016, **165**: 56–70.
The toxicity of cisplatin upon administeration is dependent on the speciation; cisplatin requires hospital stay whereas cisplatin covered by lipids (a drug referred to as Lipoplatin) is an outpatient procedure.

23. Crans DC, Levinger NE: **The conundrum of pH in water nanodroplets: sensing pH in reverse micelle water pools**. *Acc Chem Res* 2012, **45**:1637–1645.

24. Levina A, Crans DC, Lay PA: **Speciation of metal drugs, supplements and toxins in media and bodily fluids controls in vitro activities**. *Coord Chem Rev* 2017, **352**:473–498.

25. Baes CF, Mesmer RS. *The hydrolysis of cations*, vol. 81. New York: John Wiley & Sons; 1977.

26. * Rae TD, Schmidt PJ, Pufahl RA, Culotta VC, O'Halloran TV: **Undetectable intracellular free copper: the requirement of a copper chaperone for superoxide dismutase**. *Science* 1999, **284**:805–807.
This is the first evaluation of copper species present in the cell which demonstrated that there are no free copper ions present in a cell.

27. ** Beuning CN, Zocchi LJ, Malikidogo KP, Esmieu C, Dorlet P, Crans DC, Hureau C: **Measurement of interpeptidic CuII exchange rate constants of CuII-Amyloid-beta complexes to small peptide motifs by tryptophan fluorescence quenching**. *Inorg Chem* 2021, **60**:7650–7659.
In this study, the interpeptidic Cu^{II} exchange rate constants were measured from Cu(Aβ) complexes to the tryptophan- containing GHW and DAHW using a modified quantitative fluorescence quenching method. The studies provide an alternative technique for the measurement of interpeptidic exchange rates of Cu^{II} between Cu(Aβ) complexes with other peptide motifs, including N-truncated Aβ.

28. Samart N, Arhouma Z, Kumar S, Murakami HA, Crick DC, Crans DC: **Decavanadate inhibits mycobacterial growth more potently than other oxovanadates**. *Front Chem* 2018, **6**: 519.

29. Crans DC, Willging EM, Butler SR: **Vanadate tetramer as the inhibiting species in enzyme reactions in vitro and in vivo**. *J Am Chem Soc* 1990, **112**:427–432.

30. Aureliano M, Gumerova NI, Sciortino G, Garribba E, Rompel A, Crans DC: **Polyoxovanadates with emerging biomedical activities**. *Coord Chem Rev* 2021, **447**:214143, https://doi.org/10.1016/j.ccr.2021.214143.

31. Aureliano M, Joaquim N, Sousa A, Martins H, Coucelo JM: **Oxidative stress in toadfish (Halobactrachus didactylus) cardiac muscle: acute exposure to vanadate oligomers**. *J Inorg Biochem* 2002, **90**:159–165.

32. Messmore JM, Raines RT: **Decavanadate inhibits catalysis by ribonuclease A**. *Arch Biochem Biophys* 2000, **381**:25–30.

33. Kostenkova K, Arhouma Z, Postal K, Rajan A, Kortz U, Nunes GG, Crick DC, Crans DC: **Substituted decavanadates inhibit the growth of Mycobacterium smegmatis**. *J Inorg Biochem* 2021, **217**:1–10.

34. Marques-da-Silva D, Fraqueza G, Lagoa R, Vannathan AA, Mal SS, Aureliano M: **Polyoxovanadate inhibition of Escherichia coli growth shows a reverse correlation with Ca2+-ATPase inhibition**. *New J Chem* 2019, **43**: 17577–17587.

35. Missina JM, Gavinho B, Postal K, Santana FS, Valdameri G, de Souza EM, Hughes DL, Ramirez MI, Soares JF, Nunes GG: **Effects of decavanadate salts with organic and inorganic cations on Escherichia coli, Giardia intestinalis, and vero cells**. *Inorg Chem* 2018, **57**:11930–11941.

36. * Althumairy D, Postal K, Barisas BG, Nunes GG, Roess DA, Crans DC: **Polyoxometalates function as indirect activators of a G protein-coupled receptor**. *Metallomics* 2020, **12**: 1044–1061.
The paper describes the importance of speciation studies of mixed-valence polyoxovanadates in media to enhance the expression of the lutenizing hormone receptor.

37. Arena G, Rizzarelli E: **Zn(2+) interaction with amyloid-B: affinity and speciation**. *Molecules* 2019, **24**:2796.

38. Vicatos GM, Jackson GE, Hammouda AN, Bonomo RP, Valora G: **Potentiometric and spectroscopic studies of the complex formation between copper(II) and Gly-Leu-Phe or Sar-Leu-Phe tripeptides**. *Polyhedron* 2019, **170**:553–563.

39. Magri A, Grasso G, Corti F, Finetti F, Greco V, Santoro AM, Sciuto S, La Mendola D, Morbidelli L, Rizzarelli E: **Peptides derived from the histidine-proline rich glycoprotein bind copper ions and exhibit anti-angiogenic properties**. *Dalton Trans* 2018, **47**:9492–9503.

40. Paolo Destito P, Sousa-Castillo A, Couceiro JR, Lopez F, Correa-Duarte MA, Mascare JL: **Hollow nanoreactors for Pd-catalyzed Suzuki–Miyaura coupling and O-propargyl cleavage reactions in bio-relevant aqueous media**. *Chem Sci* 2019, **10**:2598–2603.

41.. ** Jang S-Y, Murale DP, Kim AD, Lee J-S: **Recent developments in metal-catalyzed bio-orthogonal reactions for biomolecule tagging**. *Chembiochem* 2019, **20**:1498–1507.
This review highlights the latest developments and progress in metal-catalyzed bio–orthogonal reactions for biomolecule labeling. All reactions are biocomptible and utilize biologically unavailable chemistry.

42. Adrio LA, Nguyen BN, Guilera G, Livingston AG, Hii KK: **Speciation of Pd(OAc)2 in ligandless suzuki–miyaura reactions**. *Catal Sci Technol* 2012, **2**:316–323.

43. Smeenk MLWJ, Agramunt J, Bonger KM: **Recent developments in bioorthogonal chemistry and the orthogonality within**. *Curr Chem Biol* 2021, **60**:79–88.

44. Vidal C, Tomás-Gamasa M, Gutiérrez-González A, Mascareñas JL: **Ruthenium-catalyzed redox isomerizations inside living cells**. *J Am Chem Soc* 2019, **141**:5125–5129.

45. Amoretti M, Amsler C, Bonomi G, Bouchta A, Bowe P, Carraro C, Cesar CL, Charlton M, Collier MJT, Doser M, Filippini V, Fine KS, Fontana A, Fujiwara MC, Funakoshi R, Genova P, Hangst JS, Hayano RS, Holzscheiter MH, Jørgensen LV, Lagomarsino V, Landua R, Lindelöf D, Rizzini EL, Macrì M, Madsen N, Manuzio G, Marchesotti M, Montagna P, Pruys H, Regenfus C, Riedler P, Rochet J, Rotondi A, Rouleau G, Testera G, Variola A, Watson TL, van der Werf DP: **Production and detection of cold antihydrogen atoms**. *Nature* 2002, **419**:456–459.

46. * Prescher JA, Bertozzi CR: **Chemistry in living systems**. *Nat Chem Biol* 2005, **1**:13–21.
A seminal paper introducing the concept of bioorthogonal reactions in living systems.

47. Suazo KF, Park K-Y, Distefano MD: **A not-so-ancient grease history: click chemistry and protein lipid modifications**. *Chem Rev* 2021, **121**:7178–7248.

48. Sherwood J, Clark JH, Fairlamb IJS, Slattery JM: **Solvent effects in palladium catalysed cross-coupling reactions**. *Green Chem* 2019, **21**:2164–2213.

49. Carole WA, Colacot TJ: **Understanding palladium acetate from a user perspective**. *Chem Eur J* 2016, **22**:7686–7695.

50. Zhang D, Yang D, Wang S, Zeng L, Xin J, Zhang H, Lei A: **The real structure of Pd(OAc)2 in various solvents**. *Chin J Chem* 2021, **39**:307–311.

51. Ghosh S: **Cisplatin: the first metal based anticancer drug**. *Bioorg Chem* 2019, **88**:102925.

52. Gambino D, Otero L: **Metal compounds in the development of antiparasitic agents: rational design from basic chemistry to the clinic**. *Met Ions Life Sci* 2019, **19**:331–358.

53. * Boros E, Dyson PJ, Gasser G: **Classification of metal-based drugs according to their mechanisms of action**. *Inside Chem* 2020, **6**:41–60.
A recent review describing different classes of metal-based drugs and correlate this to the drugs that underwent clinical trials

54. Kostelnik TI, Orvig C: **Radioactive main group and rare earth metals for imaging and therapy**. *Chem Rev* 2019, **119**: 902–956.

55. Wahsner J, Gale EM, Rodriguez-Rodriguez A, Caravan P: **Chemistry of MRI contrast agents: current challenges and new frontiers**. *Chem Rev* 2019, **119**:957–1057.

56. Englinger B, Pirker C, Heffeter P, Terenzi A, Kowol CR, Keppler BK, Berger W: **Metal drugs and the anticancer immune response**. *Chem Rev* 2019, **119**:1519–1624.

57. Chellan P, Sadler PJ: **Enhancing the activity of drugs by conjugation to organometallic fragments**. *Chem Eur J* 2020, **26**:8676–8688.

58. Murray BS, Dyson PJ: **Recent progress in the development of organometallics for the treatment of cancer**. *Curr Opin Chem Biol* 2020, **56**:28–34.

59. Chen AY, Adamek RN, Dick BL, Credille CV, Morrison CN, Cohen SM: **Targeting metalloenzymes for therapeutic intervention**. *Chem Rev* 2019, **119**:1323–1455.

60. • Savelieff MG, Nam G, Kang J, Lee HJ, Lee M, Lim MH: **Development of multifunctional molecules as potential therapeutic candidates for Alzheimer's disease, Parkinson's disease, and Amyotrophic lateraldclerosis in the last decade**. *Chem Rev* 2019, **119**:1221–1322.
A recent review of current neurodegenerative potential drug candidates and future development of drugs.

61. Bruijnincx PCA, Sadler PJ: **New trends for metal complexes with anticancer activity**. *Curr Opin Chem Biol* 2008, **12**: 197–206.

62. • Scalese G, Kostenkova K, Crans DC, Gambino D: **Metallomics and other omics approaches in antiparasitic metal-based drug research**. *Curr Chem Biol* 2022, **67**:102127.
The combination of metallomics with different omic methods allow the exploration of modes of actions of metal-based drugs in antiparasitic organisms.

Appendix XI: Electron Transport Lipids Fold Within Membrane-Like Interfaces

This manuscript describes the study of the fundamental properties of ubiquinone-2 (UQ-2). UQ-2 is a small, truncated analog of UQ-10, a lipid electron carrier in the eukaryotic electron transport chain. The study investigated the synthesis, spectroscopic characterization, 3D conformation elucidation using 1H-1H NOESY and 1H-1H ROESY NMR data of UQ-2. The study also investigated the relative locations of UQ-2 in model membrane interfaces and lipid monolayers. The results confirmed that UQ-2 adopts a folded confirmation in both organic solvents and model membranes which changes with the solvent environment (Braasch-Turi et. al, 2022).

References

Braasch-Turi, M.; Koehn, J. T.; Kostenkova, K.; Van Cleave, C.; Ives, J. W.; Crick, D. C.; Crans, D. C. Comparing the interaction of Electron Transport Lipid Analogues, Ubiquinone-2 and Menaquinone-2, with Model Membrane Systems. *Front. in Chem*. **2022**, *10,* 1-17 (article 827530).

frontiers in Chemistry

ORIGINAL RESEARCH
published: 08 March 2022
doi: 10.3389/fchem.2022.827530

Electron Transport Lipids Fold Within Membrane-Like Interfaces

*Margaret M. Braasch-Turi[1†], Jordan T. Koehn[1†], Kateryna Kostenkova[1], Cameron Van Cleave[1], Jacob W. Ives[1], Heide A. Murakami[1], Dean C. Crick[2,3] and Debbie C. Crans[1,2]**

[1]Chemistry Department, Colorado State University, Fort Collins, CO, United States, [2]Cell and Molecular Biology Program, Colorado State University, Fort Collins, CO, United States, [3]Microbiology, Immunology, and Pathology Department, Colorado State University, Fort Collins, CO, United States

OPEN ACCESS

Edited by:
Parasuraman Jaisankar, Indian Institute of Chemical Biology (CSIR), India

Reviewed by:
Sumit Sharma, Ohio University, United States
Makoto Kawamukai, Shimane University, Japan
Alokmay Datta, University of Calcutta, India

***Correspondence:**
Debbie C. Crans
debbie.crans@colostate.edu

[†]These authors have contributed equally to this work and share first authorship

Specialty section:
This article was submitted to Chemical Biology, a section of the journal Frontiers in Chemistry

Received: 06 December 2021
Accepted: 07 January 2022
Published: 08 March 2022

Citation:
Braasch-Turi MM, Koehn JT, Kostenkova K, Van Cleave C, Ives JW, Murakami HA, Crick DC and Crans DC (2022) Electron Transport Lipids Fold Within Membrane-Like Interfaces. Front. Chem. 10:827530. doi: 10.3389/fchem.2022.827530

Lipoquinones, such as ubiquinones (UQ) and menaquinones (MK), function as essential lipid components of the electron transport system (ETS) by shuttling electrons and protons to facilitate the production of ATP in eukaryotes and prokaryotes. Lipoquinone function in membrane systems has been widely studied, but the exact location and conformation within membranes remains controversial. Lipoquinones, such as Coenzyme Q (UQ-10), are generally depicted simply as "Q" in life science diagrams or in extended conformations in primary literature even though specific conformations are important for function in the ETS. In this study, our goal was to determine the location, orientation, and conformation of UQ-2, a truncated analog of UQ-10, in model membrane systems and to compare our results to previously studied MK-2. Herein, we first carried out a six-step synthesis to yield UQ-2 and then demonstrated that UQ-2 adopts a folded conformation in organic solvents using ^{1}H-^{1}H 2D NOESY and ROESY NMR spectroscopic studies. Similarly, using ^{1}H-^{1}H 2D NOESY NMR spectroscopic studies, UQ-2 was found to adopt a folded, U-shaped conformation within the interface of an AOT reverse micelle model membrane system. UQ-2 was located slightly closer to the surfactant-water interface compared to the more hydrophobic MK-2. In addition, Langmuir monolayer studies determined UQ-2 resided within the monolayer water-phospholipid interface causing expansion, whereas MK-2 was more likely to be compressed out and reside within the phospholipid tails. All together these results support the model that lipoquinones fold regardless of the headgroup structure but that the polarity of the headgroup influences lipoquinone location within the membrane interface. These results have implications regarding the redox activity near the interface as quinone vs. quinol forms may facilitate locomotion of lipoquinones within the membrane. The location, orientation, and conformation of lipoquinones are critical for their function in generating cellular energy within membrane ETS, and the studies described herein shed light on the behavior of lipoquinones within membrane-like environments.

Keywords: lipoquinone, ubiquinone, menaquinone, folded conformation, 2D NMR, electron transport, membrane interface, Langmuir monolayer

1 INTRODUCTION

Molecular conformations are paramount to the physical and chemical properties that dictate recognition and function of molecules within biological systems. The location and conformation of lipoquinones within biological membranes is not well understood and highly debated (Kingsley and Feigenson, 1981; Michaelis and Moore, 1985; Ulrich et al., 1985; Salgado et al., 1993; Soderhall and Laaksonen, 2001; Afri et al., 2004; Galassi and Arantes, 2015; Quirk et al., 2016; Koehn et al., 2018b; Koehn et al., 2019). Lipoquinones are hydrophobic membrane-bound molecules consisting of a redox-active quinone headgroup and an isoprenyl side chain. There are three major structural subgroups of lipoquinones which differ only in the structure of the headgroup. Ubiquinones (UQ), such as Ubiquinone-10 (UQ-10, **Figure 1A**), comprise of a benzoquinone ring with two methoxy substituents, plastoquinones (PQ) with a dimethylbenzoquinone, such as plastoquinone-9 (PQ-9), and menaquinones (MK), such as menaquinone-9 (MK-9, **Figure 1B**), contain a methylnaphthoquinone ring. Lipoquinones function as essential components of the respiratory electron transport system (ETS), where they shuttle electrons and protons between membrane-bound protein complexes, ultimately ending in the production of ATP (Nowicka and Kruk, 2010; Kawamukai, 2018). UQ and MK are involved in the ETS of oxidative phosphorylation in mammalian and bacterial cells, but PQ is involved in photosynthetic ETS in plants and photosynthetic bacteria (Kawamukai, 2018). For the purpose of this study, we will focus on UQ and MK. Even though the ETS is vital for life through the production of ATP, the role of lipoquinones is commonly distilled to an abbreviation within a diagram, such as "Q" for Coenzyme Q (UQ-10), the major electron transport agent in eukaryotes (Trumpower, 1981; Kawamukai, 2018), ignoring the conformation and location of these molecules as a whole. Similar to lipoquinones, polyprenyl compounds have been known to adopt preorganized, folded conformations presumably due to hydrophobic effect and π-π interactions (Woodward and Bloch, 1953; Murgolo et al., 1989). The synthesis of cholesterol relies on the preorganized conformation of squalene epoxide to produce a single stereochemical outcome out of 256 (2^8) possible conformations (Woodward and Bloch, 1953). Moreover, dolichol-19 adopts a coiled conformation (Murgolo et al., 1989). A handful of computational studies have investigated the dihedral angle (φ) about the C2C3CβCγ bond (as shown in red in **Figure 1C**) in UQs (Nilsson et al., 2001b; Ceccarelli et al., 2003; Galassi and Arantes, 2015; Eddine et al., 2020), MKs (Eddine et al., 2020), and plastoquinones (Nilsson et al., 2001a; Jong et al., 2015; Eddine et al., 2020), which determined φ was ~90°, 100°, and 90°, respectively. In this study we determined the location, orientation, and conformation of UQ-2 (**Figure 1C**), a truncated, representative analog for native UQ-10, using 1D and 2D NMR spectroscopic methods in organic solvents and in biological model membrane systems comprised of AOT reverse micelles (RM) (Van Horn et al., 2008). This analysis will allow us to compare the location and conformation of UQ-2 with MK-2 (**Figure 1D**) (Koehn et al., 2018b) in membrane-like environments to shed light on the controversies regarding the location and conformation of lipoquinones in cellular membranes.

The location of UQ-10 within the membrane has been widely studied using experimental and computational methods, but it continues to be controversial. Briefly, there is no consensus regarding the location of UQ-10 with its locations spanning the entire width of the membrane bilayer leaflet. Out of these studies, three schools of thought have emerged; the quinone headgroup is located: 1) at or near the lipid headgroups (Kingsley and Feigenson, 1981; Stidham et al., 1984; Lenaz et al., 1992; Salgado et al., 1993; Galassi and Arantes, 2015; Gómez-Murcia et al., 2016; Kaurola et al., 2016; Quirk et al., 2016; Teixeira and Arant

yl chains (Michaelis and Moore, 1985; Cornell et al., 1987; Chazotte

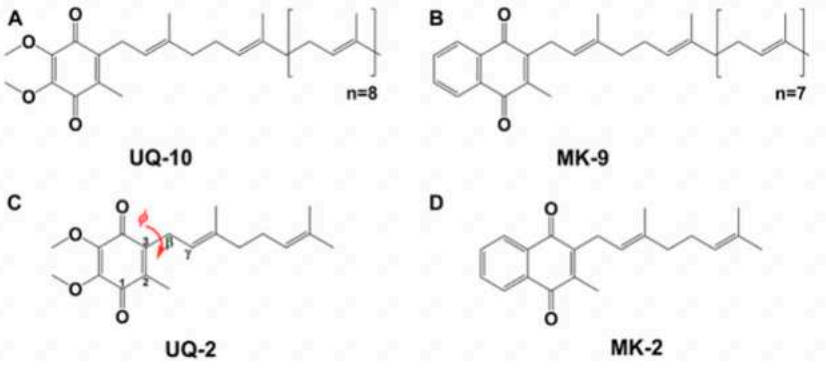

FIGURE 1 | Schematic structures of native lipoquinones: **(A)** Ubiquinone-10 (UQ-10), and **(B)** Menaquinone-9 (MK-9). Schematic structures of truncated lipoquinone analogs: **(C)** Ubiquinone-2 (UQ-2) with the C2C3CβCγ bond indicated in red with dihedral angle, φ, and **(D)** Menaquinone-2 (MK-2).

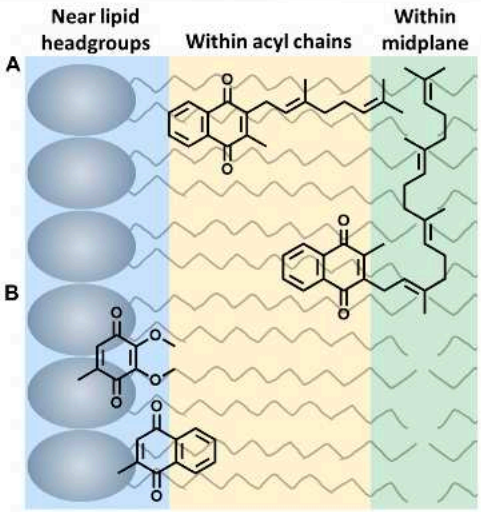

FIGURE 2 | Three possible locations of lipoquinone headgroup: **(A)** Example of the influence of the isoprenyl side chain length on location of the quinone headgroup. MK-2 and MK-4 are shown as a 2D schematics. MK-2 has been determined to fold in membrane-like interfaces (Koehn et al., 2018b). **(B)** Relative placement based on headgroup polarity (side chain omitted for clarity) (Van Cleave et al., 2020; Van Cleave et al., 2021).

et al., 1991; Salgado et al., 1993; Metz et al., 1995; Afri et al., 2004; Hauss et al., 2005), or 3) within the bilayer midplane (Ulrich et al., 1985; Ondarroa and Quinn, 1986; Soderhall and Laaksonen, 2001) (**Figure 2**). Even though the location of the headgroup is controversial, the field does seem to agree that at least part of the isoprenyl side chain is embedded within the bilayer midplane, and the headgroup is thought to extend into one of the membrane leaflets. This bend (~90° turn) in the isoprenyl side chain allows UQ-10 to be accommodated within the bilayer, which addresses the fact that UQ-10 is roughly the same length as a typical phospholipid bilayer if UQ-10 were in fully-extended conformation (Trumpower, 1981).

Two hypotheses have been reported to explain the headgroup position within the membrane. First, the length of the isoprenyl side chain was reported to affect the position of the quinone headgroup by pulling the headgroup closer to the midplane as the side chain length increases. For example, the quinone headgroup of MK-4 would be found closer to the midplane than MK-2 (**Figure 2A**). On the other hand, the polarity of the headgroup is also thought to anchor its location within the membrane. Recent computational studies by Arantes and coworkers determined UQ associates with the lipid headgroups (Galassi and Arantes, 2015; Teixeira and Arantes, 2019). Together, we recently showed for the series of MK-1, MK-2, MK-3, and MK-4 that the location of the headgroup remained constant as the side chain length increased using both experimental and computational techniques (Van Cleave et al., 2020). As a consequence of the latter, one would anticipate a difference in the location of the more polar UQ headgroup compared to the more hydrophobic MK headgroup as illustrated in **Figure 2B** (Van Cleave et al., 2020). Lipoquinone headgroup is also linked to diffusive motion. "Swimming" lipoquinones are associated with the phospholipid headgroups, and "diving" are found near the midplane. A few computational and experimental studies determined UQ and various analogs are stabilized in the swimming position (Soderhall and Laaksonen, 2001; Hoyo et al., 2017). A recent computational study determined the lipoquinone position depends on the local protein content of the membrane (Singharoy et al., 2020). If the region is lipid-rich, swimming lipoquinone is the dominant species, and diving lipoquinones are the most common in the vicinity of protein complexes (Gupta et al., 2020; Singharoy et al., 2020).

Although lipoquinone conformation is likely to be critical for function and recognition, the topic of conformation of the UQ and MK headgroup relative to the isoprenyl side chain is curiously ignored in the literature aside from a handful of computational studies (Joela et al., 1997; Bernardo et al., 1998; Lenaz et al., 1999; Nilsson et al., 2001a; Nilsson et al., 2001b; Soderhall and Laaksonen, 2001; Ceccarelli et al., 2003; Tekin and Erkoc, 2010; Galassi and Arantes, 2015; Jong et al., 2015; Ismail et al., 2016; Kaurola et al., 2016; Eddine et al., 2020; Feng et al., 2021). Additionally, a few of the computational studies investigating the location of lipoquinones in the membrane contained figures suggesting φ was ~90° (Joela et al., 1997; Bernardo et al., 1998; Lenaz et al., 1999; Soderhall and Laaksonen, 2001; Tekin and Erkoc, 2010; Ismail et al., 2016; Kaurola et al., 2016; Feng et al., 2021), leading to the expectation of a folded conformation. However, there was no discussion regarding the conformation of the headgroup relative to the isoprenyl side chain prior to our work in 2018 (Koehn et al., 2018b). The implications of conformation on lipoquinone locomotion were hypothesized by Joela and coworkers (Joela et al., 1997). Therein, they speculated the quinone headgroup is located close to the enzyme active site and moves between membrane and enzyme binding pocket by rotating about the C2C3CβCγ bond. They describe this limited movement with a stationary side chain and a mobile headgroup as if the "tail is wagging the dog." The isoprenyl chain would serve to the anchor the quinone headgroup location. Since we previously found that the side chain did not dictate the headgroup location for MK-1 through MK-4, we hypothesized that the anchoring of the headgroup drives the extension of the side chain, and that the more polar UQ-2 headgroup will be closer to the interface than the more hydrophobic headgroup of MK-2. Hence, we carried out studies in which the location and conformation of UQ-2 were elucidated in environments that allow direct comparison to previously reported MK-2, which folds within model membrane interfaces (Koehn et al., 2018b). This study will illuminate how headgroup structure changes the position, orientation, and conformation, which are critical to recognition and function, of prominent lipoquinones within membrane-like environments.

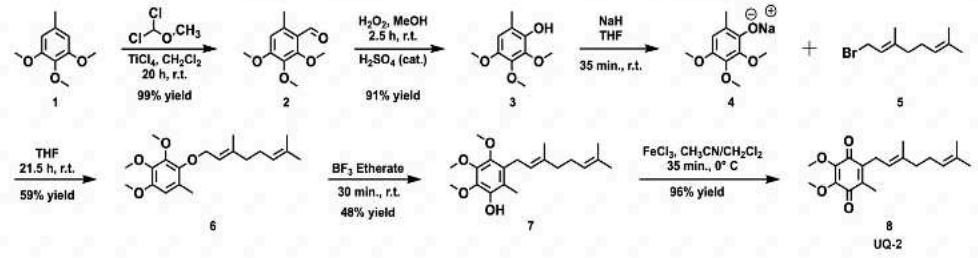

SCHEME 1 | Synthetic scheme for the six-step synthesis to obtain UQ-2 **8** from 3,4,5-trimethoxytoluene **1** using modified protocols as reported (Matsumoto et al., 1984; Lu and Chen, 2004; Bovicelli et al., 2008).

2 RESULTS AND DISCUSSION

2.1 Synthesis of UQ-2

UQ-2 **8** was prepared using a 6-step synthesis (**Scheme 1**) starting from commercially available 3,4,5-trimethoxytoluene **1**. The synthetic route has been reported in literature (Lu and Chen, 2004; Bovicelli et al., 2008); however, we scaled up the reactions and used modified procedures and conditions to overcome synthetic challenges encountered. The aldehyde **2** was prepared efficiently and was practically pure upon workup using a Rieche formylation reaction with $TiCl_4$, which is the traditional Lewis acid catalyst for this reaction. Efforts to achieve this reaction using $AlCl_3$ as the Lewis acid catalyst were low yielding and resulted in impure compound in our hands. An acid-catalyzed Dakin oxidation reaction was used to afford phenol **3** in excellent yield even after chromatographic purification (Matsumoto et al., 1984). The geranyl ether **6** was prepared via an S_N2 reaction between phenolate **4** and geranyl bromide **5** in a modest yield. Efforts to achieve the allylic rearrangement to yield compound **7** close to yields reported in literature (Bovicelli et al., 2008) was met with limited success. A 48% yield was the highest yield we obtained compared to 73% in literature (Bovicelli et al., 2008). Attempts to improve this yield failed, and reactions times longer than 30 min decreased the yield and appeared to increase the amount of unknown side products. While compound **7** was efficiently oxidized to **8** using $FeCl_3{\cdot}6H_2O$ in a mixture of dichloromethane and acetonitrile at 0°C, attempts to follow a published procedure (Bovicelli et al., 2008) using $FeCl_3$ in a mixture of ethanol and H_2O at ambient temperature yielded only starting material.

2.2 1D ^{1}H NMR Spectroscopic Studies of UQ-2 in Organic Solvents

To establish that UQ conformation is sensitive to its surrounding environment, UQ-2 was first characterized using 1D ^{1}H NMR spectroscopy. **Figure 3** shows the 1D ^{1}H NMR spectra of UQ-2 in isooctane (2,2,4-trimethylpentane), d_6-benzene, d_5-pyridine, d_6-DMSO, d_3-acetonitrile, and D_2O. The observed chemical shifts of UQ-2 vary dramatically in the different solvents shown. Different spectroscopic trends are observed in the hydrophobic (isooctane, d_5-pyridine, and d_6-benzene) and the hydrophilic

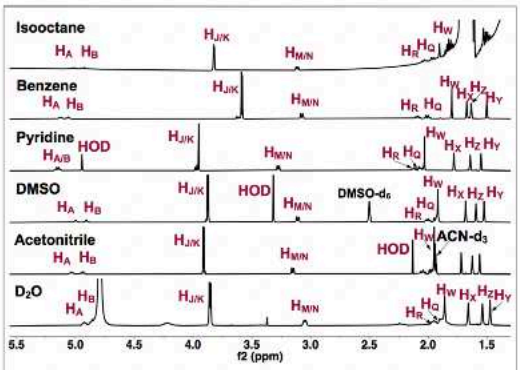

FIGURE 3 | ^{1}H NMR (400 MHz) spectra of UQ-2 in hydrophobic (isooctane (2,2,4-trimethtylpentane), d_6-benzene, and d_5-pyridine) and hydrophilic (d_6-DMSO, d_3-acetonitrile, and D_2O) solvents.

(d_3-acetonitrile, d_6-DMSO, and H_2O/D_2O) solvent environments. For example, the isoprenyl protons H_M/H_N and methoxy protons H_J/H_K are observed at significantly different chemical shifts between the two different classes of solvents. The observations could be described by conformational changes of UQ-2 in the various solvent environments investigated, alterations of the electronic state due to interaction with the solvent, or most likely, a combination of both. There were similarities and differences among the investigated solvents. For the hydrophobic solvents, protons H_M/H_N have similar chemical shifts in isooctane and benzene, but they appear more downfield in pyridine, whereas they appear in similar chemical shifts in the hydrophilic solvents. The chemical shifts for H_J and H_K are in different locations in each solvent, which suggests the methoxy groups are changing environments in the different solvents (Nilsson et al., 2001b). The chemical shifts of the vinyl protons H_A and H_B are increasingly more downfield as the polarity of the hydrophobic solvents increases. In the hydrophilic solvents, H_A and H_B are found in

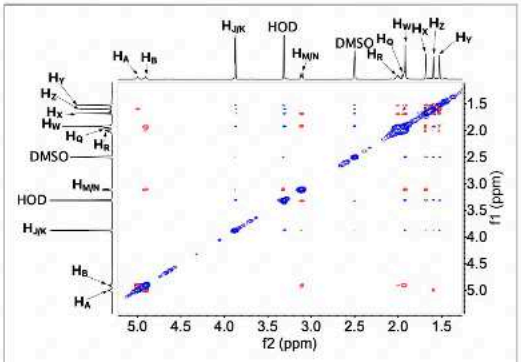

FIGURE 4 | Full ^{1}H-^{1}H 2D NOESY spectrum of UQ-2 in DMSO.

similar chemical shifts aside from D_2O where they appear slightly upfield and obscured by the HOD peak.

2.3 ^{1}H-^{1}H 2D NOESY and ^{1}H-^{1}H 2D ROESY NMR Spectroscopic Studies of UQ-2 in d_6-DMSO, d_3-Acetonitrile, d_6-Benzene, and d_5-Pyridine

To determine the conformation of UQ-2 in organic solvents, we utilized two complementary 2D NMR methods, ^{1}H-^{1}H 2D NOESY and ^{1}H-^{1}H 2D ROESY (Jones et al., 2011). We chose to highlight the NOESY and ROESY spectra of UQ-2 in d_6-DMSO for direct comparison to our previous work with MK-2 (Koehn et al., 2018b). The corresponding spectra for d_3-acetonitrile, d_6-benzene, and d_5-pyridine can be found in **Supplementary Figures S15–S23** in the Supplementary Material. Looking at the structure of UQ-2, a folded conformation, which is defined by a ~90° dihedral angle about the C2C3CβCγ bond, would be indicated by cross peaks between the headgroup and particular protons on the isoprenyl side chain such as the methyl protons H_W and protons further down the side chain, such as H_A, H_Y, and H_Z. In the full NOESY spectrum in d_6-DMSO, there is a cross peak observed between H_W and vinyl protons, H_A and H_B (**Figure 4** and proton labeling scheme is shown in **Figure 5A**). The proton H_B is close enough to H_W have NOE interactions; however, H_A would be too far away to have NOE interactions unless the molecule is in a folded conformation. In addition, there are cross peaks that confirm the 1D ^{1}H NMR spectra assignments along the isoprenyl tail, such as H_W and allylic protons H_M and H_N and between H_A/H_B and methyl protons H_X, H_Y, and H_Z. The folded conformation is also suggested by the cross peaks observed between methyl protons H_W and methyl protons, H_X, H_Y and H_Z (**Figure 5B**). These cross peaks are also observed in the ROESY spectrum (**Figures 5C,D**. Enlarged full ROESY spectrum is also shown in the Supplementary Materials: **Supplementary Figure S13**). These cross peaks are indicative of a U-shaped conformation (example shown in **Figure 6**), placing the terminal methyl groups over the quinone headgroup for UQ-2 in d_6-DMSO.

In the case of the 2D NOESY and ROESY spectra of UQ-2 in d_3-acetonitrile (**Supplementary Figures S16, S17**), there are cross peaks observed between H_W and vinyl protons, H_A and H_B, and methyl protons, H_X, H_Y, and H_Z, similar to d_6-DMSO. Together these suggest a folded, U-shaped conformation, but the results are somewhat inconclusive. The reference peak for d_3-acetonitrile, 1.93 ppm, is close to H_W (1.94 ppm) and almost overlapping. Therefore, it is hard to conclude if the cross peaks observed are a result of intramolecular NOE interactions or interactions with the solvent. For 2D NOESY and ROESY spectra of UQ-2 in d_6-benzene (**Supplementary Figures S19, S20**), there are cross peaks observed between H_W and H_X, and H_M/H_N. In both the flat-extended and folded-extended conformations (example shown in **Figure 6**), H_X, and H_M/H_N are all within the 5 Å NOE range of H_W. To distinguish between the two, we looked for cross peaks between H_W and the terminal methyl protons, H_Y and H_Z. In the folded-extended conformation, the average distance between H_W and H_Y is approximately 5.1 Å. In the ROESY spectrum, there are cross peaks present between H_W and H_Y and H_Z (**Supplementary Figure S20**) and they are present in the corresponding NOESY (**Supplementary Figure S19**). Therefore, the presence of a cross peak between H_W and H_Y in the NOESY (**Supplementary Figure S19**) suggests H_Y is inside the NOE range and therefore indicates a folded, open U-shaped conformation in d_6-benzene. Similar observations were found for 2D NOESY and ROESY spectra for UQ-2 in d_5-pyridine (**Supplementary Figures S22, S23**). There are cross peaks observed between H_W and H_A/H_B, H_X, and H_M/H_N, but there is a cross peak observed between H_W and H_Y. Similar to benzene, this together suggests UQ-2 adopts a folded, open U-shaped conformation in d_5-pyridine.

2.4 Illustrating UQ-2 Conformations Determined by NMR Using Molecular Mechanics

UQ-2 has a short repeating isoprenyl chain (C_{10}) but enough carbons with numerous degrees of rotational freedom; therefore, even the truncated version of UQ-10, UQ-2, can assume many different specific conformations and still be considered folded by our definition. We created 3D conformations (**Figure 7**) of UQ-2 for visualization using Molecular Mechanics where intramolecular distances between specific protons obtained from 2D NOESY/ROESY NMR spectra (**Supplementary Table S1**) were used as geometric constraints. While the exact position of the isoprenyl side chain varies slightly from solvent to solvent, UQ-2 adopts a folded conformation in all four solvents examined in the 2D NMR studies, where the dihedral angle about the C2C3CβCγ bond (**Figure 1C**) is ~90°.

To understand the differences between the conformations of UQ-2 and MK-2, we first had to determine the distances between the protons on the isoprenyl side chain and the headgroup methyl proton H_W. We used the volume integrals from the 2D NOESY spectra and correlated them to intramolecular distances. The

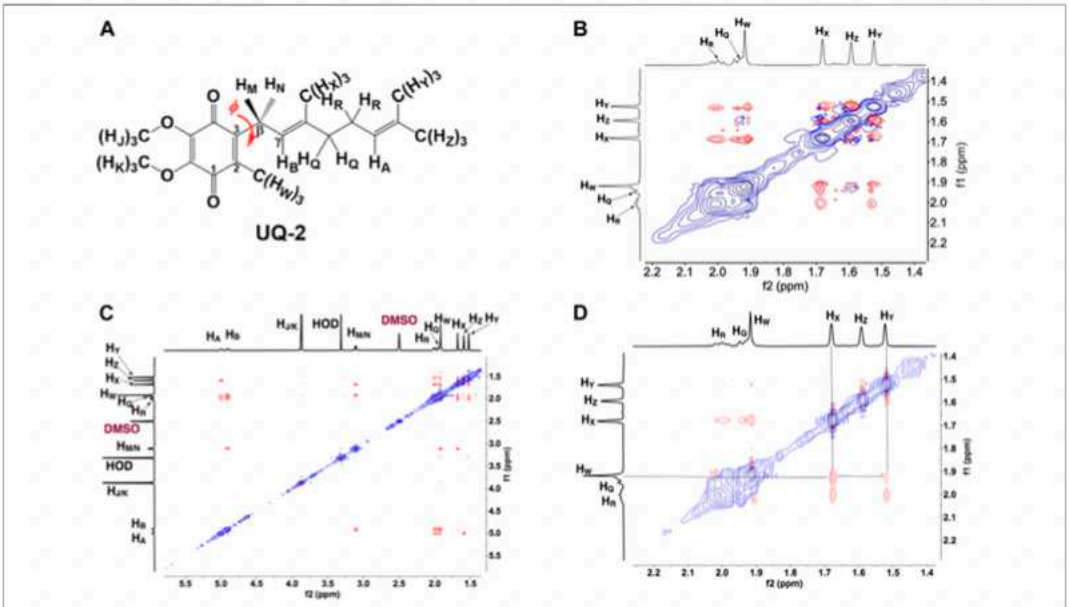

FIGURE 5 | (A) Proton labeling scheme for UQ-2. **(B)** Partial ^{1}H-^{1}H 2D NOESY spectrum of UQ-2 in DMSO. **(C)** A larger ^{1}H-^{1}H 2D ROESY spectrum of UQ-2 in DMSO. Full ROESY spectrum can also be found in the Supplementary Material, **Supplementary Figure S13**. **(D)** Partial ^{1}H-^{1}H 2D ROESY spectrum of UQ-2 in DMSO.

volume integral of the H_W and H_M/H_N cross peak, which has a known intramolecular distance of ~3.5 Å, was set to 1, and each volume integral was standardized against it. From here, the values obtained were used to determine if the cross peaks were strong (>1.5), medium (0.6–1.5), or weak (<0.6). These intensities were translated to distance in Ångstroms accordingly: 1) strong (<3 Å), 2) medium (3–4 Å), and 3) weak (>4 Å). The intramolecular distances were then used to construct the conformations, and MMFF94 minimization calculations were performed to correct bond lengths. The distances in **Supplementary Table S1** reflect the intramolecular distances post minimization.

DMSO and pyridine were chosen due to the distinctly different 1D ^{1}H NMR spectra to better illustrate the differences in conformation (Koehn et al., 2018b). Since NOESY and ROESY spectra are products of an average conformation, the intramolecular distances generated are representative of the most abundant conformation. As described previously, the interactions between headgroup methyl protons H_W and protons along the isoprenyl side chain, such as vinyl protons H_A and methyl protons H_X, H_Y, and H_Z, are critical to evaluate UQ-2 conformation in organic solvents. The distances between H_W and H_A, H_X, H_Y, and H_Z imply there is a folded conformation about the C2C3βCγ bond, and the position of the terminal methyl protons H_Y and H_Z relative to H_W suggest differences in the position of the end of the isoprenyl side chain: U-shaped or folded-extended conformation.

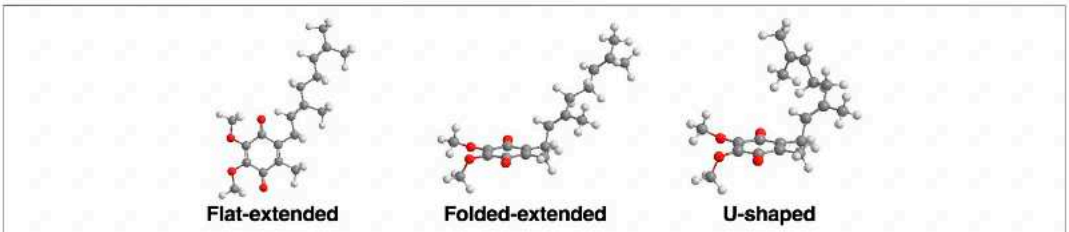

FIGURE 6 | Examples of three possible classes of UQ-2 conformations: Flat-extended, Folded-extended, and U-shaped (Koehn et al., 2018b; Koehn et al., 2019).

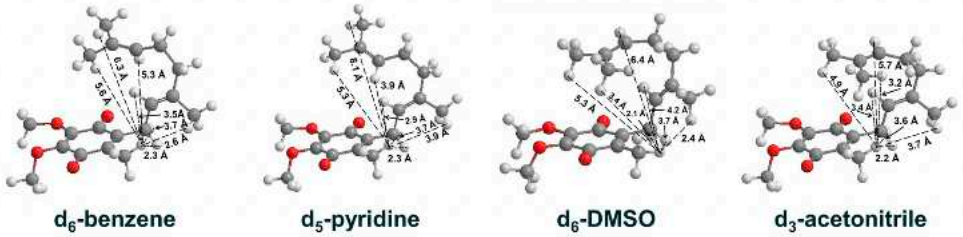

FIGURE 7 | UQ-2 conformations generated using 2D NMR data distance constraints and MMFF94 calculations to illustrate the conformations elucidated in d_6-benzene, d_5-pyridine, d_6-DMSO, and d_3-acetonitrile. Intramolecular distances (Å) between H_W and select protons on the side chain are shown (dashed lines).

For UQ-2 in d_5-pyridine, the intramolecular distance between H_W and H_X is shown to be 3.9 Å. The distance between H_W and vinyl proton, H_A, 3.9 Å, supports a folded conformation. The intramolecular distances between H_W and H_Y and H_Z were found to be 8.1 Å and 5.3 A, respectively. Although these values are outside the range of NOE influence, cross peaks were observed in the 2D NOESY and ROESY spectra (**Figures 4**, **5C**, respectively). Therefore, we cannot preclude the possibility that UQ-2 adopts both a folded-extended or a more open U-shaped conformation in d_5-pyridine. These results are in line with MK-2 in d_5-pyridine, which was previously found to adopt a folded-extended conformation (Koehn et al., 2018b).

We superimposed the conformations of UQ-2 in d_3-acetonitrile and d_6-DMSO to better visualize the minute differences observed between conformations (**Figure 8**). The superimposed conformations of UQ-2 in d_6-benzene and d_5-pyridine are found in the Supplementary Material (**Supplementary Figure S25**). In **Figure 8A**, UQ-2 in d_3-acetonitrile and d_6-DMSO are shown in green and purple, respectively. With the headgroups aligned, there is a slight variation in the dihedral angle along the C2C3CβCγ bond, and the trend continues along the sidechain through the second isoprene unit. This accounts for the differences observed in intramolecular distances toward the end of the isoprenyl side chain. The terminal methyl groups of UQ-2 in d_6-DMSO appear directly above the headgroup leading to a U-shaped conformation. The same methyl groups in d_3-acetonitrile appear to be above but not centered over the headgroup, which is consistent with the possibility of U-shaped or folded-extended conformation. In **Figure 8B**, the conformation of UQ-2 and MK-2 in d_6-DMSO are superimposed to visualize how the headgroup structure affects the conformation. The C2C3CβCγ bond in both UQ-2 and MK-2 are nearly identical to one another, but the conformation along the side chain starts to deviate past the first alkene. Taking into consideration the many degrees of freedom about the isoprenyl side chain, it is not unexpected to see deviations in conformation along the side chain.

The folded conformations observed for UQ-2 are likely a result of non-covalent interactions. Firstly, UQ-2 is folding upon itself to minimize interactions with the solvent due to the hydrophobic effect. This is especially apparent in the U-shaped conformations of UQ-2 in the hydrophilic solvents, DMSO and acetonitrile, whereas the hydrophobic solvents, pyridine and benzene, afford an open U-shaped or folded-extended conformation. Additionally, the folded conformation is likely reinforced by π-π interactions between the π bonds in the quinone headgroup and the isoprenyl side chain. This idea is supported by the work done on farnesol, where farnesol does not adopt a folded conformation, regardless of the increased number of degrees of freedom along the molecule (Zahn et al., 2000). Therefore, the presence of the quinone headgroup plays a significant role in the ability of the lipoquinone to adopt a folded conformation, but we only saw modest differences between the folded UQ-2 and MK-2 conformations. In addition to the presence of the lipoquinone headgroup, a study suggests the methyl proton, H_W, on the quinone also plays an important

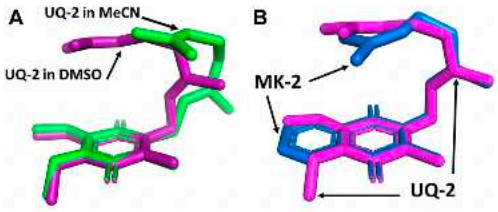

FIGURE 8 | Superimposed 3D conformations of **(A)** UQ-2 based on the 2D NMR data in d_3-acetonitrile (green) and d_6-DMSO (purple) and **(B)** UQ-2 (pink) and MK-2 (blue) based on the 2D NMR data in d_6-DMSO.

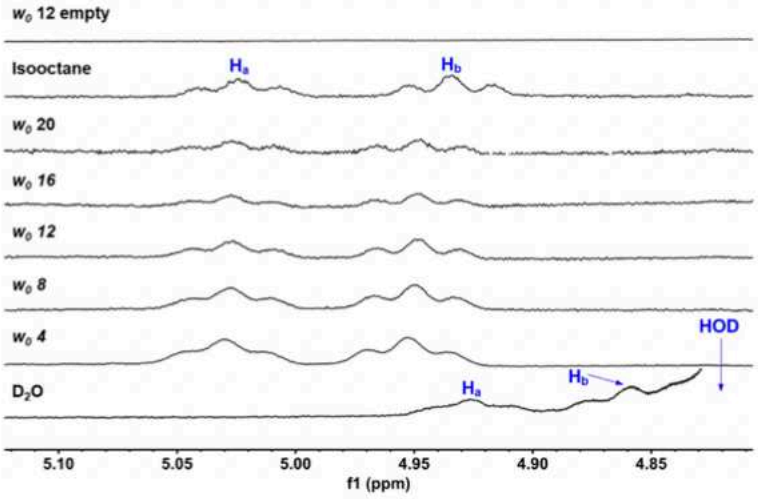

FIGURE 9 | 1D ^{1}H NMR (400 MHz) spectra of UQ-2's alkene protons, H_A and H_B, in D_2O, isooctane, and different sized RMs. An empty RM lacking UQ-2 is also shown for comparison. Peak labelling corresponds to the proton labelling scheme key in **Figure 5A**.

role in influencing a folded conformation (Eddine et al., 2020). The quinone methyl group serves as a rotational barrier by preventing the side chain from freely rotating between folded and flat conformations.

2.5 1D ^{1}H NMR Spectroscopic Studies of UQ-2 in RMs

Our ultimate objective was to determine how UQ-2 behaved with respect to membrane-like interfaces. We used a system comprised of nanosized water droplets encased in AOT surfactant to create reverse micelles (RMs) inside an isooctane (hydrophobic) solvent. This simple model system will provide useful information regarding location, orientation, and conformation of UQ-2 at an interface using NMR spectroscopy with minimal overlap between surfactant proton peaks and key UQ-2 proton peaks. 1D ^{1}H NMR spectra of varying RM sizes were collected in D_2O (w_0: 4, 8, 12, 16, 20, where $w_0 = [D_2O]/[AOT]$), shown in **Figure 9**. The placement of the UQ-2 molecules inside the membrane system was determined via the changes in chemical shift that UQ-2 protons undergo as the RM size changes. Typically, aromatic protons often offer ideal peaks to compare and analyze shifts, as they lie far from any AOT peaks. However, as there are no aromatic protons to observe in UQ-2, we instead observed the vinyl protons peaks (H_A/H_B), which are both triplet peaks that are easily discernable from the AOT peaks. The peak locations for H_A and H_B respectively are 5.02 and 4.93 ppm for isooctane, 5.03 and 4.95 ppm for w_0 20, 5.03 and 4.95 ppm for w_0 16, 5.03 and 4.95 ppm for w_0 12, 5.03 and 4.95 ppm for w_0 8, 5.03 and 4.95 ppm for w_0 4, 4.93 and 4.86 ppm for D_2O. The chemical shifts of these peaks do not change significantly enough as the RM changes in size to reliably indicate where in the RM interface the UQ-2 resides. However, the large shift between the D_2O sample and the RM samples (−0.10 ppm for H_A and −0.09 ppm for H_B from w_0 4 to D_2O) compared to the much smaller shift between the isooctane sample and the RM samples (0.01 ppm for H_a and 0.02 ppm for H_b from isooctane to w_0 20) would indicate that the UQ-2 does not reside within the bulk water or in the isooctane of the RM system, and thus UQ-2 must reside somewhere in the RM interface. However, 2D NMR studies will enable the exact location, orientation, and conformation of UQ-2 in RMs to be identified.

Dynamic Light Scattering (DLS) was used to determine the hydrodynamic radius of RMs containing UQ-2 and verify that RMs formed in the samples used and that the properties and stability of the samples were consistent with previous studies (see Section V of the **Supplementary Material**). DLS samples were prepared following the sample preparation method used for NMR spectroscopic studies except that DDI H_2O was used instead of D_2O. The results showed that RMs formed and that the sizes of the RMs made were in excellent agreement with that of the literature (Maitra, 1984). These results indicate that the introduction of UQ-2 into the RM system does not significantly affect the size or stability of the RMs.

2.6 ^{1}H-^{1}H 2D NOESY NMR Spectroscopic Studies of UQ-2 in a RM Model Membrane System

To determine the exact location, orientation, and conformation of UQ-2 within RMs, we obtained an ^{1}H-^{1}H 2D NOESY NMR of UQ-2 in a w_0 12 RM (**Figure 10**). **Figure 10A** shows a full NOESY spectrum. To elucidate the location and orientation of UQ-2 within the RM, we looked for the interactions of UQ-2 with AOT (**Figure 10C**). Methoxy protons H_J and H_K and

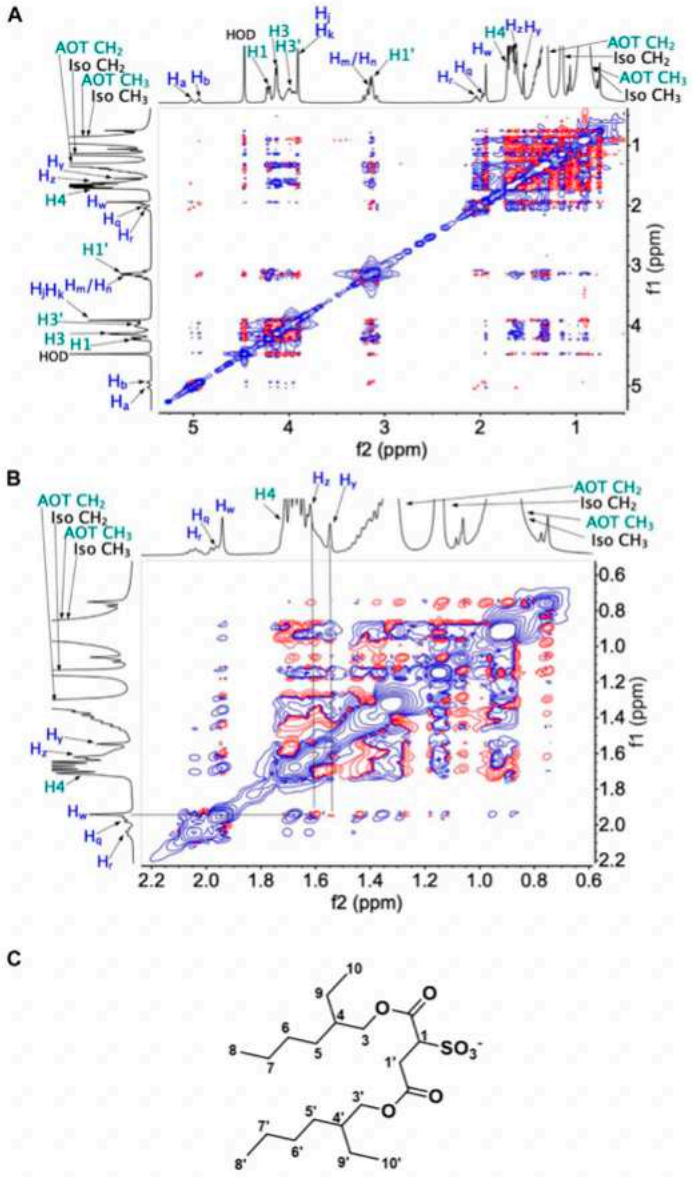

FIGURE 10 | ^{1}H-^{1}H 2D NOESY NMR spectra of UQ-2 in w_0 12 AOT-RM: **(A)** full spectrum, **(B)** partial spectrum. **(C)** Labeled structure of AOT. Blue text labels correspond to UQ-2 protons and teal text labels to AOT protons.

benzoquinone methyl protons H_W are shown to have cross peaks with AOT between H1′, H4, AOT-CH_2, and AOT-CH_3. Additionally, H_W shows cross peaks with H1, H3', and H3 of AOT. Vinyl protons H_A/H_B were found to have cross peaks with H1, H3, and H3'. Allylic protons H_M/H_N were found to have interactions with H1, H3, H3′ and AOT-CH_2, and H_Q/H_R were

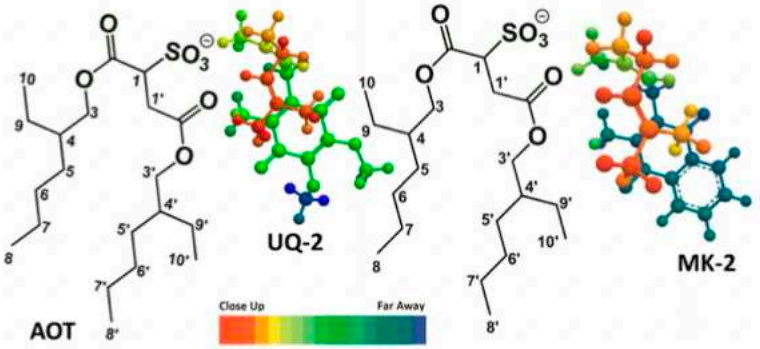

FIGURE 11 | Illustration of UQ-2 and MK-2's proposed folded, U-shaped conformations and placement within the RM interface. The arrangements are consistent with ^{1}H-^{1}H 2D NOESY and ROESY NMR spectral data obtained in a w_0 12 RM. Color depth gradient shows dark red as closer in distance and the dark blue as farther in distance from the reader. AOT proton labeling scheme key is shown.

found to have interactions with H1′. Although UQ-2 is less hydrophobic than MK-2, it is still shown to penetrate the AOT-water interface. The 2D NOESY cross peaks illustrate that UQ-2 is positioned near the interface of AOT with the methoxy groups of the headgroup oriented towards the alkyl chains of AOT (**Figure 11**). This orientation is similar to that of MK-2 (Koehn et al., 2018b), however the interactions between H_W and H_J/H_K with H1-H4 indicate the molecule is positioned closer to the interface than MK-2, which is in agreement with our previous work showing the UQ headgroup is closer to the water pool than MK-2 in phospholipid bilayers (Koehn et al., 2018b; Van Cleave et al., 2020; Van Cleave et al., 2021). The cross peaks observed between H_W and H_Y/H_Z and H_A/H_B indicate UQ-2 is in a folded conformation, specifically a U-shaped conformation. This conformation would not be possible unless the isoprenyl side chain was positioned over the headgroup (**Figure 10B**). Using methods described above in **Section 2.4**, the interproton distances of UQ-2 in a w_0 12 AOT-RM system were determined between H_W and protons along the sidechain (**Supplementary Table S2**). The intramolecular distance between H_W and H_X is shown to be 2.6 Å. Additionally, the distance between H_W and H_Y and H_Z were found to be 4.6 Å and 3.7 Å, respectively. Together this supports a U-shaped conformation for UQ-2 in AOT-RMs. As a confirmatory measure, 1D NOE experiments were performed to confirm the interactions of H_A/H_B with H_W, H_Z and H1′ within the w_0 12 AOT-RM system (**Supplementary Figure S24**). Additionally, the 2D NOESY NMR experiment in AOT-RMs was repeated multiple times, and the same conclusions were made regarding location, orientation, and conformation of UQ-2 in the interface of the AOT-RM system.

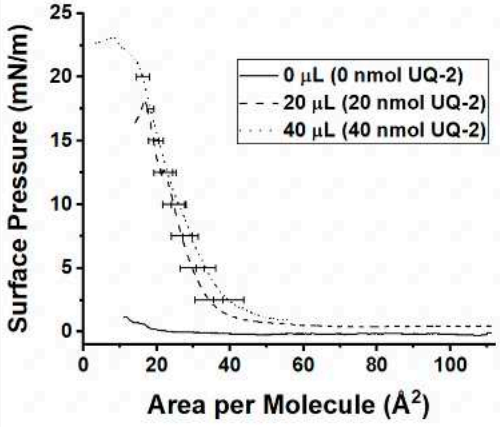

FIGURE 12 | Compression isotherms of different amounts of 1 mM UQ-2. The solid black curve represents pure phosphate buffer with no UQ-2 present, the dashed curve represents an injection of 20 µl of UQ-2, and the dotted curve represents an injection of 40 µl of UQ-2. Curves are the average of at least three measurements. Standard deviations of the area were calculated for every 5 mN/m of surface pressure.

2.7 Interaction of UQ-2 With Langmuir Phospholipid Monolayers

2.7.1 Compression Isotherms of Pure and Mixed Monolayers

Finally, we wanted to understand how UQ-2 interacted with the interface of a phospholipid-based membrane monolayer and compare these results to the RM system. UQ-2 was found to have a collapse pressure of 21 mN/m in this study (**Figure 12**). Our value was obtained by taking the second derivative of area per molecule with respect to surface pressure, with the lowest point representing the collapse pressure. Reported literature values varied widely, with some as high as 35 mN/m and others reporting that UQ-2 dissolved into the subphase (Quinn and Esfahani, 1980; Bernard et al., 2000; Hoyo et al.,

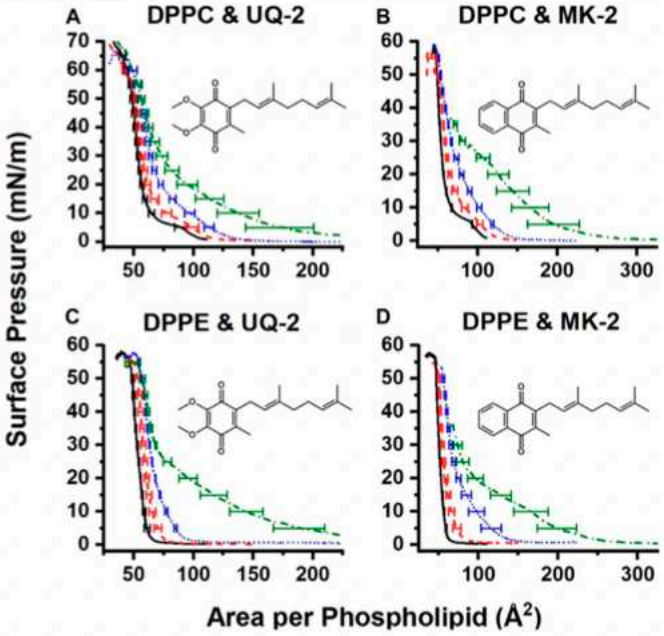

FIGURE 13 | Normalized compression isotherms of mixed monolayers of UQ-2 **(A and C)** or MK-2 **(B and D)** and either DPPC **(A and B)** or DPPE **(C and D)**. Solid black curves represent pure phospholipid monolayers, red dashed curves represent 75:25 lipid:lipoquinone films, blue dotted curves represent 50:50 lipid:lipoquinone films, and green dash-dot curves represent 25:75 lipid:lipoquinone films. Curves are the average of at least three measurements. Error bars are the standard deviation of the area at every 5 mN/m of surface pressure. MK-2 data were reproduced with permission from Koehn et al. 2018b).

2017). These discrepancies may be due to the slightly soluble nature of UQ-2, differences in the composition of the subphase, and even stirring of the subphase.

Pure films of DPPC and DPPE were in line with the literature (Patterson et al., 2016; Hoyo et al., 2017), with DPPC exhibiting its signature gas-liquid transition between 0 and 5 mN/m and its liquid-liquid condensed transition from 5 to 10 mN/m of surface pressure. The gas-liquid transition disappears upon the addition of UQ-2. The normalized 75:25 DPPC:UQ-2 curve does not overlap with the control curve. However, the variability in our measurements makes it impossible to draw a solid conclusion on whether UQ-2 is compressed out of the DPPC monolayer. Regardless, compression modulus analysis showed that increasing amounts of UQ-2 caused the DPPC monolayer to become more elastic (**Supplementary Figure S26**).

Compression isotherms with DPPE did not exhibit a significant difference in collapse pressure, as seen in **Figure 13**. The 25:75 and 50:50 DPPE:UQ-2 monolayers exhibited a liquid condensed phase, which suggests a reorganization of the monolayer. All mixed DPPE monolayers demonstrated at least a 9% increase in area per molecule at physiological surface pressure (Jones and Chapman, 1995) (30–35 mN/m) without the normalized curves overlapping with the control (see **Supplementary Tables S3, S4**). This indicates that UQ-2 is in the interface and spreading the DPPE molecules apart. UQ-2 was not compressed out of the monolayer at physiological surface pressure for DPPE.

2.7.2 Comparison of UQ-2 and MK-2 in Langmuir Monolayers

Interestingly, UQ-2 remains in the DPPC interface at physiological surface pressure, whereas MK-2 was likely to be compressed out. There is also a more distinct hump in the 25:75 DPPC:MK-2 curve at 25 mN/m than that of the 25:75 DPPC:UQ-2. In combination with the fact that mixed DPPC:UQ-2 curves do not overlap the control; we might conclude that UQ-2 is more likely to reside in the interface than MK-2. This is logical, as MK is more hydrophobic than UQ.

Both UQ-2 and MK-2 induce a liquid-condensed phase in DPPE, but it appears with a smaller mole fraction of MK-2 than UQ-2. As with DPPC, UQ-2 is always present in the interface as the mixed monolayers are at least 9% more expanded at physiological surface pressure than the DPPE control. Again, the hydrophobicity of the naphthoquinone headgroup of MK-2 is greater than that of the benzoquinone headgroup of UQ-2 which likely explains these differences. In summary, both UQ-2 and MK-2 associated with the Langmuir monolayer interface, but

UQ-2 resided closer to the interfacial water than MK-2 due to MKs more hydrophobic nature, consistent with the RM model membrane studies.

3 CONCLUSION

UQs and MKs are critical components of the ETS. UQs are found in bacteria, fungi, plants, and mammals, and MKs are mainly found in gram positive bacteria. While the interactions of these electron transport lipids with the membrane-bound protein complexes along the ETS is well-known, surprisingly their exact location and conformation within the membrane is still widely debated. In this study, we determined the location, orientation, and conformation of UQ-2, a truncated, representative analog for native UQ-10, using 1D and 2D NMR spectroscopic methods in organic solution and biological membrane-like environments. We then compared the UQ-2 results to the previously studied MK-2 to understand fundamentally how the class of lipoquinone molecules behave within membranes.

The 1D and 2D NMR studies showed that different solution environments slightly change the observed folded conformation of UQ-2. In all four solvents examined in this study (DMSO, acetonitrile, pyridine, and benzene), UQ-2 was found to adopt a folded, U-shaped conformation with a ~90° dihedral angle about the C2C3Cβ Cγ. On the other hand, UQ-2 adopts a more open U-shaped conformation in the hydrophobic solvents, benzene and pyridine, which documents the fact that the environment will impact the conformation of the UQ-2 side chain. Once we established that UQ-2 folded in solution, we wanted to determine if a folded conformation was also adopted in a membrane-like interface. Using 2D NMR spectroscopy, we determined that UQ-2 interacts similarly to MK-2 with the RM model membrane system. Both UQ-2 and MK-2 adopt a folded, U-shaped conformation but reside at slightly different places in the membrane-like interface. Not surprisingly, and consistent with other studies (Van Cleave et al., 2020; Van Cleave et al., 2021), UQ-2 resides closer to the AOT-water interface than the more hydrophobic MK-2. Both lipoquinone molecules were oriented in a manner that allowed the side chain to fold back over the quinone moiety and be accommodated in the surfactant tails. It appears that regardless of lipoquinone headgroup structure, lipoquinones adopt folded conformations at membrane-like interfaces. Langmuir monolayer studies examining the interaction of UQ-2 with DPPC and DPPE phospholipids supported the results of the RM studies. Both UQ-2 and MK-2 were found to associate with the monolayer water-lipid interface, but MK-2 was more easily compressed out of the interface, which indicates UQ-2 resides closer to the interface than MK-2.

In summary, lipoquinones UQ-2 and MK-2 adopted folded conformations in solution and within membrane-like interfaces. The more polar UQ-2 was found to reside slightly closer to the water-surfactant interface, which was supported by both the RM and Langmuir monolayer studies. It appears that the presence of a lipoquinone headgroup is important for anchoring the lipoquinone in the membrane interface and for allowing the isoprenyl side chain to adopt some variation of a folded conformation that can be accommodated within the lipid tails due to the orientation of the lipoquinone within the interface. Varying the structure of the lipoquinone (UQ vs. MK) only modestly changed the location while residing in the RM interface. However, since lipoquinones are redox-active and the polarity of the headgroup changes upon reduction to the quinol form, structural differences in the headgroup likely facilitate locomotion of headgroup within the interface between membrane-bound enzymes in the ETS (Van Cleave et al., 2020). Taken together, the results of this study and others support a model where the headgroups of the longer, native lipoquinones, such as UQ-10 and MK-9, reside close to the water-lipid interface with the side chains folded but penetrating through the acyl tails into the midplane of the membrane bilayer. The location, orientation, and conformation of lipoquinones are critical for their function in generating cellular energy within membrane ETS and the studies described herein shed light on the behavior of lipoquinones within membrane-like environments.

4 EXPERIMENTAL

4.1 General Materials

The following chemicals were used without further purification for the synthetic work: Ultra-high purity argon (99.9%, Airgas), 3,4,5-trimethoxytoluene (97%, Aldrich), α,α-dichloromethyl methyl ether (98%, Aldrich), Dichloromethane (DCM, Stabilized, 99.9%, Fisher Scientific), $TiCl_4$ (99.9%, Aldrich), *n*-pentane (98%, Merck), Ethyl Acetate (99.9%, Fisher), Diethyl ether (≥99.0%, Merck), $NaHCO_3$ (99.7%, Merck), NaCl (Fisher), Na_2SO_4 (Fisher), Methanol (Aldrich), 30% aq. H_2O_2 solution (Sigma-Aldrich), H_2SO_4 (Fisher), SiO_2 (SiliCycle® SilicaFlash® F60, 43–60 μm 60 Å), 60% NaH dispersion in mineral oil (Aldrich), THF (Fisher), Geranyl Bromide (95%, Aldrich), NH_4Cl (99.7%, Fisher), BF_3 diethyl etherate (≥46.5%, Aldrich), $MgSO_4$ (98%, Merck), Acetonitrile (99.9%, Fisher) and $FeCl_3$ hexahydrate (99.9%, Fisher). The following chemicals were used without further purification for the spectroscopic studies: D_2O (99.9%, Cambridge Isotope Laboratories), d_1-chloroform (99.8%, Cambridge Isotope Laboratories), d_3-acetonitrile (99.8%, Aldrich), d_6-DMSO (99.9%, Cambridge Isotope Laboratories), d_5-pyridine (99.8%, Merck), d_6-benzene (99.5%, Cambridge Isotope Laboratories), isooctane (99.8%, Aldrich), and AOT (≥99%, Aldrich). The following materials were used for the trough work: Sodium phosphate monobasic monohydrate (≥98%) and chloroform (≥99.8%) were purchased from Sigma Aldrich. Sodium phosphate dibasic anhydrous (≥99%) and methanol (≥99.9%) were purchased from Fisher Scientific. 1,2-dipalmitoyl-*sn*-glycero-3-phosphocholine (DPPC, >99%) and 1,2-dipalmitoyl-sn-glycero-3-phosphoethanolamine (DPPE, >99%) were purchased from Avanti Polar Lipids. Distilled deionized water (DDI H_2O) was purified with a Barnsted E-pure system (~18 MΩ-cm).

4.2 General Methods

All reactions were carried out under argon atmosphere unless otherwise noted. All reagents were used as purchased unless otherwise noted. Solvents were dried by passing through an alumina drying column (Solv-Tek Inc.) under argon pressure (DCM, THF, diethyl ether).

4.3 Syntheses

4.3.1 Preparation of 2,3,4-Trimethoxy-6-Methylbenzaldehyde (2)

To a dry 500 ml round bottom Schlenk flask was added dry dichloromethane (DCM) (150 ml) followed by 3,4,5-trimethoxytoluene **1** (9.97 g, 54.7 mmol) and α,α-dichloromethyl methyl ether (12.58 g, 109.5 mmol, 2 eq.) and then cooled to 0°C. Then, $TiCl_4$ (273.6 mmol, 137 ml, 2.0 M in dry DCM, 2.5 eq. to α,α-dichloromethyl methyl ether) was added dropwise over 30 min via a 250 ml addition funnel under argon at 0°C. After addition was complete, the red reaction mixture was stirred at ambient temperature for 20 h. Thin layer chromatography (TLC) (9:1 *n*-pentane/EtOAc) showed the reaction was complete. The reaction was then very slowly quenched with ice until the reaction color turned light blue-gray. The DCM was removed under reduced pressure at ambient temperature and the resulting off-yellow liquid was extracted with diethyl ether (3 × 100 ml). The combined organic extracts were washed with sat. $NaHCO_3$ (200 ml), washed with brine (3 × 100 ml), dried over anhydrous Na_2SO_4, and then the solvent was removed under reduced pressure at ambient temperature. The product was dried under reduced pressure (~125 Torr) for 1 h, which yielded an off-white crystalline solid (11.40 g, 54.2 mmol, 99.1%) that was pure. ^{1}H NMR (400 MHz, $CDCl_3$) δ: 10.40 (s, 1H), 6.50 (s, 1H), 3.98 (s, 3H), 3.92 (s, 3H), 3.86 (s, 3H), 2.56 (s, 3H). ^{13}C NMR (101 MHz, $CDCl_3$) δ: 191.18, 158.46, 157.78, 139.80, 138.26, 121.48, 110.53, 62.50, 61.12, 56.15, 21.91. HRMS (ESI, OTOF) m/z: $[(M + H)^+]$ Calcd for $C_{11}H_{15}O_4$ 211.0965; Found 211.0965.

4.3.2 Preparation of 2,3,4-Trimethoxy-6-Methylphenol (3)

To a 250 ml round bottom Schlenk flask was added 2,3,4-trimethoxy-6-methylbenzaldehyde **2** (11.37 g, 54.1 mmol), MeOH (110 ml), and 30% aq. H_2O_2 solution (7.97 g, 70.3 mmol, 1.3 eq.). Then, conc. H_2SO_4 (1.08 ml) was added dropwise resulting in a red-orange reaction mixture. After 2.5 h of stirring at ambient temperature under argon, the ^{1}H NMR spectrum showed no aldehyde peak present. The reaction mixture was poured into sat. $NaHCO_3$ (100 ml) and then extracted with DCM (3 × 100 ml). The combined organic extracts were washed sat. $NaHCO_3$ (100 ml), washed with brine (100 ml), dried over anhydrous Na_2SO_4, and the solvent was evaporated under reduced pressure (~125 Torr) at ambient temperature to yield 10.55 g crude red oil. The product was then purified by flash column chromatography (7:1 *n*-pentane/EtOAc, 600 ml SiO_2, 70 mm column) to yield the desired product as an off-white crystalline solid (9.75 g, 49.2 mmol, 90.9%). ^{1}H NMR ($CDCl_3$) δ: 6.43 (s, 1H), 5.43 (s, 1H), 3.95 (s, 3H), 3.86 (s, 3H), 3.80 (s, 3H), 2.21 (s, 3H). ^{13}C NMR (101 MHz, $CDCl_3$) δ:146.17, 141.24, 140.14, 140.09, 118.08, 109.63, 61.34, 61.11, 56.75, 15.65. HRMS (ESI, OTOF) m/z: $[(M + H)^+]$ Calcd for $C_{10}H_{15}O_4$ 199.0965; Found 199.0951.

4.3.3 Preparation of Geranyl 2,3,4-Trimethoxy-6-Methylphenyl Ether (6)

NaH (2.95 g of 60% NaH dispersion in mineral oil washed with *n*-pentane that was first dried over activated neutral alumina, 73.8 mmol) was added to a dry 500 ml round bottom Schlenk flask containing a solution of 2,3,4-trimethoxy-6-methylphenol **3** (9.75 g, 49.2 mmol) dissolved in dry THF (150 ml). The mixture was stirred at ambient temperature for 35 min. The solvent was removed under reduced pressure at 25°C until an off-white powder was obtained. To a dry 500 ml round-bottom Schlenk flask was added the crude powder dissolved in anhydrous THF (75 ml) and then the mixture was cooled in an ice-H_2O bath. Then, a solution of geranyl bromide (16.02 g, 73.8 mmol, 1.5 eq.) in dry THF (75 ml) was added dropwise over 15 min via an addition funnel under argon. The mixture was then warmed to ambient temperature and stirred for 21.5 h under argon. The resulting yellow reaction mixture was slowly quenched with 5% aq. NH_4Cl solution (100 ml) and then extracted with diethyl ether (3 × 100 ml). The combined yellow organic extracts were washed with sat. $NaHCO_3$ (100 ml), washed with brine (100 ml), dried over anhydrous Na_2SO_4, and then the solvent was removed under reduced pressure (~125 Torr) at ambient temperature to yield 22.4 g crude yellow oil. The crude oil was purified by flash column chromatography (9:1 *n*-pentane/EtOAc, 1,200 ml SiO_2, 70 mm column) to yield a light-yellow oil (9.75 g, 29.2 mmol, 59.4%). ^{1}H NMR ($CDCl_3$) δ: 6.44 (s, 1H), 5.55 (t, J = 7.2 Hz, 1H), 5.10 (t, J = 6.3 Hz, 1H), 4.45 (d, J = 7.1 Hz, 2H), 3.93 (s, 3H), 3.86 (s, 3H), 3.81 (s, 3H), 2.22 (s, 3H), 2.04–2.12 (m, 4H), 1.69 (s, 6H), 1.61 (s, 3H). ^{13}C NMR (101 MHz, $CDCl_3$) δ: 149.19, 147.42, 144.52, 141.48, 140.97, 131.81, 126.54, 124.11, 120.48, 108.45, 69.74, 61.37, 61.23, 56.28, 39.79, 26.53, 25.83, 17.83, 16.47, 16.43. HRMS (ESI, QTOF) m/z: $[(M + H)^+]$ Calcd for $C_{20}H_{31}O_4$ 335.2217; Found 335.2220.

4.3.4 Preparation of 5-Geranyl-2,3,4-Trimethoxy-6-Methyl-Phenol (7)

To a 500 ml round bottom Schlenk flask was added geranyl 2,3,4-trimethoxy-6-methylphenyl ether **6** (9.73 g, 29.1 mmol) dissolved in dry diethyl ether (120 ml). Then, the mixture was treated with fresh BF_3 etherate (36.9 ml, 46.5% BF_3 etherate solution, 291.0 mmol, 10 eq.) added dropwise over 5 min and then stirred under argon at ambient temperature for 30 min. After exactly 30 min, the brown colored reaction was quenched with sat. NaCl (100 ml) very slowly over 8 min and then the mixture was extracted with diethyl ether (3 × 100 ml). The combined light yellow organic extracts were washed with sat. $NaHCO_3$ (50 ml, releases CO_2), washed with brine (100 ml), dried over anhydrous $MgSO_4$, vacuum filtered, and then the solvent was removed under reduced pressure (~125 Torr) at ambient temperature to yield 9.41 g crude brown oil. The product was purified by flash column chromatography (9:1 *n*-pentane/EtOAc, 800 ml SiO_2, 70 mm) to yield the desired product (4.67 g, 14.0 mmol, 48.1%) as a light-yellow oil. ^{1}H NMR

($CDCl_3$) δ: 5.60 (s, 1H), 5.05 (q, J = 6.5, 2H), 3.93 (s, 3H), 3.91 (s, 3H), 3.75 (s, 3H), 3.33 (d, J = 6.5, 2H), 2.13 (s, 3H), 2.07 (q, J = 7.2, 2H), 1.98 (m, 2H), 1.76 (s, 3H), 1.65 (s 3H), 1.57 (s, 3H). ^{13}C NMR (101 MHz, $CDCl_3$) δ: 144.49, 143.61, 143.44, 137.85, 135.12, 131.48, 129.82, 124.43, 123.18, 117.68, 61.44, 61.32, 60.92, 39.83, 26.78, 25, 82, 25.66, 17.82, 16.34, 11.48. HRMS (ESI, QTOF) m/z: [(M + Na)$^+$] Calcd for $C_{20}H_{31}O_4Na$ 357.2036; Found 357.2004.

4.3.5 Preparation of Ubiquinone-2 (8)

To a 50 ml round bottom flask was added 5-geranyl-2,3,4-trimethoxy-6-methylphenol 7 (0.137 g, 0.410 mmol), followed by DCM (2 ml) and ACN (2 ml) and then cooled to 0°C. An excess of $FeCl_3$ (1.11 g, 4.10 mmol, 10 eq.) dissolved in ACN (4 ml) was then added. The open atmosphere mixture was stirred at 0°C for 35 min. Then, DDI H_2O (30 ml) and sat. aq. $NaHCO_3$ (30 ml) were added to the orange reaction mixture and then extracted with diethyl ether (3 × 100 ml). The combined organic extracts were washed with sat. $NaHCO_3$ (50 ml), washed with brine (50 ml), dried over anhydrous Na_2SO_4, and then the solvent was removed under reduced pressure at ambient temperature to yield UQ-2 as a red oil and practically pure (0.125 g, 0.393 mmol, 95.9%). ^{1}H NMR ($CDCl_3$) δ: 5.03 (t, J = 6.8, 1H), 4.92 (t, J = 7.0, 1H), 3.99 (s, 3H), 3.98 (s, 3H), 3.18 (d, J = 7.0, 2H), 2.01 (m, 8H), 1.72 (s, 3H), 1.64 (s, 3H), 1.57 (s, 3H). ^{13}C NMR (101 MHz, $CDCl_3$) δ: 184.91, 184.05, 144.53, 144.38, 141.84, 139.01, 137.66, 131.68, 124.13, 199.08, 61.28, 39.82, 26.66, 25.81, 25.43, 17.82, 16.43, 12.07. HRMS (DART) m/z: [(M + H)$^+$] Calcd for $C_{19}H_{27}O_4$ 319.1904; Found 319.1935.

4.4 Mass Spectrometry

High resolution mass spectrometry (HRMS) experiments were carried out using one of the following instruments: 1) an Agilent 6220 TOF LC/MS ("OTOF") interfaced to an Agilent 1200 HPLC, 2) a Maxis QTOF ("QTOF") with electrospray (ESI) mode, and 3) a Maxis QTOF in positive DART mode (DART) using jeffamine as an internal calibration standard.

4.5 NMR Spectroscopic Studies

1D and 2D ^{1}H studies were carried out both in organic solvents and a RM system. ^{1}H and ^{13}C spectra were recorded using either a Varian Model MR400 or Model Inova400 operating at 400 and 101 MHz, respectively. Chemical shift values (δ) are reported in ppm and referenced against the internal solvent peaks in ^{1}H NMR ($CDCl_3$, δ at 7.26 ppm; d_3-acetonitrile δ at 1.94 ppm; d_6-DMSO, δ at 2.50 ppm; d_6-benzene, δ at 7.16 ppm; d_5-pyridine, δ at 8.74 ppm; D_2O, δ at 4.79 ppm) and in ^{13}C NMR (d_6-DMSO, δ at 39.52 ppm; d_6-benzene, δ at 128.06 ppm). All NMR spectra were recorded at either 22°C or 26°C. When samples were prepared for RM NMR experiments, deuterium oxide was used instead of H_2O, and the pH was adjusted to consider the presence of deuterium (pD = 0.4 + pH) (Samart et al., 2014).

For 1D and 2D NMR spectroscopic studies, a sample for analytical characterization of UQ-2 was prepared by using normal phase preparative thin layer chromatography (TLC) (10:1 *n*-pentane/EtOAc). First, ~10 mg of UQ-2 (dissolved in minimal amount of DCM) was loaded onto a preparative TLC plate and then eluted (10:1 *n*-pentane/EtOAc, 45 min). The plate was briefly dried of eluent solvent and eluted a second time (10:1 *n*-pentane/EtOAc, 45 min). The orange band was illuminated under UV light and while illuminated, the band was divided into a top half and a bottom half. The bottom half was carefully removed with a razor blade, extracted with DCM, filtered through a disposable Pasteur pipette filled with glass wool (pre-rinsed with DCM) and concentrated under reduced pressure at ambient temperature to provide 6 mg of UQ-2 as a red oil for NMR spectroscopic studies.

4.5.1 Solution 1D ^{1}H NMR Spectroscopic Studies of UQ-2

Samples were prepared by dissolving 5.0 mg of UQ-2 in 0.5 ml of either d_1-chloroform, d_6-DMSO, d_5-pyridine, d_3-acetonitrile, and d_6-benzene, respectively. The NMR instrument was locked onto the respective deuterium signal in the deuterated solvent used. NMR spectra were then collected using 32 scans for each sample. The data was processed using MestReNova NMR processing software version 10.0.1. The spectra were manually phased and then the baseline was corrected using a Bernstein Polynomial Fit (polynomial order 3). The obtained spectra were referenced to the internal solvent peak.

4.5.2 Sample Preparation for ^{1}H-^{1}H 2D NOESY and ^{1}H-^{1}H 2D ROESY NMR Spectroscopic Studies of UQ-2

To prepare the samples in d_5-pyridine, d_3-acetonitrile, and d_6-DMSO, 3.2 mg of UQ-2 was dissolved in 0.5 ml of solvent to yield a 20 mM solution of UQ-2. The NMR tubes containing the UQ-2 solution were purged with argon prior to data collection. To prepare a 100 mM solution of UQ-2 in $CDCl_3$, 15.9 mg of UQ-2 was dissolved in 0.5 ml $CDCl_3$. To prepare a 20 mM sample, 3.2 mg of UQ-2 was dissolved in 0.5 ml of each respective solvent (d_1-chloroform, d_6-DMSO, d_5-pyridine, d_3-acetonitrile, and d_6-benzene).

4.5.3 ^{1}H-^{1}H 2D NOESY and ^{1}H-^{1}H 2D ROESY NMR Spectroscopic Solution Experiments of UQ-2

^{1}H-^{1}H 2D NOESY NMR and ^{1}H-^{1}H 2D ROESY NMR spectroscopic experiments were conducted using a 400 MHz Varian MR400 NMR at 26°C. A standard NOESY pulse sequence was used consisting of 256 transients with 16 scans in the f1 domain using a 500 ms mixing time, 45° pulse angle, and a 1.5 s relaxation delay. A standard ROESYAD pulse sequence was used consisting of 256 transients with 16 scans in the f1 domain using a 400 ms mixing time, 45° pulse angle, and a 2.0 s relaxation delay. The NMR was locked onto either d_5-pyridine, d_6-benzene, d_3-acetonitrile, or d_6-DMSO. The resulting spectrum was processed using MestReNova NMR software version 10.0.1 (see **Supplementary Material** for details). The spectra were referenced to the internal solvent peak.

4.5.4 Sample Preparation for RM NMR Spectroscopic Studies of UQ-2

A 0.50 M AOT stock solution was made by dissolving AOT (5.56 g, 12.5 mmol) in isooctane (25.0 ml). Empty RMs were made by mixing 0.50 M AOT stock solution with a D_2O water pool, and then vortexed. UQ-2 RMs were made in a similar matter. The only difference being a

14.3 mM for UQ-2 stock solution was made by dissolving 45.4 mg of UQ-2 in 10.0 ml of 0.50 M AOT/isooctane solution. The RMs were then prepared using the UQ-2 stock solution. First, 2.0 ml samples were made using specific amounts of the 14.3 mM UQ-2 stock solution and then diluting the sample with the 500 mM AOT/isooctane solution. From the 2.0 ml solutions, 1.0 ml RM samples were prepared using the designated amounts of 2.0 ml sample and then adding the proper amount of D_2O with pH 7.0 (see **Section 4.2** for pH measurements) for UQ-2 to form the desired size RM. The samples were then vortexed until clear. The overall concentrations for 1.0 ml UQ-2 RM samples are as follows: w_0 4, 13.8 mM; w_0 8, 6.4 mM; w_0 12, 3.5 mM; w_0 16, 2.0 mM; and w_0 20, 1.4 mM.

4.5.5 1D ^{1}H NMR Spectroscopic Studies of AOT/Isooctane RMs Containing UQ-2

NMR spectra of various size RMs and in isooctane and D_2O were obtained using a Varian Inova 400 MHz instrument at 22°C using routine parameters (pulse angle: 45°, relaxation delay of 1 s) using 64 scans. The NMR instrument was locked onto 10% D_2O signal for the RM samples and D_2O for the sample in D_2O. The 1D ^{1}H spectra of UQ-2 in isooctane were doped with 5% d_6-benzene for the NMR instrument to lock onto and to achieve properly shimmed spectra. The spectral data was processed using MestReNova NMR processing software version 10.0.1. The spectra were manually phased and then the baseline was corrected using a multipoint baseline correction (cubic splines). The spectrum in D_2O was referenced to the internal D_2O peak and the spectra in isooctane and RM samples were referenced to the isooctane methyl peak (0.904 ppm) as previously reported (Samart et al., 2014).

4.5.6 Sample Preparation for ^{1}H-^{1}H 2D NOESY and ROESY NMR Spectroscopic Studies of UQ-2 in AOT/Isooctane RMs

A 0.50 M AOT stock solution was made by dissolving AOT (5.56 g, 12.5 mmol) in isooctane (25.0 ml). A 1 ml stock solution of 112 mM UQ-2 in AOT/isooctane was made by dissolving 35.7 mg of UQ-2 in 1 ml isooctane/AOT stock solution. To make a w_0 12 RM, 893 µl of 112 mM UQ-2 AOT/isooctane stock solution and 107 µl of D_2O at pH 7 were mixed together and then vortexed. This final mixture results in a w_0 12 RM microemulsion with an overall concentration of UQ-2 being ~100 mM (~29 molecules per RM).

4.5.7 ^{1}H-^{1}H 2D NOESY NMR Spectroscopic Studies of UQ-2 in a w_0 12 AOT/Isooctane RM

2D NMR spectra were obtained using similar conditions used previously (Peters et al., 2016; Koehn et al., 2018b) using a 400 MHz Varian NMR at 26°C. A standard NOESY pulse sequence was used consisting of 256 transients with 16 scans in the f1 direction using a 200 ms mixing time, 45° pulse angle, and a relaxation delay of 1.5 s. The NMR instrument was locked onto 10% D_2O signal. The resulting spectrum was processed using MestReNova NMR software version 10.0.1. (see **Supplementary Material** for details). The spectrum was referenced to the isooctane methyl peak at 0.904 ppm as previously reported (Samart et al., 2014; Koehn et al., 2018a). The 3D structure illustration within a RM was drawn using ChemBioD Ultra 12.0 and ChemBio3D Ultra 12.0 based on spectral parameters described under results.

4.6 Langmuir Monolayer Compression Isotherm Methods

4.6.1 Instrument and Cleaning

All Langmuir monolayer studies were performed on a Kibron µTrough XS equipped with a Teflon ribbon barrier (hydrophobic) as described previously (Van Cleave et al., 2021). The trough bed was cleaned between runs by scrubbing three times with isopropanol, then scrubbing three times with absolute EtOH, and then rinsing with DDI H_2O. The ribbon was cleaned by a rinse with isopropanol, a rinse with absolute EtOH, and then a rinse with DDI H_2O.

4.6.2 Preparation of the Subphase

The subphase consisted of approximately 50 ml of 20 mM sodium phosphate buffer (pH 7.40 ± 0.02). The pH was adjusted using 1.0 M HCl or NaOH. The subphase surface was cleaned with vacuum aspiration until the surface pressure remained at 0.0 ± 0.5 mN/m throughout a quick compression.

4.6.3 Preparation of Lipid Solutions

Phospholipid solutions were prepared by dissolving powdered lipid (0.018 g DPPC, 0.017 g DPPE) into 25 ml of 9:1 chloroform/MeOH (v/v) to yield a 1 mM phospholipid stock solution. A 1 mM UQ-2 solution was prepared the same as the phospholipids, but with 0.0016 g UQ-2 dissolved into 5 ml of the chloroform/methanol solution. Stock solutions were stored at −20°C. Mixed monolayer were prepared immediately before experiments by adding appropriate amount of phospholipid stock and UQ-2 stock to a small glass vial and vortexing for ~30 s. Mixed monolayers consisted of 25:72, 50:50, and 75:25 UQ-2:phospholipid (mol fraction).

4.6.4 Formation and Compression of Monolayers

Monolayers consisted of pure DPPC, pure DPPE, pure UQ-2, or varying phospholipid:UQ-2 molar fractions (25:75, 50:50, 75:25). Films were prepared by adding 20 µl lipid stock solutions or mixtures (40 µl were used for UQ-2 and 75:25 UQ-2:phospholipid to obtain full compression) drop-wise to the surface of the subphase and were equilibrated for 15 min. Monolayers were compressed at a speed of 10 mm/min (5 mm/min from two sides). Surface pressure measurements were made via a modified Wilhelmy plate method where a wire probe was used instead of a plate. Surface pressure was calculated from surface tension with **Eq. 1**, where π is surface pressure (mN/m), γ_o is the surface tension of the subphase (72.8 mN/m), and γ is the surface tension after the addition of the monolayer.

$$\pi = \gamma_o - \gamma. \quad (1)$$

The averages of triplicate isotherms were worked up in Excel. The averages were then normalized to the amount of phospholipid according to **Eq. 2**, where A_N is the normalized area per phospholipid (Å^2), A is the experimental area per molecule (Å^2) (Van Cleave et al., 2021), and x is the mol fraction of phospholipid (0.25, 0.5, or 0.75). This method of analysis was developed from a previous study (Quinn and Esfahani, 1980).

$$A_N = A(x^{-1}). \quad (2)$$

Normalized isotherms were plotted with Origin 2021. Reported error bars are the standard deviations of the experimental area.

DATA AVAILABILITY STATEMENT

The original contributions presented in the study are included in the article/**Supplementary Material**, further inquiries can be directed to the corresponding author.

AUTHOR CONTRIBUTIONS

Project conception JK; Project management DC (Crans); Experimental design JK, DC (Crans), CC; Experiments JK, JI, CC, KK, HM; Verification MB-T, JK, DC (Crans); Manuscript preparation MB-T, JK, DC (Crans); Editing MB-T, JK, DC (Crans), KK, CC, HM; Preparation of grant funding DC (Crans) and DC (Crick). All authors helped edit and have approved the submitted manuscript.

FUNDING

DC (Crans) and DC (Crick) thank NSF for funding (Grant #CHE-1709564). DC (Crans) also thanks the Arthur Cope Foundation administered by the American Chemical Society for partial support.

ACKNOWLEDGMENTS

The authors wish to thank the Analytical Resources Core at Colorado State University for instrument access, training, and assistance with sample analysis. Additionally, the authors would like to thank Drs. Michele Mailhot and Christopher D. Rithner for experimental consultation for NMR spectroscopy.

SUPPLEMENTARY MATERIAL

The Supplementary Material for this article can be found online at: https://www.frontiersin.org/articles/10.3389/fchem.2022.827530/full#supplementary-material

REFERENCES

Afri, M., Ehrenberg, B., Talmon, Y., Schmidt, J., Cohen, Y., and Frimer, A. A. (2004). Active Oxygen Chemistry within the Liposomal Bilayer. *Chem. Phys. Lipids* 131, 107–121. doi:10.1016/j.chemphyslip.2004.04.007

Bernard, S., Roche, Y., Etienne, F., and Peretti, P. (2000). Interaction between Ubiquinones and Dipalmitoylphosphatidylcholine in Mixed Langmuir Monolayers. *Mol. Crystals Liquid Crystals Sci. Techn. Section A. Mol. Crystals Liquid Crystals* 338, 207–221. doi:10.1080/10587250008024431

Bovicelli, P., Borioni, G., Fabbrini, D., and Barontini, M. (2008). New Efficient Synthesis of Ubiquinones. *Synth. Commun.* 38, 391–400. doi:10.1080/00397910701771066

Ceccarelli, M., Procacci, P., and Marchi, M. (2003). Anab Initio Force Field for the Cofactors of Bacterial Photosynthesis. *J. Comput. Chem.* 24, 129–142. doi:10.1002/jcc.10198

Chazotte, B., Wu, E.-S., and Hackenbrock, C. R. (1991). The Mobility of a Fluorescent Ubiquinone in Model Lipid Membranes. Relevance to Mitochondrial Electron Transport. *Biochim. Biophys. Acta (Bba) - Bioenerg.* 1058, 400–409. doi:10.1016/s0005-2728(05)80136-7

Cornell, B. A., Keniry, M. A., Post, A., Robertson, R. N., Weir, L. E., and Westerman, P. W. (1987). Location and Activity of Ubiquinone 10 and Ubiquinone Analogs in Model and Biological Membranes. *Biochemistry* 26, 7702–7707. doi:10.1021/bi00398a025

de Jong, D. H., Liguori, N., van den Berg, T., Arnarez, C., Periole, X., and Marrink, S. J. (2015). Atomistic and Coarse Grain Topologies for the Cofactors Associated with the Photosystem II Core Complex. *J. Phys. Chem. B* 119, 7791–7803. doi:10.1021/acs.jpcb.5b00809

Di Bernardo, S., Fato, R., Casadio, R., Fariselli, P., and Lenaz, G. (1998). A High Diffusion Coefficient for Coenzyme Q10might Be Related to a Folded Structure. *FEBS Lett.* 426, 77–80. doi:10.1016/s0014-5793(98)00313-5

Feng, S., Wang, R., Pastor, R. W., Klauda, J. B., and Im, W. (2021). Location and Conformational Ensemble of Menaquinone and Menaquinol, and Protein-Lipid Modulations in Archaeal Membranes. *J. Phys. Chem. B* 125, 4714–4725. doi:10.1021/acs.jpcb.1c01930

Galassi, V. V., and Arantes, G. M. (2015). Partition, Orientation and Mobility of Ubiquinones in a Lipid Bilayer. *Biochim. Biophys. Acta (Bba) - Bioenerg.* 1847, 1560–1573. doi:10.1016/j.bbabio.2015.08.001

Gómez-Murcia, V., Torrecillas, A., De Godos, A. M., Corbalán-García, S., and Gómez-Fernández, J. C. (2016). Both idebenone and Idebenol Are Localized Near the Lipid-Water Interface of the Membrane and Increase its Fluidity. *Biochim. Biophys. Acta (Bba) - Biomembranes* 1858, 1071–1081. doi:10.1016/j.bbamem.2016.02.034

Gupta, C., Khaniya, U., Chan, C. K., Dehez, F., Shekhar, M., Gunner, M. R., et al. (2020). Charge Transfer and Chemo-Mechanical Coupling in Respiratory Complex I. *J. Am. Chem. Soc.* 142, 9220–9230. doi:10.1021/jacs.9b13450

Hauss, T., Dante, S., Haines, T. H., and Dencher, N. A. (2005). Localization of Coenzyme Q10 in the center of a Deuterated Lipid Membrane by Neutron Diffraction. *Biochim. Biophys. Acta* 1710, 57–62. doi:10.1016/j.bbabio.2005.08.007

Hoyo, J., Guaus, E., and Torrent-Burgués, J. (2017). Tuning Ubiquinone Position in Biomimetic Monolayer Membranes. *Eur. Phys. J. E* 40, 62. doi:10.1140/epje/i2017-11552-2

Ismail, A., Leroux, V., Smadja, M., Gonzalez, L., Lombard, M., Pierrel, F., et al. (2016). Coenzyme Q Biosynthesis: Evidence for a Substrate Access Channel in the FAD-dependent Monooxygenase Coq6. *Plos Comput. Biol.* 12, e1004690–27. doi:10.1371/journal.pcbi.1004690

Joela, H., Kasa, S., Lehtovuori, P., Bech, M., Mellikov, E., Niinistö, L., et al. (1997). EPR, ENDOR and TRIPLE Resonance and MO Studies on Ubiquinones (Q-N): Comparison of Radical Anions and Cations of Coenzymes Q-10 and Q-6 with the Model Compounds Q-2 and Q-0. *Acta Chem. Scand.* 51, 233–241. doi:10.3891/acta.chem.scand.51-0233

Jones, C. R., Butts, C. P., and Harvey, J. N. (2011). Accuracy in Determining Interproton Distances Using Nuclear Overhauser Effect Data from a Flexible Molecule. *Beilstein J. Org. Chem.* 7, 145–150. doi:10.3762/bjoc.7.20

Jones, M. N., and Chapman, D. (1995). *Micelles, Monolayers, and Biomembranes*. New York: Wiley-Liss, Inc.

Kaurola, P., Sharma, V., Vonk, A., Vattulainen, I., and Róg, T. (2016). Distribution and Dynamics of Quinones in the Lipid Bilayer Mimicking the Inner Membrane of Mitochondria. *Biochim. Biophys. Acta (Bba) - Biomembranes* 1858, 2116–2122. doi:10.1016/j.bbamem.2016.06.016

Kawamukai, M. (2018). Biosynthesis and Applications of Prenylquinones. *Biosci. Biotechnol. Biochem.* 82, 963–977.

Kingsley, P. B., and Feigenson, G. W. (1981). 1H-NMR Study of the Location and Motion of Ubiquinones in Perdeuterated Phosphatidylcholine Bilayers. *Biochim. Biophys. Acta (Bba) - Bioenerg.* 635, 602–618. doi:10.1016/0005-2728(81)90117-1

Koehn, J. T., Beuning, C. N., Peters, B. J., Dellinger, S. K., Van Cleave, C., Crick, D. C., et al. (2019). Investigating Substrate Analogues for Mycobacterial MenJ: Truncated and Partially Saturated Menaquinones. *Biochemistry* 58, 1596–1615. doi:10.1021/acs.biochem.9b00007

Koehn, J. T., Crick, D. C., and Crans, D. C. (2018a). Synthesis and Characterization of Partially and Fully Saturated Menaquinone Derivatives. *ACS Omega* 3, 14889–14901. doi:10.1021/acsomega.8b02620

Koehn, J. T., Magallanes, E. S., Peters, B. J., Beuning, C. N., Haase, A. A., Zhu, M. J., et al. (2018b). A Synthetic Isoprenoid Lipoquinone, Menaquinone-2, Adopts a Folded Conformation in Solution and at a Model Membrane Interface. *J. Org. Chem.* 83, 275–288. doi:10.1021/acs.joc.7b02649

Lenaz, G., Samorì, B., Fato, R., Battino, M., Parenti Castelli, G., and Domini, I. (1992). Localization and Preferred Orientations of Ubiquinone Homologs in Model Bilayers. *Biochem. Cel Biol* 70, 504–514. doi:10.1139/o92-078

Lenaz, G., Fato, R., Di Bernardo, S., Jarreta, D., Costa, A., Genova, M. L., et al. (1999). Localization and Mobility of Coenzyme Q in Lipid Bilayers and Membranes. *BioFactors* 9, 87–93. doi:10.1002/biof.5520090202

Lu, L., and Chen, F. (2004). A Novel and Convenient Synthesis of Coenzyme Q1. *Synth. Commun.* 34, 4049–4053. doi:10.1081/scc-200036578

Maitra, A. (1984). Determination of Size Parameters of Water-Aerosol OT-Oil Reverse Micelles from Their Nuclear Magnetic Resonance Data. *J. Phys. Chem.* 88, 5122–5125. doi:10.1021/j150665a064

Matsumoto, M., Kobayashi, K., and Hotta, Y. (1984). Acid-Catalyzed Oxidation of Benzaldehydes to Phenols by Hydrogen Peroxide. *J. Org. Chem.* 49, 4740–4741. doi:10.1021/jo00198a037

Metz, G., Howard, K. P., van Liemt, W. B. S., Prestegard, J. H., Lugtenburg, J., and Smith, S. O. (1995). NMR Studies of Ubiquinone Location in Oriented Model Membranes: Evidence for a Single Motionally-Averaged Population. *J. Am. Chem. Soc.* 117, 564–565. doi:10.1021/ja00106a078

Michaelis, L., and Moore, M. J. (1985). Location of Ubiquinone-10 (CoQ-10) in Phospholipid Vesicles. *Biochim. Biophys. Acta* 821, 121–129. doi:10.1016/0005-2736(85)90162-2

Murgolo, N. J., Patel, A., Stivala, S. S., and Wong, T. K. (1989). The Conformation of Dolichol. *Biochemistry* 28, 253–260. doi:10.1021/bi00427a035

Nilsson, J. A., Eriksson, L. A., and Laaksonen, A. (2001a). Molecular Dynamics Simulations of Plastoquinone in Solution. *Mol. Phys.* 99, 247–253. doi:10.1080/00268970010010204

Nilsson, J. A., Lyubartsev, A., Eriksson, L. A., and Laaksonen, A. (2001b). Molecular Dynamics Simulations of Ubiquinone; a Survey over Torsional Potentials and Hydrogen Bonds. *Mol. Phys.* 99, 1795–1804. doi:10.1080/00268970110072403

Nowicka, B., and Kruk, J. (2010). Occurrence, Biosynthesis and Function of Isoprenoid Quinones. *Biochim. Biophys. Acta (Bba) - Bioenerg.* 1797, 1587–1605. doi:10.1016/j.bbabio.2010.06.007

Ondarroa, M., and Quinn, P. J. (1986). Proton Magnetic Resonance Spectroscopic Studies of the Interaction of Ubiquinone-10 with Phospholipid Model Membranes. *Eur. J. Biochem.* 155, 353–361. doi:10.1111/j.1432-1033.1986.tb09498.x

Patterson, M., Vogel, H. J., and Prenner, E. J. (2016). Biophysical Characterization of Monofilm Model Systems Composed of Selected Tear Film Phospholipids. *Biochim. Biophys. Acta (Bba) - Biomembranes* 1858, 403–414. doi:10.1016/j.bbamem.2015.11.025

Peters, B. J., Groninger, A. S., Fontes, F. L., Crick, D. C., and Crans, D. C. (2016). Differences in Interactions of Benzoic Acid and Benzoate with Interfaces. *Langmuir* 32, 9451–9459. doi:10.1021/acs.langmuir.6b02073

Quinn, P. J., and Esfahani, M. A. (1980). Ubiquinones Have Surface-Active Properties Suited to Transport Electrons and Protons across Membranes. *Biochem. J.* 185, 715–722. doi:10.1042/bj1850715

Quirk, A., Lardner, M. J., Tun, Z., and Burgess, I. J. (2016). Surface-Enhanced Infrared Spectroscopy and Neutron Reflectivity Studies of Ubiquinone in Hybrid Bilayer Membranes under Potential Control. *Langmuir* 32, 2225–2235. doi:10.1021/acs.langmuir.5b04263

Salgado, J., Villalain, J., and Gomez-Fernandez, J. C. (1993). Magic Angle Spinning 13C-NMR Spin-Lattice Relaxation Study of the Location and Effects of A-Tocopherol, Ubiquinone-10, and Ubiquinol-10 in Unsonicated Model Membranes. *Eur. Biophys. J.* 22, 151–155. doi:10.1007/bf00196919

Samart, N., Beuning, C. N., Haller, K. J., Rithner, C. D., and Crans, D. C. (2014). Interaction of a Biguanide Compound with Membrane Model Interface Systems: Probing the Properties of Antimalaria and Antidiabetic Compounds. *Langmuir* 30, 8697–8706. doi:10.1021/la501600s

Seif Eddine, M., Biaso, F., Rendon, J., Pilet, E., Guigliarelli, B., Magalon, A., et al. (2020). 1,2H Hyperfine Spectroscopy and DFT Modeling Unveil the Demethylmenasemiquinone Binding Mode to *E. coli* Nitrate Reductase A (NarGHI). *Biochim. Biophys. Acta (Bba) - Bioenerg.* 1861, 148203. doi:10.1016/j.bbabio.2020.148203

Singharoy, A., Maffeo, C., Delgado-Magnero, K. H., Swainsbury, D. J. K., Sener, M., Kleinekathöfer, U., et al. (2020). Atoms to Phenotypes: Molecular Design Principles of Cellular Energy Metabolism. *Cell* 179, 1098–e23. doi:10.1016/j.cell.2019.10.021

Söderhäll, J. A., and Laaksonen, A. (2001). Molecular Dynamics Simulations of Ubiquinone inside a Lipid Bilayer. *J. Phys. Chem. B* 105, 9308–9315. doi:10.1021/jp011001w

Stidham, M. A., Mcintosh, T. J., and Siedow, J. N. (1984). On the Localization of Ubiquinone in Phosphatidylcholine Bilayers. *Biochim. Biophys. Acta (Bba) - Bioenerg.* 767, 423–431. doi:10.1016/0005-2728(84)90040-9

Teixeira, M. H., and Arantes, G. M. (2019). Effects of Lipid Composition on Membrane Distribution and Permeability of Natural Quinones. *RSC Adv.* 9, 16892–16899. doi:10.1039/c9ra01681c

Tekin, E. D., and Erkoc, S. (2010). Structural and Electronic Features of the Ubiquinone and Ubiquinol Molecules: Molecular Dynamics and Quantum Chemical Treatments. *Mol. Simulation* 36, 763–771. doi:10.1080/08927021003752838

Trumpower, B. L. (1981). New Concepts on the Role of Ubiquinone in the Mitochondrial Respiratory Chain. *J. Bioenerg. Biomembr* 13, 1–24. doi:10.1007/bf00744743

Ulrich, E. L., Girvin, M. E., Cramer, W. A., and Markley, J. L. (1985). Location and Mobility of Ubiquinones of Different Chain Lengths in Artificial Membrane Vesicles. *Biochemistry* 24, 2501–2508. doi:10.1021/bi00331a016

Van Cleave, C., Koehn, J. T., Pereira, C. S., Haase, A. A., Peters, B. J., Croslow, S. W., et al. (2021). Interactions of Truncated Menaquinones in Lipid Monolayers and Bilayers. *Int. J. Mol. Sci.* 22, 1–22. doi:10.3390/ijms22189755

Van Cleave, C., Murakami, H. A., Samart, N., Koehn, J. T., Maldonado, P., Kreckel, H. D., et al. (2020). Location of Menaquinone and Menaquinol Headgroups in Model Membranes. *Can. J. Chem.* 98, 307–317. doi:10.1139/cjc-2020-0024

Van Horn, W. D., Ogilvie, M. E., and Flynn, P. F. (2008). Use of Reverse Micelles in Membrane Protein Structural Biology. *J. Biomol. NMR.* 40, 203–211. doi:10.1007/s10858-008-9227-5

Woodward, R. B., and Bloch, K. (1953). The Cyclization of Squalene in Cholesterol Synthesis. *J. Am. Chem. Soc.* 75, 2023–2024. doi:10.1021/ja01104a535

Zahn, T. J., Eilers, M., Guo, Z., Ksebati, M. B., Simon, M., Scholten, J. D., et al. (2000). Evaluation of Isoprenoid Conformation in Solution and in the Active Site of Protein-Farnesyl Transferase Using Carbon-13 Labeling in Conjunction with Solution- and Solid-State NMR. *J. Am. Chem. Soc.* 122, 7153–7164. doi:10.1021/ja000860f

Conflict of Interest: The authors declare that the research was conducted in the absence of any commercial or financial relationships that could be construed as a potential conflict of interest.

Publisher's Note: All claims expressed in this article are solely those of the authors and do not necessarily represent those of their affiliated organizations, or those of the publisher, the editors and the reviewers. Any product that may be evaluated in this article, or claim that may be made by its manufacturer, is not guaranteed or endorsed by the publisher.

Appendix XII: Permissions for manuscripts and figures

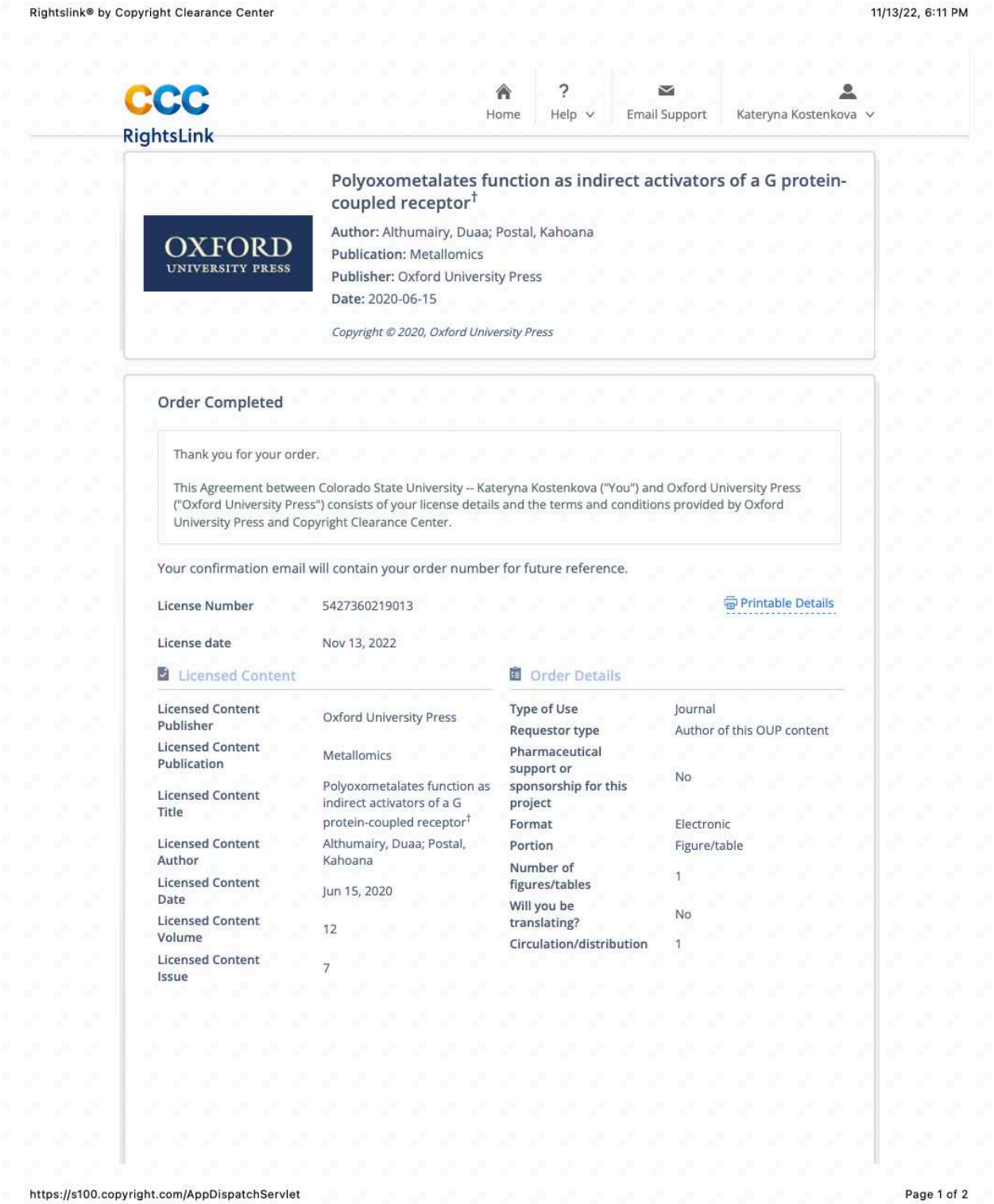

Rightslink® by Copyright Clearance Center 11/13/22, 6:11 PM

RightsLink

Home | Help | Email Support | Kateryna Kostenkova

OXFORD UNIVERSITY PRESS

Polyoxometalates function as indirect activators of a G protein-coupled receptor†

Author: Althumairy, Duaa; Postal, Kahoana
Publication: Metallomics
Publisher: Oxford University Press
Date: 2020-06-15

Copyright © 2020, Oxford University Press

Order Completed

Thank you for your order.

This Agreement between Colorado State University -- Kateryna Kostenkova ("You") and Oxford University Press ("Oxford University Press") consists of your license details and the terms and conditions provided by Oxford University Press and Copyright Clearance Center.

Your confirmation email will contain your order number for future reference.

Printable Details

License Number	5427360219013
License date	Nov 13, 2022

Licensed Content

Licensed Content Publisher	Oxford University Press
Licensed Content Publication	Metallomics
Licensed Content Title	Polyoxometalates function as indirect activators of a G protein-coupled receptor†
Licensed Content Author	Althumairy, Duaa; Postal, Kahoana
Licensed Content Date	Jun 15, 2020
Licensed Content Volume	12
Licensed Content Issue	7

Order Details

Type of Use	Journal
Requestor type	Author of this OUP content
Pharmaceutical support or sponsorship for this project	No
Format	Electronic
Portion	Figure/table
Number of figures/tables	1
Will you be translating?	No
Circulation/distribution	1

https://s100.copyright.com/AppDispatchServlet Page 1 of 2

About Your Work

Title of new article	Polyoxidovanadates V9Mo and V9Pt interact with CHO cell plasma membrane lipids causing aggregation and activation of a G protein-coupled receptor
Lead author	Kateryna Kostenkova
Title of targeted journal	Frontiers in Chemistry
Publisher	Frontiers
Expected publication date	Jan 2023

Additional Data

Portions	Figure 10

Requestor Location

Requestor Location	Colorado State University Chemistry 1301 Center Ave Fort Collins, CO 80523 United States Attn: Colorado State University

Tax Details

Publisher Tax ID	GB125506730

$ Price

Total	0.00 USD

Total: 0.00 USD

CLOSE WINDOW ORDER MORE

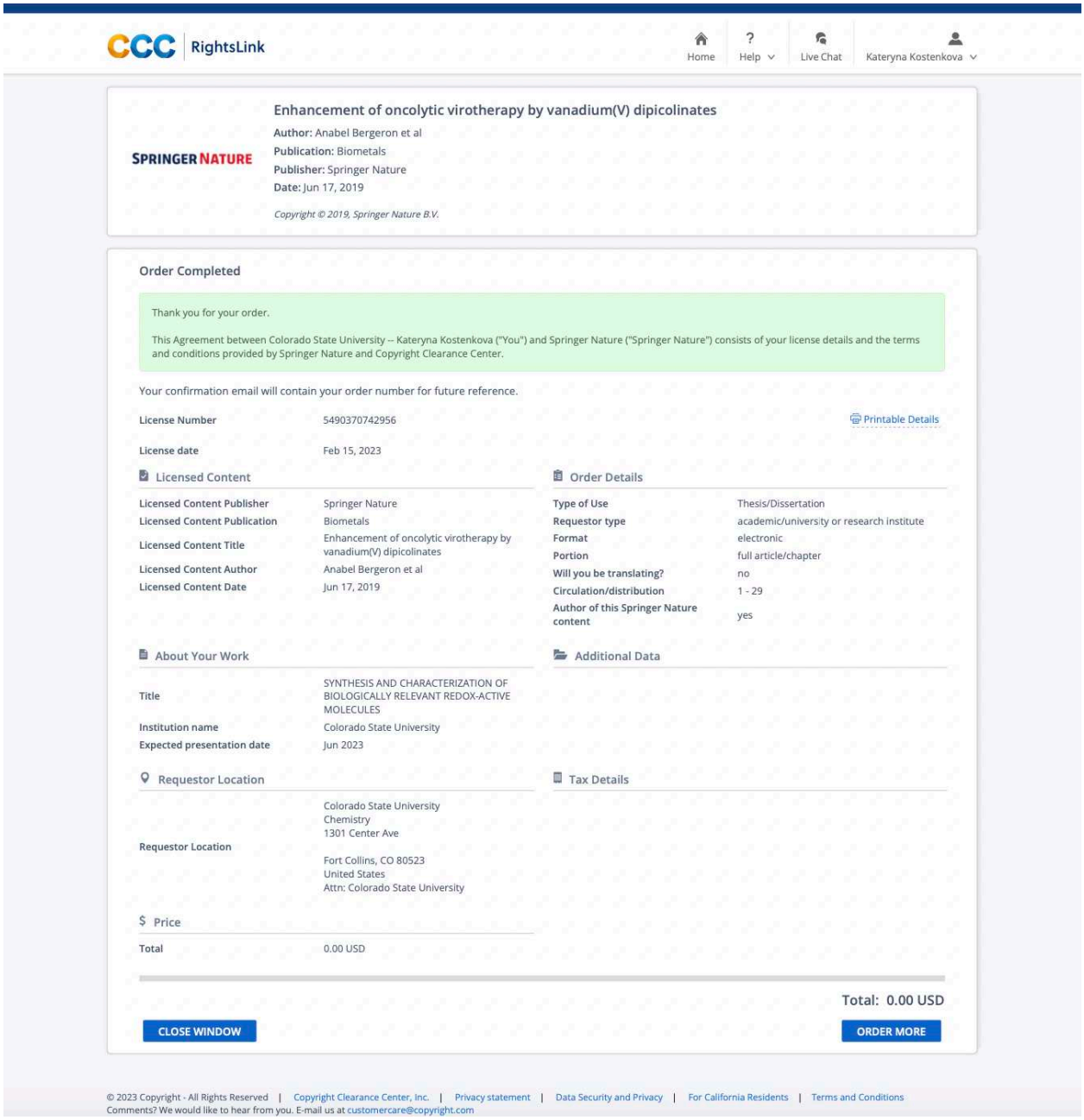
CCC RightsLink
Home
Help
Live Chat
Kateryna Kostenkova
SPRINGER NATURE
Enhancement of oncolytic virotherapy by vanadium(V) dipicolinates
Author: Anabel Bergeron et al
Publication: Biometals
Publisher: Springer Nature
Date: Jun 17, 2019
Copyright © 2019, Springer Nature B.V.
Order Completed
Thank you for your order.
This Agreement between Colorado State University -- Kateryna Kostenkova ("You") and Springer Nature ("Springer Nature") consists of your license details and the terms and conditions provided by Springer Nature and Copyright Clearance Center.
Your confirmation email will contain your order number for future reference.
License Number 5490370742956
Printable Details
License date Feb 15, 2023
Licensed Content
Licensed Content Publisher Springer Nature
Licensed Content Publication Biometals
Licensed Content Title Enhancement of oncolytic virotherapy by vanadium(V) dipicolinates
Licensed Content Author Anabel Bergeron et al
Licensed Content Date Jun 17, 2019
Order Details
Type of Use Thesis/Dissertation
Requestor type academic/university or research institute
Format electronic
Portion full article/chapter
Will you be translating? no
Circulation/distribution 1 - 29
Author of this Springer Nature content yes
About Your Work
Title SYNTHESIS AND CHARACTERIZATION OF BIOLOGICALLY RELEVANT REDOX-ACTIVE MOLECULES
Institution name Colorado State University
Expected presentation date Jun 2023
Additional Data
Requestor Location
Requestor Location Colorado State University
Chemistry
1301 Center Ave
Fort Collins, CO 80523
United States
Attn: Colorado State University
Tax Details
Price
Total 0.00 USD
Total: 0.00 USD
CLOSE WINDOW
ORDER MORE
© 2023 Copyright - All Rights Reserved | Copyright Clearance Center, Inc. | Privacy statement | Data Security and Privacy | For California Residents | Terms and Conditions
Comments? We would like to hear from you. E-mail us at customercare@copyright.com

Convergent Protein Phosphatase Inhibitor Design for PTP1B and TCPTP: Exchangeable Vanadium Coordination Complexes on Graphene Quantum Dots
Author: Xiaoda Yang, Debbie C. Crans, Bowen Zhang, et al
Publication: Advanced Functional Materials
Publisher: John Wiley and Sons
Date: Oct 27, 2021

Order Completed

Thank you for your order.

This Agreement between Colorado State University -- Kateryna Kostenkova ("You") and John Wiley and Sons ("John Wiley and Sons") consists of your license details and the terms and conditions provided by John Wiley and Sons and Copyright Clearance Center.

Your confirmation email will contain your order number for future reference.

Printable Details

License Number	5572580158407
License date	Jun 19, 2023

Licensed Content

Licensed Content Publisher	John Wiley and Sons
Licensed Content Publication	Advanced Functional Materials
Licensed Content Title	Convergent Protein Phosphatase Inhibitor Design for PTP1B and TCPTP: Exchangeable Vanadium Coordination Complexes on Graphene Quantum Dots
Licensed Content Author	Xiaoda Yang, Debbie C. Crans, Bowen Zhang, et al
Licensed Content Date	Oct 27, 2021
Licensed Content Volume	32
Licensed Content Issue	5
Licensed Content Pages	14

Order Details

Type of use	Dissertation/Thesis
Requestor type	University/Academic
Format	Electronic
Portion	Figure/table
Number of figures/tables	1
Will you be translating?	No

About Your Work

Title	SYNTHESIS AND CHARACTERIZATION OF BIOLOGICALLY RELEVANT REDOX-ACTIVE MOLECULES
Institution name	Colorado State University
Expected presentation date	Jun 2023

Additional Data

Portions	Figure 1

Requestor Location

Requestor Location	Colorado State University Chemistry 1301 Center Ave Fort Collins, CO 80523 United States Attn: Colorado State University

Tax Details

Publisher Tax ID	EU826007151

Price

Total	0.00 USD

List of Abbreviations

4TB	4-*tert*-butylcatechol
7H9	The liquid growth medium used for Mycobacteria cultures
786-0	Human renal cell carcinoma
AOT	Sodium aerosol-OT (sodium salt of bis(2-ethylhexyl)sulfosuccinate)
Aq.	Aqueous
ATP	Adenosine triphosphate
a.u.	Arbitrary units
BEOV	Bis-ethylmaltolatooxovanadium(IV)
BMOV	Bis-maltolatooxovanadium(IV)
Cat	Catechol
cAMP	Cyclic adenosine monophosphate
Cl-HSHED	N-(5-chlorosalicylideneaminato)-N'-(2- hydroxyethyl)ethane-1,2-diamine
Cl-SALIEP	N-(5-chlorosalicydeneaminato)-2-(2-aminoethylpyridine)
CV	Cyclic voltammetry
d	Doublet
dd	Doublet of doublets
DDI	Double deionized
DMEM	Dulbecco's Modified Eagle Medium
DMK	Demethylmenaquinone
DMSO	Dimethyl sulfoxide
DPPH	2,2-Diphenyl-1-picrylhydrazyl
dq	Doublet of quartets
DSS	3-trimethylsilyl-1-propanesulfonic acid sodium salt
DTB	Di-*tert*-butylcatechol
DTT	Dithiothreitol

EPR	Electron paramagnetic resonance
Equiv.	Equivalent
ETC	Electron transport chain
EtOAc	Ethyl acetate
EtOH	Ethanol
ESI	Electrospray ionization
G	Gauss
GBM	Glioblastoma multiforme
GHz	Gigahertz
GSH	Glutathione
Fc	Ferrocene
FTIR	Fourier-transform infrared spectroscopy
H_2dipic	Dipicolinic acid, 2,6-pyridinecicarboxylic acid
H_2dipic-OH	4-hydroxydipicolinic acid
H_2dipic-Cl	4-chlorodipicolinic acid
HFF-1	Human skin fibroblasts
HPI	Hours post infection
HPLC	High-performance liquid chromatography
HRMS	High-resolution mass spectrometry
HSHED	N-(salicylideneaminato)-N'-(2- hydroxyethyl)ethane-1,2-diamine
HSQC	Heteronuclear single quantum correlation
GFP	Green Fluorescent Protein
K	Kelvin
LHR	Luteinizing hormone receptor
LNPs	Lipid nanoparticles
m	Multiplet

MeCN	Acetonitrile
MHz	Megahertz
MK	Menaquinone
MOI	Multiplicity of Infection
ms	Milliseconds
NMR	Nuclear magnetic resonance
NOESY	Nuclear Overhauser Effect spectroscopy
OV	Oncolytic Virus
PDT	Photodynamic therapy
POM	Polyoxometalate
POV	Polyoxovanadate
ppm	Parts per million
PV	Vanadophosphate complex, $HVPO_7^{3-}$
RMs	Reverse micelles
ROS	Reactive oxygen species
r. t.	Room temperature
Q	Quinone
s	Singlet
SALIEP	N-(salicydeneaminato)-2-(2-aminoethylpyridine)
t	Triplet
TB	Tuberculosis
TLC	Thin-layer chromatography
tq	Triplet of quartets
T-VEC	Talimogene laherparepvec
UQ	Ubiquinone
UV-Vis	Ultraviolet–visible spectroscopy

V	Volts
V_1	Vanadate monomer, VO_4^{3-}
V_2	Vanadate dimer, $H_2V_2O_7^{2-}$
V_4	Vanadate tetramer, $V_4O_{12}^{4-}$
Vcit–	Vanadium(V) citrate complex
$[VO_2dipic]^-$	Dioxovanadium(V) dipicolinate
$[VO_2dipic\text{-}OH]^-$	Dioxovanadium(V) 4-hydroxydipicolinate
$[VO_2dipic\text{-}Cl]^-$	Dioxovanadium(V) 4-chlorodipicolinate
$VOSO_4$	Vanadyl sulfate
VSV	Vesicular Stomatitis Virus